

AD-A148 088 THE SHOCK AND VIBRATION BULLETIN PART 4 STRUCTURAL DYNAMICS SYSTEMS IDENT. (U) NAVAL RESEARCH LAB

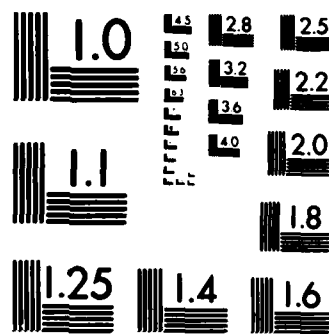
1/3

UNCLASSIFIED BULL-47-PT-4 SEP 77 F/G 20/11

PG 20/11

F/G 20/11

NL



MICROCOPY RESOLUTION TEST CHART  
NATIONAL BUREAU OF STANDARDS-1963-A

1

Bulletin 47  
(Part 4 of 4 Parts)

# THE SHOCK AND VIBRATION BULLETIN

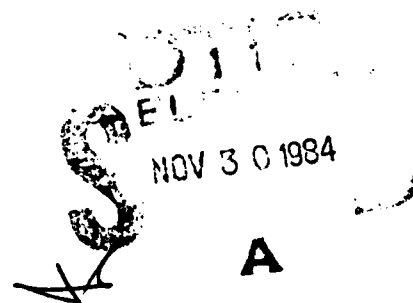
Part 4  
Structural Dynamics, Systems Identification,  
Computer Applications

SEPTEMBER 1977

A Publication of  
THE SHOCK AND VIBRATION  
INFORMATION CENTER  
Naval Research Laboratory, Washington, D.C.



Office of  
The Director of Defense  
Research and Engineering



Approved for public release; distribution unlimited.

84 11 26 18

AD-A148 088

DTIC FILE COPY

## **SYMPOSIUM MANAGEMENT**

### **THE SHOCK AND VIBRATION INFORMATION CENTER**

**Henry C. Pusey, Director**

**Rudolph H. Volin**

**J. Gordan Showalter**

**Barbara Szymanski**

**Carol Healey**

#### ***Bulletin Production***

**Graphic Arts Branch, Technical Information Division,  
Naval Research Laboratory**



**Bulletin 47**  
**(Part 4 of 4 Parts)**

# **THE SHOCK AND VIBRATION BULLETIN**

**SEPTEMBER 1977**

**A Publication of  
THE SHOCK AND VIBRATION  
INFORMATION CENTER  
Naval Research Laboratory, Washington, D.C.**

The 47th Symposium on Shock and Vibration was held at the Albuquerque Inn and Convention Center, Albuquerque, New Mexico on October 19-21, 1976. The Defense Nuclear Agency, Washington, D.C., the Field Command Defense Nuclear Agency, and the Air Force Weapons Laboratory, Kirtland Air Force Base, New Mexico were the hosts.

**Office of  
The Director of Defense  
Research and Engineering**

# CONTENTS

## PAPERS APPEARING IN PART 4

### Structural Dynamics

PREDICTION OF GAS DYNAMIC LASER MOUNTING FORCES USING ADMITTANCE TESTING TECHNIQUES, .....	1
W.R. Davis, Jr., Air Force Weapons Laboratory, Kirtland AFB, NM and D.L. Brown, Air Force Flight Dynamics Laboratory, Wright-Patterson AFB, OH	
INFLUENCE OF FLUID ON THE DYNAMIC PLASTIC RESPONSE OF A PIPE, ...	9
M.G. Srinivasan, R.A. Valentin, Argonne National Laboratory, Argonne, IL and D. Krajcinovic, University of Illinois at Chicago Circle, Chicago, IL	
A THEORETICAL ANALYSIS OF THE DYNAMIC RESPONSE OF CONSTRUCTION CABLEWAY SYSTEMS, .....	21
K.C. Tu, Stone and Webster Engineering Corporation, Denver, CO and R.S. Ayre, University of Colorado, Boulder, CO	
EMPIRICAL INVESTIGATION OF WATER-SHOCK LOADING OF A CONCRETE HALF-SPACE, .....	33
C.R. Welch and L.K. Davis, U.S. Army Engineer Waterways Experiment Station, Corps of Engineers, Vicksburg, MS	
THE EFFECT OF EARTH COVER ON THE DYNAMIC RESPONSE OF HARDENED REINFORCED CONCRETE STRUCTURES, .....	45
R.D. Crowson, and S.A. Kiger, U.S. Army Engineer Waterways Experiment Station, Vicksburg, MS	
DYNAMIC RESPONSES OF A SOIL COVERED CONCRETE ARCH TO IMPACT AND BLAST LOADINGS, .....	67
P.T. Nash, US Air Force Armament Laboratory, Eglin AFB, FL and J.H. Smith, W.P. Vann, Texas Tech University, Lubbock, TX	
INSTRUCTURE SHOCK ENVIRONMENT OF BURIED STRUCTURES SUB- JECTED TO BLAST INDUCED GROUND SHOCK, .....	75
S.A. Kiger, U.S. Army Engineer Waterways Experiment Station, Vicksburg, MS	
CRACK PATTERN OF AN UNDERGROUND, CYLINDRICAL, REINFORCED- CONCRETE STRUCTURE UNDER AN AXIAL BLAST LOADING, .....	89
L.C. Lee and M.S. Agbabian, Agbabian Associates, El Segundo, CA	
FAILURE OF ALUMINUM CYLINDRICAL SHELLS SUBJECTED TO TRANSVERSE BLAST LOADINGS, .....	111
W.S. Strickland, USAF Armament Laboratory, Eglin AFB, FL, J.E. Milton, C.A. Ross, University of Florida Graduate Engineering Center, Eglin, AFB, FL, and L.J. Mente, Kaman Avidyne, Burlington, MA	

EXTENDED TRANSFER MATRIX METHOD FOR FREE VIBRATION OF SHELLS OF REVOLUTION	121
S. Sankar, Concordia University, Montreal, Canada	

A PRACTICAL SCHEME FOR INCLUDING SHEAR WALL (OR FLOOR) STIFFNESS IN FRAME ANALYSIS	135
R.M. Mains, Washington University, St. Louis, MO	

RAIL OVERTURNING	149
F. Arbabi, Michigan Technological University, Houghton, MI	

#### Systems Identification

APPLICATION OF MODERN PARAMETER ESTIMATION METHODS TO VIBRATING STRUCTURES	155
W.R. Wells, Wright State University, Dayton, OH	

ANALYSIS OF VIBRATION RECORDS BY DATA DEPENDENT SYSTEMS	161
S.M. Pandit, Michigan Technological University, Houghton, MI	

A METHOD OF SYSTEM IDENTIFICATION WITH AN EXPERIMENTAL INVESTIGATION	175
P.H. Merritt, Air Force Weapons Laboratory, Kirtland AFB, NM and W.E. Baker, University of New Mexico, Albuquerque, NM	

A METHOD FOR THE DIRECT IDENTIFICATION OF VIBRATION PARAMETERS FROM THE FREE RESPONSE	183
S.R. Ibrahim, Old Dominion University, Norfolk, VA and E.C. Mikulcik, The University of Calgary, Calgary, Alberta, Canada	

LABORATORY IDENTIFICATION OF THE PATRIOT LAUNCHER STRUCTURE	199
T.R. Meyer and C.S. O'Hearne, Martin Marietta Aerospace, Orlando, FL	

#### Computer Applications

DIGITAL SIMULATION OF FLEXIBLE AIRCRAFT RESPONSE TO SYMMETRICAL AND ASYMMETRICAL RUNWAY ROUGHNESS	207
T.G. Gerardi, Air Force Flight Dynamics Laboratory, Wright-Patterson AFB, OH	

CHIANTI - COMPUTER PROGRAMS FOR PARAMETRIC VARIATIONS IN DYNAMIC SUBSTRUCTURE ANALYSIS	217
A. Berman and N. Giansante, Kaman Aerospace Corporation, Bloomfield, CT	

FREQUENCY RESPONSE ANALYSIS OF COMPLEX STRUCTURES	227
H.R. Radwan and P. Shunmugavel, Sargent and Lundy, Chicago, IL	

COMPUTER AIDED DERIVATION OF THE GOVERNING DYNAMICAL EQUATIONS FOR A HIGH SPEED GROUND VEHICLE	234
J. Patten and N. Isada, State University of New York	

**PAPERS APPEARING IN PART 1**

**Keynote Address**

**IMPACTS OF SHOCK AND VIBRATION CONSIDERATIONS ON WEAPON DEVELOPMENT**

Dr. Hua Lin, Assistant Director (Offensive Systems) Office Director of Defense Research and Engineering, Washington, DC

**Invited Paper**

**NUCLEAR HARDENING IN A MISSILE DEFENSE SYSTEM**

Noah J. Hurst, Ballistic Missile Defense Systems Command, Huntsville, AL

**Panel Session**

**DYNAMICS EFFECTS ON RELIABILITY**

**Shock Analysis**

**SCALING OF STRONG SHOCK HUGONIOTS**

W.E. Baker, Southwest Research Institute, San Antonio, TX

**SHOCK SPECTRA AND RESPONSES BY POCKET CALCULATOR**

C.T. Morrow, Consultant, Dallas, TX

**STUDIES OF THE TERRADYNAMICS OF A PROJECTILE  
PENETRATING SAND**

L.E. Malvern, R.L. Sierakowski, University of Florida, Gainesville, FL and  
J.A. Collins, DLYV/Air Force Armament Laboratory, Eglin AFB, FL

**HARDENED SYSTEM VULNERABILITY ANALYSIS**

J.D. Collins, J.H. Wiggins Company, Redondo Beach, CA

**Shock Testing**

**LABORATORY SIMULATION OF SEQUENTIAL SETBACK AND AERO-DYNAMIC DRAG EXPERIENCED BY ARMY ORDNANCE PROJECTILES —  
A DEVICE, THEORY AND DATA**

I. Pollin, Harry Diamond Laboratories, Adelphi, MD

**BARREL-TAMPED, EXPLOSIVELY PROPELLED ROTATING  
PLASTIC PLATES**

F.H. Mathews, B.W. Duggin, Sandia Laboratories, Albuquerque, NM

**SHOCK WAVEFORM TESTING ON AN ELECTRODYNAMIC VIBRATOR**  
W.E. Frain, Applied Physics Laboratory, The Johns Hopkins University,  
Laurel, MD

**SEISMIC SHOCK WAVEFORM REPRODUCTION AND SHOCK SPECTRA  
SYNTHESIS ON HYDRAULIC ACTUATOR**  
R.S. Nichols, White Sands Missile Range, NM

Isolation and Damping

**EXPERIENCES ON SHOCK ISOLATION OF EQUIPMENT IN THE  
SAFEGUARD SYSTEM**  
M.A. Boyd and C.C. Huang, U.S. Army Engineer Division, Huntsville,  
Huntsville, AL

**ON THE DETERMINATION AND CHARACTERISTICS OF THE CENTER  
OF ELASTICITY**  
G.L. Fox, Barry Division, Barry Wright Corporation, Watertown, MA

**DESIGN OF ELASTOMERIC COMPONENTS BY USING THE FINITE  
ELEMENT TECHNIQUE**  
R.H. Finney and B.P. Gupta, Lord Kinematics, Erie, PA

**CHARACTERIZATION OF BULK CUSHION MATERIALS UNDER IMPACT  
LOADS USING VISCOELASTIC THEORY**  
T.L. Cost, J.D. Dagen, The University of Alabama, Tuscaloosa, AL and  
J.E. Jackson, Tennessee Valley Authority, Knoxville, TN

**IMPACT RESPONSE MODELING OF BULK CUSHIONING SYSTEMS ON A  
PROGRAMMABLE DESK-TOP CALCULATOR**  
D.M. McDaniel, U.S. Army Missile Command, Redstone Arsenal, AL and  
R.M. Wyskida, J.D. Johannes, The University of Alabama in Huntsville,  
Huntsville, AL

**PAPERS APPEARING IN PART 2**

Vibration Analysis

**SOME ASPECTS OF VIBRATION CONTROL SUPPORT DESIGN**  
P. Bezler and J.R. Curreri, Brookhaven National Laboratory, Upton, NY

**RESPONSE OF A HARDENING SPRING OSCILLATOR TO  
RANDOM EXCITATION**  
J.T. Kayanickupurathu, Research Fellow and J.R. Curreri, Polytechnic  
Institute of N.Y., Brooklyn, NY

**NON-LINEAR DYNAMIC RESPONSE OF A MULTI-MASS SYSTEM  
WITH GAPS**  
B. Koplik, M. Reich, Brookhaven National Laboratory, Upton, NY

**AN IMPROVED DERIVATION OF THE DUNKERLEY-MIKHLIN FORMULA**  
J.E. Brock, Naval Postgraduate School, Monterey, CA

**RECENT ADVANCES IN FAILURE ANALYSIS BY STATISTICAL  
TECHNIQUES (FAST)**  
W.H. Rowan, TRW Defense and Space Systems Group, Redondo Beach, CA

**ON THE MEAN LIFE EVALUATION OF A MATERIAL WITH IDEAL ELASTO-  
PLASTIC BEHAVIOUR, SUBJECTED TO A STOCHASTIC LOADING  
PROGRAMME WITH A FINITE NUMBER OF STRAIN LEVELS**  
G.A. Philippin, T.H. Topper and H.H.E. Leipholz, University of Waterloo,  
Waterloo, Ontario, Canada

**FATIGUE ANALYSIS OF MULTI-DEGREE-OF-FREEDOM SYSTEMS UNDER  
RANDOM VIBRATION**  
R.G. Lambert, General Electric Company, Utica, NY

**A MATHEMATICAL MODEL FOR THE STRESS AND VIBRATIONAL  
ANALYSIS OF THE HUMAN MITRAL VALVE**  
J. Mazumdar and T.C. Hearn, The University of Adelaide, South Australia

**THE DECREMENT IN VISUAL ACUITY RELATED TO VIBRATION OF SHAKER,  
SEAT, AND OBSERVER'S HEAD**  
O.F. Hackett, David W. Taylor Naval Ship Research and Development Center,  
Bethesda, MD, W.G. Lewis, Naval Electronics Laboratory Center, San Diego, CA,  
R. Langland and T. Harder, Pacific Missile Test Center, Point Mugu, CA

**FREE VIBRATIONS OF UNSYMMETRICALLY LAMINATED CANTILEVERED  
COMPOSITE PANELS**  
E.A. Thornton, Old Dominion University, Norfolk, VA

**FUNDAMENTAL FREQUENCIES OF ORTHOTROPIC PLATES WITH VARIOUS  
PLANFORMS AND EDGE CONDITIONS**  
C.W. Bert, The University of Oklahoma, Norman, OK

**DYNAMIC RESPONSE OF LAMINATED COMPOSITE PLATES UNDER  
RESIDUAL THERMAL STRESSES**  
C.T. Sun, Iowa State University, Ames, IA

**VIBRATION OF COMPOSITE PLATES OF ARBITRARY SHAPE BY THE  
METHOD OF CONSTANT DEFLECTION LINES**  
S. Dharmarajan and F.H. Chou, San Diego State University, San Diego, CA

**COUPLED VIBRATIONS OF TURBOMACHINE BLADES**  
J.S. Rao, Indian Institute of Technology, New Delhi, India

**ACCELERATION THROUGH RESONANCE OF MULTI-DEGREE OF  
FREEDOM SYSTEMS**  
F.H. Wolff, A.J. Molnar and A.C. Hagg, Westinghouse Electric Corporation,  
Pittsburgh, PA

## PAPERS APPEARING IN PART 3

### Vibration Testing

#### **COST EFFECTIVELY EXCITING VIBRATION FAILURE MODES FOR LONG-TIME RELIABILITY DEMONSTRATIONS**

W. Tustin, Tustin Institute of Technology, Inc., Santa Barbara, CA

#### **SELF-TUNING RESONANT FIXTURES**

R.T. Fandrich, Harris Corporation, Melbourne, FL

#### **ANALYSIS OF SINUSOIDAL AND RANDOM VIBRATION ENERGIES**

J.N. Tait, Naval Air Development Center, Warminster, PA

#### **EVALUATION OF AN ADAPTIVE FILTER AS A DIGITAL TRACKING FILTER**

D.O. Smallwood and D.L. Gregory, Sandia Laboratories, Albuquerque, NM

#### **TOTAL MISSION ENVIRONMENTAL SIMULATION THROUGH DIGITALLY CONTROLLED ELECTROMAGNETIC VIBRATION**

D. Hinckley, F. Foley, Boeing Aerospace Company, Seattle, WA and

P. Moseley, W. Ross, Hewlett-Packard Company, Santa Clara, CA

#### **A COMPARISON BETWEEN SINUSOIDAL SWEEP AND BROADBAND DIGITAL TECHNIQUES FOR RESONANCE SEARCH AND TRANSMISSIBILITY MEASUREMENTS**

P. Moseley, Hewlett-Packard Company, Santa Clara, CA

#### **MODAL INVESTIGATION OF LIGHTWEIGHT AIRCRAFT STRUCTURES USING DIGITAL TECHNIQUES**

R.W. Gordon and H.F. Wolfe, Air Force Flight Dynamics Laboratory,  
Wright-Patterson AFB, OH

#### **DIGITAL CONTROL SYSTEM FOR A MULTIPLE-ACTUATOR SHAKER**

D.K. Fisher and M.R. Posehn, Lawrence Livermore Laboratory, Livermore, CA

### Instrumentation and Data Analysis

#### **MEASUREMENT OF ANGULAR VIBRATION USING CONVENTIONAL ACCELEROMETERS**

P.W. Whaley and M.W. Obal, Air Force Flight Dynamics Laboratory,  
Wright-Patterson AFB, OH

#### **THE USE OF A LOW POWER LASER AND PHOTODIODE FOR DISPLACEMENT DATA**

J.E. Cawthorn, Martin Marietta Aerospace, Orlando, FL

#### **GROUT/SOIL INTERACTION AND GROUND-MOTION MEASUREMENT**

M.B. Balachandra and J.A. Malthan, Agbabian Associates, El Segundo, CA

**COMPUTER-BASED TRANSPORTABLE DATA-ACQUISITION AND  
CONTROL SYSTEM**

D.K. Fisher, M.R. Posehn, F.L. Sindelar and H.H. Bell, Lawrence Livermore  
Laboratory, Livermore, CA

**Loads and Environments**

**VIBRATION INVESTIGATION OF A LARGE TRANSPORT HELICOPTER**

W.J. Snyder, J.L. Cross and M.B. Schoultz, NASA Langley Research Center,  
Hampton, VA

**AEROACOUSTIC ENVIRONMENT OF A STORE IN AN AIRCRAFT  
WEAPONS BAY**

L.L. Shaw, Air Force Flight Dynamics Laboratory, Wright-Patterson AFB, OH

**AN INTERIM REPORT ON SHUTTLE ORBITER VIBROACOUSTICS**

Vibration and Acoustics Unit, Space Division, Rockwell International  
Corporation, Downey, CA

**PAPERS APPEARING IN SUPPLEMENT**

**STABILITY OF NEW LIGHTWEIGHT 203MM (EIGHT INCH)  
HOWITZER IN SOILS**

H.M. Cole, Naval Surface Weapons Center, White Oak, Silver Spring, MD  
and J.C.S. Yang, University of Maryland, College Park, MD

**APPLICATION OF LIGHT-INITIATED EXPLOSIVE FOR SIMULATING  
X-RAY BLOWOFF IMPULSE EFFECTS ON A FULL SCALE  
REENTRY VEHICLE**

R.A. Benham, F.H. Mathews and P.B. Higgins, Sandia Laboratories,  
Albuquerque, NM



# STRUCTURAL DYNAMICS

## PREDICTION OF GAS DYNAMIC LASER MOUNTING FORCES USING ADMITTANCE TESTING TECHNIQUES

William R. Davis, Jr.\*  
Air Force Weapons Laboratory  
Kirtland AFB, New Mexico

and

Dansen L. Brown  
Air Force Flight Dynamics Laboratory  
Wright-Patterson AFB, Ohio

Presented are an admittance formulation and test technique for predicting the mounting point forces of a large airborne gas dynamic laser from ground measurements. Laser forces were measured during ground test stand firing, and a laser admittance matrix was determined from a shaker test on a suspended laser. Expressing the laser dynamics independently of its mounting configuration in terms of a "free response" vector, these results were combined with an admittance matrix for the aircraft mounting points from a finite element model to make the force prediction. All data processing was accomplished on a minicomputer system. The technique is generally applicable to the problem of determining the mounting point forces of a vibration source in one mounting configuration from measurements in a different configuration.

### INTRODUCTION

Because of their high speed gas flows and combustion processes, large gas dynamic lasers are a significant source of vibration which greatly affect the structures to which they are mounted. For airborne lasers the vibration environments must be characterized well before the devices are integrated with aircraft since the forces they generate can affect the structural integrity of the aircraft and the performance of sensitive optical systems.

One can measure the forces produced by a laser when it is fired in a ground test stand, but the dynamic characteristics of the test stand can be quite different than those of the aircraft and so can the resulting mounting forces. This paper presents a new mathematical approach and test technique for predicting the forces generated by a laser at its aircraft mounting points from admittance representations of the laser and aircraft and from force and acceleration measurements made during ground firing of the laser. Experimental results from the application of the technique to a large gas dynamic laser at the Air Force Weapons Laboratory are included.

Several researchers [1-6] have used admittance or impedance techniques to solve for interface vibration environments or to predict

the dynamic responses of composite systems from tests on subsystems. In particular, Karra and Vargas [1] conclude that the admittance formulation is more suited to these problems than transmission matrix or impedance methods, and they emphasize the necessity for accurate measurement techniques since the dynamic range of admittance data typically varies over several orders of magnitude.

Here we formulate the dynamics of the vibration source, i.e. the laser, in terms of a mounting point admittance matrix for an unsupported laser and a "free response" vector determined from forces and accelerations measured during ground firing of the laser. Together this information completely characterizes the dynamics of the laser independent of its mounting configuration. The airborne mounting forces are predicted by combining these results with an admittance matrix for the mounting points on the aircraft fuselage. Special force transducers were developed to measure the directional components of the ground mounting forces, and several techniques were used to insure adequate dynamic range and accuracy in the recording and analysis of experimental data. By working exclusively with random and transient analyses, advantage was taken of the digital processing and fast Fourier transform programs available with mini-computers; and considerable experimental time was saved by using random test

\*Assigned to the Air Force Flight Dynamics Laboratory, co-located at the Air Force Weapons Laboratory.

techniques rather than sine sweeps. The technique is generally applicable to the prediction of mounting point forces generated by a vibration source in one mounting configuration from measurements made in a different mounting configuration.

#### THEORETICAL FORMULATION

We begin by writing a frequency response equation for the laser mounting points. The laser consists of two identical stages each with three mounting brackets which transmit force but no moments in a total of six degrees of freedom: a forward bracket in the Y and Z directions; an aft bracket in the X, Y, and Z directions; and a drag link (assumed rigid) in the Y direction. The bracket mounting locations are labeled 1, 2, and 3, respectively, as shown schematically in Figure 1. In the following we consider only one of the two stages.

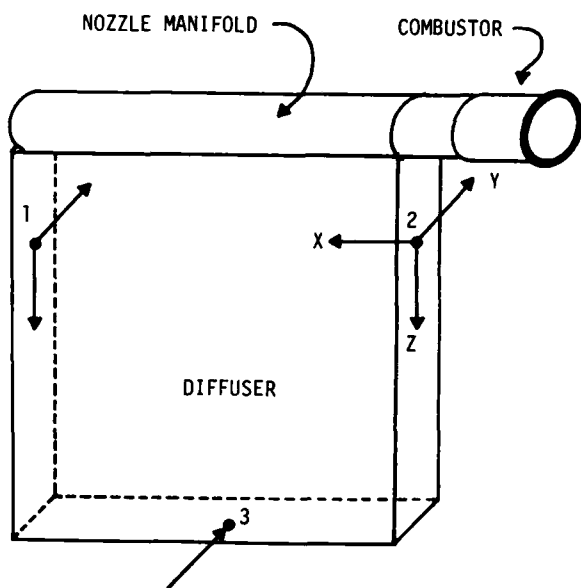


Fig. 1 - Laser Mounting Points

Since the laser produces transient rather than steady state forces, we express the forces on the laser and their corresponding accelerations in the frequency domain by their Fourier transforms  $\bar{F}_i$  and  $\bar{A}_i$ :

$$\bar{F}_1 = \begin{Bmatrix} F_{1y} \\ F_{1z} \end{Bmatrix}; \bar{F}_2 = \begin{Bmatrix} F_{2x} \\ F_{2y} \\ F_{2z} \end{Bmatrix}; \bar{F}_3 = F_{3y} \quad (1)$$

and

$$\bar{A}_1 = \begin{Bmatrix} A_{1y} \\ A_{1z} \end{Bmatrix}; \bar{A}_2 = \begin{Bmatrix} A_{2x} \\ A_{2y} \\ A_{2z} \end{Bmatrix}; \bar{A}_3 = A_{3y} \quad (2)$$

The three mounting points have linear accelerations in nine degrees of freedom even though the forces are zero in three of these dof, but we need only consider accelerations in the same dof in which we have forces.

The transformed accelerations are related to the transformed forces by a frequency response or admittance matrix:

$$\begin{Bmatrix} \bar{A}_1 \\ \bar{A}_2 \\ \bar{A}_3 \end{Bmatrix} = \begin{bmatrix} H_{11} & H_{12} & H_{13} & H_{14} \\ H_{21} & H_{22} & H_{23} & H_{24} \\ H_{31} & H_{32} & H_{33} & H_{34} \end{bmatrix} \begin{Bmatrix} \bar{F}_1 \\ \bar{F}_2 \\ \bar{F}_3 \\ \bar{F}_4 \end{Bmatrix} \quad (3)$$

Here each element,  $H_{ij}$ , of the admittance matrix is itself a matrix. The vector,  $\bar{F}_4$ , and the admittance elements,  $H_{i4}$ , represent all the internally generated forces and moments in the laser and their corresponding transfer admittances. Here we use the term admittance, although inertance might be more correct since all responses are expressed as accelerations for experimental reasons.

Re-writing Eq (3) as the sum of two parts, we have

$$\begin{Bmatrix} \bar{A}_1 \\ \bar{A}_2 \\ \bar{A}_3 \end{Bmatrix} = \begin{bmatrix} H_{11} & H_{12} & H_{13} \\ H_{21} & H_{22} & H_{23} \\ H_{31} & H_{32} & H_{33} \end{bmatrix} \begin{Bmatrix} \bar{F}_1 \\ \bar{F}_2 \\ \bar{F}_3 \end{Bmatrix} + \begin{bmatrix} H_{14} \\ H_{24} \\ H_{34} \end{bmatrix} \bar{F}_4 \quad (4)$$

The first term on the RHS of Eq (4) is the product of the admittance matrix for the laser mounting points and the transformed force vector for these points, and this product is the component of the transformed accelerations induced by the compliance of the structure to which the laser is mounted. The second term is the component of the transformed accelerations which is independent of the mounting structure. If the laser were fired while suspended in space,

the mounting point forces would be zero; and all mounting point response would come from the second term. We call this second product the "transformed free response vector" and rearrange Eq (4) as

$$\begin{Bmatrix} \bar{A}_1 \\ \bar{A}_2 \\ \bar{A}_3 \end{Bmatrix}_{FR} = \begin{Bmatrix} \bar{A}_1 \\ \bar{A}_2 \\ \bar{A}_3 \end{Bmatrix} - \begin{bmatrix} H_{11} & H_{12} & H_{13} \\ H_{21} & H_{22} & H_{23} \\ H_{31} & H_{32} & H_{33} \end{bmatrix} \begin{Bmatrix} \bar{F}_1 \\ \bar{F}_2 \\ \bar{F}_3 \end{Bmatrix} \quad (5)$$

6x1          6x1          6x6          6x1

where subscript FR denotes free response.

The free response vector is the basis for our airborne force prediction, so we must solve Eq (5). The admittance matrix may be determined by softly suspending the laser and exciting the mounting points with known forces as described in the next section. The transformed acceleration and force vectors can be determined from experimental measurement of the mounting point forces and accelerations when the laser is fired in its ground test stand.

Next to determine airborne mounting forces, we must consider the compliance of the aircraft mounting structure. Writing a frequency response equation for the aircraft mounting points, we have

$$\begin{Bmatrix} \bar{A}_1' \\ \bar{A}_2' \\ \bar{A}_3' \end{Bmatrix} = \begin{bmatrix} H_{11}' & H_{12}' & H_{13}' \\ H_{21}' & H_{22}' & H_{23}' \\ H_{31}' & H_{32}' & H_{33}' \end{bmatrix} \begin{Bmatrix} \bar{F}_1' \\ \bar{F}_2' \\ \bar{F}_3' \end{Bmatrix} \quad (6)$$

where primes denote the aircraft. Here we ignore the aircraft internal forces since their effects will be negligible compared to those of the laser. The primed admittance matrix can be determined from a finite element model of the aircraft or by experiment.

When the laser is mounted in the aircraft, we have the following coupling conditions:

$$\begin{Bmatrix} \bar{A}_1 \\ \bar{A}_2 \\ \bar{A}_3 \end{Bmatrix} = \begin{Bmatrix} \bar{A}_1' \\ \bar{A}_2' \\ \bar{A}_3' \end{Bmatrix}, \text{ and } \begin{Bmatrix} \bar{F}_1 \\ \bar{F}_2 \\ \bar{F}_3 \end{Bmatrix} = - \begin{Bmatrix} \bar{F}_1' \\ \bar{F}_2' \\ \bar{F}_3' \end{Bmatrix} \quad (7)$$

So by the first condition we can equate Eqs (4) and (6); and using the second condition, we have

$$\begin{bmatrix} H_{11}' & H_{12}' & H_{13}' \\ H_{21}' & H_{22}' & H_{23}' \\ H_{31}' & H_{32}' & H_{33}' \end{bmatrix} \begin{Bmatrix} \bar{F}_1' \\ \bar{F}_2' \\ \bar{F}_3' \end{Bmatrix} = - \begin{bmatrix} H_{11} & H_{12} & H_{13} \\ H_{21} & H_{22} & H_{23} \\ H_{31} & H_{32} & H_{33} \end{bmatrix} \begin{Bmatrix} \bar{F}_1 \\ \bar{F}_2 \\ \bar{F}_3 \end{Bmatrix} + \begin{Bmatrix} \bar{A}_1 \\ \bar{A}_2 \\ \bar{A}_3 \end{Bmatrix}_{FR} \quad (8)$$

Solving for the transform of the forces acting on the aircraft mounting points,

$$\begin{Bmatrix} \bar{F}_1' \\ \bar{F}_2' \\ \bar{F}_3' \end{Bmatrix} = \left[ \begin{bmatrix} H_{11}' & H_{12}' & H_{13}' \\ H_{21}' & H_{22}' & H_{23}' \\ H_{31}' & H_{32}' & H_{33}' \end{bmatrix} + \begin{bmatrix} H_{11} & H_{12} & H_{13} \\ H_{21} & H_{22} & H_{23} \\ H_{31} & H_{32} & H_{33} \end{bmatrix} \right]^{-1} \begin{Bmatrix} \bar{A}_1 \\ \bar{A}_2 \\ \bar{A}_3 \end{Bmatrix}_{FR} \quad (9)$$

This can be inverse Fourier transformed to produce force time histories which can be applied to the aircraft finite element model to predict laser induced responses at other points on the aircraft.

The scheme presented here can easily be generalized to an arbitrary number of degrees of freedom for application to other hardware.

#### LASER ADMITTANCE DETERMINATION

To determine the admittance matrix in Eq (5), the laser was suspended on elastic cords and excited at each mounting point in turn with a single electrodynamic shaker. Details are shown in Figure 2. The laser was essentially freely suspended above 3 Hz, the natural frequency of the suspension system.

Broadband excitation at 10 to 20 lbf RMS was applied through a force gauge to each of the six dof of interest while the acceleration response was measured in all six dof. The complex admittance elements were calculated by dividing the cross-spectral density of acceleration response and force excitation by the auto-spectral density of the force. Shaker excitation was applied in two ranges, 5-300 Hz and 5-1000 Hz, so transducer amplifier gains could be adjusted to insure adequate dynamic range in both the low and high frequency regions. The final results were combined to produce a continuous admittance function for 5-1000 Hz. The adequacy of the dynamic range of the signal conditioning system was checked during all data gathering runs by comparing spectral analyses of the data with analyses of data recordings under identical conditions but without vibration excitation. This was done using a real time spectral analyzer. As a further check on data quality, coherence functions for force and acceleration were calculated for each admittance element with good results.

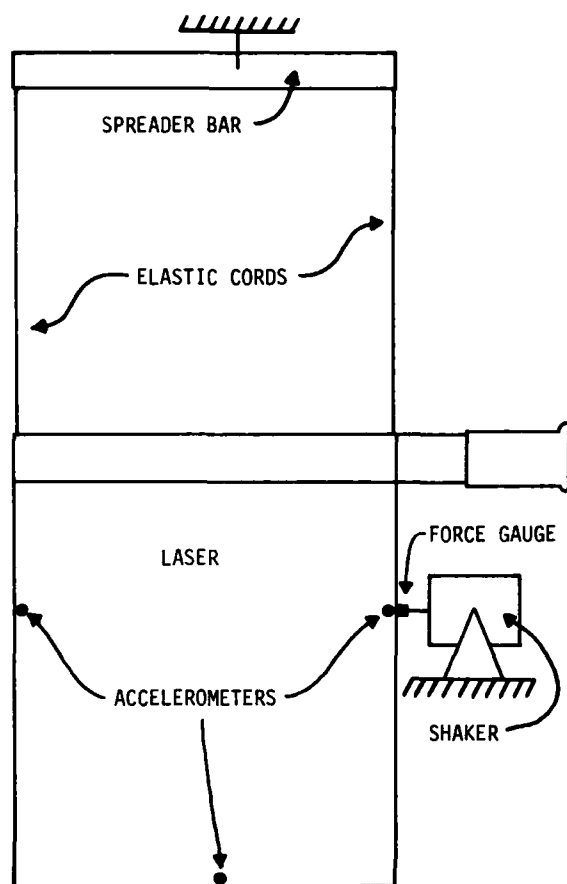


Fig. 2 - Laser Suspended for Shaker Test

Special care was taken to account for relative phase shifts between force and acceleration caused by the transducers, their signal conditioning electronics, and the tape recorder head stacks. Exciting each accelerometer and the force gauge together on the shaker and recording their outputs provided a means of measuring the phase shift from the phase of the cross spectral density of the two signals. All phase differences were linear with frequency and were corrected by time shifting the data after digitization.

Since the admittance matrix is symmetric, determination of one off-diagonal element is sufficient to determine its reciprocal. Here we experimentally determined both terms to double check the reciprocity of the data, and we found excellent results.

A typical admittance element is shown in Figure 3 (magnitude only) for the response at point 1 in the Y direction to a force at point 1 in the Y direction. The prominent peak near 30 Hz is a lateral bending mode of the laser combustor and its attachment duct. These and

all other calculations in this report were done on a Raytheon model 704 minicomputer system using standard FFT algorithms.

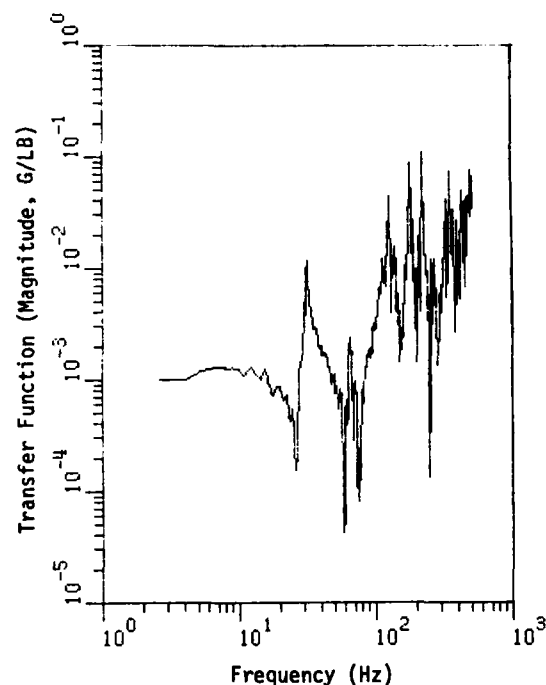


Fig. 3 - Laser Admittance Element - Forward Mount Lateral Response, Forward Mount Lateral Excitation

#### FREE RESPONSE DETERMINATION

Next we proceed to solve Eq (5) for the free response using the accelerations and forces measured during firing of the laser in its special ground test stand. Accelerometers provided the first half of the data, but the force measurements were more difficult because the forces had to be separated into their directional components.

To overcome this problem, special laser mounting brackets with strain gaged sensing elements were designed (see Figure 4). The mounts were attached to the laser stages with ball joints and, in the case of the forward and aft mounts, bolted to the test stand with four bolts each. The drag link had a ball joint at either end making it a single force member. The sensing elements were thin steel strips aligned to deflect with the mounts as they were loaded in each direction, and strain gauges attached to the strips were wired in bridge configurations so that each bridge was sensitive to deflection in only one direction. Using a static test stand, known forces were applied, both singly and in combination, to the mounts; so the strain gauge bridge outputs could be

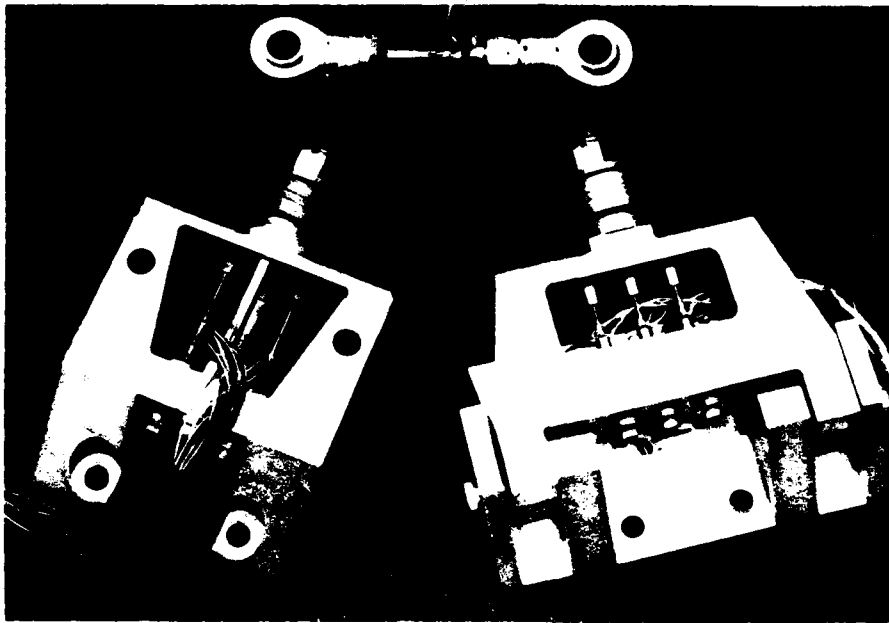


Fig. 4 - Laser Mounting Brackets with Force Measuring Elements

calibrated directly in force units. To check the calibration results, as well as to insure adequate strength of the mounts, NASTRAN finite element models were constructed for the forward and aft mounts; and good agreement was found with the experimental results.

Analysis of the initial acceleration data from the laser firings showed a large jump in response near 500 Hz, so the accelerometer outputs were low pass filtered at 500 Hz for subsequent data recordings to insure adequate dynamic range in the low frequencies. All significant force levels were below 500 Hz. Phase differences between the accelerometers and strain gauges were accounted for using the same technique mentioned in the last section. However, instead of exciting the transducers on a shaker, a broadband reference signal was inserted simultaneously into the transducer leads and recorded.

Data was recorded from ten laser firings on two sets of mounts, one set for each of the two laser stages. All firings were 1.6 sec long. Typical time histories for force and acceleration are shown in Figures 5 and 6. Since the strain gauge bridges were connected to DC amplifiers, both the static thrust and dynamic components of the laser forces were recorded. Figure 5 shows the force in the thrust direction, and the static component shows clearly in the plot. The measured static

thrust compared well with the calculated thrust, providing a double check on the mount calibrations.

The Fourier transform magnitudes of the force and acceleration time histories are also shown in Figures 5 and 6. They are only plotted to 100 Hz because this was the limit of accuracy for the final force prediction. The analysis bandwidth for these and all subsequent calculations was 0.3 Hz. Using the Fourier transforms of force and acceleration and the admittance matrix to solve Eq (5), we have the free response acceleration which is plotted in Figure 7 in both the time and frequency domains for the same dof plotted in Figures 5 and 6. Free responses were calculated for each dof for each of the ten laser firings.

#### AIRBORNE FORCE PREDICTION

Having the free response, we need only the aircraft admittance matrix to solve Eq (9) for the airborne forces, and we obtained it from a NASTRAN dynamic model of the aircraft fuselage. The model contained 54 modes up to 100 Hz which we considered to be its limit of accuracy. A typical admittance element from the model is shown in Figure 8.

Solving Eq (9) for each of the ten firings, we have an ensemble of airborne force vectors.

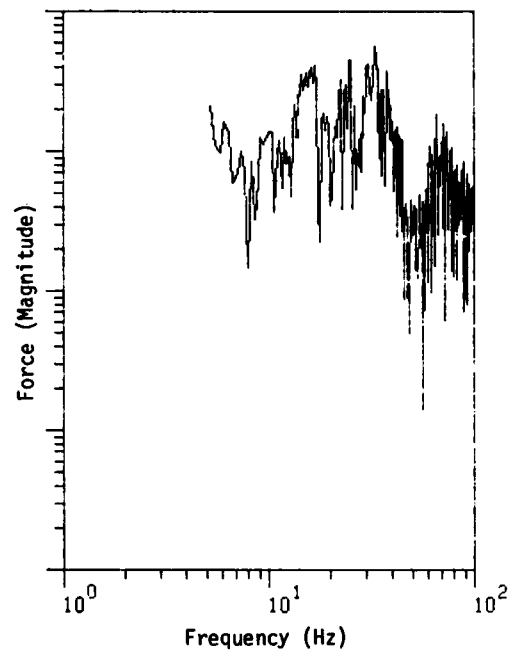
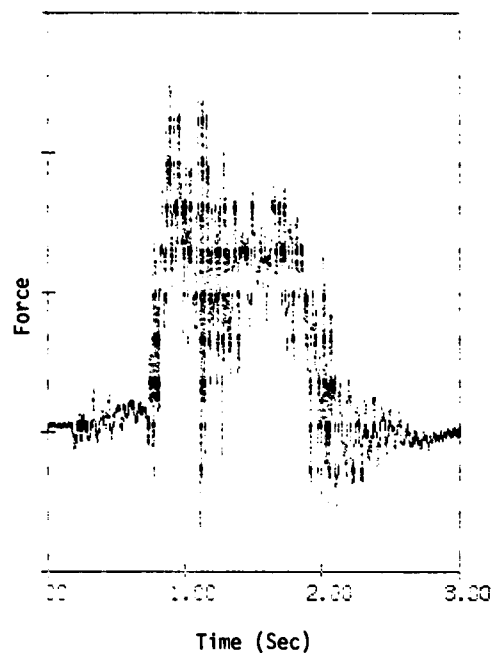


Fig. 5 - Mounting Force on Ground Test Stand - Aft Mount, Vertical

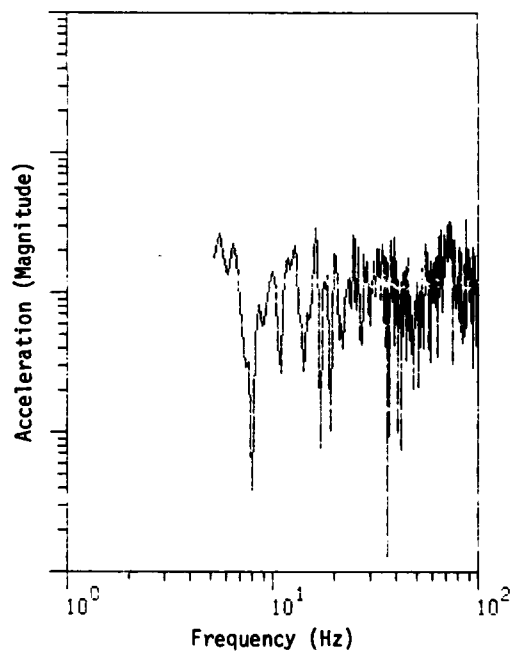
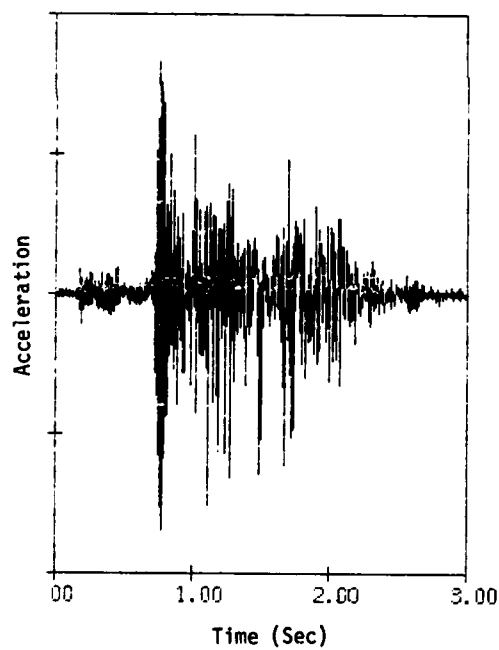


Fig. 6 - Mount Acceleration on Ground Test Stand - Aft Mount, Vertical

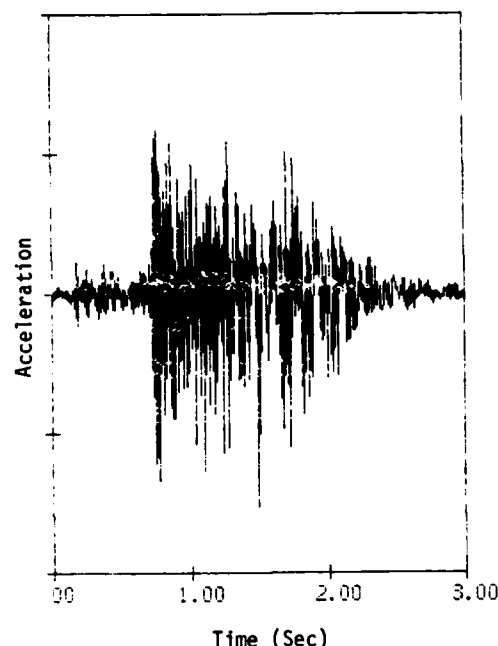


Fig. 7 - Free Response Acceleration - Aft Mount, Vertical

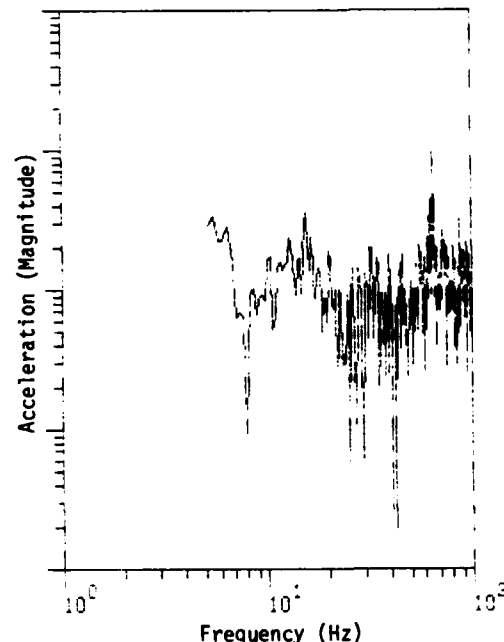


Figure 9 illustrates the airborne force time history corresponding to the time history in

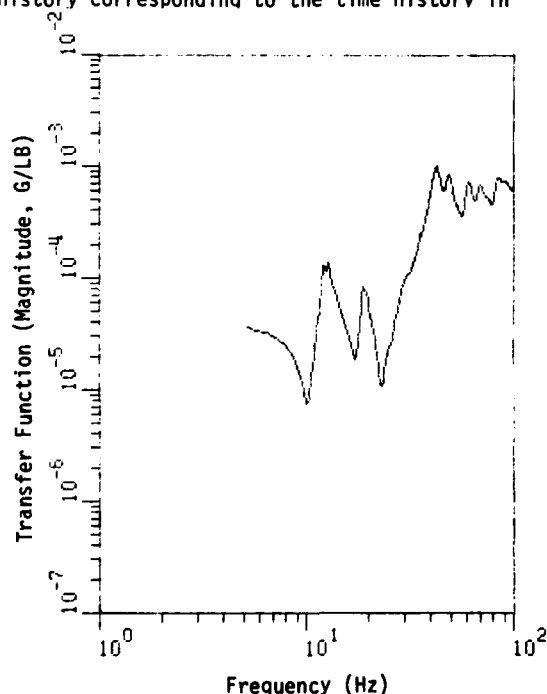


Fig. 8 - NASTRAN Admittance Element for Aircraft Mounting Points - Forward Mount Lateral Response, Forward Mount Lateral Excitation

Figure 5. There is no static thrust component in this result because the accelerometer and admittance data were not recorded below 5 Hz. The most severe time histories in the ensemble will be input to the NASTRAN model to predict responses at other locations in the aircraft.

In the future the aircraft admittance will be measured experimentally, which hopefully will enable the prediction to be carried out to 500 Hz, the frequency limit of the laser firing data.

#### CONCLUSIONS

The force prediction scheme can be implemented experimentally by taking advantage of digital processing and random shaker excitation techniques, and it provides a practical method of solving interface vibration environment problems. Further savings could be realized by automating the entire procedure on a mini-computer based analysis system and using transient impact excitations in place of shaker excitations to measure admittance functions.

Special experimental techniques must be used to assure accurate data gathering. For admittance measurements this includes calculation of coherence functions, and for all data phase shifts between transducers must be carefully accounted for.

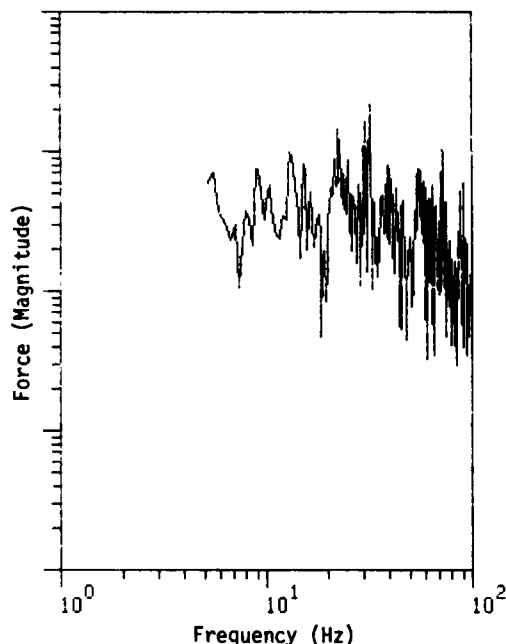
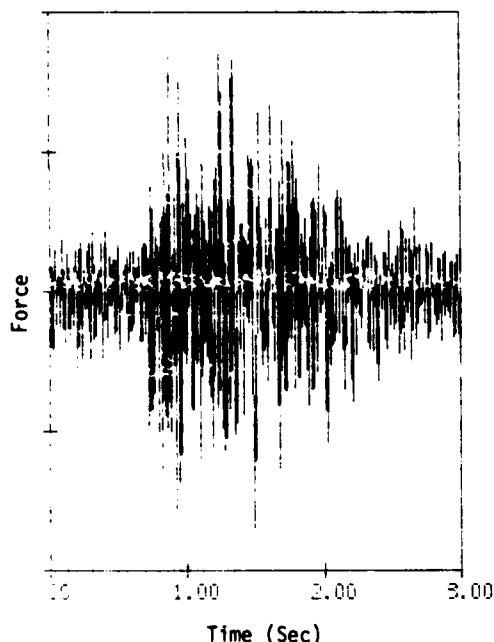


Fig. 9 - Predicted Airborne Mounting Force - Aft Mount, Vertical

#### ACKNOWLEDGMENTS

All experimental data were gathered at the Air Force Weapons Laboratory (AFWL), and all analyses were performed at the Air Force Flight Dynamics Laboratory (AFFDL). The laser force measuring mounting brackets were designed and machined by the General Dynamics Corporation under contract to the Air Force. NASTRAN analysis of the mounting brackets was done by Maj R. Bartholomew of the AFWL, and NASTRAN analysis of the aircraft fuselage was performed by both General Dynamics and the Air Force.

#### REFERENCES

1. D. D. Kana and L. M. Vargas, "Prediction of Payload Vibration Environments by Mechanical Admittance Test Techniques," *Journal of Spacecraft*, Vol 13, No. 1, January 1976, pp. 45-50.
2. G. C. Kao, J. M. Cantril, G. D. Shipway, and M. A. Boyd, "Prediction of Shock Environments by Transfer Function Measurement Techniques," *The Shock and Vibration Bulletin*, No. 44, Part 2, August 1974, pp. 65-81.
3. D. J. Ewins and M. G. Sainsbury, "Mobility Measurements for the Vibration Analysis of Connected Structures," *The Shock and Vibration Bulletin*, No. 42, Part 1, January 1972, pp. 105-122.
4. E. Heer and L. D. Lutes, "Application of the Mechanical Receptance Coupling Principle to Spacecraft Systems," *The Shock and Vibration Bulletin*, No. 38, Part 2, August 1968, pp. 239-248.
5. G. K. Jones and F. J. On, "Prediction of Interface Random and Transient Environments Through the Use of Mechanical Impedance Concepts," *The Shock and Vibration Bulletin*, No. 40, Part 3, December 1969, pp. 79-88.
6. F. J. On, "A Verification of the Practicality of Predicting Interface Dynamical Environments by the Use of Impedance Concepts," *The Shock and Vibration Bulletin*, No. 38, Part 2, August 1968, pp. 249-260.

#### Discussion

Mr. McMunn, (TRW Systems): What is the frequency content of the noise that is generated from a chemical laser or a gas dynamic laser? Is most of the noise due to combustion instability or rough burning? What is its magnitude? Did you make any measurements on this device?

Mr. Davis: The noise is very similar to that of a jet engine. It is mostly combustion noise and it is very broad band in nature. There are a few single frequency components that show up due to the natural frequencies of the laser structure itself.



# INFLUENCE OF FLUID ON THE DYNAMIC PLASTIC RESPONSE OF A PIPE\*

M. G. Srinivasan, R. A. Valentin  
Argonne National Laboratory  
Argonne, Illinois

and

D. Krajcinovic  
University of Illinois at Chicago Circle  
Chicago, Illinois

The problem of the dynamic plastic deformation of a pipe subjected to internal pressure pulse and surrounded by a fluid is studied. Through dimensional-analysis and simplifying assumptions the number of parameters influencing the solution is reduced to a minimum. The results of an analytical-numerical solution are presented and discussed in terms of these parameters.

## INTRODUCTION

In many applications of practical significance it is necessary to determine the load carrying capacity of structures immersed into fluids and subjected to dynamic loads. For example, a conventional design of heat exchangers emphasizes pipes enveloped by fluid. A sudden surge of pressure inside the pipe (associated with a postulated accident of a certain kind) might cause unacceptably large plastic deformations in the pipe. Our intuition and some previous results of beam and plate problems [1,2] indicate that the beneficial influence of surrounding fluid on final plastic deformations cannot be neglected. It is quite surprising that this problem has not been studied in the literature nearly as much as one would have expected. While the literature on hydroelasticity on one and dynamic plasticity of structures in vacuum on the other hand is rather abundant there are but few papers related to the topic at hand. It is, therefore, appropriate to discuss at least basic features of this problem.

## FORMULATION OF THE PROBLEM

An exactly formulated model of the problem would obviously comprise

- a circular cylindrical shell responding in an elastic-plastic mode with the possible influence of strain rates on the magnitude of yield stresses.
- a viscous and compressible fluid.

It is also possible (although not quite as probable as in some hydro-elastic problems) that

cavitation and turbulence might develop especially in the later stages of deformation. An analytical study of a model as complex as this is impossible. Even somewhat simplified models might pose tremendous numerical difficulties. Purely numerical schemes are quite expensive and not always entirely reliable in the case of interaction problems. It appears therefore proper to study the simplest possible problem analytically, derive basic relations and prepare the ground for a comprehensive series of experiments.

In order to establish a basis for the general formulation it is necessary to first list all of the parameters defining the response of the system.

The geometry of an infinitely long circular cylindrical shell is defined by the radius of its middle surface,  $R$ , and the wall thickness,  $H$  (Fig. 1). Since the dynamic response involves the inertia of the shell, the mass density  $\rho$  (assumed constant) is defined as the inertial parameter.

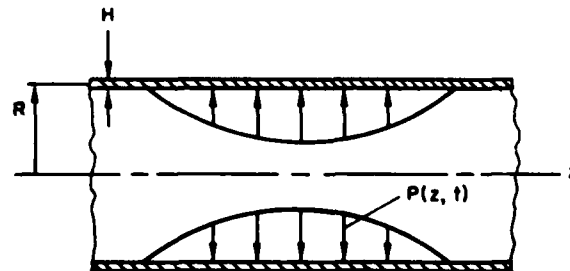


Fig. 1. Geometry and Loading of Shell Immersed in Fluid

\*Research performed under the auspices of the U.S. Energy Research and Development Administration.

The behavior of the shell material is defined by a set of parameters related by the constitutive equations. If in the first approximation we consider the material to be rigid-ideally plastic its behavior is characterized by the yield condition. The only significant generalized internal forces in the shell are the axial bending moment,  $M$  and the circumferential (hoop) normal force  $N$ . The yield condition (Fig. 2) therefore depends on  $M_y$  and  $N_y$ , the yield values, defined by

$$\begin{aligned} M_y &= \frac{1}{4} H R P_0 \\ N_y &= R P_0 \\ P_0 &= \sigma_y \frac{H}{R} \end{aligned} \quad (1)$$

where  $\sigma_y$  is the yield stress. Though  $M_y$  and  $N_y$  are defined in terms of the three independent parameters  $H$ ,  $R$ , and  $P_0$ , we need only  $P_0$  as the single parameter to characterize the material behavior, since  $H$  and  $R$  are already included among the geometry parameters.

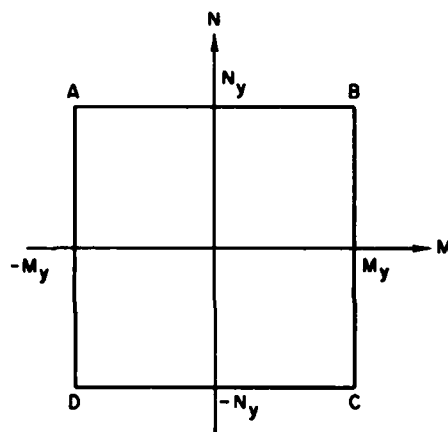


Fig. 2. Yield Condition

We should immediately note that a rigid-ideally plastic model approximates the actual material behavior sufficiently well only if [3], (a) the kinetic energy of the imparted load significantly exceeds the maximum elastic deformation energy of the structure, and (b) the duration of the load is short in comparison with the period of natural vibrations of the system. An attractive feature of the rigid-ideally plastic model is the possibility of model refinement through gradual addition of other effects (such as strain-rate sensitivity, large deformations, etc.) without necessarily compromising the tractability.

The response of the fluid, assumed to be infinite in extent, is defined by its density  $\rho_f$  (considered constant), kinematic viscosity  $\nu$  and compressibility  $K$ . (We could use the acoustic velocity instead of  $K$  to characterize compressibility).

The external load is obviously defined by its intensity, pressure-time history and dependence on spatial co-ordinates  $\theta$  and  $z$ . Even if we restrict ourselves to axisymmetric loads  $P = P(z, t)$  the variety of possibly interesting functions is still too large to allow for a reasonable discussion. Thus, it appears essential to reduce the number of load related parameters by means of a correlation technique proposed by Youngdahl [4]. Through correlation an arbitrary pressure  $P(z, t)$  is reduced to an equivalent constant pressure  $P_e$  of duration  $t_e$  uniformly distributed over a portion of length  $2 L_e$  of the cylinder (Appendix A). In effect, using the load correlation technique the load is completely defined by the set of three parameters  $P_e$ ,  $L_e$ , and  $t_e$  representing the intensity, the length of the loaded region and the duration of the load pulse, respectively. The gravity forces (i.e., the parameter  $g$ ) can be neglected in comparison with the other forces.

In addition, since the process is not stationary it is necessary to include as a parameter time  $t$ , as well as the co-ordinates  $z$  and  $r$  defining the position of the observed point.

#### DIMENSIONAL ANALYSIS

On the basis of the previous discussion it is possible to say that, for instance, the final deflection of a point on the middle surface of the shell defined by the co-ordinates  $(z, r = R)$  can be written as

$$U_f = U_f(R, H; \rho; P_0; \rho_f, \nu, K; P_e, L_e, t_e; z) \quad (2)$$

In equation (2) semicolons separate geometric, inertial, strength, fluid, load and spatial groups of parameters. Using the well known  $\pi$  theorem (see, for example [5]) the displacement  $U_f$  can be written in terms of three basic independent parameters (appropriately selected) and a set of  $11 - 3 = 8$  non-dimensional numbers. In other words, it would be necessary to examine the dependence of  $U_f$  on the magnitude of eight non-dimensional parameters characterizing the system.

This would obviously be a formidable task. An engineering approach in reducing this task to a reasonable level would obviously include a certain amount of analysis and use of previously published data related to our problem.

#### Compressibility

In a paper on a somewhat related problem of hydrodynamic impact, motivated by problems encountered in design of Apollo command module, Nevill, Morales, and Horowitz [6] studied the influence of compressibility and viscosity on the pressure exerted by fluid on the shallow spherical shell. According to their tests on two liquids (methyl acetate and water whose compressibility varies by a factor of 2.35) the variations in liquid response (within the range studied) are negligible. We should also mention

that the compressibility in hydrodynamic impact problems is of some interest only in the case of blunt bodies and even then only during an extremely short initial period while the velocity of the fluid along the contour of the impacting body is supersonic. Since in our case the velocity of deformation rises gradually from zero there is no reason to believe that the conclusion made in [6] should not be extended to our case. We should also point out that the correction for compressibility is as a rule always less significant in three dimensional cases.

#### Viscosity

The already mentioned paper [6] presents further results of a series of tests with water and castor oil. Although the Reynolds number was varied by a factor of 2447 (0.545 for castor oil and 1334 for water) and the impact speeds from 9 to 16 feet per second no significant difference in measurement of permanent deformations could be detected.

#### Adopted Analytical Model

On the basis of preceding considerations it appears reasonable to start from a model consisting of a:

- rigid-ideally plastic thin walled shell of infinite length submerged into
- an incompressible and inviscid fluid infinitely extended in all directions.

Such a formulation greatly facilitates analyses although the problem seems complex enough to prohibit a closed form analytical solution. A brief recital of analyses published elsewhere [7] is presented in Appendix B. Although the problem is still not amenable to a closed form solution in a strict sense of this word, the solution is simple enough to enable a reasonable qualitative and quantitative study of the problem without excessive computation.

In practice the main interest obviously lies in determining the maximum final, plastic deformation of the shell characterizing in a way the load carrying capacity of the structure. We should point out that in contrast to static limit analysis the dynamic response of a rigid-ideally plastic structure is characterized by finite deformation but allows (theoretically) infinitely large load intensities. Thus, instead of a collapse load (corresponding to reaching yield limits at sufficient number of locations - plastic hinges) we have a "collapse deformation" corresponding to a deformation considered excessive (either causing rupture or presenting functional failure).

According to equation (2) and previously discussed simplifications (neglecting viscosity,  $v$ , and compressibility,  $K$ , of the surrounding fluid) the maximum final deformation, i.e.,  $U_f$  at  $z=0$ , denoted by  $U_0$  can be written as:

$$U_0 = H f\left(\frac{\rho_f}{\rho}, \frac{P_e}{P_0}, \frac{L_e}{R}, \frac{H}{R}, \frac{P_0 t_e^2}{\rho H^2}\right) \quad (3)$$

Since no independent non-dimensional parameters could be formed by any combination of  $\rho$ ,  $R$ ,  $P_0$ , it is clear that  $f$  is a function only of the five non-dimensional parameters. Further, if we assume that as in the case of the shell deforming in vacuum, the maximum deformation is directly proportional to  $t_e^2$  (see Appendix B), then

$$U_0 = \frac{P_0 t_e^2}{\rho H} f_1\left(\frac{\rho_f}{\rho}, \frac{P_e}{P_0}, \frac{L_e}{R}, \frac{H}{R}\right) \quad (4)$$

where  $f_1$  is a non-dimensional function of the four given arguments only. Alternatively we can express  $U_0$  as

$$U_0 = \frac{P_0 t_e^2}{\rho H} f_2\left(\frac{\rho_f}{\rho}, \frac{P_e}{P_0}, \frac{L_e}{\sqrt{R}H}, \frac{H}{R}\right) \quad (5)$$

#### RESULTS AND DISCUSSION

Before discussing the numerical results for  $U_0$ , it is necessary to point out certain restrictions imposed on the range of  $P_e/P_0$  and  $L_e/R$  for the solution to be valid. These restrictions arise as a result of simplifying assumptions.

The mode of plastic deformation is assumed to be characterized by a stationary plastic hinge circle at  $z=0$  and two moving hinge circles at  $z=\pm\zeta$  (see Appendix B and [7]). For plastic deformation to be initiated  $P_e$  must be greater than the limit load which is obtained from the static limit analysis [4] and depends only on the parameter  $L_e/\sqrt{RH}$ . If  $P_e$  is less than the static limit load no deformation will occur.

When plastic deformation occurs in the mode described above, the condition that the bending moment cannot be less than  $-M_y$  at the hinge circle at  $z=0$  implies (see [4])

$$\frac{\partial^2 M}{\partial z^2} > 0 \text{ at } z=0$$

When the solution for  $M$  is substituted into the above inequality we find that  $P_e/P_0$  must be less than a critical value which is a function of  $H/R$ ,  $L_e/R$  and  $\rho_f/\rho$ .

Thus we note that the solution described in Appendix B is valid only if  $P_e/P_0$  is between the lower and upper critical values. Figures 3(a) to 3(e) illustrate the range of these critical values as a function of  $L_e/\sqrt{RH}$  for various values of  $H/R$ ,  $\rho_f/\rho$ . In these figures the solid line denotes the minimum value for  $P_e/P_0$ . Since this value corresponds to the limit load it depends only on  $L_e/\sqrt{RH}$  and is independent of  $H/R$ . The broken lines of Figs. 3(a) to 3(e) denote the maximum permissible values for  $P_e/P_0$  for various values of  $\rho_f/\rho$ . For a pipe

H/R= 0.0278 (1/36)

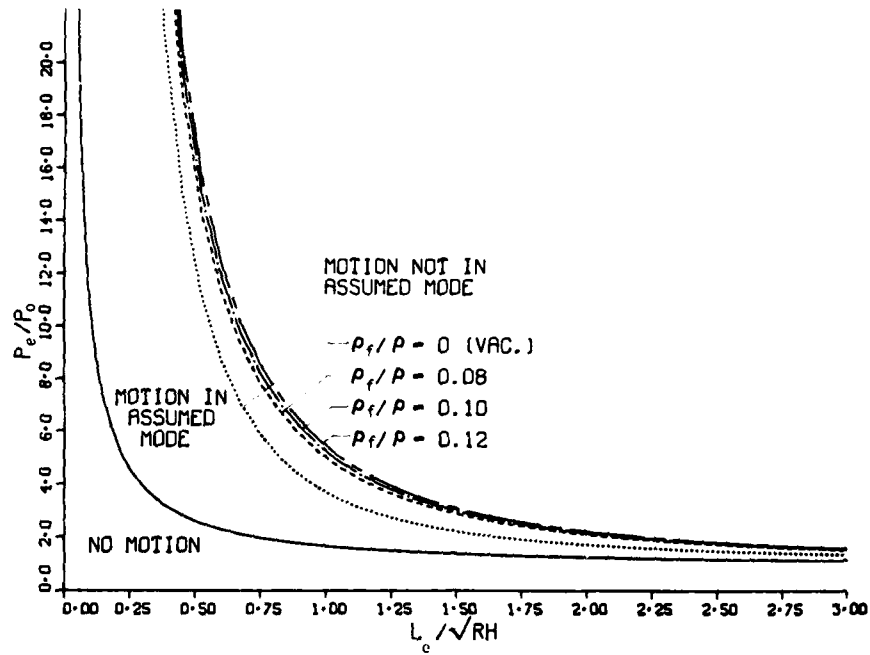


Fig. 3(a). Range of  $P_e$  Initiating Motion in Assumed Mode

H/R= 0.0417 (1/24)

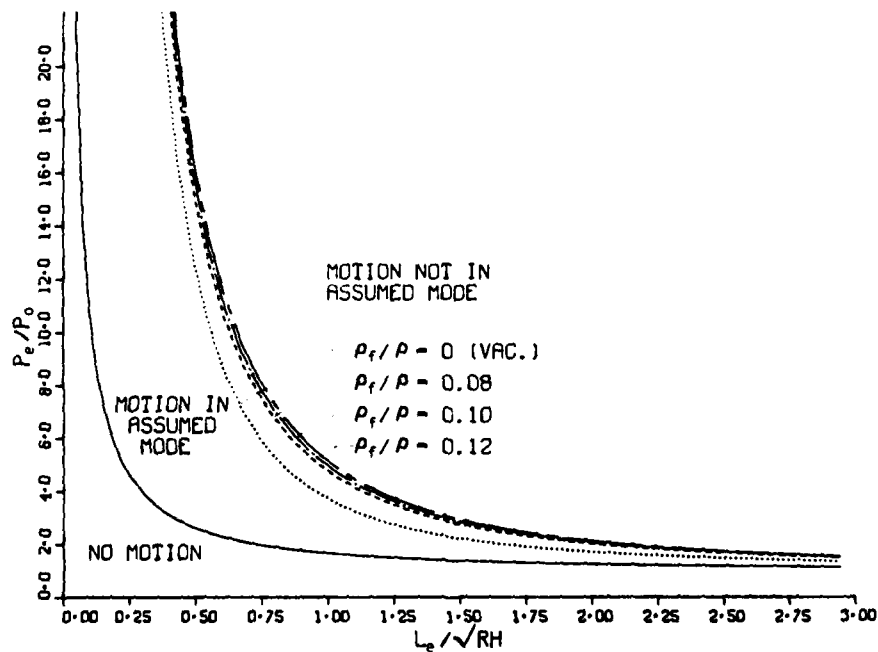


Fig. 3(b). Range of  $P_e$  Initiating Motion in Assumed Mode

H/R= 0.0556 (1/18)

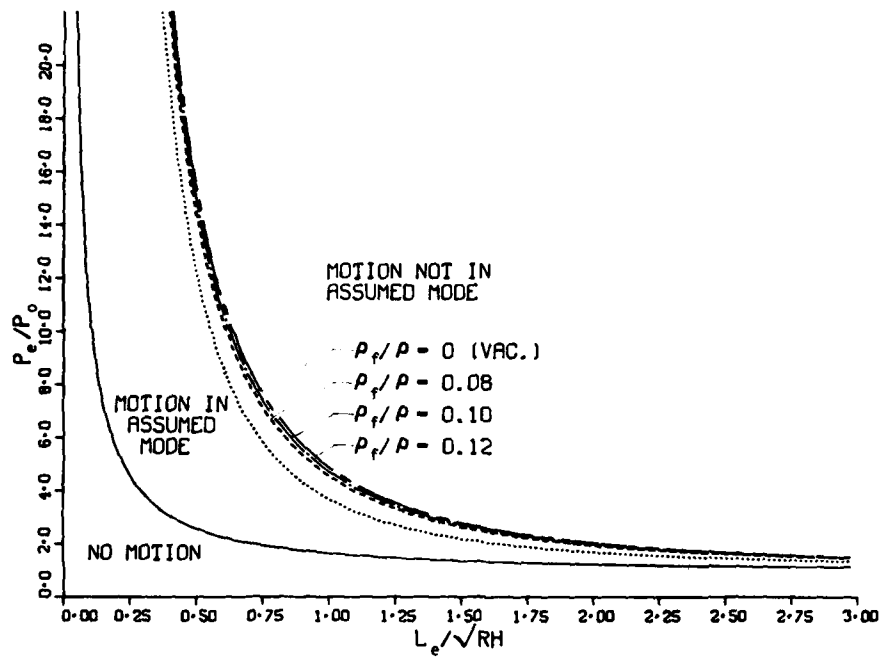


Fig. 3(c). Range of  $P_e$  Initiating Motion in Assumed Mode

H/R= 0.0694 (5/72)

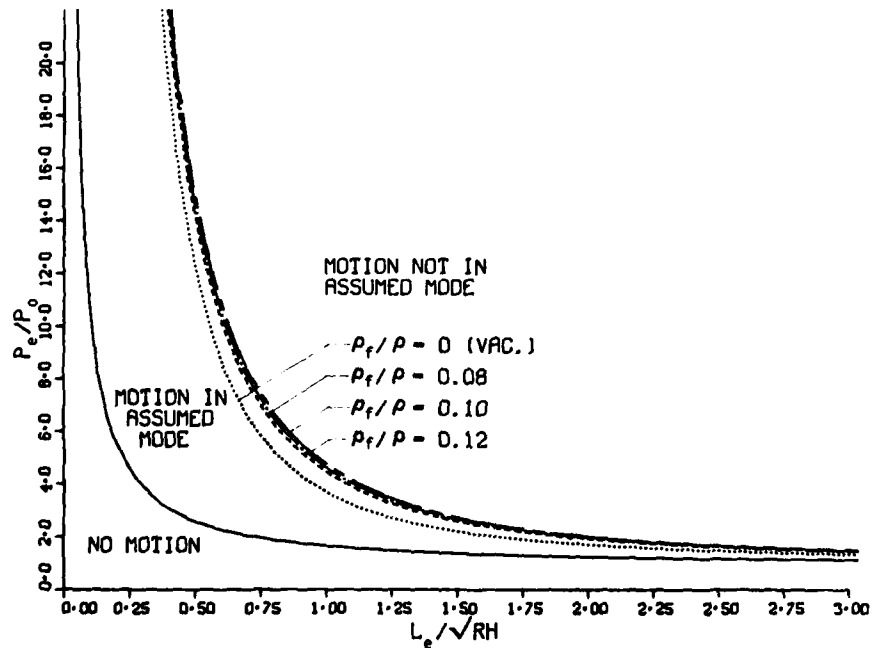


Fig. 3(d). Range of  $P_e$  Initiating Motion in Assumed Mode

H/R= 0.0833 (1/12)

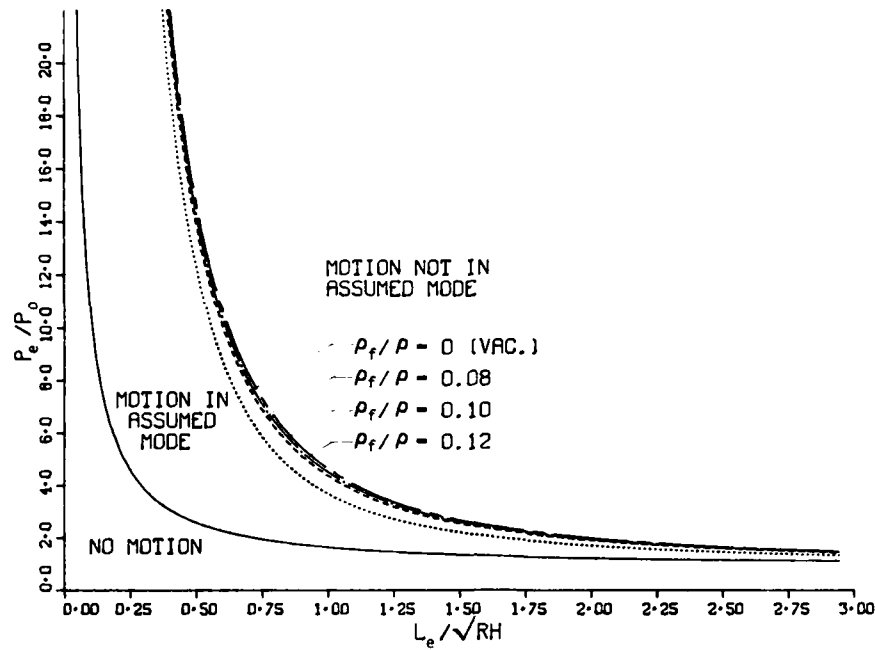


Fig. 3(e). Range of  $P_e$  Initiating Motion in Assumed Mode

H/R= 0.0278 (1/36)

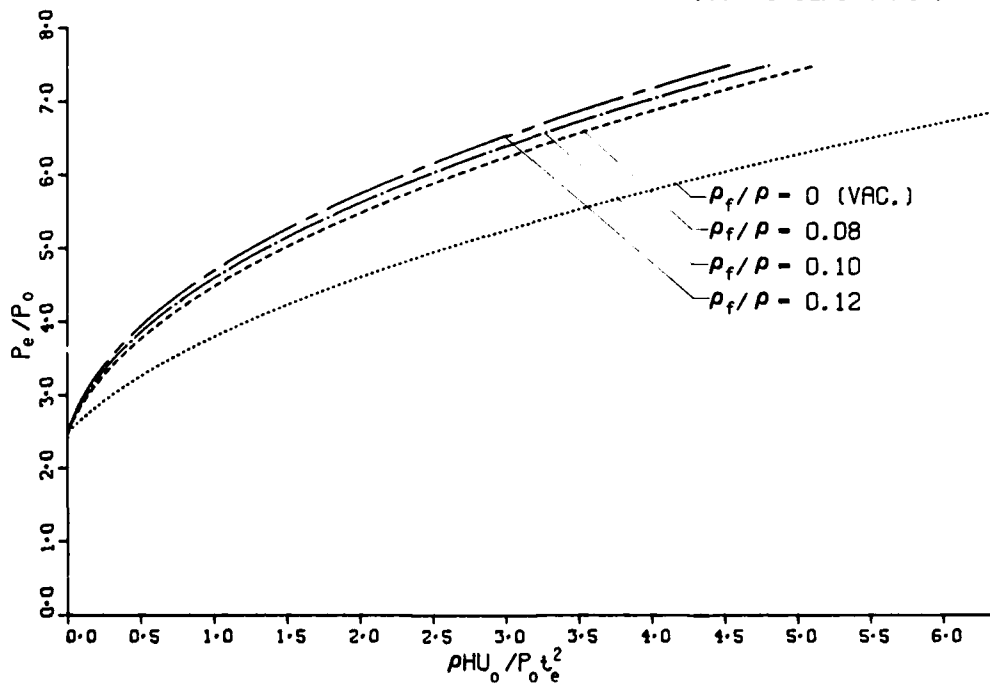


Fig. 4(a). Load-Deformation Curves for  $L_e/\sqrt{RH} = 0.52$

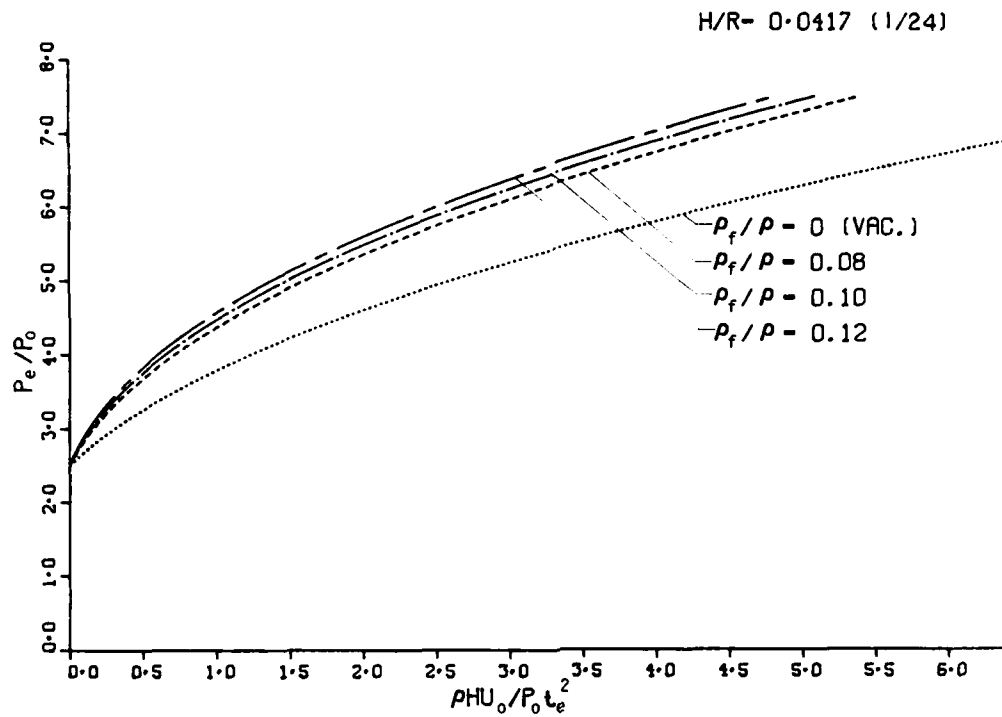


Fig. 4(b). Load-Deformation Curves for  $L_e / \sqrt{RH} = 0.52$

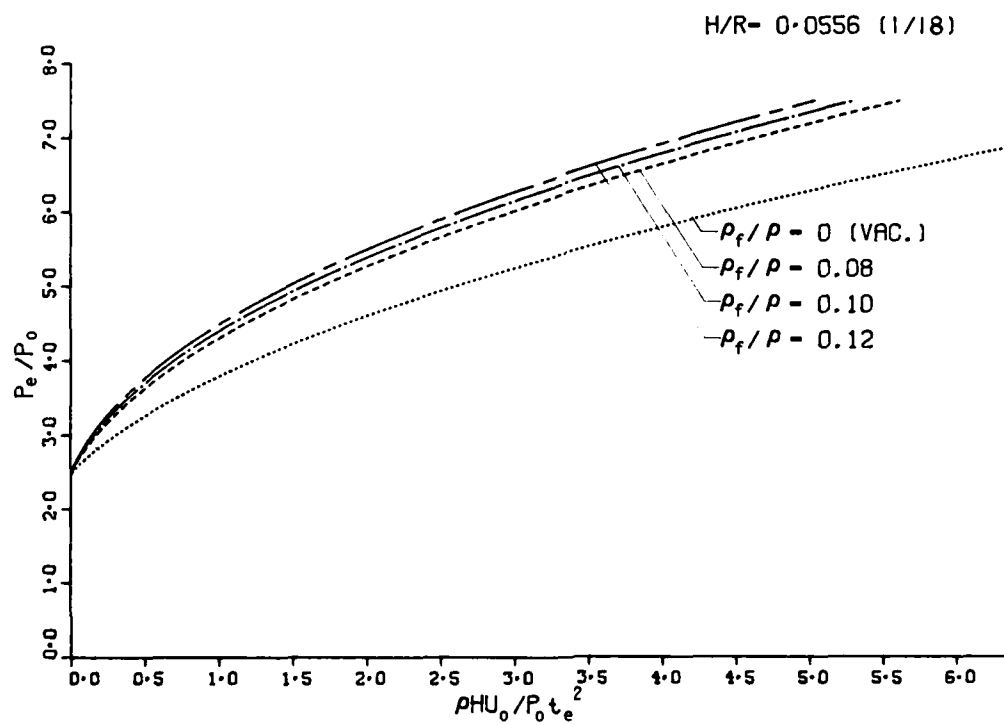


Fig. 4(c). Load-Deformation Curves for  $L_e / \sqrt{RH} = 0.52$

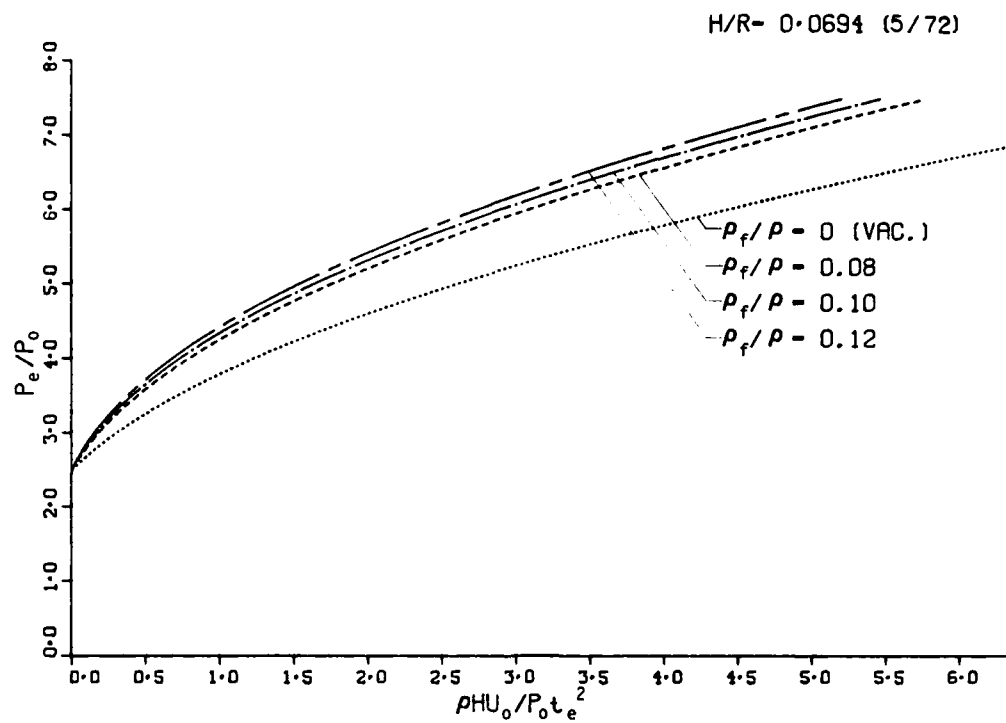


Fig. 4(d). Load-Deformation Curves for  $L_e/\sqrt{RH} = 0.52$

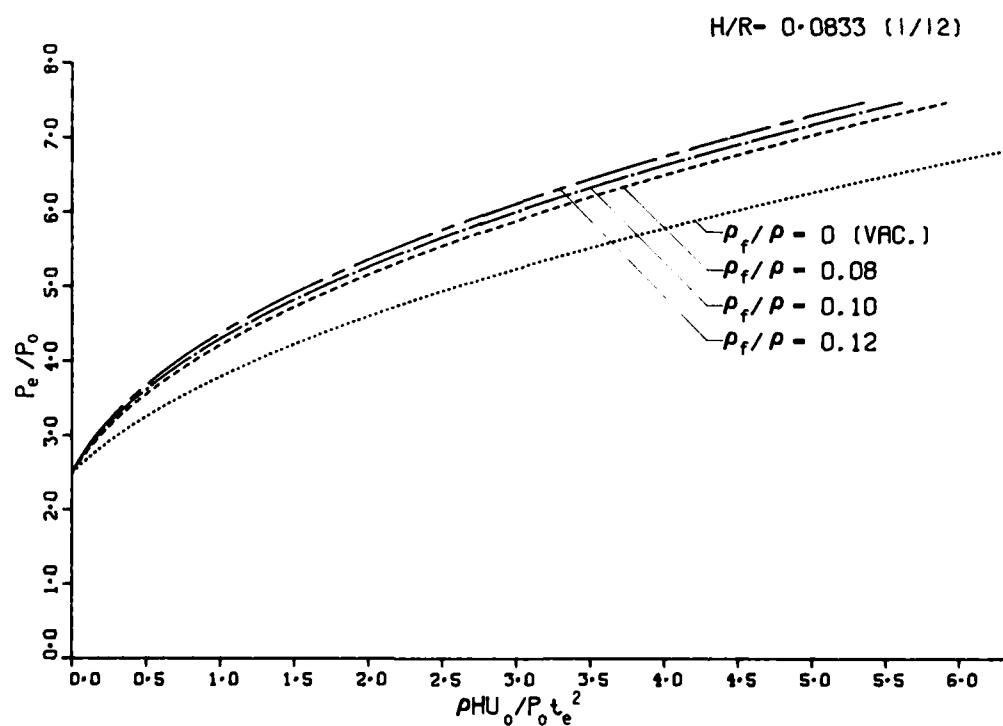


Fig. 4(e). Load-Deformation Curves for  $L_e/\sqrt{RH} = 0.52$



surrounded by vacuum  $\rho_f/\rho = 0$ . From the solution given in [4], it is seen that for this case also, the maximum permissible value of  $P_e/P_0$  depends only on  $L_e/\sqrt{RH}$  and does not depend on  $H/R$ . Three practically meaningful values of  $\rho_f/\rho$  have been chosen for illustration in these figures. These correspond to possible combinations of fluids such as liquid sodium, water and a two-phase mixture of steam and water and pipes of stainless steel and copper.

In the course of the solution for the plastic deformation  $U_0$ , it is assumed that  $\zeta/R < 1$ , in order to make the asymptotic evaluation of the fluid back-pressure possible. This is equivalent to the restriction,  $L_e/R < 1$  [7]. Therefore the solution described in Appendix B is valid only when  $P_e/P_0$  lies within the range indicated in Fig. 3(a) to 3(e) and  $L_e/R < 1$ .

From Fig. 3(a) to 3(e) we see that the permissible range of  $P_e/P_0$  narrows to a small band as  $L_e/\sqrt{RH} > 1$  for almost all practical values of  $\rho_f/\rho$ . But for  $L_e/\sqrt{RH} < 1/2$  it is seen that the upper limit for  $P_e/P_0$  is very large. Therefore we choose a value of  $L_e/\sqrt{RH} = .52$  for illustrating the results for  $U_0$ . In Fig. 4(a) to 4(e) the non-dimensionalized value of  $U_0$  is drawn as a function of  $P_e/P_0$  for various values of  $H/R$  and  $\rho_f/\rho$ .

First we note that for the case of the pipe surrounded by vacuum

$$U_0 = \frac{P_0 t^2}{\rho H} g\left(\frac{P_e}{P_0}, \frac{L_e}{\sqrt{RH}}\right) \text{ for } \rho_f/\rho = 0 \quad (6)$$

which may also be verified from the analysis in [4]. Comparing (5) and (6) it is seen that when there is no fluid surrounding the pipe,  $U_0$  does not depend on  $H/R$ . When  $\rho_f/\rho \neq 0$ , we need  $H/R$  in addition to  $L_e/\sqrt{RH}$  since the back-pressure term cannot be expressed as a non-dimensional function involving only  $L_e/\sqrt{RH}$ .

Finally Figs. 4(a) to 4(e) are seen to clearly demonstrate the beneficial influence of the presence of the fluid in reducing the plastic deformation, a measure of damage. It is seen that this influence is greatest for values of  $P_e$  only slightly larger than the limit load and that a reduction in plastic deformation of the order of 30% is observed even for large values of  $P_e/P_0$ . Therefore we conclude that for a realistic estimate of damage due to impulsive pressure pulses the influence of the fluid should be taken into account.

It should finally be noted that the present analysis can be extended to deformations in a different mode (having more than three plastic hinge rings). Solutions for the final plastic deformation  $U_0$  will again be given in form of Eq. (4) or (5). However, the function  $f_1$  or  $f_2$  will obviously depend on the non-

dimensional  $\pi$  parameters in a different way.

## REFERENCES

1. D. Krajcinovic, "Dynamic Plastic Response of Beams Resting on Fluid," Int. J. Solids and Structures, Vol. 11, pp. 1235-1243, 1975.
2. D. Krajcinovic, "Dynamic Response of Circular Rigid-Plastic Plates Resting on Fluid," J. Appl. Mech., Vol. 98, No. 1, pp. 102-106, March 1976.
3. P. S. Symonds, "Survey of Methods of Analysis for Plastic Deformation of Structures Under Dynamic Loading," Report BU/NSRDC/1-67, Division of Engineering, Brown University, 1967.
4. C. K. Youngdahl, "Correlating the Dynamic Plastic Deformation of a Circular Cylindrical Shell Loaded by an Axially Varying Pressure," Report ANL-7738, Argonne National Laboratory, 1970.
5. L. I. Sedov, Similarity and Dimensional Methods in Mechanics, Academic Press, New York, 1959.
6. G. E. Nevill, Jr., W. J. Morales, and J. M. Horowitz, "Studies of Parameter Significance in Shell-Liquid Impact," AIAA Journal, Vol. 6, No. 8, pp. 1511-1514, Aug. 1968.
7. D. Krajcinovic, M. G. Srinivasan, and R. A. Valentin, "Fluid-Plasticity of Thin Cylindrical Shells," Proceedings of the 13th Annual Meeting of the Society of Engineering Science, Nov. 1976.
8. D. C. Drucker, "Limit Analysis of Cylindrical Shells Under Axially Symmetric Loading," Proceedings of the First Midwest Conference on Solid Mechanics, pp. 158-163, 1953.
9. P. G. Hodge, Limit Analysis of Rotationally Symmetric Plates and Shells, Prentice-Hall Inc., Englewood Cliffs, New Jersey, Ch. 3, 1963.

## APPENDIX A

### Determination of the Correlation Parameters

The axisymmetric pressure  $P = P(z, t)$  is assumed to be of the form

$$P(z, t) = \phi(z)\psi(t) \quad 0 \leq |z| \leq L \quad (A.1)$$

$$= 0 \quad |z| > L$$

where  $\phi(z)$  is the load shape which decreases monotonically with  $|z|$ ,  $\psi(t)$  is the pulse shape and  $L$  is the half-length of the loaded region. An equivalent rectangular pressure distribution in space and time is determined which produces the same final plastic deformation as the

actual loading. The functions  $\phi(z)$  and  $\psi(t)$  are replaced by effective constant values  $\phi_e$  and  $\psi_e$  respectively, acting over an effective half length  $L_e$  for an effective duration  $t_e$ .

The effective values are given by

$$\phi_e = \frac{\left\{ \int_0^{z_y} \phi(z) dz \right\}^2}{2 \int_0^{z_y} z \phi(z) dz} \quad (A.2)$$

and

$$\psi_e = \frac{\left\{ \int_{t_y}^{t_f} \psi(t) dt \right\}^2}{2 \int_{t_y}^{t_f} (t - t_y) \psi(t) dt} \quad (A.3)$$

where  $z_y$  is the initial location of the plastic hinge, and  $t_y$  and  $t_f$  are the times when plastic deformation begins and ends, respectively. For the initial yield condition, standard limit analysis gives:

$$(z_y^2 - RH) \int_0^{z_y} \phi(z) dz - 2z_y \int_0^{z_y} z \phi(z) dz = 0 \quad (A.4)$$

and

$$\frac{\sigma_y H}{\psi_y R} = \frac{1}{z_y} \int_0^{z_y} \phi(z) dz \quad (A.5)$$

where  $\sigma_y$  is the yield stress and

$$\psi_y = \psi(t_y) \quad (A.6)$$

The solution of Eq. (A.4) gives  $z_y$ . Subsequently,  $t_y$  is obtained as the smallest value of time satisfying Eqs. (A.5) and (A.6). An estimate of  $t_f$  is obtained from the approximation

$$(t_f - t_y) \psi_y \approx \int_{t_y}^{t_f} \psi(t) dt \quad (A.7)$$

The effective half-length of the loaded region is given by

$$L_e = \frac{1}{\phi_e} \int_0^{L_e} \phi(z) dz, \quad (A.8)$$

and the effective duration of the pulse is given by

$$t_e = \frac{1}{\psi_e} \int_{t_y}^{t_f} \psi(t) dt \quad (A.9)$$

Finally, the effective pressure is defined as

$$P_e = \phi_e \psi_e \quad (A.10)$$

and the equivalent rectangular pulse is

$$P(z, t) = P_e \quad |z| \leq L_e \text{ and } 0 \leq t \leq t_e \\ = 0 \quad |z| > L_e \text{ or } t > t_e \quad (A.11)$$

Thus the correlation parameters  $P_e$ ,  $L_e$ , and  $t_e$  completely define the loading equivalent to the actual loading  $P(z, t)$ .

## APPENDIX B

### Dynamic Plastic Response of Pipe Surrounded by Fluid

The equation of motion for the shell is

$$\frac{\partial^2 M}{\partial z^2} = P - P_f - \frac{N}{R} - \rho H \frac{\partial V}{\partial t} \quad (B.1)$$

where  $M$  is the axial bending moment,  $N$  the hoop force,  $V$  the radial velocity of the points on the middle surface of the shell, and  $P$  and  $P_f$  are the applied pressure pulse and the fluid back-pressure respectively.

During plastic flow, four different deformation configurations or modes may appear (see [4]). Of these four, only that particular mode which is common for most loadings is considered. This mode is characterized by a stationary hinge circle at  $z = 0$  and two moving hinge circles at  $z = \pm \zeta(t)$ . Assuming that the yield condition in the  $M, N$  space is defined by the limited interaction curve (see [8,9]) we have the following boundary conditions for  $z \geq 0$

$$\begin{aligned} z = 0 & \quad M = -M_y & N = N_y \\ z = \zeta & \quad M = M_y & N = N_y \\ 0 < z < \zeta & \quad -M_y < M < M_y & N = N_y \end{aligned} \quad (B.2)$$

where the yield values  $M_y$  and  $N_y$  are given by

$$\begin{aligned} M_y &= \frac{1}{4} HR P_o \\ N_y &= R P_o \end{aligned} \quad (B.3)$$

and

$$P_o = \sigma_y \frac{H}{R}$$

with  $\sigma_y$  being the yield stress.

The deformation mode and the flow rule associated with the yield condition suggest a solution for  $V$  of the form

$$V(z, t) = \begin{cases} V_o(t) \left\{ 1 - \frac{z}{\zeta(t)} \right\} & 0 \leq z \leq \zeta \\ 0 & z > \zeta \end{cases} \quad (B.4)$$

### Expression for Back-Pressure

The governing equation for the flow of the potential fluid is

$$\frac{\partial^2 F}{\partial r^2} + \frac{1}{r} \frac{\partial F}{\partial r} + \frac{\partial^2 F}{\partial z^2} = 0 \quad (\text{B.5})$$

where  $F(r, z, t)$  is the fluid velocity potential. The boundary conditions are given by:

$$\left. \frac{\partial F}{\partial r} \right|_{r=R} = V \quad (\text{B.6})$$

$$\frac{\partial F}{\partial r} \rightarrow 0, \quad \frac{\partial F}{\partial z} \rightarrow 0 \quad \text{as } \max(r, z) \rightarrow \infty$$

The solution of Eq. (B.5) will give the fluid back-pressure on the pipe as

$$P_f = -\rho_f \left. \frac{\partial F}{\partial t} \right|_{r=R} \quad (\text{B.7})$$

But in view of Eq. (B.4) we may write

$$F(r, z, t) = V_o(t) f(r, z) \quad (\text{B.8})$$

with  $\zeta$  being treated as a constant. Then Eq. (B.7) becomes

$$P_f = -\rho_f f(R, z) \frac{dV_o}{dt} \quad (\text{B.9})$$

Substitution of Eq. (B.8) into Eq. (B.5) leads to the form

$$\frac{\partial^2 f}{\partial r^2} + \frac{1}{r} \frac{\partial f}{\partial r} + \frac{\partial^2 f}{\partial z^2} = 0 \quad (\text{B.10})$$

and the boundary conditions (B.6) become

$$\frac{\partial f}{\partial r} = \begin{cases} 1 - \frac{z}{\zeta} & r = R \quad z \leq \zeta \\ 0 & r = R \quad z > \zeta \end{cases} \quad (\text{B.11})$$

$$\frac{\partial f}{\partial r} \rightarrow 0, \quad \frac{\partial f}{\partial z} \rightarrow 0 \quad \text{as } \max(r, z) \rightarrow \infty$$

After introducing the Fourier cosine transform, we obtain a solution of Eq. (B.10) in the closed form of an integral. The argument of this integral is rather complicated and the integration is performed in three stages using asymptotic formulae and Filon's method. In order to make this numerical solution amenable to substitution into Eq. (B.1), the result is subjected to a series of polynomial regression analyses which suggest the form

$$f(R, z) = -R \left\{ g_0 \left( \frac{\zeta}{R} \right) + g_1 \left( \frac{\zeta}{R} \right) \frac{z}{\zeta} \right\} \quad (\text{B.12})$$

where  $g_0$  and  $g_1$  are non-dimensional cubic

polynomials in  $\zeta/R$ . Four numerical coefficients for each of these two polynomials are obtained from the above mentioned regression analyses. Eq. (B.9), the expression for back-pressure, is therefore given by

$$P_f = \rho_f R \left\{ g_0 \left( \frac{\zeta}{R} \right) + g_1 \left( \frac{\zeta}{R} \right) \frac{z}{\zeta} \right\} \frac{dV_o}{dt} \quad (\text{B.13})$$

### Solution of Shell Equation

Substitution of the expression for  $P_f$  given by Eq. (B.13) and the correlation parameters obtained as described in Appendix A reduce Eq. (B.1) to the form

$$\begin{aligned} \frac{\partial^2 M}{\partial z^2} = & P_e - P_o - \left[ \{\rho H + \rho_f R g_0\} - \{\rho H \right. \\ & \left. - \rho_f R g_1\} \frac{z}{\zeta} \right] \frac{dV_o}{dt} \\ & 0 \leq z \leq \zeta, \quad 0 \leq t \leq t_e \end{aligned} \quad (\text{B.14})$$

$$\begin{aligned} \frac{\partial^2 M}{\partial z^2} = & -P_o - \left[ \{\rho H + \rho_f R g_0\} - \{\rho H \right. \\ & \left. - \rho_f R g_1\} \frac{z}{\zeta} \right] \frac{dV_o}{dt} \\ & 0 \leq z \leq \zeta, \quad t > t_e \end{aligned} \quad (\text{B.15})$$

This equation is subject to the boundary conditions given by Eq. (B.2).

For the interval  $0 \leq t \leq t_e$ , we assume a trial solution of the same form as that for a shell deforming in vacuum (see [4]), viz.

$$\begin{aligned} \zeta(t) &= z_1 \\ V_o(t) &= \frac{K_1}{\rho H} t \end{aligned} \quad (\text{B.16})$$

where  $z_1$  and  $K_1$  are constants. Substituting the above expression into Eq. (B.14), integrating the resulting equation twice with respect to  $z$  and making use of the boundary conditions, we obtain two non-linear algebraic equations for  $z_1$  and  $K_1$ . These are solved by Newton's iteration method.

Integrating Eq. (B.15) twice with respect to  $z$  and making use of the boundary conditions, we obtain

$$\begin{aligned} \frac{dV_o}{dt} = & \frac{-P_o(\zeta^2 + 3RH)}{\zeta^2 \{\rho H + \rho_f R g_0\}} \equiv G_1(\zeta) \\ \frac{d}{dt} \left( \frac{V_o}{\zeta} \right) = & \frac{-6P_o RH}{\zeta^3 \{\rho H - \rho_f R g_1\}} \equiv G_2(\zeta) \end{aligned} \quad (\text{B.17})$$

where  $\zeta = \zeta(t)$ . Eqs. (B.17) are valid in  $t_e < t < t_f$  where  $t_f$  is the time at which motion ceases, i.e.,

$$V_o(t_f) = 0 \quad (B.18)$$

We also define

$$\zeta_f = \zeta(t_f) \quad (B.19)$$

and from Eqs. (B.17) and (B.18) derive a non-linear algebraic equation for  $\zeta_f$ . This equation can be solved numerically since it does not explicitly involve  $t$ . Exchanging the independent and dependent variables  $t$  and  $\zeta$ , we recast Eqs. (B.17) as

$$\frac{dV_o}{d\zeta} = \frac{dt}{d\zeta} G_1(\zeta) \quad (B.20)$$

and

$$\frac{d}{d\zeta} \left( \frac{V_o}{\zeta} \right) = \frac{dt}{d\zeta} G_2(\zeta)$$

where  $V_o(\zeta)$  and  $t(\zeta)$  are the solutions sought. The "initial" conditions for Eqs. (B.20) are given by

$$t(z_1) = t_e \quad (B.21)$$

$$V_o(z_1) = \frac{K_1 t_e}{\rho H}$$

Eqs. (B.20) which constitute a system of non-linear ordinary differential equations are solved numerically.

In view of Eqs. (B.16) and the form of the solution of Eqs. (B.20), the maximum plastic deformation is given by

$$U_o(t_f) = \frac{K_1 t_e^2}{2\rho H} + \int_{z_1}^{\zeta_f} V_o(\zeta) \frac{dt}{d\zeta} d\zeta \quad (B.22)$$

Since  $K_1$  and  $V_o(\zeta)$  are obtained numerically,  $U_o(t_f)$  is also obtained by numerical quadrature.

#### Discussion

Voice: In your second slide you showed your independent and dependent variables and your notations in dimensionless form using similitude techniques; it looked as if you had more than three repeating variables to get your non-dimensional terms.

Mr. Srinivasan: These are the only three independent dimensional quantities that cannot be put into an independent non-dimensional form.

# A THEORETICAL ANALYSIS OF THE DYNAMIC RESPONSE OF CONSTRUCTION CABLEWAY SYSTEMS

Kuen-Chun Tu  
(Former Graduate Student, University of Colorado)  
Stone & Webster Engineering Corporation  
Denver, Colorado

and

Robert S. Ayre  
Professor Emeritus,  
Department of Civil, Environmental, and Architectural Engineering  
University of Colorado  
Boulder, Colorado

Construction cableway systems were modeled mathematically in lumped parameters, the differential equations of motion written, and dynamic responses in bucket and carriage displacement and cable tension calculated. Vibration amplitudes and maximum cable tensions are presented in the form of response spectra (nonlinear system). A trial method of searching for optimum kinematic paths of the bucket is proposed and illustrated by a numerical example.

## INTRODUCTION

For many years cableways have been commonly used in heavy construction in difficult terrain, for example, in the construction of high concrete dams [1-3]. Construction cableway systems (see Fig. 1) are nonlinear, multi-degree-of-freedom vibration systems which are subject to transient excitation functions. It appears, however, that their analysis and design have generally been based on statics alone.

If they are operated slowly, static analysis is adequate, but for high speed operation it is desirable to investigate their dynamics. This paper presents, for some highly simplified cases, the maximum amplitudes of oscillation of the bucket and carriage and the maximum forces in the cables. Also investigated is the selection of the hauling and hoisting functions with the aim that the operating times and amplitudes of vibration be kept within acceptable limits.

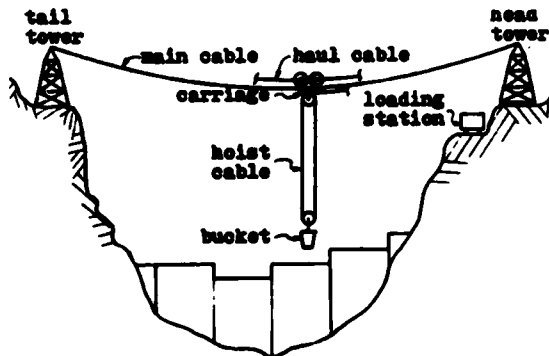


Fig. 1. Application of a cableway system in heavy construction

Cableways constitute a class of moving load systems. The transverse vibration of elastic systems under moving mass loads has long been a subject of interest. It has included studies of beams and bridges [4], plates, and tightly stretched cables, but we have found no investigations of the dynamic response of construction cableways in the published literature. There are a few references, however, which are of indirect interest [5-10]. As shown in Fig. 1, the cableway consists of the carriage, bucket, main cable, haul cable and hoist cable. The horizontal movement of the carriage is controlled by the endless haul cable. The bucket hoist cable is driven independently of the haul motion.

Three mathematical models were developed. Only the simplest one, having three degrees of freedom, is presented here. The differential equations for a much more complete model having 3 (n+2) degrees of freedom, where n is the number of lumped masses in the main cable, may be found in Ref. [11]. In addition, simplified single-degree-of-freedom systems were investigated to study the effect of wide variations in the x,y configuration of the bucket path. This led to a search by trial for optimum path configurations. The aim was to reduce the residual amplitude of horizontal oscillation of the bucket to acceptably small values and to minimum values if possible. The findings of the path studies for the single-degree-of-freedom system were then used in a reinvestigation of an example from the three-degree-of-freedom system. The investigation was carried out in the Department of Civil and Environmental Engineering at the University of Colorado at Boulder.

#### MATHEMATICAL MODEL

Basic assumptions: (a) Main cable and hoist cable are elastic and obey Hooke's Law. (b) Haul cable is inextensible. (c) Portions of the cable masses are lumped as follows: haul cable and hoist cable at the carriage and bucket; main cable in a single partial mass at the carriage. (d) Support towers are rigid. (e) Carriage and bucket are point masses. (f) Kinematic motions of carriage and bucket are specifiable functions of time (haul and hoist functions, respectively). (g) Frictional effects are neglected. (h) Motion is limited to x,y vertical plane. (i) Sag in main cable is small.

The model has three degrees of freedom in vibratory response as follows: vertical displacement of the carriage and vertical and horizontal displacements of the bucket. It may be shown that Eqs. (1) are the differential equations of motion [11].

For carriage:

$$M_c \ddot{y}_c = W_c \quad (1a)$$

$$+ A_b E_b \left\{ \frac{N(y_b - y_c)}{l_b} \left[ N + \frac{\sqrt{x_c^2 + y_c^2} - l_b}{\sqrt{(x_b - x_c)^2 + (y_b - y_c)^2}} \right] - \frac{y_c}{l_b} \left[ 1 + \frac{N \sqrt{(x_b - x_c)^2 + (y_b - y_c)^2} - l_b}{\sqrt{x_b^2 + y_b^2}} \right] \right\}$$

$$+ A_m E_m \frac{y_c}{l_m} \left[ \left[ \sqrt{x_c^2 + y_c^2} + \sqrt{(L - x_c)^2 + (y_c - d)^2} - l_m \right] \left[ \frac{1}{\sqrt{x_c^2 + y_c^2}} - \frac{1}{\sqrt{(L - x_c)^2 + (y_c - d)^2}} \right] \right]$$

For bucket:

$$M_b \ddot{x}_b = \quad (1b)$$

$$N A_b E_b \frac{x_c - x_b}{l_b} \left[ N + \frac{\sqrt{x_c^2 + y_c^2} - l_b}{\sqrt{(x_b - x_c)^2 + (y_b - y_c)^2}} \right]$$

$$M_b \ddot{y}_b = \quad (1c)$$

$$W_b + N A_b E_b \frac{y_c - y_b}{l_b} \left[ N + \frac{\sqrt{x_c^2 + y_c^2} - l_b}{\sqrt{(x_b - x_c)^2 + (y_b - y_c)^2}} \right]$$

in which  $x_c$  and  $t_b$  are the haul and hoist functions,  $M$  and  $W$  are mass or weight lumps;  $A$  and  $E$  are effective values of cross-sectional area and modulus of elasticity of cables;  $l_m$  is length of main cable;  $b$ ,  $c$  and  $m$  are subscripts referring to bucket (or hoist cable), carriage and main cable;  $N$  is number of parts in hoist cable;  $L$  is span between towers;  $d$  is vertical coordinate of top of tail tower. See Fig. 2. The equations were solved numerically by use of a CDC 6400 computer. The algorithm was based on the Runge-Kutta and predictor-corrector methods.

#### PROTOTYPE

A few construction cableways have had spans in excess of 3000 feet but their use has been limited to relatively light loads and low speeds. Normally the spans range from about 1000 to 3000 feet [12]. Important dimensions of the investigated prototype (Fig. 2) are as follows: span lengths,  $L = 1000, 2000$  and  $3000$  ft.; coordinates of initial rest position of bucket,  $x_1 = 100$  ft.,  $y_1 = 150$  ft.; coordinates of final rest position of bucket,  $x_f = 600$  ft.,  $y_f = 500$  ft.; both ends of main cable are at same level ( $d=0$ ); static sag of main cable is  $5\frac{1}{2}$  percent of span  $L$  [2]; hoist cable is in four parts ( $N=4$ ) between carriage and bucket sheaves, a value found in practice. Further details are shown in Table 1.

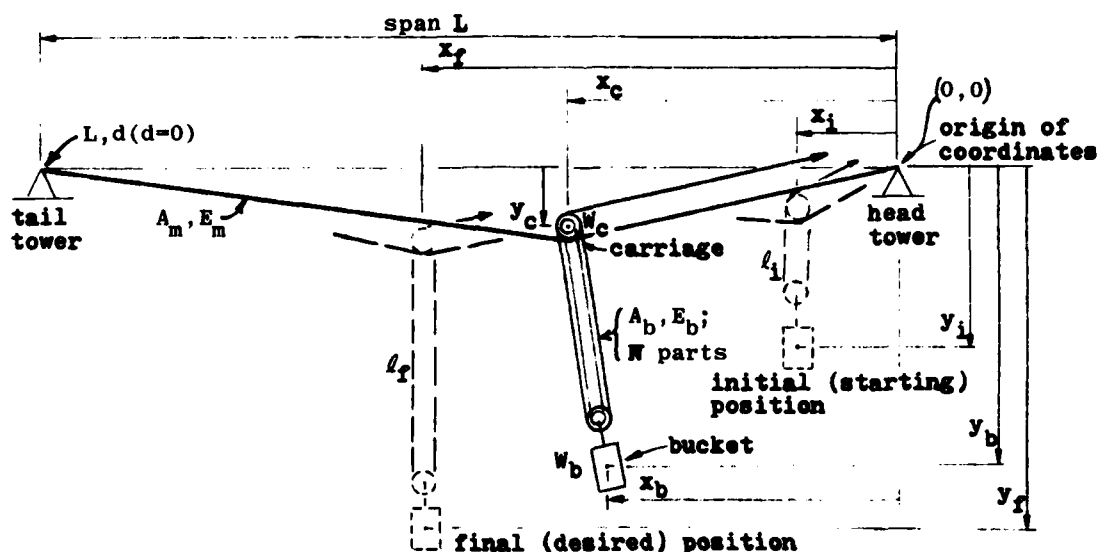


Fig. 2. Two-dimensional (x,y) model having three degrees of freedom

TABLE 1  
Load and Machinery Data.

Operational sizes and weights (cable diameters, carriage and bucket weights, etc.) are from "Handbook of Heavy Construction" by Havers and Stubbs [12]. Cable net cross-sectional areas, effective moduli of elasticity, and weights per unit length are manufacturers' catalog values.

Notation	Item	
$A_m$	Net cross-sectional area of 3 3/4 inches diameter main cable	6.7735 in <sup>2</sup>
$A_b$	Net cross-sectional area of 1 inch diameter hoist cable	0.4792 in <sup>2</sup>
$E_m$	Effective modulus of elasticity of main cable	$1.7 \times 10^7$ psi
$E_b$	Effective modulus of elasticity of hoist cable	$1.9 \times 10^7$ psi
$w_c$	Weight of carriage	14,250 lb
	Weight of 500 feet of hoist cable	850 lb
	Weight of 1000 feet of main cable	24,200 lb
	Weight of 1000 feet of haul cable (1 in. in diameter)	1,700 lb
	Total lumped weight at the carriage	41,000 lb
$w_b$	Weight of empty bucket	12,000 lb
	Weight of 8 cubic yards of fresh concrete (at approximately 150 pounds per cubic foot)	32,000 lb
	Weight of fall block and spreader	3,150 lb
	Weight of 500 feet of hoist cable	850 lb
	Total lumped weight at the bucket	48,000 lb

# HAUL-HOIST FUNCTIONS

Three displacement functions with finite rise-time  $\tau$ , having constant-slope front, versed-sine front, and cycloidal front [13] have been considered. The cycloidal front is the only one of these functions that does not require a theoretically infinite rate of change of acceleration (jerk) in passing from the initial static condition to the displacement function and in passing from the displacement function to the final static condition. It has been assumed, therefore, that the cycloidal function more nearly approaches actual operating conditions than the other two. One simple and two modified cycloidal functions were used as haul-hoist functions in the three groups of examples investigated.

The simple, symmetrical, cycloidal haul displacement function was used for "Example-One" motions. The modified cycloidal displacement functions for "Example-Two" and "Example-Three" motions were, in general, composed of an accelerating half-cycle cycloidal function, followed by a constant velocity function, which was followed by a decelerating half-cycle cycloidal function. These motions were unsymmetrical, the acceleration era being one-half the duration of the deceleration era. Under some conditions the intermediate constant-velocity era was not required. The hoist functions were the same as the haul functions in form except that the hoist time  $\tau_b$  was in all cases slightly longer than the haul time  $\tau_c$ . Fig. 3 compares the

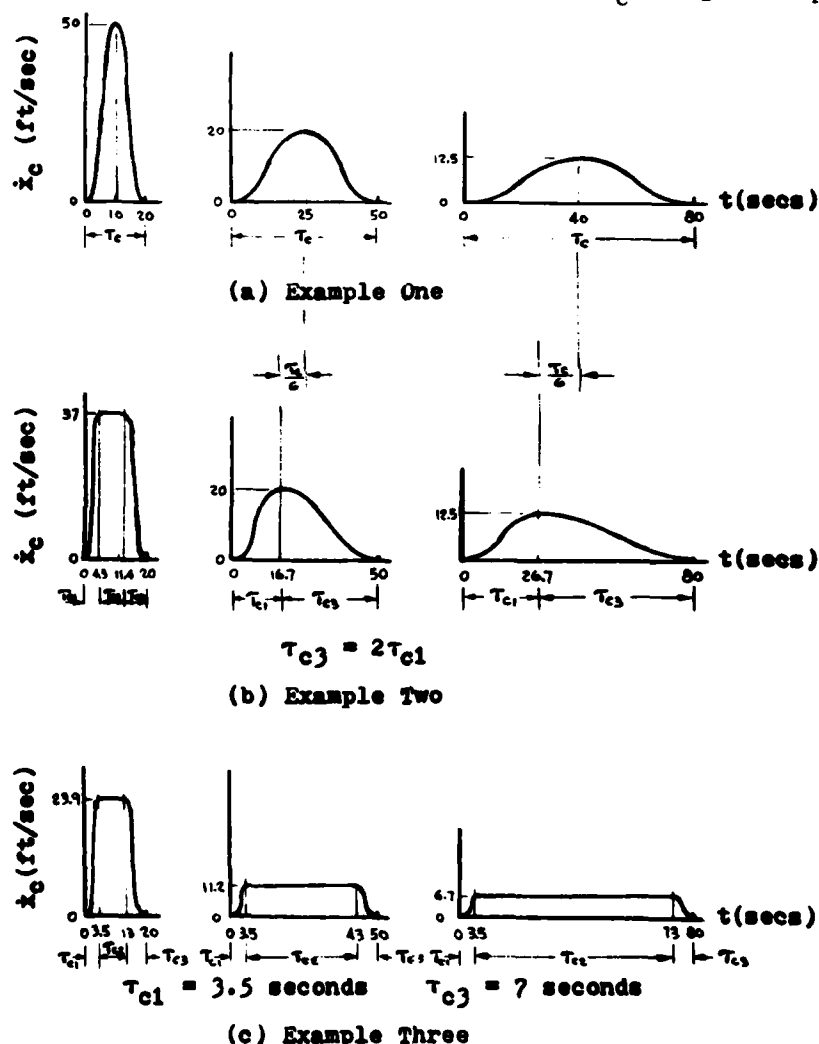


Fig. 3. Comparison of velocity-time curves for various forms of the haul-hoist function. (These curves have been labeled for the haul function.)



velocity-time haul curves (velocity pulses) for the three groups of examples for three values of  $\tau_c$  for each example. Since the haul distance ( $x_f - x_i$ ) was kept constant the areas under the velocity pulses are all equal [11].

#### DYNAMIC RESPONSE

**Example One; Simple Cycloidal Haul and Hoist Functions.** The displacement haul function consists of a cycloidal function plus a constant as follows:

$$x_c(t) = \frac{x_f - x_i}{2\pi} \left( \frac{2\pi t}{\tau_c} - \sin \frac{2\pi t}{\tau_c} \right) + x_i \quad (2)$$

where  $0 \leq t \leq \tau_c$ , and  $x_i$  and  $x_f$  are the initial and final horizontal locations. The displacement hoist function is given by:

$$l_b(t) = \frac{l_f - l_i}{2\pi} \left( \frac{2\pi t}{\tau_b} - \sin \frac{2\pi t}{\tau_b} \right) + l_i \quad (3)$$

where  $0 \leq t \leq \tau_b$ , and  $l_i$  and  $l_f$  are the initial and final lengths of the hoist cable.

The response spectra for horizontal maximum amplitudes of vibration of the bucket  $\Delta_{xb}$  have been shown in Fig. 4 for a cableway span of 1000 feet. The responses have been computed for five values of the haul duration  $\tau_c$  ranging from 20 to 90 seconds. Hoist durations  $\tau_b$  are in each case five seconds longer than the haul durations for operational reasons, that is,  $\tau_b = \tau_c + 5$ . The maximum amplitudes of vibration are very large for short durations of haul. For instance, for  $\tau_c = 20$  seconds they are:  $\Delta_{xb} = 170$ ,  $\Delta_{yb} = 38$  and  $\Delta_{yc} = 1.0$  feet for  $t < \tau_b$ ; and  $\Delta_{xb} = 180$ ,  $\Delta_{yb} = 40$  and  $\Delta_{yc} = 1.0$  feet for  $t > \tau_b$ . The bucket amplitudes for this case of very short operating time are obviously much too large for acceptable operation and have not been shown in Fig. 4. The responses for  $t > \tau_b$  are residual amplitudes of vibration. Since the vertical amplitudes of both bucket and carriage are much smaller than the horizontal amplitudes of the bucket, only the latter are shown here [11]. It is not surprising that the horizontal amplitudes for the bucket are much greater than the vertical amplitudes; the bucket is suspended as a pendulum.

In order for the operating times  $\tau_c$  and  $\tau_b$  to approach zero it would be necessary for the haul and hoist velocities to approach infinity. Such

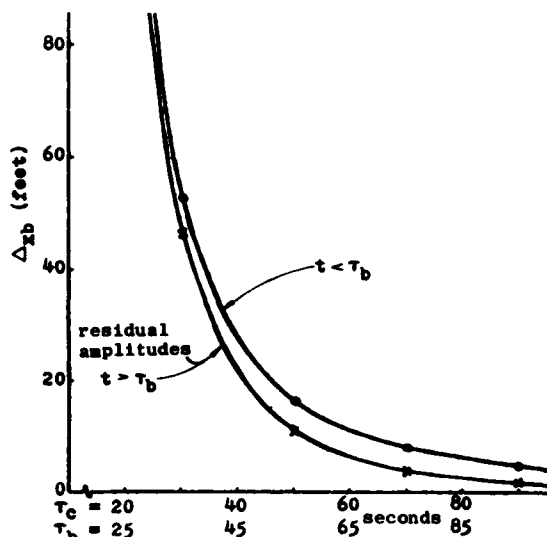


Fig. 4. Response spectra for maximum amplitudes of vibration, with simple, symmetric, cycloidal ("Example One") haul-hoist functions operating the cableway system of 1000 feet span, with haul-hoist distances as specified in a PROTOTYPE. For  $t > \tau_b$ , the amplitudes  $\Delta_{xb}$  are residual amplitudes of vibration.

conditions are physically impossible. There are thus limitations on the lower values of  $\tau_c$  and  $\tau_b$  of the prototype system and also the mathematical model. No attempt, therefore, has been made to calculate response for very small values of operating time. Within the range of investigation of operating times the maximum amplitudes of vibration decrease greatly as the operating time is increased. If the operating time is large the amplitudes approach zero and the system approaches static behavior.

Fig. 4 illustrates how response spectra may be used for setting lower limits on haul-hoist times. For example, for the particular conditions represented (span, haul-hoist distances, haul-hoist functions), if the maximum allowable horizontal residual amplitude of the bucket ( $\Delta_{xb}$  for  $t > \tau_b$ ) is 10 feet the shortest allowable haul time  $\tau_c$  is about 50 seconds.

**Example Two; Modified Cycloidal Haul and Hoist Functions.** In this example the maximum velocities for hauling the carriage and lowering the bucket have been limited to 37 and 16

feet per second, respectively, which are the maximum values found in the published literature. Span lengths of 1000, 2000 and 3000 feet were investigated. The mathematical descriptions of the displacement-time, haul-hoist functions are basically simple, but since there are three eras, the initial and terminal values as well as displacement-time functions must be given for each era. The whole becomes cumbersome and will not be included here [11].

In Example-Two motions an upper limit has been placed on the haul velocity. Consequently high values of acceleration and deceleration may be necessary under some conditions. In Fig. 3b, haul velocity functions have been shown for  $\tau_c = 20, 50$  and  $80$  seconds. The curve for the 20-second duration must include a constant velocity era if the maximum haul velocity is limited to 37 feet per second. The operating durations of 50 and 80 seconds, however, do not require the presence of constant velocity eras in order to satisfy the haul distance requirement ( $x_f - x_i$ ) within the specified durations.

For the conditions calculated the residual amplitudes ( $t > \tau_b$ ) were generally smaller than the amplitudes during the haul-hoist operation ( $t < \tau_b$ ). It is reasonable to assume that this desirable result may occur when the haul-hoist functions involve decelerations which are numerically smaller than the accelerations, but it cannot be assumed that the result will hold in all cases. No very significant difference was found in the behavior of the system as the span length was changed. Results similar to Fig. 4, consistent with change in span length, were obtained [11].

Cable strength is important. The maximum tensile forces (dynamic plus static) of the main cable and the hoist cable have therefore been calculated. The maximum static tensile force occurs when the bucket is located at the middle of the span (assuming the bucket is hauled to mid-span or beyond). In the investigation of the model the bucket is hauled in each case for the same distance (600 feet) from the head tower. In the cableway which spans 1000 feet, the bucket is thus hauled past the middle point of the span, and the static maximum tensile force is 330,000 pounds. In the cableways having spans of 2000 and 3000 feet, however, the bucket is hauled for distances equal to only three-tenths and

two-tenths of the span lengths, respectively, and the static maximum tensile forces are 305,000 and 271,000 pounds, respectively. These last two values are less than the tensile force when the bucket is at mid-span. It could be argued that the ratio of haul distance to span length should have been kept constant in the investigation. It was decided instead to keep the absolute value of haul distance a constant. The curves of the maximum tensile forces in the cables are shown in Fig. 5. At values of  $\tau_c$  greater than

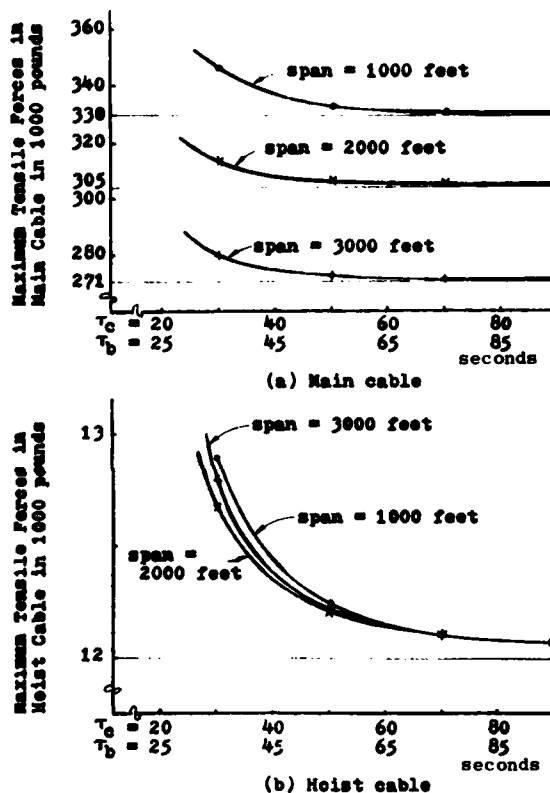


Fig. 5. Maximum tensile forces (dynamic plus static) in cables; "Example-Two" haul-hoist functions; three different span lengths; haul-hoist distances as specified in PROTOTYPE.

about 50 seconds, the maximum tensile forces in the main cable approach their asymptotes which are the maximum static tensile forces. The curves of the maximum tensile forces in the hoist cable for three different span cableways almost coincide with each other for  $\tau_b$  greater than about 60 seconds; their static asymptotes are independent of span length.

**Example Three; Modified Cycloidal Haul and Hoist Functions.** In this example, the durations for the acceleration and deceleration eras are fixed and they are not dependent on the total duration of the operating era. There always exist three eras in each operating procedure but the magnitude of the velocity in the constant velocity era is varied as the operating time is varied. In Fig. 3c three velocity haul functions are shown. All of the acceleration eras last 3.5 seconds and the deceleration eras last 7 seconds. Each of the functions includes a constant velocity era during which the velocity is a maximum. Since the durations of the acceleration and deceleration eras were very short, the maximum amplitudes of vibration were found to be very large especially for the horizontal oscillation of the bucket. The dynamic behavior of the system was concluded to be unacceptable [11]. The reason is presumably in the large accelerations involved in the haul-hoist functions.

#### SEARCHING FOR OPTIMUM PATHS

For safety and operational reasons it is necessary to limit the residual amplitudes of vibration. The calculations show that the horizontal residual amplitudes of the bucket may be of the order of ten or twenty times the vertical residual amplitudes for equal operating durations of the same example. Two methods were developed in the investigation for the purpose of reducing the horizontal residual amplitudes. They are based on the assumption that an approximately straight path from pick-up point to deposit point, as used in the calculations in the first parts of the investigation is not necessarily the best path. The idea underlying the natural period method is based on the characteristics of the response spectrum for residual amplitude for an undamped, single-degree-of-freedom, linear oscillator acted upon by an excitation function which is a simple cycloidal function of time. The important feature is the existence of zeros in the theoretical response spectrum as shown in Fig. 6 [13]. In this proposed method it is assumed that the bucket suspension length, Fig. 7, can be maintained constant until the bucket is over the desired point of deposit and that the bucket can then be lowered vertically to the deposit point. The resulting idealized path thus consists of two straight lines, one horizontal, the other vertical; Fig. 8. The bilinear path method

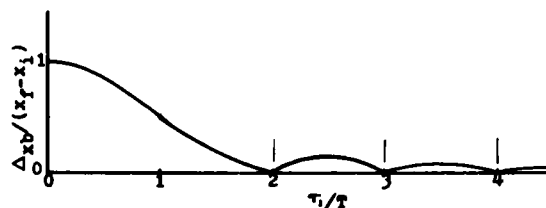


Fig. 6. Spectrum of residual amplitude resulting from the cycloidal function applied to an undamped, single-degree-of-freedom, linear oscillator [13].

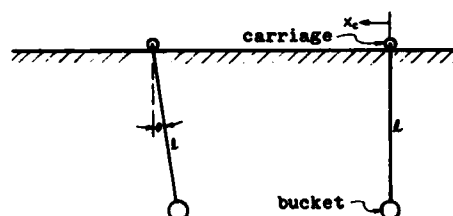


Fig. 7. A single-degree-of-freedom linear system with constant pendulum length and rigid horizontal path for the carriage; limited to small angular displacements;  $x_c$  is a specified function of time.

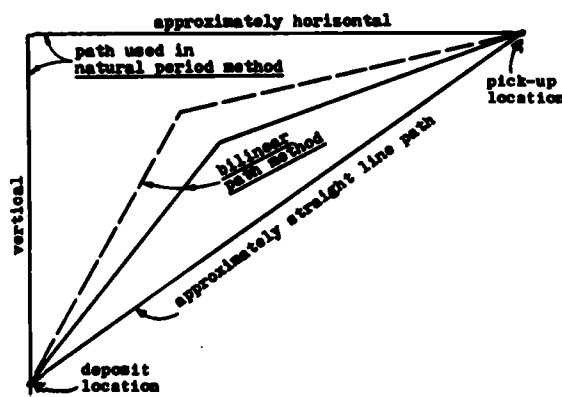


Fig. 8. The family of paths used in searching for minimum residual horizontal amplitude of vibration of bucket.

employs a limited generalization of the paths represented by the natural period

method, as one extreme, and the method employed in the earlier part of this investigation which resulted in a single, approximately straight line path.

The family of paths resulting from the three methods is shown in Fig. 8. Paths of still more general shape, either multilinear or curvilinear, can be imagined, but it seems unlikely that they would lead to a relatively simple determination of paths which approach an optimum shape. For practical reasons related to the physical topography of canyon construction sites it is generally not feasible to use paths which drop below a straight line connecting the pick-up and deposit locations. Therefore, the investigation of paths has been limited to the upper triangular region shown.

**Natural Period Method.** The "cableway" is reduced to a single-degree-of-freedom pendulum system which includes a carriage traveling on a horizontal rigid path and a bucket suspended by a massless, inextensible, constant length cable; Fig. 7. The haul function  $x_c$  which controls the displacement of the carriage is a cycloidal function of time with the duration of haul era  $\tau_1$ . It is assumed that the amplitudes of oscillation are small. The spectrum of the residual amplitude of the bucket resulting from the cycloidal function is shown in Fig. 6. The natural period of the pendulum can be found from the known relation:

$$T = 2\pi \sqrt{\frac{l}{g}} \quad (4)$$

in which  $l$  is the length of the cable. The residual amplitude of vibration is theoretically zero [13] if the duration of the haul era  $\tau_1$  is an integer multiple (excepting  $n = 1$ ) of  $T$ , that is, for  $t \geq \tau_1$ ,  $\Delta_{xb} = 0$ , if

$$\tau_1 = nT, \text{ where } n = 2, 3, 4, 5 \dots \quad (5)$$

It is assumed that this characteristic may be applied approximately to the operation of the actual cableway system in order to approach the minimum horizontal residual amplitude of vibration of the bucket. Actually, for the prototype cableway system, the path on which the carriage travels is not rigid, straight and horizontal as has been assumed here. The maximum slope of the path is small, however, so that the influence of the static shape of the path on the horizontal oscillation of the bucket can be assumed to be small.

The natural period method has been applied to the three-degree-of-freedom cableway model, having a span of 2000 feet, described previously. The initial pendulum length  $l$ , which is kept constant for the haul era ( $0 \leq t \leq \tau_1$ ), is 95 feet and  $T$  is 11 seconds. The dynamic response has been analyzed for  $\tau_1 = 2T = 22$  seconds and  $\tau_2 = 18$  seconds where  $\tau_2$  is the lowering time (hoist era). The total operating duration  $\tau = (\tau_1 + \tau_2) = 40$  seconds. The residual amplitudes of vibration are as follows:  $\Delta_{xb} = 2.8$ ,  $\Delta_{yb} = 0.5$  and  $\Delta_{yc} = 0.5$  feet. These displacements are very small compared to the results shown in the previous sections for the path consisting of one approximately straight line. The maximum tensile force in the main cable is 336,000 and in the hoist cable is 14,000 pounds. These values are far smaller than the corresponding breaking strengths of the main and hoist cables.

The obvious disadvantage of the natural period method, however, is that the path of the bucket is substantially longer (Fig. 8) and therefore the travel velocities must be higher, for the same total operating times, than in the other two methods. The more general, bilinear path method, which provides for simultaneous motion in the horizontal and vertical directions and as a result lower average velocities of travel, is developed in the next section.

**Bilinear Path Method.** As in the natural period method, the cableway system has been simplified to a single-degree-of-freedom pendulum suspended from a carriage which moves along a rigid, straight, horizontal path. The pendulum length, however, is varied during the haul-out era. The cable is assumed as before to be massless and elastically inextensible. Fig. 9.

The kinematic path of the bucket is specified as a bilinear path, but the bucket may oscillate relative to that path. The kinematic displacement of the bucket along the path from the starting position to the desired final position is a cycloidal function of time, which is

$$P_t = \frac{P_l}{2\pi} \left( \frac{2\pi t}{\tau} - \sin \frac{2\pi t}{\tau} \right), \quad (6)$$

in which  $P_t$  is the displacement of the bucket along the path at time  $t$ ,  $P_l$  is the total length of the path, and  $\tau$  is the operating duration. The location of the knee point ( $x_k, y_k$ ; Fig. 9) is the key to this method. The lengths

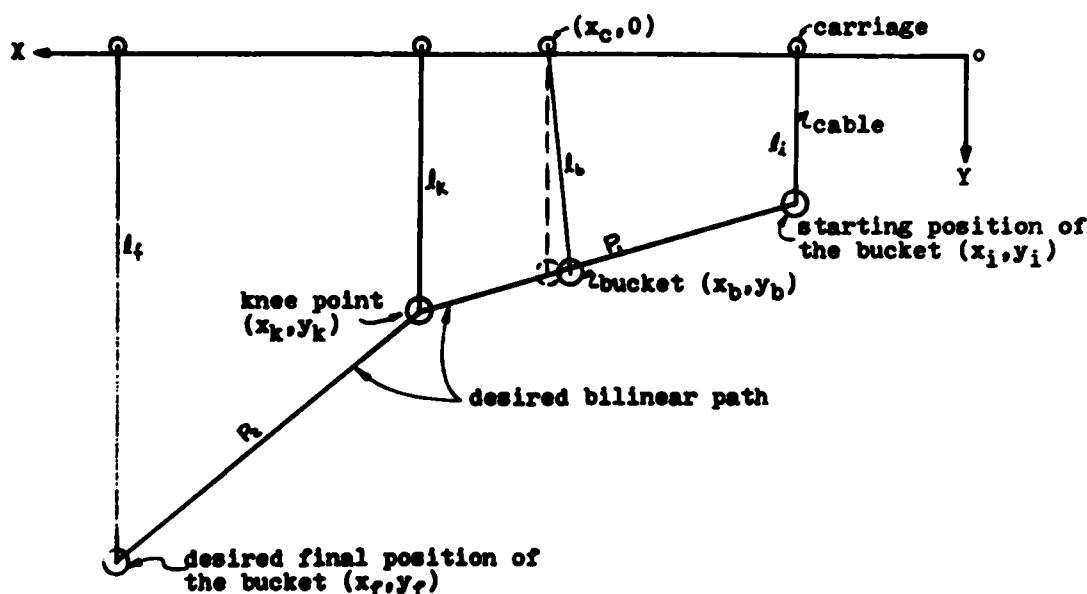


Fig. 9. A single-degree-of-freedom pendulum system with varying length of pendulum.

of the path segments are given by the expressions:

$$P_1 = \sqrt{(x_k - x_i)^2 + (y_k - y_i)^2},$$

$$P_2 = \sqrt{(x_f - x_k)^2 + (y_f - y_k)^2} \quad (7)$$

where  $P_1 + P_2 = P_t$ .

For small vibrations the differential equation of motion of the pendulum is:

$$\ddot{x}_b = (g - \ddot{y}_b) \frac{x_b - x_c}{l_b} \quad (8)$$

in which  $x_b$  is the horizontal vibratory displacement of the bucket,  $x_c$  is the horizontal displacement of the carriage (haul function),  $y_b$  is the vertical coordinate of the kinematic path of the bucket and  $l_b$  is the variable length of the pendulum (hoist function). If the carriage path is horizontal,  $l_b = y_b$ . The input time-functions  $x_c$ ,  $y_b$  and  $l_b$  depend on the specified geometry of the system (Fig. 9 and Eqs. 7) and the bucket-path time function  $P_t$  (Eq. 6) [11].

The dynamic responses of the bucket for many different bilinear paths having different locations of the knee point but all for the operating duration  $\tau = 40$  seconds have been calculated. In Fig. 10 each plotted point represents the knee point for a

bilinear path (see, for example, the dashed bilinear path with knee at coordinates  $x_k = 400$  and  $y_k = 200$  feet). The numerals written to the left of the knee points give the corresponding horizontal residual amplitudes  $\Delta_{xb}$ . Only about one-third of the approximately 150 knee points for which response calculations were made have been shown. Iso-residual-amplitude lines (lines of equal residual amplitude) have been drawn resulting in what might be called an iso-residual-amplitude map. The single-straight-line path I-F is a special case of the bilinear path and this straight line is an iso-residual-amplitude line for which the residual amplitude  $\Delta_{xb} = 36$  feet.

Fig. 10 shows that the bilinear path for which the knee point is located at about  $x_k = 380$  and  $y_k = 250$  feet results in a minimum residual amplitude for the operating duration  $\tau = 40$  seconds. Iso-residual-amplitude maps were also calculated for  $\tau = 30, 35, 50, 70$ , and 80 seconds. The knee points resulting in minimum residual amplitudes for the various values of  $\tau$  were then plotted in the  $xy$  plane. A curve drawn through these points is the locus of desired knee points [11].

The path of the carriage in the prototype system, however, is not a horizontal straight line. Since the sag in the main cable is small an

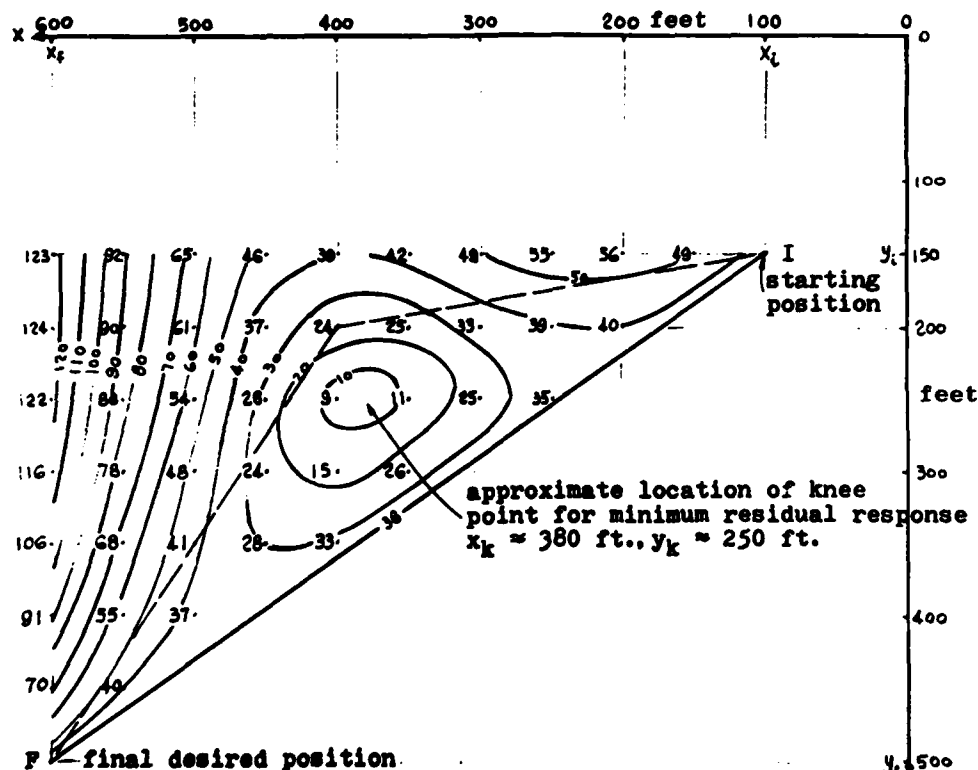


Fig. 10. Iso-residual-amplitude map for location of the knee point of the bilinear path for operating duration  $\tau = 40$  seconds. Small numbers on contour map are bucket horizontal residual amplitudes in feet.

inclined straight path may be a reasonable approximation to the curvilinear path of the carriage of an actual system. An iso-residual-amplitude map was calculated for the operating duration  $\tau = 40$  seconds for a moving pendulum system for which the rigid path of the carriage is an inclined straight line. The bilinear path knee point resulting in minimum residual amplitude was found at about  $x_k = 400$  and  $y_k = 300$  feet. These values may be compared with the previously obtained 380 and 250 feet. The iso-residual-amplitude map was strongly similar to Fig. 10 [11].

The next step was to apply the results of the optimization of path obtained for the single-degree-of-freedom model to the three-degree-of-freedom model. The three-degree-of-freedom model having 2000 foot span has been analyzed for one value of the operating time  $\tau = 40$  seconds, using a bilinear path with knee point at  $x_k = 400$  and  $y_k = 300$  feet. The calculated residual amplitudes were:  $\Delta_{xb} = 2.2$  feet,  $\Delta_{yb} = 4.0$  feet,  $\Delta_{yc} = 4.0$  feet. The great reduction in  $\Delta_{xb}$  is the

purpose of this method. It is interesting to note that the vertical maxima in this particular example are greater than the horizontal maximum. All three values are reasonably small, however. The maximum tensile forces in the main and hoist cables are 375,000 and 36,800 pounds respectively. Both values are far smaller than the breaking strength. While this procedure for securing great reduction in bucket horizontal residual amplitude was tested for only one value of  $\tau$  it seems to show significant promise.

#### CONCLUSIONS

The two principal criteria pertinent to the dynamics of construction cableway operation appear to be time consumed in operation, and safety. If the system is operated very slowly its response may be determined by statics alone but as the speed of operation is increased (operating time decreased) the dynamic effects become increasingly important as would be expected. The dynamic effects include mechanical oscillation of parts of the system, especially the possibility of large

pendular displacements of the suspended bucket, and the resulting addition of dynamic increments to the stresses in the cables and other components. Bucket oscillation is not only potentially dangerous to personnel but, if it occurs in the vicinity of the desired location of unloading, may result in lost time in waiting for the oscillation to subside in order that the load can be accurately placed.

The mathematical model presented here involves many simplifications of the prototype. Specific quantitative conclusions are presented but their application to cableway operation in general must be limited to trends and to illustrating what sorts of response calculations can be made.

Within the limits of the investigation restricted to haul and hoist (lowering) distances of 500 and 350 feet, respectively, the system shows insignificant dynamic response if the operating time is greater than about 80 seconds. If the operating time is less than about 50 or 60 seconds, however, the amplitudes of vibration increase greatly and, depending on the limits imposed, the operation may be unacceptable (Fig. 4). The vertical amplitudes of vibration of the carriage are generally smaller than those for the bucket and both are generally much smaller (by a factor of 10, 20 or more) than the horizontal amplitudes of the bucket. In most cases the residual amplitudes of vibration are significantly smaller than the amplitudes occurring during the haul-hoist operation.

The change in dynamic increments of cable force follows the same general pattern as change in vibration amplitude. Cable strength (according to the dimensions quoted in the available literature), however, appears to be a less critical consideration than bucket vibration amplitude. The ratio of breaking strength to maximum tensile force (static plus dynamic) was found to be not less than 3.5 for the main cable and 2.5 for the hoist cable (Fig. 5).

Pendulum response of the bucket (horizontal vibration amplitude), rather than vertical vibration of the bucket or carriage, or dynamic cable force, seems to control the safety limits to be placed on operating (haul-hoist) times.

Three span lengths (1000, 2000 and 3000 feet) were investigated. The

resulting variations in response do not change the conclusions already stated. In considering the effects of change in span length it should be remembered, however, that the haul-hoist distances were kept constant even though the span length was changed.

Three functional variations in the haul-hoist time functions were investigated (Fig. 3). The steep-fronted, plateau-like velocity functions (Example Three) gave much less favorable response results than the other two variations (Examples One and Two). The high accelerations required in both the acceleration and deceleration eras of Example Three functions are the apparent cause of the unacceptably large amplitudes of vibration. Examples-One-and-Two functions gave approximately equal results and both appear to be acceptable.

The search by trial for optimum configurations of the kinematic path of the bucket (Figs. 6-10) resulted in surprisingly large reductions in the horizontal residual amplitudes of vibration of the bucket. The information from the single-degree-of-freedom trial study, when applied to the three-degree-of-freedom model resulted in a reduction of bucket horizontal residual amplitude by a factor of about ten. This result was achieved for a case having the short operating time of 40 seconds.

Extensions of the investigation. The numerical results have been concerned only with the operation of hauling out and lowering the loaded bucket to the dumping position. The analysis for lifting and hauling back the empty bucket can readily be carried out. Further study of optimum path of the bucket is needed. Cableway models having  $2(n+2)$  or  $3(n+2)$  degrees of freedom can be investigated by using the equations for the more complete mathematical model presented in Ref. [11]. Wind effects can be included by using the model having  $3(n+2)$  degrees of freedom. The effect of damping could be included without difficulty by the addition of appropriate terms in the differential equations. Damping, however, is perhaps not of major importance in this transient problem.

In the operation of prototype systems a skilled, experienced human operator undoubtedly can control to some extent, through a process of human feedback, the dynamic increments of response and thus keep the oscillations of the system, particularly the

pendulous oscillations of the bucket, within reasonable limits. There is no obvious way, however, of introducing spontaneous human control into the mathematical model except perhaps through the use of interactive computer graphics.

Another consideration which has not been included is that concerned with the response of the electric drive system. It has been assumed that certain mechanical excitation functions could be specified and achieved in practical operation. This assumption is not entirely realistic, one reason being the existence of inertia in the drive system.

Finally, it seems likely that differential equations of the type of those presented, with some changes and the addition of several more degrees of freedom, can be modified to apply to other classes of cableway transportation systems. In the case of a gondola system, for example, the hoist cable would be removed from the analysis and the bucket (assumed point mass) would be replaced by the gondola (assumed rigid body) attached by a pivot at the carriage.

#### REFERENCES

1. A. J. Ackerman, "Discussion of Norris Dam Construction Cableways", Proceedings of American Society of Civil Engineers, Vol. 67, No. 8, Part 2, pp. 510-517, October 1941.
2. R. T. Colburn, and L. A. Schmidt, Jr., "Norris Dam Construction Cableways", Proceedings of American Society of Civil Engineers, Vol. 67, No. 8, Part 2, pp. 470-501, October 1941.
3. G. M. Shupe, "Dworshak Dam: Advanced Systems for Producing Aggregates and Placing Concrete", Civil Engineering, ASCE, pp. 35-38, March 1969.
4. R. S. Ayre, L. S. Jacobsen, and C. S. Hsu, "Transverse Vibration of One- and Two-Span Beams Under the Action of a Moving Mass Load", Proceedings of the First U.S. National Congress of Applied Mechanics (ASME), pp. 81-90, 1951.
5. G. M. Savin, "Basic Dynamic Equations of a Mine Lifting Cable", Applied Mechanics (in Russian), Vol. 1, No. 1, pp. 5-22, 1955.
6. V. E. Shamanskii, and V. N. Shevelo, "On Longitudinal Vibrations of an Elastic String (Cable) of Variable Length", Izv. Akad. Nauk. SSSR, Otd., Tekh. Nauk. No. 3, pp. 65-71, May/June 1959.
7. A. V. Krishna Murty, "A Lumped Inertia Force Method for Vibration Problems", Aeronautical Quarterly, Vol. 17, Part 2, pp. 127-140, May 1966.
8. R. F. Dominguez, and C. E. Smith, "Dynamic Analysis of Cable Systems", Journal of the Structural Division, Proceedings of the American Society of Civil Engineers, Vol. 98, No. ST8, pp. 1817-1834, August 1972.
9. Horace Lamb, "Higher Mechanics", 2nd Ed, The University Press, Cambridge, England, 1929.
10. S. Timoshenko, and D. H. Young, "Advanced Dynamics", McGraw-Hill Book Company, New York, 1948.
11. Kuen-Chun Tu, "A Theoretical Analysis of the Dynamic Response of Construction Cableway Systems", Ph.D. Thesis, University of Colorado, Boulder, 1974.
12. J. A. Havers, and F. W. Stubbs, Jr., eds., "Handbook of Heavy Construction", 2nd Ed. Section 14, "Cableways and Drag Scrapers", pp. 14-1 to 14-25, by R. M. Welsh, and C. H. Hubbell, McGraw-Hill Book Company, New York, 1971.
13. L. S. Jacobsen, and R. S. Ayre, "Engineering Vibrations", McGraw-Hill Book Company, New York, 1958.



## EMPIRICAL INVESTIGATION OF WATER-SHOCK LOADING OF A CONCRETE HALF-SPACE

Charles R. Welch and Landon K. Davis  
U. S. Army Engineer Waterways Experiment Station  
Corps of Engineers  
Vicksburg, Mississippi

Measurements have been made of strain induced in a simulated concrete half-space by small spherical explosive charges detonated in an overlying body of water. These measurements were used to infer peak normal stress in the concrete directly below the charge. The results indicated that peak normal stress near the vertical axis could be predicted using geometric techniques. These techniques consider the peak normal stress at the shock front to be a function of the increasing surface area of the wave.

### INTRODUCTION

The U. S. Army Engineer Waterways Experiment Station has recently conducted a series of investigations into the effects of water-shock loading from spherical charges on a concrete half-space. The investigations confirm that peak radial stress in the concrete opposite the charge can be accounted for by using a model based on geometric techniques. These techniques have been used with some success in the past to predict peak particle parameters at a free surface [1] and at various depths in a layered geologic media [2, 3].

Although the research stems from a military requirement to predict damage to concrete dams, bridge piers, and other massive concrete hydraulic structures attacked by conventional bombs and small nuclear weapons, the results will also have numerous civil applications. These include such problems as demolition and removal of obsolete underwater structures that are near newly built replacement facilities, underwater blasting for construction adjacent to existing dams or powerhouses, the removal of debris lodged against bridge piers, etc.

### DESCRIPTION OF TESTS

A concrete half-space was simulated by a large rectangular slab of unreinforced concrete of approximate dimensions 32.8 by 16.4 by 6.56 ft. The concrete used in the slab had a density of 136 lb/ft<sup>3</sup>, a dilatational wave velocity of 10,650 ft/sec, and a measured dynamic modulus of elasticity of approximately  $3.93 \times 10^6$  psi. The slab formed the bottom of a shallow (about 7 ft) basin so that various water levels could be maintained over the slab. The slab was instrumented at nine locations (see Figures 1 and

2) with vertical and slant strain gage arrays, with the slant gage arrays making an angle of approximately 20 degrees with respect to the vertical. The gages used at each location

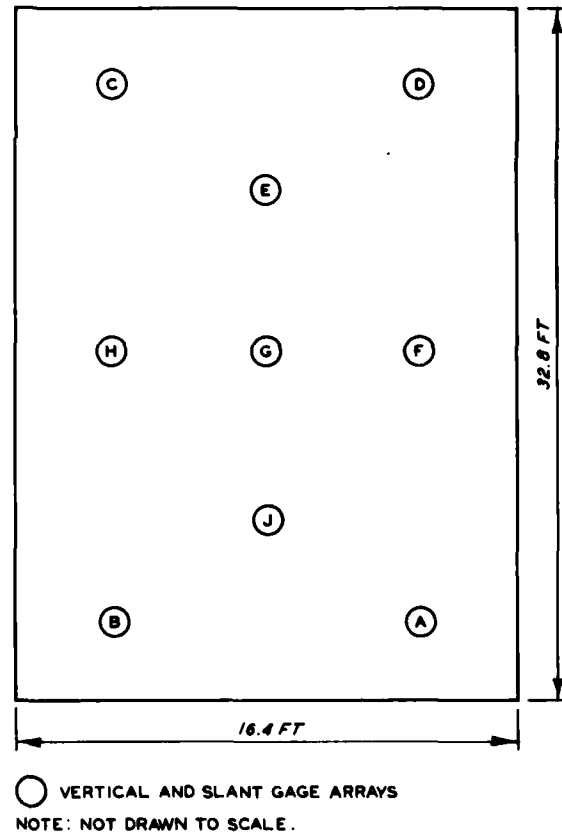


Figure 1 - Top view of test slab

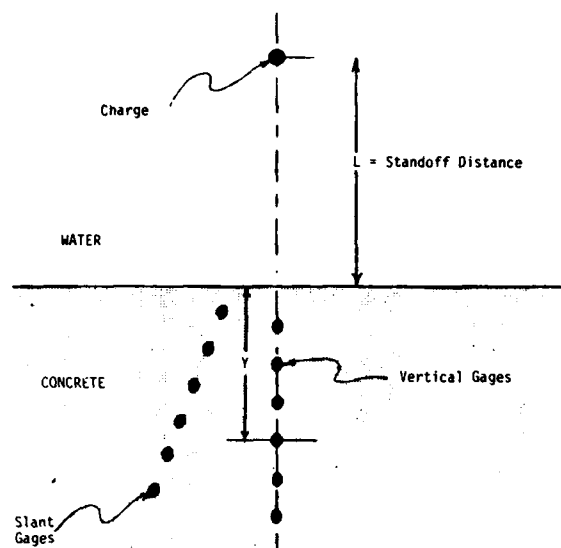


Figure 2 - Typical shot geometry showing gage locations

were 350-ohm, 1/8-in.-long, foil strain gages with gage factors of 3.18. The gages were located at approximately 1-ft intervals from a level of about 0.64 ft below the water-concrete interface to about 5.82 ft below the

interface. Output of the gages was recorded on an FM magnetic tape recording system with a linear frequency response of approximately 20 kHz.

A typical shot geometry is shown in Figure 2. Eleven shots have been fired to date over various gage locations in the slab. In each case the charge was located directly above the associated vertical gage array (see Table 1). All charges were spherical in shape. These included two 2-lb TNT charges, three 1/2-lb TNT charges, and six charges consisting of 0.188 lb of C-4 type explosive (each equivalent to 1/4 lb of TNT in producing water shock). The C-4 charges were hand molded into shape. The distance from the charge to the slab varied over a range of approximately 6 ft for the eleven tests, ranging from charges located surface-tangent to the slab to charges located at the water surface. Standard engineering No. 10 blasting caps were used to detonate the charges. The water level above the slab was approximately 6 ft for all eleven shots. The various parameters for each shot are shown in Table 1.

#### THE GEOMETRIC TECHNIQUE AS APPLIED TO CURRENT TOPIC

Cooper and Seamon [1] suggest that the peak particle velocity normal to a dilatational wave front, and hence the peak stress normal to the wave front, assuming the two

Table 1  
Test Descriptions and Derived Transmission Coefficients

Shot No.	Site Location (Refer to Figure 1)	Special Characteristics of Charge Location	Type of Charge Used	TNT Equivalent Charge Weight lb	Standoff Distance from Charge Center of Gravity to Slab	Coefficient A	Exponent $\beta$
1	J	None	C-4	1/2	3	9,365	1.595
2	J	None	C-4	1/2	3	8,112	1.465
3	B	None	C-4	1/4	3	7,301	1.810
4	B	None	C-4	1/4	2	10,210	1.601
5	B	None	C-4	1/4	1	15,870	1.224
6	B	Surface-tangent to slab	C-4	1/4	0.083	680,800	1.447
7	A	None	C-4	1/4	0.56	47,430	1.421
8	A	Surface-tangent to slab	C-4	1/4	0.083	1,364,000	1.575
9	H	Surface of water	TNT	2.00	6.00	4,065	1.654
10	H	Surface of water	C-4	1/2	5.9	2,650	2.045
11	H	None	TNT	2.00	1.00	37,150	1.307

$$\sigma_{n2} = \sigma_{n1} \left( \frac{dA_1}{dA_2} \right)^{\beta/2} \quad \beta \geq 1$$

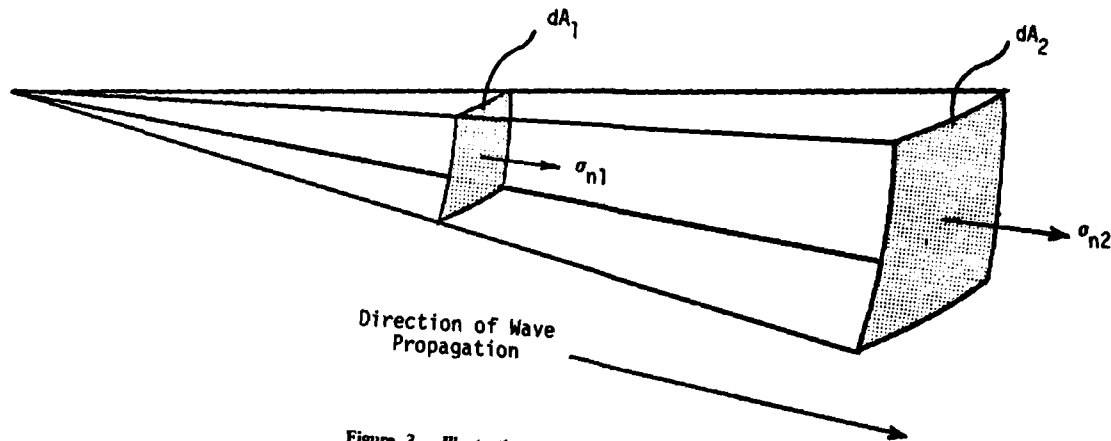


Figure 3 - Illustration of Geometric Technique

to be colinear, is a function of the increasing surface area of the wave. Referring to Figure 3, let  $\sigma_{n2}$  be the peak normal stress at a distance along the wave path from a reference point. Then  $\sigma_{n2}$  will be given by

$$\sigma_{n2} = \sigma_{n1} \left( \frac{dA_1}{dA_2} \right)^{\beta/2} \quad \beta \geq 1 \quad (1)$$

where  $\sigma_{n1}$  is the peak normal stress at a reference point and  $dA_1/dA_2$  is the ratio of an area element  $dA_1$  of the wave at the reference point to an area element  $dA_2$  of the wave located at the position of  $\sigma_{n2}$ .

A spherical shock front, upon passing a water-concrete interface, will be refracted as a result of the difference in velocities of the wave in the two media (refer to Figure 4). If acoustic behavior is assumed, this refraction process will obey Snell's Law or

$$\frac{\sin \theta_1}{\sin \theta_2} = \frac{c_1}{c_2}$$

where  $c_1$  is the velocity of the wave in the water and  $c_2$  is the velocity of the wave in the concrete. It can be shown that near the vertical axis the ratio of a wave area element at the interface to a second wave area element at a distance  $y$  in the concrete is given by

$$\frac{dA_1}{dA_2} = \left( \frac{L}{L + \frac{c_2}{c_1} y} \right)^2 \quad (2)$$

where  $L$  is the distance from the wave source to the interface. Employing the above relation along with Equation 1 gives

$$\sigma_{n2} = \sigma_{n1} \left( \frac{L}{L + \frac{c_2}{c_1} y} \right)^{\beta} \quad \beta \geq 1 \quad (3)$$

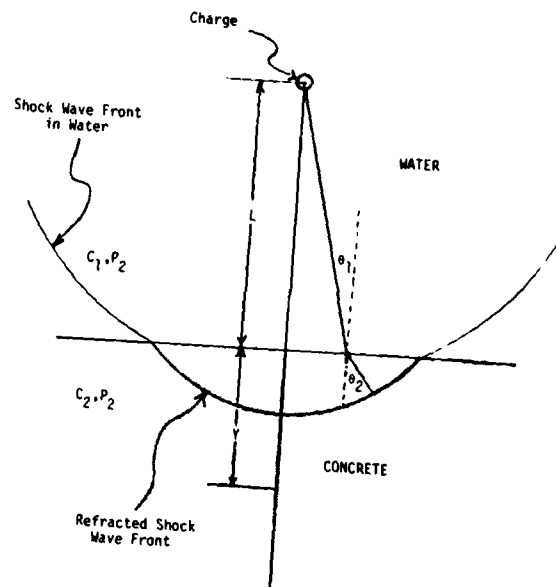


Figure 4 - Refraction of spherical wave upon crossing interface

where  $\sigma_{n2}$  is the peak stress normal to the wave front near the vertical axis at a distance  $y$  into the concrete, and  $\sigma_{n1}$  is the peak stress normal to the wave front near the vertical axis just inside the concrete boundary at the interface. The value of  $\sigma_{n1}$  can be determined from

$$\sigma_{n1} = PT \quad (4)$$

where  $P$  is the incident peak pressure at the water-concrete interface and  $T$  is the stress transmission coefficient predicted from acoustic theory. Along the vertical axis,

$$T = \frac{2\rho_2 c_2}{\rho_2 c_2 + \rho_1 c_1}$$

where  $\rho_1$  and  $c_1$  are the density and wave velocity in the water, respectively, and  $\rho_2$  and  $c_2$  are the density and wave velocity in the concrete, respectively. Using the values  $\rho_1 = 62.3 \text{ lb/ft}^3$ , and  $c_1 = 5,000 \text{ ft/sec}$  for water, and  $\rho_2 = 136 \text{ lb/ft}^3$ ,  $c_2 = 10,650 \text{ ft/sec}$  for the concrete used in the slab, the value of  $T$  becomes

$$T = 1.65 \quad (5)$$

The incident peak pressure at the water-concrete interface produced by a submerged spherical explosive charge whose center is at a distance  $L$  from the interface can be determined from the empirical equation [4].

$$P = 21,600 \left( \frac{L}{W^{1/3}} \right)^{-1.13} \quad (6)$$

where  $W$  is the TNT equivalent weight of the charge. Combining Equations 3-6, we have

$$\sigma_{n2} = 35,640 \left( \frac{L}{W^{1/3}} \right)^{-1.13} \left( \frac{L}{L + \frac{c_2}{c_1} y} \right)^\beta$$

or more simply,

$$\sigma_{n2} = 35,640 \left( \frac{L}{W^{1/3}} \right)^{-1.13} (\alpha)^\beta \quad \beta \geq 1 \quad (7)$$

where

$$\alpha = \left( \frac{L}{L + \frac{c_2}{c_1} y} \right)$$

## RESULTS OF TESTS

Following the tests the basin was emptied to determine the extent of damage to the slab caused by the detonations. There appeared to be no cratering despite the fact that some of the 1/4-lb charges were in direct contact with the concrete surface. There was, however, an apparent random scattering of pot holes on the slab surface attributed to the presence of air bubbles in the upper layer of the concrete. Two massive cracks were observed which ran the length and width of the slab, dividing it into four approximately equal parts. Since the growth of these cracks began before the advent of the test series and has continued after their termination, it appears certain that they were caused by the settling of the unreinforced concrete slab under its own weight. No other damage to the slab was observed.

Typical strain records produced by the tests are shown in Figures 5 and 6. The sample records shown were taken from tests involving the same gage site to eliminate the influence of differences in gage sites on the strain records. There seemed to be no difference between the strain records

of the vertical and the slant gages that did not fall within the data scatter of the vertical gages taken by themselves. All the strain records showed an initial compressive phase, often followed by a tensile phase. The tensile phase was observed primarily on gages near the top and bottom surfaces of the slab. The rise time of the initial compressive pulse was approximately 30  $\mu\text{sec}$ . The compressive pulse widths were in the range of 60  $\mu\text{sec}$  to 1.25 msec. For a given shot, the pulse width tended to increase with distance into the slab, with the major portion of the increase occurring in the first 1 to 2 ft from the surface. As expected, the pulse width was also observed to increase with charge weight, but showed no apparent dependence on charge standoff distance (i.e., distance from the charge center-of-mass to the slab).

Peak normal stress (i.e., stress perpendicular to the dilatational wave front) was derived from peak normal strain by assuming linear elastic theory to be applicable to the concrete, and by assuming the peak normal stress in the concrete to result from the water shock loading the concrete surface at a point directly below the charge. For peak stress in the shock front at points along the vertical axis, this relationship becomes [5]

$$\sigma_n = \left[ \frac{(1 - \nu)E}{(1 - 2\nu)(1 + \nu)} \right] \epsilon_n \quad (8)$$

where  $\nu$  is the Poisson ratio for the concrete and  $E$  is the dynamic modulus of the concrete. On the vertical axis,  $\sigma_n$  and  $\epsilon_n$  have no lateral components, and therefore Equation 8 provides a direct relationship between the peak vertical strain and the peak normal stress. Taking  $\nu = 0.25$  and  $E = 3.93 \times 10^6 \text{ psi}$ , we have

$$\sigma_n = 4.716 \times 10^6 \epsilon_n \text{ (psi)} \quad (9)$$

Equation 9 was used to convert the peak strain recorded by the vertical gages to peak normal stress.

As previously stated, the strain records of the slant gages were indistinguishable from those of the vertical gages. Accordingly, other than correcting the slant gage data to reflect the degree of tilt of the gage with respect to a normal to the wave front, the data were treated the same as the vertical data. The relationship for this correction factor is given as

$$\epsilon_n = \frac{\epsilon_{\text{mess}}}{(\cos \theta)^2}$$

where  $\epsilon_{\text{mess}}$  is the actual peak measured strain recorded by the slant gage and  $\epsilon_n$  is the associated peak strain normal to the shock front. In general these corrections amounted to no more than three or four percent of  $\epsilon_{\text{mess}}$  although in one case it was as high as 38 percent. Equation 9 was then used to calculate peak normal stress.

Figures 7-17 are graphs of  $\sigma_n$  plotted as a function of vertical distance below the concrete surface for each shot. Using Equation 7 as a guide, a least squares fit of the form

$$\sigma_n = A(\alpha)^\beta \quad (10)$$

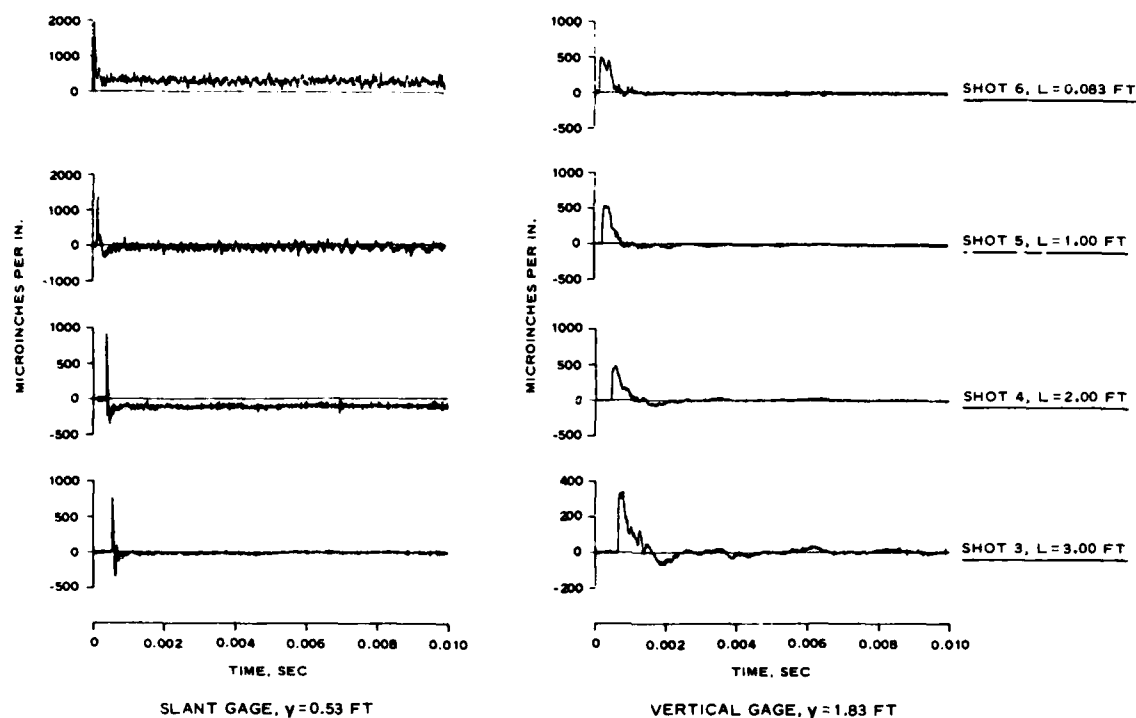


Figure 5 - Sample strain records

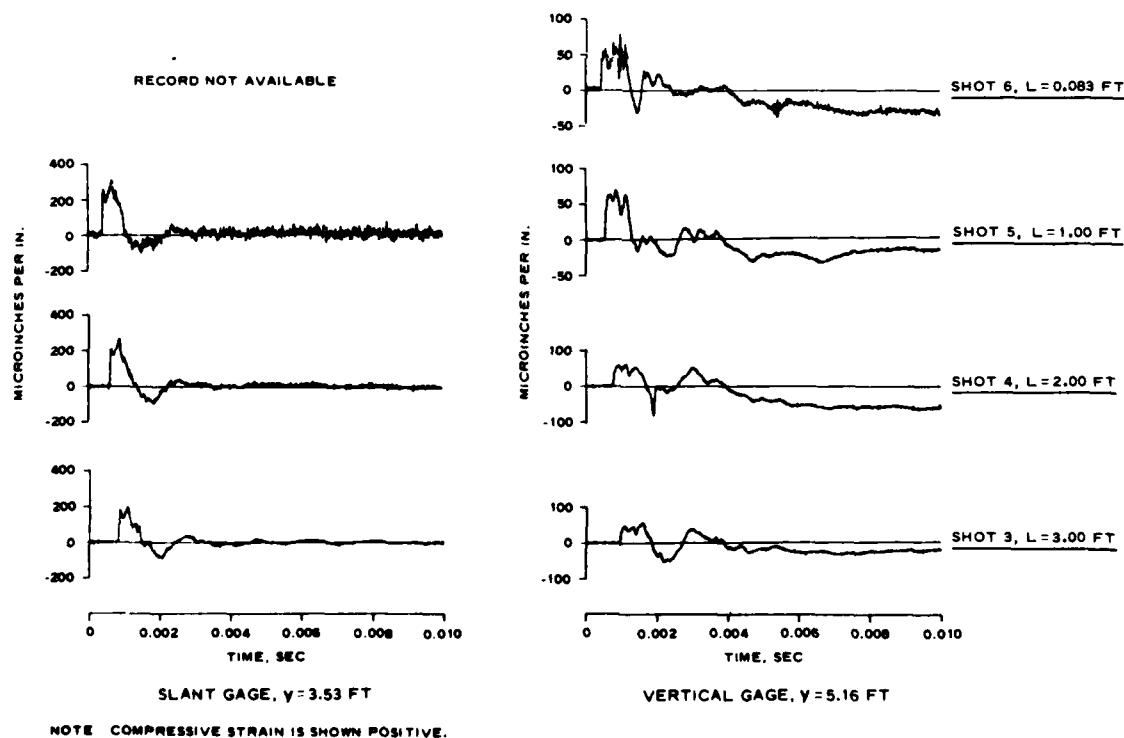


Figure 6 - Sample strain records

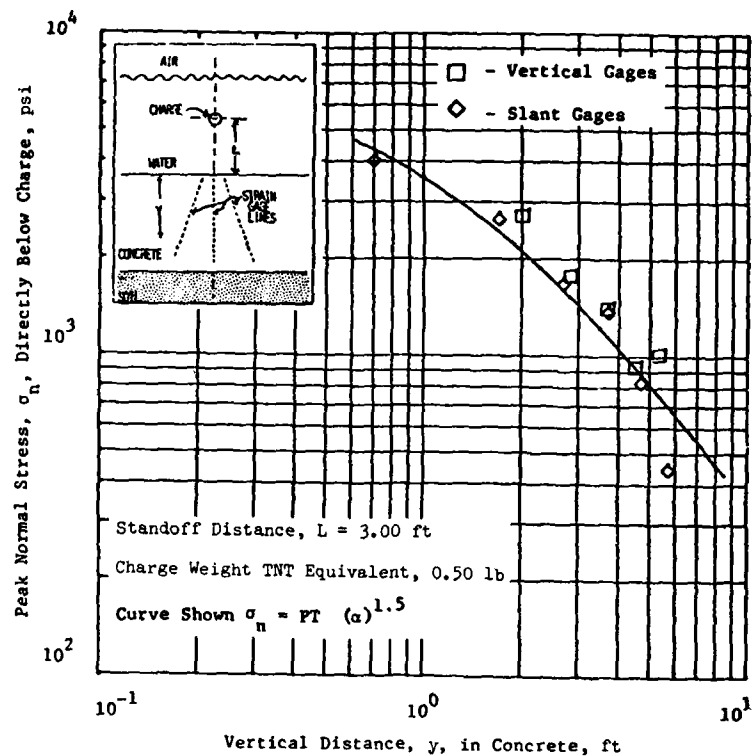


Figure 7 - Results of Shot 1

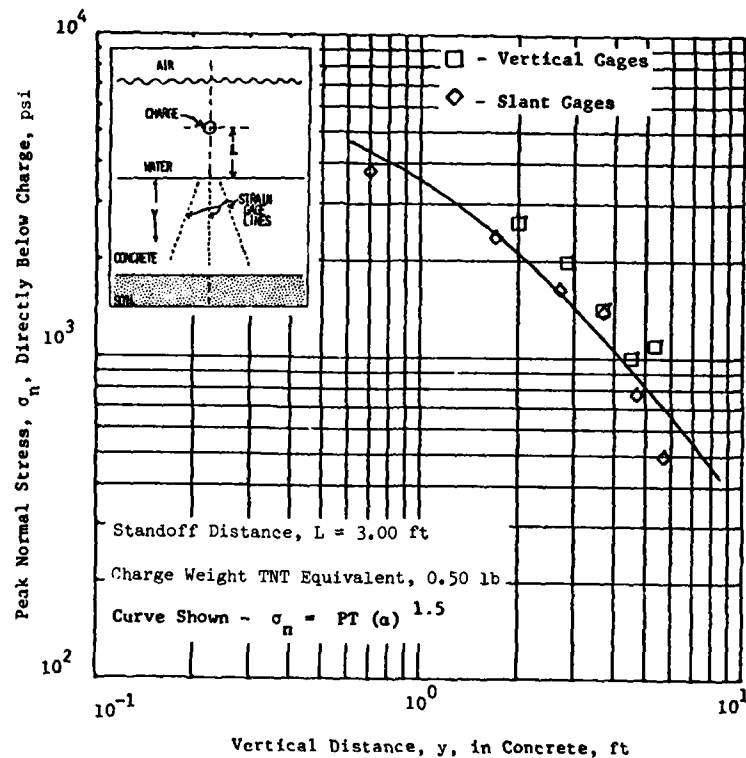


Figure 8 - Results of Shot 2

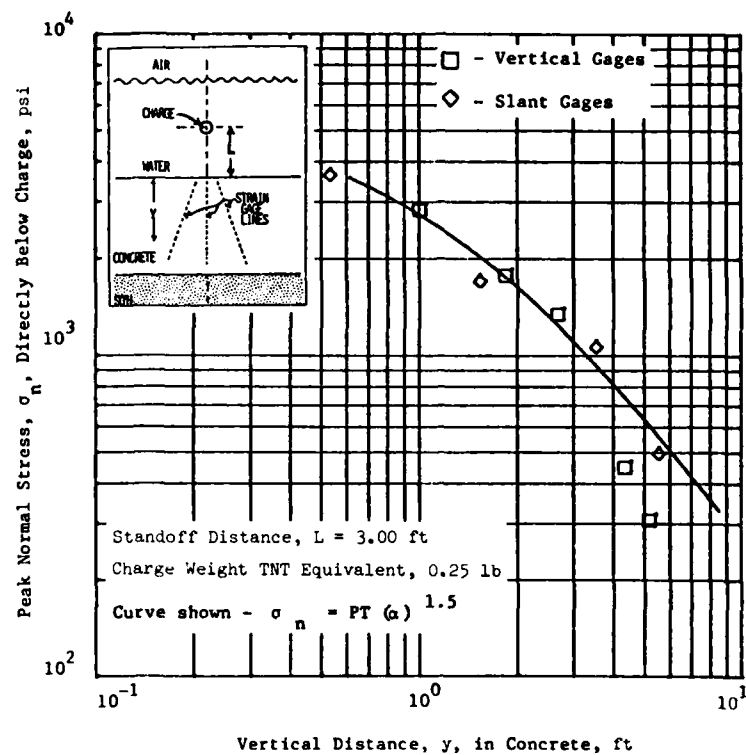


Figure 9 - Results of Shot 3

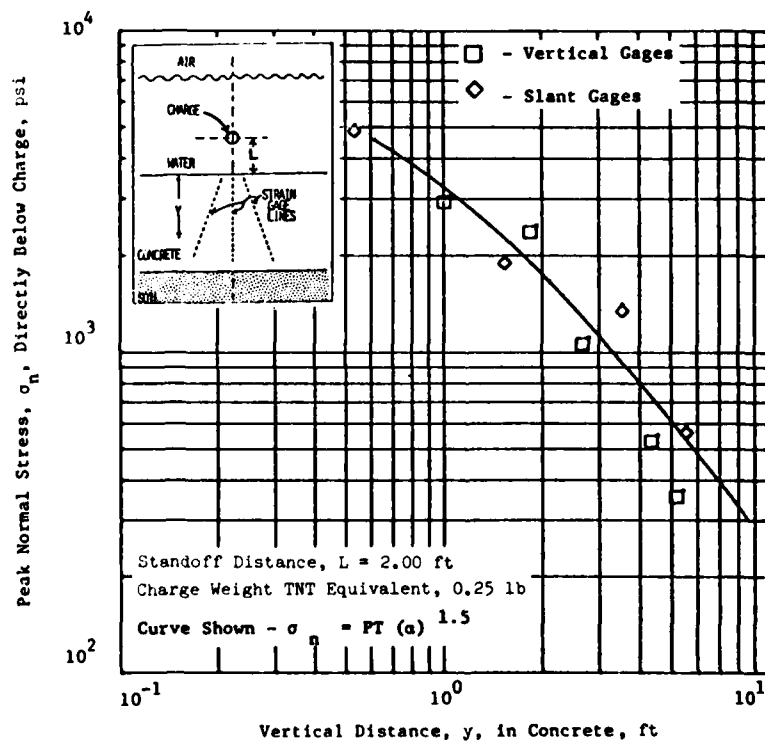


Figure 10 - Results of Shot 4

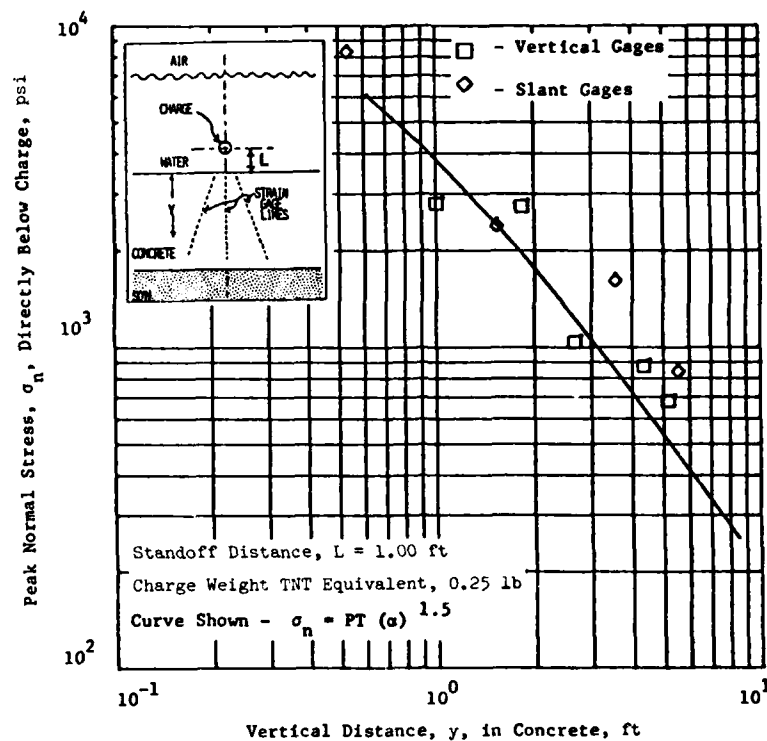


Figure 11 - Results of Shot 5

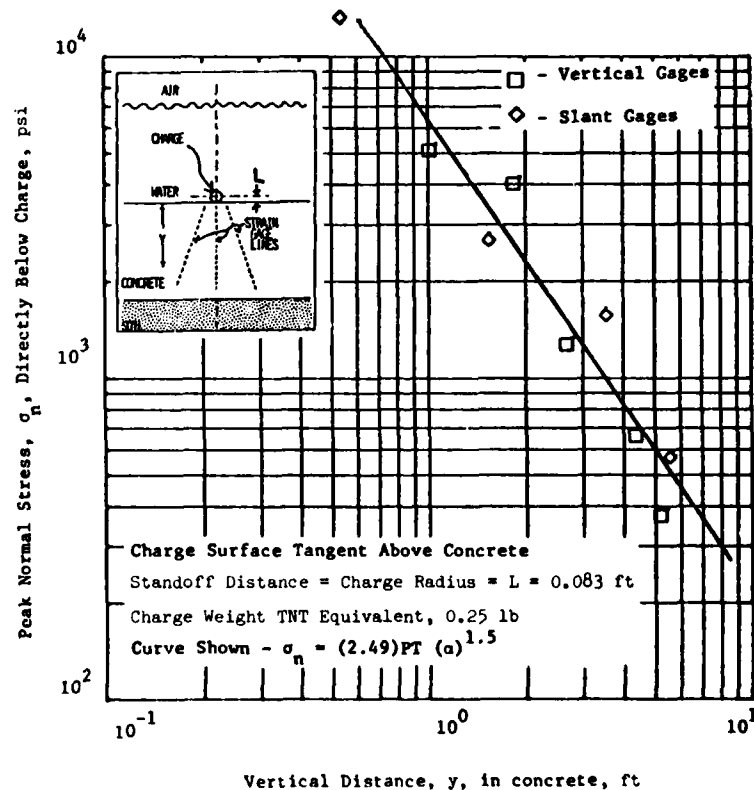


Figure 12 - Results of Shot 6



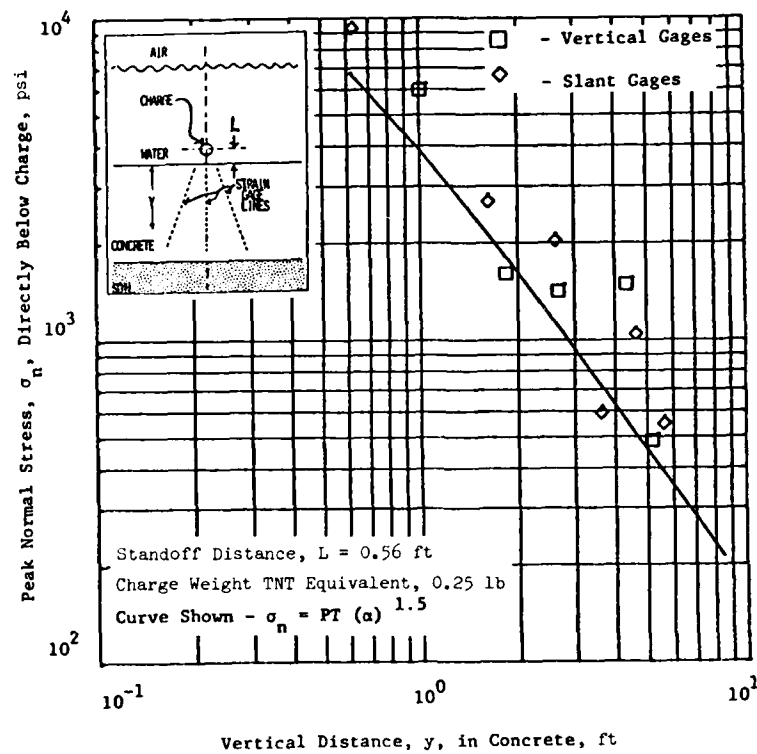


Figure 13 - Results of Shot 7

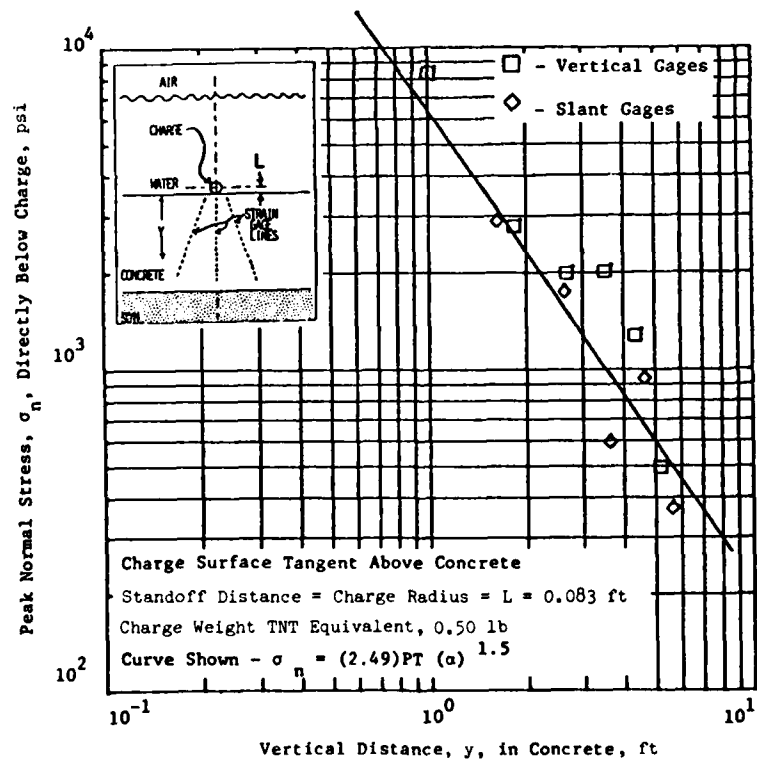


Figure 14 - Results of Shot 8

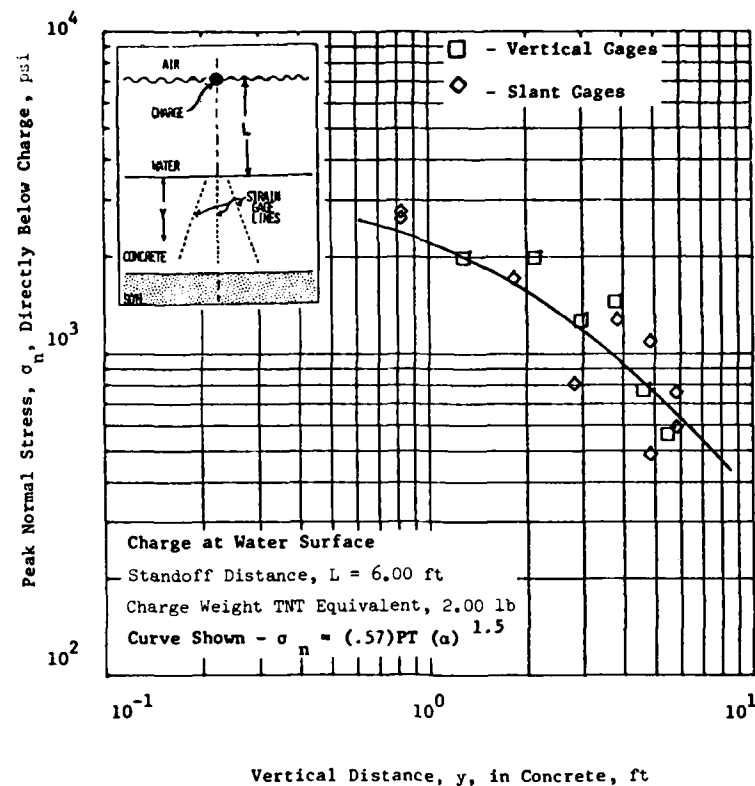


Figure 15 - Results of Shot 9

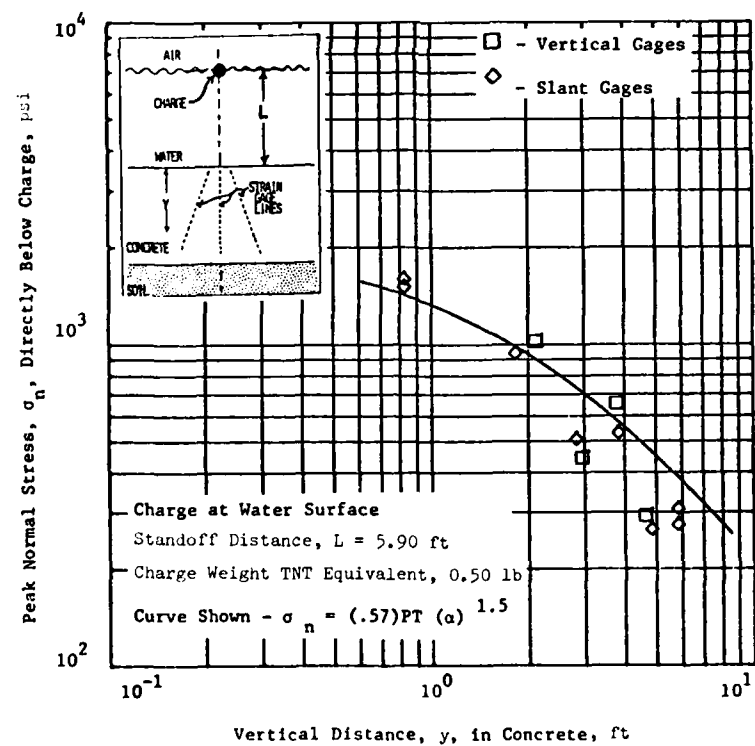


Figure 16 - Results of Shot 10

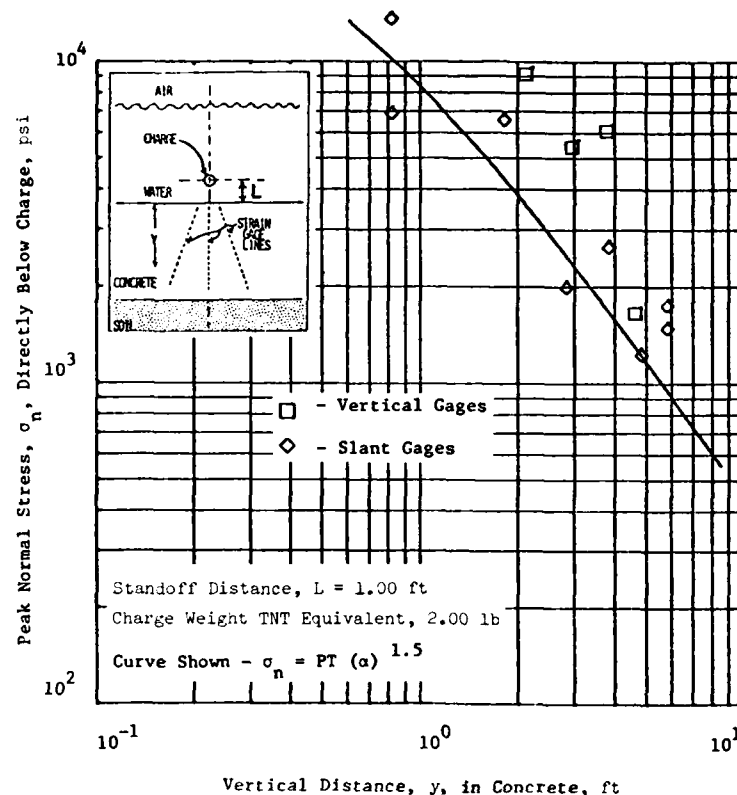


Figure 17 - Results of Shot 11

was applied to the data from each shot. The values of  $A$  and  $\beta$  derived for each data set are listed in Table 1.

The values of  $\beta$  ranged from 1.224 to 2.045, with an average value of 1.559 and a standard deviation of 0.219. Excluding the upper and lower extreme values the average value of  $\beta$  becomes 1.541, with a standard deviation of 0.140. The value of  $\beta$  was then rounded off to 1.5.

Comparing Equation 10 with Equation 7, we see that the coefficient  $A$  should be given by

$$A = PT = 35,640 \left( \frac{L}{W^{1/3}} \right)^{-1.13} \quad (11)$$

Accordingly, values of  $A$  as a function of the scaled standoff distance,  $L/W^{1/3}$ , are shown in Figure 18 along with the theoretical curve for  $A$  given by Equation 11. There appears to be good agreement between the data points and Equation 11 for all shots in which the charge was at intermediate depths in the water (i.e., not surface-tangent to the concrete and not at the water surface). It was found that the equation

$$\sigma_n = PT(\alpha)^{1.5} \quad (12)$$

fitted the stress data points for all intermediate shots fairly well (see Figures 7-11, 13, and 17).

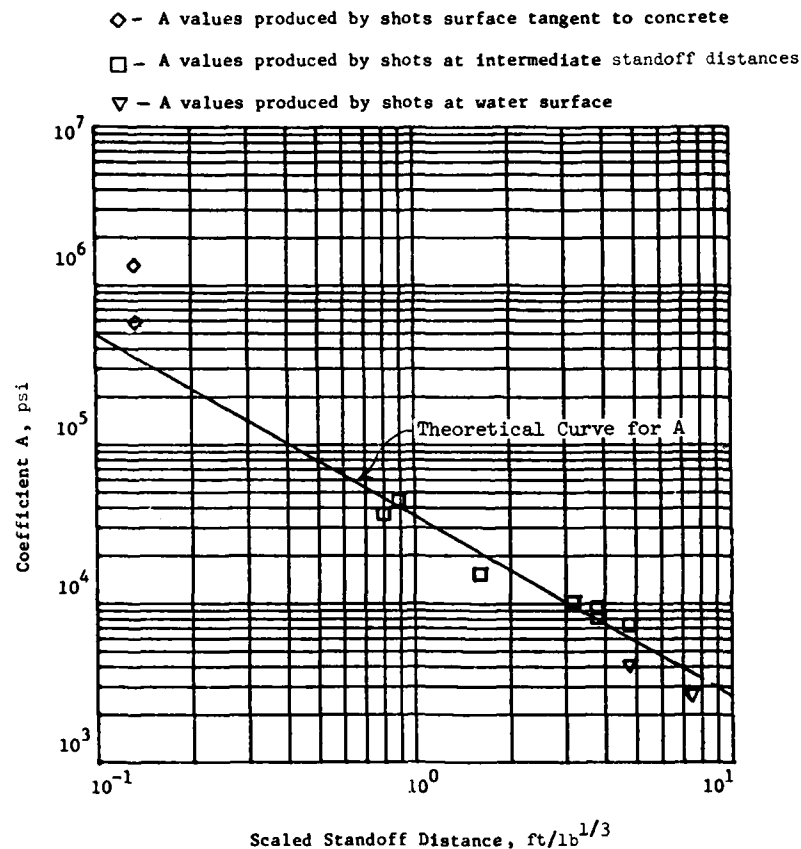
The values of  $A$  derived from shots located at the water surface (Shots 9 and 10) fell below the theoretical curve. This is to be expected since the energy coupled into the water from a charge placed at the water surface is less than that from a fully submerged charge. It was found that the stress data for both Shots 9 and 10 (Figures 15 and 16) were reasonably well fitted by an equation of the form

$$\begin{aligned} \sigma_n &= (0.57)A(\alpha)^{1.5} \\ &= (0.57)PT(\alpha)^{1.5} \end{aligned} \quad (13)$$

The values of  $A$  produced by charges located surface-tangent to the concrete (Shots 6 and 8) fell above the line given by Equation 11. This was also to be expected due to the increased amount of shock energy coupled directly into the concrete from a charge in contact with the concrete surface. It was found that a curve of the form

$$\begin{aligned} \sigma_n &= 2.49A(\alpha)^{1.5} \\ &= 2.49PT(\alpha)^{1.5} \end{aligned} \quad (14)$$

provided a good fit through the stress data points of these shots (Figures 12 and 14).



## CONCLUSIONS

Geometric techniques for predicting peak normal stress were found to be applicable to the problem of stress generation in concrete from underwater explosions. A good first order approximation of the peak normal stress,  $\sigma_n$ , near the vertical axis was found to be given by

$$\sigma_n = (\gamma) PT (\alpha)^{1.5}$$

where

$\gamma$  = Empirically determined factor that reflects the coupling efficiencies of the charge location as is given by

$\gamma = 0.57$  for charges at the water surface

$\gamma = 2.49$  for charges surface-tangent to the concrete

$\gamma = 1.00$  for charges at intermediate distances

$P$  = Peak incident water pressure at the water concrete interface =  $21,600 \left( \frac{L}{W^{1/3}} \right)^{-1.13}$

$T$  = Stress transmission coefficient for the interface = 1.65

$\alpha$  Term that describes the increasing surface area of the stress wave in the concrete =  $\left( \frac{L}{L + \frac{c_2}{c_1} y} \right)$

## REFERENCES

1. Cooper, H. F. and Seamon, J. B., "A Geologic Technique for Studying Surface Motions from Underground Nuclear Explosions in Real Geologic Media," AFWL-TR-66-123, Jan. 1967, Air Force Weapons Laboratory.
2. Cooper, H. F. and O'Kobrick, J. J. "A Geometric Method of Studying Wave Propagation Through Real Geologic Layered Media," AFWL-TR-66-125, Apr. 1966, Air Force Weapons Laboratory.
3. Cooper, H. F., "Empirical Studies of Ground Shock and Strong Motions in Rock," RDA-TR-3601-002, Oct. 1973, R&D Associates.
4. Snay, H. G., "Model Tests and Scaling (U)," NOLTR 63-257, DASA 1240-II(3), Dec. 1964, U. S. Naval Ordnance Laboratory, White Oak, Maryland.
5. Britt, J. R., Personal Correspondence, U. S. Army Engineer Waterways Experiment Station (unpublished).

## THE EFFECT OF EARTH COVER ON THE DYNAMIC RESPONSE OF HARDENED REINFORCED CONCRETE STRUCTURES

R. D. Crowson and S. A. Kiger  
U. S. Army Engineer Waterways Experiment Station  
Vicksburg, Mississippi

Forced vibration tests were conducted on three hardened reinforced concrete structures, two rectangular box structures, and a closed-end arch, both with and without backfill in order to determine the effect of backfill on dynamic characteristics, i.e., natural frequencies, mode shapes, and damping. The backfill increased equivalent viscous damping ratios in each case, ranging from a slight increase for one box structure to a substantial increase for the arch. The effect of backfill on natural frequencies was different for each structure. Finite element calculations were also performed, and it was found that two-dimensional analyses were inadequate for predicting natural frequencies, whereas, results of three-dimensional analyses compared favorably with experimental data for the uncovered structures.

### INTRODUCTION

Information about the response of buried structures subjected to dynamic loads is important when assessing the vulnerability of military targets as well as in the design of both civil and military structures. For buried structures, the effect of earth cover on dynamic parameters, i.e., natural frequencies, mode shapes, and damping ratios, is not clearly understood. This paper compares data obtained experimentally from vibration tests, in which the effect of soil cover on dynamic parameters was measured, with analytical procedures currently being used.

Normally, the first step in the dynamic analysis of a structure is the determination of the structure's fundamental frequency. To determine the natural frequency of a buried structure, one procedure (Reference 1) modifies the frequency obtained for the uncovered structure by the addition of a term to account for the mass of soil overburden. Soil stiffness and damping in such a technique are not considered. Reference 2 suggests that the effect of soil mass be neglected since in some instances the surrounding soil also acts to stiffen the structure. Finite element calculations usually consider soil stiffness, as well as mass, in the analysis of a soil-structure system. A damping term could also be included in the finite element model, however, the energy loss caused by stress waves radiating into the soil, i.e., radiation or geometric damping, require special boundary elements not available in most general purpose structural analysis programs.

### MODEL STRUCTURES

The two types of structures investigated were typical of many hardened buried structures in use today. Structures 3B and 3D were model reinforced-concrete box structures, having a roof, floor, and wall span-to-depth ratio of 10 and 4, respectively. Both box structures were 16 feet long by 4 feet wide by 4 feet high (inside dimensions); the wall thickness of Structure 3B was 5.8 inches and that of Structure 3D was 13 inches. Structure 3A was a model reinforced concrete arch, 14 feet in diameter and 24-1/2 feet long with a 12-inch-thick arch ring, 13-inch-thick floor, and 16-inch-thick end walls. For all three structures, principal reinforcing steel was 1 percent for both tension and compression. The models were fully buried with 2 feet of backfill cover at the arch crown and roofline of the boxes. The backfill material around the sides of the box structures was dense sand, having a unit weight of approximately 100 lb/cu ft. The backfill for the arch, and for the top 2 feet over the boxes, was compacted soil having a unit weight of approximately 117 lb/cu ft. Structural details are shown in Figures 1 and 2 for the box and arch structures, respectively.

### EXPERIMENTAL PROCEDURE

The box structures were instrumented (Figure 3) with vertical accelerometers along the roof and horizontal accelerometers on the side walls at midsection. Sinusoidal input forces were from two electrohydraulic vibrators located in the roof at one-third points, running inphase and then running 180 deg out of phase.

Tests were also run using a single vibrator at the center point of the roof. Frequency sweep tests from 50 to 1000 Hz were run at force levels of 50, 100, and 500 lb peak output per vibrator. The frequency sweep rate used, 0.3 decades per minute, was selected after several rates were tried and was considered to produce a quasi-steady-state condition, i.e., results at this rate were no different from those of a slower rate. The series of tests conducted on the uncovered box structures were repeated after the backfill was placed.

The uncovered arch structure was instrumented (Figure 3) with accelerometers around the interior circumference at midsection measuring radial motion and along the crown measuring vertical motion. Frequency sweeps from 50 to 1000 Hz were run using two vibrators placed at 36 deg and 144 deg from the base. The vibrators were run both inphase and 180 deg out of phase at constant force levels of 50, 100, and 500 lb peak output per vibrator. A single vibrator located at the crown at midsection was also used. Preliminary test results down to 10 Hz indicated no structural response below 50 Hz.

#### EXPERIMENTAL RESULTS

Vibration test data can be analyzed and presented a number of different ways. For this study, the measured accelerations and driving force signals were input to a signal analyzer, and the reduced data were obtained in the form of mechanical impedance ( $\frac{\text{Force}}{\text{Velocity}}$ ) versus frequency plots and component vector (Co-Quad) frequency response plots. Using such displays for each measured acceleration on a structure, the dynamics of the structure can be described completely, i.e., natural frequencies identified and mode shapes and damping ratios obtained. These experimental techniques are described in References 4, 5, and 6.

Response curves, typical of plots obtained for all measurement points on the box structures, are shown in Figure 4 for Structure 3D and Figure 5 for Structure 3B. These figures contain both mechanical impedance and component vector curves, from which the resonant peaks for the uncovered structures are readily identified. In Figure 4, resonant peaks for Structure 3D are seen to occur at 240 Hz and 415 Hz. These frequencies correspond to the first two symmetric modes. Similar plots for asymmetric loading, i.e., vibrators 180 deg out of phase, indicate the first asymmetric mode to be at 315 Hz. Curves from tests with the structure buried indicate the same 240-, 315-, and 415-Hz natural frequencies with the response curves being somewhat broader than the sharply defined peaks for the uncovered case.

From Figure 5, resonant peaks for Structure 3B, uncovered, occur at approximately 150 and 300 Hz. These frequencies correspond to the first two symmetric modes. The first

asymmetric mode, obtained in the out-of-phase tests, was at 175 Hz. However, the resonant peaks are poorly defined for the buried structure tests, as evident in the mechanical impedance curves. Such curves are indicative of high damping ratios.

Data for the arch structure are presented in Figure 6. Again, the uncovered resonant peaks are sharply defined, and the first two frequencies corresponding to symmetric modes occurred at 104 and 220 Hz. Asymmetric modes occurred at frequencies of approximately 70 and 220 Hz.

Plots similar to those of Figures 4-6 were generated for each measurement point on each structure. Since the component vector curves are both amplitude- and phase-sensitive, mode shapes were obtained by plotting the amplitude of the 90-deg component vector at the resonant frequencies for each structure. These shapes for the uncovered structures are shown in Figures 7, 8, and 9 for Structures 3D, 3B, and 3A, respectively.

From the response curves of Figures 4-6, it can be seen that the effect of the earth cover was not the same for each structure. Resonant peaks for Structure 3D after burial (Figure 4) occur at the same frequencies as those of the uncovered structure (considering only the first three modes). The general shape of the curves are quite similar with the buried structure peaks being somewhat broader, indicating higher damping ratios. The peaks at frequencies less than 100 Hz, being well below the frequency range of structure response as obtained from the uncovered tests, appear to be due to motion of the surrounding soil. Resonant peaks for Structure 3B after burial (Figure 5) are not nearly as distinct and well defined as those of Structure 3D. The response curves indicate broad peaks at frequencies of 142 and 310 Hz for symmetric loading and 175, 350, and 450 Hz for asymmetric loading. Note also the tendency of the fundamental vibration mode to be shifted to a lower frequency after burial (142 Hz compared to 150 Hz) while the higher frequencies are shifted upward (320 Hz compared to 300 Hz for the third mode). This trend is consistent with previous observations (e.g., Reference 7). From the response plots of Arch Structure 3A after burial (Figure 6), no resonant peaks are observed. These curves are the type that might be expected from a highly damped, or even critically damped, system. Mode shapes for the buried Box Structures 3B and 3D are shown in Figures 10 and 11, respectively. In order to illustrate the manner in which the structure is responding at various frequencies, deflected shapes (not mode shapes) of Structure 3A, after burial, are shown in Figure 12.

Possible explanations for the absence of resonant peaks in the response plots from Arch Structure 3A include insufficient force input from the vibrators and excessive damping.

Perhaps the most obvious cause for no resonances would be insufficient force input. However, the maximum accelerations measured in the buried arch tests were typically 0.5 g as opposed to approximately 1 g for the uncovered case, indicating ample signal strength. Maximum displacements of the arch structure were approximately  $2 \times 10^{-4}$  inches for the uncovered case and  $4 \times 10^{-5}$  inches for the buried case. Comparing these displacements with the displacements of Box Structure 3D,  $1 \times 10^{-4}$  inches - uncovered and  $4 \times 10^{-5}$  inches - buried, it is seen that the amplitude of motion at the soil/structure interface was approximately the same for both structures. Thus, insufficient input force will not explain the failure to excite natural frequencies in the buried arch.

Damping ratios of the uncovered structures, as determined from the component vector response plots, were within the range of expected values. For Box Structure 3D, measured damping ratios varied from 2 to 6 percent of critical; for Box Structure 3B, 2 to 7 percent of critical; and for the Arch Structure 3A, 2 to 5 percent of critical. Generally, the lower damping values were obtained at the higher frequencies, whereas, the larger damping values were measured at the first natural frequency.

After burial, damping ratios were found to vary from 6 to 11 percent of critical for Box Structure 3D, and for Box Structure 3B, 13 to 21 percent of critical. Due to the nature of the response curves, damping ratios could not be determined for the buried arch structure. The response curves for the buried arch are indicative of damping ratios greater than 20 to 30 percent of critical. Radiation damping was also considerably greater for the arch structure since the compressional wave velocity for the compacted soil backfill was approximately twice that of the sand backfill around the box structures. Therefore, the most likely explanation for the failure to observe resonant frequencies in the buried arch is that there was sufficient damping to suppress resonance.

#### FREQUENCY CALCULATIONS

The first step in the dynamic analysis of the uncovered structures was to make an approximation of the natural frequencies. The equations used to calculate the frequencies, in radians per second, of the extensional mode (also called the compression or breathing mode), the first antisymmetric flexural mode (also called the sway mode), and the first symmetric flexural mode of the arch were taken from Reference 1. Using these equations, the problem is formulated as one of plane strain, i.e., treating the structure as being two-dimensional (2-D).

a. For the breathing mode:

$$\omega_B = \frac{0.97}{R} \sqrt{\frac{EA}{m}} \quad (1)$$

where

R = radius of the arch  
E = Young's Modulus  
A = cross-sectional area of the arch  
m = mass per unit length of arch

b. For the flexural modes:

$$\omega_n = \frac{C_n}{S^2} \sqrt{\frac{EI}{m}} \quad (2)$$

where

$C_n$  = dimensionless coefficient depending on arch geometry and mode of vibration  
S = length of the arch axis =  $R\theta$  where R is the radius of the arch and  $\theta$  is the central angle of the arch  
I = moment of inertia of arch cross section  
m = mass per unit length of arch

c. For the breathing mode:

$$\omega_B = 4312 \text{ rad/sec (686 Hz)} \quad (3)$$

d. For the first antisymmetric flexural mode (the sway mode), assuming a fixed support arch:

$$C_1 = 43.22$$

and

$$\omega_1 = 216 \text{ rad/sec (34.4 Hz)} \quad (4)$$

e. For the first symmetric flexural mode:

$$C_2 = 84.70$$

and

$$\omega_2 = 423 \text{ rad/sec (67.3 Hz)} \quad (5)$$

Reference 1 suggests that the period of vibration will be increased somewhat by the added mass of soil cover. Since the amount of soil that vibrates with the arch is uncertain, an average depth of cover will be used. The average depth of cover is calculated as follows:

$$\begin{aligned} H_{\text{avg}} &= \frac{(2 + R) 2R - \pi R^2/2}{2R} \\ &= \frac{(2 + 7)(14) - \pi(49)/2}{14} \\ &= 3.50 \text{ ft (.106 m)} \end{aligned}$$

Distributing this mass of soil along the circumference of the arch will modify frequencies so that

$$\omega_1' = \left( \sqrt{\frac{m}{m' + m}} \right) \omega_1$$

where  $m'$  is the mass intensity of the added soil cover and  $m$  the mass intensity of the concrete arch. Thus, with 150 pcf for the weight density of concrete and 110 pcf for the weight density of soil:

$$\omega_1' = \left( \sqrt{\frac{150(1)}{(110)(3.50) + 150(1)}} \right) \omega_1 = (0.530) \omega_1$$

$$\omega_1' = 114 \text{ rad/sec (18.2 Hz)} \quad (6)$$

likewise

$$\omega_2' = 224 \text{ rad/sec (35.7 Hz)} \quad (7)$$

and

$$\omega_B' = 2283 \text{ rad/sec (364 Hz)} \quad (8)$$

The roof slab fundamental period for the box structures was calculated from an approximate simple beam equation taken from Reference 8

$$T = C \frac{L^2}{d \sqrt{p}} \quad (9)$$

where

- $T$  = natural period, seconds per cycle
- $C$  = constant =  $1.177 \times 10^{-6}$  for fixed ends
- $L$  = span length, in.
- $d$  = effective depth of beam, in.
- $p$  = tensile reinforcement ratio

For Structure 3D

$$T = 2.26 \text{ msec}$$

and the fundamental frequency  $f$  is

$$f_D = \frac{1}{T} = 442 \text{ Hz} \quad (10)$$

For Structure 3B

$$T = 5.65 \text{ msec}$$

and

$$f_B = 177 \text{ Hz} \quad (11)$$

The modified frequencies, due to the mass of the 2 ft of soil cover, become

$$f_D' = \left( \sqrt{\frac{150(1)}{110(2) + 150(1)}} \right) f_D = (0.637) f_D \quad (12)$$

$$f_D' = 281 \text{ Hz} \quad (13)$$

and

$$f_B' = (0.504) f_B = 89 \text{ Hz} \quad (14)$$

## ARCH FINITE ELEMENT ANALYSIS

A 2-D finite element analysis was conducted of the arch structure to determine the modal frequencies with and without soil cover. Soil boundaries for the problem corresponded to the excavation made for construction so that only the soil backfill was included in the grid. Two sets of frequencies were calculated, one using a soil density of 110 pcf and a soil elastic modulus of 31,000 psi and the second using zero soil density and 100 psi modulus, corresponding to the uncovered structure.

The computer code used for these calculations was SAP IV, a structural analysis program for static and dynamic response of linear systems, developed by Bathe, Wilson, and Peterson of the University of California, Berkeley (Reference 9). A plane strain 2-D element based on an isoparametric formulation was used. The grid was composed of 170 elements and 203 nodes with 340 degrees of freedom. The boundary nodes at the base and sides were fixed against translation in all directions. The first 10 mode shapes and natural frequencies of the arch and soil-arch system were determined using the subspace iteration method in SAP IV. The higher modes calculated with soil cover involved mostly soil motion with very little structure deformation. Therefore, results for only the first three modes are shown in Figure 13.

A three-dimensional (3-D) finite element analysis of the arch structure has recently been conducted by Weidlinger Associates (Reference 10). The calculated flexural mode shapes at 71 and 100 Hz were in agreement with the measured shapes at 70 and 104 Hz for the uncovered structure.

## BOX FINITE ELEMENT ANALYSIS

A 3-D finite element analysis was conducted of each box structure without the soil cover to determine the modal frequencies and shapes. A grid composed of 196 3-D shell elements, 418 nodes, with 1214 degrees of freedom was used with the SAP IV code to obtain the first 20 mode shapes and frequencies. Due to the size of the problem, only one-half the length of the structures was used; thus, only symmetric modes, with respect to length, were obtained.

Rigid body, flexural, and torsional modes were obtained. Since only a line of transducers was used in the experimental work, all the finite element mode shapes were not detected. Comparisons of the experimentally measured mode shapes with those from the finite element calculations are shown in Figures 7 and 8. Other analytical mode shapes illustrating the 3-D behavior of the Box Structures 3D are shown in Figure 14, with the shapes of Box Structure 3B being similar.



## DISCUSSION

Vibration tests were conducted on two rectangular concrete box structures and a concrete arch structure both uncovered and buried under 2 ft of soil. Natural frequencies of the uncovered structures were calculated from available formulas, and a finite element analysis was conducted for each structure. A comparison of the fundamental frequencies determined from the various methods is presented in Table 1.

Results of the buried structure tests were considerably different from accepted calculation methods, e.g., the added mass approach and linear 2-D finite element calculations. Response of the structures buried, as compared to uncovered, was different for each structure. Damping values measured were considerably different for the two box structures and appeared to be greater than 20 to 30 percent of critical for the arch. Although the buried structure problem is quite complex, a simplified 2 degree of freedom (DOF) model can be used to investigate trends in behavior of the soil-structure system as the damping and the ratio of structure stiffness to soil stiffness are changed. The transfer function approach, as presented in Reference 11, will be used to define the structure displacement. Using the physical properties of each structure and the best available soil properties data, the parameters of the problem were identified, i.e., mass (M), stiffness (K), and damping (B). For structure damping of 5 percent and soil damping of 10 percent, the responses of Figure 15 were obtained. By applying a sinusoidal input force to Mass 2 (structure), the modulus of the resulting complex mobility  $\left(\frac{\text{Velocity}}{\text{Force}}\right)$  of Mass 2 is plotted against frequency. As the stiffness ratio of structure to soil, i.e.,  $\frac{K_{\text{structure}}}{K_{\text{soil}}}$  varies from approximately 0.6 to 6, the response of the structure changes both in magnitude and frequency. Specifically, as shown in Curve A, for a structure having a fundamental frequency of 240 Hz and a damping ratio of 5 percent critical, the structure frequency shifts to 244 Hz after combining with a mass of soil, and the response is indicative of slightly higher damping. From Curve B, the response of a structure having a fundamental frequency of 150 Hz, after combining with a soil mass, appears to be highly damped and the frequency of peak response is poorly defined. The sharp peak at the lower frequency is due to the response of mass 1 (soil). Similarly, from Curve C, the response of a structure having a fundamental frequency of 70 Hz, after combining with a soil mass, is highly damped with no peak. The lower frequency peak again represents the response due to mass 1 (soil). These curves are similar to those obtained from the vibration tests. Although highly damped, evidence of response at frequencies below 50 Hz was seen in experimental curves for the

covered structures, correlating somewhat to the response at lower frequencies of the 2DOF model.

## CONCLUSIONS AND RECOMMENDATIONS

The conclusions obtained from this study are:

- (1) There was very good correlation between the 3-D finite element and experimental natural frequencies and mode shapes for the uncovered box structures.
- (2) Based upon the 3-D behavior of the structures as determined from the vibration tests, 2-D (plane strain) analyses do not adequately predict uncovered natural frequencies and mode shapes for these type structures.
- (3) The results of tests on the buried structures indicate that the effect of soil cover on natural frequencies and damping appear to be dependent upon the structure/soil stiffness ratio. Frequencies obtained by modifying the uncovered frequency with an "added soil mass" factor do not correlate with experimental results. Therefore, the results of this study suggest that commonly used, semi-empirical design manual techniques may predict erroneous modal frequencies for shallow-buried structures.

Additional experimental work is needed to expand the data base of buried structure dynamic response. Significant soil parameters, i.e., stiffness and radiation damping, also need to be more accurately defined in order to reliably predict the effect of soil cover on structure response. In particular, parametric studies employing vibration testing should be conducted on concrete structures or slabs having various span-to-thickness ratios with a variety of carefully controlled backfill conditions. Such tests would band types of response with respect to structure/soil stiffness ratio in addition to providing additional information on radiation and other types of damping mechanisms.

## REFERENCES

1. Crawford, R. E., Higgins, C. J., and Bultmann, E. H., "The Air Force Manual for Design and Analysis of Hardened Structures," AFWL-TR-74-102, Air Force Weapons Laboratory, Air Force Systems Command, Kirtland Air Force Base, NM, Oct 1974.
2. Newmark, N. M. and Haultiwanger, J. D., "Principles and Practices for Design of Hardened Structures," AFSWC-TDR-62-138, Air Force Special Weapons Center, Air Force Systems Command, Kirtland Air Force Base, NM, Dec 1962.
3. American Society for Testing and Materials, "Standard Specifications for Deformed and Plain Billet-Steel Bars for Concrete Reinforcement," A615-68, 1968 Book of ASTM Standards, Part 4, Philadelphia, PA, 1968.

4. Keller, A. C., "Vector Component Techniques: A Modern Way to Measure Modes," Sound and Vibration Reprint, Spectral Dynamics Corporation, Mar 1969.

5. Rades, M., "Methods for the Analysis of Structural Frequency-Response Measurement Data," Shock and Vibration Digest, Vol 8, No. 2, Feb 1976, p 73.

6. Jennings, P. C., Mattiesen, R. B., and Hoerner, J. B., "Forced Vibration of a Tall Steel-Frame Building," International Journal of Earthquake Engineering and Structural Dynamics, Vol 1, No. 2, Oct-Dec 1972, pp 107-132.

7. Novak, Milos and Beredugo, Y. O., "Vertical Vibration of Embedded Footings," Journal of the Soil Mechanics and Foundations Division, ASCE, Vol 98, No. SM12, Dec 1972.

8. Allgood, J. R. and Swihart, G. R., "Design of Flexural Members for Static and Blast Loading," ACI Monograph No. 5, Detroit, 1970.

9. Bathe, K., Wilson, E. L., and Peterson, F. E., "A Structural Analysis Program for Static and Dynamic Response of Linear Systems," No. EERC 73-11, Jun 1973 (revised Apr 1974), College of Engineering, University of CA, Berkeley, CA.

10. Crafton, Paul A., Shock and Vibration in Linear Systems, Harper & Brothers, Publishers, New York, 1961, pp 135-140.

11. Isenberg, J., Levine, H. S., and Pang, S. H., "Numerical Simulation of Forced Vibration Tests on a Buried Arch," Weidlinger Associates, Menlo Park, CA, Mar 1977.

TABLE 1  
Frequencies for the Fundamental Mode of Response

Structure	Experimental		Formulas		Finite Element		
	Uncovered	Buried	Uncovered	Buried	3-D Uncovered	2-D Uncovered	2-D Buried
Box 3D	240	240	442	281	226	**	**
Box 3B	150	142	177	89	144	**	**
Arch 3A	70	*	34	18	71	30	26

\* Unable to determine.  
\*\* 2-D FE analysis not performed.

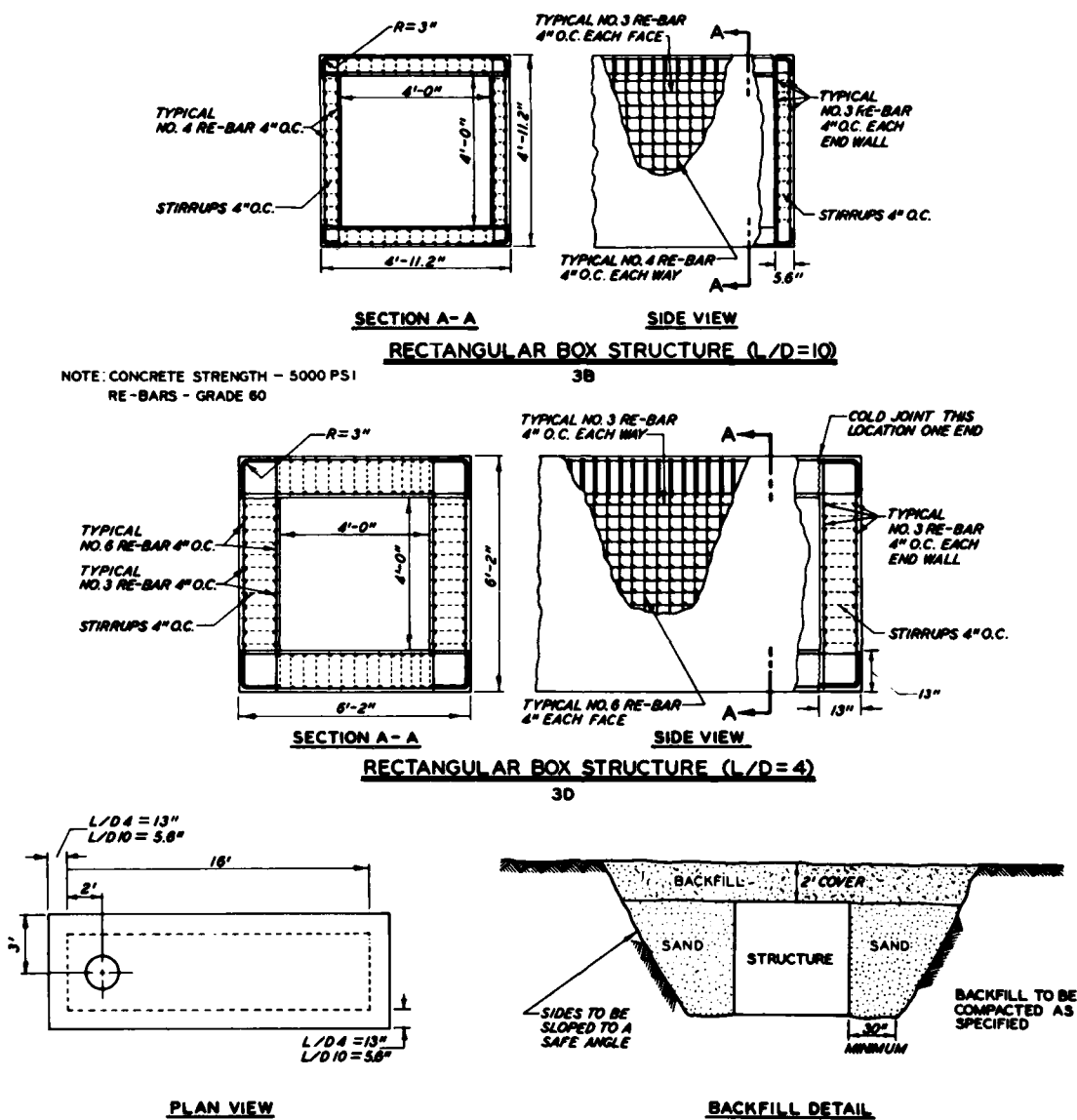
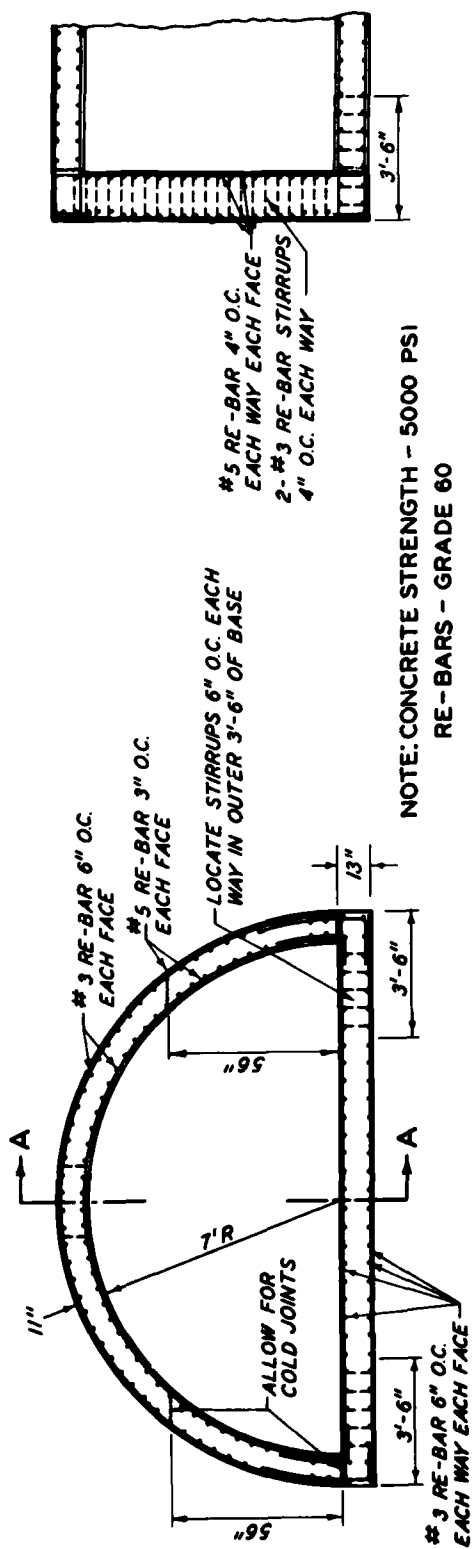


Fig. 1 - Structural details and dimensions of the box structures



CONCRETE ARCH STRUCTURE 3A

SECTION A-A

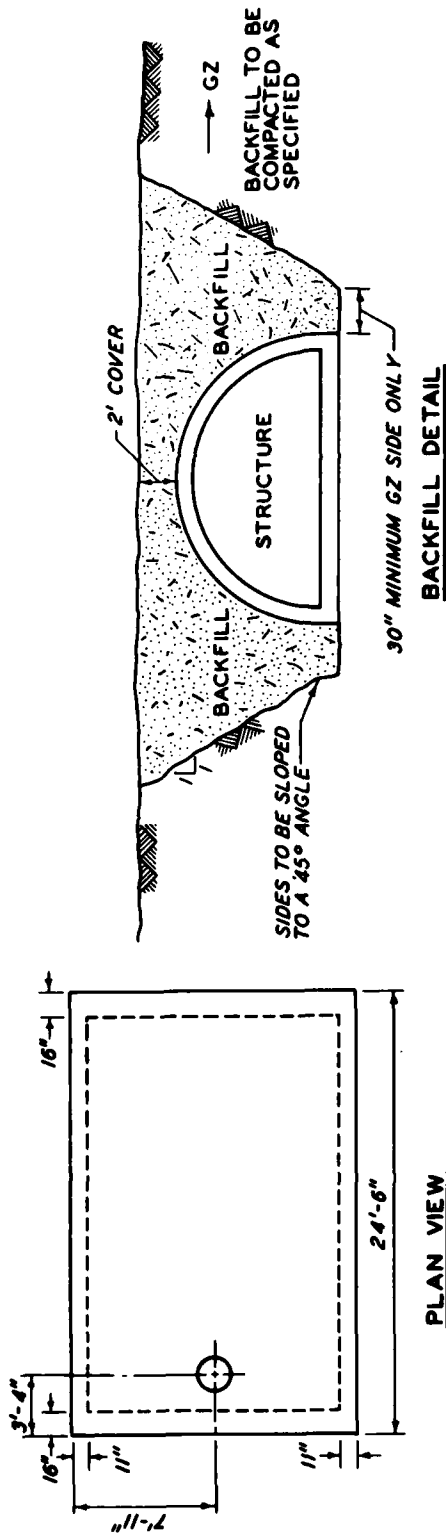


Fig. 2 - Structural details and dimensions of the arch structure

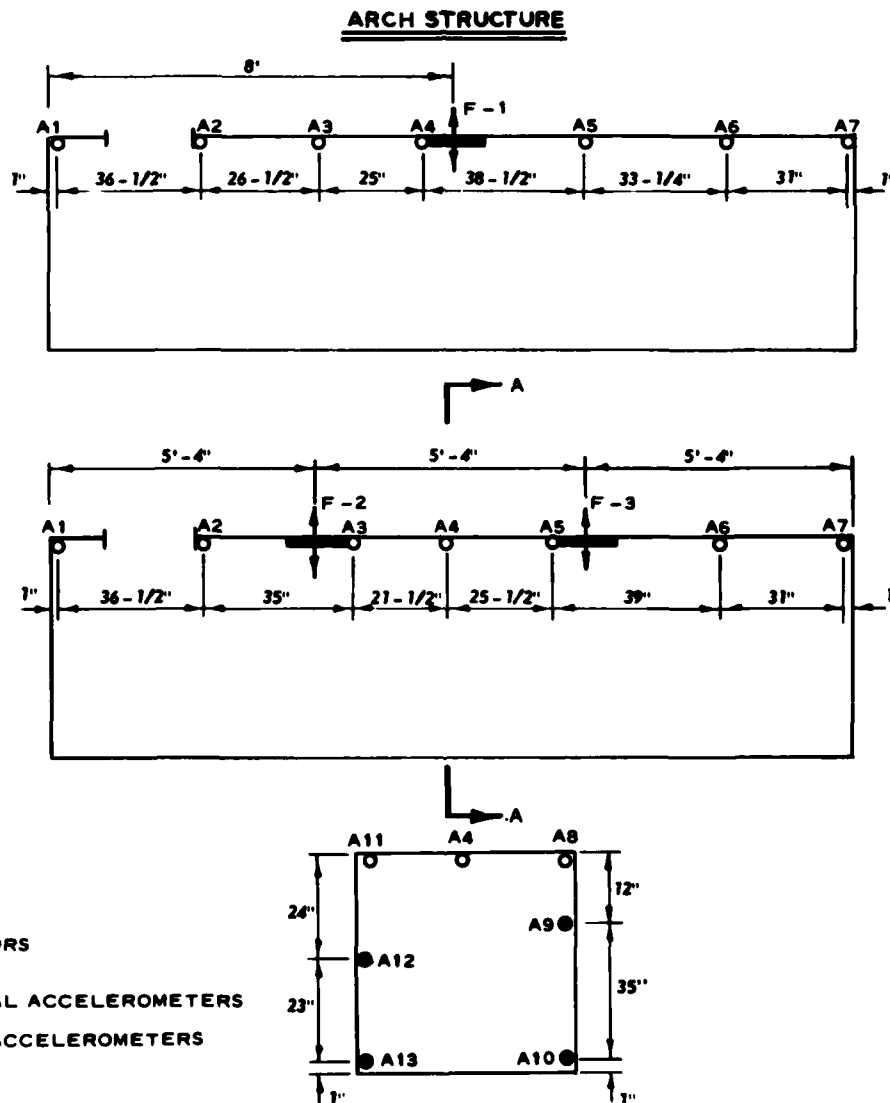
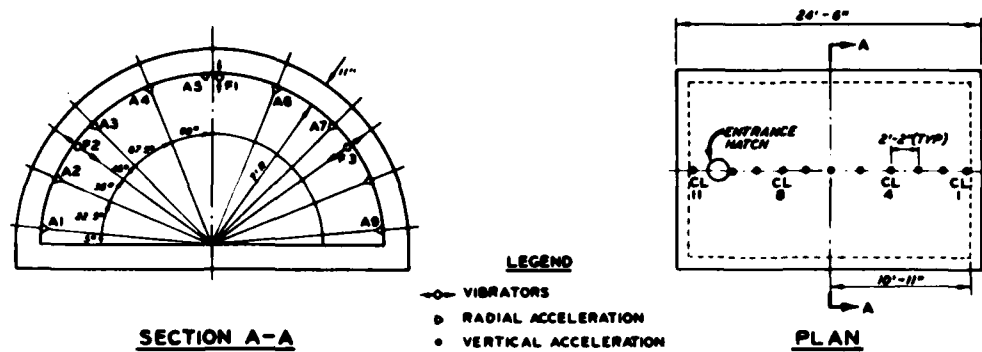
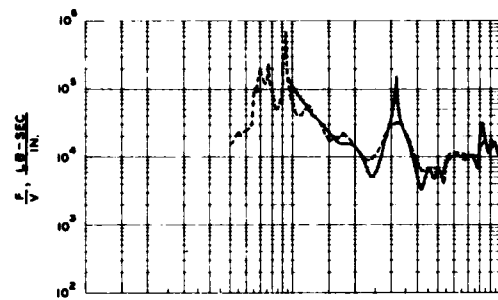
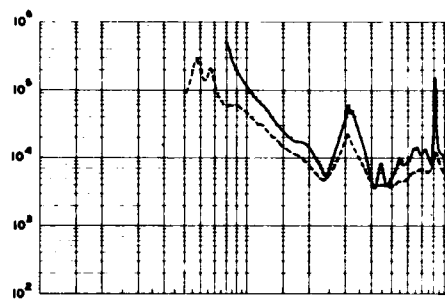


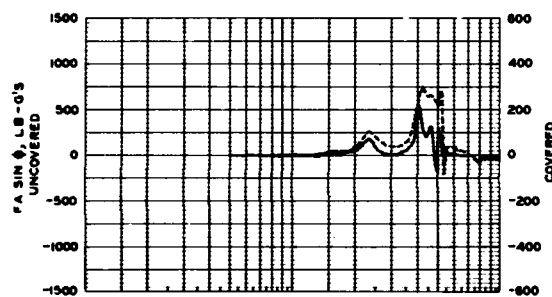
Fig. 3 - Instrumentation layout



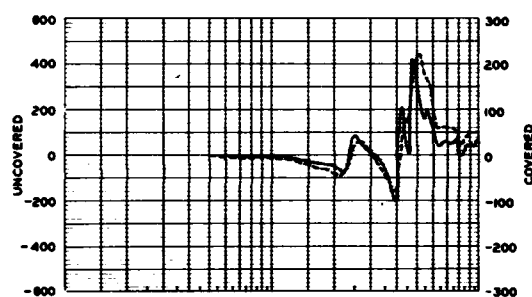
**ACCELEROMETER A3 MECHANICAL IMPEDANCE**



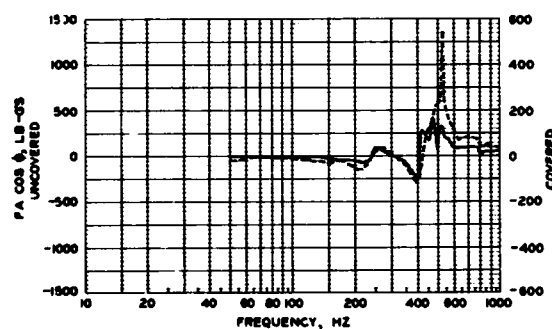
**ACCELEROMETER A5 MECHANICAL IMPEDANCE**



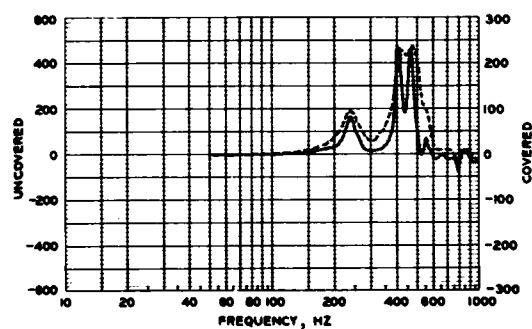
**ACCELEROMETER A3 90° COMPONENT**



**ACCELEROMETER A5 90° COMPONENT**



**ACCELEROMETER A3 IN-PHASE COMPONENT**

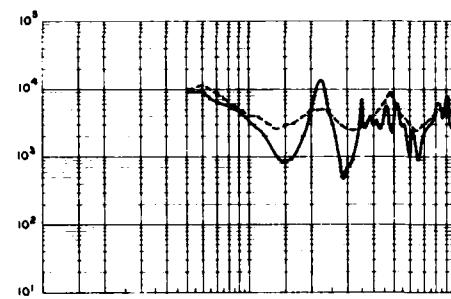
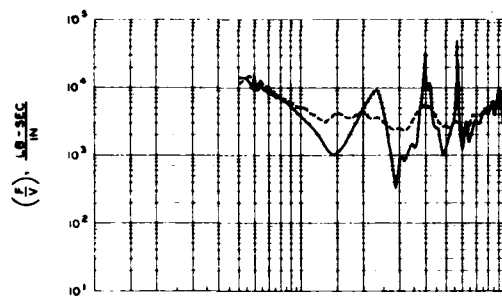


**ACCELEROMETER A5 IN-PHASE COMPONENT**

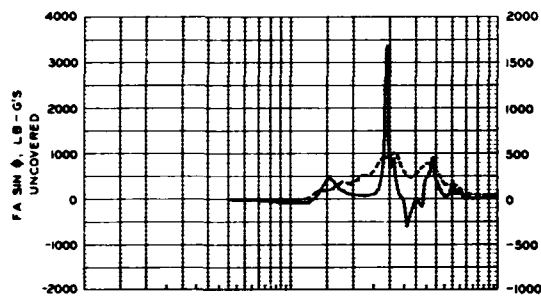
**LEGEND**  
 - - - COVERED  
 — UNCOVERED

F = FORCE  
 V = VELOCITY  
 A = ACCELERATION  
 φ = PHASE ANGLE

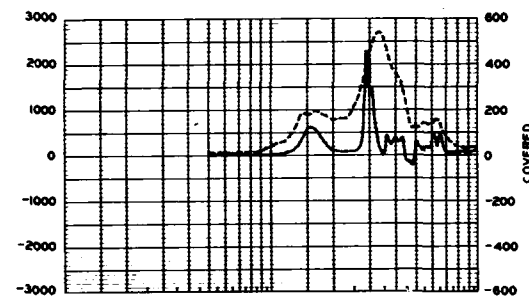
Fig. 4 - Typical response curves for Box Structure 3D with a single vibrator at F-1



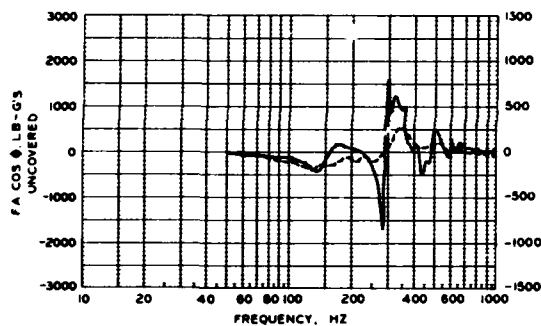
ACCELEROMETER A5 MECHANICAL IMPEDANCE



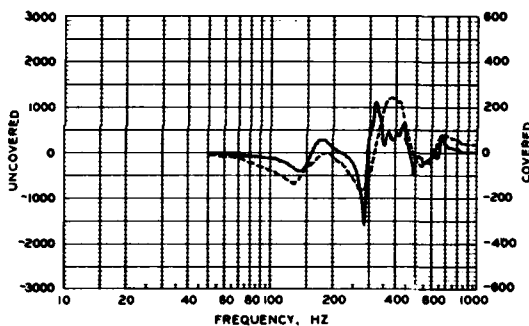
ACCELEROMETER A3 90° COMPONENT



ACCELEROMETER A5 90° COMPONENT



ACCELEROMETER A3 IN-PHASE COMPONENT

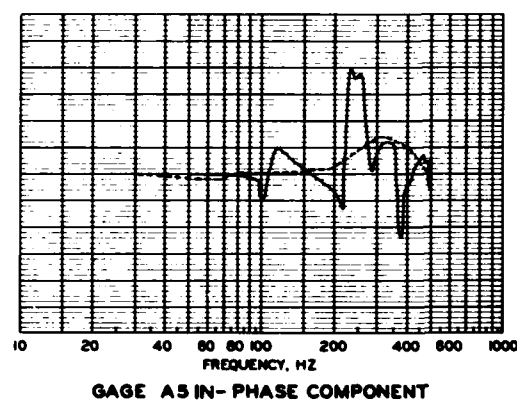
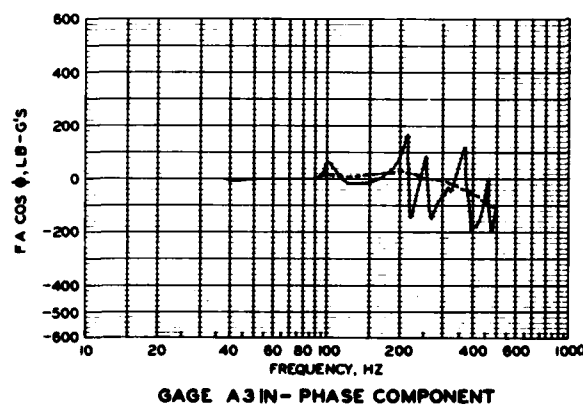
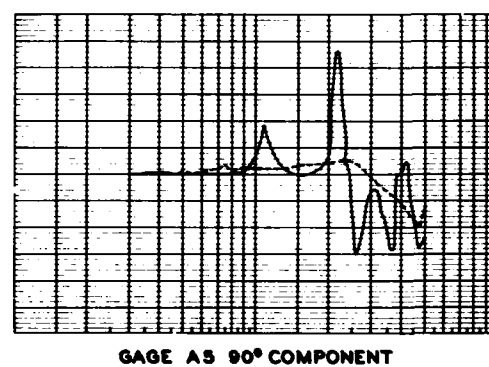
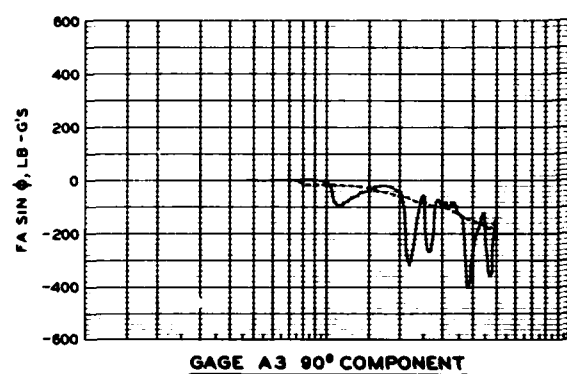
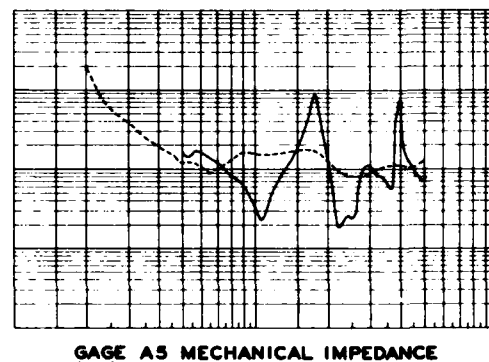
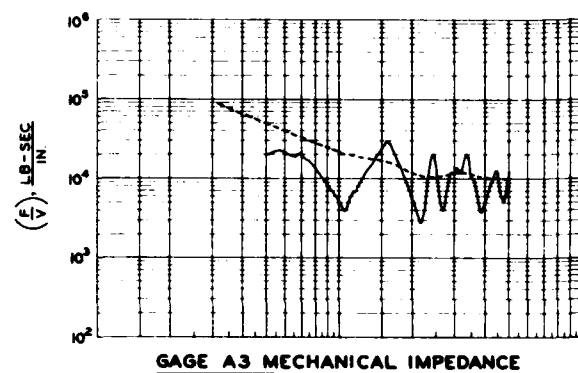


ACCELEROMETER A5 IN-PHASE COMPONENT

LEGEND  
 --- COVERED  
 — UNCOVERED

F = FORCE  
 V = VELOCITY  
 A = ACCELERATION  
 Φ = PHASE ANGLE

Fig. 5 - Typical response curves for Box Structure 3B with vibrators at F-2 and F-3, inphase



LEGEND

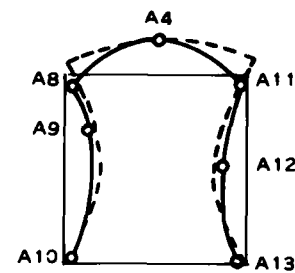
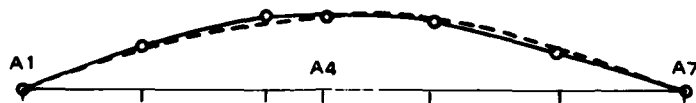
----- COVERED  
 \_\_\_\_\_ UNCOVERED

F = FORCE  
 V = VELOCITY  
 A = ACCELERATION  
 Φ = PHASE ANGLE

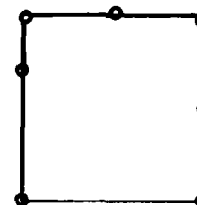
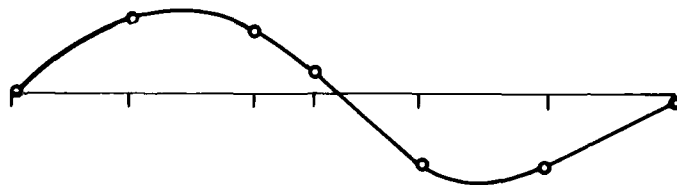
Fig. 6 - Typical response curves for Arch Structure 3A with vibrators at F-2 and F-3, inphase



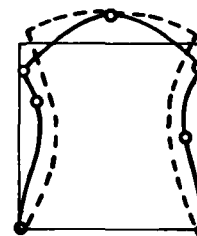
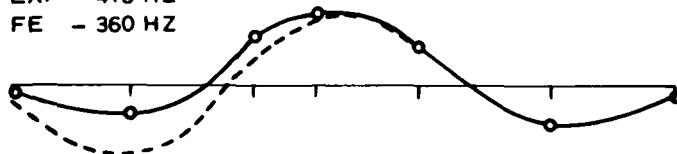
EXP - 237 HZ  
FE - 226 HZ



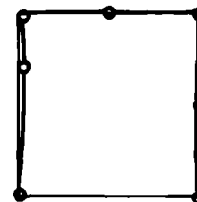
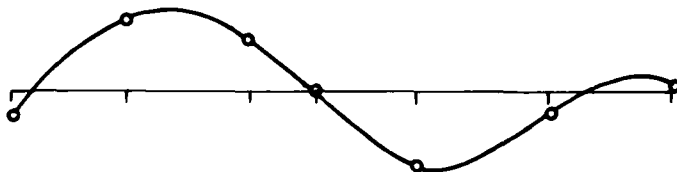
EXP - 310 HZ



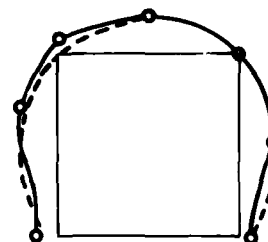
EXP - 415 HZ  
FE - 360 HZ



EXP - 465 HZ



EXP - 470 HZ  
FE - 503 HZ



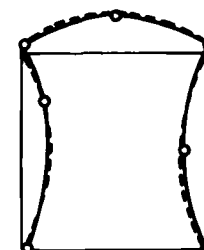
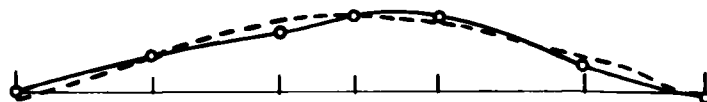
ROOF

— EXPERIMENTAL (EXP)  
- - - FINITE ELEMENT (FE)

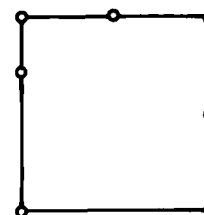
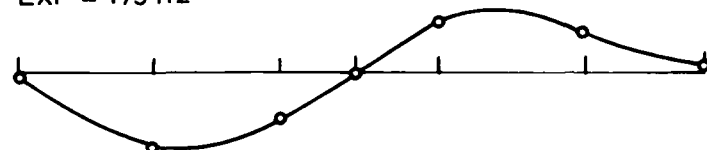
MID SECTION

Fig. 7 - Mode shapes of Box Structure 3D - uncovered

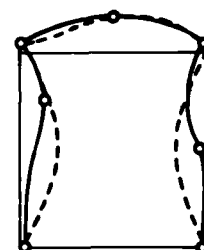
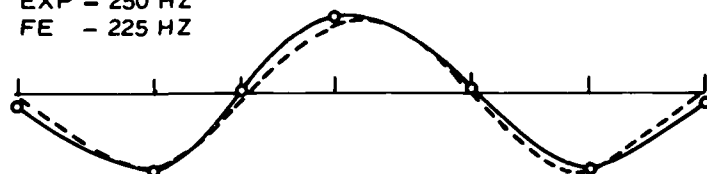
EXP - 152 HZ  
FE - 144 HZ



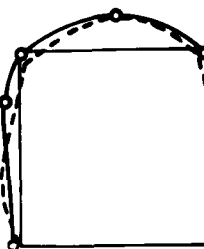
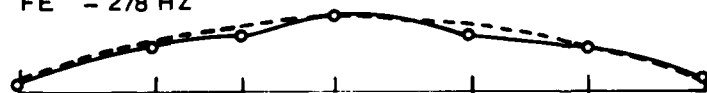
EXP - 175 HZ



EXP - 250 HZ  
FE - 225 HZ



EXP - 300 HZ  
FE - 278 HZ

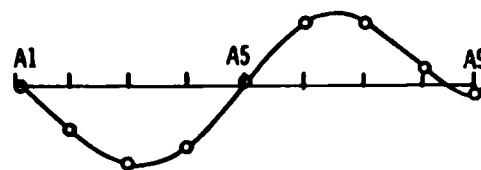


ROOF

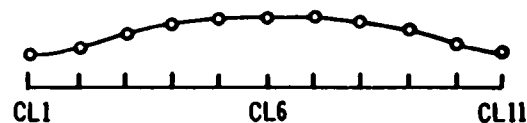
— EXPERIMENTAL (EXP)  
- - - FINITE ELEMENT (FE)

MID-SECTION

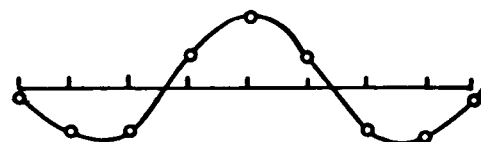
Fig. 8 - Mode shapes of Box Structure 3B - uncovered



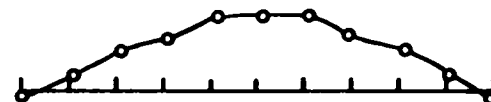
70 HZ - VIB OUT OF PHASE



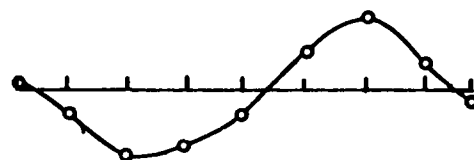
55 HZ



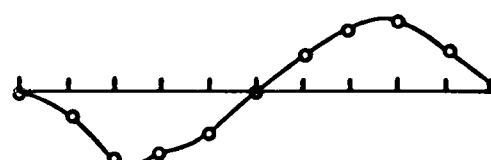
110 HZ - VIB IN PHASE



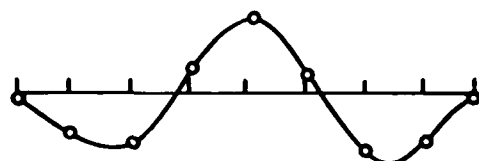
110 HZ



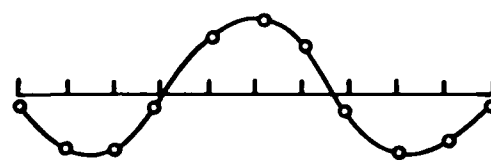
222 HZ - VIB OUT OF PHASE



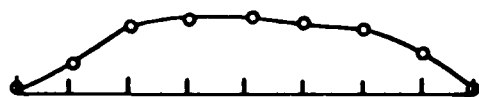
154 HZ



222 HZ - VIB IN PHASE



222 HZ

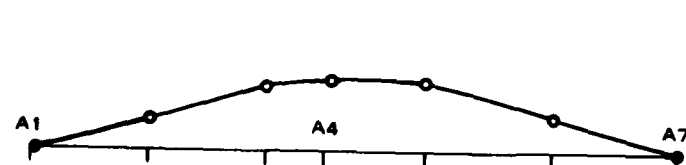


260 HZ - VIB IN PHASE

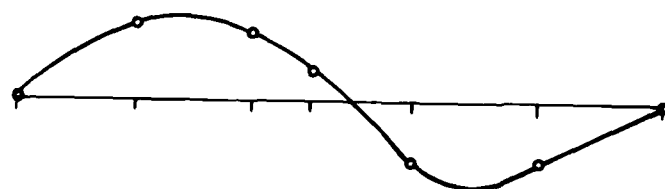
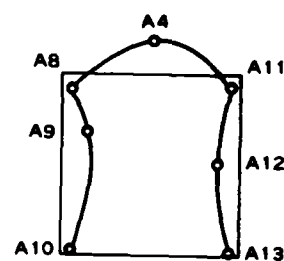
VERTICAL MOTION ALONG CROWN  
SINGLE VIB

# RADIAL MOTION AT MID-SECTION

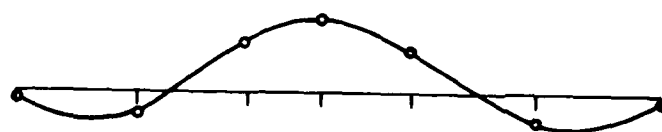
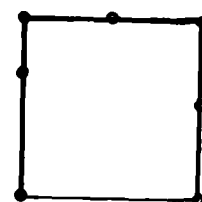
Fig. 9 - Mode shapes of Arch Structure 3A - uncovered



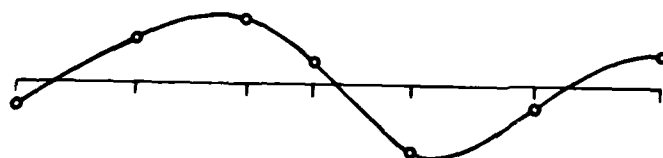
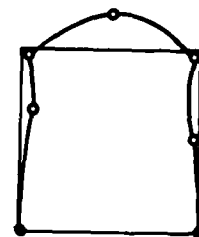
237 HZ - VIB IN PHASE



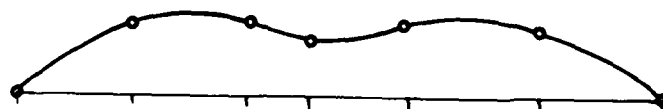
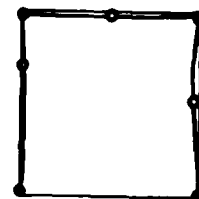
310 HZ - VIB OUT OF PHASE



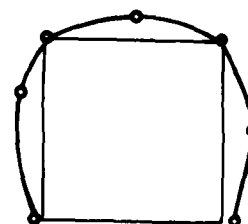
415 HZ - SINGLE VIB



465 HZ - VIB OUT OF PHASE



470 HZ - VIB IN PHASE



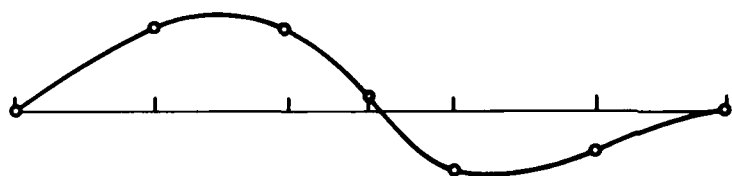
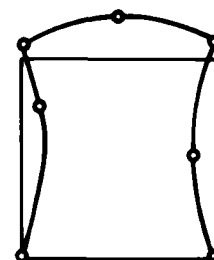
ROOF

MID SECTION

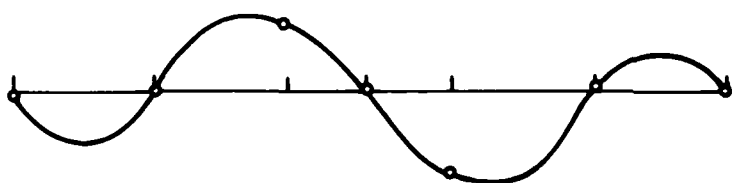
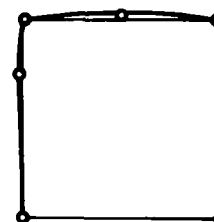
Fig. 10 - Mode shapes of Box Structure 3D - buried



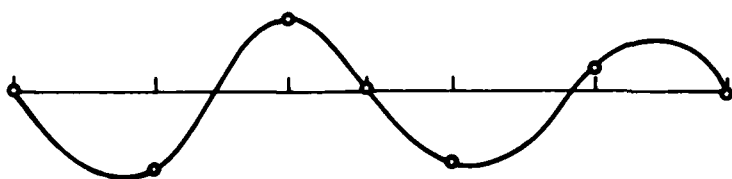
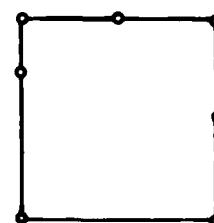
142 HZ - VIB IN PHASE



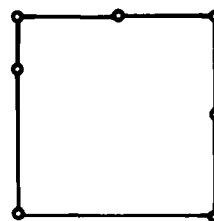
175 HZ - VIB OUT OF PHASE



350 HZ - VIB OUT OF PHASE



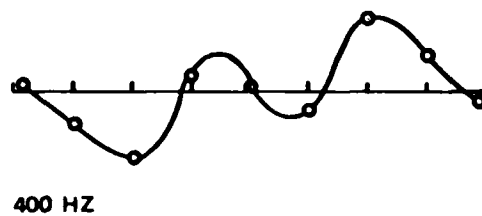
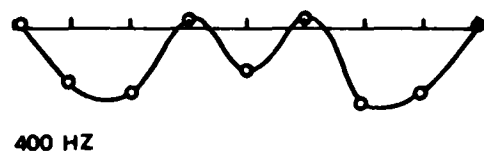
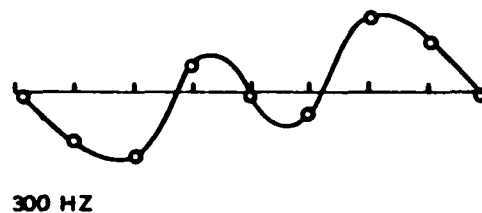
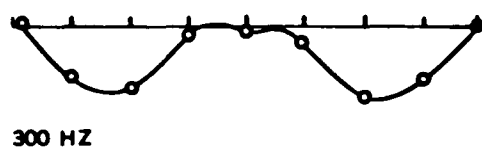
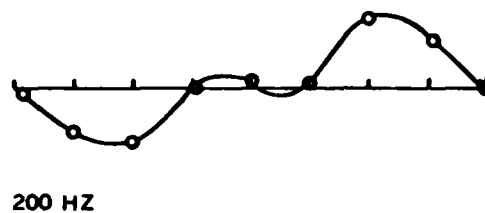
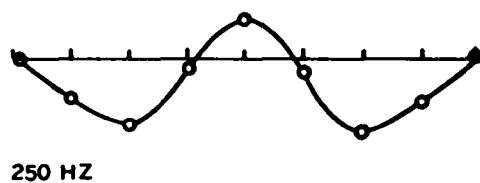
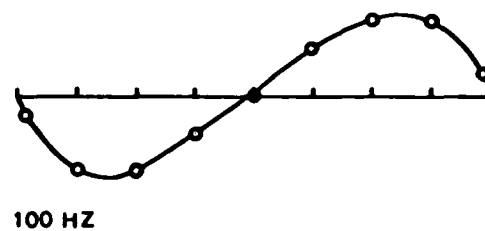
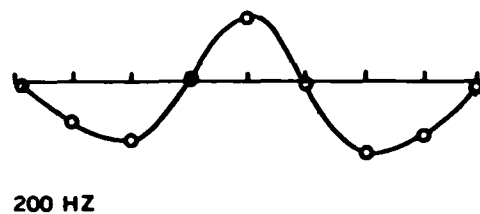
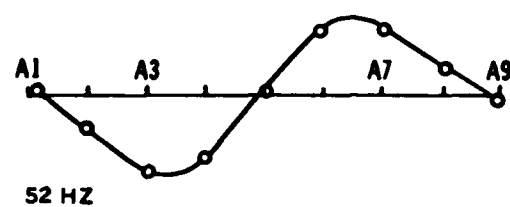
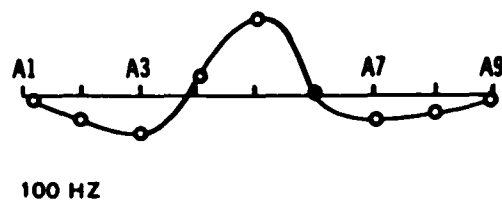
450 HZ - VIB OUT OF PHASE



ROOF

MID - SECTION

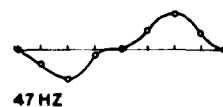
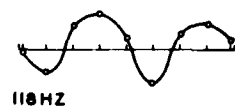
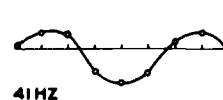
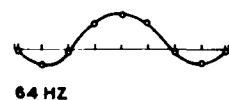
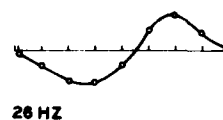
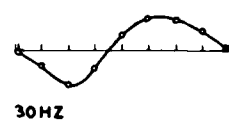
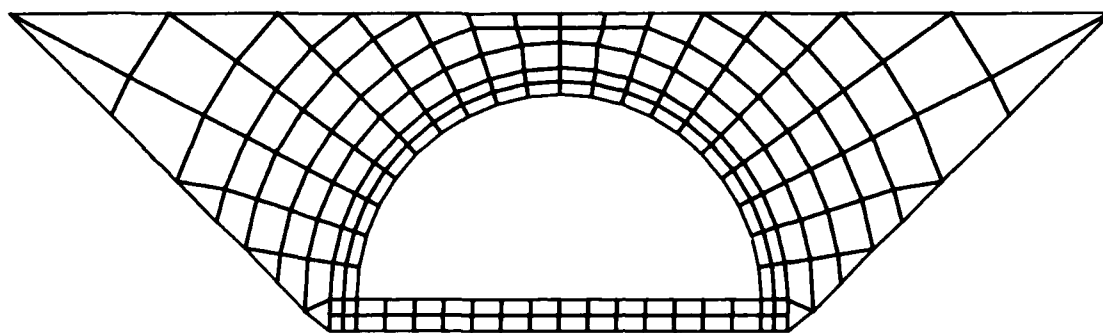
Fig. 11 - Mode shapes of Box Structure 3B - buried



VIB IN PHASE

VIB OUT OF PHASE

Fig. 12 - Deflected shapes of Arch Structure 3A - buried at selected frequencies



UNCOVERED ARCH

BURIED ARCH

Fig. 13 - Two-dimensional finite element grid and first three computed mode shapes for Arch Structure 3A

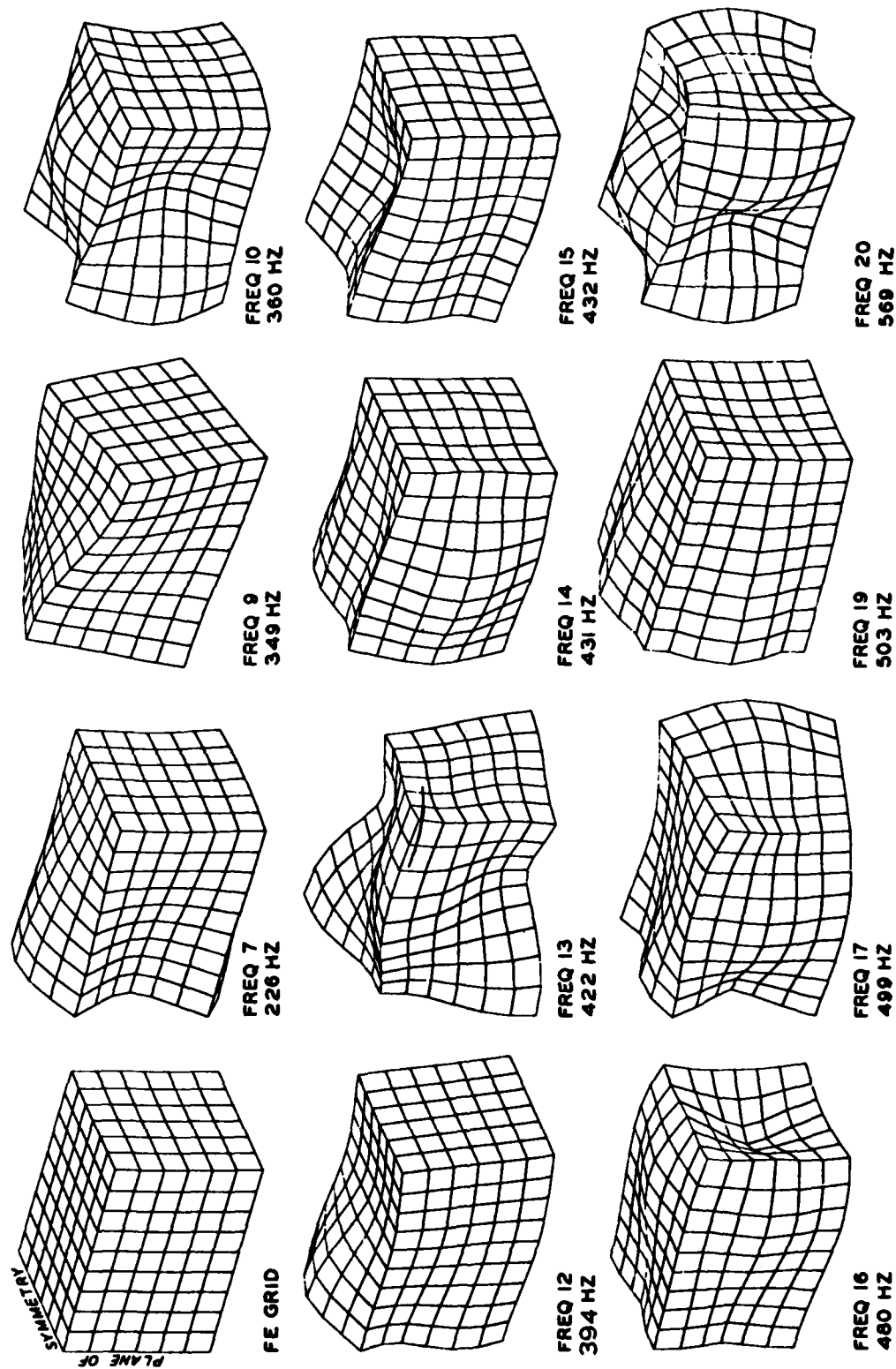


Fig. 14 - Three-dimensional finite element grid and analytical flexural mode shapes of Box Structure 3D (shapes of Box Structure 3B are similar)



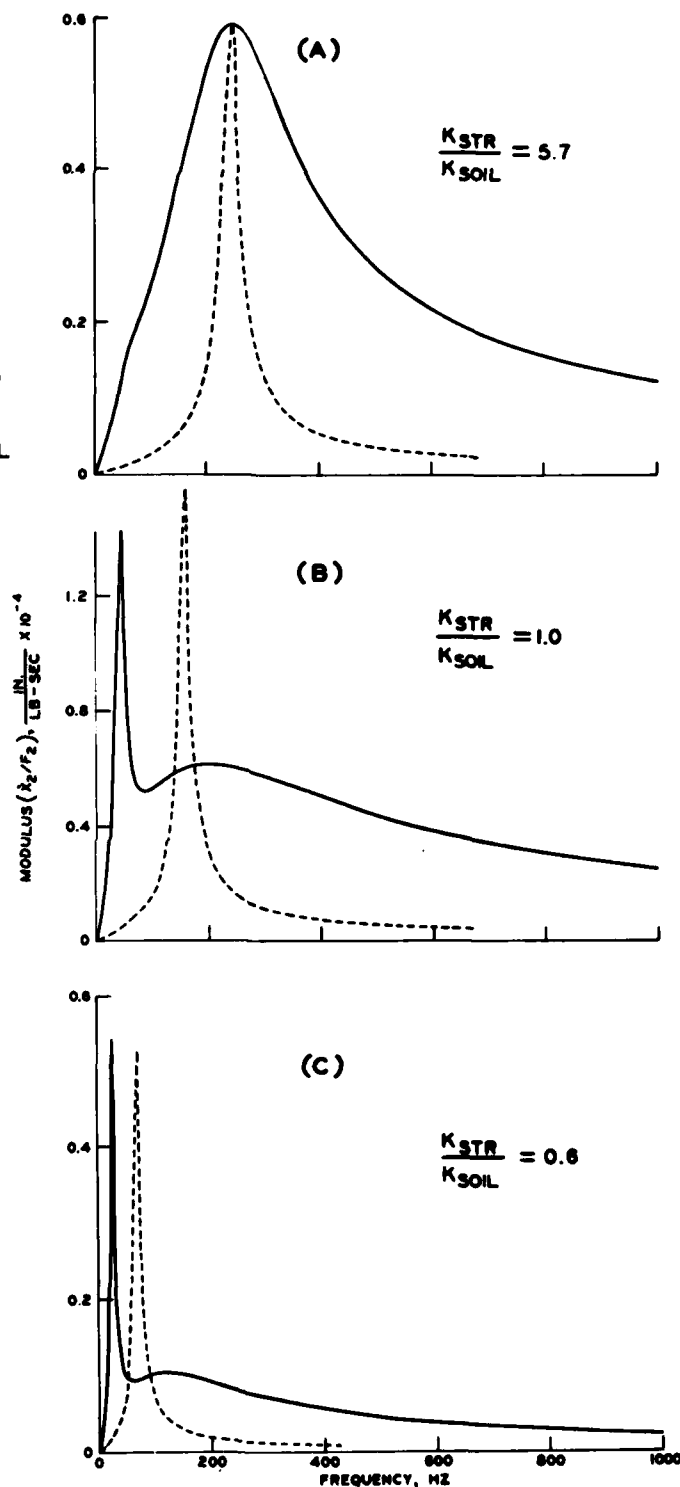
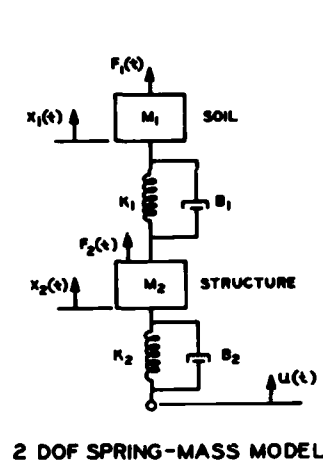


Fig. 15 - Two-degree-of-freedom model

DYNAMIC RESPONSES OF A SOIL  
COVERED CONCRETE ARCH TO IMPACT  
AND BLAST LOADINGS

Phillip T. Nash  
US Air Force Armament Laboratory  
Eglin AFB, Florida

and

Jimmy H. Smith and W. Pennington Vann  
Texas Tech University  
Lubbock, Texas

An analytical model capable of predicting responses of soil-covered concrete arches to dynamic loadings is described. Finite element techniques are used to describe the complex soil-concrete structure. Beam elements capable of inelastic bending and axial deformation are used to describe the concrete arch, and linear triangular elements describe the soil covering. Differences in the compressive and tensile properties of the soil are modeled using bilinear bar elements as connectors between the triangular elements. Numerical techniques are used to solve the differential equations involved. Blast loading functions for the arch were determined in a series of nondestructive scaled experiments and were used to develop load function generating subroutines within the analytical model.

Experiments were conducted using static impact and blast loadings on the structure. Acceleration-time histories were measured at several locations around the arch and integrated to determine velocities and displacements. Strains were measured at several points on the arch during the blast testing. Responses determined by experimentation compared favorably with those predicted using the analytical model. Total arch responses are displayed for the analytical predictions using computer graphic techniques.

INTRODUCTION

An analytical tool has been developed to help solve the complex problems involved in determining hard target vulnerability. Structural systems hardened with soil and concrete present extremely difficult problems in identifying weapon effectiveness.

Most vulnerability analyses depend heavily upon test data. Target vulnerability by nature requires a definition of possible failure mechanisms, so each test must include failure of the target. Useful empirical data must also include enough data points to ensure the reliability of the test procedures and the choices of the parameters tested. It is evident that such test programs for

complex hardened targets are very expensive, even when performed on scaled models.

Analysis techniques are therefore necessary to provide an economical means of studying hard target vulnerability. The analytical technique discussed herein is a computer program designed for Vulnerability Analysis of Non-Linear Interacting Soil and Hardened structures. Thus, the acronym VANISH.

Any such analytical technique must be proven to be accurate in order to ensure its reliability. During the development of VANISH a selected hardened target was studied experimentally, and results were correlated with predictions of the analytical model. VANISH solu-

tions were also compared with exact solutions. The test series included static, harmonic, impact, and blast loads. Comparisons between analytical and experimental results for these different cases are described herein.

#### ARCH STRUCTURE DESCRIPTION

Development of the VANISH code began with the study of an aircraft shelter similar to the one shown in Figure 1. This shelter has been used as a model target throughout the development and validation of VANISH. As shown in Figure 1, the shelter consists of a semicircular barrel arch made up of prefabricated concrete ribs, covered with soil. Each semicircular rib is made up of two quarter-circle elements bolted to adjacent ribs at four locations along each segment. Details of the scaled arches studied are shown in Figure 2. Soil is placed on the structure to a depth of two feet at the crown and slopes along the sides at the natural angle of repose for the soil.



a) Without soil cover



b) With soil cover

Fig. 1 - Hardened Aircraft Shelter

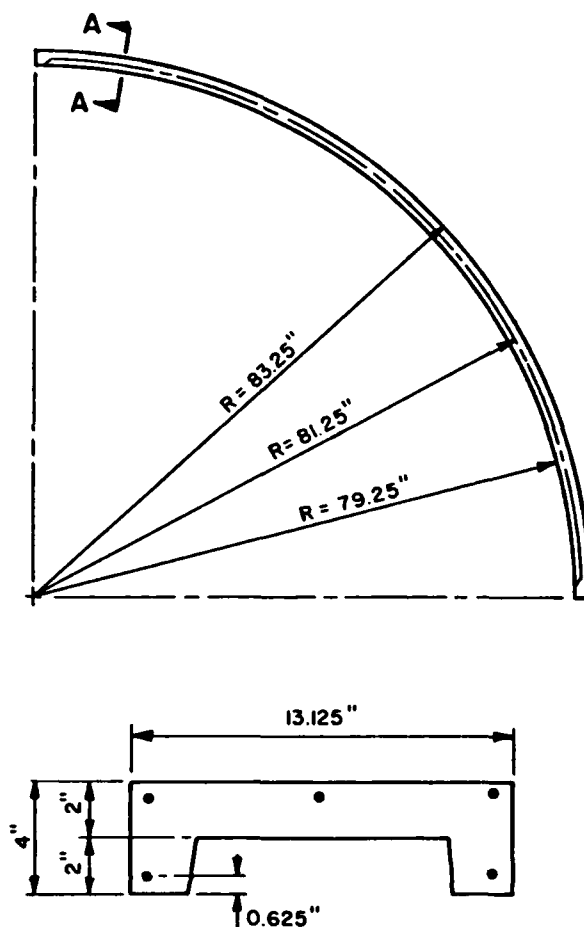


Fig. 2 - Arch Rib Geometry

#### PROGRAM DESCRIPTION (THEORETICAL PRESENTATION)

VANISH is a finite element code capable of analyzing the response of a complex target system with accuracy, reliability, and convenience. In particular, the computer code is designed to model target systems hardened with soil and concrete. While the code has special capabilities for hardened targets, it is intended to be as general as possible so that problems involving soil-structure interaction, framed structures, aircraft structures, and other structures can also be analyzed. Both static and dynamic planar problems can be solved considering either linear or nonlinear behavior of the structural materials. Dead weight loads can be included in the analysis. Static loads

are applied incrementally for static nonlinear solutions, and numerical integration is used to solve the differential equations involved in dynamic solutions.

Three basic finite elements are available in VANISH as shown in the analytically described aircraft shelter of Figure 3. First, straight prismatic planar beam elements are used to describe the concrete arch section of the shelter. These beam elements have six degrees of freedom and can undergo inelastic bending and axial deformation. A short beam element is used to model the load carrying capabilities of the joint at the crown of the arch. Second, constant strain triangles are used to describe the soil covering. These elements have six degrees of freedom but are restricted to linear behavior. Third, nonlinear behavior of the soil is modeled using bar elements as connectors between the triangular elements. The straight, prismatic bar elements are incapable of carrying moment and are thus strictly tension and compression elements. Bilinear material properties for the bar elements are used to describe the different tensile and compressive properties of the soil. The bar elements are positioned where tensile stresses are expected to produce cracks in the soil. In this study of blast loading inside the buried arch, circumferential tensile stresses were common. Bar elements were therefore placed as element connectors across radial lines emanating from the center of the arch as shown in Figure 3.

Damping of any structural system can be input as relative damping (proportional to the stiffness of the system), absolute damping (proportional to the mass of the system) or a combination of both. Loads are applied at the nodes and are specified for each time step for dynamic cases. Values of loads at each time step can be input as data or generated using force-generating subroutines. Element forces and stresses are determined for each time step and element failures are identified. A more detailed description of the computer code is presented in "Theoretical and Experimental Investigation of Buried Concrete Structures, Volume I--Analysis and Experiment," AFATL-TR-76-55.

#### PROGRAM VALIDATION

Extensive testing has been performed to ensure the accuracy of VANISH analysis. Exact solutions as well as responses in static, harmonic, impact, and blast loading tests have been correlated with VANISH predictions for the aircraft shelter structure. Agreement between analytical prediction and experimental results has been satisfactory thus far.

A. Exact Solution. Results from an exact solution of a statically loaded bare arch are compared to a VANISH solution of the same system in Figure 4. Here vertical deflection is plotted as a function of position around the arch. Two-hinged (with continuity at the crown) and three-hinged (hinged at the crown) configurations are both consider-

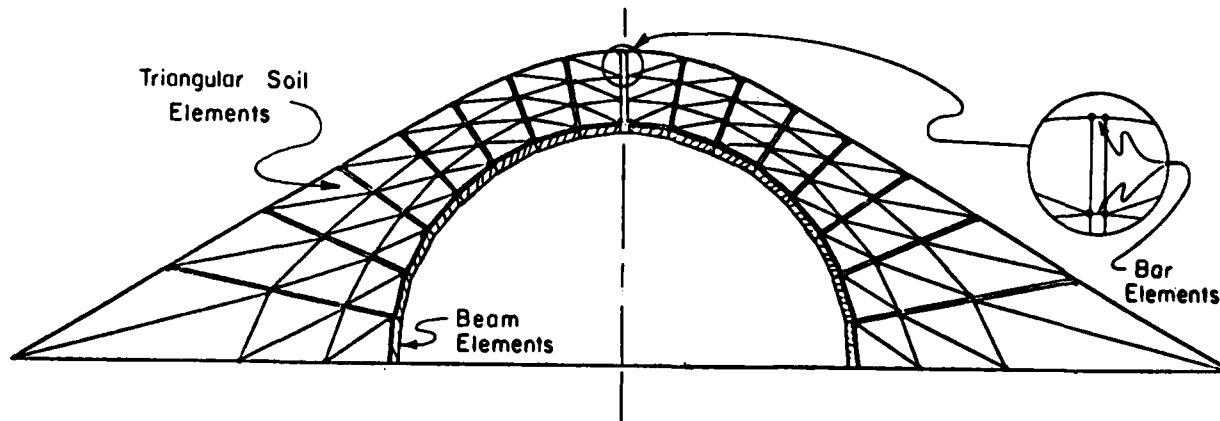


Fig. 3 - Finite Element Mesh

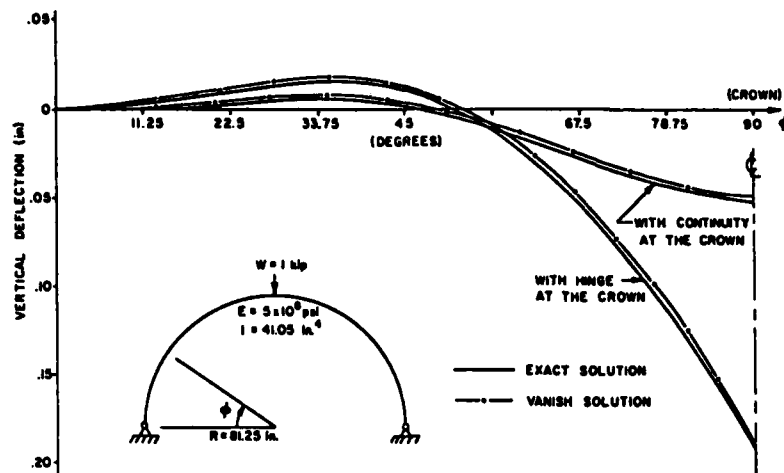


Fig. 4 - Comparison of Vanish to Exact Solution

ed. Results from the exact solution and the VANISH solution agree within 2 1/4 percent. Experiments using one-rib, three-rib, and five-rib sections of the bare concrete arch bolted at the crown and loaded with concentrated static loads at the crown reveal arch deflection values that are between those for the hinged and continuous configurations, as shown in Figure 5. Actual measured deflections can be accurately correlated with VANISH predictions by modeling the connection with a beam element having a very small percentage of the moment capacity of the other arch elements.

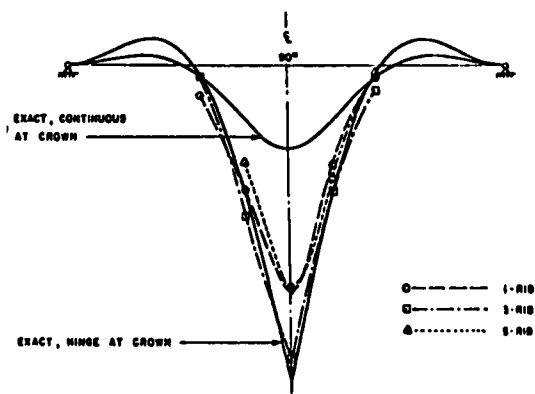


Fig. 5 - Effect of Crown Connection on Vertical Static Deflections

**B. Harmonic Loading.** Laboratory experiments were conducted using both bare and soil-covered arches subjected to harmonic loadings. Harmonic loads were imposed either horizontally or vertically at the crown and velocities and displacements were recorded at various locations around the arch. Loading frequencies were varied from 1 to 30 Hz. Natural frequencies and mode shapes were determined and correlated with VANISH predictions. The asymmetric and symmetric mode frequencies for the soil-covered arch were determined experimentally to be near 5 Hz and 9 Hz, respectively. VANISH predictions for these two frequencies were 4.9 Hz and 8.7 Hz, respectively, giving agreement within 4 percent.

Computer graphic techniques were used in conjunction with VANISH to produce the plots of the first symmetric and first asymmetric mode shapes for the soil-covered arch that are shown in Figure 6. Displacements have been exaggerated in the plots to better identify mode shapes. The radial lines chosen to model cracking in the soil due to blasts within the structure appear to act as shear planes for the modes plotted.

**C. Impact Loading.** Field tests were conducted with the aircraft shelter shown in Figure 1 using impact loads. Loads were imposed by dropping a known weight from a specific height onto a receiving frame attached to the arch as illustrated in Figure 7. Structural response was measured at the point of loading using a vertically oriented accelerometer. Acceleration-time respon-

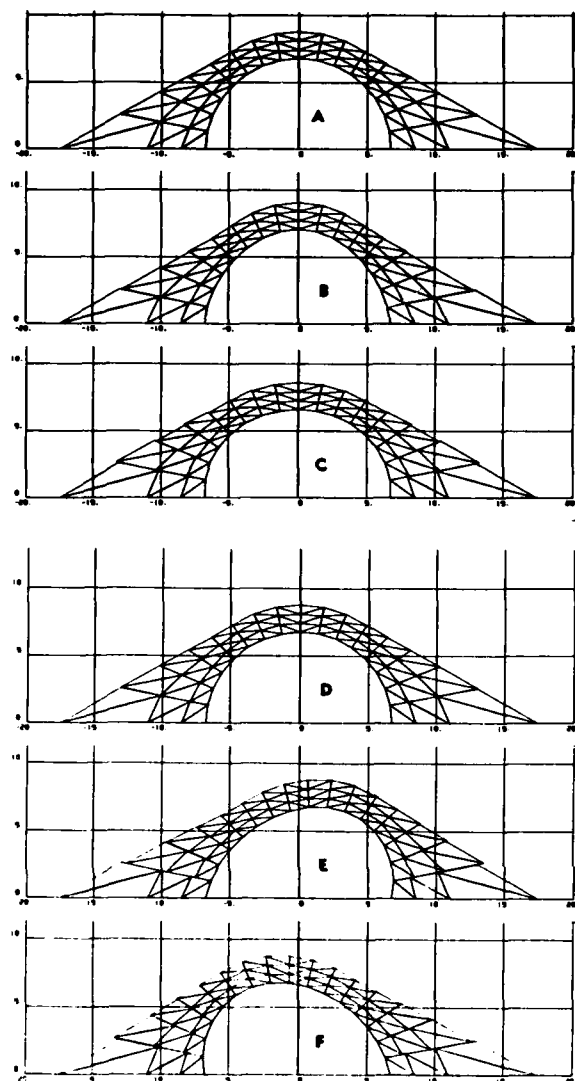


Fig. 6 - Dynamic Mode Shapes

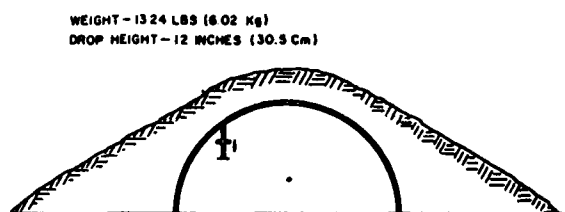


Fig. 7 - Impact Loading Test

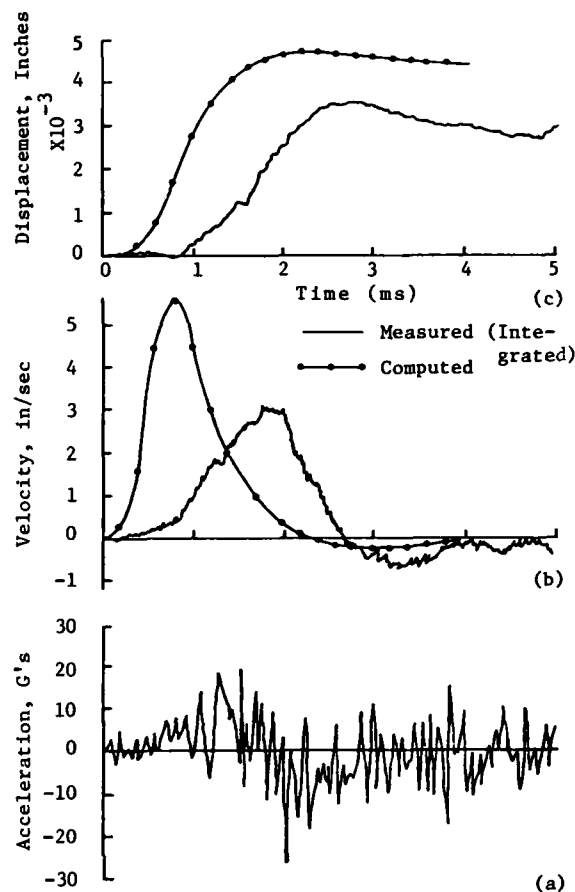


Fig. 8 - Response Comparisons - Impact Test

ses, as shown in Figure 8(A), were numerically integrated twice for comparison with the VANISH predictions shown in parts (B) and (C) of the figure. Displacements were found to be extremely small (0.004 inches) and agreed reasonably well. The high frequency response shown in the acceleration-time curve is attributed to the accelerometer mount. A phenolic block was used to orient the accelerometer vertically. The block exhibited a very high frequency response (8000-11000 cps). Integration techniques adequately filtered the response from the block for the impact test, but additional filtering was required for blast test data.

D. Blast Loading. A series of blast tests was conducted against the scaled aircraft shelter. Small, non-destructive charges were detonated inside the shelter and blast pressures were measured at eight locations around

one arch section. Vertical and horizontal accelerations and concrete strains were measured on the adjacent arch at the same locations as the blast pressure measurements. Charge positions and sizes were varied. A typical blast pressure-time history is shown in Figure 9. Measured pressure loadings were used to develop loading functions for the analytical model. Acceleration levels for the arch were difficult to discern from the measured accelerations because of the high frequency response of the accelerometer mounts, as can be seen in Figure 10. Regarding the mount as a single-degree undamped system made it possible to determine the structural responses of the arch, however. By considering the arch motion to be

$$y_a = y_{ao} \sin \Omega t$$

where

$$\begin{aligned} y_a &= \text{arch displacement} \\ y_{ao} &= \text{some magnitude of arch displacement} \\ \Omega &= \text{frequency of arch response,} \end{aligned}$$

then the measured displacement due to this input support displacement is

$$y_m = y_{ao} \omega^2 \left( \frac{\sin \Omega t}{\omega^2 - \Omega^2} - \frac{\Omega}{\omega} \frac{\sin \omega t}{\omega^2 - \Omega^2} \right)$$

where

$$\begin{aligned} y_m &= \text{measured displacement} \\ \omega &= \text{frequency of mount response.} \end{aligned}$$

The corresponding acceleration can then be determined as

$$\ddot{y}_a = -\Omega^2 y_{ao} \sin \Omega t$$

and

$$\begin{aligned} \ddot{y}_m &= y_{ao} \omega^2 \left( -\frac{\Omega^2 \sin \Omega t}{\omega^2 - \Omega^2} + \frac{\omega \Omega \sin \omega t}{\omega^2 - \Omega^2} \right) \\ &= y_{ao} \omega^2 \text{DLF} \end{aligned}$$

Therefore,

$$\ddot{y}_a = \frac{-\Omega^2 \sin \Omega t}{\omega^2 \text{DLF}} \ddot{y}_m$$

Using known values of the first arch frequency  $\Omega$  and the accelerometer frequency,  $\omega$ , the last equation was used with the measured accelerations  $\ddot{y}_m$  to obtain arch accelerations at a series of time steps. This record was then integrated numerically two times to produce a displacement-time curve that could be compared to vanish curves, as shown in Figure 11.

During the laboratory experiments using harmonic loadings, fundamental mode damping was found to be between 24 and 28 percent of critical. As shown in Figure 11, VANISH solutions consider 25 percent critical damping predicted displacements greater than those measured in the field tests. Response frequencies were also higher than those found in the test series. Increasing the damping in the VANISH solution resulted in displacement and frequency values that were closer to the field results. From Figure 11 it appears that the responses correlate best for damping between 40 and 50 percent of critical. Considering the extremely complex load-time histories imposed on the arch due to internal blasts and the construction tolerances for the shelter, the experi-

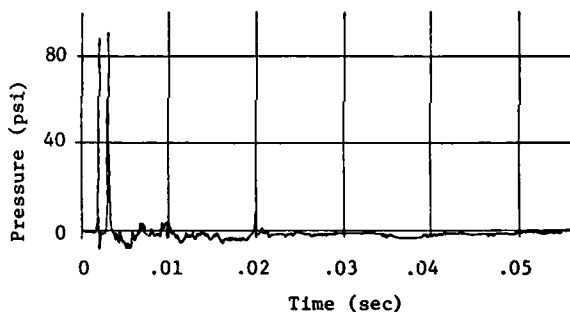


Fig. 9 - Typical Pressure-Time History

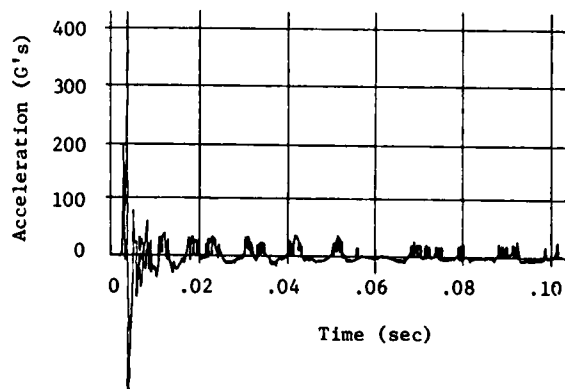


Fig. 10 - Acceleration-Time History

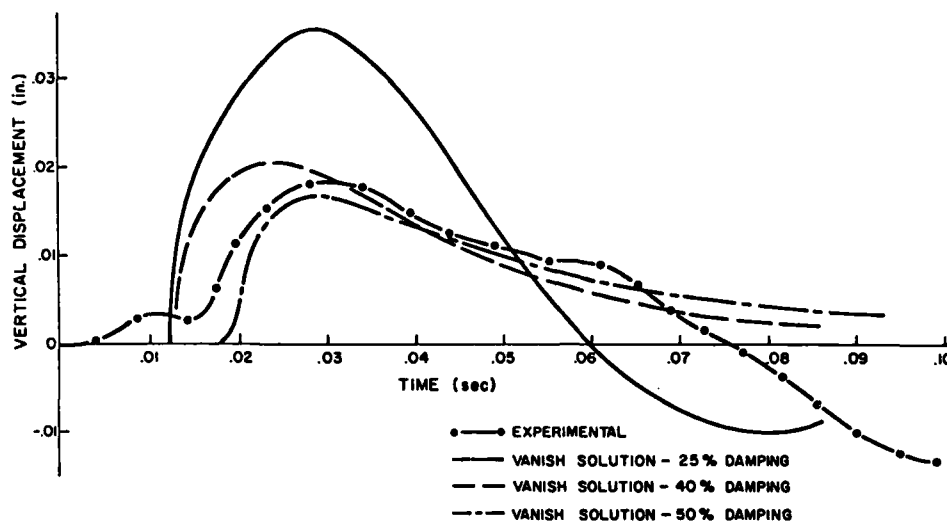


Fig. 11 - Displacement Comparisons for Blast Loading

mental and analytical results compare very well. This correlation of the results indicates a large amount of damping in the field structure and the importance of being able to incorporate damping into the analytical model.

#### CONCLUSION

VANISH has proven to be highly accurate for performing static analyses. Analytical and experimental results correlated very well for the harmonic loading experiments. Comparisons of predicted and measured responses for the impact loads agreed reasonably well. It is important to note that the deflections from the impact loading were extremely small, high-frequency responses that were determined by numerical integration of measured acceleration time histories. Results from the blast tests exhibited the same general types of response as determined analytically and agreement between predicted and measured responses was considered satisfactory. The importance of choosing proper damping factor values was illus-

trated in correlating the results. A better understanding of target response mechanism was gained during each phase of the validation series.

VANISH has proven to be an accurate method of analysis and will be a valuable tool for vulnerability analyses. Analysis techniques such as VANISH offer flexibility in approaching vulnerability studies and can be used to gain insight into target failure mechanisms. Most important of all, VANISH will be used to greatly reduce time and cost requirements of future hard target vulnerability analyses.



## Discussion

Mr. Gerardi (Air Force Flight Dynamics Lab): How did you input your forcing function of the blast into your mathematical model?

Mr. Nash: These forced generating sub-routines were special to this structure, and they were developed especially for this structure. We input them using the modified Friedlander equation for air blast. We smoothed out the multiple peaks. Since this is an impulsive loading, we don't feel that we have lost the accuracy.

Mr. Gerardi: Did you input a time function into the model?

Mr. Nash: It's just a sub-routine. I think this points out the flexibility we hope to have in the model. If you used NASTRAN or one of the larger programs, you wouldn't have this flexibility to be able to work at your desk.

Mr. Krause (Waterways Experiment Station): You stated that damping was a function of the stiffness and the mass in the system. Did you use these terms for soil damping, and if so, how did you obtain your soil properties, and what did you use for a typical soil damping term?

Mr. Nash: We haven't conducted any tests to determine the exact damping coefficients for the soil media. There are an input to the program. It goes into a matrix and this matrix, in turn, is used in the analysis process. We were able to determine some damping coefficients from the harmonic tests conducted at Texas Tech University.

Mr. Krause: Have you compared your two-dimensional model results to any other results obtained from exciting the entire structure?

Mr. Nash: Not yet. I think Rogers talked about some tests they conducted at Eglin Air Force Base a few years back.

Mr. Birchler (BDM Corporation): Will you describe your beam model and the kind of integration schemes that you used?

Mr. Nash: The integration is just a Newmark Beta method. The beam model has rotation on each of the axial forces.

Mr. Birchler: The summary said it was a non-linear model. What kind of nonlinear terms did you use?

Mr. Nash: It is really a bi-linear material property description. We had initial slope equal to the elastic modulus, then we go into the plastic region, and you're able to go out the stress strain diagram at a very small slope. Then, if there is any return of the structure, we return down the elastic curve.

Mr. Birchler: Is there any coupling between axial force and bending moments?

Mr. Nash: No.

Mr. Plamondon (Air Force Weapons Laboratory): You stated that the base of the arch was keyed into the support slab under the internal pressure loading. Could you comment on the behavior of that connection? If it separated what would that do to your analysis procedures?

Mr. Nash: We have discussed that among ourselves. I don't think there was any lifting of the arch. The joint fails long before the entire structure lifts. I think that is a ratio of the strength of the arch and the weight of the structure for an internal blast. If it were a continuous arch, it would be a different problem.

## INSTRUCTURE SHOCK ENVIRONMENT OF BURIED STRUCTURES SUBJECTED TO BLAST INDUCED GROUND SHOCK

S. A. Kiger  
USAE Waterways Experiment Station  
Vicksburg, Mississippi

Two shallow-buried reinforced-concrete structures were tested with subsurface high-explosive (HE) charges. Instructure and free-field shock spectra generated from these tests were used to develop guidelines for predicting structural response and instructure shock environment for HE generated ground shock.

### SUMMARY

The objective of this paper is to determine the shock environment in a buried protective structure subjected to the effects of nearby detonations of subsurface high-explosive (HE) charges. This investigation was conducted as a part of a Defense Nuclear Agency-sponsored study to determine the effects of localized explosions on the response of hardened command centers.

Two concrete box structures were instrumented and subjected to the explosion effects of a total of eight 21-pound spherical TNT charges. These structures were approximately 1/4-scale models of commonly found hardened structures. Measurements were made of the accelerations and velocities caused at various locations in the soil and the structure by the detonation of the spherical charges at various charge-to-structure locations and distances.

The procedures normally used for estimating peak instructure displacements, velocities, or accelerations caused by large-scale events, such as earthquakes or nuclear weapons generated ground shock, predict the instructure response to be an amplification of expected free-field motion. The shock spectra developed from these localized HE test data indicate that the horizontal free-field motion should be reduced to predict peak instructure response.

Instructure shock attenuation measurements indicate that no horizontal attenuation of the acceleration pulse occurs across the floor of the structure and, except for a peak at the leading edge of the structure, no attenuation of the vertical pulse occurs.

The instructure acceleration signals were used to generate shock spectra for various levels of damping. These spectra, along with peak values of floor displacement, velocity, and acceleration, can be used to determine

instructure amplification factors for equipment response prediction for threat-structure systems that are some scale multiple of those investigated in this study.

### INTRODUCTION

The major concern in the design of a command and control center is to prevent structural failure. However, the operation of sophisticated electronic gear within the center may be impaired at shock levels much less than those required to fail the structure, thus preventing the center from completing its mission. In order to economically design shock isolation devices to protect the various components within the structure, the internal shock environment must be well defined. For long duration ground shock, such as the ground motion associated with a nuclear event, the procedure for the modification of the free-field ground motion to predict the instructure motion is well documented. However, procedures for predicting the instructure shock environment in the case of short duration ground shock, such as that generated by conventional weapons, are not so well established.

### OBJECTIVES

The objectives of this study are threefold; first, to establish a set of suggested factors with which to modify the free-field shock spectra to predict peak instructure motions for a conventional weapon threat; second, to establish a set of shock spectra which can be used to design instructure shock isolation devices; and third, to determine the attenuation of the peak acceleration across the floor of the structure.

### PROCEDURE

A test series of eight 21-pound spherical TNT charges was conducted. The series consisted of two tests on a relatively soft structure with a span-to-depth ratio of ten and three

tests on a relatively stiff structure with a span-to-depth ratio of four. In addition, three tests were conducted to determine instructure acceleration attenuation.

#### TEST STRUCTURES

The two structures investigated were typical of many hardened buried structures of concrete slab type construction. The structures, labeled 3C and 3D, were reinforced concrete box structures, having a roof, floor, and wall span-to-depth ratio of 10 and 4, respectively. Both structures were 16 feet long by 4 feet wide by 4 feet high (inside dimensions); the overall wall thickness including concrete covers on the tension steel of 3C was 5.8 inches and that of 3D was 13 inches. Principal reinforcing steel was 1 percent for both tension and compression. The structures were fully buried with 2 feet of compacted backfill cover at the roof line. Structural details and dimensions are shown in Figure 1.

#### TEST DESCRIPTION

A sketch of the test layout and instrumentation is shown in Figure 2. Three tests were conducted for the instructure acceleration attenuation experiment. Acceleration gages measuring horizontal and vertical data were placed at five evenly spaced locations on the floor of the structure as shown in Figure 2a. The explosives used were 21-pound spheres of TNT, buried to midstructure depth and placed at ranges of 10, 8, and 6 feet from the end of structure 3D.

Tests on structure 3C were conducted at positions labeled Test 1 and Test 2 and on structure 3D at positions labeled Test 1, Test 2, and Test 3 in Figure 2b. Structure 3C was cracked during Test 2. All tests were conducted with 21-pound spheres of TNT buried to midstructure depth. Instrumentation included vertical and horizontal instructure acceleration and velocity measurements at the center of the floor and horizontal free-field acceleration and velocity measurements as shown in Figure 2b.

#### TEST RESULTS AND DATA ANALYSIS

All data were recorded on magnetic tape in analog form. Each channel was subsequently reduced to digitized format, and time-response plots made of the digitized data. Digitizing was done at the rate of 40 kHz, i.e., 40,000 samples per second. Sample acceleration, velocity, and displacement response records are given in Figures 3, 4, and 5.

The maximum values of the free-field data obtained in the project are compared to data available from other experiments in Figures 6, 7, and 8. Data points on these plots labeled Post ESSEX Box, 21 lb, are from the experiments described in this report. All other data shown in Figures 6, 7, and 8 were taken from

Reference 1 with the permission of the author.

Figure 6 is a plot of scaled acceleration versus scaled range using cube root scaling, i.e., the quantities of time and length are divided by the cube root of the charge weight. The peak acceleration data obtained in the current experiment are consistently lower than would have been predicted from previous results. This was probably due to the low compaction level of the backfill material in which the tests were conducted. The backfill was placed with a front end loader and compacted by repeated passes with the machine. This relatively low compaction of the soil should tend to decrease shock levels.

The peak velocity data collected in these tests are shown in Figure 7. These data points are very close to the values predicted from previous test results.

Maximum displacement data collected in these tests are shown in Figure 8. These data points are generally higher than would have been expected from previous test results. Again, the explanation is probably the low compaction of the soil.

Figures 9 and 10 show the 5 percent damped free-field spectra for horizontal motion at a range of 8 feet. The peak acceleration, velocity, and displacement measured at the center of the floor, with the explosive at a range of 8 feet from the leading edge of the structure for structures 3C and 3D, are also shown. The peak horizontal floor motions are shown in Figure 9 and peak vertical floor motions are shown in Figure 10. The curves in Figures 9 and 10 show that the peak floor motions are less than would have been predicted from the free-field spectra. For example, for 5 percent damping at a range of 8 feet, the reduction factors as determined from Figures 9 and 10, for structure 3C are 0.1 for horizontal acceleration and 0.04 for vertical acceleration. Reduction factors for 0, 5, and 10 percent damping are given in Table 1. The reduction factors for structure 3C are average values from tests at ranges of 8 feet and 6 feet, and those for structure 3D are averages from tests at 8, 6, and 4 feet. These reduction factors, along with the free-field shock spectra at the leading edge of the structure, can be used to predict peak values of the instructure motions.

Peak floor motions and shock spectra for the instructure response for 0, 5, and 10 percent damping are shown in Figures 11 through 20. Amplification factors for predicting peak values of the instructure response, as determined from these curves are given in Table 2. The amplification factors in Table 2 are average values obtained by approximating the shock spectra with shock spectra bounds, i.e., linear tangents to the spectra with slopes of +1, 0, and -1. As an alternative to using the amplification factors from Table 2, peak response values, obtained from the instructure shock

spectra in Figures 11 through 20, could be scaled up to predict response in a specific application.

Peak values of acceleration at various locations within the structure for tests at ranges of 6, 8, and 10 feet are shown in Figure 21. There is very little attenuation of the horizontal acceleration across the floor. However, vertical acceleration tends to peak near the leading edge of the structure.

From the shock spectra for instructure horizontal motion in Figure 22, it appears that most of the variation in horizontal motion is at relatively high frequencies. However, the shock spectra for the instructure vertical motion in Figure 23 indicate that considerable variations in the vertical accelerations occur at relatively low frequencies. Therefore, the reduction factors in Table 1 should be modified somewhat when predicting vertical acceleration near the leading edge of the structure. The amount of modification depends on the range, however, Figure 21 can be used as a guide in predicting vertical accelerations near the leading edge of a structure provided the weapon-structure system being investigated can be scaled up from the weapon-structure system in this report.

## CONCLUSIONS

1. The reduction factors given in Table 1 can be used to predict peak instructure motions from the free-field shock spectra. If the free-field shock spectra are not available, they can be approximated from the maxima ground motions by the method given in Reference 2.

2. The amplification factors given in Table 2 can be used to estimate peak motions of instructure equipment. Alternatively, the instructure shock spectra given in Figures 11 through 20 can be scaled to predict peak motion for instructure equipment.

3. Instructure attenuation of peak horizontal acceleration across the floor of the structure is negligible. The peak vertical floor acceleration has very little attenuation after an initial maximum near the leading edge of the structure.

## REFERENCES

1. J. L. Drake; "Ground Shock Threat to Buried Structures from Conventional Weapons;" presented at The Protective Design Symposium, 22-23 September 1975, NATO, Brussels, Belgium.
2. Cyril M. Harris and Charles E. Crede; Shock and Vibration Handbook Part I: Vibration of Structures Induced by Ground Motion; N. M. Newmark and W. J. Hall, 1976.

TABLE 1  
FREE-FIELD SHOCK SPECTRA REDUCTION FACTORS

Damping	Structure	Acceleration	Velocity	Displacement
<u>VERTICAL</u>				
0%	3C	.18	.056	.064
	3D	.036	.042	.031
5%	3C	.20	.069	.070
	3D	.040	.050	.036
10%	3C	.20	.056	.081
	3D	.043	.062	.041
<u>HORIZONTAL</u>				
0%	3C	.10	.22	.24
	3D	.074	.12	.14
5%	3C	.11	.26	.27
	3D	.081	.15	.092
10%	3C	.11	.32	.31
	3D	.087	.18	.18

TABLE 2  
INSTRUCTURE AMPLIFICATION FACTORS

<u>Damping</u>	<u>Structure</u>	<u>Acceleration</u>	<u>Velocity</u>	<u>Displacement</u>
<u>VERTICAL</u>				
0%	3C	1.0	2.6	2.5
	3D	1.9	3.1	2.8
5%	3C	0.78	1.9	2.0
	3D	1.4	2.2	2.2
10%	3C	0.65	1.7	1.6
	3D	1.3	1.7	1.8
<u>HORIZONTAL</u>				
0%	3C	1.5	1.5	1.3
	3D	1.8	1.9	1.5
5%	3C	1.2	1.3	1.0
	3D	1.5	1.6	1.1
10%	3C	1.0	1.1	0.84
	3D	1.3	1.4	1.0

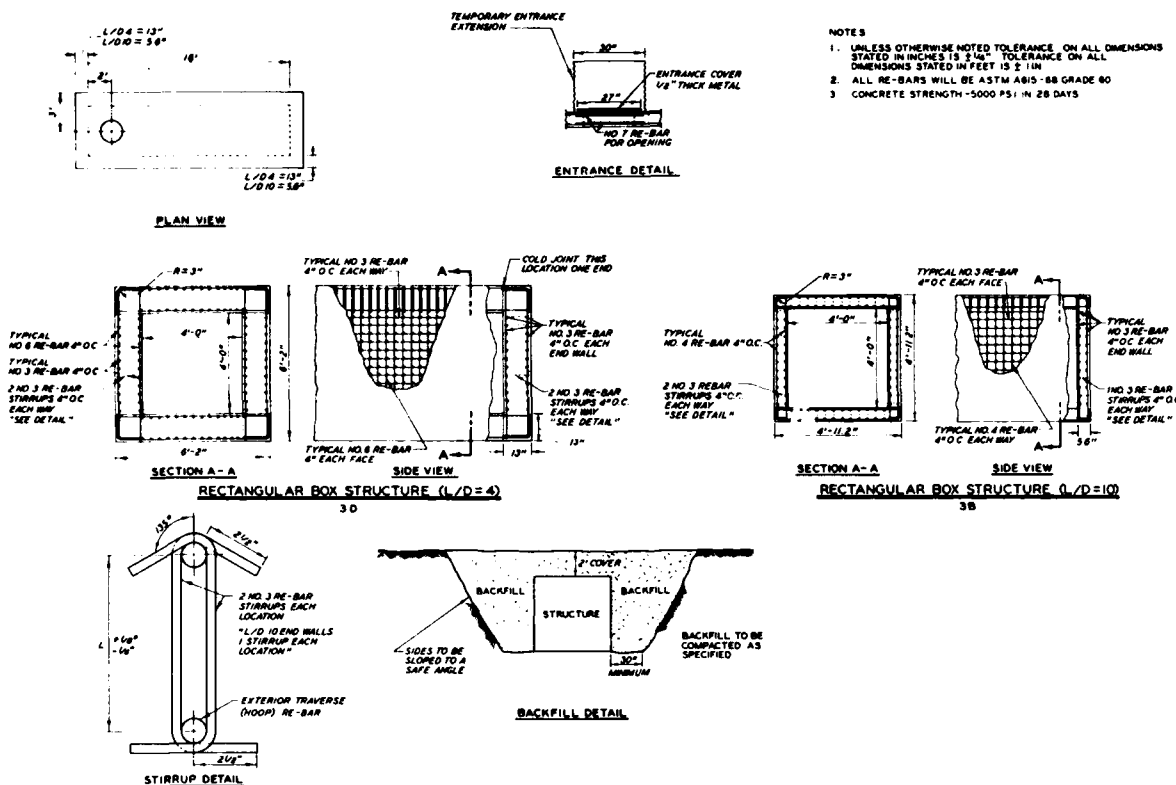


Figure 1. Structural details and dimensions

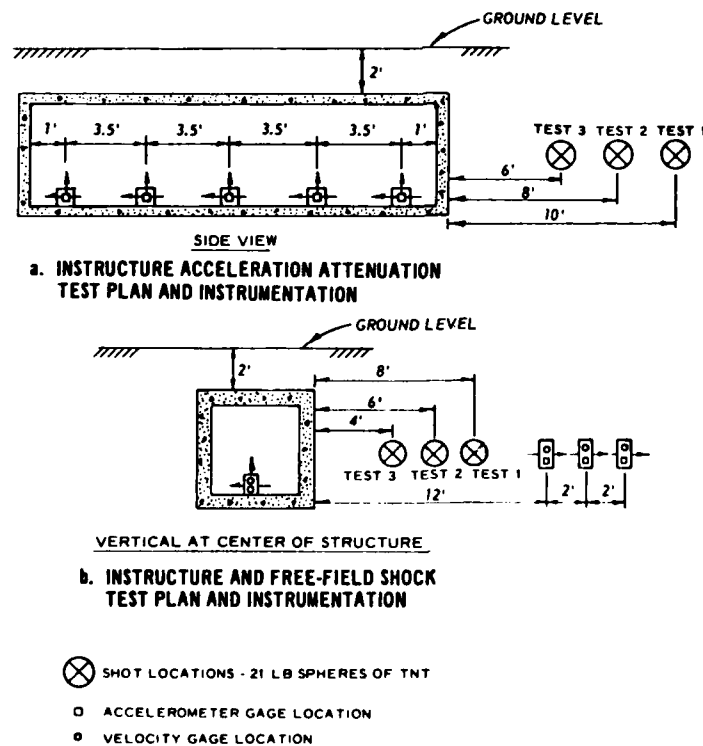


Figure 2. Test plan and instrumentation

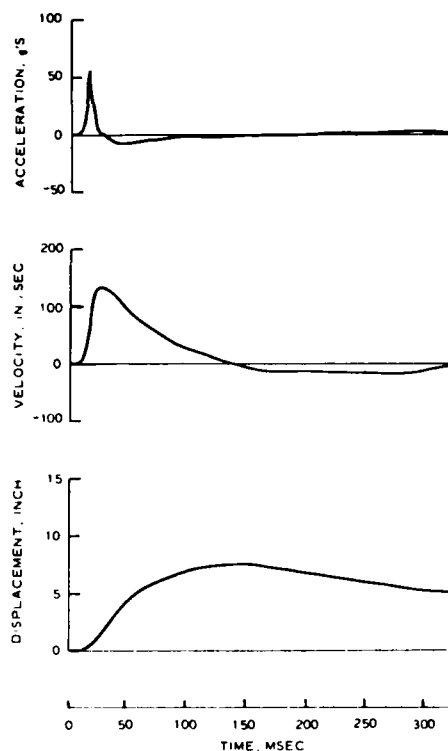


Figure 3. Sample free-field response records at range 8 ft

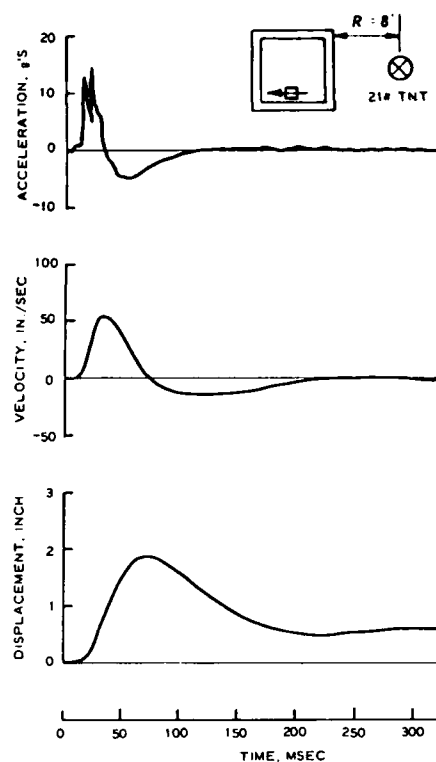


Figure 4. Instructure horizontal floor response for structure 3C, L/D = 10

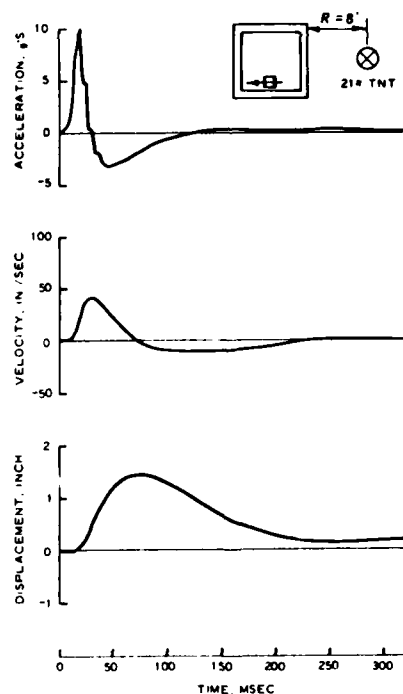


Figure 5. Instructure horizontal floor response for structure 3D, L/D = 4

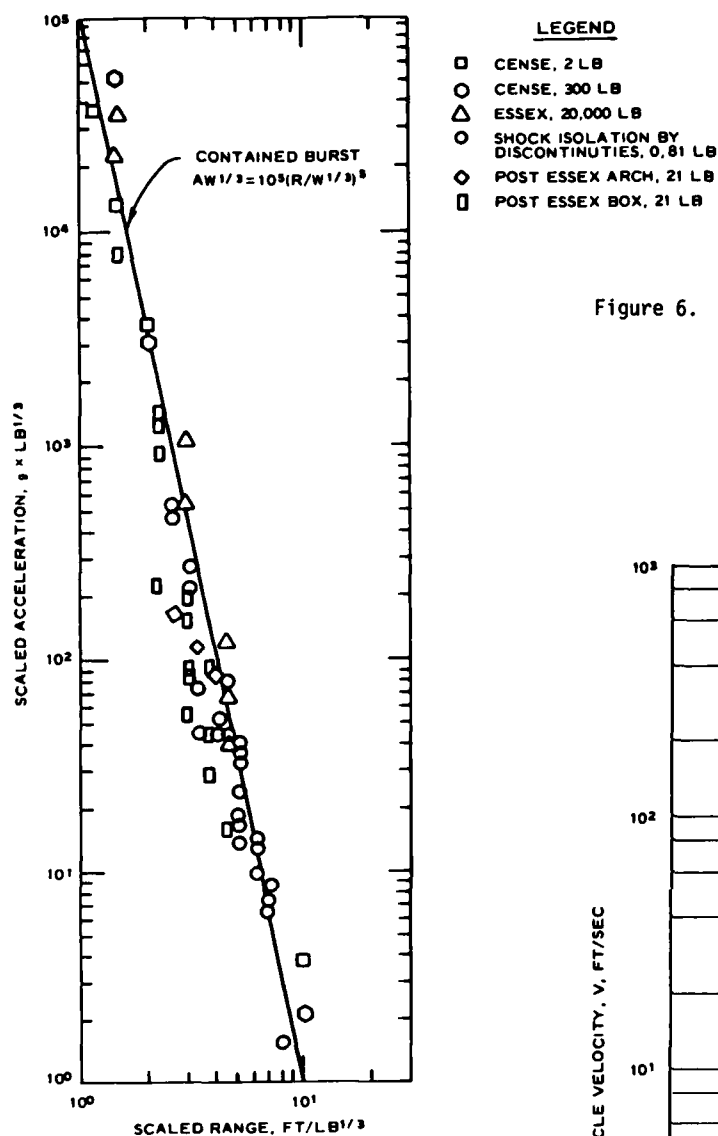


Figure 6. Peak free-field acceleration

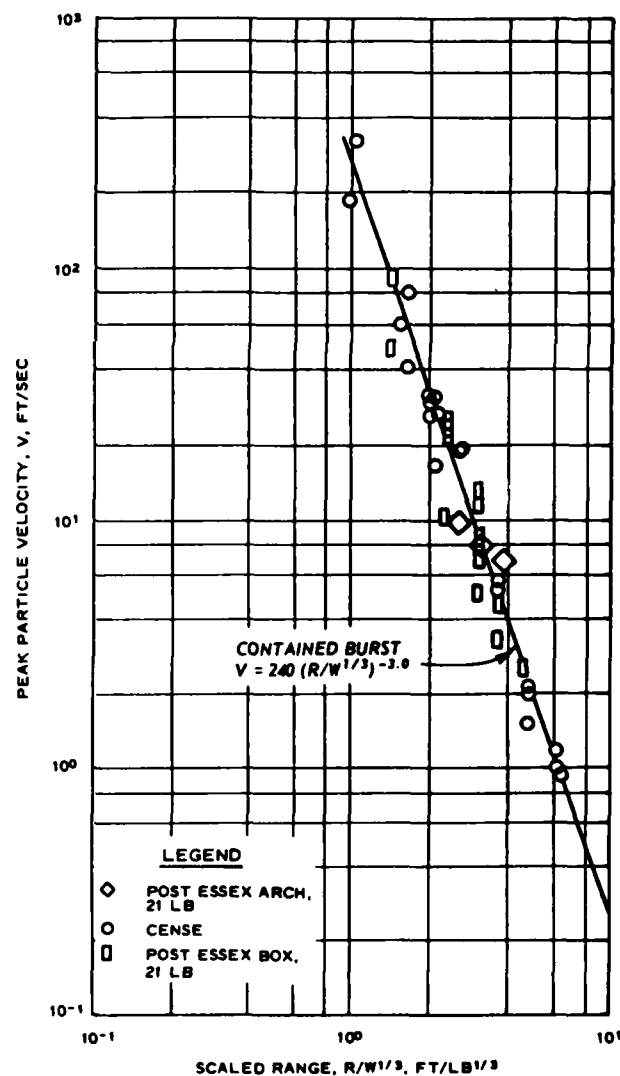


Figure 7. Peak particle velocity



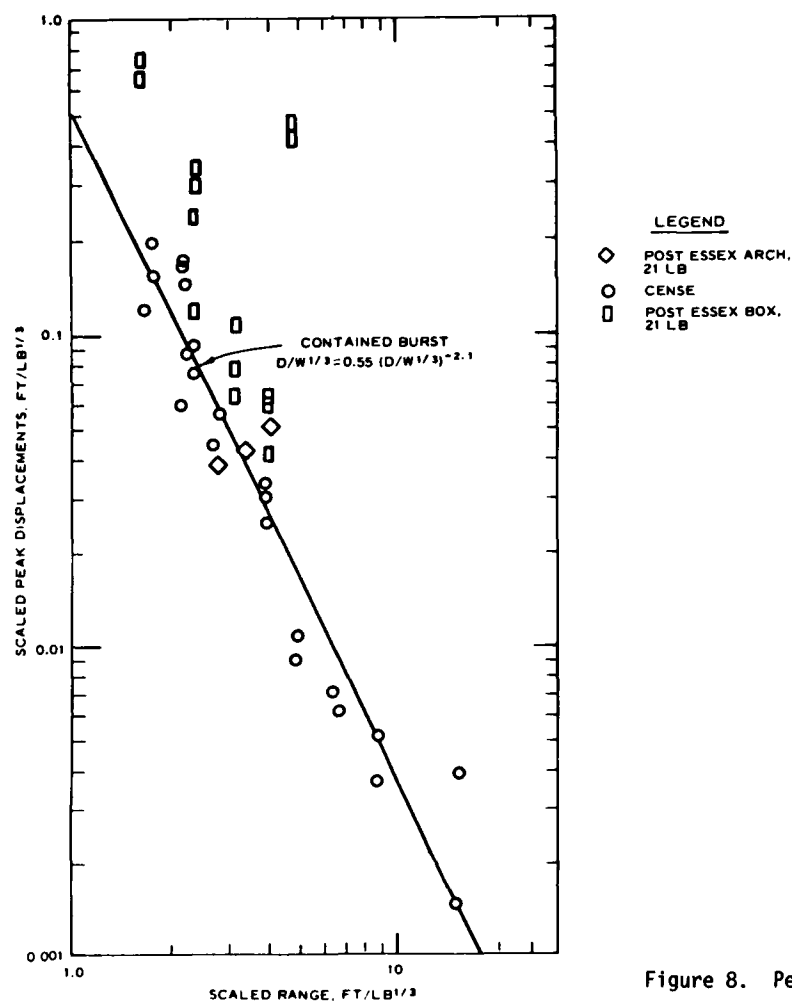


Figure 8. Peak free-field displacement

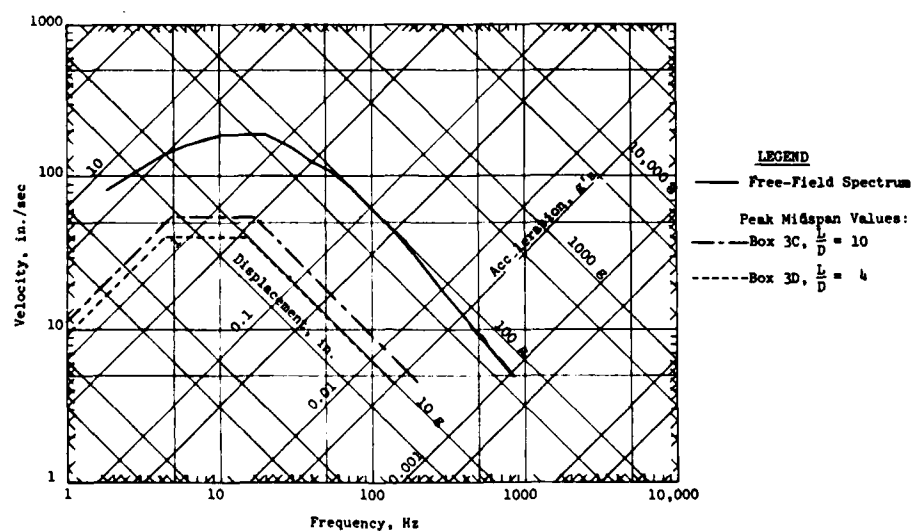


Figure 9. Instructure horizontal floor reduction factors,  
 charge = 21-lb TNT, R = 8 ft

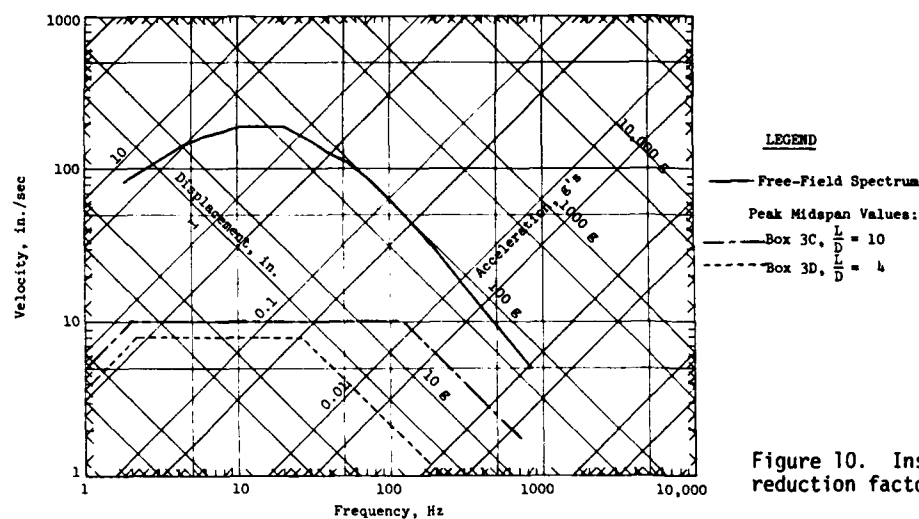


Figure 10. Instructure vertical floor reduction factors, charge = 21-lb TNT,  $R = 8$  ft

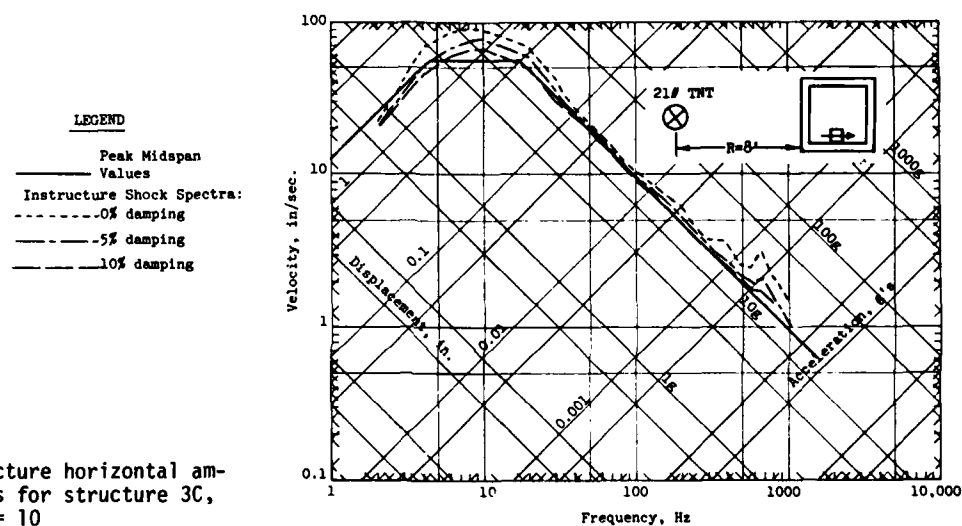


Figure 11. Instructure horizontal amplification factors for structure 3C,  $L/D = 10$

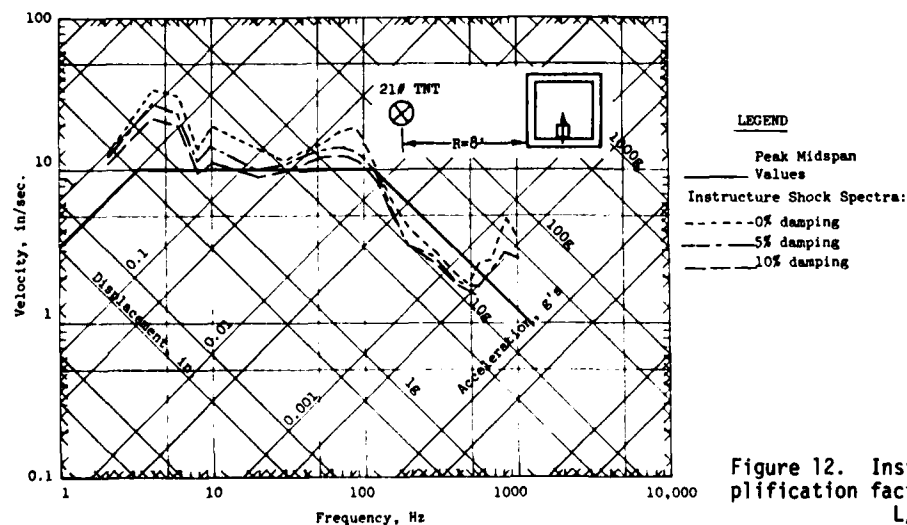


Figure 12. Instructure vertical amplification factors for structure 3C,  $L/D = 10$

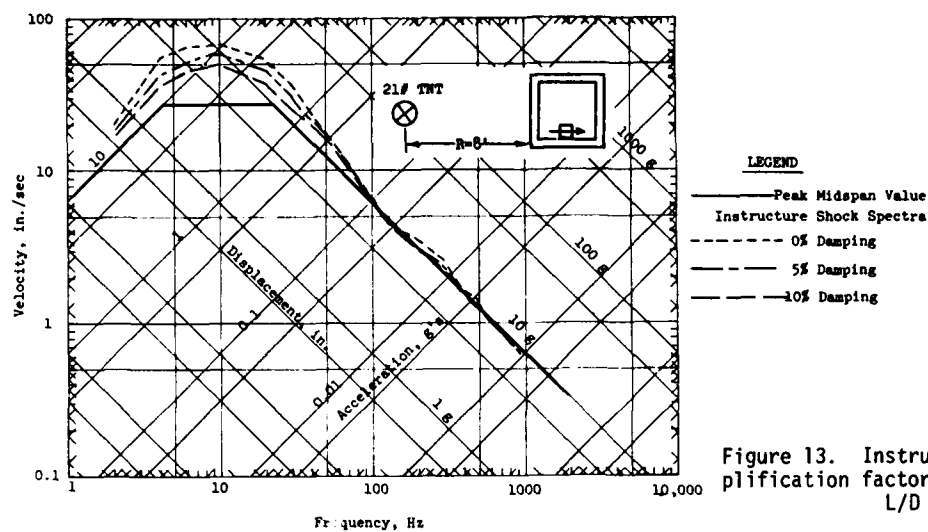


Figure 13. Instructure horizontal amplification factors for structure 3D,  $L/D = 10$

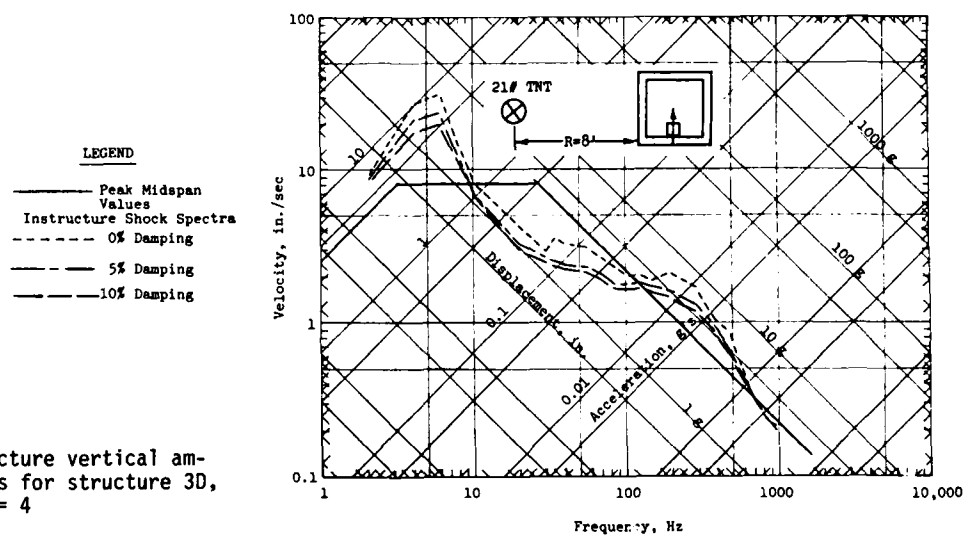


Figure 14. Instructure vertical amplification factors for structure 3D,  $L/D = 4$

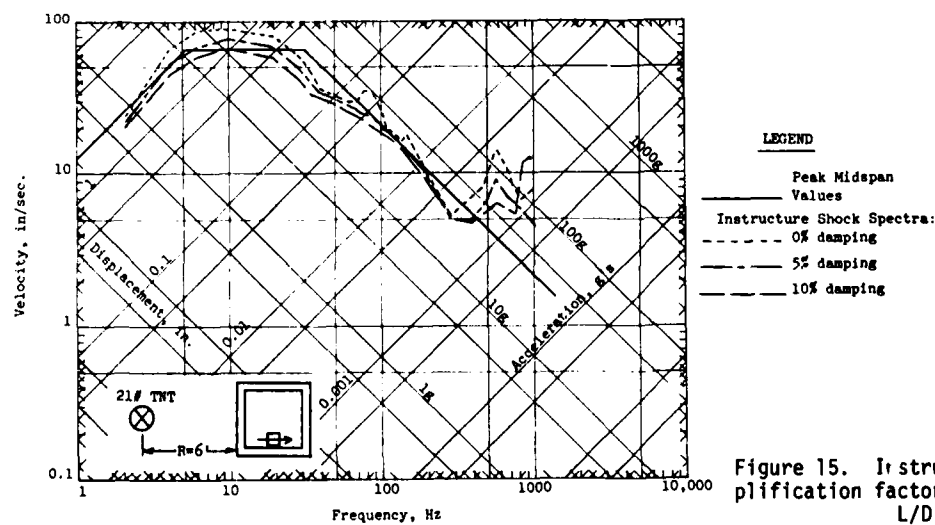


Figure 15. Instructure horizontal amplification factors for structure 3C,  $L/D = 10$

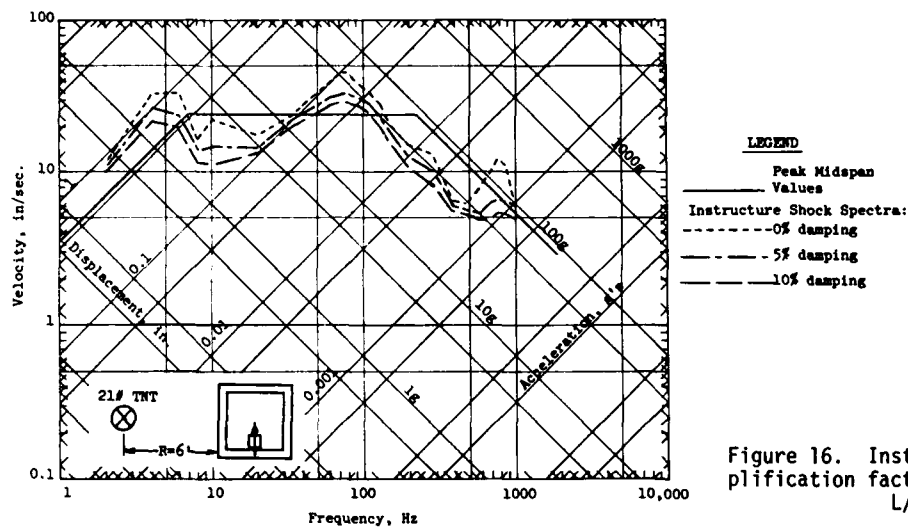


Figure 16. Instructure vertical amplification factors for structure 3C,  $L/D = 10$

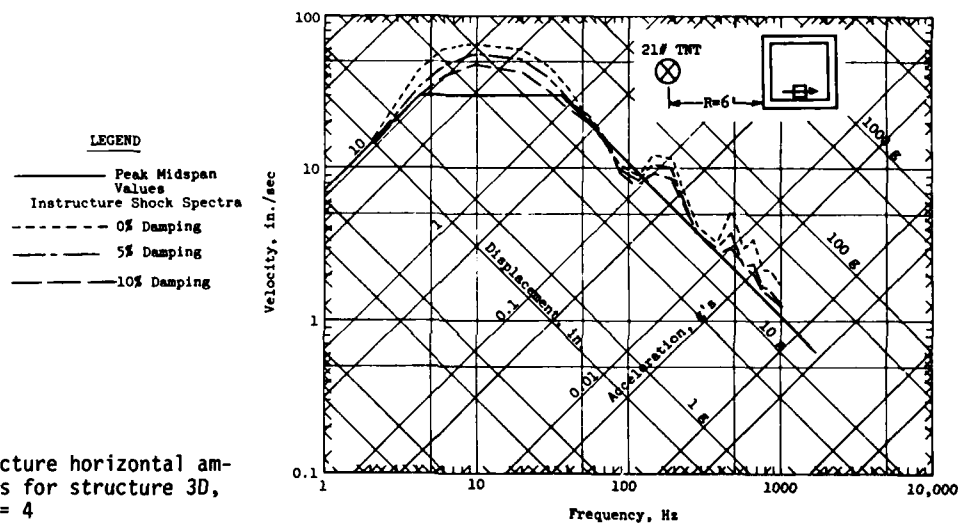


Figure 17. Instructure horizontal amplification factors for structure 3D,  $L/D = 4$

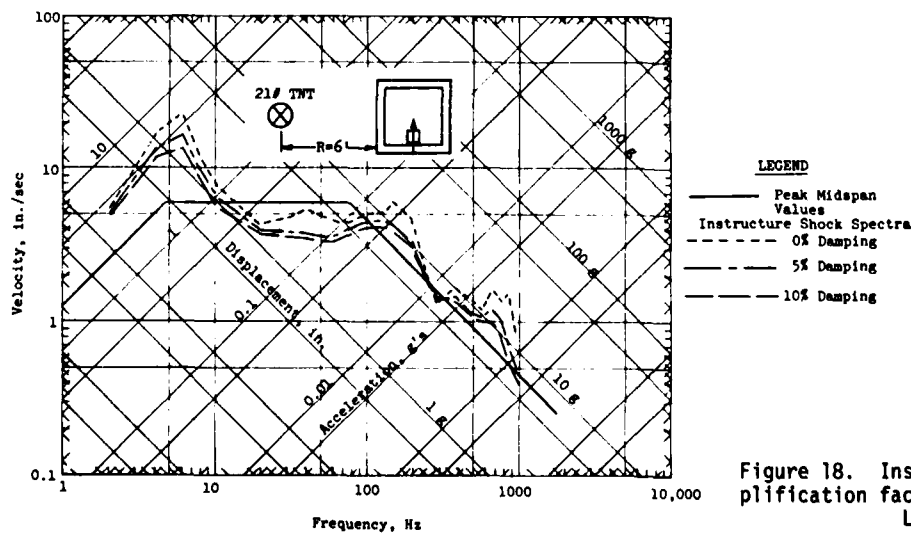


Figure 18. Instructure vertical amplification factors for structure 3D,  $L/D = 4$

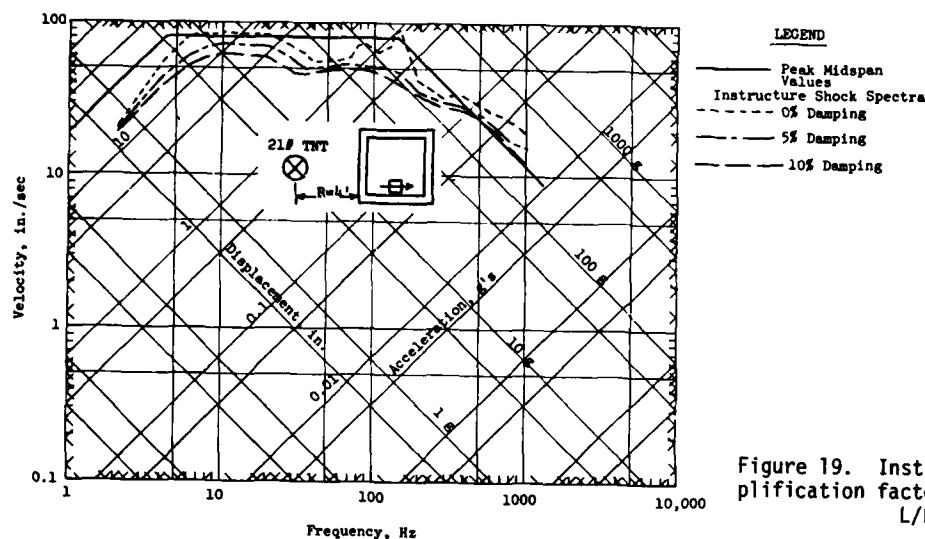


Figure 19. Instructure horizontal amplification factors for structure 3D,  $L/D = 4$

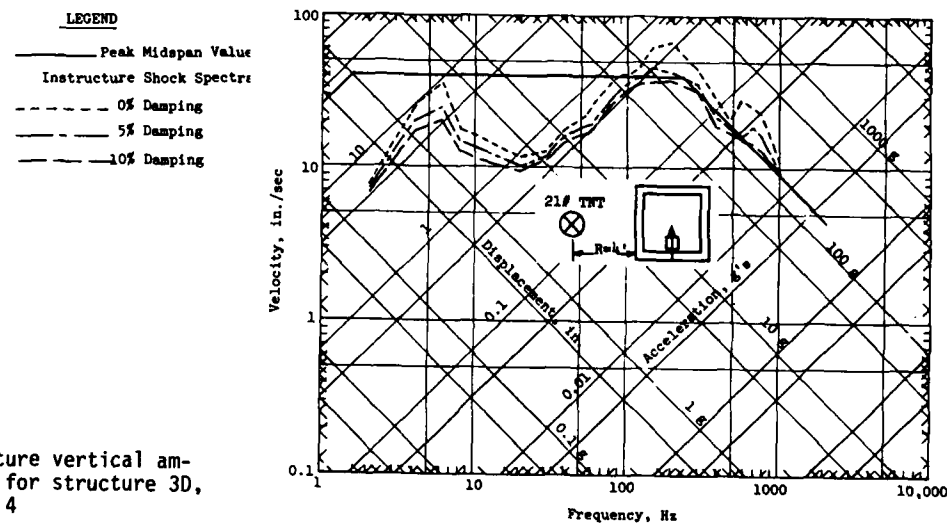


Figure 20. Instructure vertical amplification factors for structure 3D,  $L/D = 4$

		PEAK ACCELERATION, g's					
		GAGE NO.	1	2	3	4	5
RANGE	R = 10'	HORIZ.	3.2	3	3.2	3.2	3.2
		VERT.	0.8	0.6	0.4	0.4	0.5
	R = 8'	HORIZ.	10	8	7	8	8
		VERT.	-8	-3.5	± 2.5	-4.5	± 2.5
	R = 6'	HORIZ.	40	45	35	35	40
		VERT.	-30	-21	± 18	± 20	± 18

LEGEND

② GAGE AND NUMBER

LEGEND  
2 GAGE AND NUMBER

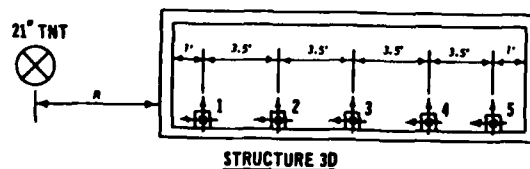


Figure 21. Instructure peak acceleration attenuation

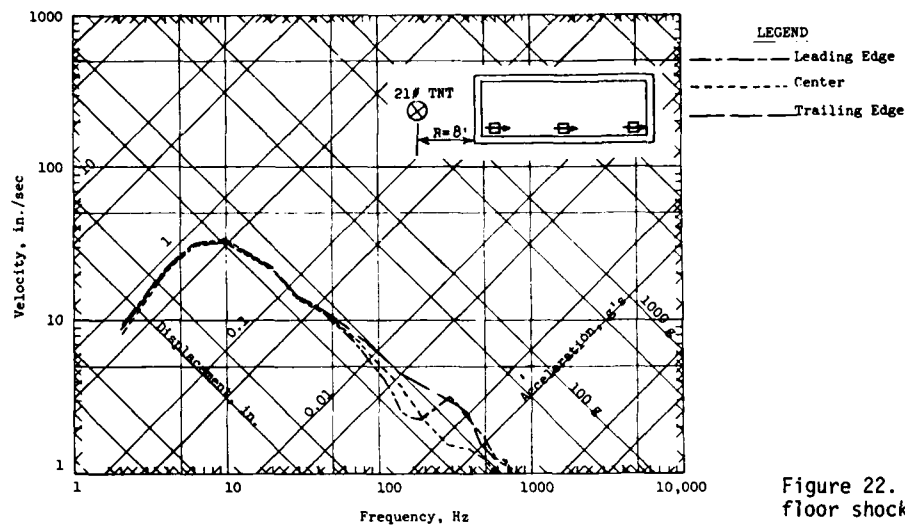


Figure 22. Instructure horizontal floor shock spectra for box 3D,  $L/D = 4$

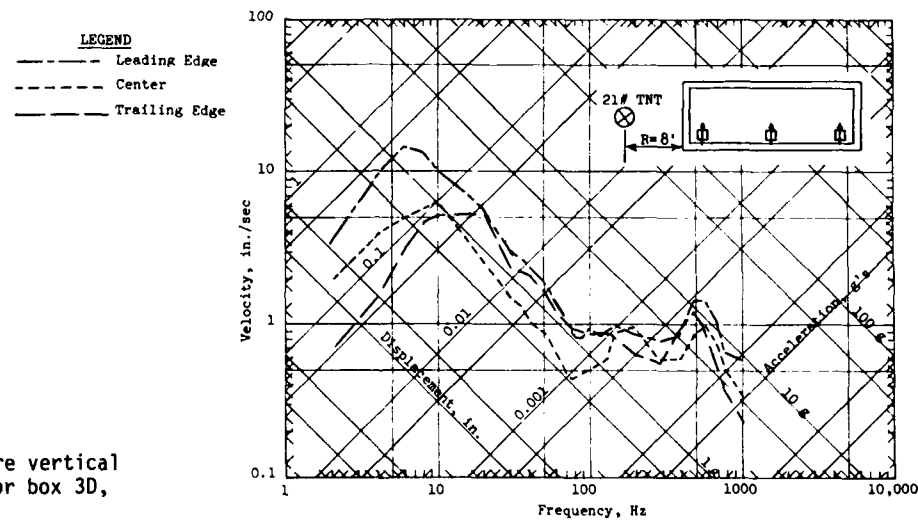


Figure 23. Instructure vertical floor shock spectra for box 3D,  $L/D = 4$

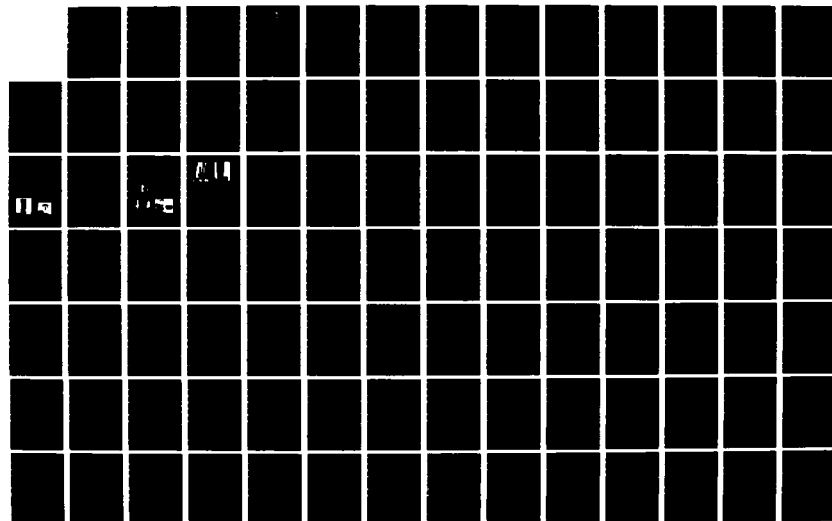
AD-A148 088

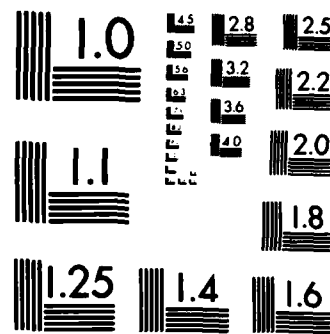
THE SHOCK AND VIBRATION BULLETIN PART 4 STRUCTURAL  
DYNAMICS SYSTEMS IDENT. (U) NAVAL RESEARCH LAB  
WASHINGTON DC SHOCK AND VIBRATION INFORMAT. SEP 77  
BULL-47-PT-4 F/G 28/11

2/3

UNCLASSIFIED

NL





MICROCOPY RESOLUTION TEST CHART  
NATIONAL BUREAU OF STANDARDS-1963-A



# CRACK PATTERN OF AN UNDERGROUND, CYLINDRICAL, REINFORCED-CONCRETE STRUCTURE UNDER AN AXIAL BLAST LOADING

L.C. Lee and M.S. Agbabian  
Agbabian Associates  
El Segundo, California

A blast type of loading is applied to the top of an underground, cylindrical, reinforced-concrete structure. The problem is analyzed by the finite element step-by-step integration method, incorporating a variable modulus model for the soil and a nonlinear composite model for the reinforced concrete. Results of calculations show the step-by-step development of a crack pattern as the blast load is propagated down through the structure. This crack pattern is shown to be related to the sequence of development of the deformation, the displacement, and the stress, both in the structure and in the surrounding soil. Differences in cracking patterns in the structure due to dynamic and quasi-static loads are noted. Because of the difference between wave speeds in the concrete and the soil, the structure is initially unconfined by the surrounding soil. This uncoupling of the soil/structure interaction proves to be a powerful mechanism in generating cracks. In contrast, no such uncoupling takes place when the pressure is applied statically. It is shown that equivalent static analyses generate stress responses that are significantly lower than those obtained for a dynamic environment.

## INTRODUCTION

Two approaches are generally used to analyze the response of underground reinforced-concrete structures subjected to air-blast loading: (1) the testing of scaled or prototype structures under air-blast simulators and (2) mathematical modeling and modern numerical analysis techniques. The major drawback of the experimental approach is that, except for small-scale testing, only a limited number of tests can be economically performed. The mathematical approach is generally much more economical, and the analysis can be repeated with relatively little effort if the test configuration is changed. The major drawback of the mathematical approach is that its accuracy is limited by uncertainties in the definition of material properties and in the modeling of the boundary conditions.

Although both model tests and numerical analyses are performed for some protective types of structures, most soil/structure interaction problems rely on the accuracy of numerical analyses for insight into the dynamic responses of both the soil and the structure. Using recent

developments in finite element techniques, numerical solutions of interaction problems have become very effective and highly reliable.

This paper reports the results of a refined finite element analysis employing a reinforced-concrete model capable of cracking. A "crack-pattern analysis" gives detailed descriptions of the progressive crack development in the concrete and the dynamic response characteristics of the structure and the soil media.

## DESCRIPTION OF THE PROBLEM

The soil/structure interaction problem selected for the demonstration of the crack analysis is an embedded, cylindrical, reinforced-concrete structure subjected to a blast type of loading applied uniformly from overhead, as shown in Fig. 1. The three sections of this underground structure are shown in Fig. 2. The bottom section, called the lower structure, is a reinforced-concrete tube approximately 27.5 ft long with an open top and a closed, 2-ft-thick

bottom. The top section, called the upper structure, is a broader, heavier, reinforced-concrete cylinder with a massive top portion, slender walls, and a thick-ring footing at the bottom. The neck of the lower structure fits inside the ring of the upper structure with about a 3-in. clearance between their surfaces. The third section is a circular reinforced-concrete disk cover countersunk into the upper structure, flush with the top plane.

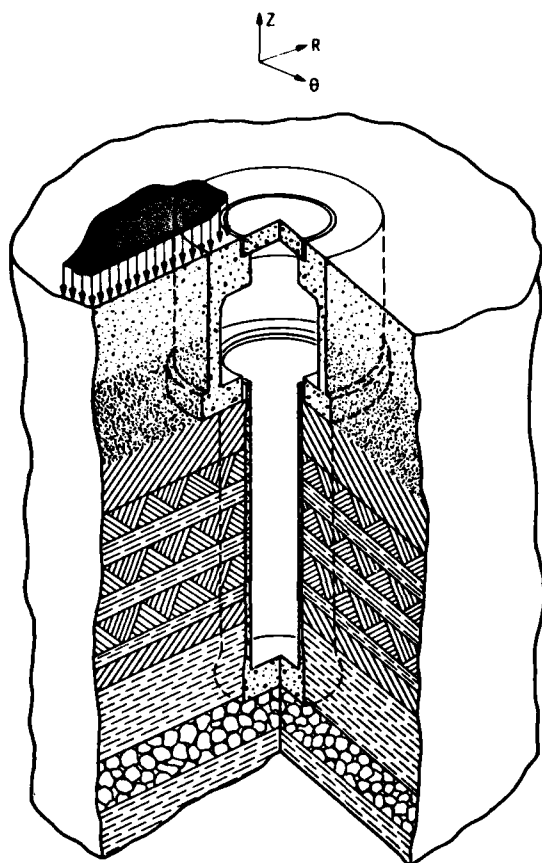


Fig. 1 - Site of underground reinforced-concrete structure subjected to overhead blast loading

The entire structure is embedded in a geological site, with the top of the upper structure and the cover disk level with the ground surface. The upper structure itself rests directly on top of the relatively hard limestone layer (Layer 3) and is surrounded by a soft backfill material. This material extends above the limestone layer, and to a radial distance of 12.3 ft from the center line of the upper structure. The idealized free-field geological profile of the test site is shown in Fig. 3.

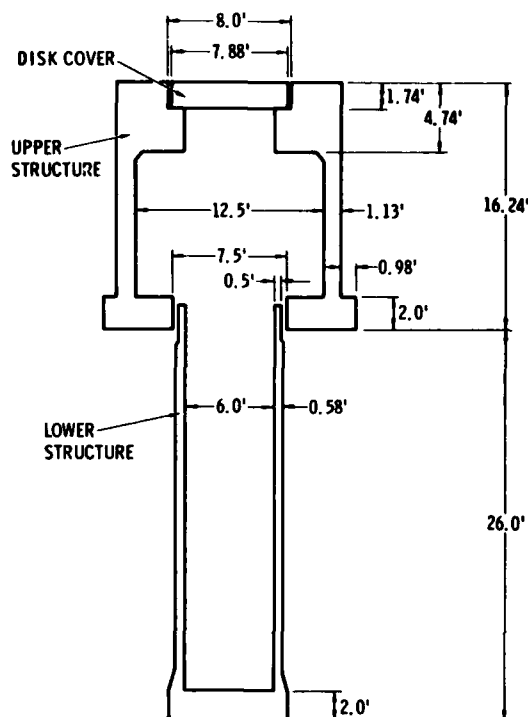


Fig. 2 - Underground structure

DEPTH, FT	MATERIAL DESCRIPTION	LAYER NUMBER	REFRACTION SEISMIC VELOCITY, FPS	ESTIMATED ARRIVAL TIME OF WAVE FRONT, SEC
0				0
5	DRY CLAY	1	1,600	
8.77				0.0055
10	WET CLAY	2	4,300	
16.24				0.0072
20.44	LIMESTONE	3	18,000	0.0075
25	INTER-BEDDED LIMESTONE AND SHALE	4	8,500	
32.84				0.0089
35.24	LIMESTONE	5	8,500	0.0092
40	SHALE	6	6,000	
41.64				0.0103
45.24	COAL	7	2,800	0.0115
50	SHALE	8	7,000	
51.74				0.0125
55	LIMESTONE	9	10,900	
60.84				0.0133

Fig. 3 - Free-field geological profile

## Finite Element Idealization of the Soil/Structure Interaction Problem

A nonlinear axisymmetric finite element computer code called FEDRC was used for the soil/structure interaction analysis. The approximate equation of motion applied in FEDRC at time  $t$  has the following form:

$$M\ddot{u}_t + K_{t-\Delta t} du_t = P_t - F_{t-\Delta t} \quad (1)$$

in which

$M$  = Nodal point masses

$\ddot{u}_t$  = Nodal point accelerations at time  $t$

$K_{t-\Delta t}$  = Global stiffness at time  $t-\Delta t$

$du_t$  = Generalized incremental displacements between time  $t-\Delta t$  and  $t$

$P_t$  = Externally applied forces at time  $t$

$F_{t-\Delta t}$  = Internal resisting forces at time  $t-\Delta t$

The step-by-step integration of Eq. (1) is carried out using the so-called implicit scheme, which incorporates the Wilson  $\theta$ -method for numerical stability. A special feature of this code is a composite reinforced-concrete model that takes into account such important characteristics as the cracking and crushing of concrete, the yielding of steel, and the debonding and rebonding between the concrete and steel. A general description of the FEDRC code can be found in [1] and [2].

The finite element idealization of the structure and the surrounding "soil island," including the backfill region, is shown in Fig. 4. In this model, the bodies of the structure and the soil are represented by axisymmetric isoparametric elements. In addition, special slip elements are used to simulate the slippage between two contiguous bodies. Mathematical formulations of these elements are given in App. A.

The boundary conditions specify that the vertical boundaries a-b, c-d, and e-f in Fig. 4 are restrained from all horizontal motion. On the other hand, the bottom boundary d-c is quieted by a technique that eliminates unwanted reflection originating from this artificial boundary, as described in the *User's Guide* [1].\* A detailed discussion of the boundary conditions is given in App. B.

\*The quiet boundary technique is formulated for 90-deg impingement. The two-dimensional nature of the wave propagation problem imposes certain restrictions on the validity of using such techniques. In this analysis, reflections from the bottom would have arrived at the upper structure in about 15 msec. Any possible errors due to the assumption of 90-deg impingement will not affect the significant part of the dynamic response, which occurs in the first 15 msec (see App. B).

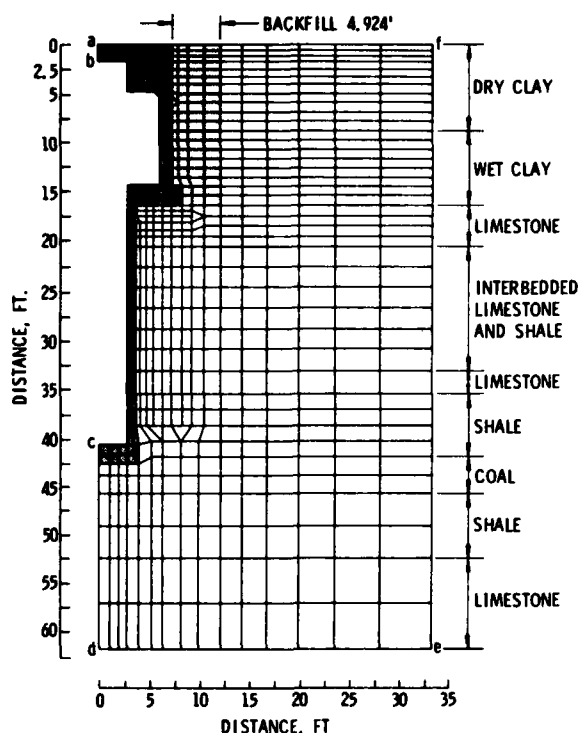


Fig. 4 - Finite element idealization of the site structure

## Material Modeling

A hysteretic, piecewise linear stress/strain relationship with a Mohr-Coulomb failure envelope is used to model the nine geological soil layers. However, to use this model for the backfill materials, where a sharp variation in the moduli occurs in the high-strain range, may in some circumstances lead to numerical instabilities. To circumvent this difficulty, the piecewise linear loading curve is replaced by a single continuous polynomial curve. All ten soil models are assumed to be isotropic and homogeneous, with constant Poisson ratios.

The composite reinforced concrete is modeled as two component materials [3]. The plain concrete is treated as an orthotropic nonlinear material, whereas the steel is treated as a linearly elastic, perfectly plastic material. A combination of these two component materials yields an orthotropic, variable modulus continuum

that takes into account the following effects known to exist in the reinforced concrete:

- a. Behavior of steel reinforcement, which includes the elasticity of steel
- b. Debonding between steel and concrete
- c. Dowel action
- d. Tensile cracking and rebonding in concrete
- e. Crushing of concrete in compression
- f. Anisotropy in concrete

Mathematical formulation of the steel and concrete materials and the slip elements are given in App. C.

## RESULTS OF ANALYSES

Two separate calculations were performed using essentially the same finite element mesh. In the static calculations, a uniform load was applied to the top boundary in steps of small load increments; in the dynamic calculations, a blast load was applied to the same boundary. The restart capability of the FEDRC code permits both calculations to terminate at any predetermined step and to continue after the results have been examined at this intermediate step. The static calculation was performed to provide a reference for selecting a dynamic load amplitude and to help isolate some of the dynamic effects characteristic of the present problem.

### Static Analysis and Geometry of Cracks

Due to the relatively high degree of non-linearity of the backfill material, the load increment in the static calculation was selected such that the entire static calculation was accomplished in 29 steps. Gravity loading was also applied during the first two steps of loading. The results of the static analysis are summarized in Figs. 5 to 9. Fig. 5 shows the relationship between the total number of cracks and the load.

As depicted in Fig. 6, cracks that develop inside an element can be categorized as two types. The first type, conical cracks, includes all cracks that form conical surfaces of revolution. Hence, conical crack surfaces may range from a cylindrical surface at one extreme to a cross-sectional plane, at the other extreme. In a single element, such a crack produces a crack surface perpendicular to the R-Z plane. By

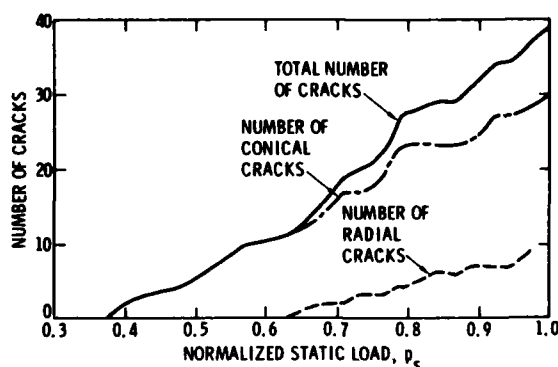


Fig. 5 - Number of cracks vs. static load

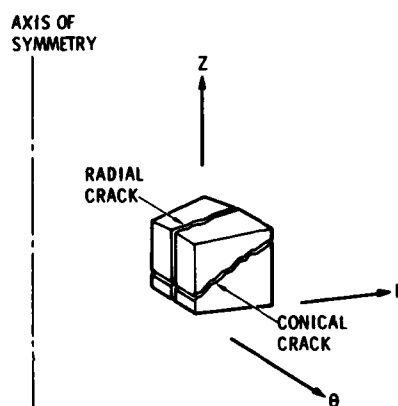


Fig. 6 - Conical and radial cracks

giving the stress components in the cylindrical coordinate system, the orientation of the crack surface (that is, the orientation where maximum tension occurs) can be calculated by the application of Mohr circles. Since a crack is formed when the tensile stress across a surface within an element exceeds a certain limit, conical cracks are generally the result of excessive bending and/or excessive axial load.

Cracks of the second type, radial cracks, are developed when the hoop stress  $\sigma_\theta$  exceeds a certain limit in tension. In a single element a radial crack produces a crack surface that appears to fall on the R-Z plane (the crack gap opens in the  $\theta$ -direction and propagates in the R and Z directions). Theoretically, radial cracks will develop simultaneously and uniformly in all circumferential directions, thereby presenting axisymmetry. In reality this is seldom the case, since any small imperfection may cause a radial

crack to develop first in the region that includes the imperfection. Thus the radial stresses in the remaining "identically located" elements are relieved, and the development of further radial cracks is prevented. Since radial cracks are developed as a result of the radial expansion, or bulging, of a ring section, this type of crack can result from excessive axial compression applied with little or no lateral confinement.

Based on these observations, it can be concluded that the combination of the crack load history and the crack distribution plots together provide some qualitative information on the overall distribution of stresses, as well as describing the critically stressed areas in the structure.

Fig. 5 shows that the first conical crack occurs when the normalized applied load  $p_s$  reaches about 0.37, and no radial cracks are developed until the load reaches 0.63. From 0.63 to the maximum applied load of 1, both conical cracks and radial cracks increase at an essentially steady rate. Consequently, the number of radial cracks developed remains substantially below that of the conical cracks at the end of the calculation. The intensity corresponding to the maximum normalized load  $p_s = 1$  is selected such that significant crack activities can be detected in the structure. It also provides a reference for selecting a peak dynamic load intensity. It has no other physical significance. Experimental data are generally needed for a further definition of  $p_s$ .

The zones in which cracks are developed and the orientation of these cracks are shown at  $p_s = 0.758$  (Fig. 7[a]), which approximately corresponds to the peak dynamic load, and at the maximum load  $p_s = 1$  (Fig. 7[b]). It is obvious in both plots that the conical cracks outnumber the radial cracks. All of the radial cracks are found in the bottom part of the disk cover and the upper part of the lower structure. The conical cracks are concentrated in essentially the same regions and also in the footing of the upper structure.

One of the most prominent characteristics of the static analysis is the fact that the development of the radial cracks trails that of the conical cracks, both in the initiation time and the number. (As will be shown later in the dynamic analysis, this characteristic demonstrates a very interesting distinction between the static and the dynamic results.) Such an outcome can be understood in part by examining the formation of plastic zones in the free-field media. Fig. 8(a) shows the extent of plastic zones (dark area) at  $p_s = 0.368$ . Fig. 8(b) shows the plastic zone at  $p_s = 0.632$ , when the first radial crack is registered. Finally,

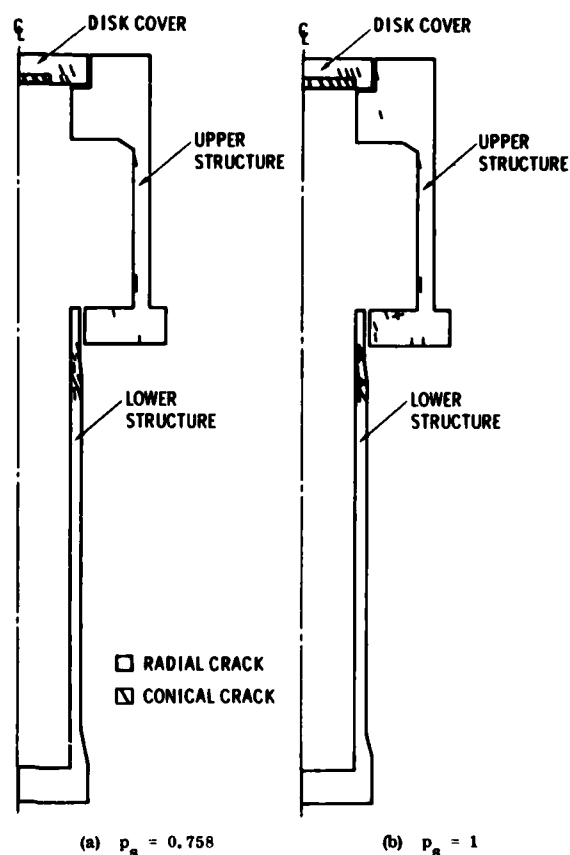


Fig. 7 - Crack zones under static load

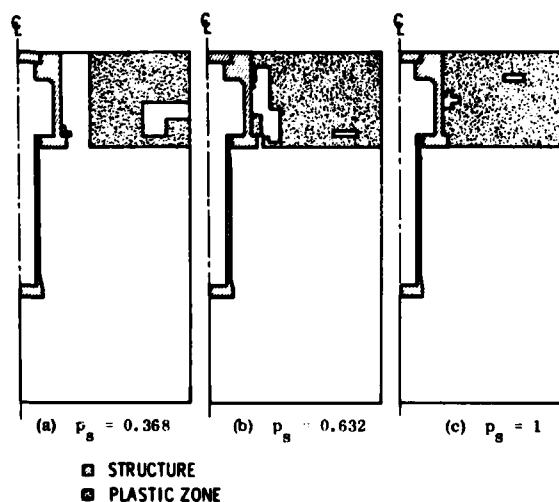


Fig. 8 - Plastic zones in the surrounding soil media under static load

Fig. 8(c) shows the plastic zones at the maximum load of  $p_s = 1$ . It can be seen that at the onset of the cracking there is an extensive plastic region surrounding the upper structure. Since the top soil layers exhibit very little strain hardening (Table 1, App. C), they behave essentially like compressible fluids after the yield point is reached. Therefore, the lateral pressures exerted on the structure by these materials are approximately equal to the applied pressure from the top. These lateral pressures prevent the structure from undergoing excessive bulging. As a result, no radial cracks are developed until the applied load is increased to such a level that the lateral confining pressure is overcome.

Fig. 9 shows the vertical deflections at various locations in the structure. Although there is no flattening of the curves, which could be interpreted as the sudden collapsing of the structure, the deflection at nodes in the upper structure increases at a faster rate than the increase of the applied load; whereas the deflection curve corresponding to the node at the bottom section of the lower structure indicates the reverse trend. The transition appears to occur at the bottom of the upper structure (Node 438, Fig. 9), where an approximately linear load-deflection curve is observed. This can be explained by the fact that the upper structure rests directly on a very stiff limestone layer that provides a relatively firm foundation, which allows the upper structure to bulge in addition to sinking downward. The load-deflection curve at the bottom structure merely reflects the stiffening effects of the soil layers below the level of the bottom of the structure.

## Dynamic Analysis

The input pressure pulse applied uniformly to the top boundary of the finite element mesh is shown in Fig. 10. This pulse has a rise time of 1.5 msec, a duration of 22 msec, and a maximum amplitude equivalent to about 0.758  $p_s$ . The shape and the amplitude of the pulse was chosen somewhat arbitrarily to generate significant crack activity in the structure.

The step-by-step integration routine was carried out following the schedule shown in Fig. 10. Because of the potential for instability caused by some highly nonlinear soil properties, caution was exercised in the choice of the time-step sizes; and the restart capability was used to safeguard against the occurrence of instability.

Because of the difference between the loading and the unloading characteristics in all material models, some numerical oscillations may be induced as a result of the different loading and unloading stiffnesses. To suppress these unwanted oscillations, some stiffness-proportional damping was introduced in the numerical integration. This type of damping can be related to critical damping ratios by the following formula

$$\lambda_n = \frac{\beta \omega_n}{2} \quad (2)$$

in which

$\lambda_n$  = Critical damping ratio corresponding to the  $n^{\text{th}}$  node

$\beta$  = Damping constant

$\omega_n$  = Natural period of the  $n^{\text{th}}$  node

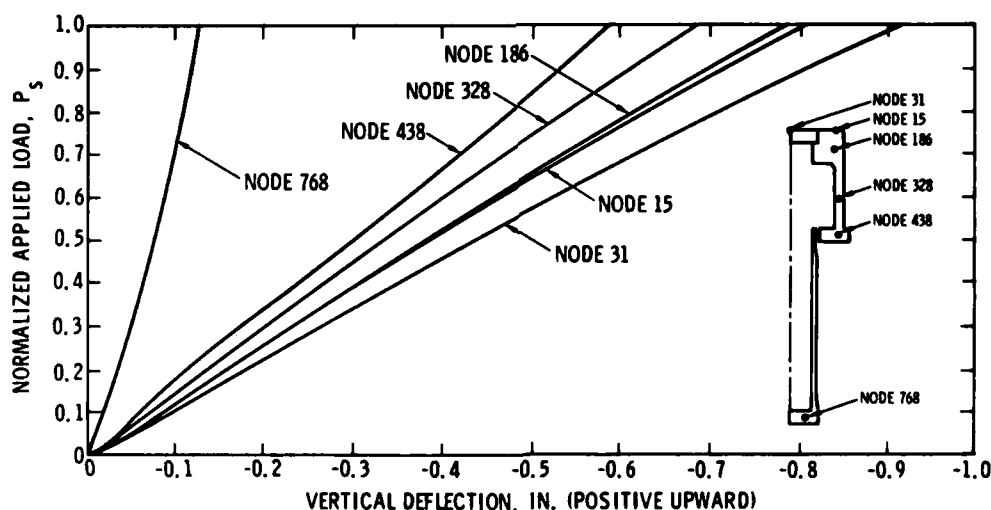


Fig. 9 - Load deflection curves in the structure for static loading

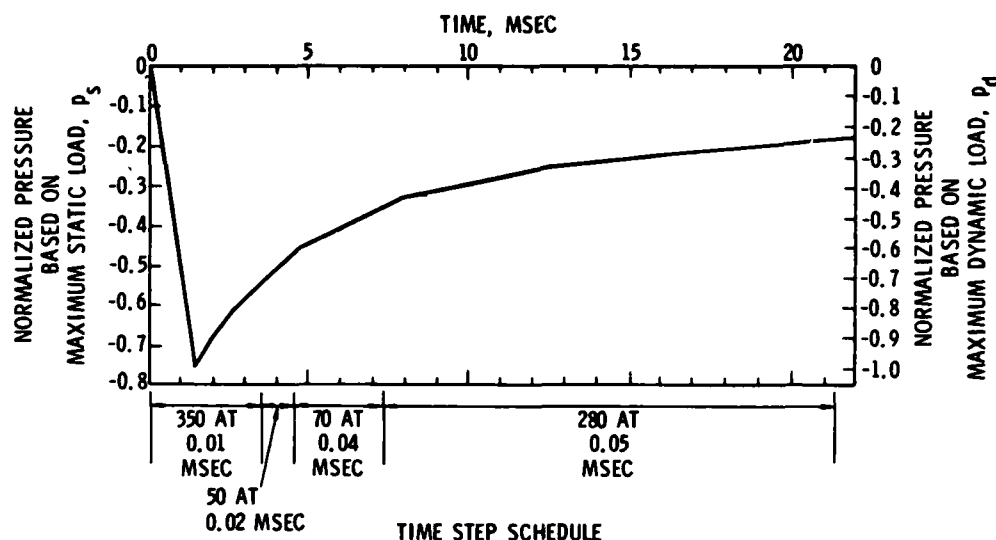


Fig. 10 - Input pressure pulse for dynamic calculation

In the present calculation,  $\beta$  is taken equal to 0.00005 and is applied uniformly to all materials of the mesh throughout the duration of the calculation. When this value of  $\beta$  is used, Eq. (2) yields 2% critical damping when the natural frequency  $f (= \omega_n / 2\pi)$  is taken to equal 100 Hz.

#### Crack Formation

The study of the formation of cracks in the dynamic analysis is carried out in a manner

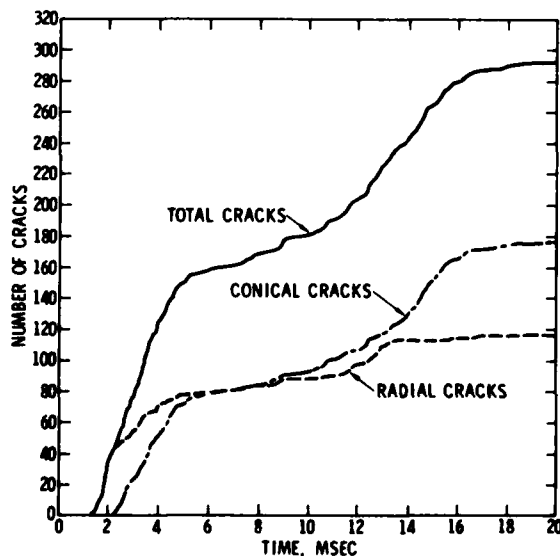


Fig. 11 - Crack time history in the dynamic calculation

similar to that in the static case. Using the terminology previously introduced, Fig. 11 shows separately the time histories of the number of conical cracks, the number of radial cracks, and the total number of cracks developed in the structure. It is of interest to note that prior to about 8 msec the radial cracks lead both in the time of crack initiation and the number of cracks developed. After about 8 msec the number of conical cracks overtakes that of the radial cracks; and after about 13.5 msec, the increase in the number of radial cracks practically ceases. However, the formation of conical cracks continues at a substantial rate until about  $t = 16$  msec. It can also be observed in Fig. 11 that there is a temporary reduction of the rate of increase for both types of cracks between approximately  $t = 5$  msec and  $t = 10.5$  msec.

Figs. 12(a) to 12(c) show the progressive development of crack zones at three different times, namely,  $t = 3.5$  msec,  $t = 7.3$  msec, and  $t = 14.3$  msec, respectively. At early time  $t = 3.5$  msec (Fig. 12(a)), radial cracks are formed in the bottom side of the disk cover, and the middle portion of the upper structure. Conical cracks are formed in the bottom side of the cover and in the shear region in the upper part of the upper structure, because of bending and shear, respectively.

At 7.3 msec (Fig. 12(b)) radial cracks propagate downward toward the lower part of the upper structure. Numerous new conical cracks are also formed, extending the crack zone established in the earlier times. In addition, some nearly vertical conical cracks are formed in the upper structure wall. The generation of

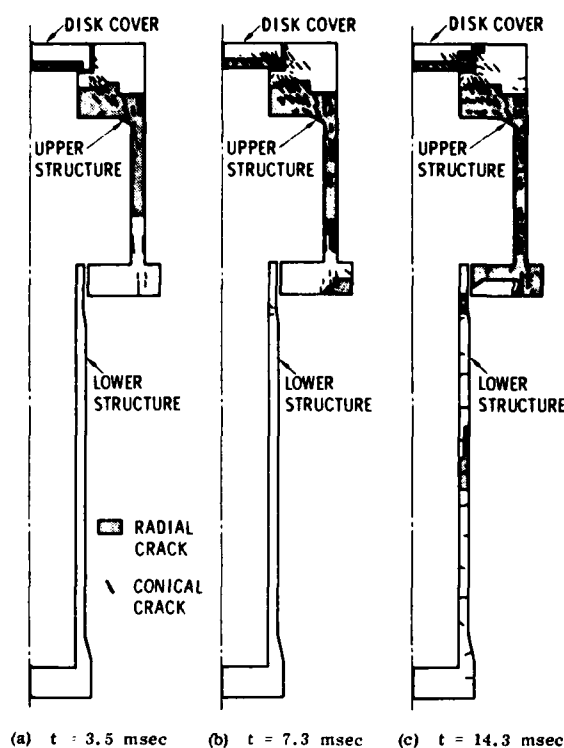


Fig. 12 - Crack zones under dynamic load

these spalling types of cracks indicates that the wall experiences predominantly vertical loads with very little bending and lateral pressure. This is probably owing to the fact that the upper structure footing rests on a relatively hard limestone layer. This stiff layer provides a firm foundation so that high vertical compressive stresses can be developed in the wall of the upper structure.

At  $t = 14.3$  msec (Fig. 12[c]) the radial cracks have engulfed approximately two-thirds of the footing of the upper structure. They also have propagated in the outer bottom portion of the disk cover. Of particular interest is the formation of some nearly horizontal cracks along the outside and the inside of the upper structure wall. The development of these horizontal cracks indicates that the structure is subjected to significant bending moment. This bending moment is probably introduced by the lateral pressure exerted through the surrounding soil. Only a few radial cracks are formed in the lower structure. However, nearly horizontal conical cracks are formed in the entire length of the lower structure wall. Since the applied pressure is exerted on the lower structure only through the surrounding soil, the principal loading transmitted from the soil is through radial compression and

shear. It is therefore expected that only bending cracks will be found in the lower structure.

The different stages of crack development support the observation that, owing to the difference in wave speed, the applied pressure propagates downward through the structure much faster than through the surrounding soil. Because the footing of the upper structure rested directly on a relatively hard limestone layer, significant vertical stresses were developed in portions of the upper structure while the surrounding soil was still relatively unstressed.

The slow buildup of soil stresses is demonstrated by Figs. 13(a), (b), and (c), where the plastic zones in the surrounding soil regions are shown at three different times. In contrast to those of the static case (Figs. 8[a] to 8[c]), plastic zones did not develop in the adjacent soil regions under dynamic loading until very late times. The absence of lateral soil pressure at early times thus permitted the upper structure to bulge, i.e., to swell or expand radially, forming radial cracks in the process. As the axial load increased, spalling cracks also developed in the upper structure wall region. This was followed by the lateral pressure buildup as the peak overpressure propagated through the soil. This downward propagating lateral pressure caused bending cracks to develop and, as shall be seen later, at the same time applied an inward crushing load to the upper structure wall that exceeded the compressive strength of the concrete. Finally, the cracking activity in the top and the wall portions of the upper structure subsided after the peak of the overpressure

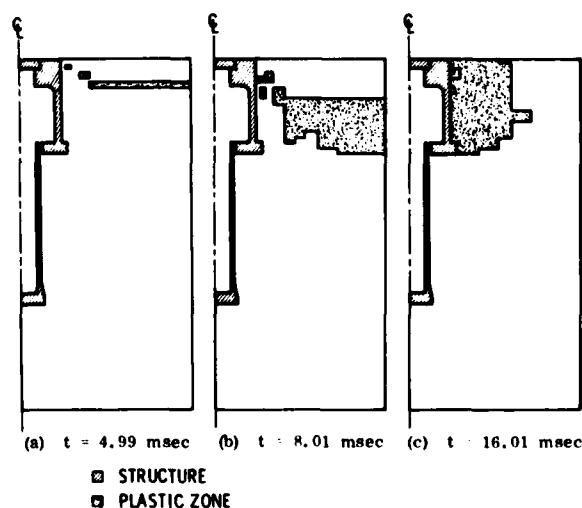


Fig. 13 - Plastic zone in the surrounding soil media under dynamic load



propagated through the soil. The rate of crack formation started to climb again as new cracks developed in the footing and the lower structure regions. Cracks generated in the footing appear to have been caused by both bulging and bending, while those in the lower structure appear primarily due to bending.

#### Deformed Shapes

The deformed shapes of the upper structure computed for two instances are plotted in Figs. 14(a) and 14(b). Because of differences in the degree of deformation, the early time response is shown on a scale with a five-fold difference from the late-time response, for easier visibility of the lesser deformation. The deformed upper structure, shown at  $t = 3.53$  msec, represents the configuration when the peak of the applied load propagated through the concrete has already passed the footings of the upper structure, whereas the same load propagated through the free field has only passed a depth corresponding to the midheight of the upper structure.

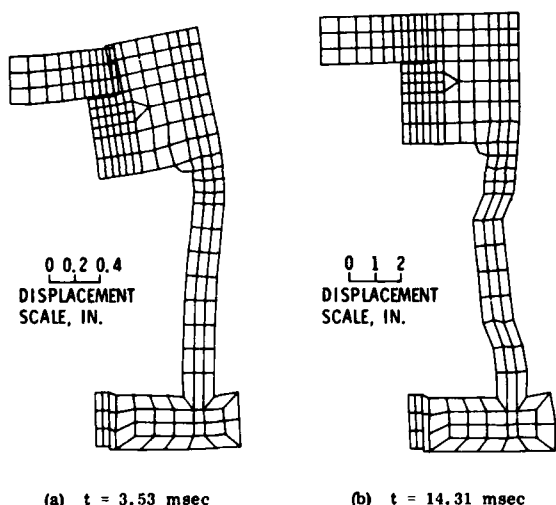


Fig. 14 - Deformed shapes of the upper structure in the dynamic calculation

At this time the deformation is concentrated in the top portion of the structure. The disk cover is significantly deformed, primarily due to bending. The massive top portion appears to have undergone a combination of shear and bending deformation that causes the bottom part to expand radially where it joins the cylinder wall, and the top part to move inward. The wall is vertically compressed and is slightly expanded at the top.

Those regions that undergo radial expansions coincide with the zone where radial cracks initiated and propagated (Fig. 12[a]). The fact that the vertical load has been transmitted to the bottom of the wall is shown by the relative vertical displacement between the footing and the top of the lower structure, and also the sinking of the wall into the footing.

At  $t = 14.31$  msec (Fig. 14[b]), which uses one-fifth the displacement exaggeration used previously, the plot shows significant inward compression of the cylindrical wall. As the amplitude of the applied overpressure decreases after the passage of the peak value, the bending of the top portion of the upper structure also diminishes. The lateral soil pressure on these parts of the structure has replaced the direct overpressure as the major driving force. The weakest portion in the structure to resist this combined axial compression and radially inward pressure is the upper structural wall, as shown in this deformed plot.

#### Displacements

Displacement time histories for selected free-field and structural locations are discussed below. The vertical displacements for these vertically aligned nodal points in the free field are superimposed in Fig. 15. Node 4 is located at the ground surface, Node 223 is located in the middle of the top (dry clay) layer, and Node 523 is located in the middle of the limestone layer. This comparison shows the amount

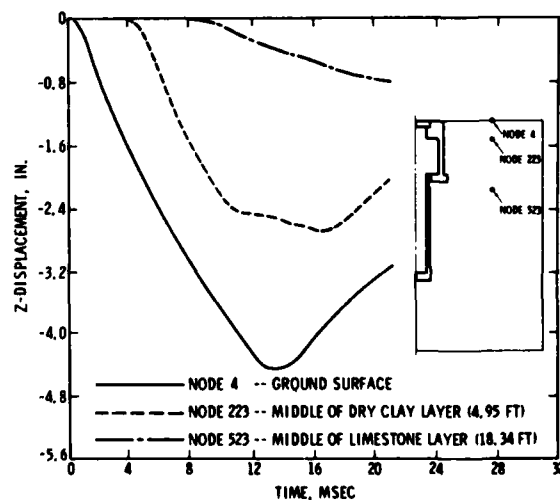


Fig. 15 - Vertical displacement comparison for three free-field locations

of attenuation, as well as the smearing or broadening of the peak as the target location moves downward.

At the ground surface, the displacement reaches a peak value of about 4.52 in. at approximately 13.8 msec before a rebound occurs and the ground begins to move upward. The peak occurs at approximately the time when the reflection from the top interface of the limestone layer (Layer 3, Fig. 3) first reaches the ground surface. The rate of the upward motion indicates that the reflection is a strong one.

At Node 223 the motion is characterized by a blunt peak region occurring approximately between 11 and 16.6 msec. In this broadened peak region, a slowly but continuously increasing trend in displacement is observed. Since an idealized perfect reflection without attenuation would have produced a horizontal plateau region, this increase indicates that the reflected wave from the limestone interface is slightly weaker than the initial incident wave. At about 16.6 msec the unloading wave, initiated when the reflected wave reached the surface, arrives. This third pulse of upward velocity is sufficient to overcome the downward velocity produced by a combination of the original pulse and the reflected pulse originated from the limestone interface.

At Node 523, the amplitude of the particle velocity is strongly reduced. This reduction reflects the increase in material impedance and the strong reflection that occurs at the interface between the clay and the limestone. At problem termination, slightly before peak displacement is expected, the displacement at Node 523 is about 0.8 in., or 18% of the peak value attained at the surface. This rather strong peak attenuation is not out of line when the ten-fold impedance ( $\rho c$ ) mismatch at the clay limestone interface is considered.

Fig. 16 shows the horizontal displacement of Node 232 located at the top of the upper structure wall, superimposed on that of Node 414 located at the foot of the same wall. The displacement at Node 232 is outward up to about 7.3 msec. This outward motion has been shown to be primarily responsible for the development of radial cracks in the upper structure. Inward movement begins at about 5 msec with net inward displacement after about 7.3 msec. At Node 414 the same outward-inward sequence of motion is preceded by a period of small-amplitude inward displacement up to about 11 msec. A major difference in the characters of the two curves is the amplitude of the outward motion. The positive peak (outward motion) displacement of the bottom node is only about 20% of that of the top

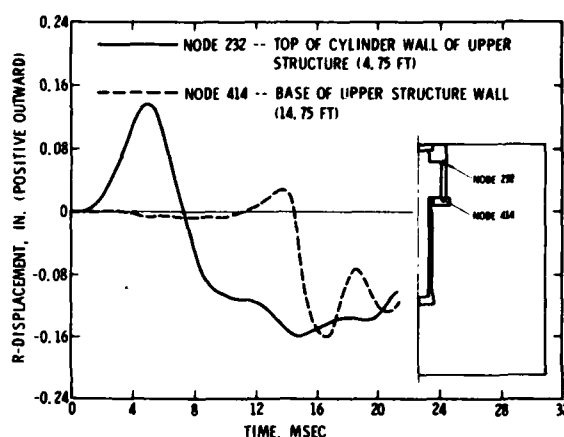


Fig. 16 - Horizontal displacement at two locations in the upper structure

mode. This can be explained by the fact that the outward motion of the cylinder wall is primarily caused by a moment and a radial shear force applied to the top end of the cylinder, whereas the inward motion of the cylinder wall is due to the lateral pressure transmitted by the surrounding soil.

Finally, Fig. 17 shows the vertical displacement time histories of Node 263 located near the top of the upper structure wall and Node 523 at the middle of the limestone layer in the free field. The curve corresponding to Node 263 shows an early downward peak at approximately 7.8 msec. This is followed by a brief upward motion before moving downward again at about 12.4 msec. The second downward

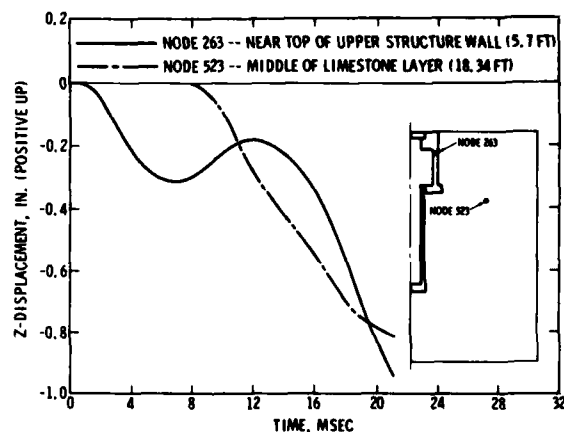


Fig. 17 - Vertical displacement comparison for locations in upper structure and free field

motion is much stronger and is still increasing at the end of the calculation. This curve is superimposed on the free-field displacement time history representing roughly the displacement at the base of the upper structure. The first peak, which is completely absent in the free field, is probably due to wave propagating in the structure. This is followed by an upward rebound motion as the wave is reflected from the hard limestone layer. The main motion, however, appears to be caused by waves propagating through the surrounding soil that result in the downward movement of the supporting limestone layer. The history of crack development (Fig. 11) indicates that most cracks are initiated prior to 16 msec. Therefore, the strong vertical motion occurring after this time appears mainly to be composed of rigid body motion.

### Stresses

Selected stress plots at various free field and structural locations are presented and discussed in this section. Vertical stress time histories for three free-field locations are superimposed in Fig. 18. These stresses are normalized based on the maximum dynamic load amplitude  $p_d$ . At Element 4, which is located at the ground surface, the time history very closely follows the input pressure pulse (Fig. 10). At Element 205 near the middepth of the top (dry clay) layer, the curve has a first peak that is nearly identical to the peak of the surface element. A second peak has an amplitude comparable to the first peak. The arrival time of this peak (12.6 msec) can be readily identified with that of the wave reflected from the interface between the clay and the hard limestone layers.

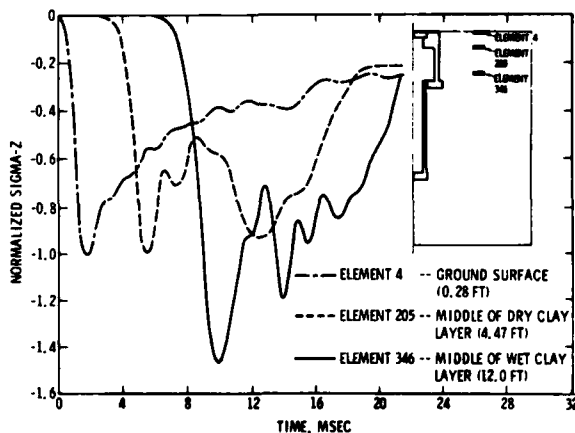


Fig. 18 - Vertical stress comparison for three free-field locations

At Element 346 near the middepth of the second (wet clay) layer, the first peak is amplified approximately 1.5 times, and the second peak 1.3 times from the previous values because of the impedance mismatch and the superposition of the primary and reflected waves. The two peaks are now closer together because this target point is now closer to the reflecting interface.

Vertical stress time histories for three elements at the top of the upper structure wall are shown in Fig. 19. This comparison shows that prior to about 6 msec the section undergoes a buildup in both compression and bending. This is followed by a brief period of unloading until the middle element cracks in tension at 9 msec. In the second stage the inner element reloads again in compression while the middle and the outer element both undergo tension, and consequently the crack developed in Element 261 remains open. In view of the previous discussions on cracks and displacements, it is obvious that the first state of loading is due primarily to the directly applied pressure loading. As the vertical load decays, the horizontal load exerted by the soil increases. The inward bending of the cylindrical wall section again introduces new buildup of bending moment at this section. However, there is not enough compressive load at this state to prevent the development of tension for the two outside elements.

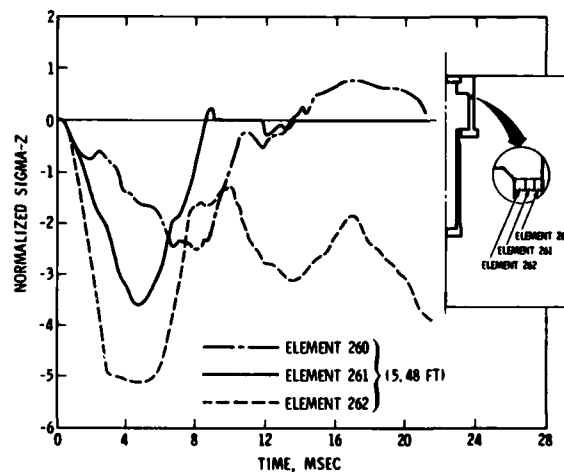


Fig. 19 - Vertical stress comparisons across the top of the upper structure wall

Fig. 20 presents a comparison of vertical stresses in the elements across a section at approximately the midheight of the upper structure wall. The vertical stresses show essentially the same sequence of events seen in Fig. 19 for

the top of the wall section. A noticeable difference is that the first compressive peaks in Fig. 20 have a nearly equal amplitude. This rather uniform compressive stress distribution indicates that prior to about 9 msec, the bending moment at the midheight section is small compared to that at the top. This observation is supported by the deformed mesh plots. In Fig. 14(a) it was shown that the massive top portion of the upper structure rotates in a counterclockwise direction. Therefore, in addition to transmitting the vertical overpressure, it also transmits a counterclockwise moment and an outward shear force to the top section of the cylindrical wall.

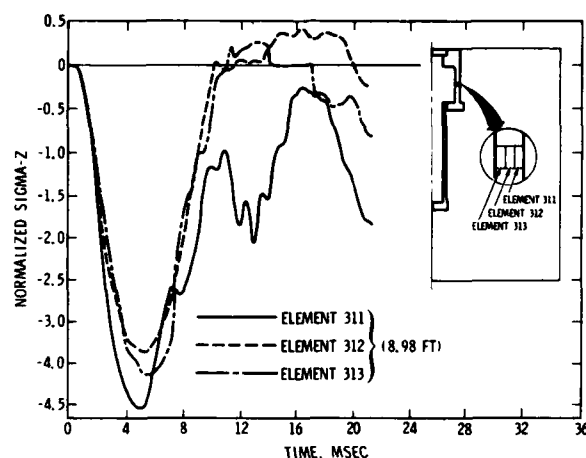


Fig. 20 - Vertical stress comparisons across a mid-height section of the upper structure wall

Since the bending moment induced by the applied end-moment and by the end shear-force are significant only within a small local region near the end, and their effects appear to be self-canceling, the major loading in the lower part of the cylinder is from the uniform vertical compression. A second noticeable difference is observed in the second stage of loading caused by the inward compression of the soil. The distribution of stresses across the wall thickness indicates that the sign of the moment at the midheight is reversed from that at the top of the wall. The sign of the bending moment represented by these plots corresponds to the case of a built-in cylinder loaded externally by radial compression.

Fig. 21 shows the representative radial stress time histories at the top and the midheight of the upper-structure wall. Both curves indicate almost identical behavior patterns. The two sections first crack radially in tension and stay

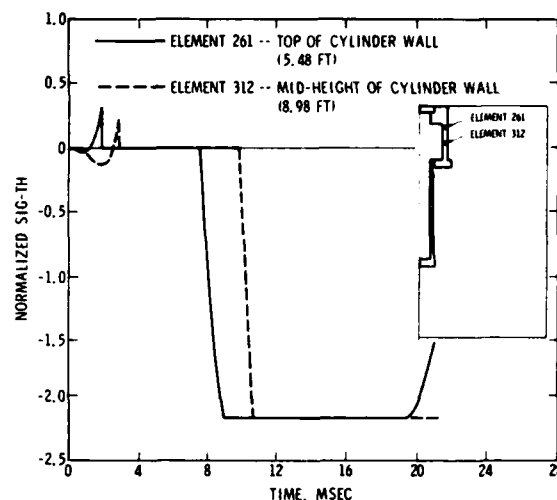


Fig. 21 - Radial stresses in the upper structure wall

under tension until a large compression generated from the loading in the surrounding soil develops. The strong compression quickly crushes both sections and they remain crushed until near the end of the calculation.

## SUMMARY AND CONCLUSIONS

The finite element analysis reported in this paper illustrates some of the recent results of a very important area of development in solving soil/structure interaction problems. To improve the performance of a finite-element analysis, more refined material models are used that account for a number of aspects of the material behavior. One of the main features of this analysis is the inclusion of the composite reinforced-concrete material model reported in [3]. Based on experimental data, this model is constructed to predict macroscopic cracking and crushing in the reinforced concrete. Other important characteristics taken into account are the debonding and rebonding between concrete and steel, the dowel action, and the inelasticity in the reinforcement. A crack analysis demonstrates the crack growth quantitatively as the loading proceeds. The results show a distinct pattern that facilitates the isolation of the dynamic interaction effects. Strong correlations are also found between cracking and the deformation of the structure, as well as in the displacement and the stress buildups in both the structure and the soil. The main results of the crack analysis can be summarized as follows:

- a. The main feature of the crack analysis is the classification of all cracks into

two groups: those associated with the bulging mode of deformation, called "radial" cracks; and those associated with compressive and bending loads, called "conical" cracks. Making such distinctions between these two types of cracks facilitates the interpretation of results and the identification of critically stressed areas in the structure.

- b. Due to the difference between the wave speeds in the concrete and those in the soil media, the structure is freed momentarily from the constraint of the surrounding soil. Consequently, the first major loading the structure experiences is dominated by the direct overhead pressure. The second stage of loading develops as the effect of waves propagating through the soil is felt. This "uncoupling" of the soil/structure interaction effects proves to be a powerful mechanism for generating cracks. In contrast, no such uncoupling is possible when the overhead pressure is applied statically. The deformation of the structure is always "confined" by the surrounding soil media, thus preventing a large number of cracks from occurring.
- c. In the case studied, the blast type of loading is a very powerful mechanism in generating cracks. Compared to a static loading of the same maximum amplitude, the dynamic loading shown in Fig. 10 generates about 14 times more cracks. Therefore, an "equivalent" static analysis may generate stress responses that are significantly lower than could occur in the dynamic environment.
- d. The cracking of concrete affects the structural behavior on two important counts: (1) The concrete's loss of ability to transmit tension in a local region causes the tensile load to be redistributed and high tension regions are therefore more widespread than they would be otherwise; and (2) by reducing the compressive strength in the postcracking phase, the cracked regions are weakened and can be more easily crushed when the loading is reversed.

#### ACKNOWLEDGMENTS

The work reported in this paper is based on an analysis performed by Agbabian Associates

for SAMSO under Contract F04701-69-C-0209. The authors would like to express sincere gratitude to Capt. J. Kaiser, project monitor at SAMSO, for giving permission to publish this paper; to Mr. L.E. Carlson, project manager at Agbabian Associates, for his general guidance throughout the entire phase of the reported work; and to Drs. D.P. Reddy and J.W. Workman for their constructive comments in the preparation of the original report.

#### REFERENCES

1. User's Guide for FEDRC Code, U-7523-2-3868, Agbabian Associates, El Segundo, CA, May 1975
2. K.P. Chuang and J. Isenberg, A Study of Implicit and Explicit Step-by-Step Integration Techniques for Finite Element Application, R-7243-5-2954, Agbabian Associates, El Segundo, CA, Jun. 1973
3. S.A. Adham, A.K. Bhaumik, and J. Isenberg, Reinforced Concrete Constitutive Relations, R-7322-3300, Agbabian Associates, El Segundo, CA, Jun. 1974 (AD A007-886)
4. T.C.Y. Liu, A.H. Nilson, and F.O. Slate, "Biaxial Stress-Strain Relations for Concrete," Proc., ASCE Struct. Div., Vol. 98, No. ST5, May 1972

#### APPENDIX A

##### TYPES OF TWO-DIMENSIONAL ELEMENTS

##### Axisymmetric Isoparametric Elements

The axisymmetric isoparametric element used to model the structure and the soil is depicted in Fig. 22. These elements are defined by the shape functions that are quadratic functions in terms of the local coordinates  $s$  and  $t$ .

$$\left. \begin{aligned} r(s,t) &= \sum_{i=1}^4 h_i r_i \\ z(s,t) &= \sum_{i=1}^4 h_i z_i \\ u(s,t) &= \sum_{i=1}^4 h_i u_i \\ v(s,t) &= \sum_{i=1}^4 h_i v_i \end{aligned} \right\} \quad (3)$$

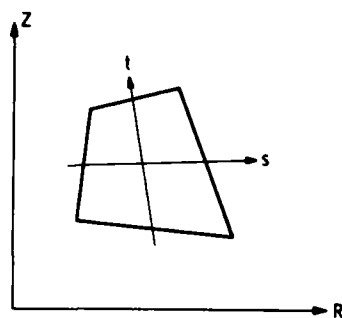
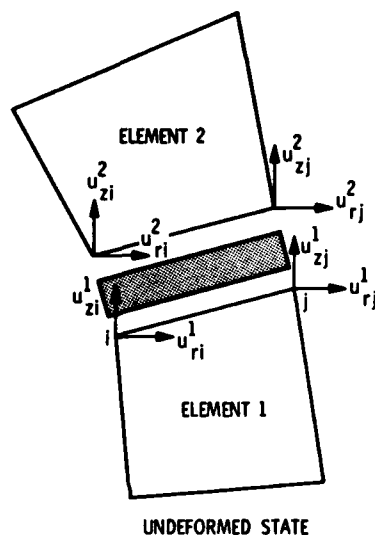


Fig. 22 - Axisymmetric isoparametric continuum used in FEDRC code



R, Z - GLOBAL COORDINATES  
r, s - LOCAL COORDINATES

Fig. 23 - Deformation geometry of slip element

in which  $r, z$  are the cartesian coordinates and  $u, v$  are the velocity components. The subscript  $i$  identifies one of the four corner nodes of the elements. The shape coefficients  $h_i$  are defined by

$$\left. \begin{aligned} h_1 &= \frac{(1-s)(1-t)}{4} \\ h_2 &= \frac{(1+s)(1-t)}{4} \\ h_3 &= \frac{(1+s)(1+t)}{4} \\ h_4 &= \frac{(1-s)(1+t)}{4} \end{aligned} \right\} \quad (4)$$

The strain-displacement relations are obtained by differentiating the above displacement functions with respect to coordinates  $r$  and  $z$ . From this the strain-displacement transformation matrix  $[S]$  is calculated and finally the element stiffness matrix  $[k]$  is derived by evaluating the integral

$$[k] = \int_{\text{volume}} S^T C S dV \quad (5)$$

where  $C$  is a matrix composed of the generalized tangent stress/strain moduli of the material.

#### Slip Elements

A special slip element is used to simulate the slippage between two contiguous bodies. The added degrees of freedom are introduced by relating the displacement components at nodal points on two sides of the common interface by the following set of equations:

$$\left. \begin{aligned} u_{ri}^2 &= u_{ri}^1 + \Delta u_{ri} \\ u_{zi}^2 &= u_{zi}^1 + \Delta u_{zi} \\ u_{rj}^2 &= u_{rj}^1 + \Delta u_{rj} \\ u_{zj}^2 &= u_{zj}^1 + \Delta u_{zj} \end{aligned} \right\} \quad (6)$$

The superscripts 1 and 2 refer to the two sides of the interface as shown in Fig. 23;  $i$  and  $j$  denote the two pairs of nodal points and the two  $\Delta u$ 's are the relative displacement components of the pair of initially coinciding nodal points.

The displacement field is assumed to vary linearly along the interface. It can be defined in

terms of the local coordinate  $s$  along the length of the interface by the following set of equations

$$\left. \begin{aligned} \Delta u_r &= h_i \Delta u_{ri} + h_j \Delta u_{rj} \\ \Delta u_z &= h_i \Delta u_{zi} + h_j \Delta u_{zj} \\ u_r^1 &= h_i u_{ri}^1 + h_j u_{rj}^1 \end{aligned} \right\} \quad (7)$$

in which  $h_i = \frac{1}{2}(1 - s)$  and  $h_j = \frac{1}{2}(1 + s)$

It is convenient to transform the relative displacement components into the local coordinates  $n$  and  $s$  which are normal to and along the direction of the interface. The resulting components are:

$$\left. \begin{aligned} \Delta u_n &= -\Delta u_r \sin \phi + \Delta u_z \cos \phi \\ \Delta u_s &= \Delta u_r \cos \phi + \Delta u_z \sin \phi \end{aligned} \right\} \quad (8)$$

The element stiffness matrix of the slip element is obtained based on the above displacement field.

## APPENDIX B

### BOUNDARY CONDITIONS

The vertical boundaries a-b, c-d, and e-f in Fig. 4 are roller in the vertical direction, that is, the horizontal displacement is restrained. Pressure loading is applied uniformly over the top boundary a-f. Since, generally speaking, the motion and the deformation of the entire mesh are predominantly vertical and are expected to approach those of the free field a short distance away from the structure and the backfill region, the approximation of roller on the outer boundary e-f appears to be justified. The roller on the innermost vertical boundary a-b, c-d not only eliminates certain numerical singularities at the axis of symmetry, but also ensures that this boundary is the axis of symmetry.

The mesh has a total depth of 60.84 ft. The one-way transit time across the free-field profile is estimated to be 13.3 msec (Fig. 3). If the bottom boundary were indeed free, a reflected signal would have arrived at the vicinity of the upper structure footing at about 19.1 msec. Because the wave travels much faster in the concrete, the corresponding arrival time of the reflected signal when the wave is propagated through the concrete is estimated to be approximately 11.1 msec. In reality, the initial arrival time of the reflected signal probably falls somewhere in between. Therefore, after approximately

15 msec, the response at the foot of the upper structure will be distorted by the fictitious signals reflected from the bottom boundary of the finite element mesh. To avoid these reflected signals, the bottom boundary is "quieted" using a technique described in [1]. This technique is intended to eliminate unwanted reflections from a boundary so that this boundary can be considered to lie beyond the physical limits of the finite element mesh. In the static analysis all bottom boundary nodes are hinged to provide fixity.

## APPENDIX C

### MATERIAL MODELS

#### Material Model for Soils

The idealized material model used to represent the nine geological soil layers exhibits a hysteretic, piecewise linear stress/strain behavior and a Mohr-Coulomb-type failure envelope as shown in Fig. 24. Property coefficients of these nine materials based on laboratory data are shown in Table 1.

Definitions of these coefficients are given below:

Virgin Loading for  $\mu \leq \mu_m, \dot{\mu} \leq 0$

$$\left. \begin{aligned} B &= B_1 \text{ for } \mu_2 > \mu \geq \mu_1 \\ B &= B_2 \text{ for } \mu_1 > \mu \geq \mu_2 \end{aligned} \right\} \quad (9)$$

$$G = \frac{3B(1 - 2\nu)}{2(1 + \nu)} \quad (10)$$

Unloading/Reloading for  $\mu > \mu_m$

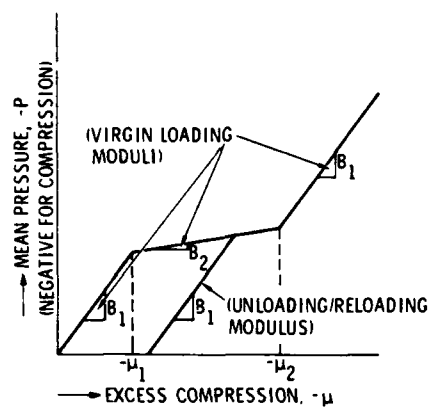
$$B = B_1 \quad (11)$$

#### Yield Criteria

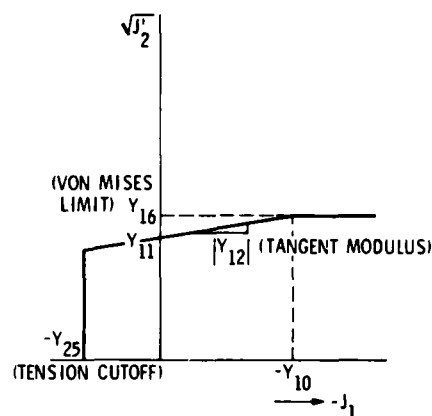
$$\left. \begin{aligned} F &= Y_{11} + Y_{12} J_1 \\ &\quad - \sqrt{J_2'} \geq 0 \quad (\text{for } J_1 \geq Y_{10}) \\ F &= Y_{25} - J_1 \geq 0 \end{aligned} \right\} \quad (12)$$

$$F = Y_{16} - \sqrt{J_2'} \geq 0 \quad (\text{for } J_1 < Y_{10})$$

$$F < 0 \text{ not permitted}$$



(a) Pressure/volume change curve



(b) Failure envelope curve

Fig. 24 - Idealized model for free-field materials

TABLE 1  
Properties of Free-Field Materials

Material		Depth, ft	Density, psf	Poisson's Ratio, $\nu$	Excess Compression, in./in.		Bulk Modulus, psi				Yield Criteria		
							B <sub>1</sub> Loading	B <sub>2</sub> Loading	B <sub>u</sub> Tensile	B <sub>u</sub> Unloading	Y <sub>T</sub> , psi Tension Cutoff	Y <sub>11</sub> , psi Cohesion	Y <sub>12</sub> Envelope Slope
No.	Description				$\mu_1$	$\mu_2$							
1	Dry Clay	0 to 4.77	110	0.4	$-2.41 \times 10^{-4}$	-0.02	$4.1494 \times 10^4$	$2.657 \times 10^4$	$4.1494 \times 10^4$	$4.1494 \times 10^4$	10.0	100.0	-0.0033
2	Wet Clay	4.77 to 16.24	130	0.4	$-1.57 \times 10^{-5}$	-0.005	$6.3694 \times 10^5$	$5.778 \times 10^5$	$6.3694 \times 10^5$	$6.3694 \times 10^5$	30.0	10.0	-0.0033
3	Limestone	16.24 to 20.44	167	0.35	$-8.3 \times 10^{-7}$	-0.005	$1.2048 \times 10^7$	$4.879 \times 10^6$	$1.2048 \times 10^7$	$1.2048 \times 10^7$	48.0	5000.0	-0.1667
4	Interbedded Limestone and Shale	20.44 to 32.44	160	0.36	$-6.4 \times 10^{-6}$	-0.005	$1.5625 \times 10^6$	$8.791 \times 10^5$	$1.5625 \times 10^6$	$1.5625 \times 10^6$	76.0	500.0	-0.1
5	Limestone	32.44 to 35.24	167	0.35	$-8.3 \times 10^{-7}$	-0.005	$1.2048 \times 10^7$	$4.879 \times 10^6$	$1.2048 \times 10^7$	$1.2048 \times 10^7$	100.8	5000.0	-0.1667
6	Shale	35.24 to 41.64	155	0.38	$-5.86 \times 10^{-6}$	-0.005	$1.7065 \times 10^6$	$1.13 \times 10^6$	$1.7065 \times 10^6$	$1.7065 \times 10^6$	115.3	5000.0	-0.1
7	Coal	41.64 to 45.24	90	0.41	$-8.0 \times 10^{-6}$	-0.005	$1.25 \times 10^6$	$8.694 \times 10^5$	$1.25 \times 10^6$	$1.25 \times 10^6$	129.1	500.0	-0.1
8	Shale	45.24 to 51.74	155	0.38	$-5.86 \times 10^{-6}$	-0.005	$1.7065 \times 10^6$	$1.13 \times 10^6$	$1.7065 \times 10^6$	$1.7065 \times 10^6$	143.0	500.0	-0.1
9	Limestone	51.74 to 60.84	167	0.35	$-8.3 \times 10^{-7}$	-0.005	$12.048 \times 10^7$	$4.879 \times 10^6$	$1.2048 \times 10^7$	$1.2048 \times 10^7$	168.8	5000.0	-0.1667



In these equations

- $J_1$  = First stress invariant ( $\sigma_{ii}$ )  
 $J_2'$  = Second stress deviator invariant  $\frac{1}{2}(\sigma_{ij}\sigma_{ij})$   
 $B$  = Bulk modulus  
 $G$  = Shear modulus  
 $\nu$  = Poisson's ratio (assumed to be constant)  
 $\mu = (1 + \epsilon_r)(1 + \epsilon_z)(1 + \epsilon_\theta) - 1$   
 = Excess compression (negative for compressive strains)  
 $\dot{\mu}$  = Time derivative of  $\mu$   
 $\mu_m$  = Maximum excess compression reached in previous load history  
 $\epsilon_r, \epsilon_z,$  and  $\epsilon_\theta$  are the three axial strains  
 $B_1, B_2, \mu_1, \mu_2, Y_{11}, Y_{12}, Y_{16},$  and  $Y_{25}$  are empirical constants

#### Material Model for Backfill Material

The idealized uniaxial-loading stress/strain curve for the backfill material based on laboratory data is shown in Fig. 25. Because of a potential numerical instability problem induced by the rapid variation of the constraint modulus at about 4% strain, the piecewise linear uniaxial stress/strain curve is approximated by a single continuous fourth-order polynomial curve. This variable modulus model represented by a single smooth virgin-loading curve is defined by Eqs. (13) through (22).

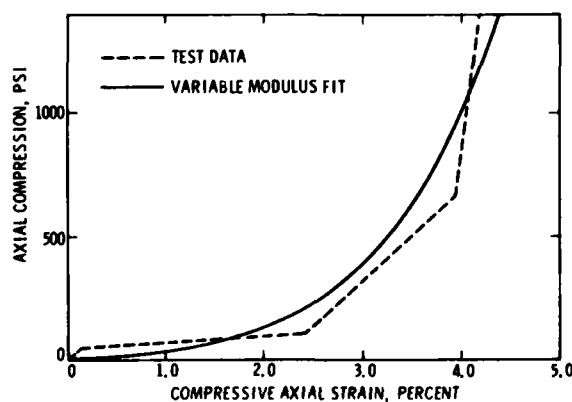


Fig. 25 - Uniaxial stress/strain fit for backfill material

Virgin Loading for  $\mu \leq \mu_m, \dot{\mu} \leq 0$

$$B = D_0 + D_1\mu + D_2\mu^2 + D_3\mu^3 \quad (13)$$

$$G = \frac{B(1 - 2\nu)}{2(1 + \nu)} \quad (14)$$

Unloading/Reloading for  $\mu > \mu_m$

$$B_m = D_0 + D_1\mu_m + D_2\mu_m^2 + D_3\mu_m^3 \quad (15)$$

$$P_m = \left[ \sigma_x(\mu_m) + \sigma_y(\mu_m) + \sigma_z(\mu_m) \right] / 3 \quad (16)$$

$$\mu_R = \left[ 1 - \exp\left(\frac{\mu_m}{\mu_0}\right) \right] \bar{\mu} \quad (17)$$

$$B'_0 = B_m + \frac{P_m - B_m(\mu_m - \mu_R)}{\mu^* \left[ 1 - \exp\left(\frac{\mu_R - \mu_m}{\mu^*}\right) \right]} \quad (18)$$

$$B = \left. \begin{aligned} &B_m - [B_m - B'_0] \exp[-(\mu - \mu_R)/\mu^*] \\ &\quad \text{(for } B_0 < B_m) \end{aligned} \right\} \quad (19)$$

$$B = \left. \begin{aligned} &B_m \text{ (or maximum } B) \\ &\text{encountered in load history} \end{aligned} \right\} \quad \text{(for } B'_0 \geq B_m)$$

$$G = \text{Maximum of } \frac{3}{2} B_m \frac{(1 - 2\nu_u)}{(1 + \nu_u)} \quad (20)$$

or largest  $G$  encountered in load history

#### Yield Criteria

$$\left. \begin{aligned} F &= Y_{11} + Y_{12}J_1 \\ &\quad - \sqrt{J_2'} \geq 0 \end{aligned} \right\} \quad \text{(for } J_1 \geq Y_{10}) \quad (21)$$

$$F = Y_{25} - J_1 \geq 0$$

$$F = Y_{16} - \sqrt{J_2'} \geq 0 \quad \text{(for } J_1 < Y_{10}) \quad (22)$$

$F < 0$  not permissible

In these equations,

$\mu_u$  = Unloading Poisson's ratio

$D_0, D_1, D_2, D_3, \mu_0, \mu^*, \bar{\mu}$ , and  $Y_{10}$  are empirical constants determined from the loading/unloading uniaxial stress/strain curve and the yield criteria

All other variables are as defined in Eqs. (9) through (12). Numerical values of the parameters used for the backfill are given in Table 2.

TABLE 2  
Uniaxial Test Data for Backfill Material

Range of Axial Strain, in./in.	Constraint Modulus $M_c$ , psi
$\epsilon > -0.0015$	31,111
$-0.0015 > \epsilon > -0.0244$	2,667
$-0.0244 > \epsilon > -0.0394$	37,037
$-0.0394 > \epsilon$	310,588

#### Material Model for Reinforced Concrete

The reinforced concrete model used in the present analyses is a continuum model based on considering separately the properties of plain concrete and the steel. The resulting material is orthotropic and homogeneous, and possesses the main characteristics of both materials.

##### Plain Concrete

The plain concrete is represented by a variable modulus model in which the elastic moduli in orthogonal directions under virgin compressive loading are assumed to be functions of both the strain and the confinement [3].

The functional relationships of the two elastic moduli originally suggested by Liu, Nilson, and Slate [4] are given by:

$$E_c^i = \frac{E_c \left[ 1 - \left( \frac{\epsilon_i}{\epsilon_m} \right)^2 \right]}{\left[ 1 + \left( \frac{1}{1 - \nu \beta_1} \frac{E_c \epsilon_m}{\sigma_m} - 2 \right) \left( \frac{\epsilon_i}{\epsilon_m} \right) + \left( \frac{\epsilon_i}{\epsilon_m} \right)^2 \right]^2} \quad (23)$$

$$G_{ij} = \frac{E_c^i E_c^j}{(1 + \nu)(E_c^i + E_c^j)} \quad (24)$$

in which

$E_c^i, E_c^j$  = Tangent moduli in two orthotropic directions

$G_{ij}$  = Shear modulus between the  $i$ th and the  $j$ th orthotropic directions

$E_c$  = Initial tangent modulus of concrete, constant for all directions (tangent modulus corresponding to zero strain)

$\epsilon_i$  = Strain in the direction considered

$\sigma_m$  = Peak stress in biaxial compressive loading

$\epsilon_m$  = Strain corresponding to the peak stress

$\nu$  = Poisson's ratio for concrete, assumed to be a constant

$\beta_1 = \frac{\sigma_1}{\sigma_i}$  = Ratio of principal stress in the direction considered to the stress in the principal stress direction considered

The directions of orthotropy are assumed to coincide with the principal directions of stresses until tensile cracking occurs, after which they remain frozen permanently. Unloading and reloading in compression assume a constant modulus  $E_c$ . The complete loading, unloading, and reloading characteristics of the plain concrete are shown in Fig. 26. In tension, a constant  $E_c$  is assumed in all cases until cracking occurs. Then the concrete modulus is set to zero until rebonding. After rebonding the post-rebonding modulus is set to  $0.5 E_c$ .

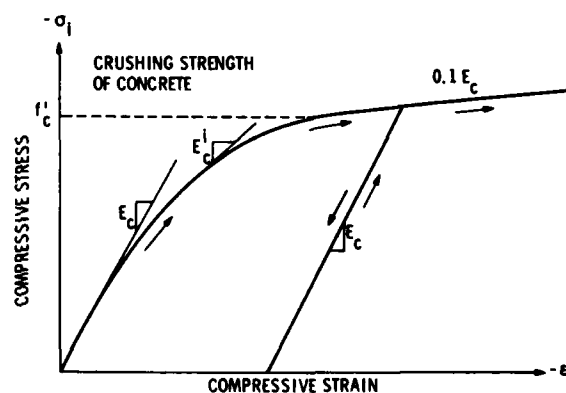


Fig. 26 - Virgin loading and unloading/reloading behavior of concrete model in compression

The cracking strength of concrete,  $f_t'$ , where  $\sigma_1 \leq f_t'$ , in any given direction  $x$ , is assumed to be

$$f_t' = f_t - \eta \sigma_2 \quad (25)$$

for  $\sigma_2 < \sigma_3$  and  $\sigma_2 \leq 0$ ,  $\sigma_2$  and  $\sigma_3$  are the confinement stress components in which

$f_t$  = Unconfined tensile strength of concrete

$\eta$  = Slope of cracking envelope =  $f_t/f_c'$

$f_c'$  = Unconfined compressive strength of concrete

$\sigma_2$  = Minimum nonpositive normal stress

The stress/strain behavior of concrete in tension is depicted in Fig. 27.

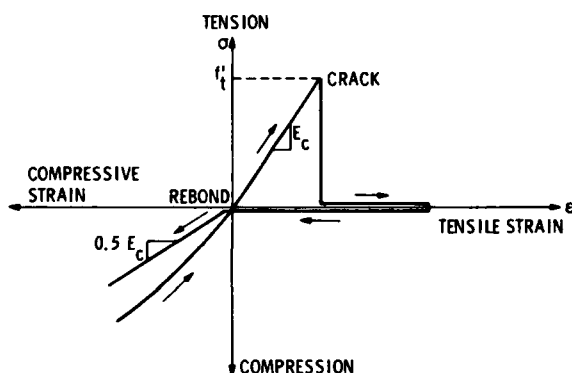


Fig. 27 - Behavior of concrete model under cracking and rebonding

#### Steel Reinforcement

The main properties of the reinforcing steel treated in the composite model are the area of the steel (percentages of steel area) and its stress/strain behavior. Both of these properties are prescribed in the so-called steel coordinates, or in other words, in directions parallel to the axes of the steel bars. These areas are then transformed to the principal directions of orthotropy, where they are incorporated together with the tangent moduli of the steel to form the composite moduli. The stress/strain behavior of the steel is assumed to be linearly elastic and perfectly plastic, and is identical for both tension and compression (Fig. 28). Numerical values used are given in Table 3.

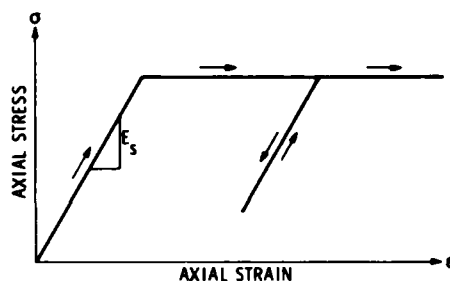


Fig. 28 - Stress/strain behavior for reinforcing steel

TABLE 3  
Material Properties of Steel

Specific Weight, pcf	Young's Modulus, psi	Shear Modulus, psi	Yield Strength, psi
490	$29.8 \times 10^6$	$11.5 \times 10^6$	50,000

#### Composite Reinforced-Concrete Model

Based on the transformed percentage of steel areas in the three principal directions of orthotropy, the effective modulus  $E_{comp}^i$  of the uncracked composite material is given by the weighted mean between steel and concrete moduli, using respective steel-area percentages as weighting factors.

$$E_{comp}^i = E_c^i A_c^i + E_s^i A_s^i \quad (26)$$

in which the superscript  $i$  denotes a principal direction,

$E_{comp}^i$  = Effective modulus of the composite material in the  $i$ th direction

$E_c^i$  = Elastic modulus of concrete (Eq. [23])

=  $E_c$  for unloading or reloading in compression and for loading and unloading in tension

$E_s$  = Elastic modulus of steel

$A_s^i$  = Projected steel-area fraction in the  $i$ th direction

$A_c^i = 1 - A_s^i$  = Concrete-area fraction in the  $i$ th direction

After the occurrence of cracking, one or all of the directions of orthotropy are fixed. The effective modulus is then given by

$$E_{comp}^i = \frac{(E_c A_c^i + E_s A_s^i) E_s A_s^i}{E_s A_s^i + (1 - \lambda) E_c A_c^i} \quad (27)$$

in which  $\lambda$  is a bond-slip parameter to be determined based on experimental data. In the present case this parameter is defined by

$$\lambda = 1 - \frac{10X}{3} \quad (\text{for } X \leq 0.15)$$

$$= \frac{10(1 - X)}{17} \quad (\text{for } 0.15 < X \leq 1.0)$$

and  $X = \frac{\text{tensile stress in steel}}{\text{yield stress of steel}}$

The onset of cracking is determined when the stress carried by concrete  $\sigma_i$  has exceeded its tensile strength; that is, whenever  $\sigma_i > f'_t$  where  $\sigma_i$  is calculated by

$$\sigma_i = \frac{E_c \sigma_{comp}^i}{E_c A_c^i + E_s A_s^i} \quad (28)$$

in which  $\sigma_{comp}^i$  is the effective average  $i$ th principal stress computed for the element of interest and  $f'_t$  is given by Eq. (25).

In the present crack model a maximum of three mutually perpendicular cracks are permitted to develop inside an element. On account of the radial symmetry, one of the three crack planes has to be on the radial plane. Therefore, all three crack directions are defined, provided one of the remaining two crack planes is known.

After cracking and before the occurrence of "rebonding," concrete is assumed to lose all its strength in the cracked direction, and the stress in the reinforcement is not allowed to exceed the yield stress of steel. The effective modulus of the composite material during loading, unloading, or reloading is given by

$$E_{comp}^i = E_s A_s^i \quad (29)$$

In the absence of reinforcement ( $A_s^i = 0$ ) the effective modulus is set equal to a nominal minimum value to avoid numerical difficulties.

Rebonding occurs when, during unloading, the strain in an element becomes negative (i.e.,

compressive). The composite modulus is composed of a weighted average (according to the percentage of steel area) of the steel modulus and a fraction of the virgin-concrete modulus. Thus

$$E_{comp}^i = n E_c A_c^i + E_s A_s^i \quad (30)$$

where  $n$  is taken to be 0.5 in the present analysis.

The current reinforced-concrete model also takes into account the bond-slip behavior and the dowel-action effects. Detailed discussions of these two effects can be found in [3]. The material properties used in the calculation are given in Table 4.

TABLE 4  
Properties of Reinforced Concrete

Properties	Value
Specific Weight, pcf	145
Young's Modulus of Concrete, psi	$4.454 \times 10^6$
Young's Modulus of Reinforcing Steel, psi	$30 \times 10^6$
Compressive Strength of Concrete (20% below nominal value), psi	6100
Yield Strength of Reinforcing Steel, psi	56,648
Poisson's Ratio of Concrete	0.2
Unconfined Tensile Strength of Concrete, psi	650
Shear Modulus of Reinforcing Steel, psi	$11.5 \times 10^6$
$\eta = f_t/f'_c$	0.10656

#### Materials for Slip Elements

The slip elements are assumed to be of unit thickness with no mass. In addition, stiffness properties and a Mohr-Coulomb-type yield surface in the shear stress/strain relationship are selected to simulate interface friction. In the current model, three different slip zones are introduced. The first one simulates any slippage that may occur between the structure and the surrounding soil. The second slip material simulates the free surface in the air gap between the bottom of the upper structure and the top of the lower structure. The third slip material simulates the contact zone between the upper structure and the seat of the circular disk cover.

TABLE 5  
Properties of Slip Materials  
(Terms are defined in Figs. 12 and 13.)

Interface	Normal Modulus, psi	Shear Modulus, psi	Cohesion, psi	Mohr-Coulomb Tangent Modulus	von Mises Limit, psi
Concrete and Backfill	$10^6$	100	10	-0.016667	58
Concrete* and Air	$10^6$	100	$10^5$	0	$10^5$
Concrete and Steel	$10^8$	$11.5 \times 10^6$	500	-0.3	27,787

\* The values for normal modulus, cohesion, and the von Mises limit of air are artificial. They are selected to prevent normal penetration and yielding.

Material parameters for the three slip materials used in the calculations are listed in Table 5. Typical normal and typical shear stress/strain relationships are illustrated in Figs. 29(a) and (b). The modified Mohr-Coulomb criterion

governing the maximum allowable shear stress is depicted in Figure 30.

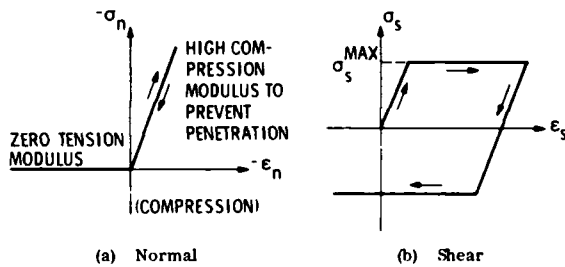


Fig. 29 - Stress/strain curves for a slip element

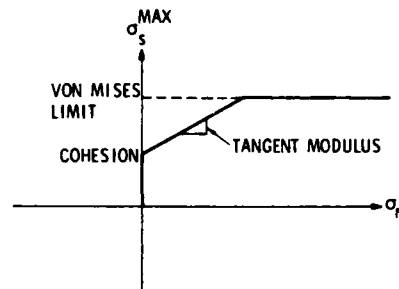


Fig. 30 - Modified Mohr-Coulomb criterion for maximum shear stress in the slip material

FAILURE OF ALUMINUM CYLINDRICAL  
SHELLS SUBJECTED TO TRANSVERSE BLAST LOADINGS

W. S. Strickland  
USAF Armament Laboratory  
Eglin AFB, Florida

and

J. E. Milton and C. A. Ross  
University of Florida Graduate Engineering Center  
Eglin AFB, Florida

and

L. J. Mente  
Kaman Avidyne  
Burlington, Massachusetts

The failure of 6061-T6 aluminum cylindrical shells was investigated both experimentally and analytically. Cylinders of various thicknesses and lengths with a constant diameter (30.48 cm) were subjected to blast loadings using both fuel air explosives FAE and high explosives HE. Test cylinders were held fixed against rotation and deflection at the ends and two kinds of loads were applied using a FAE gas bag technique with MAPP gas and HE Pentolite spheres. Both planar and cylindrical surface pressure measurements were recorded and utilized to determine loading functions for analytical models.

The dynamic response of these cylindrical shells is a complicated problem involving both elastic and plastic buckling before failure begins to occur. The buckling phenomenon depends on the loading function as well as the geometrical dimensions of the cylinder. Analytical predictions of the buckling mode prior to actual material fracture appear to be the major task in the overall solution of the failure problem. Empirical solutions to this portion of the problem have shown some promise.

Experimental tests on fixed end cylinders show the cylinders begin to buckle circumferentially on the leading edge normal to the blast wave front with buckling occurring very early in time after the blast wave touches the cylinder. The circumferential buckling then proceeds tangentially around the cylinder as the fundamental longitudinal mode begins to form with maximum deflection occurring at the midpoint of the cylinder length. Failure then begins as a crack at the fixed end of the cylinder and running tangentially away from the leading edge. All tests were performed for intermediate pressures of two to ten megapascals and positive pressure phase durations of one to three milliseconds. For these type loadings only 25% to 30% of the cylinder, measured tangentially (90°), is active in the deformation process.

Analytical methods based on both finite difference and modal solution techniques were used to calculate response of typical cylindrical shells and results were compared to experimental results.

## INTRODUCTION

Dynamic plastic response of metal cylindrical shells subjected to sharp edge blast loads is mathematically very complex. The overall plastic deformation process is complicated by the buckling phenomenon associated with the compressive load. Due to the highly complicated nature of the overall response only approximate analytical solutions coupled with experimental observations are to be expected. The general results of typical approximate solutions [1-3] are expressions for a given level of damage often displayed as iso-damage curves. These curves are generally a plot of impulse verses peak blast pressure for varying values of the geometric parameters of the cylinder. Considerable experimental work using actual blast loads by Schuman [4-5], Lindberg [3] and presently by the authors has not completely verified the approximate solutions.

Iso-damage curves, for a given damage level, may be drawn using the experimental observations and the approximate methods, but a prediction of failure for actual material separation is not available. Even the large and more complex computer codes [7-8] are limited in this area due to the lack of adequate failure criteria.

The main objective of this study is to further define plastic response of cylindrical shells exposed to actual mild transverse blast loads which produce actual material rupture. The study is essentially experimental in nature and comparisons are made with some analytical methods.

## ANALYTICAL RESULTS

The analysis of the dynamic response and subsequent failure of cylindrical shells is a rather complex problem. Several different models have been developed, many of which are response type models where emphasis is placed on a detailed description of the deflection. In all cases these models must take into account large deflection theory, kinematic and material hardening, elastic and plastic buckling and utilize finite difference or finite element techniques. In this study only transverse loading was considered and any reference to buckling or response is assumed to be as a result of this type loading. Response models, presented in detail in References [6] and [7], are summarized in the following paragraphs. These models were used to predict response of selected

cylindrical shells included in the experimental tests.

Analytical solutions were obtained for a cylinder tested under both HE pentolite and FAE gas bag techniques by assuming simple pressure distributions to represent the loading. The DEPICS-2 and PETROS-3 shell computer programs, based on both geometrically and physically nonlinear behavior, were used to analyze the large displacement transient elastic-plastic response of the selected cylinder. DEPICS-2 is a recently developed elastic-plastic version of the elastic DEPICS shell analysis presented in Reference [6], and is based on a modal approach for solving the cylindrical shell equations of motion established through the virtual work method. The PETROS-3 program, presented in Reference [7], employs a finite-difference approach for solving the general shell equations of motion. The selected 6061-T6 aluminum cylindrical shell has a radius of 15.32 cm., a length of 57.54 cm. and a thickness of 0.16 cm. This cylinder was tested by both loading techniques which produced different deformation patterns on the windward side of the shell, probably caused by differences in the pressure distribution on the shell. The shell response analyses DEPICS-2 and PETROS-3 were used to examine the response sensitivity to assumed frontal cosine squared and cosine pressure distributions on the shell with peak pressures and decays similar to those obtained experimentally. These simple loadings also imply an assumed instantaneous engulfment of the shell.

The results of this analysis are illustrated in Figures 1 through 4. Figure 1 shows the analytical time histories of the midlength radial displacement at  $\theta = 0^\circ$  as predicted by DEPICS-2 and PETROS-3. The figure also shows the response of this cylinder relative to the experimental permanent set measured at this point resulting from the HE pentolite. Figure 2 illustrates the estimated permanent set deformation patterns on the windward side of the shell obtained from DEPICS-2 and PETROS-3 for the cosine squared loading. Both patterns are similar to the experimental final deformed shape of the cylinder tested using the HE pentolite technique. Figures 3 and 4 show similar plots for the frontal cosine loading distribution which produced a different deformation pattern than from the cosine squared loading. However, neither analytical pattern was similar to the experimental patterns. The large differences between the DEPICS and PETROS results for the cosine

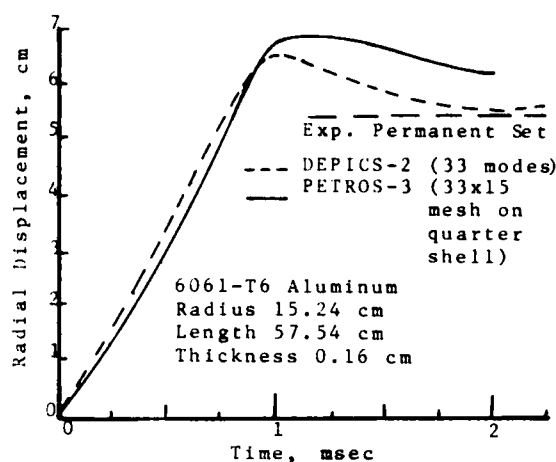


Figure 1. Radial displacement response at  $\theta=0$  and mid-length of cylinder assuming a cosine squared loading over front half. Assumed pressure load of  $p=(P_r \cos^2 \theta) \exp(-t/t_0)$ ,  $-\pi/2 \leq \theta \leq \pi/2$ , where  $P_r=5.52$  MPa and  $t_0=.1875$  milliseconds.

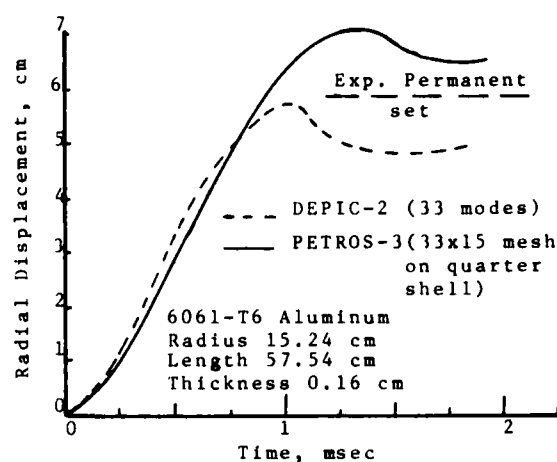


Figure 3. Radial displacement response at  $\theta=0$  and mid-length of cylinder assuming a cosine loading over front half. Assumed pressure load of  $p=(P_r \cos \theta) \exp(-t/t_0)$ ,  $-\pi/2 \leq \theta \leq \pi/2$ , where  $P_r=5.52$  MPa and  $t_0=.275$  milliseconds.

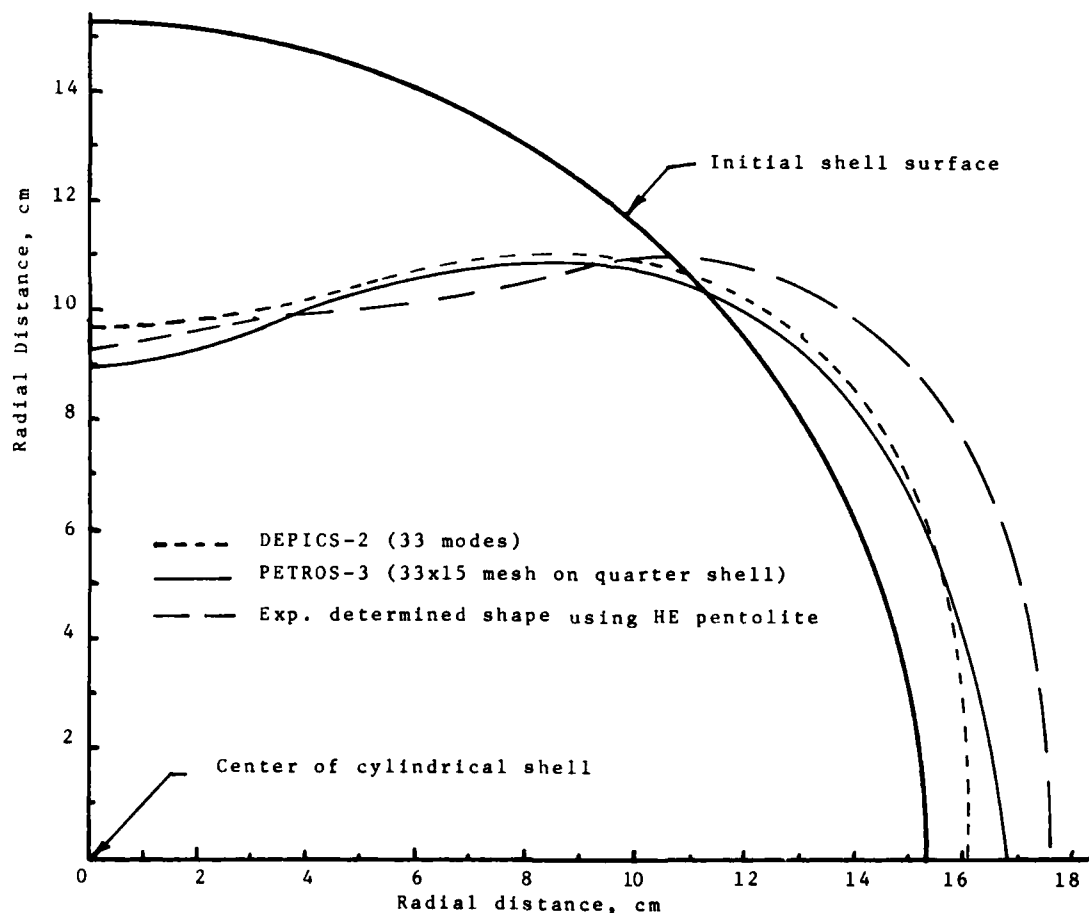


Figure 2. Calculated permanent set at mid-length of cylinder of Figure 1. Photograph of deformed cylinder shown in Figure 14.



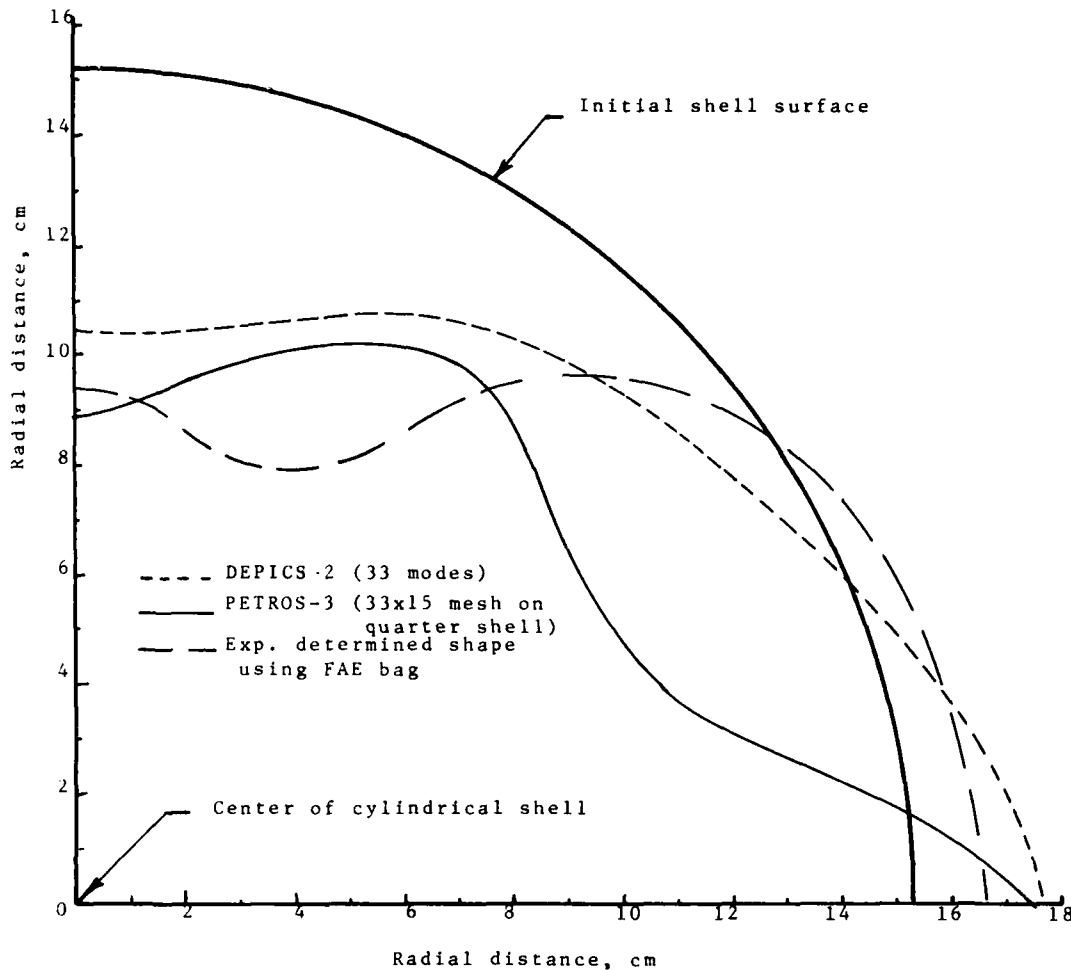


Figure 4. Calculated permanent set at mid-length of cylinder of Figure 3. Photograph of deformed cylinder shown in Figure 13.

loading may be an indication that more modes are needed in this case for the DEPICS solution. Both analytical and experimental results appear to indicate that the deformation pattern of the shell is quite sensitive to the pressure distribution and the engulfment process.

Several simple vulnerability type models were developed by the authors using large strain theory, rigid work hardening constitutive relations, and energy methods in a Lagrangian formulation. Three of these methods are listed in Reference (8). Some of the methods showed promise in predicting failure but gave very large over predictions for deflection at failure. The basic conclusion here is the process of buckling and resulting response of the shells is too complicated and complex to be modelled by the simple

fundamental mode shapes.

#### EXPERIMENTAL TESTS

Cylindrical shells of a constant radius of 15.24 cm of varying lengths and thicknesses were tested in both a fuel air explosion (FAE) and high energy (HE) environment.

Testing in a FAE device was accomplished using a gas bag technique developed previously and shown schematically in Figure 5. Construction of the bag was accomplished using polyurethane plastic stretched taut on a galvanized pipe frame and held together with 3M Paklon<sup>®</sup> transparent tape. A 100 gram disc of green Data sheet and detonator were placed at the end of the bag. The bag was then partially filled with .91 kg of (MAPP) gas. The gas-air

mixture was then mixed for ten minutes using a shaded pole electric motor.

Detonation of the Data sheet produces a Chapman-Jouget wave of constant velocity and reflected pressure which impinges on the shell at the opposite end of the bag. The magnitudes of the peak pressure and impulse were varied by adjusting the distance  $d$ , between the end of the bag and the cylinder. The experimental pressure is highly reproduceable and typical pressure and impulse values are given in Table I. The reflected pressure measurements presented were made on a thick-walled steel cylinder using PCB

piezoelectric transducers.

Pressure measurements were taken around the periphery of the cylinder as shown schematically in Figure 6. This type measurement allows for determination of pressure and impulse as a function of angular position. A typical pressure distribution is shown in Figure 6.

Testing of identical cylinders was also completed in a HE environment using .79 kg 50/50 pentolite sphere 21 cm in diameter hanging directly above the cylinder. A schematic of this test is shown in Figure 7. The charge radius  $X/A$  was varied to give

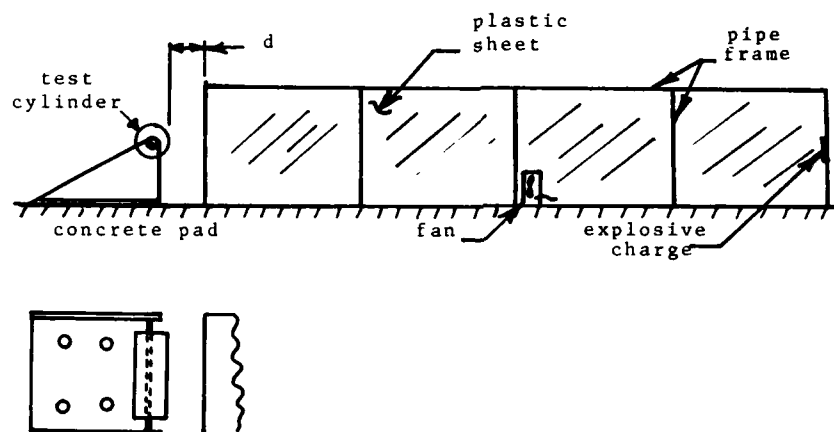


Figure 5. Fuel air explosion blast loading fixture.

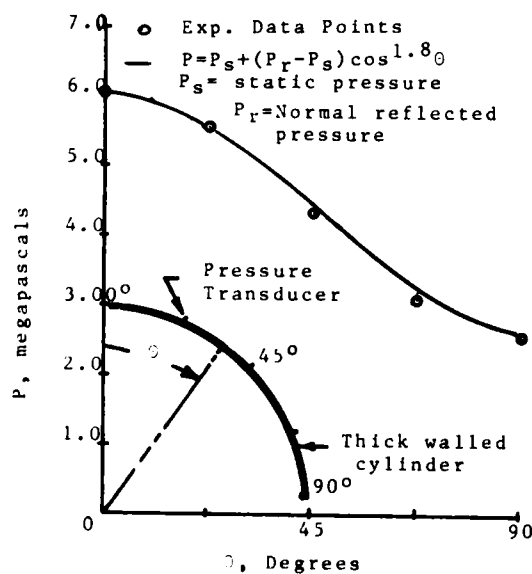


Figure 6. Pressure instrumented cylinder and resulting pressure distribution.

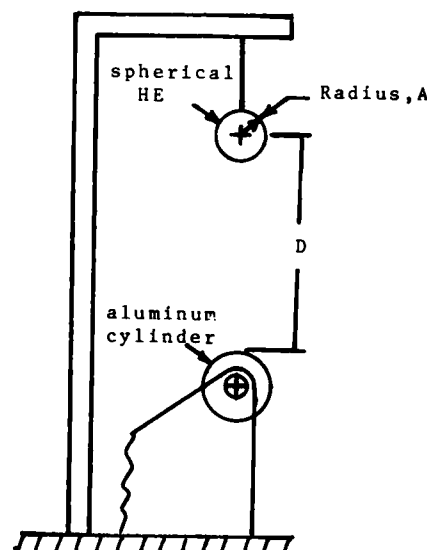


Figure 7. HE blast loading test fixture.

peak pressures and specific impulse similar to that of the FAE output. Calibration shots of the spherical devices were accomplished and good agreement was found with the analytical and experimental values given by Goodman (9).

#### EXPERIMENTAL RESULTS

A total of twenty-six cylindrical shells were subjected to blast loads from fuel air and conventional explosives to observe plastic buckling and failure characteristics. All shells were made of 6061-T6 aluminum and had a diameter of 30.48 cm. Cylinder thickness and length were varied in an effort to determine the effects of these parameters on failure and buckling modes. The magnitude of the blast load was controlled to produce material rupture or near rupture whenever possible.

A summary of the test results appears in Table 1. The pressure and impulse,  $P$  ( $\theta=0$ ) and  $I$  ( $\theta=0$ ), are those reflected values as seen by the leading edge of the shell. The circumferential mode number,  $n$ , represents the number of full buckled waves around the shell circumference assuming the cylinder was fully buckled. This number, however, is not truly representative of the deformation process, in that only a portion of the shell buckles circumferentially. The percentage of shell deformed was relatively constant and column (10) of Table 1 shows that only 20% to 35% of the cylinder circumference was

plastically deformed.

Before examining the experimental data points in Table 1, certain general deformation characteristics should be mentioned. For all cylinders tested, a fundamental mode shape was observed in the axial direction; ie,  $m=1$ , for the clamped end conditions. Figure 8 shows this fundamental shape for a .18 cm thick shell. Failure in the cylinders was always initiated at the clamped boundary and at the  $\theta=0$  point. Rupture of the material generally propagated from this point around the cylinder circumference; and the resulting failure surface resembled simple tensile type failure. A typical failure is shown in Figure 9. The modes or shape of the cylinders circumferentially, as represented by  $n$ , are believed to be functions of the shell geometry, material type, and the applied shock loads. If analytical methods are to be used to predict deformation and failure, the circumferential mode shape must be properly determined; as the shell stiffness is strongly influenced by the number of buckles generated.

The circumferential mode is the most difficult to analyze or observe from the experiments. Many buckling formulas have been authored, a majority of which were determined empirically. Most of these were generated for static loads, or radial loads uniformly applied around the shell, and were not applicable for the conditions of transverse blast loads as applied in these experiments. The experimental data gathered here tended to support theories of Greenspon [1-2] which suggests that a given cylindrical shell may be forced into a collapse mode, where  $n$  might be considered 1, or a buckling mode where  $n$  has some large value that is a function of the shell length, thickness, radius, and

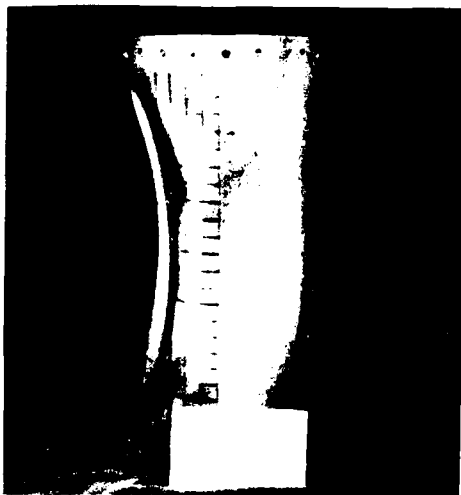


Figure 8. Typical side view of axial mode shape.

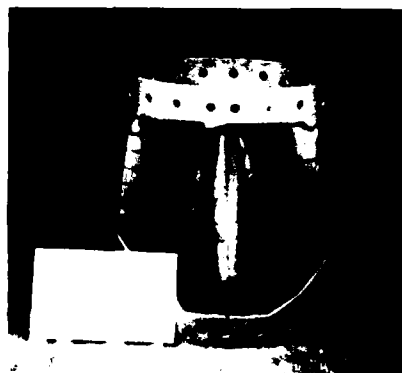


Figure 9. Typical shell failure.

TABLE 1  
SUMMARY OF RESULTS

(1)	(2)	(3)	(4)	(5)	(6)	(7)	(8)	(9)	(10)	(11)
DATA	a/h	L/D	P ( $\theta=0$ )	I ( $\theta=0$ )	n	Center Pt. Defl.	Mat'l Failure	Load Device	X	% of Circum. Buckled
1	188	.39	2.41	0.52	28	1.63	NO	BAG	1.37	30
2	188	.39	2.96	0.59	38	2.03	YES	BAG	1.22	30
3	188	.39	3.65	0.67	34	2.87	YES	BAG	1.07	--
4	188	.39	4.48	0.76	36	10.41	YES	BAG	.91	--
5	117	.39	4.48	0.76	22	2.24	NO	BAG	.91	32
6	117	.39	6.03	0.90	25	2.31	NO	BAG	0	34
7	117	.39	8.27	1.28	30	3.02	NO	PENT. SPH.	1.71	25
8	95	.39	6.03	0.90	26	1.02	NO	BAG	0	24
9	95	.39	6.03	0.90	26	0.74	NO	BAG	0	24
10	85	.39	17.24	1.93	25	2.64	NO	PENT. SPH.	1.25	34
11	85	.39	23.44	2.33	23	1.37	NO	PENT. SPH.	1.10	30
12	188	.89	2.96	0.59	32	6.10	YES	BAG	1.22	34
13	188	.89	3.65	0.67	32	>11.43	YES	BAG	1.07	--
14	188	.89	4.48	0.76	33	>11.43	YES	BAG	.91	--
15	117	.89	4.48	0.76	26	3.96	NO	BAG	.91	32
16	117	.89	6.89	0.83	34	6.05	YES	BAG	.61	36
17	117	.89	6.03	0.90	22	8.26	YES	BAG	0	--
18	95	.89	6.03	0.90	18	3.05	NO	BAG	0	34
19	95	.89	5.52	1.03	1	0.86	NO	PENT. SPH.	1.98	24
20	95	.89	10.34	1.45	1	>11.43	YES	PENT. SPH.	1.55	--
21	85	.89	6.03	0.90	19	2.41	NO	BAG	0	32
22	85	.89	6.89	1.18	1	8.26	YES	PENT. SPH.	1.83	--
23	85	.89	8.27	1.31	26	1.60	NO	PENT. SPH.	1.71	22
24	188	1.89	1.28	0.37	13	4.32	YES	BAG	1.83	34
25	188	1.89	1.52	0.40	13	---	NO	BAG	1.68	34
26	188	1.89	1.86	0.45	19	>11.43	YES	BAG	1.52	--
27	117	1.89	2.96	0.59	1	3.66	NO	BAG	1.22	29
28	117	1.89	3.65	0.67	1	7.87	YES	BAG	1.07	--
29	117	1.89	4.48	0.76	1	7.32	YES	BAG	.91	--
30	95	1.89	6.03	0.90	10	6.99	YES	BAG	0	--
31	95	1.89	5.52	1.03	1	5.56	YES	PENT. SPH.	1.98	32
32	85	1.89	6.03	0.90	10	6.50	NO	BAG	0	37
33	85	1.89	6.89	1.18	1	3.56	NO	PENT. SPH.	1.83	32
34	85	1.89	8.27	1.31	25	7.21	YES	PENT. SPH.	1.71	30
35	85	1.89	10.34	1.45	25	7.06	NO	PENT. SPH.	1.55	33

P ( $\theta=0$ ) = Normally Reflected Pressure in Megapascals

I ( $\theta=0$ ) = Normally Reflected Impulse in Megapascal-millisecond.

CENT. PT. DEFL. in Centimeters

L/D = Length to Diameter Ratio of Cylinder

a/h = Radius to Thickness Ratio

n = Circumferential Mode Number

D = Distance to Explosive in Meters

material type. Greenspon further suggests the use of Reynolds [10] buckling formula to determine  $n$ . Comparison of this formulation to Table 1 showed reasonable agreement for cylindrical shells of  $L/D$  less than one and the hypothesis of a given shell deforming in either a "collapse" pattern, or buckled pattern appears to be supported by the present data.

The data points in Table 1 are ordered in three groups of constant  $L/D$  values. The data points for  $L/D = .39$ , given for decreasing  $a/h$  values in Figure 10-12, show a decrease in  $n$  as the thickness increases. This trend continues for  $L/D$  values of .89. This grouping, however, contains three data points, 19, 20, and 22, which did not buckle, but apparently deformed in the collapse pattern.

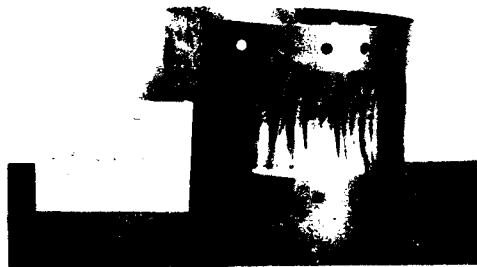


Figure 10. Cylinder representing Data Point 2, Table I.  $L/D = .39$ ,  $a/h = 188$ , 2.96 MPa reflected pressure.

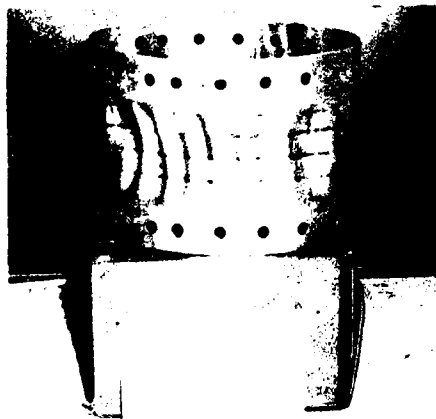


Figure 11. Cylinder representing Data Point 6, Table I.  $L/D = .39$ ,  $a/h = 177$ , 6.03 MPa reflected pressure.

The data for  $L/D$  values of 1.89 show five collapse patterns at data points 27, 28, 29, 31 and 33. The shells of this group that did buckle all had  $n$  values between 10 and 25. This indicates that for  $L/D$  values of approximately one and larger the higher buckling modes are less dominate.

The appearance of a collapse mode and buckling mode in the same cylinder size, shown in Figures 13 and 14, is apparent in data points (18, 19) (21, 22), (30, 31), and (32, 33). Each set of data represent cylindrical shells tested with the same  $L/D$ , and  $a/h$  values but with different applied loads. This suggests that for a given shell size there exists a critical load that determines if buckling occurs or a fundamental collapse pattern is formed. Almroth (11) calculated such critical loads for small deflections and elastic deformation. Experimental determination of dynamic critical load values would require extensive testing and it appears that peak pressure or impulse alone is not a sufficient description of the load to use as critical values to determine collapse or buckling. To vary both experimentally appears impractical outside a shock tunnel.

The failure, as defined in this report, was considered to be material rupture. Briefly discussed in the above paragraphs, this was observed to initiate along the clamped edge at the  $\theta = 0$  point. Column (8) of Table 1 indicates fracture or nonfracture of the shell material. The approximate centerpoint deflection is shown in column (7). As would be expected, the longer shells deflected more before

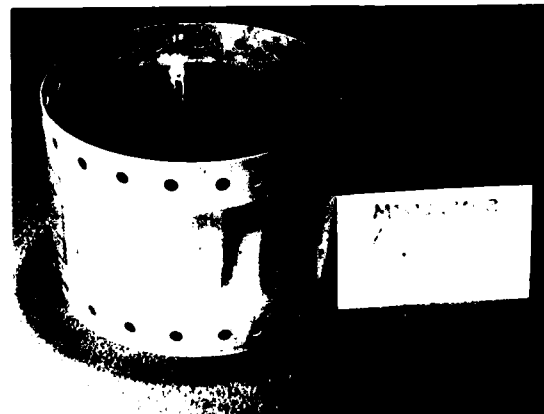


Figure 12. Cylinder representing Data Point 9, Table I.  $L/D = .39$ ,  $a/h = 95$ , reflected pressure.



Figure 13. Buckled pattern for Data Point 22, Table I. Length 57.54 cm, thickness 0.16 cm FAE test. Mid-length permanent set shown in Figure 4.

failure, but due to lack of control over the degree of fracture little else may be determined from the data. It is believed, however, that failure could be related to the centerpoint deflection, and for a given shell there exists a critical centerpoint deflection for failure.

#### CONCLUSIONS

Blast loaded cylinders, deformed plastically, show two types of permanently deformed patterns; i.e. a collapse pattern and a buckled pattern. The permanent mode shape is dependent upon the loading function as well as the geometric dimensions of the cylinder, however, a satisfactory prediction technique is not available. Based on tests performed for short duration blast only 25 to 30% of the leading edge of the cylinder is deformed. Failure of all cylinders occurred at the fixed boundaries and appears to be a simple tensile failure as a result of the axial strain.

#### REFERENCES

1. Greenspon, J. E., "Collapse, Buckling and Post Failure Behavior of Cylindrical Shells Under Elevated Temperature and Dynamic Loads," J. G. Eng. Res. Assoc. TR-6 Nov. 1965. DDC No. AD 630-269.

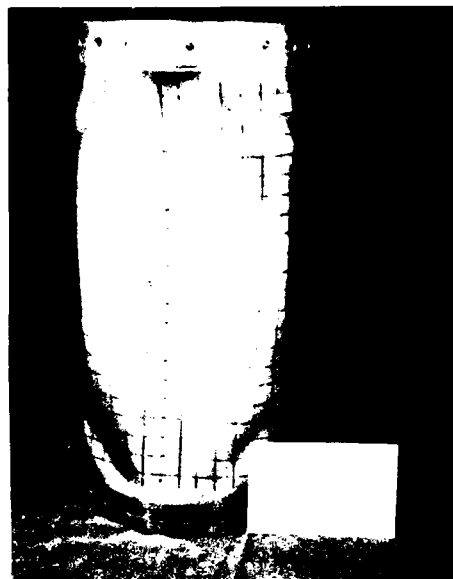


Figure 14. Collapse pattern for Data Point 22, Table I. Length 57.54 cm, thickness 0.16 cm HE test. Mid-length permanent set shown in Figure 2.

2. Greenspon, J. E., "Theoretical Calculation of Iso-Damage Characteristics" J. G. Eng. Res. Assoc. TR-10 Feb. 1970. DDC No. AD-869093.
3. Lindberg, H. E., Anderson, D. L., Firth, R. D., and Parker, L. V. "Response of Reentry Vehicle-Type Shells to Blast Loads" Stanford Res. Inst. Menlo Park, Calif. USAF Contract AF04 (694)-655 Sept. 1965.
4. Schuman, W. J. Jr., "The Response of Cylindrical Shells to External Blast Loading" BRL Memo Dept. 1461, Ballistic Res. Lab. Aberdeen Proving Ground, March 1963.
5. Schuman, W. J. Jr., "The Response of Cylindrical Shells to External Blast Loading-Part II" BRL Memo Dept. 1560 Ballistic Res. Lab. Aberdeen Proving Ground, May 1964.
6. Mente, L. J., "Dynamic Nonlinear Response of Cylindrical Shells to Asymmetric Pressure Loading" AIAA Journal, Vol. 11, No. 6, June 1973, pp 793-800.
7. Atluri, S. Witmer, E. A. Leech, J. W. and Morins, L., "PETROS 3: A Finite-Difference Method and Program for the Calculation of Large Elastic-Plastic Dynamically-Induced Deformations of Multi-Layer, Variable-Thickness Shells," BRL CR 60 (MIT-ASRL TR 152-2), Nov. 1971.

8. Ross, C. A., and Milton, J. E., "Study of Dynamic Response of Shell Structures to Blast Loads" AFATL-TR-75-117 USAF Armament Laboratory, Eglin AFB, Fla., Sept. 1975.
9. Goodman, H. J., "Compiled Free-Air Blast Data on Bare Spherical Pentolite," BRL Dept. No. 1092, Ballistic Res. Lab. Aberdeen Proving Ground, Feb. 1960.
10. Reynolds, T. E., "Inelastic Lobar Buckling of Cylindrical Shells Under External Hydrostatic Pressure," David Taylor Model Basin Dept. 1392, Aug. 1960.
11. Almroth, B. O., "Buckling of a Cylindrical Shell Subjected to Non-uniform External Pressure," Journal of Applied Mechanics, Vol. 29, Ser. E, No. 4, Dec. 1962, pp 675-682.

#### ACKNOWLEDGEMENT

The work described in this paper was conducted as an in-house test and research program by the U. S. Air Force Armament Laboratory, Eglin AFB, Florida.

#### DISCUSSION

Mr. Smith (Texas Tech University): Did you ever look at just the bending that the side-on force puts on the shell to see what interaction that has with the force on the shell?

Mr. Strickland: No, not experimentally.

Mr. Smith: You had a steel shaft running through there and it looked rather rigid but I couldn't see what the far ends looked like. Did that keep it from bending much?

Mr. Strickland: If it did move, it probably moved very little because that was a pretty rigid system. We have looked into that and I feel that that is the stiffness you have to overcome to fail that.

## EXTENDED TRANSFER MATRIX METHOD FOR FREE VIBRATION OF SHELLS OF REVOLUTION

Seshadri Sankar  
Department of Mechanical Engineering  
Concordia University, Montreal, Canada

Free vibration of shells of revolution is analyzed using an extended transfer matrix method to determine the natural frequencies and mode shapes. The proposed method utilizes Newton-Raphson iteration technique for determining the natural frequencies from within a range on either side of the true natural frequencies and hence allows a greater degree of error in the selection of trial frequency. The fundamental equations for free vibration are derived based on the classical bending theory. From these equations, a transfer matrix relation between the state vectors at the boundaries are obtained using fourth order Runge Kutta integration method. By applying the boundary conditions, the natural frequencies correspond to those trial frequencies for which a residual quantity of a certain determinant is zero. However this paper utilizes an improved procedure of modifying the basic method so that the derivative of the residual quantity of the determinant is also computed simultaneously along with the residual quantity itself. The derivative of the residual quantity are determined by formulating an extended transfer matrix relation which relates the extended state vectors at the boundaries. This extended state vector consists of the original state vector and its derivatives with respect to the frequency  $\omega$ . Finally, Newton-Raphson iteration technique which utilizes both the residual quantity and its derivatives is used for the characteristic determinant to obtain the next trial frequency. Numerical examples are given to illustrate the simplicity and straightforwardness of the proposed method in finding the natural frequencies. Results indicate that the method is accurate and allows a greater degree of error in the selection of trial frequencies.

### INTRODUCTION

The shell of revolution is an important structural element which has found wide use as a load carrying member in various turbomachinery components, refinery equipments, nuclear reactor vessels, pressure vessels, and the like. The failure of any of these structural elements are often suspected due to either adverse dynamic vibrations or repeated cyclic stress alterations. A knowledge of the free vibration characteristics of these structures is important in order to avoid the destructive effect of resonance with nearby rotating or oscillating equipment. This paper presents an extended transfer matrix method for analyzing free vibration modes and natural frequencies of

shells of revolution.

Since free vibrations occur in the absence of all external loads, the free vibration analysis of shells of revolution concern only with the solution of a homogeneous system of partial differential equations governing the free shell vibration with homogeneous boundary conditions. The natural frequencies of the shell are determined by finding the roots of a determinant whose elements are related to the solutions of these homogeneous field equations. For simple shell configurations such as cylindrical and spherical shells, these solutions are known hypergeometric functions [1]. However, for more complicated shells, numerical methods employing finite difference



approach [2, 3] or direct integration techniques [4, 5] have been used to obtain the solution. Free vibration of cantilever shells using the Rayleigh-Ritz method [6] and by matrix progression method [7] have been investigated. In this paper the free vibration characteristics of shells of revolution are obtained by an extended matrix approach [8]. This extended transfer matrix relates the state vectors consisting of displacements, stress resultants and their derivatives with respect to frequency  $\omega$  at the two boundaries of the shell and is formulated using the regular transfer matrix method [9]. Finally the paper presents the use of this extended transfer matrix relation in the determination of natural frequencies via Newton-Raphson iterative technique. The proposed method gives a quadratic convergence to a natural frequency from within a range on either side of the true natural frequency and hence allows a greater degree of error in the selection of trial frequency.

#### FUNDAMENTAL SYSTEM OF EQUATIONS FOR FREE VIBRATION OF SHELLS OF REVOLUTION

Based on classical bending theory, the fundamental equations governing the stresses and deformations of shell of revolution are:

- Equations relating force equilibrium;
- Stress - strain relations, and
- Strain - displacement relations.

For an arbitrary shell of revolution as shown in Figure 1 and vibrating under arbitrary edge loads, the governing system of equations are given in [1] which are derived by Reissner [10] based on linear classical theory of shells. Denoting the first and second derivatives with respect to any coordinate by ( ),  $x$  and ( ),  $xx$ , the fundamental set of equations are given below.

The dynamic equilibrium equations which include the translatory inertia can be written from Figure 2 as:

$$N_{\phi,\phi} + (r_\phi/r) N_{\theta\phi,\theta} + (r_\phi/r) (N_\phi - N_\theta) \cos\phi + Q_\phi = r_\phi \rho h K_1 U_{\phi,tt} \quad (1a)$$

$$N_{\theta\phi,\theta} + (r_\phi/r) N_{\theta,\theta} + 2(r_\phi/r) \cos\phi N_{\theta\phi} + (r_\phi/r) Q_\theta \sin\phi = r_\phi \rho h K_1 U_{\theta,tt} \quad (1b)$$

$$Q_{\phi,\phi} + (r_\phi/r) Q_{\theta,\theta} + (r_\phi/r) Q_\phi \cos\phi - N_\phi - (r_\phi/r_\theta) N_\theta \sin\phi = r_\phi \rho h K_1 W_{,tt} \quad (1c)$$

$$M_{\phi,\phi} + (r_\phi/r) M_{\theta\phi,\theta} + (r_\phi/r) (M_\phi - M_\theta) \cos\phi - r_\phi Q_\phi = (r_\phi/r) (\rho h^3/6) U_{\phi,tt} \quad (1d)$$

$$M_{\theta\phi,\theta} + (r_\phi/r) M_{\theta,\theta} + 2(r_\phi/r) \cos\phi M_{\theta\phi} - r_\phi Q_\theta = (r_\phi/r) (\rho h^3/6) U_{\theta,tt} \quad (1e)$$

Stress - strain relations are:

$$N_\theta = K(\epsilon_\theta + \nu \epsilon_\phi) \quad (2a)$$

$$N_\phi = K(\epsilon_\phi + \nu \epsilon_\theta) \quad (2b)$$

$$N_{\theta\phi} = N_{\phi\theta} = (1-\nu) K \epsilon_{\theta\phi} \quad (2c)$$

$$M_\theta = D(K_\theta + \nu K_\phi) \quad (2d)$$

$$M_\phi = D(K_\phi + \nu K_\theta) \quad (2e)$$

$$M_{\theta\phi} = M_{\phi\theta} = (1-\nu) D K_{\theta\phi} \quad (2f)$$

Strain - displacement relations are:

$$\epsilon_\theta = (1/r) (U_{\theta,\theta} + U_\phi \cos\phi + W \sin\phi) \quad (3a)$$

$$\epsilon_\phi = (1/r_\phi) (U_{\phi,\phi} + W) \quad (3b)$$

$$2\epsilon_{\theta\phi} = (1/r) (U_{\phi,\theta} - U_\theta \cos\phi) + (1/r_\phi) U_{\theta,\phi} \quad (3c)$$

$$K_\theta = (1/r) (\beta_{\theta,\theta} + \beta_\phi \cos\phi) \quad (3d)$$

$$K_\phi = (1/r_\phi) \beta_{\phi,\phi} \quad (3e)$$

$$2K_{\theta\phi} = (1/r) (\beta_{\phi,\theta} - \beta_\theta \cos\phi) + (1/r_\phi) \beta_{\theta,\phi} \quad (3f)$$

$$\beta_\theta = -(1/r) W_{,\theta} + (\sin\phi/r) U_\phi \quad (3g)$$

$$\beta_\phi = -(1/r_\phi) W_{,\phi} + (1/r_\phi) U_\phi \quad (3h)$$

It is assumed in the above set of equations that the shell is sufficiently thin, so that

$$1+h^2/12r^2 \approx 1$$

where  $r$  is the minimum principal radius of curvature.

Now combining the three sets of equations and expressing effective transverse and tangential shear resultants by the equations

$$Q = Q_\phi + (1/r) M_{\theta\phi,\theta} \quad (4a)$$

$$N = N_{\theta\phi} + (\sin\phi/r) M_{\theta\phi} \quad (4b)$$

the fundamental equations can be reduced to eight differential equations with eight generalized variables consisting of four displacements  $W$ ,

$U_\phi$ ,  $U_\theta$  and  $\beta_\phi$ , and four stress resultants  $Q$ ,  $N_\phi$ ,  $N$  and  $M_\phi$ .

Assuming that the shell is rotationally symmetric, the shells of revolution will consist of complete latitude circles. Then the fundamental variables for free vibration can be assumed to be separable of the form

$$\begin{bmatrix} W \\ U_\phi \\ \beta_\phi \\ N_\phi \\ M_\phi \\ Q \end{bmatrix} = \begin{bmatrix} W_n \\ U_{\phi n} \\ \phi n \\ N_{\phi n} \\ M_{\phi n} \\ Q_n \end{bmatrix} \cos n\theta \cos \omega t \quad (5a)$$

$$\begin{bmatrix} U_\theta \\ N \end{bmatrix} = \begin{bmatrix} U_{\theta n} \\ N_n \end{bmatrix} \sin n\theta \cos \omega t \quad (5b)$$

where  $n$  is a circumferential wave number and  $\omega$  is a circular frequency.

Substituting equations (5a) and (5b) in the resultant eight differential equations formed by combining equations (1-4), the governing equations for free vibration reduces to a vector differential equation of the form.

$$\frac{d}{d\phi}[z(\phi)] = [A(\phi)][z(\phi)] \quad (6)$$

where  $\phi$  is the independent variable,  $[z(\phi)]$  is a  $(8 \times 1)$  force and displacement vector, and  $[A(\phi)]$  is a  $(8 \times 8)$  coefficient matrix.

Replacing the independent variable  $\phi$  by the length parameter  $s$  measured along the meridian as shown in Figure 3, the following transformation can be written:

$$\frac{d(\cdot)}{ds} = (1/r_\phi) \frac{d(\cdot)}{d\phi}$$

Then using the above transformation, equation (6) can be rewritten in the following form,

$$\frac{d}{ds}[z(s)] = [A(s)][z(s)] \quad (7)$$

where

$$[z(s)]^T = [W_n(s), U_{\phi n}(s), U_{\theta n}(s), \beta_{\phi n}(s), Q_n(s), N_{\phi n}(s), N_n(s), M_{\phi n}(s)]$$

and the elements of the coefficient matrix  $[A(s)]$  which depend on the material properties, geometry and natural frequencies of the shell are expressed as follows:

$$A_{12} = 1/r_\phi, A_{14} = -1$$

$$A_{21} = -P, A_{22} = -v \cos \phi / r, A_{23} = -vn/r,$$

$$A_{26} = 1/K$$

$$A_{31} = nGD \sin 2\phi / Kr^3,$$

$$A_{32} = n(1-GDJ \sin \phi / Kr) / r,$$

$$A_{33} = (1-GDH \sin \phi / Kr) \cos \phi / r,$$

$$A_{34} = 2nGD \sin \phi / Kr^2,$$

$$A_{37} = 2(1-GD \sin^2 \phi / Kr^2) / (1-v)K$$

$$A_{41} = -vn^2/r^2, A_{43} = -vn \sin \phi / r^2,$$

$$A_{44} = -v \cos \phi / r, A_{48} = 1/D$$

$$A_{51} = 2n^2GD(1-v) \cos^2 \phi / r^4 + K(1-v^2) \sin^2 \phi / r^2 - \omega^2 \rho h (1 + \frac{h^2 n^2}{12r^2}),$$

$$A_{52} = K(1-v^2) \sin 2\phi / 2r^2 - n^2GDJ(1-v) \frac{\cos \phi}{r^3},$$

$$A_{53} = n(1-v^2) (K + \frac{n^2D}{r^2}) \frac{\sin \phi}{r^2} - nGDH(1-v) \frac{\cos^2 \phi}{r^3} - n\omega^2 \rho h^3 \sin \phi / 12r^2,$$

$$A_{54} = n^2D(1-v)(1+v+2G) \cos \phi / r^3,$$

$$A_{55} = -\cos \phi / r, A_{56} = P, A_{57} = -A_{31},$$

$$A_{58} = -A_{41}$$

$$A_{61} = K(1-v^2) \sin 2\phi / 2r^2 - n^2GDJ(1-v) \cos \phi / r^3,$$

$$A_{62} = K(1-v^2) \cos^2 \phi / r^2 + n^2GDJ^2(1-v) / 2r^2 - \omega^2 \rho h,$$

$$A_{63} = nK(1-v^2) \cos^2 \phi / r^2 + nGDJH(1-v) \frac{\cos \phi}{2r^2}$$

$$A_{64} = -n^2GDJ(1-v) / r^2, A_{65} = 1/r_\phi,$$

$$A_{66} = -(1-v) \cos \phi / r, A_{67} = -n(1-GDJ \sin \phi / Kr) / r$$

$$A_{71} = A_{53}, A_{72} = A_{63},$$

$$A_{73} = n^2 (K + D \frac{\sin^2 \phi}{r^2}) (1-v^2) / r^2 + GDH^2(1-v) \frac{\cos^2 \phi}{2r^2} - \omega^2 \rho h (1 + h^2 \sin^2 \phi / 12r^2),$$

$$A_{74} = -nD(1-\nu) [GH - (1+\nu) \sin\phi/r] \cos\phi/r^2,$$

$$A_{76} = -A_{23}, A_{77} = -(2-GDH \sin\phi/Kr)$$

$$\cos\phi/r,$$

$$A_{78} = -A_{43},$$

$$A_{81} = A_{54}, A_{82} = A_{64}, A_{83} = A_{74},$$

$$A_{84} = D(1-\nu) [(1+\nu) \cos^2\phi + 2n^2G]/r^2 - \omega^2 \rho h^3/12,$$

$$A_{85} = 1, A_{87} = -A_{34}, A_{88} = -(1-\nu) \cos\phi/r$$

#### FORMULATION OF TRANSFER MATRIX RELATION

The eight fundamental variables given in equation (7) represent the natural boundary conditions on the axisymmetric edge of the shell. Depending on the physical nature of the problem the boundary conditions are characterized by four known displacements at one end of the shell and by four known stress resultants at the other end. Hence the problem of free vibration of shells of revolution reduces to a two point boundary value problem with a differential equation (7) together with the associated boundary conditions. The solution for this two point boundary value problem has been carried out by reducing to an initial value problem by using numerical integration methods. However, in this paper a transfer matrix, relating the state vectors at the two ends of the shell has been formulated which reduces the differential equation (7) into a set of algebraic equations. Moreover the elements of the transfer matrix depend only on the values of the coefficients of  $[A(s)]$  and hence can be easily evaluated.

In order to compute the transfer matrix, the entire meridian of the shell is approximated to be an assemblage of conical shell segments of short length  $L$  as shown in Figure 3. Now integrating equation (7) numerically from station  $i$  with a step size equal to the length of the segment, then the value of the state variables at station  $(i+1)$  can be obtained. Relating the two state vectors  $[z^i]$  and  $[z^{i+1}]$ , the local transfer matrix relationship can be written as

$$[z^{i+1}] = [T^i][z^i] \quad (8)$$

where  $[T^i]$  is the local transfer matrix which depends on the values of  $[A(s)]$

at stations  $i$ ,  $i+1$  and at a station midway between  $i$  and  $i+1$ .  $[z^{i+1}]$  and  $[z^i]$  are the state vectors at stations  $i+1$  and  $i$  respectively.

In this paper the fourth order Runge Kutta numerical integration method is used for integrating equation (7) and hence the relationship between  $[z^{i+1}]$  and  $[z^i]$ , is given by

$$[z^{i+1}] = [z^i] + \frac{1}{6}([k_0] + 2[k_1] + 2[k_2] + [k_3]) \quad (9)$$

where

$$[k_0] = L[A^i(s)][z^i]$$

$$[k_1] = L[A^i(s+L/2)][z^i + k_0/2] \quad (10)$$

$$[k_2] = L[A^i(s+L/2)][z^i + k_1/2]$$

$$[k_3] = L[A^i(s+L)][z^i + k_2]$$

The matrices  $[A^i(s)]$ ,  $[A^i(s+L)]$  and  $[A^i(s+L/2)]$  are the values of the matrix  $[A(s)]$  at station  $i$ ,  $i+1$  and at the station midway between  $i$  and  $i+1$ . Now substituting equation (10) in (9) and rearranging in the form of equation (8), the local transfer matrix  $[T^i]$  can be expressed as

$$\begin{aligned} [T^i] = & [I] + \frac{L}{6}([A^i(s)] + 4[A^i(s+L/2)] + \\ & [A^i(s+L)]) + \frac{L^2}{6}([A^i(s+L/2)][A^i(s)] + \\ & [A^i(s+L)][A^i(s+L/2)] + \\ & [A^i(s+L/2)]^2) + \frac{L^3}{12}([A^i(s+L/2)]^2 \cdot \\ & [A^i(s)] + [A^i(s+L)]) \cdot \\ & [A^i(s+L/2)]^2 + \frac{L^4}{24}([A^i(s+L)] \\ & [A^i(s+L/2)]^2 [A^i(s)]) \end{aligned}$$

Successive application of equation (8), the local transfer matrix relationships for other stations along the meridian of the shell can be written as

$$[z^{i+2}] = [T^{i+1}][z^{i+1}],$$

$$[z^{i+3}] = [T^{i+2}][z^{i+2}],$$

etc.

Now combining the individual local transfer matrix relationship, the global transfer matrix relationship between the two boundary state vectors of the shell can be obtained as

$$\{z^n\} = [T] \{z^1\} \quad (12)$$

where the global transfer matrix is

$$[T] = [T^{n-1}] [T^{n-2}] \dots [T^2] [T^1]$$

#### CALCULATION OF NATURAL FREQUENCIES USING NEWTON-RAPHSON ITERATION TECHNIQUE

By partitioning the matrix and vectors in equation (12) gives

$$\begin{bmatrix} z_1^n \\ z_2^n \end{bmatrix} = \begin{bmatrix} A^* & B^* \\ C^* & D^* \end{bmatrix} \begin{bmatrix} z_1^1 \\ z_2^1 \end{bmatrix} \quad (13)$$

The coefficients of matrices  $A^*$ ,  $B^*$ ,  $C^*$  and  $D^*$  are functions of frequency  $\omega$ . In general, the boundary conditions are characterized by known displacement vectors  $\{z_1\}$  at one edge of the shell and by known stress resultants  $\{z_2\}$  at the other edge. For example, if station 1 is fixed and station  $n$  is free, then the boundary conditions are given by

$$\{z_1^1\} = \{z_2^n\} = 0$$

Substituting these boundary conditions in equation (13), the natural frequencies are determined from the roots of the polynomial

$$\Delta(\omega) = \det D^*(\omega) = 0 \quad (14)$$

The natural frequencies for free vibration are those frequencies for which the  $\det [D^*]$  in equation (14) vanishes and are normally obtained by trial and error search procedure. However in this paper an improvement to this basic method is presented. The improved procedure consists of computing the derivative of  $\det [D^*]$  with respect to  $\omega$  together with  $\det [D^*]$  itself at the chosen trial frequency. Newton-Raphson technique which incorporates the values of  $\det [D^*]$  and its derivative with respect to  $\omega$  is used to obtain the next trial frequency.

The recurrence relation between the trial frequencies based on Newton-Raphson iteration method is given by

$$\omega_{\text{new}} = \omega_{\text{trial}} - \quad (15)$$

$$\frac{\det [D^*]}{(\det [D_1] + \det [D_2] + \det [D_3] + \det [D_4])}$$

In equation (15) the determinants are evaluated at  $\omega = \omega_{\text{trial}}$  and the coefficients of the matrices  $D_1$ ,  $D_2$ ,  $D_3$  and  $D_4$  are identical to that of matrix  $D^*$  except for the following coefficients which are related to the coefficients of matrix  $\dot{D}^*$ .

$$\begin{aligned} D_1(I, 1) &= \dot{D}^*(I, 1) \\ D_2(I, 2) &= \dot{D}^*(I, 2) \\ D_3(I, 3) &= \dot{D}^*(I, 3) \\ D_4(I, 4) &= \dot{D}^*(I, 4) \end{aligned} \quad I = 1, 4$$

$$\text{where } [\dot{D}^*] = \frac{d}{d\omega} [D^*]$$

Hence knowing the matrices  $[D^*]$  and  $[\dot{D}^*]$ , the natural frequencies can be calculated using the systematic procedure outlined in equation (15).

The number of steps for convergence using this method depends on the closeness of the initial trial frequency to the true natural frequency. However, within the vicinity of a root, convergence is quadratic as compared to super-linearly convergent root iteration method such as inverse interpolation method. Since Newton-Raphson iteration technique requires a derivative of the function at each step, the computation time doubles per step. However this increase in computational time per step is offset by the fewer number of steps for the same final accuracy. An Additional advantage of the Newton-Raphson method is that it is a single point method requiring only one initial trial value. Further it has a known sufficient condition for convergence [11] given by

$$\left| \frac{\omega_{\text{trial}} - \omega_{\text{true}}}{\omega_{\text{trial}}} \right| \leq \frac{d}{(n^2 - 1)}$$

where  $d$  is the separation between the true natural frequency under consideration and its nearest neighbouring natural frequency, and  $n$  is the degree of polynomial  $\Delta(\omega)$  under consideration.

#### EXTENDED TRANSFER MATRIX RELATIONSHIP FOR FREE VIBRATION

Suppose equation (8) is differentiated with respect to  $\omega$  and then if

combined with itself gives an extended local transfer matrix relation which can be written as

$$\begin{bmatrix} z^{i+1} \\ \dot{z}^{i+1} \end{bmatrix} = \begin{bmatrix} T^i & 0 \\ \dot{T}^i & T^i \end{bmatrix} \begin{bmatrix} z^i \\ \dot{z}^i \end{bmatrix} \quad (16)$$

where a dot represents differentiation with respect to  $\omega$  and  $[T^1]$  is the extended local transfer matrix found by differentiating equation (11) with respect to  $\omega$ . The new state vector in equation (16) consists of the original state vector of four displacements and four stress resultants and its derivatives with respect to  $\omega$  and is referred to as the extended state vector.

Successive application of equation (16) results in an extended global transfer matrix relation for the whole system relating the extended state vectors at the boundaries. This relationship can be written as

$$\begin{bmatrix} z^n \\ \dot{z}^n \end{bmatrix} = \begin{bmatrix} T^{n-1} & 0 \\ \dot{T}^{n-1} & T^{n-1} \end{bmatrix} \begin{bmatrix} T^{n-2} & 0 \\ \dot{T}^{n-2} & T^{n-2} \end{bmatrix} \dots \begin{bmatrix} T^1 & 0 \\ \dot{T}^1 & T^1 \end{bmatrix} \begin{bmatrix} z^1 \\ \dot{z}^1 \end{bmatrix}$$

Rewriting the above equation gives

$$\begin{bmatrix} z_1^n \\ z_2^n \\ \dot{z}_1^n \\ \dot{z}_2^n \end{bmatrix} = \begin{bmatrix} A^* & B^* & 0 & 0 \\ C^* & D^* & 0 & 0 \\ \hline E^* & F^* & A^* & B^* \\ G^* & H^* & C^* & D^* \end{bmatrix} \begin{bmatrix} z_1^1 \\ z_2^1 \\ \dot{z}_1^1 \\ \dot{z}_2^1 \end{bmatrix}$$

As before, if it is assumed that station 1 is fixed and station n is free, then the boundary conditions are given by

$$[z_1^1] = [\dot{z}_1^1] = 0$$

$$[z_2^n] = [\dot{z}_2^n] = 0$$

Inserting the boundary conditions at station 1 in equation (17) give

$$[z_2^n] = [D^*] [z_2^1] \quad (18)$$

$$[\dot{z}_2^n] = [H^* D^*] \begin{bmatrix} z_2^1 \\ \dot{z}_2^1 \end{bmatrix} \quad (19)$$

Substituting the boundary condition  $[z_2^n] = 0$  in equation (18), a non-trivial solution exists only if the det  $[D^*]$  vanishes as stated previously in equation (13). Suppose if the det  $[D^*]$  does not vanish for a chosen value of the trial frequency  $\omega$ , then there is a residual quantity of  $[z_2^n]$  according to equation (18). Hence  $[z_2^n]$  is a function of the trial frequency  $\omega$ . Now differentiating equation (18) with respect to  $\omega$  and comparing with equation (19) gives

$$H^* = \frac{d}{d\omega} [D^*]$$

Hence the coefficients of  $[D^*]$  are known through the extended transfer matrix approach which can be used to identify the coefficients of matrices  $D_1, D_2, D_3$  and  $D_4$ . Once the matrices  $D_1, D_2, D_3$  and  $D_4$  are known, then the Newton-Raphson iteration technique in equation (15) can be used for finding the natural frequencies systematically.

After determining the natural frequencies, the corresponding solution for  $[z_2^1]$  is obtained from

$$z_2^1(i) = d(-1)^{i+1} \Delta_i \quad (20)$$

where  $z_2^1(i)$  denotes the  $i$ th element of  $[z_2^1]$ ,  $d$  is an arbitrary constant, and  $\Delta_i$  is the determinant of a submatrix of  $[D^*]$  by deleting the  $i$ th column. Once  $[z_2^1]$  are calculated from equation (20), the mode shapes at other stations along the meridian are calculated from equation (8).

#### ILLUSTRATIVE EXAMPLES AND RESULTS

To illustrate the accuracy of the method described in the paper, the following test examples are considered. The first example is an axisymmetric free vibration of a truncated conical shell in the shape of a loudspeaker cone with a semi-cone angle of  $30^\circ$ . The cone was assumed to be free at the outer edge and clamped at the inner edge. The values of the three lowest frequencies and the corresponding mode shapes are obtained by the present method and found to have an excellent agreement with the results obtained in [4, 5]. The results

are illustrated in Table 1. The method outlined in this paper completely eliminates the trial and error procedure; that is, by selecting an arbitrary initial value, the method utilizes a systematic, efficient and accurate procedure in determining the nearest natural frequency in a limited number of steps. Hence by using different trial values, all the required natural frequencies can be determined. Table 2 shows the range over which a trial frequency may converge to the critical required frequency. It can be seen that the range of convergence for initial values higher than the natural frequency is appreciably greater than the range for initial values lower than the natural frequency. Also, this range of convergence decreases with the mode number. From the above results, it can be concluded that the present method allows a greater degree of error in the trial frequency for values greater than the true natural frequency.

The second example is to determine the natural frequencies of free vibration of cantilever cylindrical shell. Results obtained using the extended transfer matrix method presented in this paper are compared in Tables 3 and 4 with those calculated using matrix progression method [6], exact solution based on Rayleigh-Ritz method [7], and using Green functions [12]. The results show that there is good agreement between the corresponding results.

Hence it can be said that the extended transfer matrix method is a simple, efficient and accurate alternate method for calculating the natural frequencies and mode shapes of free vibration of shells of revolution and is applicable to rotationally symmetric shells with meridional variations in Young's modulus, Poisson's ratio, radii of curvature, and thickness. However the method is not suitable for long shells with the meridional length exceeding a critical value because of the loss of accuracy of the results [5]. The loss of accuracy is caused by the subtraction of almost equal, very large numbers in the calculation of the frequency determinant [11]. By the use of Gaussian elimination method [5] such loss of accuracy can be eliminated in analyzing long shells. However the method presented in this paper is not extended for long shells and will be the subject for future investigation.

#### CONCLUSIONS

This paper presents a novel numerical method for the investigation of free

vibration of shells of revolution. The method is general, straightforward, compact and economical for determining the natural frequencies of thin shells of revolution. Unlike the methods found in the literature, the fundamental system of equations which are in the form of differential equations are reduced to algebraic equations through the formulation of an extended transfer matrix. Such a method automatically eliminates any trial and error procedure in the calculation of natural frequencies. Finally, a single frequency dependent determinant is obtained whose value reduces to zero at true natural frequencies to satisfy the boundary conditions.

The proposed method also introduces a systematic procedure for finding automatically the roots of the frequency determinant based on the Newton-Raphson iterative technique which incorporates both the residual quantity of the determinant and its derivative. The paper also presents the formulation of an extended transfer matrix from which the values of the derivative of the determinant are directly calculated.

Natural frequencies of cantilevered conical and cylindrical shells are calculated and found to have good agreement with the results found by other investigators. Major advantages of the method presented are that it allows a greater degree of error in the selection of trial frequencies and gives a quadratic convergence in calculating natural frequencies.

The method presented here is not limited to vibration analysis of shells of revolution but also applicable to vibration problems in plates, beams and torsional systems.

#### ACKNOWLEDGMENT

The present work is a part of the research program for the developing techniques for analysis and design of mechanical systems. The support of the National Research Council of Canada, Grant No. A3685 is acknowledged.

#### REFERENCES

- (1) Kraus, H., *Thin Elastic Shells*, John Wiley & Sons, Inc., New York, N.Y., 1967, pp. 289-360
- (2) Penny, R.K., "Symmetric Bending of the General Shell of Revolution by Finite Difference Method", *Journal of Mechanical Engineering Science*, Vol. 3, 1961, pp. 369-377

- (3) Radkowaski, P.P., Davies, R.M., and Bolduc, M.R., "Numerical Analysis of Equations of Thin Shells of Revolution", American Rocket Society Journal, Vol. 32, 1962, pp. 36-41
- (4) Goldberg, J.E., and Bogdanoff, J.L., "On the Calculation of the Axisymmetric Modes and Frequencies of Conical Shells", The Journal of the Acoustical Society of America, Vol. 32, No. 6, 1960, pp. 738-742
- (5) Kalnins, A., "Free Vibration of Rotationally Symmetric Shells", The Journal of the Acoustical Society of America, Vol. 36, No. 7, 1964, pp. 1355-1365
- (6) Warburton, G.B., and Higgs, J., "Natural Frequencies of Thin Cantilever Cylindrical Shells", Journal of Sound and Vibration, Vol. 11, No. 3, 1970, pp. 335-338
- (7) Tottenham, H., and Shimizer, K., "Analysis of the Free Vibration of Cantilever Cylindrical Thin Elastic Shells by the Matrix Progression Method", International Journal of Mechanical Science, Vol. 14, 1972, pp. 293-310
- (8) Dawson, B., and Davies, M., "An Improved Transfer Matrix Procedure", International Journal for Numerical Methods in Engineering, Vol. 8, 1974, pp. 111-117
- (9) Pestel, E.C., and Leckie, F.A., Matrix Methods in Elasto Mechanics, McGraw Hill, New York, N.Y., 1963
- (10) Reissner, E., "A New Derivation of the Equations for the Deformation of Elastic Shells", American Journal of Mathematics, Vol. 63, 1941, pp. 171-184
- (11) Lancaster, P., "Convergence of the Newton-Raphson Method of Arbitrary Polynomials", Mathematical Gazette, Vol. 48, 1964, pp. 291-295
- (12) Srinivasan, R.S., and Sankaran, S., "Vibration of Cantilever Cylindrical Shells", Journal of Sound and Vibration, Vol. 40, No. 3, 1975, pp. 425-430
- (13) Sepetoski, W.K., Pearson, C.E., Dingwell, I.W. and Adkins, A.W., "A Digital Computer Program for the General Axially Symmetric Thin-Shell Problem", Journal of Applied Mechanics, Trans. ASME, Vol. 84, Series E, 1962, pp. 655-661

# NOMENCLATURE

A(s)	(8x8) matrix
D	$Eh^3/12 (1-\nu^2)$
E	Young's modulus
G	$1/(1+D \sin^2\phi/Kr^2)$
H	$(1/r_\phi) - (\sin\phi/r)$
h	thickness of shell
I	unit matrix
J	$[(1/r_\phi) + (\sin\phi/r)]$
$K_1$	$Eh/(1-\nu^2)$
K	$1+h^2/12r_\phi^2$
L	some characteristic length of shell
$M_\phi, M_\theta, M_{\theta\phi}$	moment resultants
n	integer, denotes Fourier component
N	effective tangential - shear resultant
$N_\phi, N_\theta, N_{\theta\phi}$	membrane - stress resultants
P	$[(\nu \sin\phi/r) + (1/r_\phi)]$
Q	effective transverse - shear resultants
$Q_\phi, Q_\theta$	transverse - shear resultants
r	distance from axis of symmetry
$r_\phi, r_\theta$	radii of curvatures
s	distance along meridian in positive direction of
t	time
T	transfer matrix
$U_\phi, U_\theta, W$	displacements of middle surface in meridional circumferential and normal directions
z	(8x1) column vector of fundamental variables
$\beta_\phi, \beta_\theta$	angle of rotation of normal
$\theta$	polar angle on the latitude circles

$\nu$	Poisson's ratio
$\rho$	mass density
$\phi$	angle between normal and axis of symmetry
$\omega$	circular frequency, rad/sec
$( )_{,x}$	derivative with respect to any coordinate
[.]	capital letter inside square bracket represents a matrix and small letter a vector
$[ ]^T$	transpose

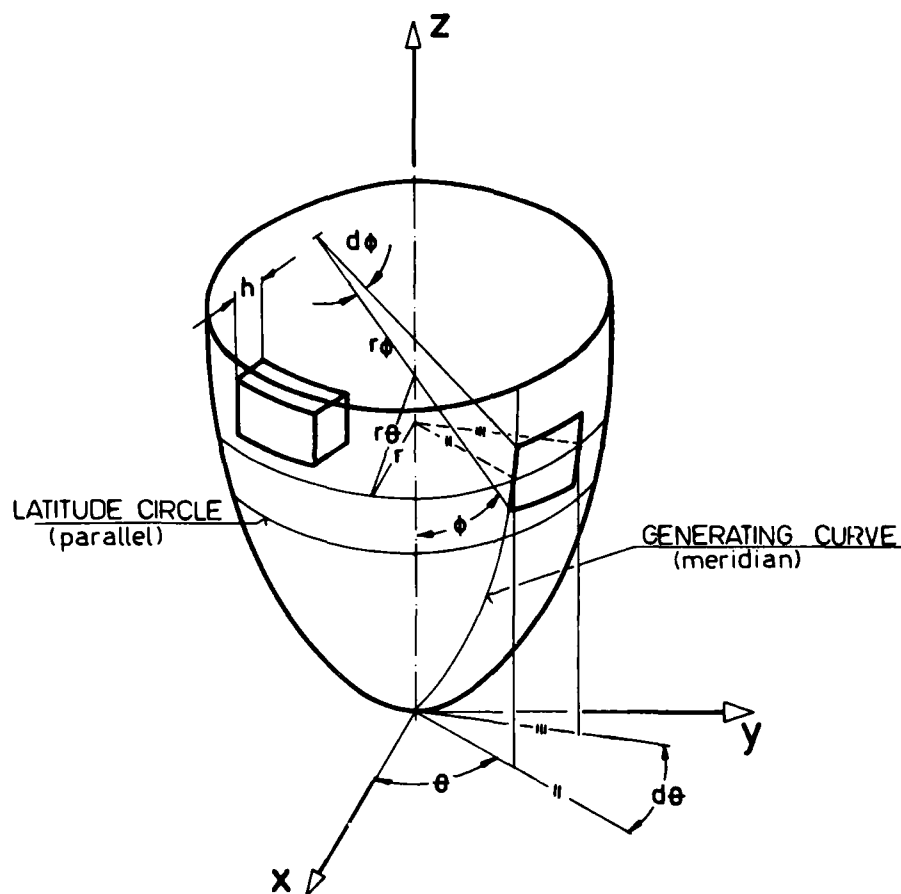


Fig. 1 - Shell geometry and co-ordinate systems



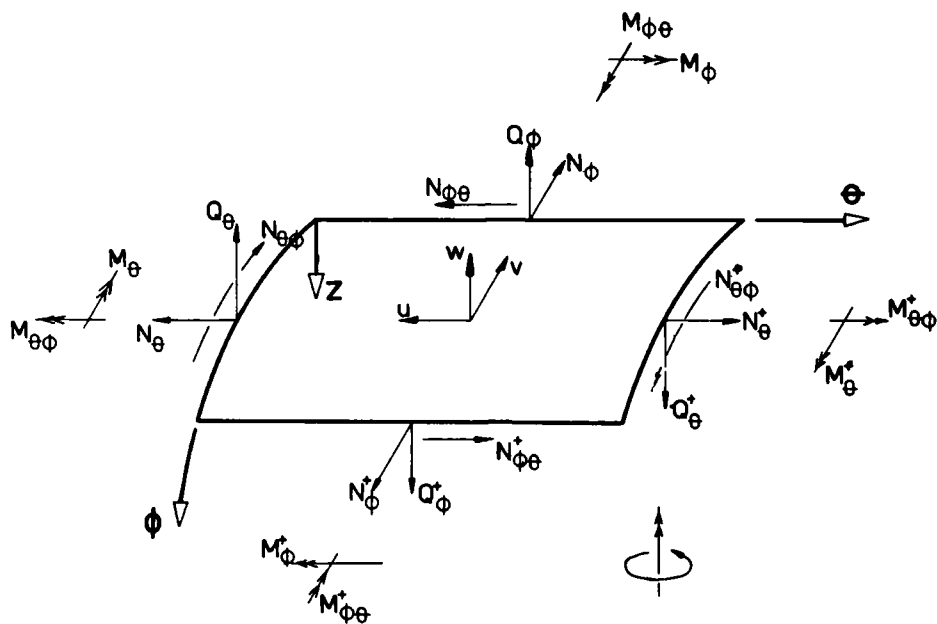


Fig. 2 - Element of a shell of revolution

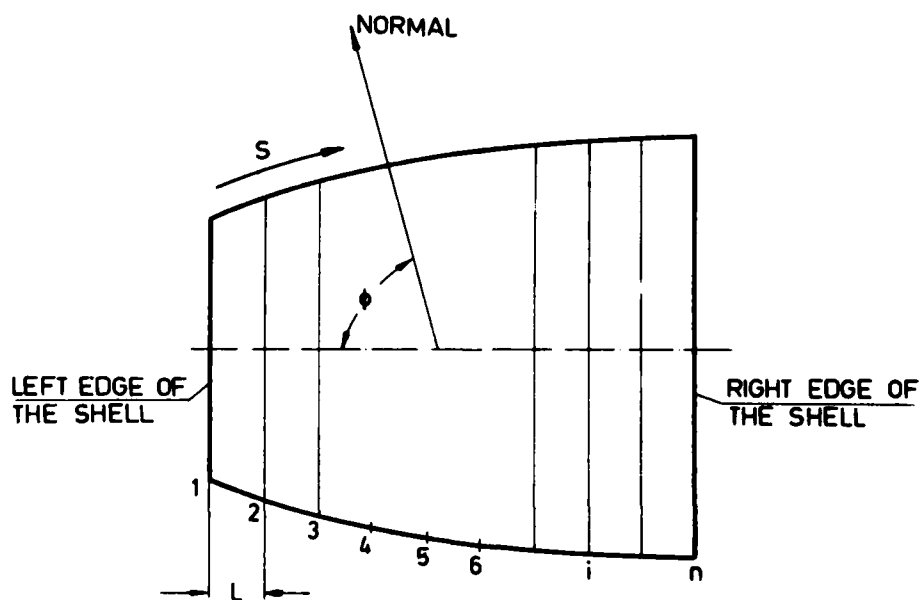


Fig. 3 - Schematic of a shell of revolution as an assemblage of conical shell segments

TABLE 1  
Natural Frequencies of Axisymmetric Vibration of Truncated Conical Shell

$$h = 0.0625 \text{ cm,}$$

$$\nu = 0.25$$

$$E = 4.66 \times 10^4 \text{ Kg/cm}^2,$$

$$\rho = 1.43 \times 10^{-3} \text{ Kg/cm}^3,$$

Mode Number	Natural Frequencies (Hz)		
	Reference 4	Reference 5	Extended Transfer Matrix Method
1	1071	1072	1072
2	1314	1315	1315
3	1608	1611	1610

TABLE 2  
Convergence Range to a Root

Vibration of a cantilevered conical shell  
described in Table 1

$$|\omega_{\text{new}} - \omega_{\text{trial}}| \leq 0.1$$

Mode Number	Computed $\omega$ value (rad./sec.)	Percentage Range of Convergence to Root	
		From Lower Limit	From Higher Limit
1	1072	22	48
2	1315	16	21
3	1610	8	12

TABLE 3  
Natural Frequencies of a Cantilevered Cylindrical Shell

$E = 2.11 \times 10^6 \text{ Kg/cm}^2$ ,       $\nu = 0.3$ ,       $r = 10.16 \text{ cm}$   
 $\rho = 7.84 \times 10^{-3} \text{ Kg/cm}$ ,       $r/h = 100$ ,       $r/L = 0.448$

Mode Number	Circumferential Wave Number	Natural Frequencies (Hz)		
		Extended Transfer Matrix Method	Matrix Progression Method [7]	Green Functions Method [12]
1	2	998	1002	990* 985 <sup>†</sup>
	4	491	489	483* 550 <sup>†</sup>
	5	620	617	670* 735 <sup>†</sup>
2	2	3438	3440	3420* 3400 <sup>†</sup>
	4	1612	1608	1635* 1670 <sup>†</sup>
	5	1301	1296	1370* 1425 <sup>†</sup>
3	2	5738	5732	5700* 5650 <sup>†</sup>
	4	3308	3305	3300* 3280 <sup>†</sup>
	5	2632	2623	2640* 2670 <sup>†</sup>

\* Integral equation solution with 7 internal points in reference [12].

† Integral equation solution with 5 internal points in reference [12].

TABLE 4  
Comparison of First Mode Frequencies with Different Circumferential Wave Number

$$E = 2.11 \times 10^6 \text{ Kg/cm}^2,$$

$$\nu = 0.3,$$

$$h/r = 0.01$$

$$\rho = 7.84 \times 10^{-3} \text{ Kg/cm}^3,$$

$$r = 10.16 \text{ cm},$$

Circumferential Wave Number	L/r	Natural Frequencies (HZ)			
		Extended Transfer Matrix Method	Matrix Progression Method [7]	Exact Solution [6]	Green Function Method [12]*
2	1.18	15091	15100	14988	15316
	2.16	6548	6550	6490	6535
4	1.22	6198	6220	6270	6693
	1.39	5218	5210	5307	5304

\*Integral equation solution with 5 internal points in reference [12].

# A PRACTICAL SCHEME FOR INCLUDING SHEAR WALL (OR FLOOR)

## STIFFNESS IN FRAME ANALYSIS

Robert M. Mains  
Department of Civil Engineering  
Washington University  
St. Louis, Missouri

The stiffness representation of shear walls (or floors) is developed in terms of a general triangular element in plane stress. This triangular element is used to make up a rectangular element from two and four triangles. The results are compared with the Argyris-Przemieniecki formulation of stiffness. Combinations of rectangular and triangular elements to handle walls with openings are discussed. A tabulation of stiffness coefficients for a rectangular wall for a range of aspect ratios and Poisson's ratio of 0.3 is given in the appendix.

### INTRODUCTION

In considering specifically how to include shear-wall stiffness and shear-floor stiffness in frame analysis, the author was unable to find in the literature explicit information which could be directly applied in an analysis. A study of several strength-of-material approaches produced unsatisfying, or unsymmetric, or unsuitable stiffness matrices. Consequently a development of a rectangular element stiffness matrix which would be directly useable in a frame analysis was undertaken. Rectangular and triangular element stiffnesses in plane stress, and combinations thereof, are presented in forms which lend themselves to clear physical understanding of what is being done or assumed. No claim is made that the principles involved are new, but the results are directly applicable in frame analysis and are not restricted to orthogonal frames.

### THE GENERAL TRIANGULAR ELEMENT IN PLANE STRESS

Assume a general triangular element in plane stress as in Fig. 1. Lines in the element which are initially straight remain straight after deformation. Hence the strain field within an element is constant and edge stresses are constant. Then, if  $u$  is the  $x$  displacement, and  $v$  is the  $y$  displacement,

$$u(x,y) = u_1 + c_1x + c_2y \quad (1)$$

$$v(x,y) = v_1 + c_3x + c_4y \quad (2)$$

From elastic theory,

$$\epsilon_x = \frac{\partial u}{\partial x} = c_1 \quad (3)$$

$$\epsilon_y = \frac{\partial v}{\partial y} = c_4 \quad (4)$$

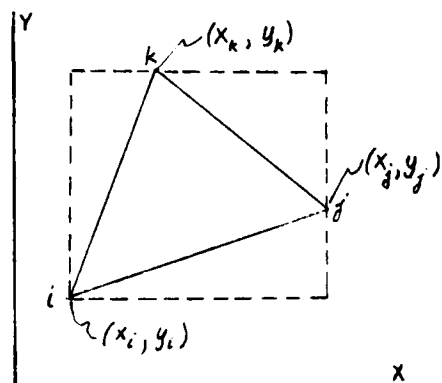
$$\gamma_{xy} = \frac{\partial u}{\partial y} + \frac{\partial v}{\partial x} = c_2 + c_3 \quad (5)$$

If the  $u$  and  $v$  nodal displacements are substituted into eq. (1) and (2),

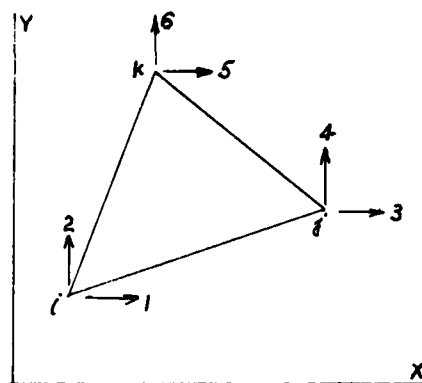
$$\left. \begin{aligned} u_1 &= u_1 + c_1(x_1 - x_1) + c_2(y_1 - y_1) \\ u_j &= u_1 + c_1(x_j - x_1) + c_2(y_j - y_1) \\ u_k &= u_1 + c_1(x_k - x_1) + c_2(y_k - y_1) \\ v_1 &= v_1 + c_3(x_1 - x_1) + c_4(y_1 - y_1) \\ v_j &= v_1 + c_3(x_j - x_1) + c_4(y_j - y_1) \\ v_k &= v_1 + c_3(x_k - x_1) + c_4(y_k - y_1) \end{aligned} \right\} \quad (6)$$

In matrix form, eq. (6) becomes

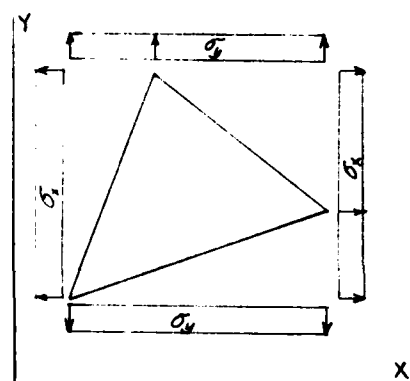
$$\begin{bmatrix} (x_j - x_1) & (y_j - y_1) & 0 & 0 \\ (x_k - x_1) & (y_k - y_1) & 0 & 0 \\ 0 & 0 & (x_j - x_1) & (y_j - y_1) \\ 0 & 0 & (x_k - x_1) & (y_k - y_1) \end{bmatrix} \begin{bmatrix} c_1 \\ c_2 \\ c_3 \\ c_4 \end{bmatrix} = \begin{bmatrix} u_j - u_1 \\ u_k - u_1 \\ v_j - v_1 \\ v_k - v_1 \end{bmatrix} \quad (7)$$



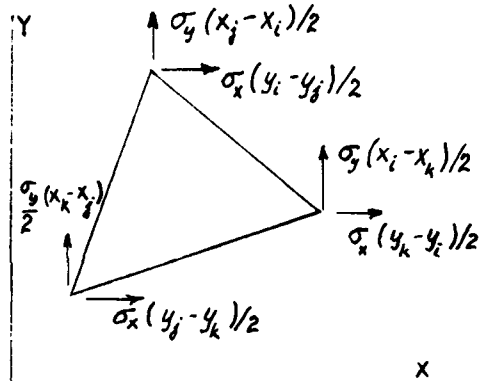
(a) Notation



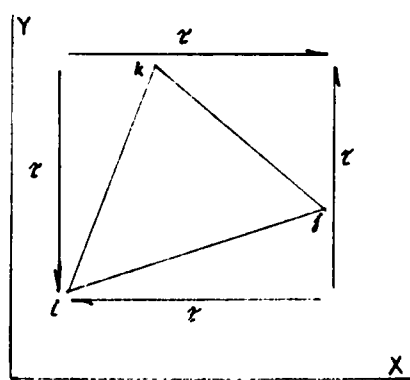
(b) Coordinate Sequence



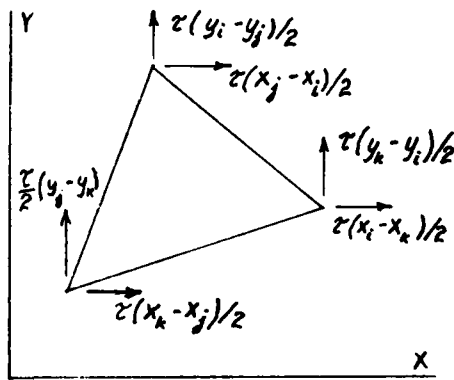
(c) Normal Stress



(d) Equivalent Nodal Forces



(e) Uniform Edge Shear



(f) Equivalent Nodal Forces

Fig.1 General Triangular Element

The solution of eq. (7) for  $c$  gives:

$$\begin{bmatrix} c_1 \\ c_2 \\ c_3 \\ c_4 \end{bmatrix} = \frac{1}{D} \begin{bmatrix} +(y_k - y_i) - (y_j - y_i) & 0 & 0 \\ -(x_k - x_i) + (x_j - x_i) & 0 & 0 \\ 0 & 0 & +(y_k - y_i) - (y_j - y_i) \\ 0 & 0 & -(x_k - x_i) + (x_j - x_i) \end{bmatrix} \begin{bmatrix} u_j - u_i \\ u_k - u_i \\ v_j - v_i \\ v_k - v_i \end{bmatrix} \quad (8)$$

$$\text{in which } D = (x_j - x_i)(y_k - y_i) - (x_k - x_i)(y_j - y_i) \quad (9)$$

Equation (8) can be rearranged to give:

$$\begin{bmatrix} c_1 \\ c_2 \\ c_3 \\ c_4 \end{bmatrix} = \frac{1}{D} \begin{bmatrix} (y_j - y_k) & 0 & (y_k - y_i) & 0 & (y_i - y_j) & 0 \\ (x_k - x_j) & 0 & (x_i - x_k) & 0 & (x_j - x_i) & 0 \\ 0 & (y_j - y_k) & 0 & (y_k - y_i) & 0 & (y_i - y_j) \\ 0 & (x_k - x_j) & 0 & (x_i - x_k) & 0 & (x_j - x_i) \end{bmatrix} \begin{bmatrix} u_i \\ v_i \\ u_j \\ v_j \\ u_k \\ v_k \end{bmatrix} \quad (10)$$

Substitute eq. (3), (4), (5) into (10) and get:

$$\begin{bmatrix} \epsilon_x \\ \epsilon_y \\ \gamma_{xy} \end{bmatrix} = \frac{1}{D} \begin{bmatrix} (y_j - y_k) & 0 & (y_k - y_i) & 0 & (y_i - y_j) & 0 \\ 0 & (x_k - x_j) & 0 & (x_i - x_k) & 0 & (x_j - x_i) \\ (x_k - x_j) & (y_j - y_k) & (x_i - x_k) & (y_k - y_i) & (x_j - x_i) & (y_i - y_j) \end{bmatrix} \begin{bmatrix} u_i \\ v_i \\ u_j \\ v_j \\ u_k \\ v_k \end{bmatrix} \quad (11)$$

In compact form:

$$\epsilon = T_{ue} * u \quad (12)$$

where

$\epsilon$  = strain vector

$T_{ue}$  = transformation matrix, deformation to strain

$u$  = displacement vector

The relation between strain and stress from elastic theory is, for plane stress:

$$\begin{bmatrix} \epsilon_x \\ \epsilon_y \\ \gamma_{xy} \end{bmatrix} = \frac{1}{E} \begin{bmatrix} 1 & -\mu & 0 \\ -\mu & 1 & 0 \\ 0 & 0 & 2(1+\mu) \end{bmatrix} \begin{bmatrix} \sigma_x \\ \sigma_y \\ \tau_{xy} \end{bmatrix} \quad (13)$$

in which  $E$  = Young's modulus  
 $\mu$  = Poisson's ratio

and the solution of eq. (13) for  $\sigma$  gives:

$$\begin{bmatrix} \sigma_x \\ \sigma_y \\ \tau_{xy} \end{bmatrix} = \frac{E}{(1-\mu^2)} \begin{bmatrix} 1 & +\mu & 0 \\ +\mu & 1 & 0 \\ 0 & 0 & \frac{1-\mu}{2} \end{bmatrix} \begin{bmatrix} \epsilon_x \\ \epsilon_y \\ \gamma_{xy} \end{bmatrix} \quad (14)$$

or in compact notation:

$$\sigma = E_1 * \epsilon \quad (15)$$

The equivalent nodal forces for the stresses are shown in Fig. 1 (d) and (f). In matrix form these are:

$$\begin{bmatrix} f_{ix} \\ f_{iy} \\ f_{jx} \\ f_{jy} \\ f_{kx} \\ f_{ky} \end{bmatrix} = \frac{1}{2} \begin{bmatrix} (y_j - y_k) & 0 & (x_k - x_j) \\ 0 & (x_k - x_j) & (y_j - y_k) \\ (y_k - y_i) & 0 & (x_i - x_k) \\ 0 & (x_i - x_k) & (y_k - y_i) \\ (y_i - y_j) & 0 & (x_j - x_i) \\ 0 & (x_j - x_i) & (y_i - y_j) \end{bmatrix} \begin{bmatrix} \sigma_x \\ \sigma_y \\ \tau_{xy} \end{bmatrix} \quad (16)$$

and in compact notation:

$$F = T_{of} * \sigma \quad (17)$$

Now substitute eq. (12) into (15) and (15) into (17) to get:

$$F = T_{of} * E_1 * T_{ue} * u \quad (18)$$

Next examine eq. (11) and note that  $T_{ue}$  is the transpose of  $T_{of}$  in eq. (16) except for the  $\frac{1}{2}$  and  $\frac{1}{D}$ . Hence

$$T_{ue} = \frac{1}{D} T^T$$

$$T_{of} = \frac{1}{2} T$$

and if  $E_1$  is written as:

$$E_1 = \frac{E}{1-\mu^2} * E_2$$

then eq. (18) can be written as:

$$F = \frac{E}{2(1-\mu^2)} * \frac{1}{D} * T * E_2 * T^T * u \quad (19)$$

Note that eq. (19) presumes a unit thickness of plate. To account for plate thickness other than unity, the factor  $\frac{E}{2(1-\mu^2)}$  must be changed

to  $\frac{Et}{2(1-\mu^2)}$ . Then the terms between  $F$  and  $u$  constitute the stiffness matrix for the general triangular element in plane stress.

$$K = \frac{Et}{2(1-\mu^2)} * \frac{1}{D} * T * E_2 * T^T \quad (20)$$

It is worthwhile to note that for a particular material,  $E$  and  $\mu$  are constants, that  $\frac{1}{D} * T * T^T$  is dimensionless, and that the only dimension dependent factor in eq. (20) is  $t$ . The expansion of eq. (20) follows.

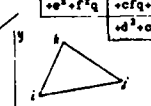
$$\begin{matrix} u_i & v_i & u_j & v_j & u_k & v_k \\ \begin{matrix} +h^2+g^2q & -ghq-g^2p & -fh-egq & +fgq+ehp & +dh+cgq & -dgq-chp \\ +g^2+h^2q & +ghq+f^2p & -fg-fhq & -chq-dgp & +cg+dhq & +dg+chp \\ c=x-x_i & d=y-y_i & e=x-x_j & f=y-y_j & g=x-x_k & h=y-y_k \\ f=y-y_i & g=x-x_j & h=y-y_j & i=x-x_k & j=y-y_k & k=x-x_i \\ p=\text{Poisson's ratio} & q=(1-p)/2 \end{matrix} \\ \text{symmetric} \end{matrix} * \frac{1}{cf-ed} \frac{Et}{2(1-p^2)}$$


Fig.2 Stiffness Matrix for General Triangular Element

#### THE RECTANGULAR ELEMENT AS SUM OF TWO TRIANGLES

With the expanded element stiffness matrix of Fig. 2, it is now feasible to put together the stiffness for a rectangular element either:

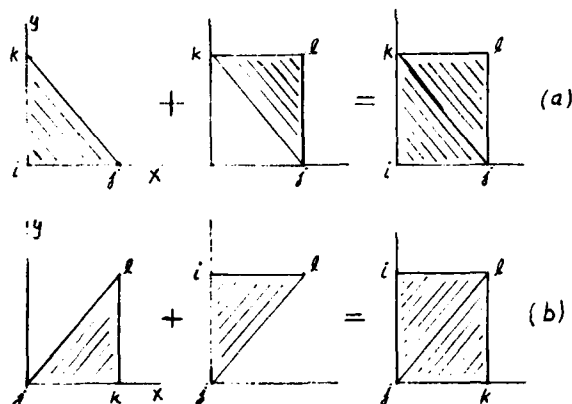


Fig.3 Rectangular Element from 2 Triangles

The two different forms of composition, 3(a) and 3(b), give diagonal elements that are identical, but the off-diagonal elements differ in sign and in  $\mu_j$  and  $\mu_i$ . If the sum of  $K_{3a}$  and  $K_{3b}$  is formed and divided by 2, the resulting stiffness looks right, satisfies statics, and seems generally acceptable (see Fig. 4). However, there is an anomaly of constraint on strain within the rectangle because of the superposition of two different solutions.

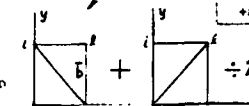
$$\begin{matrix} u_i & v_i & u_j & v_j & u_k & v_k & u_l & v_l \\ \begin{matrix} +a & -c/2 & +e-a/2 & -f & 0 & +c/2 & -e-a/2 & +f \\ +b & +f & -d-b/2 & +c/2 & 0 & -f & +d-b/2 & -c/2 \\ a=2r+(1-p)/r & b=2/r+(1-p)r & c=1+p, r=b/a & d=1/r-(1-p)r/2 & e=r-(1-p)/2r & f=(1-3p)/2 & p=\text{Poisson's ratio} \end{matrix} \\ \text{symmetric} \end{matrix} * \frac{Et}{4(1-p^2)}$$


Fig.4 Stiffness Matrix for Rectangular Element

#### THE RECTANGULAR ELEMENT AS SUM OF FOUR TRIANGLES

The anomaly of constraint on strain in the matrix of Fig. 4 led to the consideration of a rectangular element composed of 4 triangles as shown in Fig. 5.

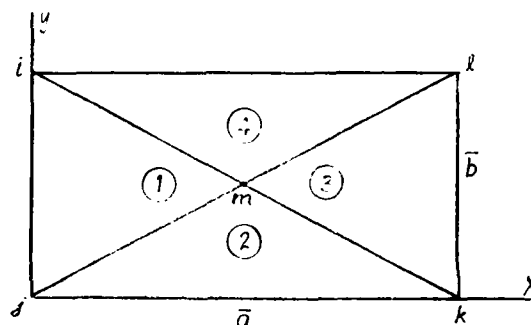
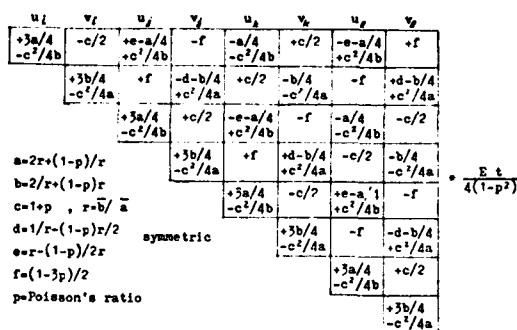
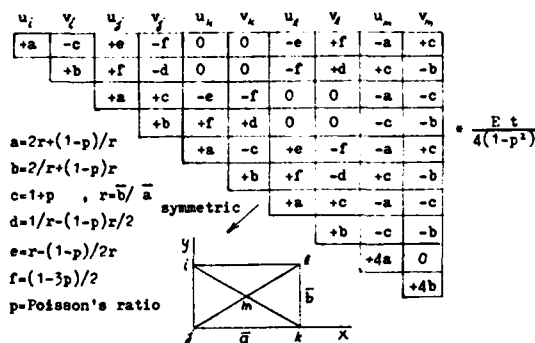


Fig.5 Rectangular Element from 4 Triangles

The assembly of a stiffness matrix from these 4 triangles would lead to a  $10 \times 10$  matrix when only an  $8 \times 8$  was wanted. Stiffness reduction from 10 to 8 is easy, if done numerically by computer, but that would not produce a general stiffness matrix in algebraic terms. To use rectangular elements in shear walls and floors which were to be added to rectangular beam-column frames would require an algebraic statement of the stiffness for general use. The matrix reduction was accomplished by a combination of hand work and computer work by representing matrix elements by prime numbers and verifying the hand work in the computer. Results are shown in Fig. 6 and 7.





The 8x8 stiffness of Fig. 7 differs significantly from the 8x8 of Fig. 4, with the diagonal elements of the latter all larger and the off diagonal elements mixed. The difference, Fig. 7-Fig. 4 in abc terms is:

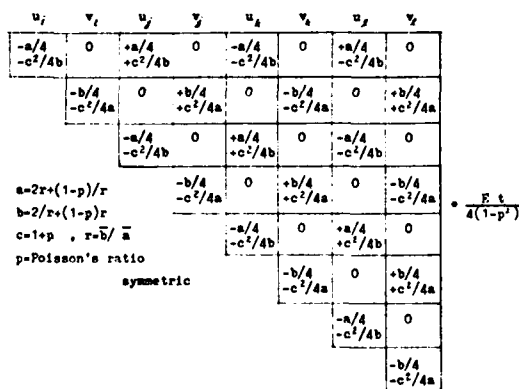


Fig. 8 Difference Matrix, Fig. 7 - Fig. 4

The matrix of Fig. 7 gives a smaller stiffness for the rectangular element than the matrix of Fig. 4, and so would be a smaller estimate for combination with a rectangular frame, both with regard to stiffness and frequency. The matrix elements are readily calculated in the computer, and the elements of the upper triangle (numbered sequentially by rows) have been computed for a range of values of  $\rho = \frac{b}{a}$  and  $\nu = 0.30$ . The results are listed in the appendix and need only to be multiplied by  $Et/3.64$  to be used for a specific application.

Since, except for  $t$ , the element stiffness matrix is dimensionless, it was desirable to investigate the effect of subdivision of a single rectangular element into various numbers of sub-elements. Conventional wisdom would have it that the larger the number of sub-elements, the better (more precise) the representation. But how was this compatible with the non-dimensionality of the stiffness? To study this, a stiffness compilation was made for 1, 4, 9, 16, 36 and 64 elements of identical shape, as shown in Fig. 9. The compiled stiffnesses were then reduced to 8x8 (the corner coordinates) by stiffness condensation.

1	4	9	16	25	36	49	64
2	3	8	15	24	35	48	63
5	6	7	14	23	34	47	62
10	11	12	13	22	33	46	61
17	18	19	20	21	32	45	60
26	27	28	29	30	31	44	59
37	38	39	40	41	42	43	58
50	51	52	53	54	55	56	57

Fig. 9 Successive Assembly Plan

The results of this assembly and reduction were:

Table 1. Comparative Stiffness of Successively Greater Number of Elements

Number Elements	x Stiffness (el 1,1)	y Stiffness (el 2,2)	x + y
1	2.400	4.300	6.700
4	1.263	2.154	3.417
9	0.950	1.466	2.416
16	0.803	1.129	1.932
36	0.660	0.806	1.466
64	0.587	0.654	1.241

As may be seen in Table 1, the stiffness gets continuously smaller as the number of elements

increases, just as if there were some dimensional effect. This was puzzling for a while, until it was realized that the stiffness condensation process frees the nodes which are condensed out, from any constraint other than that supplied by attached structure. Hence, the edge nodes which were constrained to lie in a straight line may now lie on a segmented line, making the assembly more flexible. In the limit, it would be akin to pulling on a membrane at the corners.

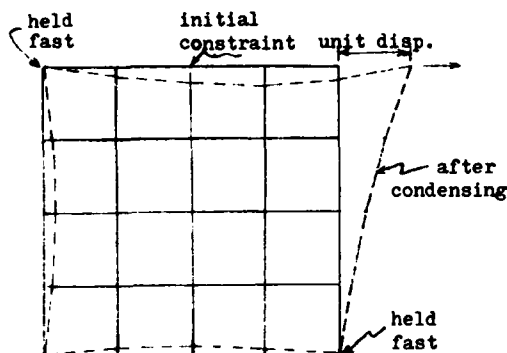
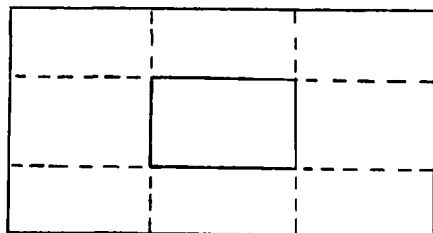


Fig. 10 Effect of Condensation

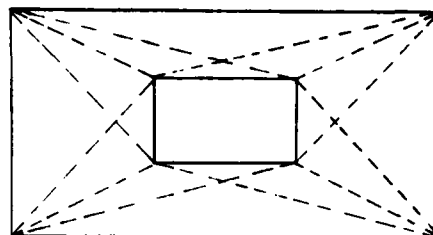
The foregoing reasoning leads to the conclusion that if a shear wall (or floor) is to be joined to a rectangular frame, with analytic nodes at the corners and beams and columns constraining the edges, then a single rectangular element is a better representation of the shear wall than is an assembly of rectangular elements condensed into an  $8 \times 8$  of corner coordinates.

#### WALLS WITH OPENINGS

In a real-life structure, some shear walls can be solid and some must have openings of such size that their effect must be included in the analysis. It would be tempting to model a wall with a window as an assembly of rectangular elements and condense out all but the corner coordinates as in Fig. 11a. This would be all right for the nodes around the window, but the 8 non-corner edge nodes cannot be condensed out until after they have been assembled into any constraining structure which joins them. This limitation can be gotten around by using triangles which have no nodes along the edges, as in Fig. 11b.



(a) Rectangular Elements



(b) Triangular Elements

Fig. 11 Wall with Window

With a window, the interior nodes can be condensed out before further assembly, which helps on the size and cost of computation. A doorway, on the otherhand, must have its bottom nodes preserved until after assembly into constraining structure.

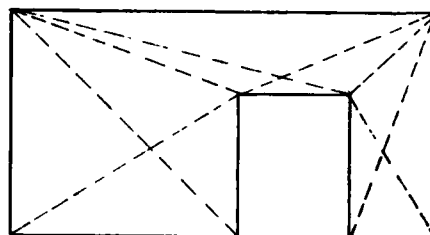


Fig. 12 Wall with Doorway

When a doorway is repeated for several floors, a combination of triangular and rectangular elements may be convenient.

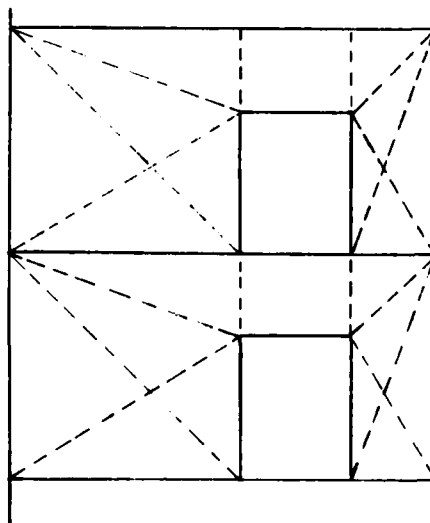


Fig. 13 Wall with Repeated Door

A note of caution is appropriate here, to point out that the constraints on strain distribution implicit in the division of a rectangular wall into triangles, make the resulting stiffnesses very shape sensitive. Long, narrow triangles, as in the upper part of Fig. 12 are to be avoided wherever possible, just as in any triangulation problem. The more nearly equilateral the triangle is, the more precisely determined it is trigonometrically, and the same is true of its stiffness. It would be better to introduce more interior nodes and condense them out later in order to avoid long, narrow triangles.

#### THE RECTANGULAR ELEMENT PER ARGYRIS-PRZEMIENIECKI

A source was found in the literature\*, which presented the stiffness for a rectangular element in a form which could be adapted for frame analysis. This stiffness was developed from the application of Castigliano's Theorem to the total strain energy of the element under an assumed constant-stress, linear-strain variation condition, characterized by:

$$u_x = c_1\xi + c_2\xi\eta + c_3\eta + c_4$$

$$v_y = c_5\xi + c_6\xi\eta + c_7\eta + c_8$$

in which

$$\xi = \frac{x}{a}$$

$$\eta = \frac{y}{b}$$

The displacement distribution is represented by a second-degree surface, in which the variation of displacement in the direction of  $\xi$  or  $\eta$  is linear for constant values of  $\xi$  or  $\eta$ . The resulting stiffness matrix (transformed into a form consistent with Fig. 7) is shown in Fig. 14, and it satisfies statics and symmetry, just as did the matrices of Fig. 4 and Fig. 7. The main diagonal elements of Fig. 14 are smaller than Fig. 4 and larger than Fig. 7, showing that the implicit constraints on strain lie between those of Fig. 4 and Fig. 7. The differences, Fig. 4-Fig. 14, and Fig. 7-Fig. 14, are shown in Fig. 15 and Fig. 16, respectively. The similarity in pattern of the matrix elements between Fig. 7, Fig. 15, and Fig. 16 is interesting, and demonstrates that the formulation of the various matrices is consistent.

$u_i$	$v_i$	$u_j$	$v_j$	$u_k$	$v_k$	$u_l$	$v_l$
$+2a/3$	$-c/2$	$+a-a/6$	$-f$	$-a/3$	$+c/2$	$-a-a/6$	$+f$
	$+2b/3$	$+f$	$-d-b/6$	$+c/2$	$-b/3$	$-f$	$+d-b/6$
		$+2a/3$	$+c/2$	$-a-a/6$	$-f$	$-a/3$	$-c/2$
			$+2b/3$	$+f$	$+d-b/6$	$-c/2$	$-b/3$
$a=2r/(1-p)/r$				$+2a/3$	$-c/2$	$+a-a/6$	$-f$
$b=2/r/(1-p)r$					$+2b/3$	$+f$	$+d-b/6$
$c=1+p$	$r=b/\bar{a}$					$+2a/3$	$+c/2$
$d=1/r/(1-p)r/2$							$+2b/3$
$e=r/(1-p)/2r$							
$f=(1-3p)/2$							
$p$ =Poisson's ratio							

Fig. 14 Stiffness Matrix for Rectangular Element from Przemieniecki

$u_i$	$v_i$	$u_j$	$v_j$	$u_k$	$v_k$	$u_l$	$v_l$
$+a/3$	0	$-a/3$	0	$+a/3$	0	$-a/3$	0
	$+b/3$	0	$-b/3$	0	$+b/3$	0	$-b/3$
		$+a/3$	0	$-a/3$	0	$+a/3$	0
			$+b/3$	0	$-b/3$	0	$+b/3$
$a=2r/(1-p)/r$				$+a/3$	0	$-a/3$	0
$b=2/r/(1-p)r$					$+b/3$	0	$-b/3$
$r=b/\bar{a}$						$+a/3$	0
$p$ =Poisson's ratio							$+b/3$

Fig. 15 Difference Matrix, Fig. 4 - Fig. 14

$u_i$	$v_i$	$u_j$	$v_j$	$u_k$	$v_k$	$u_l$	$v_l$
$+a/12$	0	$-a/12$	0	$+a/12$	0	$-a/12$	0
	$-c^2/4b$		$-c^2/4b$		$-c^2/4b$		$-c^2/4b$
		$+b/12$	0	$-b/12$	0	$+b/12$	0
			$+c^2/4a$		$+c^2/4a$		$+c^2/4a$
		$+a/12$	0	$-a/12$	0	$+a/12$	0
			$-c^2/4b$		$-c^2/4b$		$-c^2/4b$
		$+b/12$	0	$-b/12$	0	$+b/12$	0
			$-c^2/4a$		$-c^2/4a$		$-c^2/4a$
$a=2r/(1-p)/r$				$+a/12$	0	$-a/12$	0
$b=2/r/(1-p)r$					$+c^2/4b$		$-c^2/4b$
$c=1+p$						$+b/12$	0
$r=b/\bar{a}$							$-b/12$
$p$ =Poisson's ratio							$+c^2/4a$

Fig. 16 Difference Matrix, Fig. 7 - Fig. 14

To evaluate the importance of the difference between the matrices of Fig. 7 and Fig. 14, the calculation shown in Table 2 was made.

\*Theory of Matrix Structural Analysis, T. S. Przemieniecki, McGraw-Hill, 1968, p. 94.

Table 2. Ratio Fig. 16/Fig. 14

$$\mu = 0.30$$

$\rho$	$\frac{a}{12} - \frac{c^2}{4b}$ + $\frac{b}{12} - \frac{c^2}{4a}$	$\frac{2}{3} a$ + $\frac{2}{3} b$	Ratio
1.00	0.137	3.600	0.038
1.25	0.153	3.690	0.041
1.50	0.183	3.900	0.047
2.00	0.289	4.500	0.064
2.50	0.407	5.220	0.078

a, b, c are defined in Fig. 14

$$\rho = \bar{b}/\bar{a}$$

It can be seen that the difference between the matrices of Fig. 7 and Fig. 14 is a small percentage of the main diagonal values in the practical range of values of  $\rho$ . Consequently, whether one uses the formulation of Fig. 7 or Fig. 14 (or Fig. 4), the effect on the final stresses would be almost the same, and design decisions would be also.

#### CONCLUSIONS

For inclusion of the stiffness of a shear wall (or floor) into a beam-column frame analysis, the author recommends the matrix of Fig. 7 for two reasons:

1. It is the smallest of the three matrices, and should give the least stiffness and the lowest frequency.
2. For walls (or floors) with openings, it lends itself most readily to combination with triangular elements for a consistent stiffness representation of the whole wall (or floor) panel.

The stiffnesses of the corner nodes (as in Fig. 7) may be added directly to the beam-column stiffnesses for those nodes, and the static or dynamic deflection calculations carried through to produce a deformation matrix,  $u$  (see Eq. (18)). The deformations appropriate to each wall (or floor) panel may be selected from the total  $u$  and used to get stresses in each rectangular element, after restoration to the full deformation set by the reverse condensation process. (See Appendix A for a brief treatment of the condensation process.)

#### APPENDIX

##### A. Condensation

It is frequently desirable to reduce the size (number of coordinates) of the problem in order to keep within core size limitations or to reduce the cost of computation. The process is called "condensation", and is similar to using a truncated Fourier series in place of the full series, or a selected portion of the modal matrix instead of the full one. The author prefers to consider the condensation process as a coordinate transformation, as follows:

Consider the dynamic equation

$$M\ddot{x} + C\dot{x} + Kx = f(t) \quad (a1)$$

in which  $M$  = mass matrix,  $n \times n$

$C$  = damping coefficient matrix,  $n \times n$

$K$  = stiffness matrix,  $n \times n$

$x$  = displacement coordinate vector,  $n \times 1$

$\dot{x}, \ddot{x}$  = time derivatives of  $x$

$f(t)$  = force vector time function,  $n \times 1$

The Fourier transform of eq. (a1) is

$$(-\omega^2 M + i\omega C + K) * x(i\omega) = f(i\omega) \quad (a2)$$

Let

$$Z(i\omega) = (-\omega^2 M + i\omega C + K) \quad (a3)$$

and call this the "impedance". Then eq. (a2) becomes

$$Z(i\omega) * x(i\omega) = f(i\omega) \quad (a4)$$

To condense eq. (a4) from dimension  $n$  to some smaller dimension,  $m$ , introduce a transformation matrix,  $R$ , of dimension  $(n-m) \times m$ , such that a new displacement vector,  $y$ , is defined by:

$$[x(i\omega)] = \begin{bmatrix} I \\ R \end{bmatrix} [y(i\omega)] \quad (a5)$$

in which  $x(i\omega)$  is size  $n \times 1$

$I$  = identity matrix, size  $m \times m$

$R$  = transformation matrix, size  $(n-m) \times m$

$y(i\omega)$  = transformed vector, size  $m \times 1$

If the transformation of eq. (a5) is applied to

eq. (a4), and a premultiplication by  $\begin{bmatrix} I \\ R \end{bmatrix}^T$  is performed, then eq. (a4) becomes,

$$\begin{bmatrix} I \\ R \end{bmatrix}^T * [z(i\omega)] * \begin{bmatrix} I \\ R \end{bmatrix} * [y(i\omega)] = \begin{bmatrix} I \\ R \end{bmatrix}^T * [f(i\omega)] \quad (a6)$$

$m \times n$      $n \times n$      $n \times m$      $m \times 1$      $m \times n$      $n \times 1$

and reduction of size has been achieved. When responses,  $y(i\omega)$ , of the reduced set of coordinates to the driving function have been obtained by solution of eq. (a6), the responses,  $x(i\omega)$ ,

of the full set of coordinates are available through the application of eq. (a5). So eq. (a6) is "forward condensation", and eq. (a5) is "reverse condensation".

For the zero frequency case, only the stiffness remains in eq. (a3), and eq. (a5) becomes

$$\begin{bmatrix} x_1 \\ x_2 \end{bmatrix} = \begin{bmatrix} I & \\ -K_{22}^{-1} & K_{21} \end{bmatrix} [y_1] \quad (a7)$$

in which the matrices have been partitioned

$$\begin{bmatrix} K_{11} & K_{12} \\ K_{21} & K_{22} \end{bmatrix} \begin{bmatrix} x_1 \\ x_2 \end{bmatrix} = \begin{bmatrix} f_1 \\ f_2 \end{bmatrix} \quad (a8)$$

When the transformation of eq. (a7) is applied to eq. (a8), the result is

$$[K_{11} - K_{12} K_{22}^{-1} K_{21}] [y_1] = [f_1 - K_{12} K_{22}^{-1} f_2] \quad (a9)$$

This is the familiar "stiffness condensation".

In the dynamic case, the transformation matrix, R, should be a selected set of the modal matrix, if the transformation is to be orthogonal. Using the modal matrix, however, requires the prior solution of the eigenvalue problem, which is costly. The use of the matrix  $R = [-K_{22}^{-1} K_{21}]$  in eq. (a5) has been applied to dynamic problems with satisfactory results for the lower frequency register. This transformation with stiffness is known as Guyan's condensation.\*

#### B. Stiffness Coefficient Tables

The elements of the upper triangle of the 8x8 stiffness matrix of Fig. 7 were calculated for a value of  $\mu = 0.3$ , and a range of values of  $\rho$  from 0.333 to 3.0. The results are listed, with the element number key shown below. For rectangular elements without openings, it should be satisfactory to interpolate in the listing for  $\rho$  values not explicitly shown.

$$\rho = \bar{b}/\bar{a} = \text{aspect ratio (see Fig. 4)}$$

1	2	3	4	5	6	7	8
	9	10	11	12	13	14	15
		16	17	18	19	20	21
			22	23	24	25	26
				27	28	29	30
					31	32	33
						34	35
							36

Fig.A1 Positions of Element Numbers

\*R. J. Guyan, "Reduction of Stiffness and Mass Matrices", AIAA Jour. v3 n2, Feb. 1965.

TABLE A1. Stiffness Coefficients for Rectangular Walls or Floors. (multiply by Et/3.64)

	MU	RHO	EL 1	EL 2	EL 3	EL 4
1	0.300000	0.323333	0.200720	-0.650000	-0.134061	-0.500000
2	0.300000	0.344830	0.196980	-0.650000	-0.128020	-0.500000
3	0.300000	0.357140	0.193350	-0.650000	-0.121920	-0.500000
4	0.300000	0.370370	0.189840	-0.650000	-0.115770	-0.500000
5	0.300000	0.384620	0.186470	-0.650000	-0.109540	-0.500000
6	0.300000	0.400000	0.183250	-0.650000	-0.103250	-0.500000
7	0.300000	0.416670	0.180200	-0.650000	-0.968690	-0.500000
8	0.300000	0.434780	0.177350	-0.650000	-0.903960	-0.500000
9	0.300000	0.454550	0.174730	-0.650000	-0.838180	-0.500000
10	0.300000	0.476190	0.172360	-0.650000	-0.771210	-0.500000
11	0.300000	0.500000	0.170290	-0.650000	-0.702870	-0.500000
12	0.300000	0.526320	0.168560	-0.650000	-0.632980	-0.500000
13	0.300000	0.555560	0.167240	-0.650000	-0.561300	-0.500000
14	0.300000	0.588240	0.166400	-0.650000	-0.487540	-0.500000
15	0.300000	0.625000	0.166130	-0.650000	-0.411350	-0.500000
16	0.300000	0.666670	0.166560	-0.650000	-0.332290	-0.500000
17	0.300000	0.714290	0.167800	-0.650000	-0.249830	-0.500000
18	0.300000	0.769230	0.170170	-0.650000	-0.163260	-0.500000
19	0.300000	0.833330	0.173840	-0.650000	-0.717130	-0.500000
20	0.300000	0.909090	0.179220	-0.650000	-0.266040	-0.500000
21	0.300000	1.000000	0.186850	-0.650000	0.131480	-0.500000
22	0.300000	1.100000	0.196400	-0.650000	0.235970	-0.500000
23	0.300000	1.200000	0.206890	-0.650000	0.331050	-0.500000
24	0.300000	1.300000	0.218130	-0.650000	0.418710	-0.500000
25	0.300000	1.400000	0.229960	-0.650000	0.500420	-0.500000
26	0.300000	1.500000	0.242270	-0.650000	0.577270	-0.500000
27	0.300000	1.600000	0.254990	-0.650000	0.650150	-0.500000
28	0.300000	1.700000	0.268030	-0.650000	0.719710	-0.500000
29	0.300000	1.800000	0.281350	-0.650000	0.786520	-0.500000
30	0.300000	1.900000	0.294900	-0.650000	0.851010	-0.500000
31	0.300000	2.000000	0.308650	-0.650000	0.913540	-0.500000
32	0.300000	2.100000	0.322560	-0.650000	0.974420	-0.500000
33	0.300000	2.200000	0.336610	-0.650000	0.103390	-0.500000
34	0.300000	2.300000	0.350790	-0.650000	0.109210	-0.500000
35	0.300000	2.400000	0.365060	-0.650000	0.114940	-0.500000
36	0.300000	2.500000	0.379430	-0.650000	0.120570	-0.500000
37	0.300000	2.600000	0.393870	-0.650000	0.126130	-0.500000
38	0.300000	2.700000	0.408380	-0.650000	0.131620	-0.500000
39	0.300000	2.800000	0.422950	-0.650000	0.137050	-0.500000
40	0.300000	2.900000	0.437570	-0.650000	0.142430	-0.500000
41	0.300000	3.000000	0.452230	-0.650000	0.147770	-0.500000
	RHO	EL 5	EL 6	EL 7	EL 8	EL 9
1	0.333333	-0.759450	0.650000	0.927810	0.500000	0.452230
2	0.344830	-0.749850	0.650000	0.601930	0.500000	0.437570
3	0.357140	-0.740790	0.650000	0.265080	0.500000	0.422950
4	0.370370	-0.732340	0.650000	-0.839910	0.500000	0.408380
5	0.384620	-0.724560	0.650000	-0.446730	0.500000	0.393870
6	0.400000	-0.717520	0.650000	-0.824810	0.500000	0.379430
7	0.416670	-0.711310	0.650000	-0.122020	0.500000	0.365060
8	0.434780	-0.706040	0.650000	-0.163530	0.500000	0.350790
9	0.454550	-0.701820	0.650000	-0.207270	0.500000	0.336610
10	0.476190	-0.698790	0.650000	-0.253590	0.500000	0.322560
11	0.500000	-0.697130	0.650000	-0.302870	0.500000	0.308650
12	0.526320	-0.697020	0.650000	-0.355620	0.500000	0.294900
13	0.555560	-0.698700	0.650000	-0.412410	0.500000	0.281350
14	0.588240	-0.702460	0.650000	-0.474010	0.500000	0.268030
15	0.625000	-0.708650	0.650000	-0.541350	0.500000	0.254990
16	0.666670	-0.717710	0.650000	-0.615630	0.500000	0.242270
17	0.714290	-0.730170	0.650000	-0.698400	0.500000	0.229960
18	0.769230	-0.746740	0.650000	-0.791730	0.500000	0.218130
19	0.833330	-0.768290	0.650000	-0.898380	0.500000	0.206890
20	0.909090	-0.796000	0.650000	-1.022220	0.500000	0.196400
21	1.000000	-0.831480	0.650000	-1.168500	0.500000	0.186850
22	1.100000	-0.872330	0.650000	-1.327770	0.500000	0.179220
23	1.200000	-0.914380	0.650000	-1.485610	0.500000	0.173840
24	1.300000	-0.957170	0.650000	-1.642800	0.500000	0.170170
25	1.400000	-1.000400	0.650000	-1.799600	0.500000	0.167800
26	1.500000	-1.043900	0.650000	-1.956100	0.500000	0.166560
27	1.600000	-1.087600	0.650000	-2.112400	0.500000	0.166130
28	1.700000	-1.131500	0.650000	-2.268500	0.500000	0.166400
29	1.800000	-1.175400	0.650000	-2.424600	0.500000	0.167240
30	1.900000	-1.219400	0.650000	-2.580600	0.500000	0.168560
31	2.000000	-1.263500	0.650000	-2.736500	0.500000	0.170290
32	2.100000	-1.307700	0.650000	-2.892300	0.500000	0.172360
33	2.200000	-1.352100	0.650000	-3.047900	0.500000	0.174730
34	2.300000	-1.396500	0.650000	-3.203500	0.500000	0.177350
35	2.400000	-1.441000	0.650000	-3.359000	0.500000	0.180200
36	2.500000	-1.485700	0.650000	-3.514300	0.500000	0.183250
37	2.600000	-1.530500	0.650000	-3.669500	0.500000	0.186470
38	2.700000	-1.575400	0.650000	-3.824600	0.500000	0.189840
39	2.800000	-1.620500	0.650000	-3.979500	0.500000	0.193350
40	2.900000	-1.665700	0.650000	-4.134300	0.500000	0.196980
41	3.000000	-1.711000	0.650000	-4.289000	0.500000	0.200720

	RHO	EL 10	EL 11	EL 12	EL 13	EL 14
1	0.33333D 00	0.5C000D-01	-0.42890D 01	0.65000D 00	-0.17110C 01	-0.5CCCCD-01
2	0.34483D 00	0.5C000D-01	-0.41343D 01	0.65000D 00	-0.16657D 01	-0.5CCCCD-01
3	0.35714D 00	0.5C000D-01	-0.39795D 01	0.65000D 00	-0.16205C 01	-0.5CCCCD-01
4	0.37037D 00	0.5C000D-01	-0.38246D 01	0.65000D 00	-0.15754D 01	-0.5CCCCD-01
5	0.38462D 00	0.5C000D-01	-0.36695D 01	0.65000D 00	-0.15303C 01	-0.5CCCCD-01
6	0.40000D 00	0.5C000D-01	-0.35143D 01	0.65000D 00	-0.14857D 01	-0.5CCCCD-01
7	0.41667D 00	0.5C000D-01	-0.33590D 01	0.65000D 00	-0.14410C 01	-0.5CCCCD-01
8	0.43478D 00	0.5C000D-01	-0.32035D 01	0.65000D 00	-0.13965C 01	-0.5CCCCD-01
9	0.45455D 00	0.5C000D-01	-0.30479D 01	0.65000D 00	-0.13521C 01	-0.5CCCCD-01
10	0.47619D 00	0.5C000D-01	-0.28923D 01	0.65000D 00	-0.13077D 01	-0.5CCCCD-01
11	0.50000D 00	0.5C000D-01	-0.27365D 01	0.65000D 00	-0.12635C 01	-0.5CCCCD-01
12	0.52632D 00	0.5C000D-01	-0.25806D 01	0.65000D 00	-0.12194C 01	-0.5CCCCD-01
13	0.55556D 00	0.5C000D-01	-0.24246D 01	0.65000D 00	-0.11754C 01	-0.5CCCCD-01
14	0.58824D 00	0.5C000D-01	-0.22685D 01	0.65000D 00	-0.11313C 01	-0.5CCCCD-01
15	0.62500D 00	0.5C000D-01	-0.21124D 01	0.65000D 00	-0.10876D 01	-0.5CCCCD-01
16	0.66667D 00	0.5C000D-01	-0.19561D 01	0.65000D 00	-0.10439C 01	-0.5CCCCD-01
17	0.71429D 00	0.5C000D-01	-0.17996D 01	0.65000D 00	-0.10004C 01	-0.5CCCCD-01
18	0.76923D 00	0.5C000D-01	-0.16428D 01	0.65000D 00	-0.95717D 00	-0.5CCCCD-01
19	0.83333D 00	0.5C000D-01	-0.14856D 01	0.65000D 00	-0.91438C 00	-0.5CCCCD-01
20	0.90909D 00	0.5C000D-01	-0.13277D 01	0.65000D 00	-0.87233C 00	-0.5CCCCD-01
21	1.00000D 01	0.5C000D-01	-0.11685D 01	0.65000D 00	-0.83148C 00	-0.5CCCCD-01
22	0.11000D 01	0.5C000D-01	-0.10222D 01	0.65000D 00	-0.79600D 00	-0.5CCCCD-01
23	0.12000D 01	0.5C000D-01	-0.89838D 00	0.65000D 00	-0.76829C 00	-0.5CCCCD-01
24	0.13000D 01	0.5C000D-01	-0.79173D 00	0.65000D 00	-0.74674C 00	-0.5CCCCD-01
25	0.14000D 01	0.5C000D-01	-0.69840D 00	0.65000D 00	-0.73017C 00	-0.5CCCCD-01
26	0.15000D 01	0.5C000D-01	-0.61563D 00	0.65000D 00	-0.71771C 00	-0.5CCCCD-01
27	0.16000D 01	0.5C000D-01	-0.54135D 00	0.65000D 00	-0.70865C 00	-0.5CCCCD-01
28	0.17000D 01	0.5C000D-01	-0.47401D 00	0.65000D 00	-0.70246C 00	-0.5CCCCD-01
29	0.18000D 01	0.5C000D-01	-0.41241D 00	0.65000D 00	-0.69870C 00	-0.5CCCCD-01
30	0.19000D 01	0.5C000D-01	-0.35562D 00	0.65000D 00	-0.69702C 00	-0.5CCCCD-01
31	0.20000D 01	0.5C000D-01	-0.30287D 00	0.65000D 00	-0.69713C 00	-0.5CCCCD-01
32	0.21000D 01	0.5C000D-01	-0.25359D 00	0.65000D 00	-0.69875C 00	-0.5CCCCD-01
33	0.22000D 01	0.5C000D-01	-0.20727D 00	0.65000D 00	-0.70182C 00	-0.5CCCCD-01
34	0.23000D 01	0.5C000D-01	-0.16353D 00	0.65000D 00	-0.70604D 00	-0.5CCCCD-01
35	0.24000D 01	0.5C000D-01	-0.12202D 00	0.65000D 00	-0.71131C 00	-0.5CCCCD-01
36	0.25000D 01	0.5C000D-01	-0.82481D-01	0.65000D 00	-0.71752C 00	-0.5CCCCD-01
37	0.26000D 01	0.5C000D-01	-0.44673D-01	0.65000D 00	-0.72456C 00	-0.5CCCCD-01
38	0.27000D 01	0.5C000D-01	-0.83991D-02	0.65000D 00	-0.73234C 00	-0.5CCCCD-01
39	0.28000D 01	0.5C000D-01	0.26508D-01	0.65000D 00	-0.74079D 00	-0.5CCCCD-01
40	0.29000D 01	0.5C000D-01	0.60193D-01	0.65000D 00	-0.74985C 00	-0.5CCCCD-01
41	0.30000D 01	0.5C000D-01	0.92781D-01	0.65000D 00	-0.75945C 00	-0.5CCCCD-01

	RHO	EL 15	EL 16	EL 17	EL 18	EL 19
1	0.33333D 00	0.14777D 01	0.20072D 01	0.65000D 00	0.92781D-01	-0.5CCCCD-01
2	0.34483D 00	0.14243D 01	0.19698D 01	0.65000D 00	0.60193D-01	-0.5CCCCD-01
3	0.35714D 00	0.137C5D 01	0.19335D 01	0.65000D 00	0.26508D-01	-0.5CCCCD-01
4	0.37037D 00	0.13162D 01	0.18984D 01	0.65000D 00	-0.83991C-02	-0.5CCCCD-01
5	0.38462D 00	0.12613D 01	0.18647D 01	0.65000D 00	-0.44673C-01	-0.5CCCCD-01
6	0.40000D 00	0.12057D 01	0.18325D 01	0.65000D 00	-0.82481C-01	-0.5CCCCD-01
7	0.41667D 00	0.11494D 01	0.18020D 01	0.65000D 00	-0.12202C 00	-0.5CCCCD-01
8	0.43478D 00	0.10921D 01	0.17735D 01	0.65000D 00	-0.16353C 00	-0.5CCCCD-01
9	0.45455D 00	0.10339D 01	0.17473D 01	0.65000D 00	-0.20727C 00	-0.5CCCCD-01
10	0.47619D 00	0.97442D C0	0.17236D 01	0.65000D 00	-0.25359D 00	-0.5CCCCD-01
11	0.50000D 00	0.91354D C0	0.17029D 01	0.65000D 00	-0.30287C 00	-0.5CCCCD-01
12	0.52632D 00	0.85101D 00	0.16856D 01	0.65000D 00	-0.35562C 00	-0.5CCCCD-01
13	0.55556D 00	0.78652D 00	0.16724D 01	0.65000D 00	-0.41241C 00	-0.5CCCCD-01
14	0.58824D 00	0.71971D 00	0.16640D 01	0.65000D 00	-0.47401C 00	-0.5CCCCD-01
15	0.62500D 00	0.65015D 00	0.16613D 01	0.65000D 00	-0.54135D 00	-0.5CCCCD-01
16	0.66667D 00	0.57727D 00	0.16656D 01	0.65000D 00	-0.61563D 00	-0.5CCCCD-01
17	0.71429D 00	0.50042D 00	0.16784D 01	0.65000D 00	-0.69840D 00	-0.5CCCCD-01
18	0.76923D 00	0.41871D 00	0.17017D 01	0.65000D 00	-0.79173C 00	-0.5CCCCD-01
19	0.83333D 00	0.33105D 00	0.17384D 01	0.65000D 00	-0.89838C 00	-0.5CCCCD-01
20	0.90909D 00	0.23597D C0	0.17922D 01	0.65000D 00	-0.10222C 01	-0.5CCCCD-01
21	1.00000D 01	0.13148D C0	0.18685D 01	0.65000D 00	-0.11685C 01	-0.5CCCCD-01
22	0.11000D 01	-0.26004D-01	0.19640D 01	0.65000D 00	-0.13277C 01	-0.5CCCCD-01
23	0.12000D 01	-0.71713D-01	0.20689D 01	0.65000D 00	-0.14856C 01	-0.5CCCCD-01
24	0.13000D 01	-0.16326D 00	0.21813D 01	0.65000D 00	-0.16428C 01	-0.5CCCCD-01
25	0.14000D 01	-0.24983D 00	0.22996D 01	0.65000D 00	-0.17996C 01	-0.5CCCCD-01
26	0.15000D 01	-0.33229D 00	0.24227D 01	0.65000D 00	-0.19561C 01	-0.5CCCCD-01
27	0.16000D 01	-0.41135D C0	0.25499D 01	0.65000D 00	-0.21124D 01	-0.5CCCCD-01
28	0.17000D 01	-0.48754D 00	0.26803D 01	0.65000D 00	-0.22685D 01	-0.5CCCCD-01
29	0.18000D 01	-0.56130D 00	0.28135D 01	0.65000D 00	-0.24246D 01	-0.5CCCCD-01
30	0.19000D 01	-0.63298D 00	0.29490D 01	0.65000D 00	-0.25806D 01	-0.5CCCCD-01
31	0.20000D 01	-0.70287D 00	0.30865D 01	0.65000D 00	-0.27365D 01	-0.5CCCCD-01
32	0.21000D 01	-0.77121D 00	0.32256D 01	0.65000D 00	-0.28923D 01	-0.5CCCCD-01
33	0.22000D 01	-0.83818D 00	0.33661D 01	0.65000D 00	-0.30479D 01	-0.5CCCCD-01
34	0.23000D 01	-0.90396D C0	0.35079D 01	0.65000D 00	-0.32035D 01	-0.5CCCCD-01
35	0.24000D 01	-0.96869D 00	0.36506D 01	0.65000D 00	-0.33590D 01	-0.5CCCCD-01
36	0.25000D 01	-0.10325D 01	0.37943D 01	0.65000D 00	-0.35143D 01	-0.5CCCCD-01
37	0.26000D 01	-0.10957D 01	0.39387D 01	0.65000D 00	-0.36695D 01	-0.5CCCCD-01
38	0.27000D 01	-0.11577D 01	0.40838D 01	0.65000D 00	-0.38246D 01	-0.5CCCCD-01
39	0.28000D 01	-0.12192D 01	0.42295D 01	0.65000D 00	-0.39795D 01	-0.5CCCCD-01
40	0.29000D 01	-0.12802D 01	0.43757D 01	0.65000D 00	-0.41343D 01	-0.5CCCCD-01
41	0.30000D 01	-0.13406D 01	0.45223D 01	0.65000D 00	-0.42890D 01	-0.5CCCCD-01

	RHD	EL 20	EL 21	EL 22	EL 23	EL 24
1	0.33333D 00	-0.75945D 00	-0.65000D 00	0.45223D 01	0.50000C-01	0.14777D 01
2	0.34483D 00	-0.74985D 00	-0.65000D 00	0.43757C 01	0.50000C-01	0.14243D 01
3	0.35714D 00	-0.74079D 00	-0.65000D 00	0.42295C 01	0.50000C-01	0.13705D 01
4	0.37037D 00	-0.73234D 00	-0.65000D 00	0.40838C 01	0.50000C-01	0.13162D 01
5	0.38462D 00	-0.72456D 00	-0.65000D 00	0.39387C 01	0.50000C-01	0.12613C 01
6	0.40000D 00	-0.71752D 00	-0.65000D 00	0.37943D 01	0.50000C-01	0.12057D 01
7	0.41667D 00	-0.71131D 00	-0.65000D 00	0.36506C 01	0.50000C-01	0.11494D 01
8	0.43478D 00	-0.70604D 00	-0.65000D 00	0.35079C 01	0.50000C-01	0.10921D 01
9	0.45455D 00	-0.70182D 00	-0.65000D 00	0.33661D 01	0.50000C-01	0.10339D 01
10	0.47619D 00	-0.69879D 00	-0.65000C 00	0.32256D 01	0.50000C-01	0.97442D 00
11	0.50000C 00	-0.69713D 00	-0.65000C 00	0.30865C 01	0.50000C-01	0.91354D 00
12	0.52632D 00	-0.69702D 00	-0.65000D 00	0.29490C 01	0.50000C-01	0.85101D 00
13	0.55556D 00	-0.69870D 00	-0.65000D 00	0.28135D 01	0.50000C-01	0.78652D 00
14	0.58824D 00	-0.70246D 00	-0.65000D 00	0.26803C 01	0.50000C-01	0.71971D 00
15	0.62500C 00	-0.70865D 00	-0.65000C 00	0.25499D 01	0.50000C-01	0.655015D 00
16	0.66667D 00	-0.71771D 00	-0.65000C 00	0.24227C 01	0.50000C-01	0.5951727D 00
17	0.71429D 00	-0.73017D 00	-0.65000D 00	0.22996D 01	0.50000C-01	0.53042D 00
18	0.76923D 00	-0.74674D 00	-0.65000D 00	0.21813C 01	0.50000C-01	0.41871D 00
19	0.83333D 00	-0.76825D 00	-0.65000D 00	0.20689C 01	0.50000C-01	0.33105D 00
20	0.90909D 00	-0.79660D 00	-0.65000D 00	0.19540C 01	0.50000C-01	0.23597D 00
21	0.10000C 01	-0.83148D 00	-0.65000D 00	0.18685C 01	0.50000C-01	0.13148D 00
22	0.11000C 01	-0.87233D 00	-0.65000D 00	0.17922D 01	0.50000C-01	0.02600C 00
23	0.12000C 01	-0.91438D 00	-0.65000D 00	0.17384C 01	0.50000C-01	-0.11113D 00
24	0.13000D 01	-0.95717D 00	-0.65000D 00	0.17017C 01	0.50000C-01	-0.16326D 00
25	0.14000C 01	-0.10004D 01	-0.65000D 00	0.16784D 01	0.50000C-01	-0.24983D 00
26	0.15000C 01	-0.10439D 01	-0.65000D 00	0.16656C 01	0.50000C-01	-0.33225C 00
27	0.16000C 01	-0.10876D 01	-0.65000D 00	0.15513C 01	0.50000C-01	-0.41135D 00
28	0.17000C 01	-0.11315D 01	-0.65000D 00	0.16640C 01	0.50000C-01	-0.48754D 00
29	0.18000C 01	-0.11754D 01	-0.65000D 00	0.16724D 01	0.50000C-01	-0.56133D 00
30	0.19000C 01	-0.12194D 01	-0.65000D 00	0.16856C 01	0.50000C-01	-0.63258D 00
31	0.20000D 01	-0.12635D 01	-0.65000D 00	0.17029D 01	0.50000C-01	-0.70287D 00
32	0.21000C 01	-0.13077D 01	-0.65000C 00	0.17236C 01	0.50000C-01	-0.77121D 00
33	0.22000C 01	-0.13521D 01	-0.65000C 00	0.17473C 01	0.50000C-01	-0.83818D 00
34	0.23000C 01	-0.13965D 01	-0.65000D 00	0.17735C 01	0.50000C-01	-0.90396D 00
35	0.24000D 01	-0.14410D 01	-0.65000D 00	0.18020C 01	0.50000C-01	-0.96869D 00
36	0.25000C 01	-0.14857D 01	-0.65000D 00	0.18325D 01	0.50000C-01	-0.10325D 00
37	0.26000C 01	-0.15305D 01	-0.65000D 00	0.18647C 01	0.50000C-01	-0.10955D 00
38	0.27000C 01	-0.15754D 01	-0.65000D 00	0.18984C 01	0.50000C-01	-0.11577D 00
39	0.28000C 01	-0.16205D 01	-0.65000D 00	0.19335D 01	0.50000C-01	-0.12192D 00
40	0.29000C 01	-0.16657D 01	-0.65000C 00	0.19698C 01	0.50000C-01	-0.12802D 00
41	0.30000D 01	-0.17110D 01	-0.65000D 00	0.20072C 01	0.50000C-01	-0.13406D 01

	RHD	EL 25	EL 26	EL 27	EL 28	EL 29
1	0.33333D 00	-0.65000D 00	-0.17110D 01	0.20072C 01	-0.65000C 00	-0.13406D 01
2	0.34483D 00	-0.65000D 00	-0.16657D 01	0.19698C 01	-0.65000C 00	-0.12802D 00
3	0.35714D 00	-0.65000D 00	-0.16205D 01	0.19335D 01	-0.65000C 00	-0.12192D 00
4	0.37037D 00	-0.65000D 00	-0.15754D 01	0.18984C 01	-0.65000C 00	-0.11577D 00
5	0.38462D 00	-0.65000D 00	-0.15305D 01	0.18647D 01	-0.65000C 00	-0.10955D 00
6	0.40000D 00	-0.65000D 00	-0.14857D 01	0.18325C 01	-0.65000C 00	-0.10325D 00
7	0.41667D 00	-0.65000C 00	-0.14410D 01	0.18020D 01	-0.65000C 00	-0.96869D 00
8	0.43478D 00	-0.65000C 00	-0.13965D 01	0.17735C 01	-0.65000C 00	-0.90396D 00
9	0.45455D 00	-0.65000D 00	-0.13521C 01	0.17473C 01	-0.65000C 00	-0.83818D 00
10	0.47619D 00	-0.65000D 00	-0.13077D 01	0.17236D 01	-0.65000C 00	-0.77121D 00
11	0.50000C 00	-0.65000D 00	-0.12635D 01	0.17029C 01	-0.65000C 00	-0.70287D 00
12	0.52632D 00	-0.65000C 00	-0.12194D 01	0.16856C 01	-0.65000C 00	-0.63258D 00
13	0.55556D 00	-0.65000D 00	-0.11754D 01	0.16724C 01	-0.65000C 00	-0.56133D 00
14	0.58824D 00	-0.65000D 00	-0.11315D 01	0.16640D 01	-0.65000C 00	-0.48754D 00
15	0.62500C 00	-0.65000C 00	-0.10876C 01	0.16613D 01	-0.65000C 00	-0.41135D 00
16	0.66667D 00	-0.65000C 00	-0.10439D 01	0.16566C 01	-0.65000C 00	-0.33225D 00
17	0.71429D 00	-0.65000D 00	-0.10004D 01	0.16784C 01	-0.65000C 00	-0.24983D 00
18	0.76923D 00	-0.65000D 00	-0.95717D 00	0.17017C 01	-0.65000C 00	-0.16326D 00
19	0.83333D 00	-0.65000C 00	-0.91438D 00	0.17384D 01	-0.65000C 00	-0.11113D 00
20	0.90909D 00	-0.65000D 00	-0.87233D 00	0.17922C 01	-0.65000C 00	0.02600C 00
21	0.10000C 01	-0.65000D 00	-0.83148D 00	0.18685C 01	-0.65000C 00	0.13148D 00
22	0.11000C 01	-0.65000D 00	-0.79660D 00	0.19540C 01	-0.65000C 00	0.23597D 00
23	0.12000C 01	-0.65000C 00	-0.76825D 00	0.20689C 01	-0.65000C 00	0.33105D 00
24	0.13000D 01	-0.65000D 00	-0.74674D 00	0.22068D 01	-0.65000C 00	0.41871D 00
25	0.14000C 01	-0.65000D 00	-0.73017D 00	0.22996D 01	-0.65000C 00	0.50042D 00
26	0.15000C 01	-0.65000C 00	-0.71754D 00	0.24227C 01	-0.65000C 00	0.57127D 00
27	0.16000C 01	-0.65000D 00	-0.70865D 00	0.25499C 01	-0.65000C 00	0.655015D 00
28	0.17000C 01	-0.65000D 00	-0.70246D 00	0.26803C 01	-0.65000C 00	0.71971D 00
29	0.18000C 01	-0.65000C 00	-0.69870D 00	0.28135D 01	-0.65000C 00	0.78652D 00
30	0.19000C 01	-0.65000C 00	-0.69702D 00	0.29490C 01	-0.65000C 00	0.85101D 00
31	0.20000D 01	-0.65000D 00	-0.69713D 00	0.30865D 01	-0.65000C 00	0.91354D 00
32	0.21000C 01	-0.65000D 00	-0.69879D 00	0.32256C 01	-0.65000C 00	0.97442D 00
33	0.22000C 01	-0.65000C 00	-0.70182D 00	0.33661C 01	-0.65000C 00	0.10339D 00
34	0.23000C 01	-0.65000D 00	-0.70604D 00	0.35079C 01	-0.65000C 00	0.10921D 00
35	0.24000D 01	-0.65000D 00	-0.71131D 00	0.36506C 01	-0.65000C 00	0.11494D 00
36	0.25000C 01	-0.65000D 00	-0.71752D 00	0.37943D 01	-0.65000C 00	0.12057D 00
37	0.26000C 01	-0.65000D 00	-0.72456D 00	0.39387C 01	-0.65000C 00	0.12613C 00
38	0.27000C 01	-0.65000D 00	-0.73234D 00	0.40838C 01	-0.65000C 00	0.13162D 00
39	0.28000C 01	-0.65000D 00	-0.74079D 00	0.42295C 01	-0.65000C 00	0.13705D 00
40	0.29000C 01	-0.65000C 00	-0.74985D 00	0.43757C 01	-0.65000C 00	0.14243D 00
41	0.30000D 01	-0.65000D 00	-0.75945D 00	0.45223C 01	-0.65000C 00	0.14777D 00



	RHO	EL 30	EL 31	EL 32	EL 33	EL 34
1	0.33333D 00	-C.5CCCCD-01	0.45223D 01	0.50000E-01	-0.42890E 01	0.2CC72D 01
2	0.34483D 00	-C.5CCCCD-01	0.43757D 01	0.50000E-01	-0.41343E 01	0.15698D 01
3	0.35714D 00	-C.5CCCCD-01	0.42295D 01	0.50000E-01	-0.39795E 01	0.14335D 01
4	0.37037D 00	-C.5CCCCD-01	0.40838D 01	0.50000E-01	-0.38246E 01	0.13054D 01
5	0.38462D 00	-C.5CCCCD-01	0.39387D 01	0.50000E-01	-0.36695E 01	0.11864D 01
6	0.40000D 00	-C.5CCCCD-01	0.37943D 01	0.50000E-01	-0.35143E 01	0.10832D 01
7	0.41667D 00	-C.5CCCCD-01	0.36506D 01	0.50000E-01	-0.33590E 01	0.10020D 01
8	0.43478D 00	-C.5CCCCD-01	0.35079D 01	0.50000E-01	-0.32035E 01	0.17735D 01
9	0.45455D 00	-C.5CCCCD-01	0.33661D 01	0.50000E-01	-0.30479E 01	0.17473D 01
10	0.47619D 00	-C.5CCCCD-01	0.32256D 01	0.50000E-01	-0.28923E 01	0.17236D 01
11	0.50000D 00	-C.5CCCCD-01	0.30865D 01	0.50000E-01	-0.27365E 01	0.17029D 01
12	0.52632D 00	-C.5CCCCD-01	0.29490D 01	0.50000E-01	-0.25806E 01	0.16856D 01
13	0.55556D 00	-C.5CCCCD-01	0.28135D 01	0.50000E-01	-0.24246E 01	0.16724D 01
14	0.58824D 00	-C.5CCCCD-01	0.26803D 01	0.50000E-01	-0.22685E 01	0.16640D 01
15	0.62500D 00	-C.5CCCCD-01	0.25499D 01	0.50000E-01	-0.21124E 01	0.16613D 01
16	0.66667D 00	-C.5CCCCD-01	0.24227D 01	0.50000E-01	-0.19561E 01	0.16656D 01
17	0.71429D 00	-C.5CCCCD-01	0.22996D 01	0.50000E-01	-0.17996E 01	0.16784D 01
18	0.76923D 00	-C.5CCCCD-01	0.21813D 01	0.50000E-01	-0.16428E 01	0.17017D 01
19	0.83333D 00	-C.5CCCCD-01	0.20689D 01	0.50000E-01	-0.14856E 01	0.17384D 01
20	0.90909D 00	-C.5CCCCD-01	0.19640D 01	0.50000E-01	-0.13277D 01	0.17922D 01
21	0.10000D 01	-C.5CCCCD-01	0.18685D 01	0.50000E-01	-0.11685E 01	0.18685D 01
22	0.11000D 01	-C.5CCCCD-01	0.17922D 01	0.50000E-01	-0.10222E 01	0.19564D 01
23	0.12000D 01	-C.5CCCCD-01	0.17384D 01	0.50000E-01	-0.89838E 00	0.20689D 01
24	0.13000D 01	-C.5CCCCD-01	0.17017D 01	0.50000E-01	-0.79173E 00	0.21813D 01
25	0.14000D 01	-C.5CCCCD-01	0.16784D 01	0.50000E-01	-0.69840E 00	0.22996D 01
26	0.15000D 01	-C.5CCCCD-01	0.16656D 01	0.50000E-01	-0.61563E 00	0.24227D 01
27	0.16000D 01	-C.5CCCCD-01	0.16613D 01	0.50000E-01	-0.54135E 00	0.25499D 01
28	0.17000D 01	-C.5CCCCD-01	0.16640D 01	0.50000E-01	-0.47401E 00	0.26803D 01
29	0.18000D 01	-C.5CCCCD-01	0.16724D 01	0.50000E-01	-0.41241E 00	0.28135D 01
30	0.19000D 01	-C.5CCCCD-01	0.16856D 01	0.50000E-01	-0.35562E 00	0.29490D 01
31	0.20000D 01	-C.5CCCCD-01	0.17029D 01	0.50000E-01	-0.30287E 00	0.30865D 01
32	0.21000D 01	-C.5CCCCD-01	0.17236D 01	0.50000E-01	-0.25359E 00	0.32256D 01
33	0.22000D 01	-C.5CCCCD-01	0.17473D 01	0.50000E-01	-0.20727E 00	0.33661D 01
34	0.23000D 01	-C.5CCCCD-01	0.17735D 01	0.50000E-01	-0.16353E 00	0.35079D 01
35	0.24000D 01	-C.5CCCCD-01	0.18020D 01	0.50000E-01	-0.12202E 00	0.36506D 01
36	0.25000D 01	-C.5CCCCD-01	0.18325D 01	0.50000E-01	-0.82481E-01	0.37943D 01
37	0.26000D 01	-C.5CCCCD-01	0.18647D 01	0.50000E-01	-0.44673E-01	0.39387D 01
38	0.27000D 01	-C.5CCCCD-01	0.18984D 01	0.50000E-01	-0.83991E-02	0.40838D 01
39	0.28000D 01	-C.5CCCCD-01	0.19335D 01	0.50000E-01	0.26508E-01	0.42295D 01
40	0.29000D 01	-C.5CCCCD-01	0.19698D 01	0.50000E-01	0.60193E-01	0.43757D 01
41	0.30000D 01	-C.5CCCCD-01	0.20072D 01	0.50000E-01	0.92781E-01	0.45223D 01

	RHO	EL 35	EL 36
1	0.33333D 00	C.65000D 00	0.45223D 01
2	0.34483D 00	C.65000D 00	0.43757D 01
3	0.35714D 00	C.65000D 00	0.42295D 01
4	0.37037D 00	C.65000D 00	0.40838D 01
5	0.38462D 00	C.65000D 00	0.39387D 01
6	0.40000D 00	C.65000D 00	0.37943D 01
7	0.41667D 00	C.65000D 00	0.36506D 01
8	0.43478D 00	C.65000D 00	0.35079D 01
9	0.45455D 00	C.65000D 00	0.33661D 01
10	0.47619D 00	C.65000D 00	0.32256D 01
11	0.50000D 00	C.65000D 00	0.30865D 01
12	0.52632D 00	C.65000D 00	0.29490D 01
13	0.55556D 00	C.65000D 00	0.28135D 01
14	0.58824D 00	C.65000D 00	0.26803D 01
15	0.62500D 00	C.65000D 00	0.25499D 01
16	0.66667D 00	C.65000D 00	0.24227D 01
17	0.71429D 00	C.65000D 00	0.22996D 01
18	0.76923D 00	C.65000D 00	0.21813D 01
19	0.83333D 00	C.65000D 00	0.20689D 01
20	0.90909D 00	C.65000D 00	0.19640D 01
21	0.10000D 01	C.65000D 00	0.18685D 01
22	0.11000D 01	C.65000D 00	0.17922D 01
23	0.12000D 01	C.65000D 00	0.17384D 01
24	0.13000D 01	C.65000D 00	0.17017D 01
25	0.14000D 01	C.65000D 00	0.16784D 01
26	0.15000D 01	C.65000D 00	0.16656D 01
27	0.16000D 01	C.65000D 00	0.16613D 01
28	0.17000D 01	C.65000D 00	0.16640D 01
29	0.18000D 01	C.65000D 00	0.16724D 01
30	0.19000D 01	C.65000D 00	0.16856D 01
31	0.20000D 01	C.65000D 00	0.17029D 01
32	0.21000D 01	C.65000D 00	0.17236D 01
33	0.22000D 01	C.65000D 00	0.17473D 01
34	0.23000D 01	C.65000D 00	0.17735D 01
35	0.24000D 01	C.65000D 00	0.18020D 01
36	0.25000D 01	C.65000D 00	0.18325D 01
37	0.26000D 01	C.65000D 00	0.18647D 01
38	0.27000D 01	C.65000D 00	0.18984D 01
39	0.28000D 01	C.65000D 00	0.19335D 01
40	0.29000D 01	C.65000D 00	0.19698D 01
41	0.30000D 01	C.65000D 00	0.20072D 01

## RAIL OVERTURNING

Freydoon Arbabi

Assistant Professor of Civil Engineering  
Michigan Technological University  
Houghton, Michigan 49931

The number of train accidents has increased in recent years. This may be partially attributed to the use of high speed trains and elimination of expansion joints. Derailments are among the significant causes of accident and may be caused by overturning of rail. A better understanding of rail overturning is thus a significant step toward the safe operation and adequate design of the rail system. This paper is concerned with the identification of the significant parameters affecting the instability of the rail system and an improved method of solution. In the first part, the equations governing the behavior of the system are set up. Axial loads induced by a temperature change or braking of locomotives are included in the formulation in addition to the vertical and lateral loads. The torsional and lateral stiffness of the rail, fasteners and ties are represented by means of springs. A parametric study is performed by a direct variational method to establish the values of the significant parameters. The finite element method is then applied, using the derived stiffness matrix, to obtain an accurate solution.

### INTRODUCTION

The number of train accidents has increased in recent years. This is especially true (1)\* with track related accidents. In view of the growth in the gross ton-miles transported and higher speeds, train accidents can be costly in terms of damages and human lives. In 1970 alone, reported derailments cost the American railroads 200 million dollars and led to the death and injury (2) of over 300 people. The problem is often aggravated (3) by the loss of loading of cars carrying hazardous materials. Derailments are among the most significant causes of accidents (4) and are often caused by rail overturning. The use of high speed trains results in higher overturning moments, particularly on curved tracks (5,6). Furthermore, elimination of the expansion joints can induce, under temperature changes or braking of locomotives, axial loads that affect (7-13) the stability of the track. A better understanding of the overturning mechanism can improve the design and safety of the operation of the railroad systems.

### GOVERNING EQUATIONS

For the rail element shown in Figure 1, the  $x$  coordinate is taken along the longitudinal axis of the rail. Thus, the cross-section of the rail is in the  $y-z$  plane of the left handed

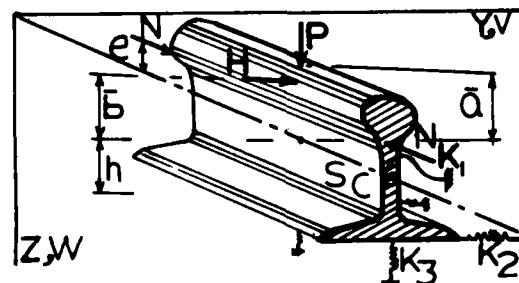


FIG. 1. RAIL SYSTEM

\* Numbers in parentheses refer to the entries in the list of references.

coordinate system. The displacements in the y and z directions are denoted by v and w and the rotation about the x-axis by  $\beta$ . Because of the high yield point of the rail material and the observation that during overturning the stresses remain below the plastic range, in the following derivations only elastic analysis is considered.

The governing equations may be obtained either by a direct method or by an energy approach. The latter method is adopted here. The total energy of the system  $\Pi$ , is the algebraic sum of the elastic energy and the potential energy of the external loads. The elastic energy is composed (14) of two parts: the internal energy of the rail,  $U$ , and the elastic energy of the springs modeling the ties and the fasteners,  $U_s$  where

$$U = \frac{1}{2} \int_0^L [EI_z(v'')^2 + GJ(\beta')^2 + EI_y(w'')^2] dx \quad (1a)$$

and

$$U_s = \frac{1}{2} \int_0^L [K_1\beta^2 + K_2(v-h\beta)^2 + K_3w^2] dx \quad (1b)$$

In the above equations  $E$  is the modulus of elasticity,  $G$  is the shear modulus,  $I_y$ ,  $I_z$  the moments of inertia about the y and the z axes.  $J$  and  $\Gamma$  are torsion and warping constants.  $K_1$ ,  $K_2$ , and  $K_3$  are the torsional, lateral and vertical stiffness of the tie and the fasteners.  $h$  is the distance of the shear center from the base of the rail. A prime indicates derivative with respect to  $x$ . The potential energies of the axial and lateral loads (14) are:

$$V_n = -\frac{1}{2} \int_0^L [N(v')^2 + 2N(Z_0 + e) v'\beta' + N(\frac{I_p}{A_0} + \frac{eX}{I_y}) (\beta')^2 + N(w')^2] dx \quad (1c)$$

$$V_p = -\int_0^L \delta(x-\frac{L}{2}) [P(v\beta + \bar{\alpha}\beta^2 + w) + H(v + \bar{\beta}\beta)] dx \quad (1d)$$

$Z_0$  is the z coordinate of the shear center and  $x$  is a property of the section (14) defined as

$$x = 2Z_0 I_y - \int_A z(y^2 + z^2) dA \quad (1e)$$

$N$  is the axial load,  $p$  and  $H$  are concentrated vertical and horizontal loads transmitted by a wheel acting at  $a$  and  $b$  from the shear center.  $\delta$  is the Dirac function.  $I_p$  is the polar moment of inertia,  $A$  is the area of the cross-section of the rail and  $e$  the eccentricity of the axial load from the shear center. The total energy of the system is:

$$\Pi = U + U_s + U_n + U_p \quad (1e)$$

This expression is used to develop the solution to the problem. As a first step in identifying the significant parameters a direct variational

method is utilized. A more accurate solution is provided by the finite element method which is discussed in a subsequent section.

## DIRECT METHOD

The Rayleigh - Ritz method is used to obtain a solution which is appropriate for parametric studies. Assuming

$$v = A \sin \left( \frac{\pi x}{L} \right) \quad (2a)$$

$$w = B \sin \left( \frac{\pi x}{L} \right) \quad (2b)$$

$$\beta = C \sin \left( \frac{\pi x}{L} \right) \quad (2c)$$

which satisfy the boundary conditions and introducing relations (2) into equations (1), the total potential energy is obtained in terms of the unknown coefficients  $A$ ,  $B$ , and  $C$ . The latter coefficients are then determined by minimizing the total energy of the system. This is done by requiring that the variation of the total potential energy must vanish. The coefficients are obtained as

$$A = (2H\theta_3 - 5H\theta_4)/\Delta \quad (3a)$$

$$B = P/(2\theta_2) \quad (3b)$$

$$C = (25H\theta_1 - H\theta_4)/\Delta \quad (3c)$$

where

$$\theta_1 = \frac{EI_z \pi^4}{4L^3} + \frac{K_2 L}{4} - \frac{N \pi^2}{4L} \quad (3d)$$

$$\theta_2 = \frac{EI_y \pi^4}{4L^3} + \frac{K_3 L}{4} - \frac{N \pi^2}{4L} \quad (3e)$$

$$\theta_3 = \frac{GJ \pi^4}{4L} + \frac{EI_y \pi^4}{4L^3} + \frac{K_1 L}{4} + \frac{K_2 L}{4} h^2 -$$

$$\frac{N \pi^2}{4L} \left( \frac{I_p}{A_0} + \frac{eX}{I_y} \right) - \frac{P \bar{\alpha}}{2} \quad (3f)$$

$$\theta_4 = -\frac{N(Z_0 + e) \pi^2}{2L} + \frac{K_2 L h}{2} + p \quad (3g)$$

$$\Delta = 4\theta_1 \theta_3 - (\theta_4)^2 \quad (3h)$$

Eqs. 2 then give the displacements and rotations at any point along the rail. Discontinuous elastic foundations can be easily handled by the use of Dirac function. The formulas obtained agree for special cases with the available solutions (14).

# DERIVATION OF THE STIFFNESS MATRIX

A major step in this solution technique is the derivation of the element stiffness matrix. Once this is done, the stiffness matrix for the overall system can be obtained and the solution can be carried out. Using interpolation functions.

$$v = A_1 + A_2x + A_3x^2 + A_4x^3 \quad (4a)$$

$$w = B_1 + B_2x + B_3x^2 + B_4x^3 \quad (4b)$$

$$\beta = C_1 + C_2x + C_3x^2 + C_4x^3 \quad (4c)$$

to represent the deformations and rotation within an element the matrix notation is adopted to outline the procedure with T indicating transpose

$$\{x\}^T = (1 \ x \ x^2 \ x^3) \quad (5a)$$

$$\{A\}^T = (A_1 \ A_2 \ A_3 \ A_4)$$

$$\{B\}^T = (B_1 \ B_2 \ B_3 \ B_4)$$

$$\{C\}^T = (C_1 \ C_2 \ C_3 \ C_4)$$

then

$$v = \{x\}^T \{A\} \quad (6a)$$

$$w = \{x\}^T \{B\} \quad (6b)$$

$$\beta = \{x\}^T \{C\} \quad (6c)$$

The derivatives of equations (6) are

$$v'' = \{x''\}^T \{A\} \quad (7a)$$

$$w'' = \{x''\}^T \{B\} \quad (7b)$$

$$\beta' = \{x'\}^T \{C\} \quad (7c)$$

where

$$\{x'\}^T = \langle 0 \ 1 \ 2x \ 3x^2 \rangle \quad (7d)$$

and

$$\{x''\}^T = \langle 0 \ 0 \ 2 \ 6x \rangle$$

Evaluating  $v$ ,  $v'$ ,  $w$ ,  $w'$ ,  $\beta$  and  $\beta'$  in terms of the constant parameters  $\{A\}$ ,  $\{B\}$  and  $\{C\}$  at both ends of the rail segment, i.e. at  $x = 0$  and  $x = l$  results in

$$\begin{Bmatrix} v_1 \\ v'_1 \\ v_2 \\ v'_2 \end{Bmatrix} = \begin{bmatrix} 1 & 0 & 0 & 0 \\ 0 & 1 & 0 & 0 \\ 1 & l & l^2 & l^3 \\ 0 & 1 & 2l & 3l^2 \end{bmatrix} \begin{Bmatrix} A_1 \\ A_2 \\ A_3 \\ A_4 \end{Bmatrix}$$

$v_1$  and  $v_2$  are the displacements in the  $y$  direction at the two ends of the rail segment and  $v'_1$ ,  $v'_2$  rotations at the same points. Similar relationships can be derived for  $w$  and  $\beta$ . These may be obtained by simply replacing  $v$  in eq. 8a by  $w$  or  $\beta$  and  $A$  by  $B$  or  $C$ . Inversion of eq. 8a yields.

$$\begin{Bmatrix} A_1 \\ A_2 \\ A_3 \\ A_4 \end{Bmatrix} = \begin{bmatrix} 1 & 0 & 0 & 0 \\ 0 & 1 & 0 & 0 \\ \frac{-3}{l^2} & \frac{-2}{l} & \frac{3}{l^2} & \frac{-1}{l} \\ \frac{2}{l^3} & \frac{1}{l^2} & \frac{-2}{l^3} & \frac{1}{l^2} \end{bmatrix} \begin{Bmatrix} v_1 \\ v'_1 \\ v_2 \\ v'_2 \end{Bmatrix}$$

or in compact form

$$\{A\} = [a] \{v\} \quad (9a)$$

similarly

$$\{B\} = [a] \{w\} \quad (9b)$$

$$\{C\} = [a] \{\beta\} \quad (9c)$$

Here vector  $\{v\}$  represents the values of  $v$  and its derivatives at both ends of the rail segment.  $\{w\}$  and  $\{\beta\}$  are defined in a similar manner. Substitution of the above equations in the energy expressions for the system yields

$$U = \langle \{v\}^T \ \{w\}^T \ \{\beta\}^T \rangle \begin{bmatrix} EI_z [L^4] & 0 & 0 \\ 0 & EI_y [L^4] & 0 \\ 0 & 0 & GJ [L^3] + EI' [L^4] \end{bmatrix} \begin{Bmatrix} \{v\} \\ \{w\} \\ \{\beta\} \end{Bmatrix} \quad (10a)$$

$$U_s = \langle \{v\}^T \ \{w\}^T \ \{\beta\}^T \rangle$$

$$\begin{bmatrix} K_2 [L] & 0 & -K_2 [L] \\ 0 & K_3 [L] & 0 \\ -hK_2 [L] & 0 & (K_1 + h^2 K_2) [L] \end{bmatrix} \begin{Bmatrix} \{v\} \\ \{w\} \\ \{\beta\} \end{Bmatrix}$$

$$U_n = \langle \{v\}^T \{w\}^T \{\beta\}^T \rangle$$

$$\begin{bmatrix} [L'] & 0 & (Z_0+e)[L'] \\ 0 & [L'] & 0 \\ (Z_0+e)[L'] & 0 & \frac{I_p + e^2 x}{A_0 I_y} [L'] \end{bmatrix} \begin{Bmatrix} \{v\} \\ \{w\} \\ \{\beta\} \end{Bmatrix}$$

where

$$[L] = \int_0^L [a]^T \{x\} \{x\}^T [a] dx$$

$$[L'] = \int_0^L [a]^T \{x'\} \{x'\}^T [a] dx$$

$$[L''] = \int_0^L [a]^T \{x''\} \{x''\}^T [a] dx$$

carrying out the algebra results in

$$[L] = \begin{bmatrix} \frac{48L^3}{35} & \frac{11L^2}{210} & \frac{9L}{70} & -\frac{13L^2}{420} \\ & \frac{L^3}{105} & \frac{13L^2}{420} & \frac{31L^3}{140} \\ \text{Sym} & & \frac{13L}{35} & -\frac{11L^2}{210} \\ & & & \frac{12L^3}{35} \end{bmatrix}$$

$[L']$  and  $[L'']$  are obtained similarly.  $U_p$  does not enter in the calculation of the stiffness matrix. The total potential energy is then

$$\Pi = \langle \{v\}^T \{w\}^T \{\beta\}^T \rangle$$

$$([K_E] + [K_G]) \begin{Bmatrix} \{v\} \\ \{w\} \\ \{\beta\} \end{Bmatrix}$$

$[K_E]$  and  $[K_G]$  are the elastic and geometric stiffness matrices as given below

$$[K_E] = \begin{bmatrix} EI_z [L''] + K_2 [L] & 0 & -hK_2 [L] \\ 0 & EI_y [L''] + K_3 [L] & 0 \\ -hK_2 [L] & 0 & GJ [L'] + EI [L''] + (K_1 + h^2 K_2) [L] \end{bmatrix}$$

$$[K_G] = -N \begin{bmatrix} [L'] & 0 & (Z_0+e)[L'] \\ 0 & [L'] & 0 \\ (Z_0+e)[L'] & 0 & \left( \frac{I_p}{A_0} + \frac{e^2 x}{I_y} \right) [L'] \end{bmatrix}$$

and the element stiffness matrix  $[K]$  is the sum of these two items. The element stiffness matrix is used to form the overall stiffness matrix for the rail system.

#### FINITE ELEMENT SOLUTION TECHNIQUE

Once the stiffness matrices are obtained for different elements or subdivision of the rail, they are assembled to obtain the structural stiffness matrix. The boundary conditions are then imposed and the nodal displacements are computed by solving a system of simultaneous equations. Stresses can be determined from these displacements. This portion of the solution process is the same as for other finite element problems. Since substantial bibliography exists on the subject (15, 16) the details will not be given here.

The critical lateral loads are the values for which the determinant of the structural stiffness matrix vanishes. Thus, the critical values of the loads can be calculated by increasing their values gradually and calculating the determinant. When the determinant changes its sign the approximate value of the critical loads are obtained. More accurate results may be obtained by using smaller load increments and starting from the loads calculated at the previous step. A simpler procedure is to check the diagonal term instead of the determinant. As soon as a diagonal term becomes negative the process is restarted using a smaller load increment. Ref. 17 gives the details of this procedure for obtaining the critical load.

#### NUMERICAL RESULTS

The finite element analysis gives accurate information on the behavior of the rail system. For parametric studies, however, it might be costly in terms of computer time and data preparation efforts. The variational method can be used to depict the significance of the different parameters and to obtain the appropriate model which would then be analyzed by the finite element method.

The overturning of a 100 lb. (45.4 kg) standard rail segment was studied under a set of concentrated horizontal and vertical loads applied at the mid-section. The length varied from 105 to 420 inches (267 to 1067 cm) with the following properties

$$\begin{aligned} E &= 29000 \text{ ksi } (2.04 \times 10^6 \text{ kg/cm}^2) \\ G &= 12000 \text{ ksi } (0.84 \times 10^6 \text{ kg/cm}^2) \\ J &= 2.34 \text{ in}^4 (97.40 \text{ cm}^4) \\ I &= 2.34 \text{ in}^6 (628.4 \text{ cm}^6) \\ I_y &= 42.6 \text{ in}^4 (1773.2 \text{ cm}^4) \\ I_z &= 9.1 \text{ in}^4 (378.8 \text{ cm}^4) \\ I_p &= 51.1 \text{ in}^4 (2127 \text{ cm}^4) \\ K_1 &= 61 \text{ Kips/rad/in } (10893 \text{ kg/rad/cm}) \\ K_2 &= 15 \text{ ksi } (1054 \text{ kg/cm}^2) \\ K_3 &= 29 \text{ ksi } (2039 \text{ kg/cm}^2) \\ A_0 &= 9.82 \text{ in}^2 (63.36 \text{ cm}^2) \\ b &= 3.75 \text{ in } (9.53 \text{ cm}) \\ h &= 1.625 \text{ in } (4.13 \text{ cm}) \end{aligned}$$

Other non-zero values are shown in the figures. Because of the rather high stiffness of the rail system, the length of the rail segment is a significant parameter and must be chosen such that the effect of the boundary conditions are not significant at the section considered. The axial load commonly caused by temperature changes or by braking of locomotives was much below the critical axial load. Furthermore, the eccentricity of the axial load did not have a significant effect. Figures 2 and 3 show the variation of the rotation at the mid-section of the rail segment with the axial load under a lateral load of 20 Kips (9090 kg) and a lateral and vertical load of 40 Kips (18180 kg) each. The rotation increases due to increases in the horizontal and vertical forces.

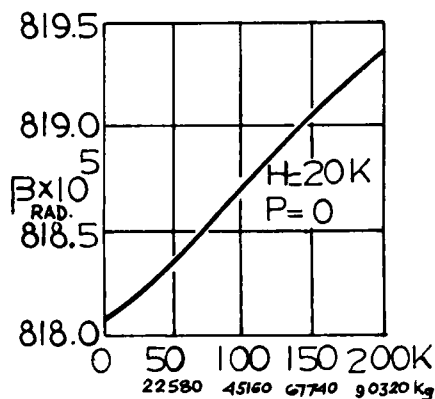


FIG. 2. N

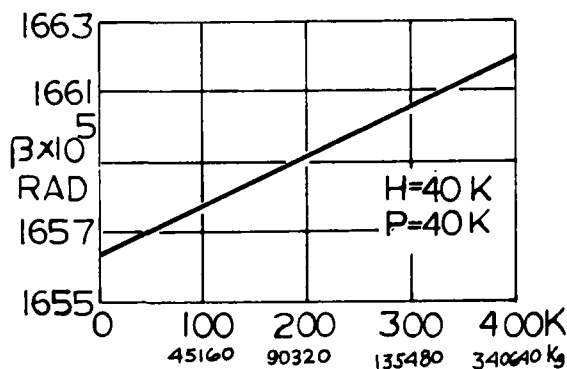


FIG. 3. N

The variation of the lateral displacement with respect to the horizontal force is shown in Fig. 4. The lateral displacement directly increases with the horizontal force. The effect of the lateral load on the rotation is shown in Fig. 5. For small values of horizontal loads the relationship is almost linear. For higher values of horizontal load the rotation increases very rapidly.

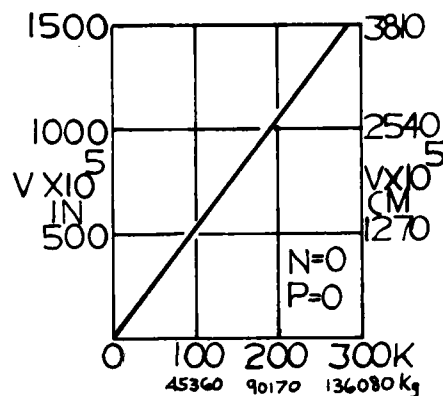


FIG. 4. N

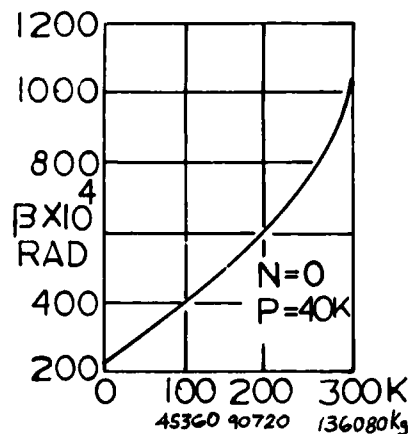


FIG. 5. H

#### CONCLUSION

The stability of a rail system was examined against overturning. A variational solution was used to study the effect of the different parameters affecting the stability. The derivation of the stiffness matrix and a finite element solution technique were then discussed. The variational method was used to establish the values of parameters for which the accurate solution could be obtained by the finite element method.

# LIST OF REFERENCES

1. "Analysis of Nine Years of Railroad Accident Data 1968-1974," Association of American Railways, Report No. R-223 (1975).
2. Proceeding, Conference on Track-Train Dynamic Interactions, pp. 204-205, Vol. 1 of 2, Chicago, Ill. (Dec. 1971).
3. Hohenemser, K. H., Diboll, W. B., Yin, S.K. and Szabo, B. A., "Computer Simulation of Tank Car Head Puncture Mechanism," Department of Transportation Report No. FRA-OR & 75-23 prepared at Washington University (Feb. 1975).
4. Rose, C. F., "Railway Accidents," Her Majesty's Stationary Office, London, England (1970).
5. "Tracking Test of an Eighty-five Foot Flat Car Trailer Carrier on the Burlington Railroad," Association of American Railroads Report No. ER-69 (Oct. 1966).
6. "Lateral Forces on Track and Equipment Due to Dynamic Braking on the Southern Pacific Line," Association of American Railroads Report No. ER-69 (Oct. 1966).
7. Martinet, M. A., "Flambement des Voies sans Joint sur Ballast et Rails de Grande Longueur," Revue Genral des Chemin de Fer (1936).
8. Hay, H. H., Railroad Engineering, Vol. 1. John Wiley & Sons, Inc. New York, N.Y., (1953).
9. Kawaguchi, M. "Thermal Buckling of Continuous Pavements," Proc. of the Japan Soc. of Civil Eng. No. 170 (Oct. 1969).
10. Kerr, A. D., "On the Stability of the Railroad Track in the Vertical Plane," Rail International pp. 132-142 (Feb. 1974).
11. Kerr, A.D., "A Model Study of Vertical Track Buckling," High Speed Gound Transportation Journal, Vol. 7, No. 3 pp. 251-368 (1973).
12. Kerr, A. D., "Lateral Buckling of Tracks Due to Constrained Thermal Expansions," Proc. of the Sym. of Track Mechanics, Princeton University, Princeton, N. J. (Apr. 1975).
13. Marek, P. V., and Daniels, J. H., "Behavior of Continous Crane Rails," ASCE J. of Struc. Div. Vol. 97, No. ST4, Proc. paper 8067, pp. 1081-1095 (Apr. 1971).
14. Bleich, F., Buckling Strength of Metal Structures, McGraw Hill (1952).
15. Clough, R. W., "The Finite Element Method in Structural Mechanics," in Stress Analysis by Zienkiewicz, O. C. and Holister, G. S. (1965).
16. Zienkiewicz, O. C., The Finite Element Method in Engineering Science, McGraw Hill (1971).
17. Powell, G. and Klingner, R., "Elastic Lateral Buckling of Steel Beams," ASCE Journal of Struc. Div. (Sept. 1970).

# SYSTEMS IDENTIFICATION

## APPLICATION OF MODERN PARAMETER ESTIMATION METHODS TO VIBRATING STRUCTURES

William R. Wells  
Wright State University  
Dayton, Ohio

The application of modern parameter estimation methods to the problem of identifying the mass, stiffness, and damping matrices of vibrating systems is discussed. In particular, emphasis is given to the use of the combined disciplines of estimation and optimal control theory in the design of forcing functions for efficient system parameter extraction. Numerical results are presented for the case of a vibrating spring-mass-damper system.

### INTRODUCTION

Hart [1] has investigated via least squares and regression methods, the identification of the natural periods of vibration associated with high rise buildings. Wells [2] has applied the Newton-Raphson algorithm to the identification of the stiffness constant in a simple vibrating system. However, the wide applicability of current parameter identification techniques has not been addressed to the more general problem of improvement in sensor design and data processing for more complicated systems. In addition, further improvement in structural system modeling may be forthcoming by combining the disciplines of modern optimal control theory and identification to achieve more efficient input functions in vibration testing. [3] - [5]

A typical design problem is to choose the forcing input which sufficiently excites the modes of vibration to allow for reliable estimates of the physical parameters. One means of achieving this is to maximize the trace of the information matrix which arises in the estimation formulation.

### PROBLEM FORMULATION

The equations for the forced small motions of a vibrating system can be written in conventional form as [6]

$$m \ddot{q}(t) + c \dot{q}(t) + k q(t) = Q(t) \quad (1)$$

where  $m$ ,  $c$ , and  $k$  are the mass, damping and stiffness matrices respectively. Since system identification is generally performed in state space instead of configuration space as

represented by equation (1), the  $n$  second order equations (1) are transformed into  $2n$  first order equations having the matrix form

$$\dot{x}(t) + G x(t) = u(t) \quad (2)$$

where

$$\begin{aligned} x(t) &= [\dot{q}^T(t) : q^T(t)]^T \\ u(t) &= [Q^T(t) : 0^T]^T \end{aligned} \quad (3)$$

are the  $2n$ -dimensional state vector and associated generalized input vector, respectively, and

$$M = \begin{bmatrix} 0 & I & m \\ m & & c \end{bmatrix} \quad G = \begin{bmatrix} -m & 0 \\ 0 & k \end{bmatrix} \quad (4)$$

are  $2n \times 2n$  "inertia and stiffness matrices", respectively.

Finally, the system dynamics are written as

$$\dot{x} = f(x, p) + g(p) u \quad (5)$$

where

$$f(x, p) = -M^{-1} G x, \quad g(p) = M^{-1} \quad (6)$$

are denoted as explicit functions of the system parameter vector  $p$  to be estimated. The system output or measurement from which the vector  $p$  is to be extracted is assumed to consist of the system state components and a gaussian white noise process with zero mean and covariance  $R$ ,

$$y = x + v \quad (7)$$



and

$$E[v(t_i)] = 0, \quad E[v(t_i) v^T(t_j)] = R \delta_{ij} \quad (8)$$

Further the initial and final times are considered known and fixed and the input amplitude may or may not be constrained according to

$$|u_i| \leq U_i, \quad (i = 1, 2, \dots, r) \quad (9)$$

#### MAXIMUM LIKELIHOOD ESTIMATION

The popularity of the maximum likelihood estimate lies in the fact that it gives asymptotically unbiased minimum variance estimates of the unknown parameters; that is, it results in an unbiased estimate with variance which approaches the Cramer-Rao lower bound as the data record increases without bound. In case of negligible process noise, the method simplifies to the modified Newton-Raphson method and in the case of negligible measurement noise, the method simplifies to the weighted least squares method.

The likelihood function to be maximized is taken as

$$L(p, R) = -\frac{1}{2} \sum_{i=1}^N v^T(t_i) R^{-1} v(t_i) - \frac{N}{2} \log |R| \quad (10)$$

This function can be put into a form convenient for maximizing if  $x$  is expanded in a Taylor's series about a nominal guess at  $p_0$  and only linear terms retained.

If  $L(p, R)$  is maximized with respect to  $p$  and  $R$  the following expressions result

$$\hat{p} = p_0 + \left[ \sum_{i=1}^N A^T(t_i) R^{-1} A(t_i) \right]^{-1} \left[ \sum_{i=1}^N A(t_i) R^{-1} v(t_i) \right] \quad (11)$$

$$\hat{R} = \frac{1}{N} \sum_{i=1}^N v(t_i) v^T(t_i) \quad (12)$$

where  $A$  is the system sensitivity matrix  $\frac{\partial x}{\partial p}$

whose elements satisfy

$$\frac{d}{dt} \left( \frac{\partial x_i}{\partial p_j} \right) = \sum_{k=1}^N \frac{\partial f_i}{\partial x_k} \frac{\partial x_k}{\partial p_j} + \frac{\partial f_i}{\partial p_j} \quad (13)$$

with initial conditions

$$\frac{\partial x_i}{\partial p_j}(t_0) = 0, \quad (i=1, 2, \dots, 2n; j=1, 2, \dots, m) \quad (14)$$

and

$$v(t_i) = y(t_i) - x(p_0, t_i) \quad (15)$$

The asymptotic value of the covariance of the error in the estimate is

$$E \left[ (p - \hat{p}) (p - \hat{p})^T \right] = \left[ \sum_{i=1}^N A^T(t_i) \hat{R}^{-1} A(t_i) \right]^{-1} \quad (16)$$

which is the Cramer-Rao lower bound on the covariance of the estimate for the case of  $N$  discrete measurements.

#### OPTIMAL INPUT DESIGN

In addition to the state equation expressed by equation (15), it will prove useful to introduce additional state variables defined by the elements of the sensitivity matrix and the time dependent continuous form of the Cramer-Rao lower bound matrix which satisfies the equations

$$\dot{C}(t) = -C(t) A^T(t) R^{-1} A(t) C(t) \quad (17)$$

$$C(t_f) = \left[ \int_{t_0}^{t_f} A^T(t) R^{-1} A(t) dt \right]^{-1} \quad (18)$$

This results in an augmented state vector

$$x = [x^T \ C^{(1)T} \dots C^{(m)T} \ A^{(1)T} \dots A^{(n)T}]^T \quad (19)$$

where

$$C^{(1)} = [C_{11}, C_{22}, \dots, C_{mm}]^T$$

$$C^{(2)} = [C_{12}, C_{23}, \dots, C_{m-1, m}]^T$$

$$C^{(m)} = C_{1m}$$

$$A^{(1)} = \left[ \frac{\partial x_1}{\partial p_1}, \frac{\partial x_1}{\partial p_2}, \dots, \frac{\partial x_1}{\partial p_m} \right]^T$$

$$A^{(n)} = \left[ \frac{\partial x_n}{\partial p_1}, \frac{\partial x_n}{\partial p_2}, \frac{\partial x_n}{\partial p_2}, \dots, \frac{\partial x_n}{\partial p_m} \right]^T$$

The performance index to be minimized for the optimal input can now be stated in the

conventional form as

$$J = \phi[X(t_f)] + \int_{t_0}^{t_f} L[X(t), u(t), t] dt \quad (20)$$

For instance, one might wish to minimize individual elements of the trace of the covariance matrix which represent the quality of the estimate. Another choice might be to minimize or to reduce a high statistical correlation between various parameters in the system.

#### ILLUSTRATIVE EXAMPLE

The system shown in Fig. 1(a) can be regarded as an idealized mathematical model of an automobile. The body is a rigid bar with mass  $\mu$  with mass center at distances  $a$  and  $b$  from the springs  $k_1$  and  $k_2$  and dampers  $c_1$  and  $c_2$  which simulate the suspension system. The body has a mass moment of inertia  $I$  about its center. The automobile rests on a horizontal table which can be accelerated vertically by application of a forcing function  $F(t)$  at the center of gravity of the body. Fig. 1(b) shows a free-body diagram for the body in a displaced position. The displacements are the vertical translation  $z(t)$  of the mass center from equilibrium and a rotation  $\theta(t)$  about the mass center.

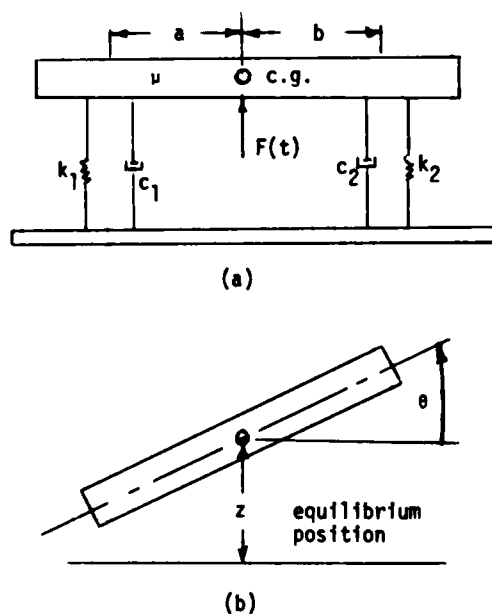


Fig. 1 - Vibrating system

The linearized equations of motion for the system are

$$\begin{aligned} \mu \ddot{z} + (c_1 + c_2) \dot{z} - (c_1 a - c_2 b) \dot{\theta} \\ + (k_1 + k_2) z - (k_1 a - k_2 b) \theta = F(t) \\ I \ddot{\theta} - (a c_1 - b c_2) \dot{z} - (c_1 a - c_2 b) \dot{\theta} \\ + (k_1 + k_2) z + (k_1 a^2 + k_2 b^2) \theta = 0 \end{aligned}$$

The corresponding mass, damping and stiffness matrices are, respectively

$$m = \begin{bmatrix} \mu & 0 \\ 0 & I \end{bmatrix}, \quad c = \begin{bmatrix} c_1 + c_2 - (c_1 a - c_2 b) \\ - (c_1 a - c_2 b) \quad c_1 a^2 + c_2 b^2 \end{bmatrix}$$

and

$$k = \begin{bmatrix} k_1 + k_2 & - (k_1 a - k_2 b) \\ - (k_1 a - k_2 b) & k_1 a^2 + k_2 b^2 \end{bmatrix}$$

The state and control vectors are

$$x(t) = [\dot{z}, \dot{\theta}, z, \theta]^T, \quad u(t) = [F(t), 0]^T$$

and the 4 x 4 inertia and stiffness matrices are

$$M = \begin{bmatrix} 0 & 0 & \mu & 0 \\ 0 & 0 & 0 & I \\ \mu & 0 & c_1 + c_2 & - (c_1 a - c_2 b) \\ 0 & I & - (c_1 a - c_2 b) & c_1 a^2 + c_2 b^2 \end{bmatrix}$$

and

$$G = \begin{bmatrix} -\mu & 0 & 0 & 0 \\ 0 & -I & 0 & 0 \\ 0 & 0 & k_1 + k_2 & - (k_1 a - k_2 b) \\ 0 & 0 & - (k_1 a - k_2 b) & k_1 a^2 + k_2 b^2 \end{bmatrix}$$

For purposes of data gathering, an accelerometer is assumed placed at the body center of mass to measure  $\ddot{z}(t)$  from which  $z(t)$  is obtained. This gives a scalar measurement

$$y = z + v$$

with covariance  $R = r$ .

For this example, the unknown parameter vector is taken as

$$p = [k_1, k_2, c_1, c_2]^T$$

for which the sensitivity matrix is

$$A(t) = \begin{bmatrix} \frac{\partial \dot{z}}{\partial k_1} & \frac{\partial \dot{z}}{\partial k_2} & \frac{\partial \dot{z}}{\partial c_1} & \frac{\partial \dot{z}}{\partial c_2} \\ \frac{\partial \ddot{z}}{\partial k_1} & \frac{\partial \ddot{z}}{\partial k_2} & \frac{\partial \ddot{z}}{\partial c_1} & \frac{\partial \ddot{z}}{\partial c_2} \\ \frac{\partial \dot{\theta}}{\partial k_1} & \frac{\partial \dot{\theta}}{\partial k_2} & \frac{\partial \dot{\theta}}{\partial c_1} & \frac{\partial \dot{\theta}}{\partial c_2} \\ \frac{\partial \ddot{\theta}}{\partial k_1} & \frac{\partial \ddot{\theta}}{\partial k_2} & \frac{\partial \ddot{\theta}}{\partial c_1} & \frac{\partial \ddot{\theta}}{\partial c_2} \end{bmatrix}$$

The computational aspects of this type problem are basically to treat the minimization problem as one of determining the switching history of the resulting bang-bang control law; that is, consider  $J$  to be an explicit function of a finite unknown set of constants representing switching times,  $T_1, T_2, \dots, T_N$ . The switching times are then determined by a direct search method of Hooke and Jeeves [7] with modifications developed by Weisman [8].

Shown in Figure 2 are an initial non-optimal forcing function and the corresponding optimal design obtained from the analysis. The correlations between the elements of the parameter vector for the two inputs are presented in Table I. High correlations near unity exist between the stiffness coefficients and damping coefficients for the non-optimal design. These correlations are reduced by about 50 percent in the case of the optimal forcing function.

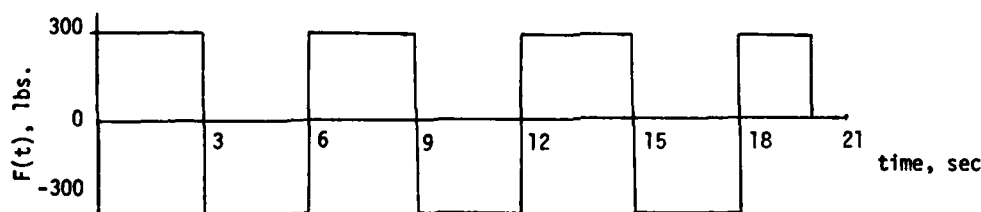


Fig. 2(a) - Non-optimal excitation

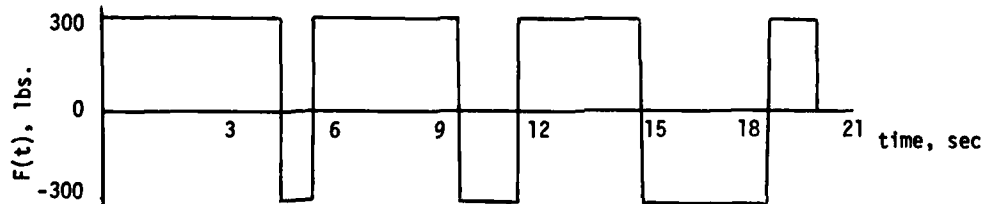


Fig. 2(b) - Optimal excitation

## CONCLUSIONS

The feasibility of improving upon the estimation of physical parameters by combining the disciplines of modern optimal control theory and identification has been considered. Numerical simulations were performed which suggest high confidence levels in the predicted values using specially designed input of forcing functions. However, at this time no comparison has been made to ascertain the relative improvement, if any, over the more conventional sweep test.

## REFERENCES

- 1) Hart, Gary C., and Torkamani, M.A.M., "Structural System Identification", Stochastic Problems in Mechanics, Univ. of Waterloo Press, 1974.
- 2) Wells, W.R., "Stochastic Parameter Estimation for Dynamic Systems", Shock and Vibration Digest, Vol. 7, No. 2, Feb. 1975.
- 3) Mehra, R.K., "Optimal Inputs for Linear System Identification", IEEE Transactions on Automatic Control, Vol. AC-19, No. 3, June 1974.
- 4) Goodwin, G.C., "Input Synthesis for Minimum Covariance State and Parameter Estimation", Electronics Letters, Vol. 5, No. 21, October 16, 1969.
- 5) Aoki, M. and Staley, R.M., "On Input Signal Synthesis in Parameter Identification", Automatica, Vol. 6, 1970.
- 6) Meirovitch, L., "Elements of Vibration Analysis", McGraw-Hill Book Company, New York, 1975.
- 7) Hooke, R., and Jeeves, T.A., "Direct Search Solution of Numerical and Statistical Problems", J. Assoc. Com. Mach., Vol. 8, No. 2, 1961.
- 8) Weisman, J. et.al., "Optimal Design of Chemical Process Systems", Chem. Engr. Progr. Symp. Ser., Vol. 61, No. 55, 1965.

TABLE I  
Correlation Matrix

Non-Optimal Exciting Function					Optimal Exciting Function				
	$k_1$	$k_2$	$c_1$	$c_2$		$k_1$	$k_2$	$c_1$	$c_2$
$k_1$	1.000	-0.841	-0.006	0.020		1.000	-0.437	-0.002	-0.009
$k_2$		1.000	-0.108	-0.004			1.000	0.004	-0.002
$c_1$			1.000	-0.862				1.000	-0.484
$c_2$				1.000					1.000

ANALYSIS OF VIBRATION RECORDS BY  
DATA DEPENDENT SYSTEMS

Sudhakar M. Pandit  
Associate Professor  
Department of Mechanical Engineering -  
Engineering Mechanics  
Michigan Technological University  
Houghton, Michigan 49931

The paper outlines a recently developed methodology called Data Dependent Systems (DDS), which provides mathematical models derived from and dependent upon the recorded or observed data alone, without requiring an a priori knowledge of the underlying systems. After summarizing the concept, basic theorems, and related mathematical results of DDS, its modeling procedure is given which directly leads to the differential equations from the descriptized vibration records. By means of machine-tool chatter vibration records, it is shown how the DDS provides smooth and readily interpretable plots of spectra and autocorrelation, and gives a complete modal analysis including natural frequency, damping ratio and proportion of power/energy for each mode. Decomposition of a complex high order system into simple subsystems to aid the physical identification and stability assessment is illustrated. The strength and versatility of the methodology is underlined by a brief survey of its applications in the literature.

INTRODUCTION

With the phenomenal advances in instrumentation and data processing in recent years, accurately recorded data are available in many diverse fields: Machine-tool chatter or seismic records in engineering and physical sciences, cardiograms or electroencephalograms (EEG) in biological sciences, and stock prices or sales history in business and economics are a few typical examples. Many of the data sets exhibit a periodic or pseudo-periodic behavior, and hence may be broadly termed as vibration records, or more precisely random vibration records.

A good understanding of the underlying system useful for design, prediction and control requires a mathematical model, which fits the data well and also describes the system in a physically meaningful way. To get such models by the existing methods, one has to idealize the system by some simplifying

assumptions and then alter these assumptions so that the resultant model provides a response similar to the available data. It is impossible to get meaningful models by such a method for many of the present-day complex systems. Then, one has to be satisfied with the qualitative and often deceptive information provided by the characteristics such as autocorrelations or spectra of the records obtained by suitable instrumentation from the random vibration signals [1]. The extensive literature on system identification [e.g. 2] is of little help when the model is unknown.

This paper presents a recently developed methodology called Data Dependent Systems (DDS) which provides accurate mathematical models directly from the recorded data without requiring any other knowledge of the system. Once obtained by feeding the data to the available computer routines, these models in the form of differential/

difference equations can be used for mathematical system analysis, design, prediction and control in much the same way as the classical models. Moreover, these models also provide smooth qualitative plots of characteristics such as the autocorrelation function, the spectrum and the impulse response function, which are clearer, closer to the true ones, and much easier to interpret compared to those obtained by instrumentation or by statistical estimation and time series analysis.

The first section of this paper briefly summarizes the philosophy and the concept of the DDS. The principal theorems and mathematical results on which it is founded are given in section 2. A modeling procedure based on these results is outlined in section 3. The salient features of the methodology are illustrated by the analysis of machine-tool chatter vibration records in section 4 and some of its recent applications in the literature are reviewed in section 5. Although this paper is restricted to single or univariate records, extensions and suitable references for multivariate records and their application to design, prediction, control and optimization are indicated in section 6.

## 1. Data Dependent Systems

A quantitative analysis of the system underlying the observed data requires a mathematical model for its behavior. Usually certain unknown parameters of the model are estimated on the basis of observed data as well as other factors and then the model response is used for analysis, prediction, design and control. The formulation of the model requires a rather thorough understanding of the system. Based on such an understanding the system is idealized and some general laws such as Newton's laws of motion are applied to it. This yields a set of, say, differential equations, which form the mathematical model describing the system behavior [3].

Such an approach is often ineffective to deal with the vibration records obtained from many of the modern complex systems, typified at the beginning of the paper. It is not possible to idealize these systems sufficiently accurately to apply some general laws from physics, mechanics or chemistry. It is also virtually impossible to conjecture general laws about the microscopic or macroscopic behavior of these systems which can lead us to the desired mathematical model.

Our lack of understanding of the physical mechanism giving rise to the observed data prevents us from formulating the mathematical model. However, the observed data or vibration record fully incorporates this missing knowledge of the basic mechanism relevant to the measured variable. Therefore, a systematic quantitative analysis of the observed data should be able to provide us with this missing knowledge. Then the system equations, which cannot be derived from the unknown physical mechanism, can now be developed from the observed data alone. The system as represented by these equations derived from and dependent upon the data, may be called as the "Data Dependent System", (DDS). This concept of obtaining system equations from the observed data alone was advanced in [4] and later elaborated and developed with the requisite mathematical formulation in [5].

The DDS approach uses least square techniques to fit a series of differential/difference equations to the observed data until statistically adequate approximation is reached. When the data gathering procedure is such that the data "truly" reflects the behavior of the underlying physical system, the DDS provides its true representation and can be used for the purposes of system analysis in much the same way as the conventional methods. Even when the data is such that no such underlying physical system can be identified, the DDS models can still be used for characterization, prediction, and control, on the basis of an abstract system represented by the model. The methodology is diagrammatically represented in Fig. 1.

## 2. Basic Mathematical Results

The DDS approach is founded on two basic theorems. These theorems, together with some related results, are summarized in this section from [5,6], wherein their detailed proof may be found.

A DDS is inherently stochastic in nature due to the presence of random influences. For the purpose of mathematical analysis it may be assumed to be stationary over a reasonable length of recorded data, which implies a fixed mean and covariance structure. In practice these assumptions are not restrictive since non-stationary components, if present, can be removed by sinusoidal, linear, or exponential trends.

The first question, therefore, is what kind of models or equations can be used to represent such a system. This

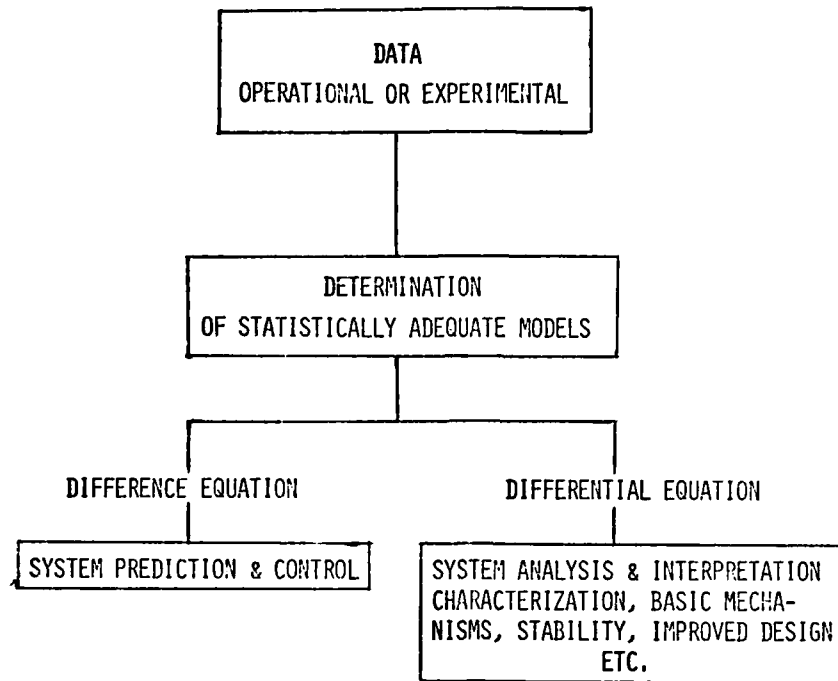


Fig. 1 Diagram of the DDS Methodology

question is answered by the first basic theorem called the "Fundamental Theorem" of stationary stochastic systems (or time series). The Fundamental Theorem states that an arbitrary stationary stochastic system can be represented as closely as we want by a model

$$\begin{aligned}
 & \frac{d^n X(t)}{dt^n} + \alpha_{n-1} \frac{d^{n-1} X(t)}{dt^{n-1}} + \dots \\
 & + \alpha_1 \frac{dX(t)}{dt} + \alpha_0 X(t) \\
 & = b_{n-1} \frac{d^{n-1} Z(t)}{dt^{n-1}} + \dots \\
 & + b_1 \frac{dZ(t)}{dt} + Z(t) \\
 & E[Z(t)] = 0 \\
 & E[Z(t)Z(t-u)] = \delta(u)\sigma_z^2
 \end{aligned} \tag{1}$$

where  $Z(t)$  is the white noise,  $X(t)$  is the system response,  $E$  denotes the expectation operator,  $\delta(u)$  is the Dirac delta function,  $\alpha_0, \alpha_1, \dots, \alpha_{n-1}$  are autoregressive parameters (AR), and  $b_1, b_2, \dots, b_{n-1}$  are moving average (MA) parameters. The model (1) is called an Autoregressive Moving average model of

order  $n$  and  $n-1$  respectively and denoted by  $AM(n, n-1)$ . In particular some of the  $b_i$ 's,  $i=n-1, n-2, \dots, 1$ , may be zero so that we get an  $AM(n, m)$  model with  $m \leq n-1$ . When all the  $b_i$ 's are zero we get a pure Autoregressive model denoted by  $A(n)$ .

The  $AM(n, m)$  models considered above give the system response in continuous time. However, it is more convenient to record and analyze the discrete data obtained from the system, sampled at uniform intervals. It is therefore important to know the discrete representation of such a uniformly sampled system. This is provided by the Uniform Sampling Theorem, which states that when an  $AM(n, m)$  system is sampled at uniform intervals  $\Delta$  it can be represented by a stochastic difference equation

$$\begin{aligned}
 & X_t - \phi_1 X_{t-1} - \phi_2 X_{t-2} - \dots \\
 & - \phi_n X_{t-n} = a_t - \theta_1 a_{t-1} - \theta_2 a_{t-2} \\
 & - \dots - \theta_{n-1} a_{t-n+1} \\
 & E[a_t] = 0 \\
 & E[a_t a_{t-k}] = \delta_k \sigma_a^2
 \end{aligned} \tag{2}$$

where  $\delta_k$  is the Kronecker delta which is zero for  $k \neq 0$ , and one for  $k = 0$ . Equation (2) is called a Uniformly Sampled Autoregressive Moving-average model of order  $n, m$  and denoted by USAM( $n, m$ ). In the special case when  $m = 0$  it is denoted by USA( $n$ ).

The parametric relationships between the two representations AM( $n, m$ ) and USAM( $n, m$ ) are given by

$$(1 - \phi_1 B - \phi_2 B^2 - \dots - \phi_n B^n) \equiv (1 - \lambda_1 B) \cdot (1 - \lambda_2 B) \dots (1 - \lambda_n B) \quad (3a)$$

$$\text{i.e.} \quad \phi_k = (-1)^{k+1} \sum_{\substack{i_1, i_2, \dots, i_k=1 \\ i_1 < i_2 < \dots < i_k}}^n \lambda_{i_1} \lambda_{i_2} \dots \lambda_{i_k}, \quad k=1, 2, \dots, n \quad (3b)$$

$$\theta_\ell = \sum_{i,j=1}^n R(\mu_i) \bar{R}(\mu_j) \frac{V_i \bar{V}_j}{\mu_i + \bar{\mu}_j} \cdot (\lambda_i \bar{\lambda}_j - 1) \sum_{k=0}^{\ell} \phi_k \lambda_i^{\ell-k} \quad (4)$$

$$\sum_{i,j=1}^n R(\mu_i) \bar{R}(\mu_j) \frac{V_i \bar{V}_j}{\mu_i + \bar{\mu}_j} (\lambda_i \bar{\lambda}_j - 1) \quad (5)$$

$$\phi_0 = -1$$

$$\ell = 1, 2, \dots, n-1$$

$$\sigma_a^2 = \frac{\sigma_z^2}{|V|^2} \sum_{i,j=1}^n R(\mu_i) \bar{R}(\mu_j) V_i \bar{V}_j \cdot \frac{(\lambda_i \bar{\lambda}_j - 1)}{(\mu_i + \bar{\mu}_j)}$$

where the bar denotes complex conjugates,  $\mu_1, \mu_2, \dots, \mu_n$  are the characteristic roots of the differential eq. (1), i.e.

$$D^n + \alpha_{n-1} D^{n-1} + \dots + \alpha_1 D + \alpha_0 = (D - \mu_1)(D - \mu_2) \dots (D - \mu_n) \quad (6)$$

$$\lambda_i = e^{\mu_i \Delta}, \quad i=1, 2, \dots, n \quad (7)$$

and

$$V = \prod_{\substack{i,j=1 \\ i>j}}^n (\mu_i - \mu_j) \quad (8)$$

$$V_k = (-1)^{n+k} \prod_{\substack{i,j=1 \\ i,j \neq k \\ i>j}}^n (\mu_i - \mu_j)$$

$k=1, 2, \dots, n$

$$R(\mu) = b_m \mu^m + b_{m-1} \mu^{m-1} + \dots + b_1 \mu + 1 \quad (9)$$

It can be shown that for the USAM( $n, m$ ) model eq. (2) the inverse function  $I_j$  defined by

$$X_t = \sum_{j=1}^{\infty} I_j X_{t-j} + a_t \quad (10)$$

satisfies

$$\phi_k = I_k - \theta_1 I_{k-1} - \theta_2 I_{k-2} - \dots - \theta_m I_{k-m}, \quad k=1, 2, \dots \quad (11)$$

with  $I_0 = -1$ ,  $\phi_k = 0$  for  $k > n$ ,

$$m = \min(k, n-1).$$

Good estimates of the  $I_j$  function can be obtained by truncating the infinite series in eq. (10) as

$$X_t = \hat{I}_1 X_{t-1} + \hat{I}_2 X_{t-2} + \dots + \hat{I}_p X_{t-p} + a_t \quad (12)$$

for large enough  $p$  and then estimating  $I_j$ 's by linear least squares method. Substituting these  $I_j$  in eq. (11) one can get rough estimates of  $\phi_i$  and  $\theta_i$  and then the relations (3-4) can be used to get the initial estimates of  $\alpha_i$  and  $b_i$ .

The explicit expression for the autocovariance function of an AM( $n, m$ ) model is

$$\gamma(s) = E[X(t)X(t-s)]$$

$$= - \frac{\sigma_z^2}{|V|^2} \sum_{i,j=1}^n R(\mu_i) \bar{R}(\mu_j) V_i \bar{V}_j \cdot \frac{e^{\mu_i s}}{(\mu_i + \bar{\mu}_j)} \quad (13)$$



whereas its Fourier transform, the auto-spectrum, is given by

$$f(\omega) = \sigma_z^2 |b_m(i\omega)^m + b_{m-1}(i\omega)^{m-1} + \dots + 1|^2 / 2\pi |i\omega|^n + \alpha_{n-1}(i\omega)^{n-1} + \dots + \alpha_0|^2 \quad (14)$$

where  $i = \sqrt{-1}$

The spectral moments defined by

$$m_{2k} = \int_{-\infty}^{\infty} \omega^{2k} f(\omega) d\omega \quad (15)$$

can be evaluated, when they exist, as

$$m_{2k} = \frac{(-1)^k \sigma_z^2}{ds^{2k}} [\gamma(s)] \Big|_{s=0} = (-1)^{k+1} \frac{\sigma_z^2}{|V|^2} \sum_{i,j=1}^n \quad (16)$$

$$\cdot R(\mu_i) \bar{R}(\mu_j) V_i \bar{V}_j \frac{\mu_i^{2k}}{(\mu_i + \mu_j)}$$

It follows from eqs. (13-16) that the variance

$$m_0 = \gamma(0) = \sum_{i=1}^n R(\mu_i) V_i \quad (17)$$

$$\cdot \left( \sum_{j=1}^n \frac{-\sigma_z^2}{|V|^2} \bar{R}(\mu_j) \bar{V}_j \frac{1}{\mu_i + \mu_j} \right)$$

where each term in the outer summation gives the contribution to the variance or power by the characteristic roof  $\mu_i$ . It is thus seen that once an AM(n,m) model is known the autospectrum and its moments, important in many applications dealing with excursions of random vibrations, can be immediately obtained by eqs. (14-16). It should be noted that for an AM(n,m) model only moments of the order  $2k$ , with  $k < (n-m)$ , exist.

### 3. Modeling Procedure

A modeling procedure developed for

obtaining AM(n,m) models from a set of uniformly sampled data on a system will now be described briefly. Since the Fundamental Theorem assures us that any stationary stochastic system can be approximated as closely as we want by an AM(n,n-1), the procedure consists of fitting models of higher and higher order  $n$  until statistically adequate fit is obtained. If the adequate model is AM(n,m) with  $m < n-1$ , including A(n), this will be indicated by the corresponding  $b_i$  parameters close to zero. For practical as well as theoretical reasons it is advisable to increase  $n$  in steps of two, that is, successively fit AM(2n, 2n-1) models for  $n=1,2,\dots$ .

As the available data is in the form of a discrete set of  $N$  observations it is the USAM(n,m) model which is used for fitting. For each  $n$  the form of this model is completely determined. Then the estimates of the parameters  $\alpha_0, \alpha_1, \dots, \alpha_n$  and  $b_1, b_2, \dots, b_m$  can be obtained by a nonlinear least squares computer routine which minimizes the sum of squares of  $a_t$ 's in the USAM(n,m) model given by eq. (2). The required parameters  $\phi_1, \phi_2, \dots, \phi_n$  and  $\theta_1, \theta_2, \dots, \theta_{n-1}$  are set as functions of  $\alpha_0, \alpha_1, \dots, \alpha_n$  and  $b_1, b_2, \dots, b_m$  by incorporating the relationships (3 to 9) in the computation.

The iterative nonlinear least squares routine requires initial values to start with. These initial values can be obtained by substituting the estimates obtained by eqs. (10-12) as discussed in section 2. Once the initial values are provided the nonlinear least square routine will monitor the values of  $\alpha_0, \alpha_1, \dots, \alpha_n, b_1, b_2, \dots, b_m$  and the mean  $\mu$  if necessary, until the sum of squares of  $a_t$ 's is minimized. The  $a_t$ 's are recursively computed for each set of parameters chosen by the routine from eq. (2), i.e.

$$a_t = X_t - \phi_1 X_{t-1} - \dots - \phi_n X_{t-n} + \theta_1 a_{t-1} + \theta_2 a_{t-2} + \dots + \theta_{n-1} a_{t-n+1}$$

The computation is started from  $t=n+1$  and  $a_t$ 's for  $t \leq n$  are taken as zero.

AM(n,n-1) models of higher and higher order are fitted until the reduction in the minimum sum of squares of  $a_t$ 's obtained by increasing  $n$  is insignificantly small. The final model is examined to see if some of the  $b_i$ 's and the last  $\phi_i$  are close to zero. If so, then these parameters are dropped and the resultant model refitted to see

if it also gives an adequate fit. Comparing the sum of squares of this model with the AM(n,n-1) model, the adequate AM(n,m) model can be chosen.

The statistical significance of the reduction in the sum of squares of  $a_t$ 's after increasing the number of parameters can be checked by the F-criterion:

$$F = \frac{(A_1 - A_0)(N-r)}{sA_0} \quad (18)$$

where  $A_0$  = sum of squares of the model with more parameters

$A_1$  = sum of squares of the model with less parameters

$r$  = number of parameters in the model with more parameters

$s$  = difference in the number of parameters

$N$  = number of observations

and  $F(s, N-r)$  denotes the F-distribution with  $s$  and  $(N-r)$  degrees of freedom. If the F-value computed from eq. (18) is larger than that from the F-distribution table at given probability level such as 95%, then the model with less number of parameters is considered inadequate, otherwise it can be considered as adequate at the same level. Reference may be made to [5] for further details regarding confidence intervals, tolerances, etc.

#### 4. Illustrative Application to Machine-Tool Chatter

Some of the salient features of the DDS methodology can be well illustrated by analyzing the machine-tool chatter vibration records collected under different cutting conditions. Three records of milling machine vibration, such as the one shown in Fig. 2, were collected under different speeds; the experimental set up for these signals is given in [7]. These digitized records were modeled by the method of section 3 and the respective models, their parameter values and the characteristic roots are shown in Table 1. Some of the qualitative as well as quantitative characteristics of the DDS can be obtained from the mathematical results of section 2 after substituting the appropriate values from Table 1.

(i) Spectra and autocorrelations - These most commonly used characteristics of the random vibration records can be readily obtained from expressions (13-14)

and are plotted in Fig. 3. They provide a qualitative signature of the vibrations in frequency and time domain respectively. Note that because the plots are obtained from differential equations they are much smoother and easier to interpret compared to those obtained by instrumentation or by Fast Fourier Transform methods [8]. It can be shown they are also better in terms of statistical estimation [5,12,17].

At the lowest speed of 40 RPM, no peaks appear in the spectrum and therefore the system is highly damped and stable. At the medium speed 90 RPM a high frequency peak appears in the spectrum and a low frequency peak starts developing, signalling the beginning of two modes, one at low and the other at high frequency. It is seen from Table 1 that the variances  $\gamma_0$  reduces from 0.2003 to 0.1244, so that there is a redistribution of power without any significant change in the stability as measured by the amplitude.

For the highest speed of 302 RPM, the power under low as well as high frequencies increases, as indicated by the increased area under the spectrum, and also quantified by almost doubling of  $\gamma_0$  to 0.3849 in Table 1. The low frequency component which was not clear at the speed of 90 RPM now becomes significant. The autocorrelation also exhibits the sinusoidal behavior corresponding to the low frequency peak.

Besides a clear signature providing a qualitative picture of the system behavior, the DDS also provides precise quantitative indices. This is possible because of the analytical expressions for spectra, transfer function and other characteristics, directly available from the differential equation (1). Some of these quantitative features will now be discussed.

(ii) Vibration modes - The characteristic roots or the eigen-values of the differential equation (1) for the respective cases listed in Table 1 immediately enable us to identify the different modes of vibration of the DDS. The real roots indicate a heavily damped mode corresponding to a first order system, whereas each complex pair provides an oscillatory mode. The imaginary part of the complex pair gives the damped frequency  $\omega_d$  of the oscillatory mode in radians per unit time. Using both the real and imaginary parts, the natural frequency  $\omega_n$  and the damping ratio  $\zeta$  can be easily computed for each mode by the standard one-degree-of-freedom vibration calculations.

TABLE 1  
MODELS, PARAMETERS AND CHARACTERISTIC ROOTS

Speed	40 RPM		90 RPM		302 RPM	
Model	AM(2,1)		AM(4,2)		AM(6,2)	
	Param.	Roots	Param.	Roots	Param.	Roots
$\gamma_0$	0.2003		0.1244		0.3849	
$\alpha_0$	0.0086	-8.30	0.4071		1.2896	
$\alpha_1$	8.1408	-0.001	3.6592	$0.21 \pm i0.063$	6.7391	$-0.11 \pm i0.20$
$\alpha_2$			9.8210		29.0264	
$\alpha_3$			4.8985	$-2.22 \pm i1.68$	13.4388	$-1.27 \pm i0.81$
$\alpha_4$					3.0748	
$\alpha_5$					0.5026	$-0.14 \pm i3.11$
$b_1$	0.6173		1.0537		0.7866	
$b_2$			2.1003		2.0615	

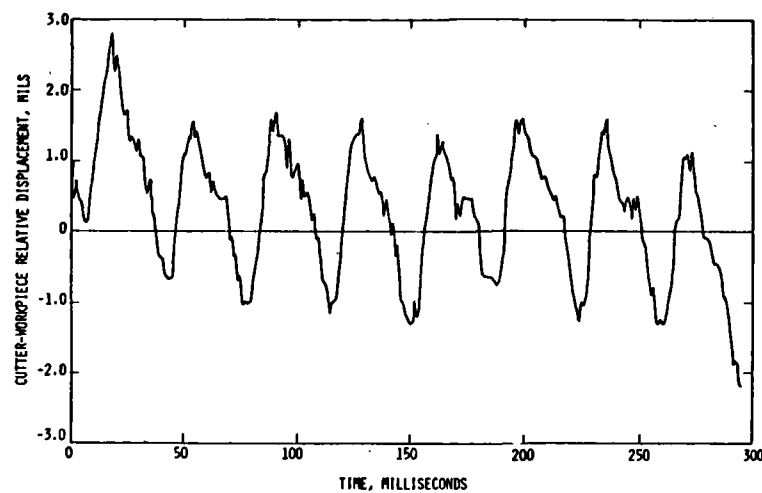


Fig. 2 A Typical Chatter Vibration Record

40 RPM —————  
 90 RPM - - - - -  
 302 RPM .....

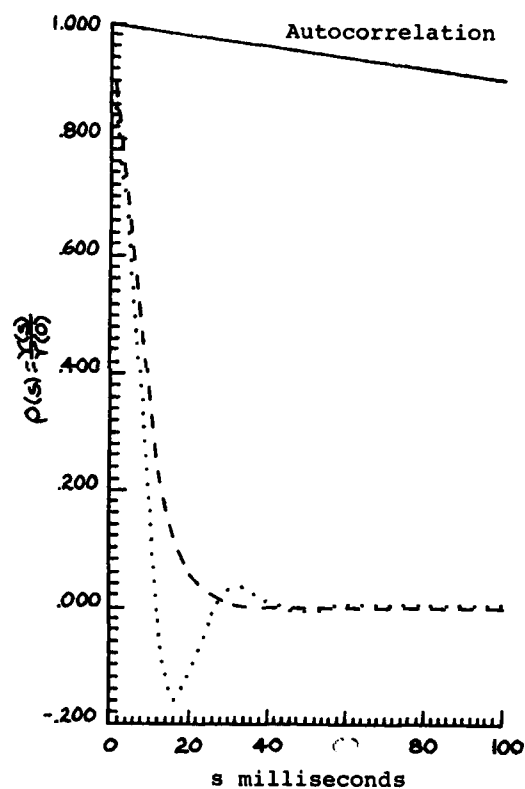
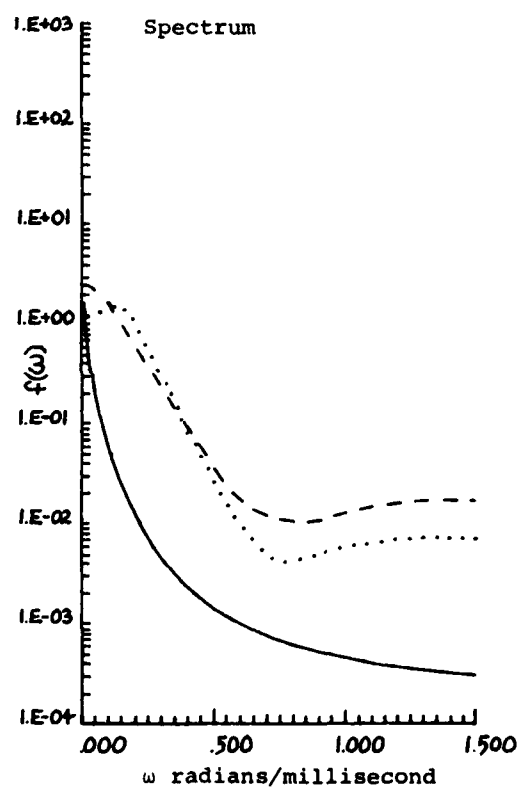


Fig. 3

Spectra and Autocorrelations

At the lowest speed of 40 RPM both the roots are real so that there are no oscillatory modes. At 90 RPM two oscillatory modes appear: one with the damped frequency  $\omega_d = 0.063$  rad/millisecond and the other with  $\omega_d = 1.68$  rad/millisecond. The corresponding natural frequencies  $\omega_n$  and the damping ratios  $\zeta$  are given in Table 2. It is seen that since the damping ratios are as high as 0.96 and 0.78, these modes do not give distinct peaks in the spectrum of Fig. 3.

At the highest speed of 302 RPM an additional oscillatory mode appears and there are three modes with damped frequencies  $\omega_d = 0.20, 0.81$  and  $3.11$  rad/millisecond. It can be seen from Table 2 that the natural frequency of the first mode remains unchanged from 90 RPM to 302 RPM but the damping ratio is now 0.48 and therefore it provides a low frequency peak in the spectrum. Reduction in the damping ratio from 0.96 to 0.48 indicates the deterioration in the stability of the system with increasing speed, which is also corroborated by increase in the variance  $\gamma_0$ .

Table 2 shows that the single mode with  $\omega_d = 1.68$  rad/millisecond at 90 RPM, splits into two modes with  $\omega_d = 0.81$  and  $3.11$  rad/millisecond, and the natural

frequencies  $1.51$  and  $3.11$  rad/millisecond respectively. Of these the first mode does not appear as a peak in the spectrum since the damping ratio is 0.84 but the second one has a damping ratio of 0.0450 and tends to give a somewhat flat peak at the end of the spectrum plot in Fig. 2.

(iii) Power/energy decomposition by modes - Although the characteristics of each mode of vibration become clear from the characteristic roots, this knowledge is not enough to understand the DDS or the underlying physical system, unless the relative contribution of each mode is known. For example, even if the mode  $\omega_d = 3.11$  at 302 RPM is quite unstable, no sharp peak appears in the spectrum and hence the relative instability of this mode does not seem to have much importance. It is therefore necessary to know the relative importance or effect of each mode on the whole system.

Such a relative importance can best be measured by the proportion of power or energy shared by each mode. The total power or energy of the vibrating signal can be represented by the variance  $\gamma_0$ , which is also the area under the spectrum, as shown by eq. (15) for  $k=0$ . Therefore the power or energy

TABLE 2  
VIBRATION MODES, THEIR FREQUENCIES AND % CONTRIBUTION TO POWER/ENERGY

Speed	90 RPM		302 RPM		
	Mode 1	Mode 2	Mode 1	Mode 2	Mode 3
Damped Frequency $\omega_d$ rad./millisec.	0.063	1.68	0.20	0.81	3.11
Natural Frequency $\omega_n$ rad./millisec.	0.219	2.784	0.228	1.506	3.113
Damping Ratio $\zeta$	0.958	0.784	0.482	0.843	0.045
% Contribution to Power/Energy	82.04	17.96	85.40	7.54	7.06

decomposition of the vibration is provided by eq. (17). Each term in the outer sum gives the contribution by the mode represented by the root  $\mu_i$ . For real  $\mu_i$ , the term gives the contribution by the first order mode, for complex  $\mu_i$  we add the contributions of the complex conjugate pair to get the contribution of the corresponding second order mode.

The percentage contribution of each mode to  $\gamma_0$  is given in the last column of Table 2. It is seen that at both the speeds about 82 to 85% power is in the low frequency mode, which therefore practically dominates the system. At 302 RPM the remaining 15% power is shared almost equally by the two high frequency modes.

(iv) Overall stability - The quantitative information provided by (ii) and (iii) enables us to get an overall index of stability. As in classical vibrations, the stability of a DDS can be determined by the characteristic roots. A negative real root represents a damped first order system and therefore need not be considered for stability analysis. For a complex conjugate pair either the real part or the damping ratio may be taken as index of stability. The closer it is to zero the more unstable is that particular mode. However, the instability of a mode would not be of consequence for the overall system unless the mode contributes significantly to the power. Therefore, it is best to choose that mode, which has maximum contribution as given by eq. (17) and then choose either the real part or the damping ratio of that mode as the index of overall stability. A more detailed analysis based on static and dynamic stability can also be performed as discussed in [9].

It can be seen from Tables 1 and 2 that when the speed is increased from 90 to 302 RPM, the real part of the characteristic root with maximum contribution changes from -0.5 to -0.11, and the damping ratio goes down from 0.98 to 0.48. Therefore, the overall stability reduces, which is also apparent from the increased variance  $\gamma_0$ . Note that actually the damping ratio of the third mode at 302 RPM is the lowest,  $\zeta = 0.045$ . But since this mode contributes only 7%, its low stability does not affect the overall system significantly.

(v) Decomposition and physical system identification - The analysis presented above provides a comprehensive description of the DDS in both qualitative and quantitative terms. However, for the purpose of design, performance

optimization and other applications, it is necessary to relate this description to the physical constituents of the system from which the data has been collected. Since it is difficult to directly conceive of systems represented by models such as AM(2,1), AM(4,2) or AM(6,2) in the present illustration, the physical system identification of the DDS is facilitated a great deal if it is decomposed into simple first or second order systems. This can be easily done by starting from the transfer function of the AM(n,m) model and using D-operator or Laplace transforms as illustrated in [7,10]. The three models for the vibration records can be decomposed as follows:

A) 40 RPM - AM(2,1):

$$(D^2 + \alpha_1 D + \alpha_0)X(t) = (b_1 D + 1)Z(t)$$

is decomposed as

$$(D + 1/\tau)X(t) = Z'(t) - Y(t)$$

$$(D + 1/\tau_f)Y(t) = K X(t)$$

B) 136 RPM - AM(4,2):

$$(D^4 + \alpha_3 D^3 + \alpha_2 D^2 + \alpha_1 D + \alpha_0)X(t)$$

$$= (b_2 D + b_1 D + 1)Z(t)$$

is decomposed as

$$(D^2 + 2\zeta_1 \omega_{n1} D + \omega_{n1}^2)X(t) = Z'(t) - Y(t)$$

$$(D^2 + 2\zeta_f \omega_{nf} D + \omega_{nf}^2)Y(t) = (MD + K)X(t)$$

C) 302 RPM - AM(6,2):

$$(D^6 + \alpha_5 D^5 + \alpha_4 D^4 + \alpha_3 D^3 + \alpha_2 D^2 + \alpha_1 D + \alpha_0)$$

$$= (b_2 D^2 + b_1 D + 1)Z(t)$$

is decomposed as

$$(D^2 + 2\zeta_1 \omega_{n1} D + \omega_{n1}^2)(D^2 + 2\zeta_2 \omega_{n2} D + \omega_{n2}^2)$$

$$\cdot X(t) = Z'(t) - Y(t)$$

$$(D^2 + 2\zeta_f \omega_{nf} D + \omega_{nf}^2)Y(t)$$

$$= (MD + K)X(t)$$

In each of the decomposed pairs, the first equation represents the primary path and the second equation represents the feedback path. The block diagrams for the corresponding transfer functions are shown in Fig. 4, and the constants of the systems are given in

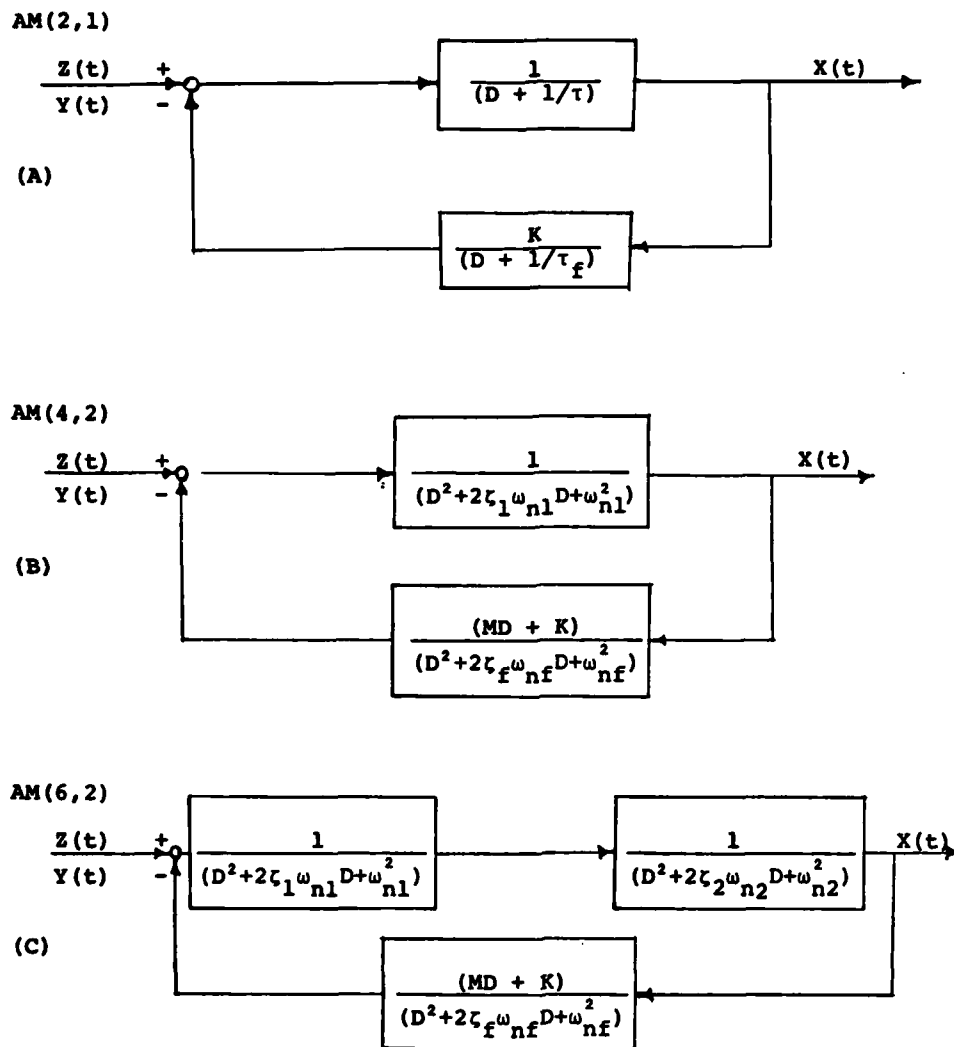


Fig. 4 Block Diagrams of the Decomposed AM Models

Table 3 from reference [7], where additional experimental evidence is given to show that the primary path can be related to the cutting process, whereas the feedback path appears to originate from the machine-tool structure.

Once the parameters of the decomposed subsystems are related to the physical constituents, their relation to the whole system can be used to determine the effects of changes in the design and to arrive at an optimum design. The characteristics such as the stability of the individual subsystems and

their interactions can also be studied by these decompositions as illustrated in [11].

#### 5. Some Applications in the Literature

Some of the diverse applications of the DDS methodology in the literature are listed in this section to illustrate its strength and versatility.

(i) *Characterization of grinding wheels* [12] - Grinding wheel profiles were modeled adequately by A(2) models and it was shown that the parameters

$\omega_n$ ,  $\zeta$  and  $\gamma_0$  can be used to quantitatively describe the profile characteristics useful in grinding.

(ii) *Model for the grinding process* [13] - An AM(3,1) model was found to adequately describe the ground metal surfaces. The decomposition discussed in section 4 was employed to model the grinding process as the cutting process in the main path and the wheel-metal interaction in the feedback path.

(iii) *Study of lathe chatter* [9,14] - Chatter vibration signals from a lathe were used to analyze chatter as random vibration ascertaining its stability. Two of the three vibration modes were related to the workpiece and the cutting tool.

(iv) *Machine-tool dynamics* [7,11] - By modeling the milling machine vibration signals collected under actual working conditions, it has been shown that the dynamics of the machine-tool structure and the cutting process can be estimated.

(v) *System identification and control* [15] - Measurements from a paper-making process control system were used to identify the dynamics of the process and the disturbance. This

provides the transfer function necessary for optimal control.

(vi) *Stochastic geometry of random surfaces* [16] - The mathematical results of section 2, especially expression (16) was used to obtain the properties of random surfaces such as the density of peaks and summits, distribution of slopes, etc.

(vii) *Prediction or forecasting and quality control* [10] - The well known technique of exponential smoothing is shown to be a special case of forecasting using AM(2,1) model; this illustrates the application of the DDS for prediction and quality control.

(viii) *Alias-free estimates of spectra* [17] - The common problem of aliasing in spectral estimation can be avoided by the DDS methodology, which therefore provides better plots of spectra.

## 6. Extensions to Multivariate Records

Although this paper concentrates on univariate or single records at a time, the DDS methodology is also applicable to multiple vibration records collected for more than one variable. For multiple records,  $\mathbf{X}(t)$  is treated as a multivariate vector of observations at time  $t$

TABLE 3: CHARACTERISTICS OF DECOMPOSED SUBSYSTEMS [7]

Parameters	Speed		
	40 RPM	90 RPM	302 RPM
$\tau$ sec	152		
$\tau_f$ sec	625		
$\omega_{n1}$ cps		425	491
$\zeta_1$		0.84	0.06
$\omega_{n2}$ cps			366
$\zeta_2$			0.94
$\omega_{nf}$ cps		109	111
$\zeta_f$		0.4	0.3
M		-2	-9
K	-11	-3	-5



and the coefficients  $g_i$ ,  $b_i$  then become matrices in eq. (1). The extensions of the mathematical results of section 2 and the modeling procedure of section 3 for the multivariate case are given in [5].

The multivariate DDS models provide smooth plots of cross-correlations and cross-spectra including coherence; these are extremely useful in design. The multivariate analog of the difference equation (2) is ideally suited for predictions or forecasting and control as illustrated for a blast furnace operation in [18]. These models are also useful for identification and analysis of closed-loop systems [19] and economic forecasting by leading indicators [20].

The multivariate versions of eqs. (15-17) can be used for performance optimization since they provide explicit expressions for the effect of one variable on another. The design implementing such optimization can be achieved by means of the relations to physical constituents obtained by the decomposition similar to the one discussed in section 4.

#### ACKNOWLEDGMENT

Experimental work and computer programming assistance from Dr. F. A. Burney and Mr. Shiv Kapoor is gratefully acknowledged.

#### REFERENCES

- [1] S. H. Crandall and W. D. Mark, *Random Vibrations in Mechanical Systems*, Academic Press, New York, 1963.
- [2] D. Graupe, *Identification of Systems*, Van Nostrand Reinhold, New York, 1972.
- [3] R. H. Cannon, Jr., *Dynamics of Physical Systems*, McGraw-Hill, New York, 1967.
- [4] S. M. Pandit, "A Bayesian Approach to Time Series Analysis in Adaptive Control," M.S. Thesis, The Pennsylvania State University, University Park, 1970.
- [5] S. M. Pandit, "Data Dependent Systems: Modeling Analysis and Optimal Control via Time Series," Ph.D. Thesis, University of Wisconsin - Madison, 1973.
- [6] S. M. Pandit and S. M. Wu, "Data Dependent Systems: A New Approach to Manufacturing System Analysis," *Proc. Int'l Conference in Production Engineering, Part I*, Tokyo, Japan, pp. 82-87, 1974.
- [7] F. A. Burney, S. M. Pandit and S. M. Wu, "A Stochastic Approach to Characterization of Machine Tool System Dynamics Under Actual Working Conditions," *Trans. ASME, J. of Engr. for Industry*, Vol. 98, Series B, pp. 614-619, 1975.
- [8] G. M. Jenkins and D. G. Watts, *Spectral Analysis*, Holden-Day, San Francisco, 1969.
- [9] S. M. Pandit, T. L. Subramanian and S. M. Wu, "Stability of Random Vibrations with Special Reference to Machine-Tool Chatter," *Trans. ASME, J. of Engr. for Industry*, Vol. 97, Series B, pp. 216-219, 1974.
- [10] S. M. Pandit and S. M. Wu, "Exponential Smoothing as a Special Case of a Linear Stochastic System," *Operations Research*, Vol. 22, pp. 868-879, 1974.
- [11] F. A. Burney, S. M. Pandit and S. M. Wu, "A New Approach to the Analysis of Machine Tool System Stability Under Working Conditions," To appear in *Trans. ASME, J. of Engr. for Industry*, Paper No. 76-WA/Prod-11, 1976.
- [12] S. M. Pandit and S. M. Wu, "Characterization of Abrasive Tools by Continuous Time Series," *Trans. ASME, J. of Engr. for Industry*, Vol. 95, Series B, pp. 821-826, 1972.
- [13] S. M. Pandit, P. T. Suratkar and S. M. Wu, "Mathematical Model of a Ground Surface Profile with the Grinding Process as a Feedback System," *Wear*, Vol. 39, pp. 205-217, 1976.
- [14] S. M. Pandit, T. L. Subramanian and S. M. Wu, "Modeling Machine Tool Chatter by Time Series," *Trans. ASME, J. of Engr. for Industry*, Vol. 97, pp. 211-215, 1974.
- [15] S. M. Pandit, T. N. Goh and S. M. Wu, "Modeling of System Dynamics and Disturbance From Paper-Making Process Data," *Trans. ASME, J. of Dynamic Systems, Measurement, and Control*, Vol. 98, pp. 197-199, 1976.

- [16] S. M. Pandit, F. Nassirpour and S. M. Wu, "Stochastic Geometry of Anisotropic Random Surfaces With Application to Coated Abrasives," To appear in Trans. ASME, J. of Engr. for Industry, Paper No. 76-WA/Prod-9, 1976.
- [17] S. M. Pandit and S. M. Wu, "Unique Estimates of the Parameters of a Continuous Stationary Stochastic Process," Biometrika, Vol. 62, pp. 497-501, 1975.
- [18] S. M. Pandit, "Data Dependent Systems: A New Approach to Prediction and Control in Steel-making," Proc. CAPC Symposium on the Control of Basic Oxygen Steel-making, Ed. K. R. Barnes, C.I.M., Toronto, Canada, September 2-4, 1975.
- [19] S. M. Pandit and S. M. Wu, "Modeling and Analysis of Closed-Loop Systems from Operating Data," To be published, 1976.
- [20] S. M. Pandit and S. M. Wu, Time Series and System Analysis: Modeling, Forecasting and Control, Forthcoming book, to be published, 1976.

A METHOD OF SYSTEM IDENTIFICATION WITH AN  
EXPERIMENTAL INVESTIGATION

P. H. MERRITT  
Air Force Weapons Laboratory  
Kirtland Air Force Base, New Mexico

and

W. E. BAKER  
University of New Mexico  
Albuquerque, New Mexico

System Identification is the problem of determining a mathematic relationship between the input and output of a system. In this paper the desired mathematical relationship is a differential equation which adequately describes a real dynamic system. This paper develops an approach to the identification problem and then demonstrates the method by applying it to a real system. The method is applicable to systems described by ordinary differential equations, either linear, or nonlinear, and yields explicit estimates of the coefficients of the equation. Included in the method is a means of evaluating the form of the differential equation after the coefficients are determined.

The development of the necessary equations is accomplished by utilizing a simple single degree-of-freedom mechanical spring mass system as an example. The method requires assuming the form of a candidate differential equation to start the identification technique. Once the equation is assumed the analysis is direct and equations are developed to permit use of the necessary test data. The solution yields explicit estimates of all unknown coefficients. The required data is frequency response data such as obtained in a laboratory by sweeping a sinusoidal forcing function through a broad frequency range. Specifically the measurements are the frequency, magnitude, and phase of the input and output of the system.

The paper then demonstrates the technique by applying it to test data obtained in laboratory tests of a spring-mass system. The springs were rubber and could not be considered as linear elastic components. Three different forms of differential equations are hypothesized for this system, the Kelvin model, the Zener model, and the Duffing equation with nonlinear damping added. Utilizing data from vibration tests on this system, numerical values for the coefficients in each of these differential equations were computed. The resulting equations were compared, differences were discussed, and the one which best represented the test device selected. The technique described permits this to be done on a rational basis.

The main advantages of the method presented in this paper are as follows: it characterizes the system as a differential equation; it can be applied to nonlinear systems; no initial estimates of values for the coefficients are required; and it utilizes all of the available test data.

## INTRODUCTION

The problem of determining a mathematical relation to describe the relationship between the input and output of a system is called "System Identification." For a dynamic system, the relationship must be time dependent. Arnold and Narendra [1] show four different ways that linear time-invariant systems may be characterized; these are by the impulse response, the transfer function, the differential equation, and orthogonal decomposition. In this work, a method of identifying the form and coefficients of the differential equation characterization was developed and an evaluation made utilizing test data from an actual dynamic system.

Bellman [2] has done considerable work utilizing the differential equation description for dynamic systems, and has developed two methods, quasilinearization and differential approximation to identify the equations from available data. Quasilinearization is well described in the literature [3] [4]. The differential approximation technique utilizes a predetermined form of the differential equation to operate on the measured input and output signals and form an equation error. The integral of the error is minimized with respect to the parameter being evaluated to obtain equations that may be solved for the parameter. While differential approximation has been applied to simulated data with a computer study, it has the limitation that numerical differentiation is required and this process limits the accuracy of the results.

Another method found in the literature [7] [9] was to fit the frequency function with a polynomial in "s", the Laplace variable. The main limitation of this method was that the approach was only applicable to linear equations.

The method developed in this study utilized the initial formulation proposed in the method of differential approximation. The limitation of numerical differentiation was avoided by utilizing sinusoidal data where explicit equations relate all derivatives of the dependent variable. The method was augmented with a regression equation to permit the inclusion of a large amount of test data. Finally, a method was developed to evaluate the resulting differential equation for accuracy determination and comparison purposes.

## DEVELOPMENT OF THE IDENTIFICATION METHOD

There are two principal steps in the identification method, parameter identification and residual evaluation. These will first be described briefly, and then an example will be presented for clarification.

Figure 1 shows the step-by-step procedure for the parameter identification.

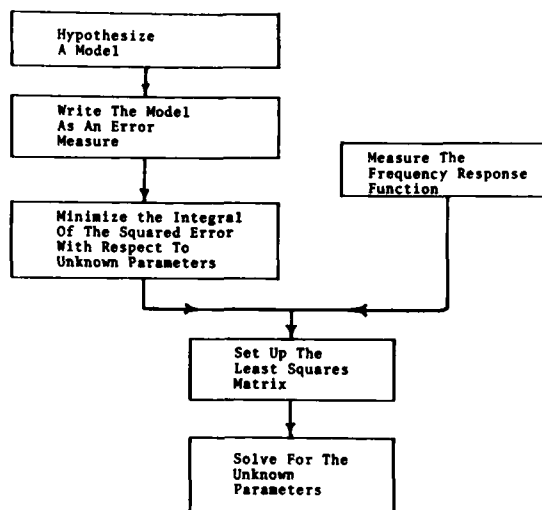


Fig. 1 - Parameter Identification

The initial task is to hypothesize the form of a differential equation that may represent the system. This task relies on the investigator's knowledge of the system and the underlying physics. While this is a large step, and one into which errors will be introduced, subsequent steps will expose these errors to permit elimination of incorrect or inadequate forms. The coefficients are carried in the equation as unknown variables. The equation is then used to set up an error function, where the error is defined as the difference between the forcing function and the dependent variable and its derivatives. This approach is referred to as the "equation error," [6]. This error is squared and integrated over a time period. The integrated and squared error is then minimized with respect to the unknown coefficients. A set of integral equations will be obtained at this point. These equations are used with the test data to evaluate the integrals, and the resulting algebraic equations are solved using a least-squares approach. Numerical values for the coefficients are the final result.

Step 2 of the procedure is required to evaluate the validity of the originally assumed equation and the computed values of the coefficients. The step-by-step procedure is shown in Figure 2.

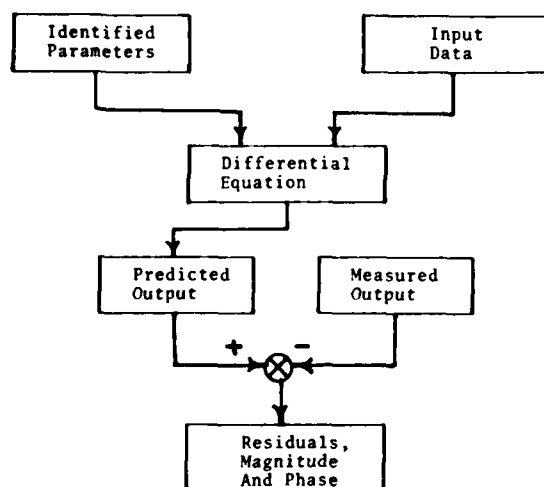


Fig 2. - Residual Evaluation

Quantities called "residuals" are computed. The residuals are defined as the difference between the measured output and the output as predicted by the identified differential equation. The magnitudes of the residuals will indicate if the hypothesized equation is adequate to describe the system being tested.

The method described may be greatly clarified by illustrating its use on a simple example, specifically a second order, time invariant, non-homogeneous, ordinary differential equation.

$$m \ddot{x} + c \dot{x} + kx = f(t) \quad (1)$$

The error model for this equation would be

$$e = [m \ddot{x} + c \dot{x} + kx] - [f(t)] \quad (2)$$

and if this is squared and integrated over some time period, the result is

$$\int_0^T e^2 dt = \int_0^T [m \ddot{x} + c \dot{x} + kx - f(t)]^2 dt \quad (3)$$

Equation 3 is next minimized with respect to each of the unknown coefficients,  $m$ ,  $c$  and  $k$ . When the partial derivative of 3 with respect to  $m$  is determined and equated to zero, and the coefficients removed from the integrand since they are constants in time, the following equation is obtained:

$$m \int_0^T \ddot{x}^2 dt + c \int_0^T \dot{x} \ddot{x} dt + k \int_0^T x \ddot{x} dt - \int_0^T f(t) \ddot{x} dt = 0 \quad (4)$$

Repetition of this process, but considering  $k$  as the variable yields a similar result. Considering " $c$ " as the variable and repeating this step gives

$$m \int_0^T \ddot{x}^2 dt + c \int_0^T \dot{x}^2 dt + k \int_0^T x \dot{x} dt - \int_0^T f(t) \dot{x} dt = 0 \quad (5)$$

Equations 4 and 5 are now combined with the experimental data.

In this work a harmonic, or sinusoidal, forcing function was used to excite the system. The advantage of this type of forcing function is that it results in a unique and known relation between the output variable and all its derivatives, specifically, for acceleration being the measured output quantity,

$$\ddot{x} = A \sin \omega t \quad (6)$$

$$\dot{x} = \frac{-A}{\omega} \cos \omega t \quad (7)$$

$$x = \frac{-A}{\omega^2} \sin \omega t \quad (8)$$

$$f(t) = F \sin(\omega t + \phi) \quad (9)$$

where  $\omega$  is the frequency of the forcing function and  $\phi$  is the phase angle between input and output. The constants of integration are normally set to zero based on physical constraints.

If equations 6 through 9 are combined with equation 4 and then with equation 5, and the limits on integral specified as a time interval covering an integer number of cycles of vibration the integrals may be evaluated in closed form. The resulting equations are as follows:

$$mA - \frac{kA}{\omega^2} = F \cos \phi \quad (10)$$

$$c \frac{A}{\omega} = F \sin \phi \quad (11)$$

Since the above equations are valid in any particular frequency, and the experimental data may be obtained over a broad frequency sweep, the problem appears overspecified. However, the method developed utilized data at  $N$  discrete frequencies. In the following development, the measured quantities will be identified with a subscript to specify the frequency, i.e.,  $F_i$ ,  $A_i$ , and  $\phi_i$  are the peak force, peak acceleration, and phase angle at  $\omega_i$ .

For use of four test frequencies on a given system, the following matrix would be constructed from equation 10.

$$\begin{bmatrix} A_1 & -\frac{A_1}{\omega_1^2} \\ A_2 & -\frac{A_2}{\omega_2^2} \\ A_3 & -\frac{A_3}{\omega_3^2} \\ A_4 & -\frac{A_4}{\omega_4^2} \end{bmatrix} \begin{bmatrix} m \\ k \end{bmatrix} = \begin{bmatrix} F_1 \cos \phi_1 \\ F_2 \cos \phi_2 \\ F_3 \cos \phi_3 \\ F_4 \cos \phi_4 \end{bmatrix} \quad (12)$$

or, in matrix shorthand,  $\underline{A} \underline{x} = \underline{b}$  (13)

The procedure of least squares is now used to obtain an estimation of  $\underline{x}$ , denoted  $\hat{\underline{x}}$ .

$$\hat{\underline{x}} = (\underline{A}^t \underline{A})^{-1} \underline{A}^t \underline{b} \quad (14)$$

A solution to estimate the damping,  $c$ , is easily obtained following a similar approach. This completes the first step of the identification process as shown in Figure 1.

The next step is to use the estimated values of  $m$ ,  $c$ , and  $k$ , insert them into equation 1 and calculate  $\hat{\underline{x}}$  and  $\phi$  for the measured input levels and frequencies. By comparing these predicted outputs with the measured outputs it is possible to see if the equation adequately describes the system. If not, plots of the residuals over the frequency range aid in determining the missing terms of the hypothesized equation, [8].

This method may be utilized for nonlinear as well as linear equations. If the nonlinearities produce harmonics in the output, then the harmonics may be measured and carried through the minimization scheme, or a describing function approach, which retains only the fundamental frequencies may be used. This describing function approach was used to develop the equations used in the experimental investigation that is next described. The experimental equipment automatically excluded harmonics by utilizing tracking filters.

#### EXPERIMENTAL INVESTIGATION OF IDENTIFICATION METHOD

One of the test items used to evaluate the identification method consisted of four rubber vibration isolators supporting a steel cube. A

sketch of the experimental setup is shown in Figure 3.

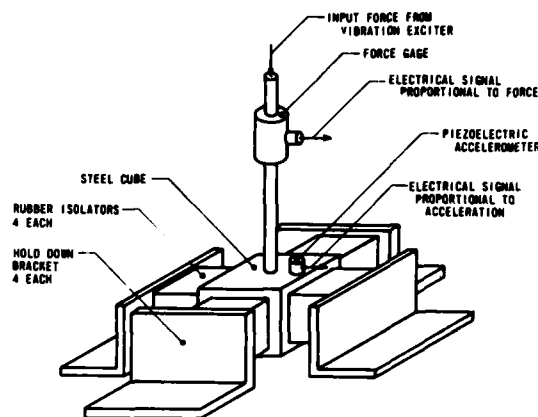


Fig. 3 - Test Item Construction for the Rubber Isolator

The instrumentation system for the series of tests on this item is shown as Figure 4. The data which were obtained by sweeping the test setup through a frequency range is shown as Figures 5 and 6.

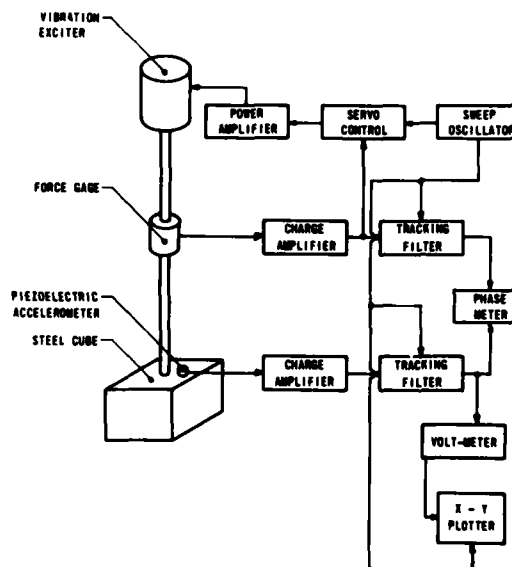


Fig. 4 - Instrumentation for the Rubber Isolator

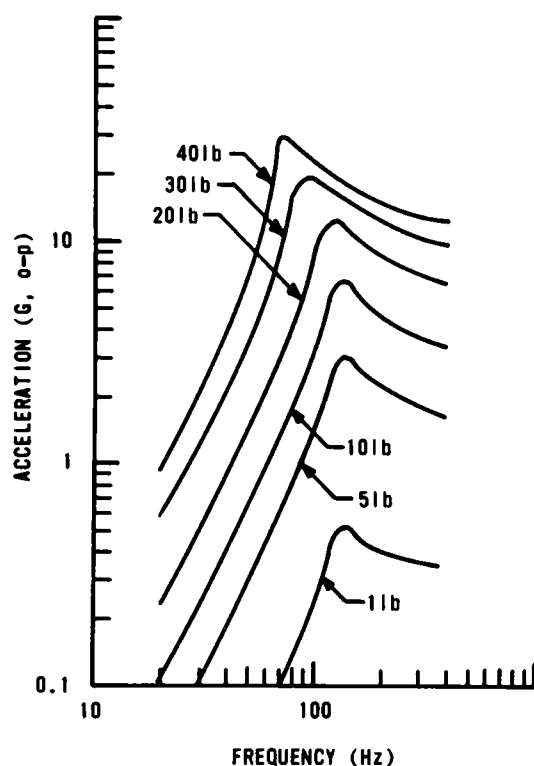


Fig. 5 - Measured Acceleration Data for Rubber Isolator

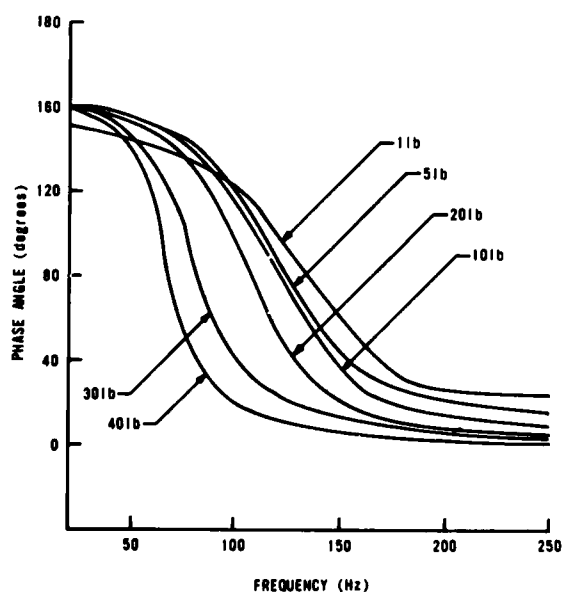


Fig. 6 - Measured Phase Angles for the Rubber Isolator Tests

In the study of this system, three models were hypothesized, their coefficients calculated, and residuals compared to demonstrate the method.

The first model utilized was a simple second order equation as described in the previous section and shown schematically as Figure 7.

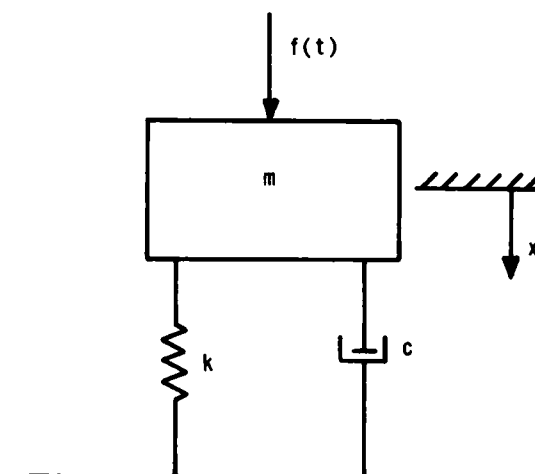


Fig. 7 - Kelvin Model

This model is often called the Kelvin Model, and the appropriate equation is given in the previous section as equation 1.

The second model hypothesized for the test item is shown schematically as Figure 8 and is often referred to as the Zener or relaxation model.

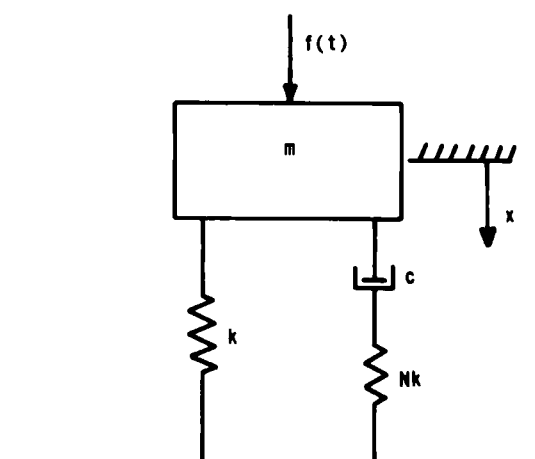


Fig 8. - Zener Model

This model has been suggested to be a good model for a rubber isolator such as utilized here [10]. The differential equation which describes the system is as follows:

$$\frac{mc}{NK} \ddot{x} + m \dot{x} + c \frac{(N+1)}{N} \dot{x} + kx = f(t) + \frac{C}{NK} f(t) \quad (15)$$

The coefficients were redefined as follows:

$$\left. \begin{aligned} a_1 &= \frac{mc}{NK} \\ a_2 &= m \\ a_3 &= \frac{c(N+1)}{N} \\ a_4 &= k \\ a_5 &= \frac{C}{NK} \end{aligned} \right\} \quad (16)$$

The algebraic equations developed for calculating the values of the coefficients were as follows:

$$\omega^2 A a_1 - A a_3 - (\omega^2 F \cos \phi) a_5 = \omega F \sin \phi \quad (17)$$

$$A a_2 - \frac{A}{\omega^2} a_4 + (\omega F \sin \phi) a_5 = F \cos \phi \quad (18)$$

The last model used to describe the test item was a nonlinear equation, which was written to include nonlinearities for both the damping and stiffness coefficients. The differential equation was postulated as:

$$m \ddot{x} + c \dot{x} + d \dot{x}^3 + kx + h x^3 = f(t) \quad (19)$$

The algebraic equations that were derived were:

$$-\omega^2 m + k + \frac{3A^2}{4\omega^2} h = \frac{-F\omega^2 \cos \phi}{A} \quad (20)$$

$$c + \frac{3A^2}{4\omega^2} d = \frac{-F\omega \sin \phi}{A} \quad (21)$$

The test data shown in Figures 5 and 6 were digitized and used with each of the models to calculate numerical values for the coefficients in each of the three hypothesized equations. Sixteen frequency points across the range from 20 to 200 Hz were used for each of the six force levels for a total of 96 measurements. The results, expressed utilizing the differential

equations, were as follows:

Kelvin Model,

$$.0077 \ddot{x} + 3.57 \dot{x} + 1662 x = f(t) \quad (22)$$

Zener Model,

$$-.55 \times 10^{-5} \ddot{x} + .01 \dot{x} + .55 x + 1310 x = f(t) + .7 \times 10^{-3} \dot{f}(t) \quad (23)$$

Nonlinear Model,

$$.0085 \ddot{x} + 3.93 \dot{x} - .012 \dot{x}^3 + 3980 x - 2.1 \times 10^6 x^3 = f(t) \quad (24)$$

where the forcing function is in units of pounds and the displacement is in inches.

These equations were next utilized to evaluate the residuals for each model. This was accomplished by using the measured acceleration values and the derived velocity and displacement values to calculate the input forcing function and phase angle. These values were subtracted from the measured forcing functions and phase angles to obtain residuals for any one force level. Two of these residual plots are shown as Figures 9 and 10.

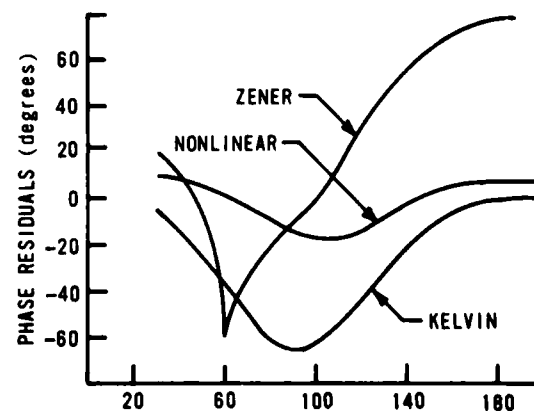
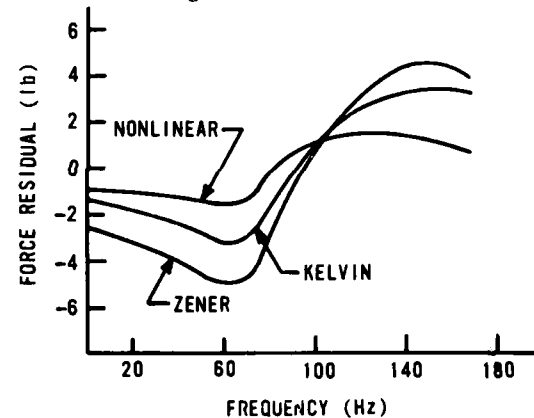


Fig 9. - Residual Plots for Five Pound Force



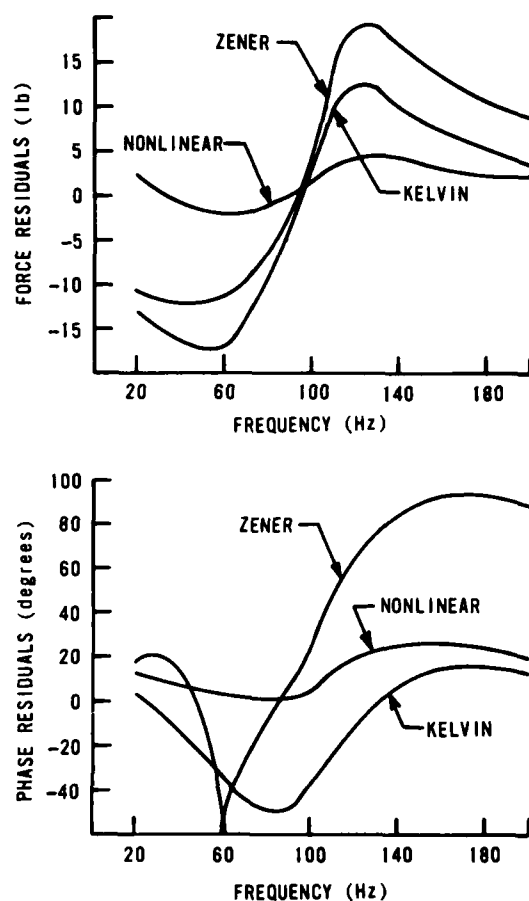


Fig. 10 - Residual Plots for Twenty Pound Force

It should be noted in these figures, for a given model, the residuals show the same behavior. This indicates the method is not highly dependent on the magnitude of the forcing function. A study of the residual plots showed that the nonlinear model best described the physical system tested. Clearly, both the phase residual and force residual came closer to zero with this model. Another indication of the effectiveness of the technique for this particular model was by comparison of the mass in the physical system with the calculated values for the three models. The mass of the springs were included by assuming they moved as if they were pinned at both ends. The resulting difference between measured and calculated mass for the nonlinear model was only 1.2%. For the Kelvin model, the difference was 8.6% while for the Zener model the difference was 18%.

## CONCLUSIONS

A method was developed to permit calculating the coefficients of a hypothesized differential equation using test data. The method was demonstrated by applying it to data from a laboratory vibration test. It was shown that the method permits evaluating the hypothesized models versus the test data and permits comparisons between models. The method is considered to be simple to apply and should be applicable to a wide range of problems.

## REFERENCES

1. Arnold, Charles R., and Narenda, Kumpati S., "The Characterization and Classification of Systems," Technical Report 471, Cruft Laboratory, Harvard, Cambridge, MA., 1965.
2. Bellman, R., "On the Construction of a Mathematical Theory of the Identification of Systems," The Rand Corp., Santa Monica, CA., RM-4769-PR, 1966.
3. Bellman, R., and Kalaba, R., "Quasilinearization and Nonlinear Boundary Value Problems," Elsevier Publishing Co., NY, NY, 1965.
4. Bellman, R., Kalaba, R., and Sridhar, R., "Adaptive Control via Quasilinearization and Differential Approximation," The Rand Corp., Santa Monica, CA., RM-3928-PR, 1963.
5. Detchmندی, D. M., and Sridhar, R., "On the Experimental Determination of the Dynamics of Physical Systems," Proceedings of National Electronics Conference, 1965.
6. Eykhoff, Pieter, "System Identification, Parameter and State Estimation," John Wiley and Sons, 1974.
7. Levy, E. C., "Complex Curve Fitting," IRE Transactions on Automatic Control AC-4, 1959.
8. Merritt, Paul H., "A Method of System Identification with Experimental Investigations of Real Systems," PhD. Dissertation, The University of New Mexico, Albuquerque, NM, 1974.
9. Manetje, J.J., "Transfer Function Identification Using a Complex Curve Fitting Technique," Journal of Mechanical Engineering Science, V 15 (5), 1973.
10. Ruzicka, J., and Derby, T., "Influence of Damping in Vibration Isolation," Shock and Vibration Monograph Series, the Shock and Vibration Information Center, Washington, D. C., 1971.

## A METHOD FOR THE DIRECT IDENTIFICATION OF VIBRATION PARAMETERS FROM THE FREE RESPONSE

S. R. Ibrahim  
Department of Mechanical Engineering and Mechanics  
Old Dominion University  
Norfolk, Virginia

and

E. C. Mikulcik  
Department of Mechanical Engineering,  
The University of Calgary,  
Calgary, Alberta, Canada

This paper describes the theory and application of a method which utilizes the free response of a structure to determine its vibration parameters.

The time domain free response is digitized and used in a digital computer program to determine the number of modes excited, the natural frequencies, the damping factors, and the modal vectors. The underlying theory is developed, including the basis of the computational procedures required, as well as the requirements regarding the sampling rate in the digitizing procedure. Consideration is given to the practical application of the theory. The paper includes the description of a laboratory experiment in which the method described was used to determine the parameters related to the first three modes of vibration of a cantilever beam. The technique is also applied to a more complex generalized payload model previously tested using sine sweep method and analyzed by NASTRAN. Ten modes of the payload model are identified.

### INTRODUCTION

The experimental determination of the natural frequencies and modes of structures is usually pursued through the application of frequency response or other frequency domain methods. Many test procedures have been proposed [1-10] differing in the manner in which the structure is excited, the quantities which are measured, and the manner in which the experimental data are analysed. Analysis of frequency domain methods have shown that there are limits on the degree of damping and the closeness of natural frequencies, beyond which frequency response methods cannot yield accurate information about the vibration parameters [11-14]. These limitations are essentially due to modal interference which can obscure the separate observation of individual modes and natural frequencies. Most modal vibration test methods are, then, based on assumptions of negligible mode coupling, although some methods have been introduced to deal with modal interference [15-17]. Special methods, though, have the main disadvantage that it must somehow be determined in advance that special attention is, in fact, required.

These particular problems encountered using frequency response methods have led to the consideration of time domain based methods in vibration testing. The direct use of time response information, without transformation to the frequency domain, should not necessarily require assumptions about the interference of modes due to heavy damping or closely spaced natural frequencies, and would thus eliminate the necessity for special procedures in these cases.

The theory and application of such a time domain method were presented in [18] and [19]. The method involves the use of transient response data in determining the differential equations of a lumped parameter model of the system under test, followed by analysis of the mathematical model to determine the vibration parameters. An alternative time domain technique is described in this paper. This method differs from the one noted previously in that, here, a mathematical model or differential equation of the structure is not developed; rather, the structure's free response is used directly in a computational procedure which yields the vibration parameters. In both

methods, either the acceleration, velocity or displacement response may be used, but in the earlier method it was required that the recorded response be numerically integrated twice in the computational procedure, while in the present case no such integration is necessary.

## THEORY

The test procedure described utilises the free response of the structure under test. As for the previously referenced time domain method [18,19], the free response is generated after the sudden termination of excitation of the structure by a forcing function containing contributions in the frequency range of interest. It is necessary that a mode contribute to the response in order that it can be detected. Narrow band random excitation and rapid frequency sweeps have been used with success in laboratory experiments. In this way, a considerable amount of energy may be built up in the structure during excitation, to be dissipated during the free response. This contrasts with transient procedures which depend upon, and can be seriously limited by, the amount of energy which can be imparted to the structure by a pulse or a step.

Dependent upon the form of excitation, the response may, in theory, contain an infinite number of modes, although it is not physically possible in practice. For the theoretical development described here, it is assumed that a finite, but for the present known, number of modes is excited. While this assumption is necessary and fundamental to the technique described, it also allows the testing of a complex structure to be done in a series of tests, each of which covers a frequency spectrum only as wide as desired. This makes the procedure analogous to a series of tests on simple systems rather than a single test of a large system, keeping both instrumentation and computational complexities to a lower level.

It is convenient to imagine the response that is thus monitored as being equivalent to that of an hypothetical  $n$ -degree of freedom lumped parameter system with all modes excited, and in which the masses undergo the same motions as the measuring stations on the structure under test. The natural frequencies of the hypothetical lumped system are the same as those of the structure, and the mode shapes of the lumped system are equivalent to the modal displacements of the structure measured at the measuring stations. The identification of the vibration parameters of the structure is now pursued through the determination of the vibration parameters of the lumped system.

The lumped system is assumed to be described by the following equation during its free response:

$$\underline{M} \ddot{\underline{x}} + \underline{C} \dot{\underline{x}} + \underline{K} \underline{x} = \underline{0} \quad (1)$$

$\underline{M}$ ,  $\underline{C}$ , and  $\underline{K}$  are  $n \times n$  matrices, while  $\underline{x}$ ,  $\dot{\underline{x}}$ , and  $\ddot{\underline{x}}$  are  $n$ -dimensional vectors. The solution of this equation is assumed to be

$$\underline{x} = \underline{p} e^{\lambda t} \quad (2)$$

whence

$$[\lambda^2 \underline{M} + \lambda \underline{C} + \underline{K}] \underline{p} = \underline{0} \quad (3)$$

Equation (3) defines  $2n$  values for  $\lambda$ , which are also the roots of the characteristic equation of the system. For each root, there is a corresponding vector,  $\underline{p}$ , of relative displacements of the coordinates of the system.  $\lambda$  and the elements of  $\underline{p}$  are real for overdamped modes, but for underdamped modes they are complex, and occur in conjugate pairs. Each conjugate pair combines to produce a real mode shape corresponding to a single natural frequency and damping factor. For a complex conjugate pair of modal vectors having the first element of each normalized to unity and having the  $k$ th elements  $c \pm id$ , the displacement of the  $k$ th coordinate is  $\sqrt{c^2 + d^2}$ , and its motion lags that of the first coordinate by  $\tan^{-1}(d/c)$ . For a complex conjugate pair of roots  $a \pm ib$ , the damped natural frequency is  $\omega_{nd} = b$ , the undamped natural frequency is  $\omega_n = \sqrt{a^2 + b^2}$  and the damping ratio is

$$\eta = \frac{a}{\sqrt{a^2 + b^2}}$$

The problem of modal vibration testing is to determine, from the test data, the values of  $\lambda$  and  $\underline{p}$  which satisfy Eq. (3). The test data required may be any one of the displacement, velocity or acceleration response assumed for the present to be measured at the  $n$  stations. The response, be it displacement, velocity or acceleration, consists of a sum of contributions made by all the modes, and can be written as

$$\underline{x} = \sum_{j=1}^{2n} \underline{p}_j e^{\lambda_j t} \quad (4)$$

The response at time  $t_i$  is

$$\underline{x}(t_i) = \underline{x}_i = \sum_{j=1}^{2n} \underline{p}_j e^{\lambda_j t_i} \quad (5)$$

and the response vectors measured at  $2n$  different instances of time can be written in matrix form as

$$[\underline{x}_1 \ \underline{x}_2 \ \dots \ \underline{x}_{2n}] =$$

$$[p_1 \ p_2 \ \dots \ p_{2n}] \begin{bmatrix} e^{\lambda_1 t_1} & e^{\lambda_1 t_2} & e^{\lambda_1 t_{2n}} \\ e^{\lambda_2 t_1} & \dots & e^{\lambda_2 t_{2n}} \\ \vdots & & \vdots \\ e^{\lambda_{2n} t_1} & \dots & e^{\lambda_{2n} t_{2n}} \end{bmatrix} \quad (6)$$

or

$$\underline{X} = \underline{P} \underline{\Lambda} \quad (7)$$

Responses that occur at time  $\Delta t$  later with respect to those of Eq. (7) are

$$[y_1 \ y_2 \ \dots \ y_{2n}] = [p_1 \ p_2 \ \dots \ p_{2n}] \begin{bmatrix} e^{\lambda_1(t_1+\Delta t)} & \dots & e^{\lambda_1(t_{2n}+\Delta t)} \\ \vdots & & \vdots \\ e^{\lambda_{2n}(t_1+\Delta t)} & \dots & e^{\lambda_{2n}(t_{2n}+\Delta t)} \end{bmatrix} \quad (8)$$

where

$$y_i = x_i(t_i + \Delta t), \quad i = 1, 2, \dots, 2n$$

Eq. (8) can be rewritten as

$$[y_1 \ y_2 \ \dots \ y_{2n}] = [q_1 \ q_2 \ \dots \ q_{2n}] \underline{\Lambda} \quad (9)$$

or

$$\underline{Y} = \underline{Q} \underline{\Lambda} \quad (10)$$

where

$$q_i = p_i e^{\lambda_i \Delta t}, \quad i = 1, 2, \dots, 2n \quad (11)$$

In a similar manner, responses that occur at time  $\Delta t$  later with respect to those of  $\underline{Y}$  are

$$[z_1 \ z_2 \ \dots \ z_{2n}] = [r_1 \ r_2 \ \dots \ r_{2n}] \quad (12)$$

or

$$\underline{Z} = \underline{R} \underline{\Lambda} \quad (13)$$

where

$$z_i = x_i(t_i + 2\Delta t), \quad i = 1, 2, \dots, 2n \quad (14)$$

and

$$r_i = q_i e^{\lambda_i \Delta t} = p_i e^{2\lambda_i \Delta t}, \quad i = 1, 2, \dots, 2n \quad (15)$$

The responses given by Eqs. (7), (10) and (13) can be manipulated to solve for the eigenvalues and modal vectors. First, Eqs. (7) and (10) are grouped to be written as

$$\begin{bmatrix} \underline{X} \\ \underline{Y} \end{bmatrix} = \begin{bmatrix} \underline{P} \\ \underline{Q} \end{bmatrix} \underline{\Lambda} \quad (16)$$

or

$$\underline{\Phi} = \underline{\Psi} \underline{\Lambda} \quad (17)$$

and (10) and (13) are written as

$$\begin{bmatrix} \underline{Y} \\ \underline{Z} \end{bmatrix} = \begin{bmatrix} \underline{Q} \\ \underline{R} \end{bmatrix} \underline{\Lambda} \quad (18)$$

or

$$\underline{\hat{\Phi}} = \underline{\hat{\Psi}} \underline{\Lambda} \quad (19)$$

It is shown in the appendix that the inverses of the matrices  $\underline{\Phi}$  and  $\underline{\hat{\Phi}}$  exist. Also, the inverse of  $\underline{\Psi}$  and  $\underline{\hat{\Psi}}$  exist, because their columns are proportional to the modal vectors, which must be linearly independent. Hence, Eqs. (17) and (19) can be manipulated to eliminate  $\underline{\Lambda}$ , giving the result

$$\underline{\hat{\Phi}} \underline{\Phi}^{-1} \underline{\Psi} = \underline{\hat{\Psi}} \quad (20)$$

This equation relates each column,  $\underline{\Psi}_i$ , of  $\underline{\Psi}$  to the corresponding column,  $\underline{\hat{\Psi}}_i$ , of  $\underline{\hat{\Psi}}$  through

$$\underline{\hat{\Phi}} \underline{\Phi}^{-1} \underline{\Psi}_i = \underline{\hat{\Psi}}_i, \quad i = 1, 2, \dots, 2n \quad (21)$$

The column vectors  $\underline{\Psi}_i$  and  $\underline{\hat{\Psi}}_i$  are also related through Eqs. (11) and (15) by

$$\underline{\hat{\Psi}}_i = e^{\lambda_i \Delta t} \underline{\Psi}_i \quad (22)$$

Equations (21) and (22) can be combined to give

$$\underline{\hat{\Phi}} \underline{\Phi}^{-1} \underline{\Psi}_i = e^{\lambda_i \Delta t} \underline{\Psi}_i \quad (23)$$

This equation is an eigenvalue problem which enables the measured response to be used in the calculation of eigenvectors and eigenvalues which are related to the vibration parameters of the structure. The modal vectors are merely the first  $n$  elements of the eigenvectors of  $\underline{\hat{\Phi}} \underline{\Phi}^{-1}$ , but the relationship between the eigenvalues and  $\lambda_i$ , the characteristic roots of Eq. (1), requires further analysis. This relationship is discussed below with reference to an eigenvalue  $\beta + i\gamma$ , of  $\underline{\hat{\Phi}} \underline{\Phi}^{-1}$ , which is related to a characteristic root  $a + ib$ . It is to be noted that the eigenvalue  $\beta - i\gamma$  and the corresponding

characteristic root  $a - ib$  would also exist but for simplicity it will henceforth be assumed that  $b \geq 0$  with the understanding that for every  $b > 0$  the conjugate root  $a + ib$  also exists. The eigenvalue  $\beta + i\gamma$  is related to  $a + ib$  through

$$\beta + i\gamma = e^{(a+ib)\Delta t} \quad (24)$$

Thus,

$$\beta = e^{a\Delta t} \cos b\Delta t$$

and

$$\gamma = e^{a\Delta t} \sin b\Delta t$$

from which

$$a = \frac{1}{2\Delta t} \ln (\gamma^2 + \beta^2) \quad (25)$$

and

$$b = \frac{1}{\Delta t} \tan^{-1} \left( \frac{\gamma}{\beta} \right) \quad (26)$$

Hence, real eigenvalues of  $\hat{\Phi} \Phi^{-1}$  correspond to critically or overdamped modes because they represent real characteristic roots. Natural frequencies of underdamped modes are represented by complex conjugate eigenvalues, and must be determined using Eqs. (25) and (26).

#### SAMPLING RATE

Equation (26) does not allow the natural frequencies to be determined uniquely, because it can be written as

$$b = \frac{1}{\Delta t} [\tan^{-1} \left( \frac{\gamma}{\beta} \right) + k\pi] \dots \begin{cases} 0 < \tan^{-1} \left( \frac{\gamma}{\beta} \right) < \pi \\ k = 0, 1, 2, \dots \end{cases} \quad (27)$$

Thus for each damped natural frequency  $b$ , there is a relationship between  $\Delta t$  and the value of  $k$  which should be used in Eq. (27).  $\Delta t$  is the time delay used to generate the delayed response matrices  $\underline{Y}$  and  $\underline{Z}$  from  $\underline{X}$ , and thus  $\frac{1}{\Delta t}$  represents the sampling rate required to obtain these delayed responses, although consecutively sampled response vectors need not be used as the columns of  $\underline{X}$ .

To avoid ambiguity in the use of Eq. (27) it is necessary to specify that all the modes which contribute to the response correspond to frequencies which can be calculated from the equation by using only a single value for  $k$ . It is required then that for all values of  $b$  in the frequency range of interest, that

$$\frac{k\pi}{\Delta t} < b < \frac{(k+1)\pi}{\Delta t} \quad (28)$$

for some value of  $k$ . Writing the minimum and maximum values of damped natural frequencies as related to the minimum and maximum values of the frequency range of interest as

$$b_{\min} > 2\pi f_{\min}$$

$$b_{\max} < 2\pi f_{\max}$$

and the sampling frequency  $f_s$  as

$$f_s = \frac{1}{\Delta t},$$

Eq. (28) requires that

$$\left. \begin{aligned} f_s k &< 2f_{\min} \\ f_s (k+1) &> 2f_{\max} \end{aligned} \right\} k = 0, 1, 2, \dots$$

or

$$\frac{2f_{\max}}{k+1} < f_s < \frac{2f_{\min}}{k}, \quad k = 0, 1, 2, \dots \quad (29)$$

This equation can be used to relate the frequency range of interest to the acceptable value or values of  $k$  for use in Eq. (27) through

$$\frac{2f_{\max}}{k+1} < \frac{2f_{\min}}{k}$$

or

$$\frac{f_{\max}}{f_{\min}} < \frac{k+1}{k}, \quad k = 0, 1, 2, \dots \quad (30)$$

The determination of frequencies in a range from  $f_{\min}$  equal to zero, to some upper limit  $f_{\max}$  requires, from Eq. (30), that  $k = 0$ . In addition Eq. (29) requires that

$$f_s > 2f_{\max} \quad (31)$$

This requirement on  $f_s$  may present practical difficulties if  $f_{\max}$  is excessively high, but it is seen below that the requirement for determining high frequencies can be made less demanding if testing is done for a frequency range having a lower limit greater than zero and thus allowing values other than zero to be used for  $k$ . Equation (30) defines the maximum width of the frequency range which can be used with the various values of  $k$  or, conversely, it can be thought of as defining the possible values of  $k$  which can be used for a desired frequency band. This information can then be used in Eq. (29) to determine the allowable sampling frequencies. The maximum width of the frequency range is  $f_{\max}/f_{\min}$  equal to two for which the lowest sampling frequency is  $f_{\max}$

and  $k$  equals unity. As the frequency range decreases, the sampling rate may be chosen from an allowable range, and with frequency ranges that are sufficiently narrow it becomes possible to choose sampling frequencies from several allowable ranges, each range corresponding to a different value of  $k$ . This is demonstrated in an illustrative example below.

It is supposed that all the natural frequencies up to 1000 Hz are to be determined for a structure. Two approaches can be taken; either the entire range can be covered at once, or it may be subdivided into several narrower ranges, each to be covered separately.

A single test covering the range from 0-1000 Hz would require, from Eq. (31), that the sampling frequency be any value above 2000 Hz, and  $k = 0$  should be used in Eq. (27).

Division into narrower frequency ranges must keep in mind that, for any range having a non-zero lower limit, the upper frequency limit must be not more than twice the lower frequency limit. (If the upper frequency limit is more than twice the lower frequency limit,  $k$  should be 0). Suitable ranges for the case being considered would be 0-400 Hz, 400-700 Hz, and 700-1000 Hz. Each frequency range must be studied using response information which contains (through filtering or other means) only frequency components in the range of interest. The frequency range 0-400 Hz must be studied using a sampling frequency of at least 800 Hz, with  $k=0$  in Eq. (27). The 400-700 Hz range requires, from Eq. (30), that

$$\frac{700}{400} < \frac{k+1}{k}$$

hence  $k = 0, 1$  are acceptable, with corresponding sampling rates as determined from Eq. (29). These rates are  $f_s > 1400$  Hz for  $k = 0$ , and  $700 \text{ Hz} < f_s < 800$  Hz for  $k = 1$  in Eq. (29). For the 700-1000 Hz range,  $k = 0, 1, 2$  are acceptable with sampling rates  $f_s > 2000$  Hz for  $k = 0$ ,  $1000 \text{ Hz} < f_s < 1400$  Hz for  $k = 1$  and  $667 \text{ Hz} < f_s < 700$  Hz for  $k = 2$ .

In comparison of sampling rates for the two approaches, the first requires a rate of at least 2000 Hz, while the second requires a rate of at least 800 Hz. The requirements for the second approach can be reduced still further if narrower frequency ranges are chosen

Another solution to the problem of requiring high sampling rates for a certain frequency range of interest is the use of a tape recorder at a high recording speed, with the recorded response then played back at a lower speed during the digitization process. This can reduce the required sampling rate by a factor of the ratio of the two recorder speeds that have been used. This ratio is to be used later

as a correction factor to obtain the actual structural frequencies.

## PRACTICAL APPLICATION

An important assumption made in deriving the theory is that the number of measuring stations on the structure equals the number of degrees of freedom of the hypothetical lumped parameter system with all modes excited. Thus in performing a test it would be necessary to know in advance the number of equivalent degrees of freedom to be excited, so that the correct number of measuring stations could be employed. In practice, this information is not usually available, and even if it were, it might not be possible or desirable to use the same number of measuring stations as there are equivalent degrees of freedom. This section describes a procedure whereby the theory developed thus far may be used in conjunction with any convenient number of measuring stations. As few as a single station may be used for determining any number of frequencies in a single test, and modal displacements at any number of points may be determined using as few as two stations at a time in a series of tests using one station as a reference.

Three possibilities exist in the relationship between the equivalent number of degrees of freedom excited, and the number of stations at which measurements are made. The number of stations used may be greater than, equal to, or fewer than the number of degrees of freedom. Each situation requires a different computational approach, so the determination of which of the three possibilities is actually present is the first goal in the analysis of experimental data. These same possibilities arise and are dealt with in [19] and parallel procedures are used in dealing with them here. Verification is dealt with fully in [19], so emphasis here is placed only on describing the procedures employed.

The first step in the analysis of experimental data is the determination of the number of degrees of freedom of the associated hypothetical lumped parameter system. This is done by determining the number of independent modal vectors which contribute to the response, on the basis that the rank of the matrix  $\Phi$  is equal to the number of independent modal vectors,  $2k$ , used to make up its columns. It is kept in mind that a pair of complex conjugate modal vectors corresponds to a single real underdamped mode, and thus for a structure in which all modes are underdamped, the number of real modes is half the number of modal vectors. Also, overdamping results in two real modal vectors corresponding to a single degree of freedom. Hence, the existence of  $2k$  independent modal vectors corresponds to a corresponding lumped parameter system having  $k$  degrees of freedom.

First, the matrix  $\Phi$  is formed using the responses obtained from all the measuring stations which have been used. Then, in theory, it should only be necessary to successively calculate the determinants of sub-matrices of  $\Phi$ , using the first  $m$  elements of the responses of  $m$  stations at  $2m$  instants of time, where  $m$  takes on values from unity up to a value at which the determinant becomes zero. This value of  $m$  equals  $k+1$  whence the response of only  $k$  stations need to be used to identify the vibration parameters of the structure. In practice the computed determinant is never zero due to measurement noise and computer round-off, hence instead of using the value of the determinant itself, the ratio of two successively calculated determinants should be used [20]. The responses of the excess measurement stations may be used in a modification of the computational procedure as described in [19].

If the determinant check described above does not reveal the number of modes excited, then the number of modes is either equal to or greater than the number of measuring stations. In either case, it is required to increase the apparent number of stations through the generation of response vectors of higher order, with a corresponding increase in the number of time instances considered, thus increasing the order of  $\Phi$  and allowing the determinant check to be continued. The response vectors of higher order takes the form

$$\underline{x}' = \begin{bmatrix} \underline{x} \\ \underline{x}_a \end{bmatrix} \quad (32)$$

where

$$\underline{x}_a = \underline{x}(t + \Delta\tau) \quad (33)$$

in which  $\Delta\tau$  is any convenient value which must be different from  $\Delta t$ . The procedure can be repeated to triple, quadruple, etc., the order of the apparent response vector using other values for  $\Delta\tau$ , using the determinant check after each increase until the number of modes is determined. The frequencies are then computed for the appropriately enlarged  $\Phi$ , and the mode shapes are given by the eigenvector elements which correspond to the original measuring stations.

Another problem of practical importance which arises is in the introduction of errors due to measurements and recording noise. In the next section, two methods are suggested to reduce the effect of measurements errors on the identified parameters. These methods were used in the second (payload model) experiment.

## MEASUREMENTS AND RECORDING NOISE

Two methods are used to minimize the effect of different kinds of noise on the identified

parameters. These two methods are:

### 1- Least Square Error Minimization:

This can be accomplished by using more data than needed and find the parameters with least error that satisfy the data. In such a case  $\hat{\Phi}$  and  $\Phi$  will be rectangular matrices and Eq. (23) will be:

$$[\hat{\Phi} \Phi^T] [\Phi \Phi^T]^{-1} \underline{\psi}_i = e^{\lambda_i \Delta t} \underline{\psi}_i \quad (34)$$

### 2- The Use of Overspecified Math Model:

In this case the number of degrees of freedom of the mathematical model is larger than the number of modes to be identified. This will give an escape for some of the noise thus improve the accuracy of the identified modes.

## EXPERIMENTAL RESULTS

### 1. Cantilever Beam

An experiment using the technique described in the preceding sections was carried out using a steel cantilever beam. The dimensions of the beam are shown in Fig. 1; also shown are the locations of two accelerometers which were used in measuring the response.

The range for which frequency and modal information were to be obtained was chosen as 0-500 Hz. The beam was excited at a location about 3/4" from the free end with a narrow band random signal, and the accelerometer outputs were filtered to eliminate frequency components higher than 500 Hz.

According to Eq. (31), the sampling rate should be greater than 1000 Hz; a rate of 7500 Hz was used.

The results of the analysis of the experimental results are summarized in Tables I and II. The determinant check using the direct results of the two measuring stations is inconclusive, thus higher order response vectors were generated according to equations (32) and (33), in which  $\Delta\tau$  was taken as  $\frac{20}{8 \cdot 7500}$  sec. and  $\frac{40}{7500}$  sec.;  $\Delta t$  was taken as  $\frac{1}{7500}$ . It is seen that the direct use of the determinants is inconclusive, but the use of determinant ratios indicates that there are three equivalent degrees of freedom. The results of 30 sets of calculations using different sets of response vectors from a single test were used in generating this information. The record length that was used to perform the necessary calculations was 0.2 sec.

In Table II, the results are shown in comparison with those identified using the peak amplitude method in conjunction with a simple frequency sweep, and with the theoretical (undamped) parameters using Bernoulli equation

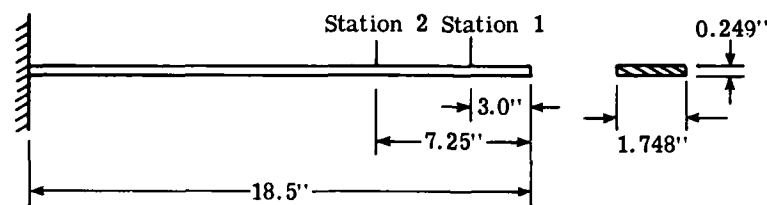


Fig. 1 - Geometry of the cantilever beam

TABLE I  
Determinant Check

No. of Stations (N)	$ \text{Det} _N$	$ \text{Det} _N /  \text{Det} _{N+1}$
1	$0.2705 \times 10^0$	$0.1863 \times 10^4$
2	$0.1452 \times 10^{-3}$	$0.1044 \times 10^5$
3	$0.1391 \times 10^{-7}$	$0.3662 \times 10^{12}$
4	$0.3799 \times 10^{-19}$	$0.1587 \times 10^{11}$
5	$0.2394 \times 10^{-29}$	$0.8317 \times 10^{12}$
6	$0.2879 \times 10^{-41}$	



AD-A148 088

THE SHOCK AND VIBRATION BULLETIN PART 4 STRUCTURAL

3/3

DYNAMICS SYSTEMS IDENT. (U) NAVAL RESEARCH LAB

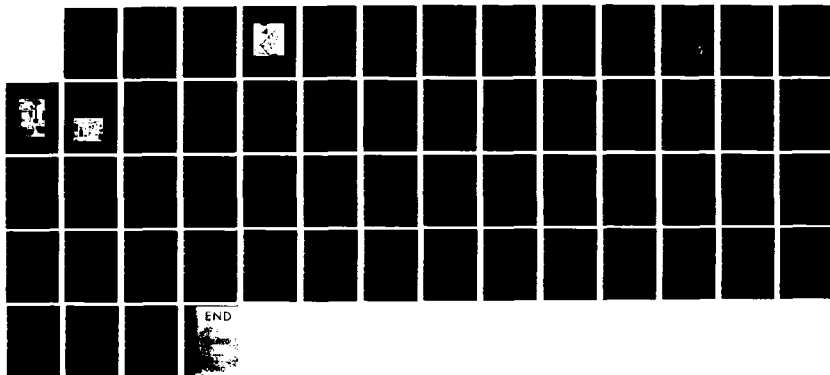
WASHINGTON DC SHOCK AND VIBRATION INFORMAT. SEP 77

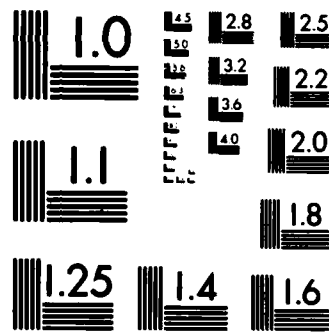
UNCLASSIFIED

BULL-47-PT-4

F/G 20/11

NL





MICROCOPY RESOLUTION TEST CHART  
NATIONAL BUREAU OF STANDARDS-1963-A

TABLE II  
Vibration Parameters of the Beam

Mode No.		Theoretical Undamped	IDENTIFIED							
			Present Technique			Method of [19]			Peak Amplitude	
			$f_n$ (Hz)	Principal Mode*	$f_d$ (Hz)	$\eta$	Principal Mode*	$f_d$ (Hz)		
1	23.82	100.00	22.86	0.0018	100.00	22.87	0.00162	100.00	22.2	100.00
		60.66			58.62 - i0.84			58.73 - i0.81		51.80
2	149.06	100.00	145.63	0.00055	100.00	145.58	0.00055	100.00	143.2	100.00
		-243.63			-213.54 + i18.09			-213.64 + i18.53		-217.00
3	417.61	100.00	404.85	0.00141	100.00	404.41	0.00129	100.00	401.4	100.00
		260.64			237.25 + i9.24			237.11 + i9.20		286.00

\*Mode shapes are presented as displacements at stations 1 and 2, with that at station 1 having a reference value of 100 units; imaginary values indicate the phase difference between the motion at the two stations.

for beams, and with results obtained using the method of [19]. There is a good comparison of the results for frequencies and mode shapes obtained by all three experimental methods, particularly between the two time domain procedures. It is noted that the time domain methods give phase information regarding the coordinates in addition to the amplitude ratios. The damping ratios as obtained by the two time domain methods do not agree so well. The determination of damping ratios in both cases depends upon the relative amplitudes of the real and imaginary parts of characteristic roots. For modes which are as lightly damped as those encountered in the beam used in this experiment, even small errors in the relative amplitudes of the real and imaginary parts can cause large differences in the damping ratios obtained.

## 2. Generalized Payload Model

The payload model is shown in Fig. 2. Sixteen accelerometers were fixed to the eight bulkheads; eight accelerometers on each side, Fig. 3. Two data groups were used. Data group one had accelerometers 1 to 8. Data group two had accelerometers 9 to 16 and accelerometer 8 as a common accelerometer for the two data groups. A random input was applied at station 8. The input was cut off and free responses from data group one were recorded on a tape recorder. The procedure was repeated for data group two. A two-way switch was used to cut off the random input and at same time generate a D.C. signal of about 1 volt. The start of the D.C. signal, recorded on a separate channel of the tape recorder, was used to determine the start of the free response.

The free responses were filtered to eliminate frequency components higher than 350 Hz and then digitized at a sampling rate of 2000 sample/second. Only 500 points for each channel were stored to be used as data for the identification program. This corresponds to a record length of 0.25 second.

The noise/signal ratio for the resulting data was estimated at about 22%. This estimate was based on comparing two responses from station 8 that were recorded simultaneously on two channels of the tape recorder. The root mean square of the two records, rms and RMS, were calculated and the noise/signal ratio was estimated using the following formula:

$$N/S = \sqrt{\frac{(RMS - rms)^2}{RMS \times rms}}$$

Higher order response vectors were generated using Eqs. (32) and (33). Results of the determinant check are shown in Table III from which it is indicated that the system had ten modes in its response. The determinant check indication is not as strong as in the cantilever beam case because of the higher level of noise in the payload model response.

Although it was known from the determinant check that the system's responses contained about 10 modes, a mathematical model with 20 degrees of freedom was used to identify the system. Also a math model of 40 D. O. F. was used. Structures mode can be differentiated from noise modes by observing that the system's modes occur consistently in different computer runs. Table IV shows the frequencies of the ten modes obtained by this technique using a math model of 20 and 40 D. O. F. Also listed are frequencies obtained by sine sweep test and NASTRAN. Figures 4-a to 4-f show some of the identified mode shapes.

## CONCLUSION

The theory and application of a time domain modal vibration testing technique are presented. The results of the two experiments reported in this work are very encouraging. The second experiment (payload model) proved that the technique is insensitive to measurements noise. While the data used for this experiment had about 22% noise, the identified frequencies compared extremely well with the analytical (NASTRAN) and the other experimental (sine sweep) frequencies. Maximum error in the identified frequencies was in the range of 2.5%.

Another important feature of this technique is the ability to use an overspecified math model to identify a number of modes much less than the number of degrees of freedom of the math model. This is very useful when the number of modes in the structure's response is not exactly known because the determinant check, due to high noise levels in the data, might be inconclusive.

Simplicity and economy of the experimental procedure was the main factor in designing this technique. Any structure, however complex, can be identified in stages using only two stations at a time. Also the data needed for the identification program was minimized. The free response needed can be either displacement, velocity acceleration or strain response. The length of record needed to identify a certain structure was noted to be relatively small. Only 0.25 seconds of data was used to identify the ten modes of the payload model.

## ACKNOWLEDGEMENT

The work described in this paper was supported by the National Research Council of Canada Grant No. A7094, The National Research Council of the U.S. and NASA Grant NSG 1325.

## REFERENCES

1. Charles C. Kennedy and C.D.P. Pancu, "Use of Vectors in Vibration Measurement and Analysis", J. of the Aeronautical Sciences, Vol. 14, No. 11, pp. 603, 1947

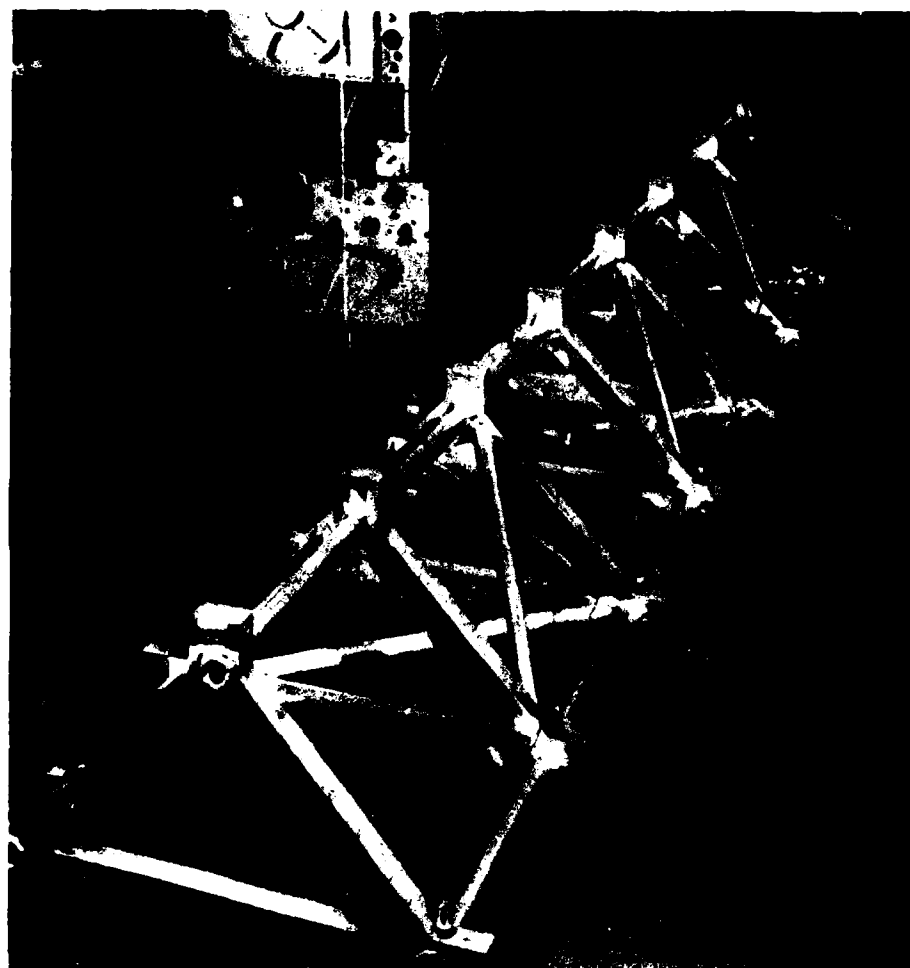


Fig. 2 - Payload Model

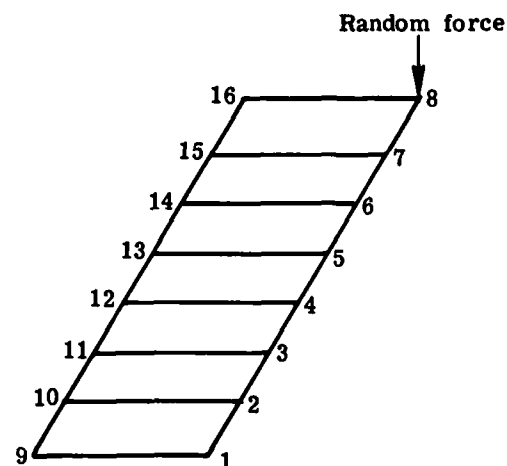


Fig. 3 - Location of stations

TABLE III  
Derterminant Check

No. of Stations (N)	$ \text{Det} _N$	$ \text{Det} _N /  \text{Det} _{N+1}$
1	$0.50 \times 10^0$	$0.35 \times 10^1$
2	$0.14 \times 10^0$	$0.32 \times 10^2$
3	$0.46 \times 10^{-2}$	$0.10 \times 10^3$
4	$0.43 \times 10^{-4}$	$0.10 \times 10^3$
5	$0.45 \times 10^{-6}$	$0.11 \times 10^3$
6	$0.40 \times 10^{-8}$	$0.13 \times 10^5$
7	$0.31 \times 10^{-12}$	$0.88 \times 10^4$
8	$0.35 \times 10^{-16}$	$0.66 \times 10^4$
9	$0.52 \times 10^{-20}$	$0.12 \times 10^6$
10	$0.44 \times 10^{-25}$	$0.20 \times 10^{10}$
11	$0.25 \times 10^{-34}$	$0.10 \times 10^{10}$
12	$0.25 \times 10^{-43}$	$0.24 \times 10^{11}$
13	$0.10 \times 10^{-53}$	$0.34 \times 10^{10}$
14	$0.30 \times 10^{-63}$	$0.77 \times 10^{10}$
15	$0.39 \times 10^{-73}$	$0.13 \times 10^{11}$
16	$0.30 \times 10^{-83}$	$0.24 \times 10^{11}$
17	$0.13 \times 10^{-93}$	$0.13 \times 10^{13}$
18	$0.97 \times 10^{-106}$	$0.46 \times 10^{11}$
19	$0.21 \times 10^{-116}$	$0.16 \times 10^{12}$
20	$0.13 \times 10^{-127}$	

TABLE IV  
Frequencies for the Payload Model

Mode No.	Motion	Time Domain		Frequency Sweep	NASTRAN
		20 D.O.F.	40 D.O.F.		
1	1st Bending	74.20	74.15	74.6	73.4
2	1st Torsion	78.75	78.75	79.7	80.1
3	1st Bending (Yaw)	119.88	119.83	120.7	117.3
4	2nd Torsion	156.63	156.63	158.5	158.9
5	2nd Bending	161.95	161.93	163.1	159.9
6	3rd Torsion	216.51	216.44	219.2	218.6
7	3rd Bending	245.00	245.18	246.7	244.6
8	2nd Bending (Yaw)	259.55	261.04	263.7	253.1
9	4th Torsion	280.95	280.94	283.7	283.0
10	5th Torsion	325.31	325.31	328.0	—

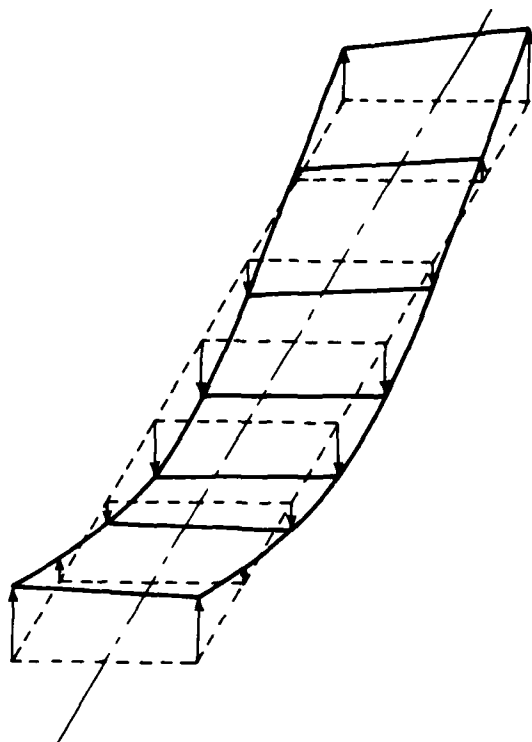


Fig. 4a - Mode No. 1 First Bending

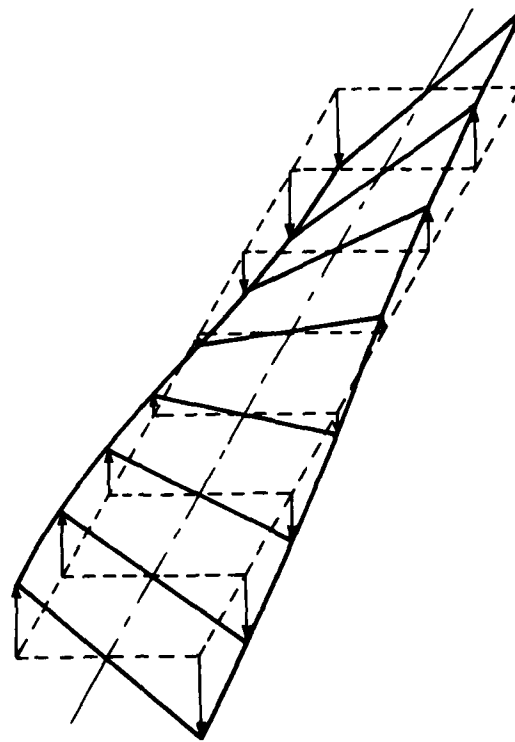


Fig. 4b - Mode No. 2 First Torsion

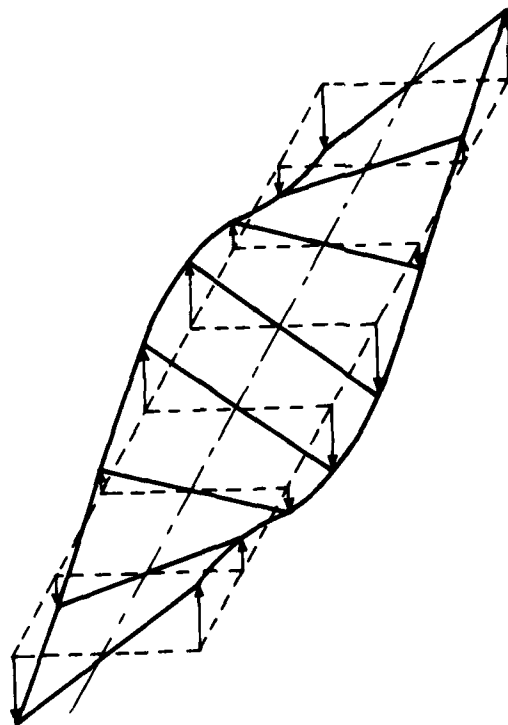


Fig. 4c - Mode No. 4 2nd Torsion



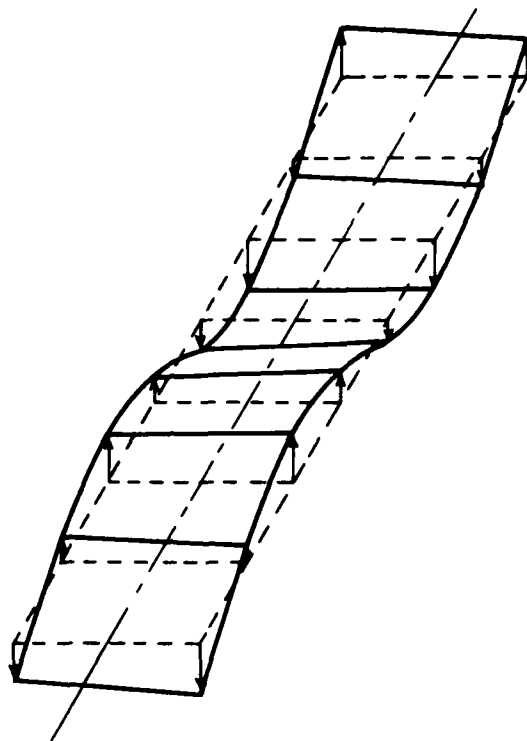


Fig. 4d - Mode No. 5 2nd Bending

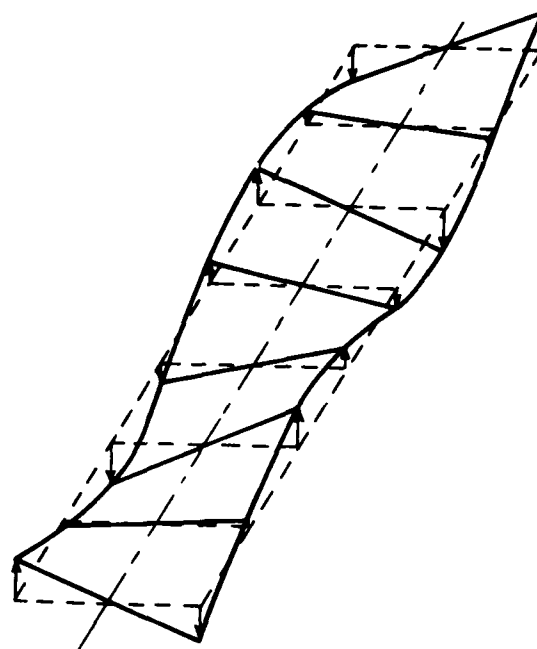


Fig. 4e - Mode No. 6 3rd Torsion

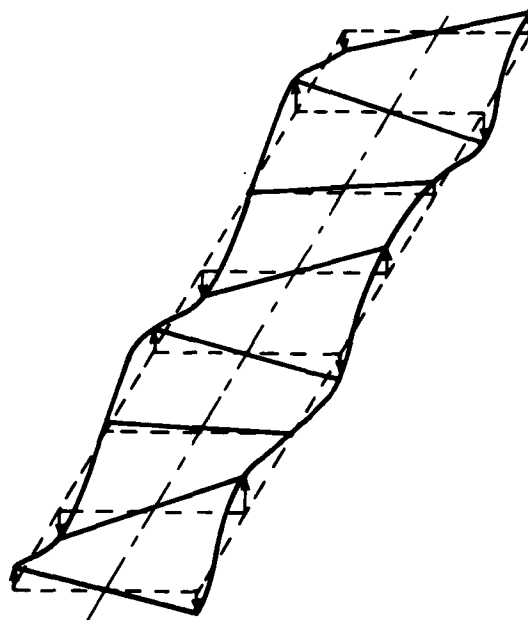


Fig. 4f - Mode No. 10 5th Torsion

2. R.C. Lewis and O.L. Wrisley, "A System For Excitation of Pure Natural Modes of Complex Structures", J. of Aerospace Sciences, Vol. 17, No. 11, Nov. 1950
3. R.W. Trail-Nash, "On the Excitation of Pure Natural Modes in Aircraft Resonance Testing", J. of Aerospace Sciences, Vol. 25, pp. 775, 1958
4. Strether Smith and A.A. Woods, Jr., "Multi-Driver Admittance Technique for Vibration Testing", The Shock and Vibration Bulletin, Bulletin 42, Part 3, Jan. 1972
5. J.P. Raney, "Identification of Complex Structures Using Near Resonance Testing", The Shock and Vibration Bulletin, Bulletin 38, Part 2, Aug. 1968
6. John D. Favour, MaClom C. Mitchell and Norman L. Olson, "Transient Test Techniques For Mechanical Impedance and Modal Survey Testing", The Shock and Vibration Bulletin, Bulletin 42, Part 1, Jan. 1972
7. R.G. White, "Evaluation of Dynamic Characteristics of Structures by Transient Testing", Symposium on Structural Dynamics, University of Technology, Loughborough, England, Mar. 1970
8. B.L. Clarkson and C.A. Mercer, "Use of Cross-Correlation in Studying the Response of Lightly Damped Structures to Random Forces", AIAA Journal, Vol. 3, No. 12, Dec. 1965
9. John V. Otts and Norman F. Hunter, Jr., "Random Force Vibration Testing", The Shock and Vibration Bulletin, Bulletin 38, Part 2, Aug. 1968
10. Robert G. Christiansen and Wallace W. Parmenter, "An Experimental Technique for Determining Vibration Modes of Structures with Quasi-Stationary Random Forcing Function", The Shock and Vibration Bulletin, Bulletin 42, Part 4, Jan. 1972
11. R.E.D. Bishop and G.M.L. Gladwell, "An Investigation into the Theory of Resonance Testing", Phil. Trans. A1963, 255, (No. 1055), pp. 241.
12. J.W. Pendered, "Theoretical Investigation into the Effect of Close Natural Frequencies in Resonance Testing", J. Mechanical Engineering Science, Vol. 7, No. 4, pp. 372, 1965
13. J.W. Pendered and R.E.D. Bishop, "A Critical Introduction to Some Industrial Resonance Testing Techniques", J. Mechanical Engineering Science, Vol. 5, No. 4, pp. 345, 1963
14. J.W. Pendered and R.E.D. Bishop, "The Determination of Modal Shapes in Resonance Testing", J. Mechanical Engineering Science, Vol. 5, No. 4, pp. 379, 1963
15. J.B. Hoerner and P.C. Jennings, "Modal Interference in Vibration Testing", J. of the Engineering Mechanics Division, pp. 827, Aug. 1969
16. N.F. Hunter, Jr. and J.V. Otts, "The Measurement of Mechanical Impedance and its Use in Vibration Testing", The Shock and Vibration Bulletin, Bulletin 42, Part 1, Jan. 1972
17. C.V. Stahl, Jr., "Phase Separation Technique for Ground Vibration Testing", Aerospace Engineering, July 1962
18. S.R. Ibrahim and E.C. Mikulcik, "A Time Domain Modal Vibration Test Technique", The Shock and Vibration Bulletin, Bulletin 43, Part 4, June 1973
19. S.R. Ibrahim and E.C. Mikulcik, "The Experimental Determination of Vibration Parameters from Time Responses", The Shock and Vibration Bulletin, Bulletin 46, 1976
20. C.M. Woodside, "Estimation of the Order of Linear Systems", IFAC Symposium on Identification in Automatic Control Systems, Prague, 1970
21. Charles G. Cullen, Matrices and Linear Transformations, Addison-Wesley Publishing Co., 1972

#### APPENDIX

According to Eqs. (17) and (19), the matrices  $\underline{\Phi}$  and  $\underline{\hat{\Phi}}$  are the results of multiplying the two matrices  $\underline{\Psi}$  and  $\underline{\Lambda}$  and  $\underline{\hat{\Psi}}$  and  $\underline{\Lambda}$ . For  $\underline{\Phi}$  and  $\underline{\hat{\Phi}}$  to have inverses,  $\underline{\Psi}$ ,  $\underline{\hat{\Psi}}$  and  $\underline{\Lambda}$  should be nonsingular. The columns of  $\underline{\Psi}$  and  $\underline{\hat{\Psi}}$  are the modal vectors, which are known to be linearly independent hence neither  $\underline{\Psi}$  or  $\underline{\hat{\Psi}}$  can be singular. Thus, for  $\underline{\Phi}$  and  $\underline{\hat{\Phi}}$  to be nonsingular the requirement is that  $\underline{\Lambda}$  be nonsingular.

$\underline{\Lambda}$  is a  $2n \times 2n$  matrix having elements of the form

$$\lambda_{ij} = e^{\lambda_i t_j} \quad (A-1)$$

If  $t_j$  is arbitrarily chosen to be zero and the time between samples is always the same, then

$$t_j = (j-1) \delta t \quad (A-2)$$

and  $\underline{\Delta}$  takes the form

$$\underline{\Delta} = \begin{bmatrix} 1 & e^{\lambda_1 \delta t} & e^{2\lambda_1 \delta t} & \dots & e^{(2n-1)\lambda_1 \delta t} \\ 1 & e^{\lambda_2 \delta t} & e^{2\lambda_2 \delta t} & \dots & e^{(2n-1)\lambda_2 \delta t} \\ \vdots & \vdots & \vdots & \ddots & \vdots \\ 1 & e^{\lambda_{2n} \delta t} & e^{2\lambda_{2n} \delta t} & \dots & e^{(2n-1)\lambda_{2n} \delta t} \end{bmatrix} \quad (\text{A-3})$$

Substituting  $e^{\lambda_i \delta t} = \alpha_i$ ,

$$\underline{\Delta} = \begin{bmatrix} 1 & \alpha_1 & \alpha_1^2 & \dots & \alpha_1^{2n-1} \\ 1 & \alpha_2 & \alpha_2^2 & \dots & \alpha_2^{2n-1} \\ \vdots & \vdots & \vdots & \ddots & \vdots \\ 1 & \alpha_{2n} & \alpha_{2n}^2 & \dots & \alpha_{2n}^{2n-1} \end{bmatrix} \quad (\text{A-4})$$

$\underline{\Delta}$  is written as the Vandermonde matrix (21), for which the determinant is

$$\begin{aligned} |\underline{\Delta}| &= \prod_{1 \leq i < j \leq 2n} (\alpha_i - \alpha_j) \\ &= \prod_{1 \leq i < j \leq 2n} (e^{\lambda_i \delta t} - e^{\lambda_j \delta t}) \end{aligned} \quad (\text{A-5})$$

Equation (A-5) shows that  $\underline{\Delta}$  is singular only if there are equal  $\lambda$ 's, which is unlikely. Thus in the usual case the inverse of  $\underline{\Delta}$  exists, and  $\underline{\Phi}$  and  $\underline{\hat{\Phi}}$  are non-singular.

## LABORATORY IDENTIFICATION OF THE PATRIOT LAUNCHER STRUCTURE

Thomas R. Meyer and Clifford S. O'Hearne  
Martin Marietta Aerospace  
Orlando, Florida

The changes in alignment under environmental loads of a large, mobile, multi-missile launcher were to be limited by design to small values. Deformations of the launcher structure changing missile pointing in the milliradian range, were predicted for applied loads on the order of thousands of pounds. The predictions were shown to be acceptably accurate by laboratory measurements. The contribution of the paper lies in the demonstration of prediction feasibility, and in the description of test features which allowed efficient test procedures and data reduction.

### INTRODUCTION

PATRIOT is an air defense missile system in the final phase of engineering development for the U. S. Army Materiel Command. Raytheon Company is the prime contractor and Martin Marietta Aerospace (MMA) is principal subcontractor responsible for development of the launcher, canister, and missile subassemblies.

The missile launcher is mobilized on a semi-trailer (Figure 1). The mobile unit is designated launcher station/guided missile (LS/GM). At emplacement, the trailer is stabilized on four outrigger jacks, and the launcher is trained in azimuth and elevation. The launcher carries four missile rounds, each consisting of a canister with a missile. The canister functions as shipping container and launch rail.

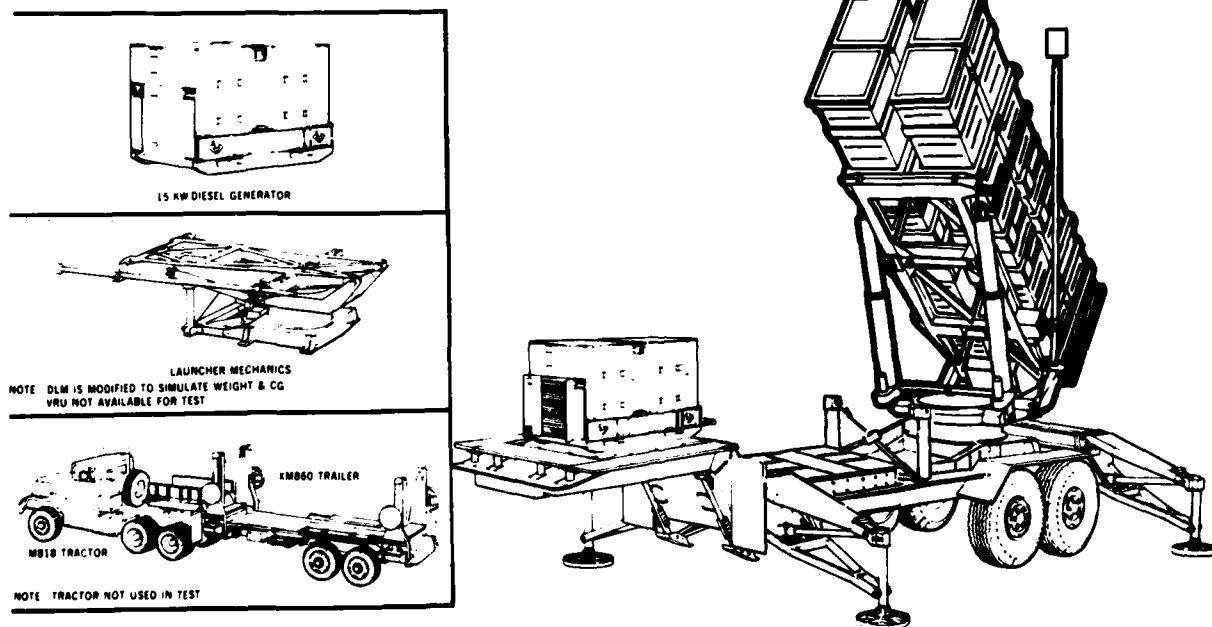


Figure 1. Launching Station/Guided Missile - Test Configuration

The PATRIOT missile is captured in flight by ground radar and command-guided through midcourse. The missile also has an onboard radar seeker antenna. The engagement control station must determine the seeker spatial orientation with a specified total acquisition error (TAE) to acquire the target. An important component of the TAE is the initial alignment error (IAE) which is the difference in actual spatial orientation of the missile at launch and orientation values used by the computer.

The only source of IAE of interest here is the elastic deformation of the structure under environmental and operational loads. Wind, snow, ice, and payload variations are thousands of pounds, while corresponding allocations to the IAE error are on the order of milliradians. In addition to these steady loads, a transient load is created by the plume impingement pressure of departing rounds. Informally, this is called "dynamic pointing error" and the steady load IAE "static pointing error."

#### MEASUREMENT PLAN

The theoretical analysis used to predict errors employed a finite-element structural analysis computer code (Reference 1). Predictions based on a large order finite-element model were calculated in single precision on an IBM 360. Results showed positive margins against all allocations, and predictions were of the same magnitude as the allocations. The adequacy of margins depended strongly on the predicted proximity of rectilinear load centers to the centers of rotation (elastic centers) in the static deformation modes. Due to the vicissitudes of large order finite-element system analysis and the sensitivity of predictions to elastic center location, an experimental verification program was desired.

In the LS/GM configuration analyzed, lateral tension ties were positioned between each canister at the main frames. The requirement for these ties had been created by a need to transfer blast-load-induced momentum across the canister stacks. The strength requirement for the tension ties was eliminated, and there was some reason to believe that their contribution to overall stiffness was negligible in holding deformation-type alignment errors within specified limits. It would have been very expensive to reconstruct the input data sets and rerun the analyses to demonstrate this, however. Instead of recalculation, three static test runs were made with ties installed for direct comparison to runs in which the same loads were applied to the structure without ties.

The turntable is an important "soft spot" in the structure. Static moments about the turntable axis are reacted elastically through a small drive on the pedestal. A pinion on the drive engages a ring gear at the circumfer-

ence of the turntable, and a brake, which prevents turntable rotation, is located at the motor end of the high ratio drive transmission. Overall yaw compliance is significantly influenced by wrap-up in the drive transmission and local deformation of the drive housing support structure. This region was particularly sensitive to inadequate modeling.

Pointing error prediction verification was accomplished indirectly: static influence coefficient measurements and the measurement of decay rates in "ringdowns" following quick release of loads were used. The static influence coefficient test was designed to:

- verify the analytical model by direct comparison of selected analytical and experimental influence coefficients;
- provide a basis for re-estimation of error by having the missile spatial alignments among the output displacements and selecting the load inputs such that the environmental loads could be composed from smoothed linear combinations of inputs at the test load stations;
- develop data to identify the critical "soft spots" in the structure if negative margins were discovered.

The problem of finding "hard points" to apply point loads of the magnitude of distributed loads, as well as minimizing task time and cost demanded that the above goals be achieved with a low number of inputs and outputs. At the same time, a good distribution of inputs and outputs over the structural system was needed. The loads, displacements, and end instruments selected for the test are listed in Table I.

The LS/GM test item consisted of the PATRIOT shop queen launcher mechanics, an XM860 trailer, ballast, a 15-kW diesel generator, and four simulated guided missile (GM) rounds, one representative of a tactical unit. The three remaining canisters were ballasted to tactical weight and center of gravity.

#### INSTRUMENTATION CONSIDERATIONS

Rectilinear and angular displacement measuring devices using remote laser beam guns for displacement reference were developed to satisfy two significant requirements. Firstly, the rigid base reference for displacements undisturbed by loads or ringdown dynamics was needed. This would have been difficult to obtain using ordinary position pots attached to light scaffolding around the loading framework. Secondly, an accurate single axis measurement in the presence of tri-axial motion was needed.

TABLE I  
Static Influence Coefficient Test\*

Measure- ment No.	Load Line Input No.	Measurement/Load Line Input Location	Load Axis	Measure- ment Axis	End Instrument	Max Deflection Range in Axis
1	1	Roadside elevation actuator/platform interface pivot	+Z'	+Z'	Laser and detector	+1.0 in
2	2	Lower roadside canister aft end frame at upper curbside corner	+X'	+X'	Laser and detector	+1.0 in
3	3	Lower roadside canister forward main frame at upper roadside corner	+Y	+Y	Laser and detector	+1.0 in
4	4	Upper curbside canister aft main frame at upper curbside corner	+Y	+Y	Laser and detector	+1.0 in
5	5	Upper roadside canister aft main frame at upper roadside corner	+Y	+Y	Laser and detector	+1.0 in
6	6	Roadside platform/turntable elevation pivot	+X''	+X	Laser and detector	+0.5 in
7	7	Curbside platform/turntable elevation pivot	+X	+Z	Laser and detector	+0.5 in
8	8	Curbside elevation actuator/platform interface pivot	+Z'	+Z'	Laser and detector	+1.0 in
9	9	Roadside elevation actuator/platform interface point	+Y	+Y	Laser and detector	+1.0 in
10	10	Upper curbside canister aft end frame at lower curbside corner	+X'	+X'	Laser and detector	+1.0 in
11	11	Aft trailer chassis longitudinal centerline	+X	+X	Disp transducer	+0.5 in
12	12	Radar support bracket at Tra Sta 434, WL 43, BL +29.75	+Y''	+Y	Disp transducer	+0.25 in
13	13	Radar support bracket at Tra Sta 434, WL 43, BL +29.75	+Z''	+Z	Disp transducer	+0.25 in
14	14	Radar support bracket at Tra Sta 515, WL 43, BL +40	+Y''	+Y	Disp transducer	+0.25 in
15	15	Radar support bracket at Tra Sta 515, WL 43, BL +40	+Z''	+Z	Disp transducer	+0.25 in
16	NA	Curbside platform/turntable elevation pivot	+X	+X	Laser and detector	+1.0 in
17		Upper roadside canister forward end frame at upper roadside corner	+Y	+Y	Laser and detector	+1.0 in
18		Curbside platform/turntable elevation pivot	+Z	+Z	Laser and detector	+1.0 in
19		Missile, Sta 309	+U'	+U'	Laser, mirror, GP target	+10.0 mr
20		Missile, Sta 303, roadside vertical centerline	+V	+V	Laser, mirror, biaxial, auto collimator, ch 1	+10.0 mr
21		Missile, Sta 303, roadside vertical centerline	+W'	+W'	Laser, mirror, biaxial, auto collimator, ch 1	+10.0 mr
22		Launcher base at Sta 538.0, BL -12.0, WL 48.25	+U	+U	Laser, mirror, biaxial, auto collimator, ch 2	+5.0 mr
23		Launcher base at Sta 538.0, BL -12.0, WL 48.25	+V	+V	Pendulum disp	+2.0 mr
24		Launcher base at Sta 538.0, BL -12, WL 48.25	+W	+W	Laser, mirror, biaxial, auto collimator, ch 2	+2.0 mr
25		Turntable/launcher base (tangential motion)	+W	+W	Disp transducer	+15.0 mr
26		Outrigger vertical strut, forward roadside	+Z	+Z	Strain gage	25K
27		Outrigger vertical strut, aft roadside	+Z	+Z	Strain gage	25K
28		Outrigger vertical strut, forward curbside	+Z	+Z	Strain gage	25K
29		Outrigger vertical strut, aft curbside	+Z	+Z	Strain gage	25K
30+		Pinion gear rotation	+W	+W	Disp transducer	+222 mr
31		Input load			20K dual output load cell	20K
32		Radar support bracket at Tra Sta 434, WL 43, BL -29.75	+Y	+Y	Disp transducer	+0.25 in
33		Radar support bracket at Tra Sta 434, WL 43, BL -29.75	+Z	+Z	Disp transducer	+0.25 in
34		Radar support bracket at Tra Sta 515, WL 43, BL -40	+Y	+Y	Disp transducer	+0.25 in
35		Radar support bracket at Tra Sta 515, WL 43, BL -40	+Z	+Z	Disp transducer	+0.25 in
36		Turntable/launcher base	+Z	+Z	Disp transducer	+0.25 in
37	NA	Test identification (three digit number sequence)			Manual data entry	

Notes:

\*Tentative, may be changed if dictated by test data or structural analysis.

Quick look measurements - input load, load line measurement, measurement numbers 1, 2, and 3.

+Turntable backlash test.

A deformation survey was conducted of the structural test laboratory to ensure that effectively rigid backup of the LS/GM existed at the floor interface and that displacement reference stations would not be disturbed by test loads or motions.

#### INSTRUMENTATION

Measurements 11 through 15, 23, 25, 30, and 32 through 36 used moving core-type displacement transducers from the Hewlett/Packard 7-DCDT Series. Measurements 11 through 15 and 32 through 36 were made with moving cores attached to their displacement stations by aircraft cable. The instrument core shaft was spring-loaded at the rear of the transducer case to hold the cable in tension, thereby permitting bidirectional measurement.

For Measurement 30, the cable was wrapped around the undercut of the pinion gear so the core moved rectilinearly in proportion to pinion gear rotation. The core of Measurement 36 was spring-loaded in compression. The shaft/test item interface allowed low friction transverse sliding. For Measurement 25, the trans-

ducer was mounted to detect tangential motion at the turntable to pedestal interface. Measurement 23 incorporated a displacement transducer to detect motion of a pendulum moving in the launcher base pitch plane.

Measurements 1 through 10 and 16 through 18 employed Spectra Physics Model 132 helium-neon lasers and United Detector Technology Model LSC-4 laser detectors. Each measurement employed a laser gun with a MMA-designed optical attachment which fanned out the emitted laser beam and changed its cross-section to a narrow line. This optical modification eliminated cross-axis motion effects. The line bisected the laser detector at a 90-degree angle to the sensing direction, and cross-axis motion left the detector impingent light pattern virtually unchanged. Rectilinear displacements were measured as the laser detector, which was mounted to the test item, moved during application of load. The relative motion of the laser beam on the surface of the detector produced a change in resistance in a bridge balance circuit (Reference 2).

Angular displacement Measurements 20 through 22 and 24 used a novel technique. The

Spectra Physics Model 132 laser gun was used to illuminate a mirror attached to the test item. The reflected beam was projected on a plexiglas target, which was sandblasted to diffuse the intense laser spot. A Phystec Model 440 auto-collimator optical system, which has bidirectional spot tracking capability, was used to lock-on the spot position at the back of the target. The Phystec thereby provided signals proportional to missile pitch and yaw displacements (Figure 2). Launcher base roll

and yaw were measured similarly. The laser beam was aligned close to the mirror surface-normal direction to eliminate the effect of mirror-normal motion on the measurement.

Measurements 26 through 29 used BLH Model SR-4 strain gages. These measurements were closely proportional to the outrigger pad vertical loadings. Measurement 31, the input load, employed a BLH Model U3G2 20K load cell.

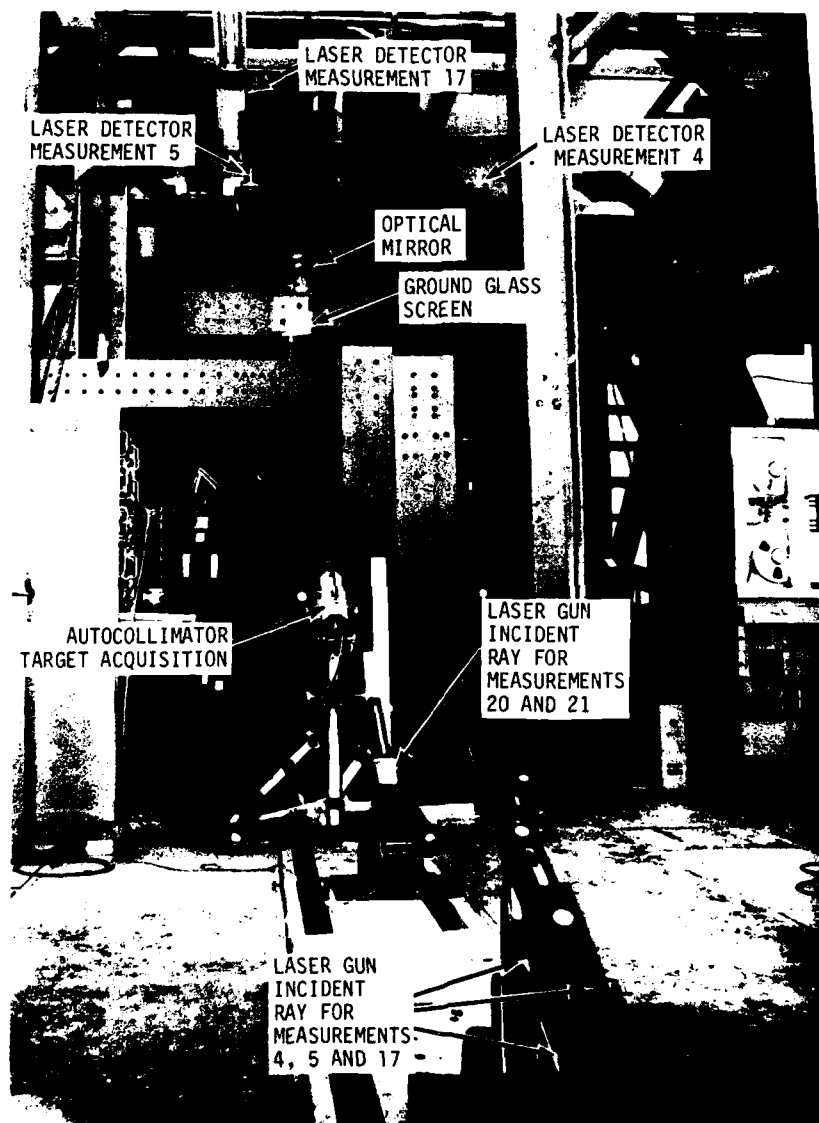


Figure 2. Aft View of Test Setup

#### STATIC INFLUENCE COEFFICIENT TEST

The LS/GM, in the emplacement configuration was set up in the MMA structural test laboratory (Figure 2), and a steel test fixture

was erected adjacent to the test item. A load line, consisting of a hydraulic jack with electronic load cell and attachment fittings, was mounted on the test fixture and attached to the

test item at one of the fourteen prescribed input locations. Instrumentation was set up to record the measurements as indicated in Table I. Instrument data were sampled and recorded

digitally using a Systems Engineering Laboratories Model 600 data acquisition system. The input control, output recording, and safety feedback are shown in Figures 3 and 4.

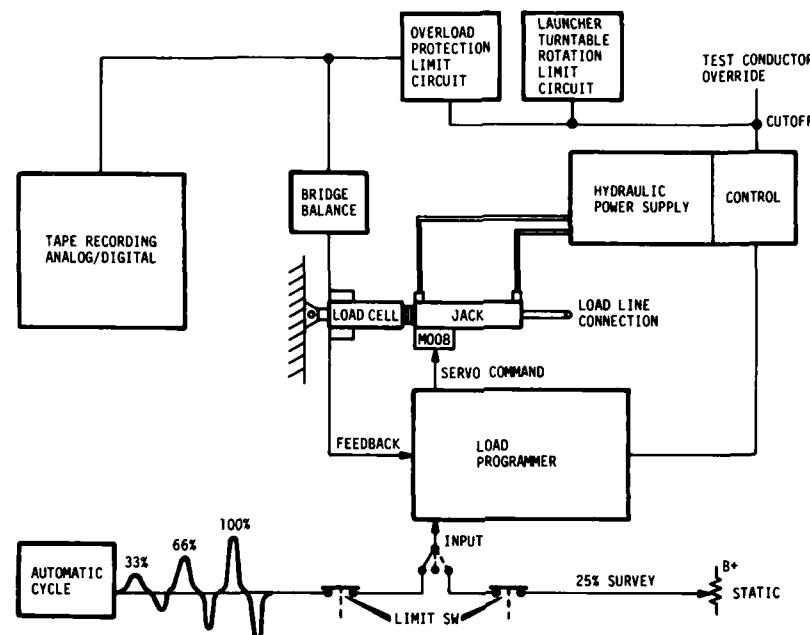


Figure 3. Influence Coefficient Test Load Application

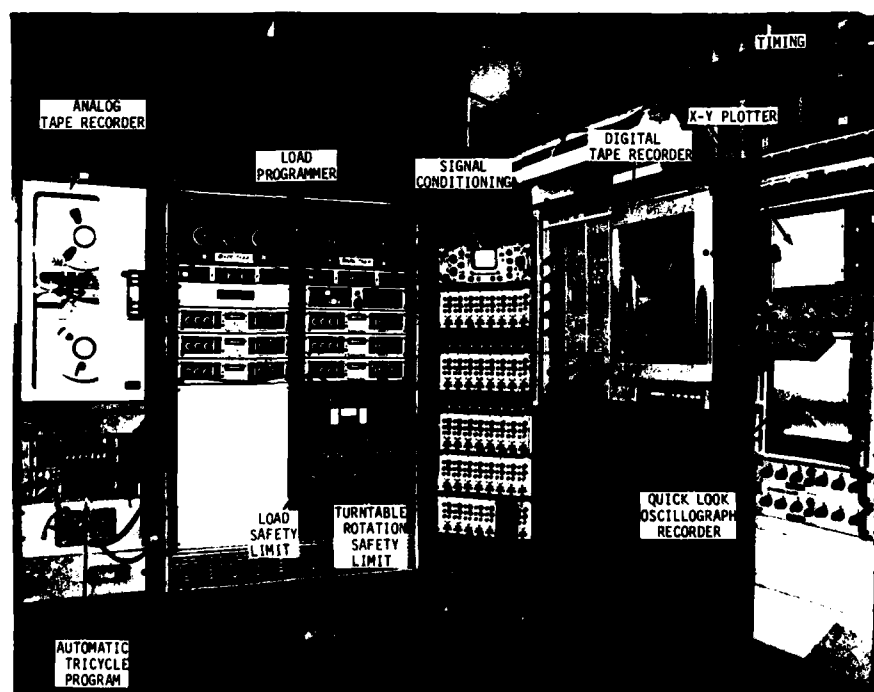


Figure 4. Instrumentation Recording



Test loads were applied (Figure 5) in three adjoining cycles at a low rate of application. The load function was supplied by an MTS Model 480 load programmer. Each cycle contained a tension load followed by a compression load. The cyclic loading rate was 25 seconds per cycle to avoid significant dynamic forces.

The first cycle peaked at 1/3 of the maximum specified for that particular load point. The second and third cycles peaked at 2/3 and 3/3 of maximum load, respectively. The motive for this application formula and the modified versine shape of the load function was to obtain point density near the origin of the displacement versus load plots based on digital

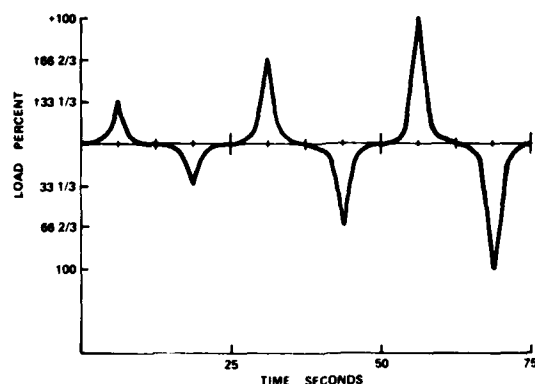
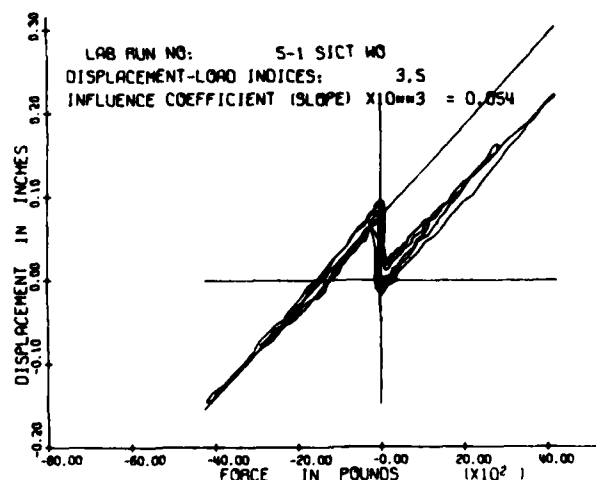


Figure 6. Measurement No. 3 versus Applied Load Load Line No. 2



data sampled at a constant rate. This helped define friction-backlash nonlinearities near the origin, and produced a better distribution of data points in the linear load-displacement range. Approximately 800 data samples per channel, per cycle were recorded.

Measurement 19, a reflected laser beam spot, was visually observed and manually plotted on graph paper. All other instrumentation was recorded on magnetic tape. The tape-recorded data were re-recorded on IBM OS/360 tape files, edited, and plotted on a CalComp. The plotting program also calculated the influence coefficient value using a modified least square fit of a linear function. Typical plots are shown in Figures 6 and 7.

Figure 5. Modified Versine Tricycle

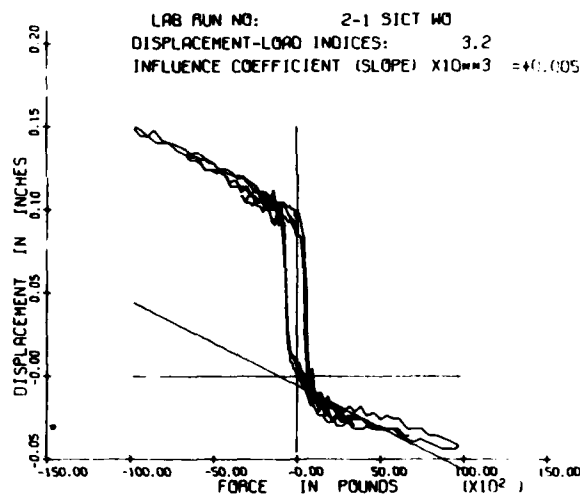


Figure 7. Measurement No. 3 versus Applied Load Load Line No. 5

# FREE MOTION DECAY MEASUREMENT

Free motion decay measurement was accomplished in the static influence coefficient test setup, except the load line was a manually controlled jack with a quick release mechanism. Test runs were made using three of the influence coefficient points selected to obtain decays in the lowest symmetric and antisymmetric modes of motion.

To produce deflection time histories, measurements recorded on analog magnetic tape were processed through an X-Y plotter at reduced speed. All responses were recorded on digital channels as backup. The analog plots were reduced manually to obtain linear damping rates.

These damping values were calculated by fitting linear plots to the sequential variations (peak to peak absolute values) in the decays as plotted on semilog paper.

## RESULTS

Selected static influence coefficient results for seven load lines comparing predicted and measured values are shown in Tables II and III. The nonentries in Table III represent measurements so small that they fall within only a few quantization levels and a slope could not be calculated. The table column indices designate load number and the row indices displacement number.

TABLE II  
Measured and Predicted Influence Coefficients  
(Inch/Pound  $\times 10^{-3}$ )

Measured Values of Influence Coefficients, Matrix M							
	1	2	3	4	5	8	9
1	0.080	0.054	-0.023	0.045	0.035	0.042	-0.042
2	0.054	0.069	-0.020	0.031	0.032	0.027	-0.029
3	-0.009	-0.005	0.173	0.041	0.054	0.012	0.149
4	0.040	0.019	0.038	0.179	0.096	-0.028	0.011
5	0.028	-0.001	0.043	0.105	0.156	-0.040	0.006
8	0.040	0.044	0.020	-0.035	-0.038	0.080	0.034
9	-0.027	-0.011	0.171	0.016	0.019	0.025	0.174
Predicted Values of Influence Coefficients, Matrix P							
	1	2	3	4	5	8	9
1	0.120	0.061	-0.018	0.032	0.032	0.071	-0.033
2	0.061	0.067	-0.011	0.001	0.001	0.055	-0.012
3	-0.018	-0.011	0.211	0.048	0.048	0.021	0.195
4	0.032	0.001	0.048	0.097	0.097	-0.028	0.019
5	0.032	0.001	0.048	0.097	0.097	-0.028	0.019
8	0.071	0.055	0.021	-0.028	-0.028	0.119	0.035
9	-0.033	-0.012	0.195	0.019	0.019	0.035	0.198

TABLE III  
Measured and Predicted Missile Angular Displacement  
Values versus Load Line (MR per 1000 Pounds)

Measured							
	1	2	3	4	5	8	9
Roll	-0.634	-0.132	0.352	-1.100	-1.490	0.625	0.857
Pitch	0.533	0.409				0.472	
Yaw	0.339	0.146	-1.493	0.458	0.410	-0.244	-1.446
Predicted							
	1	2	3	4	5	8	9
Roll	-0.545	-0.064	0.323	-1.044	-1.060	0.526	0.703
Pitch	0.659	0.456	-0.030	0.019	0.019	0.590	-0.048
Yaw	0.271	0.079	-1.348	0.135	0.138	-0.265	-1.348

Test results showed the design was within its allocated error budget. The largest discrepancy occurred in yaw under load lines 4 and 5. By recomposing to the environmental loads, it was shown that the yaw margin was, in fact, close to the predicted value. Other criteria showed adequately close correspondence of test data and predictions. As expected, the lateral ties had a negligible effect on structural compliances.

Damping rates of 0.03 and 0.07 were obtained in the fundamental symmetric and anti-symmetric modes of motion. These corresponded to a value of 0.05 which had been estimated on the basis of experience with similar structure.

#### COMMENTS

Particularly interesting features of the test were:

- the laser instrumentation
- the automatic input and computer retrievable data collection
- the data reduction and plotting using large computer software and hardware.

The laser instrumentation is detailed in Reference 2. The automatic input-output features helped compress laboratory run time. The accumulation of test data in a form easily accessible at a time sharing scope terminal permitted a quick look at any displacement-load plot on a CRT scope.

It would have been desirable to examine results in the laboratory, virtually on-line, but a local computer was not available, and the data acquisition system could not be directly connected to a time sharing terminal. Software used for the quick-look scope plots was the same as that used for computer graphics plots produced for the engineering report. Because extensive plotting software and hardware were accessible from the same terminal as the

#### DISCUSSIONS

Mr. Dyrda (Boeing Company): Was this mainly an aiming error analyses?

Mr. O'Hearne: The requirement was basically one that came out of systems analysis. We allocate so many milliradians for environmental load due to structural deformation. There is the complete budget due to mechanical tolerances and delaying tolerances, etc. Our job was to predict whether or not we met that budget and show that our predictions were accurate.

data sets, programming and plot production were easily accomplished.

The scrupulosity of the title of this paper has been questioned. A reviewer wrote: "The title is misleading in that no 'structural identification' is performed." It may be that many structural engineers would not use the term for a static influence coefficient measurement; others perhaps would resent the introduction of a neologism adumbrating an old locution. The authors maintain that using input-output to determine parameters of any system equation is "system identification." The terminology is recent, but solidly ensconced in the literature.

#### CONCLUSION

This structural identification program could have been extraordinarily difficult. Generating the data, handling the large volume of information, and making the transformations to meaningful reduced representations could have been, in the hands of the sorcerer's apprentices, a boundless work. Actually, it was a remarkably quick and easy job, facilitated by the selection of appropriate end instruments and the use of digital recording, digital computation, and digital computer graphics. Predictions of large multilauncher deformations affecting critical alignments in the milliradian range can be made with useful accuracy using ordinary engineering analysis. Test laboratory verification can be accomplished expeditiously.

#### REFERENCES

1. O'Hearne, C.S. and Shipley, J.W. "Structural Dynamics Computations Using an Approximate Transformation," Bulletin 44, Part 2, The Shock and Vibration Bulletin, No. 44, Part 2, August, 1974.
2. Cawthorn, John E., "The Use of a Low Power Laser and Photodiode for Displacement Data, Bulletin of the 47th Shock and Vibration Symposium.

## COMPUTER APPLICATIONS

### DIGITAL SIMULATION OF FLEXIBLE AIRCRAFT RESPONSE TO SYMMETRICAL AND ASYMMETRICAL RUNWAY ROUGHNESS

Tony G. Gerardi  
Air Force Flight Dynamics Laboratory  
Wright-Patterson Air Force Base, Ohio

A method has been developed for determining the dynamic response of a flexible aircraft to symmetric and asymmetric runway roughness during takeoff or constant speed taxi. The mathematical model has been programmed and run on a CDC 6600 digital computer and uses a Calcomp plotter for part of the output. The solution algorithm is a direct three term Taylor series solution yielding a ratio of solution time to real time of 1.75. Peak value vertical acceleration level comparison of simulated results to limited measured results were satisfactory. The mathematical model demonstrated the capability of accomplishing the intended purpose of locating the rough areas of a runway.

#### INTRODUCTION

A common problem that occurs during take-off and taxiing operations of aircraft is high acceleration levels caused by a rough runway. Due to these accelerations, runways must be evaluated with respect to roughness in order to ensure timely pavement maintenance to control aircraft structural loads and fatigue. Also, rough runways adversely affect the normal functional ability of the crew members by reduced instrument readability and reduced crew comfort. Figure 1 shows criterion<sup>1</sup> used to set maximum allowable vertical acceleration levels from a human comfort standpoint. Reference 2 addressed the runway roughness problem at considerable length and contains the development of a mathematical model and subsequent computer program called "TAXI" to simulate the dynamic response of aircraft to runway roughness on a symmetrical runway. For a symmetric runway, only one runway profile is required. Normally this is sufficient for representing a paved runway. With the advent of the AMST (Advanced Medium STOL Transport) and in some cases with conventional airplanes operating off of semi-prepared or very rough paved surfaces, the rolling motion of an aircraft became significant. This rolling motion was the result of operating the aircraft on an asymmetric runway. Therefore, in order to properly simulate this response, it became necessary to include the runway profile encountered by each landing gear.

The primary purpose of this study was to develop a computer program capable of simula-

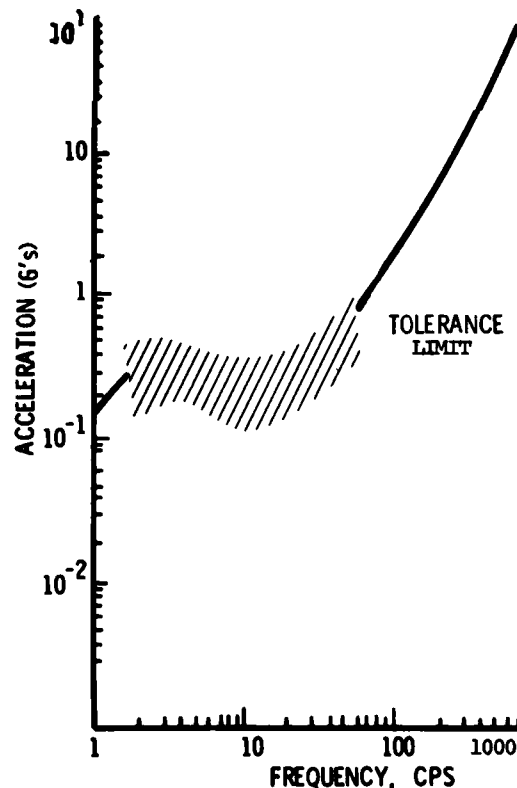


Figure 1. Human Comfort Vertical Acceleration Criteria

ting an aircraft during takeoff from or constant speed taxi over an asymmetrical runway. The mathematical model includes roll, pitch, vertical and horizontal translation as rigid body degrees of freedom, plus a vertical translation degree of freedom for each landing gear. In addition, up to 30 flexible airplane modes can be included in the simulation.

is controlled by the landing gear strut forces, lift, drag, thrust and the resisting parameters of aircraft mass and inertia.

The landing gear struts are nonlinear, single or double acting oleo pneumatic energy absorbing devices (Figure 2) and are represented in the model as the sum of the three forces,

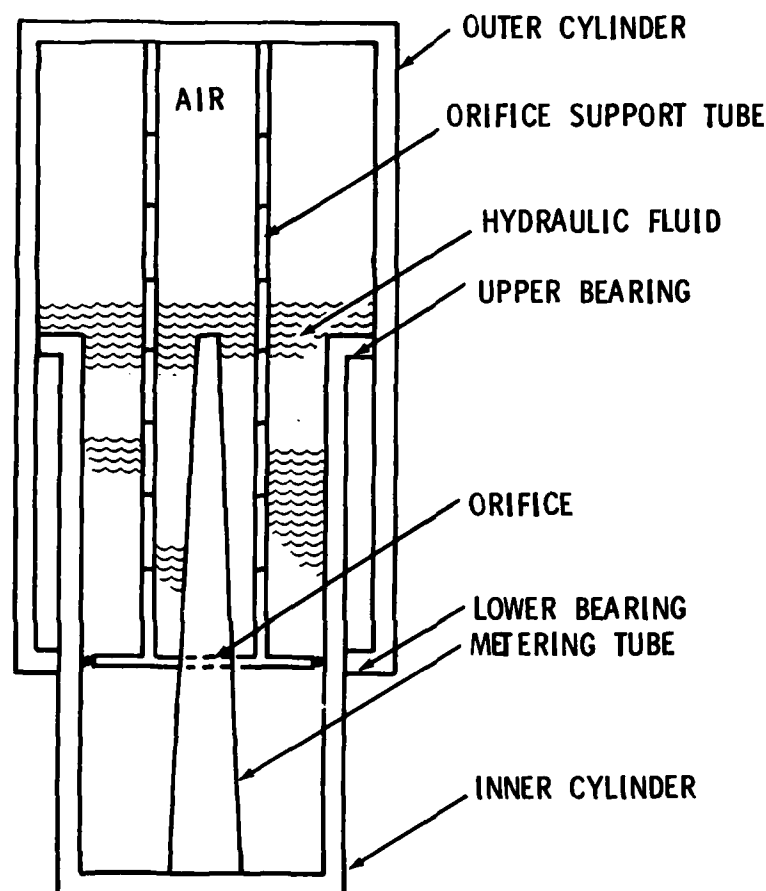


Figure 2. Typical Single Acting Oleo Pneumatic Landing Gear Strut

#### General Airplane/Runway Model

The general model is represented as an asymmetrical body with a nose, and a right and left main landing gear. Each landing gear strut is assumed to have point contact with the profile and it is assumed that each landing gear traverses a different profile. The model has aerodynamic life and drag, and thrust applied at the aircraft's center of gravity.

The airplane is free to roll, pitch, plunge and translate horizontally and, in addition, each landing gear unsprung mass is free to translate vertically. To these rigid body degrees of freedom, up to 30 flexible modes of vibration are included. The airplane motion

pneumatic, hydraulic and strut bearing friction forces. The pneumatic force, resulting from compression of the air in the upper cylinder, which is the largest of the three, is represented by the equation:

$$F_A = \frac{PV}{\frac{V}{A} - S} \quad (\text{For Single Chambered Strut}) \quad (1)$$

where:

P = the fully extended strut pressure

V = the fully extended strut volume

A = the pneumatic piston area

S = strut stroke

The hydraulic or damping force is given by the equation:

$$F_h = \frac{\rho_h A_h^3 \dot{S} |\dot{S}|}{2 (C_d A_o)^2} \quad (2)$$

where:

$\rho_h$  = density of the hydraulic fluid

$A_h$  = the hydraulic piston area

$A_o$  = effective orifice area (constant orifice minus metering pin area)

$C_d$  = orifice coefficient (use .9)

$\dot{S}$  = strut piston velocity

The third strut force is the strut bearing friction force and is expressed as follows:

$$F_F = (\mu |F_u| + \mu |F_l|) \frac{\dot{S}}{|S|} \quad (3)$$

where:

$\mu$  = the sliding coefficient of friction (usually .1)

$F_u$  and  $F_l$  = upper and lower bearing forces required to balance the lateral loading

$\dot{S}$  = strut velocity

and

$$F_l = \frac{F_s X_a}{X_b + S} \quad (4)$$

$$F_u = (1.0 - \frac{X_a}{X_b + S}) \quad (5)$$

where:

$F_s$  = total wheel drag force

$X_a$  = strut piston length

$X_b$  = minimum bearing separation

S = strut stroke

The force  $F_s$  can be large during landing spinup or braking. During taxi however, the strut friction force is very small compared to the total strut static force for symmetrically loaded struts. For this reason it is usually neglected in the simulation (See Reference 2).

The tire force is represented by the linear equation:

$$F_T = k T_D \quad (6)$$

where:

$T_D$  = tire deflection

k = linear tire spring constant

The runway elevation data (See Figure 3) is input into the model in two foot length increments. The profile is made continuous by fitting the following polynomial through the three elevation data points and the slope at the end of the previous profile segment:

$$y(x) = a_1 + a_2x + a_3x^2 + a_4x^3 \quad (7)$$

where:

$a_{1,2,3,4}$  = coefficients derived from the elevation and slope data

This is done for each of the three lines of runway profile data.

#### Rigid Body Equations of Motion

The differential equations of motion for the mathematical model were derived by application of the method of Lagrange. The general form of these equations are shown below and corresponds to the notation shown in Figure 4.

$$\ddot{Z} = (F_{s1} + F_{s2} + F_{s3} + L - W)/M_{cg} \quad (6)$$

[c.g., vertical acceleration]

$$\ddot{Z}_1 = (F_{t1} - F_{s1} - W_1)/M_1 \quad \text{Landing gear} \quad (9)$$

$$\ddot{Z}_2 = (F_{t2} - F_{s2} - W_2)/M_2 \quad \text{Vertical} \quad (10)$$

$$\ddot{Z}_3 = (F_{t3} - F_{s3} - W_3)/M_3 \quad \text{Accelerations} \quad (11)$$

$$\ddot{\theta} = (F_{s1}A + F_{s2}B + F_{TD}\epsilon_1 - F_{s3}C)/I_{yy} \quad (12)$$

[pitching acceleration]

$$\ddot{\phi} = (F_{s3} - F_{s2})C/I_{xx} \quad (13)$$

[rolling acceleration]

$$\ddot{X} = (F_T - F_{TD} - F_{AD})/(M_{cg}) \quad (14)$$

[horizontal translation acceleration]

where:

$F_{s1}, F_{s2}, F_{s3}$  = total landing gear strut forces

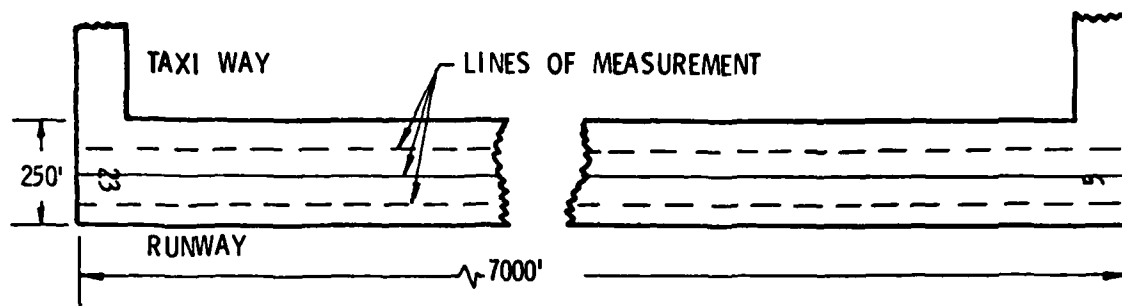
$F_{t1}, F_{t2}, F_{t3}$  = tire forces

$M_{cg}, W, I_{yy}, I_{xx}$  = aircraft mass, weight, and pitching and roll inertias

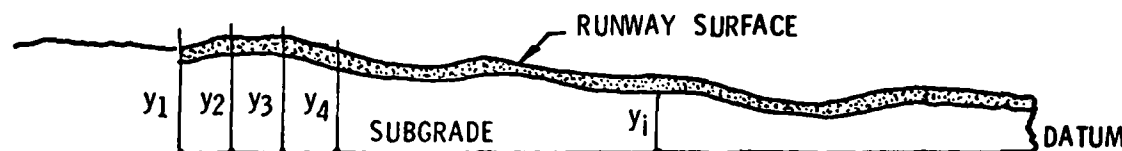
$W_1, W_2, W_3$  = unsprung landing gear weights

A, B, C,  $\epsilon_1$  = moment arms

L,  $F_T, F_{TD}, F_{AD}$  = lift, thrust, and tire aerodynamic drag forces



(a) TYPICAL RUNWAY (NOT TO SCALE)



(b) TYPICAL RUNWAY ELEVATION PROFILE

Figure 3. Runway Profile Representation

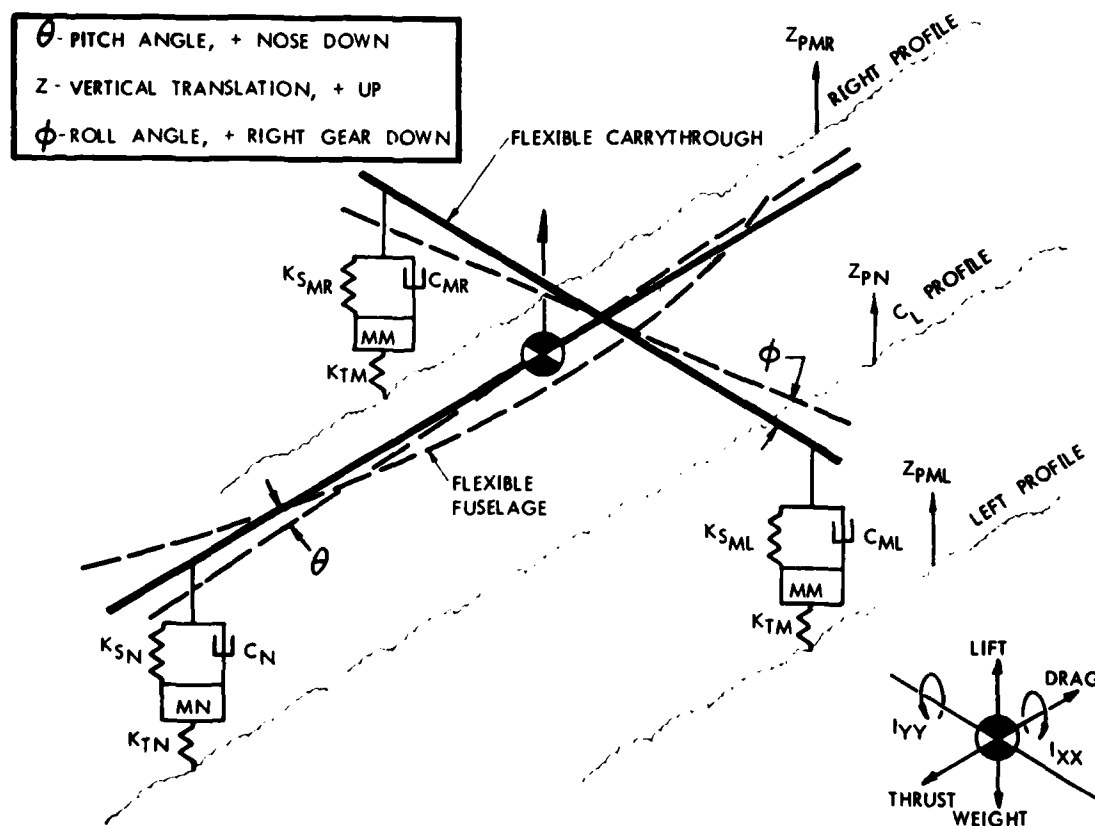


Figure 4. Free Body Diagram Used to Develop the Mathematical Model

The subscript 1, 2 and 3 corresponds to the nose, right main and left main landing gears respectively.

[ $F_T$  and  $F_{AD}$  act through the center of gravity]

#### Flexibility Equations of Motion

$$M_i \ddot{q}_i = \xi_{i1} F_{s2} + \xi_{i2} F_{s2} + \xi_{i3} F_{s3} - 2\zeta_i \dot{q}_i - \omega_i^2 M_i q_i \text{ for the } i\text{th mode} \quad (15)$$

where:

$M_i$  = the generalized mass

$\xi_{i1}, \xi_{i2}, \xi_{i3}$  = modal deflections at gear location 1, 2 and 3

$\omega_i$  = modal frequency

$\zeta$  = damping factor

$q_i, \dot{q}_i, \ddot{q}_i$  = generalized coordinates and their time derivatives

The sign convention is as follows:

$Z$  = Vertical Displacement + up  
 $\theta$  = Pitch + nose down  
 $\phi$  = Roll + roll right  
 $q$  = Deflection Due to Bending + up  
 $X$  = Horizontal Translation + forward

#### Solution Technique

The technique used for solving the coupled nonlinear differential equations of motion that describe the simulated aircraft is the same as described in reference 2; a three-term Taylor series. For example, the equation:

$$\ddot{x} = -c\dot{x} - kx \quad (16)$$

The three-term Taylor series representation can be written as:

$$x_{(I+1)} = x_{(I)} + \dot{x}_{(I)} (\Delta t) + \ddot{x}_{(I)} \frac{(\Delta t)^2}{2} \quad (17)$$

where:  $I = 1 \rightarrow N$

The values for  $x, \dot{x}$  and  $\ddot{x}$  from the previous step are substituted into equation (17) and a new value for  $x$  is obtained. Differentiating equation (17) we obtain for the velocity  $\dot{x}$ , the expression:

$$\dot{x}_{(I+1)} = \dot{x}_{(I)} + \ddot{x}_{(I)} (\Delta t) \quad (18)$$

The values for  $\dot{x}$  and  $\ddot{x}$  are then substituted into equation (14) and a new value of  $\ddot{x}$  is found. This entire process is repeated with

the new values of  $x$  and  $\dot{x}$  to obtain the next point in the solution.

#### RESULTS

The results of the computer program are displayed in two forms, one, a standard digital listing, and two, a Calcomp plotted time history of the runway profile, the pilot's station vertical acceleration and the center-of-gravity vertical acceleration.

Many simulations have been made using the mathematical model described herein. Included in this paper are several simulations of a large commercial jet, which were of interest:

Figure	Profile	Remarks
6	1-cos dip	Taxi Head-on
7	1-cos dip	Taxi 45°
8	Rough Commercial Airfield	Without a roll degree freedom
9	Rough Commercial Airfield	With a roll degree freedom

Figure 5 is a drawing of the 1-cos dip used in these simulations. The dip is contin-

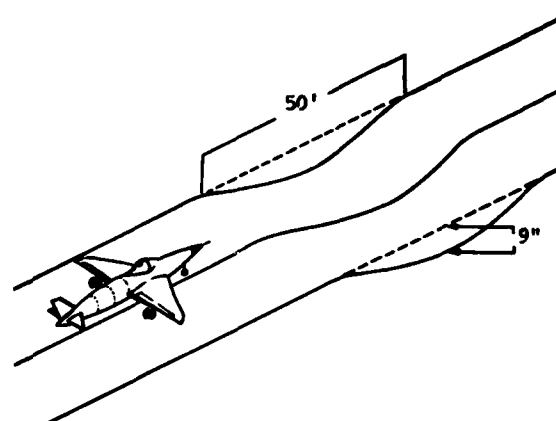


Figure 5. (1-cos) Dip used in Simulations

uous laterally across the runway. In this way the "trough" can be approached at any angle by inputting the appropriate runway profile data.

Figure 6 shows the plotted results of a simulated large commercial jet during a 50 foot per second constant speed taxi over a 1-cos dip. The approach angle was 90°. The maximum vertical acceleration at the pilot's station was slightly over 1g and occurred after the nose landing gear had completely traversed the dip. The center-of-gravity vertical acceleration maximum of .75g occurred at the point when the nose landing gear passed through the



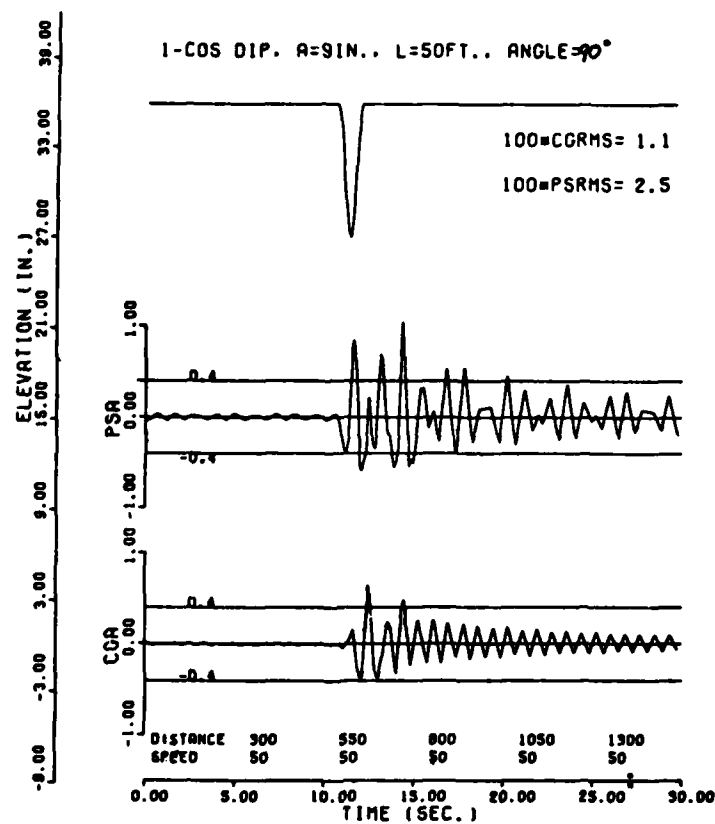


Figure 6. Boeing 727-100 Constant Speed Taxi Simulation over a 1-cos Bump Head-on

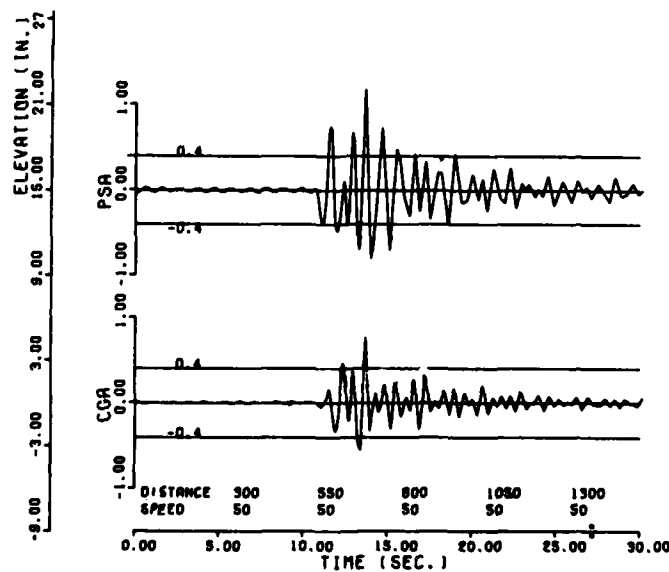


Figure 7. Boeing 727-100 Constant Speed Taxi over a 1-cos Bump at a 45° angle of approach

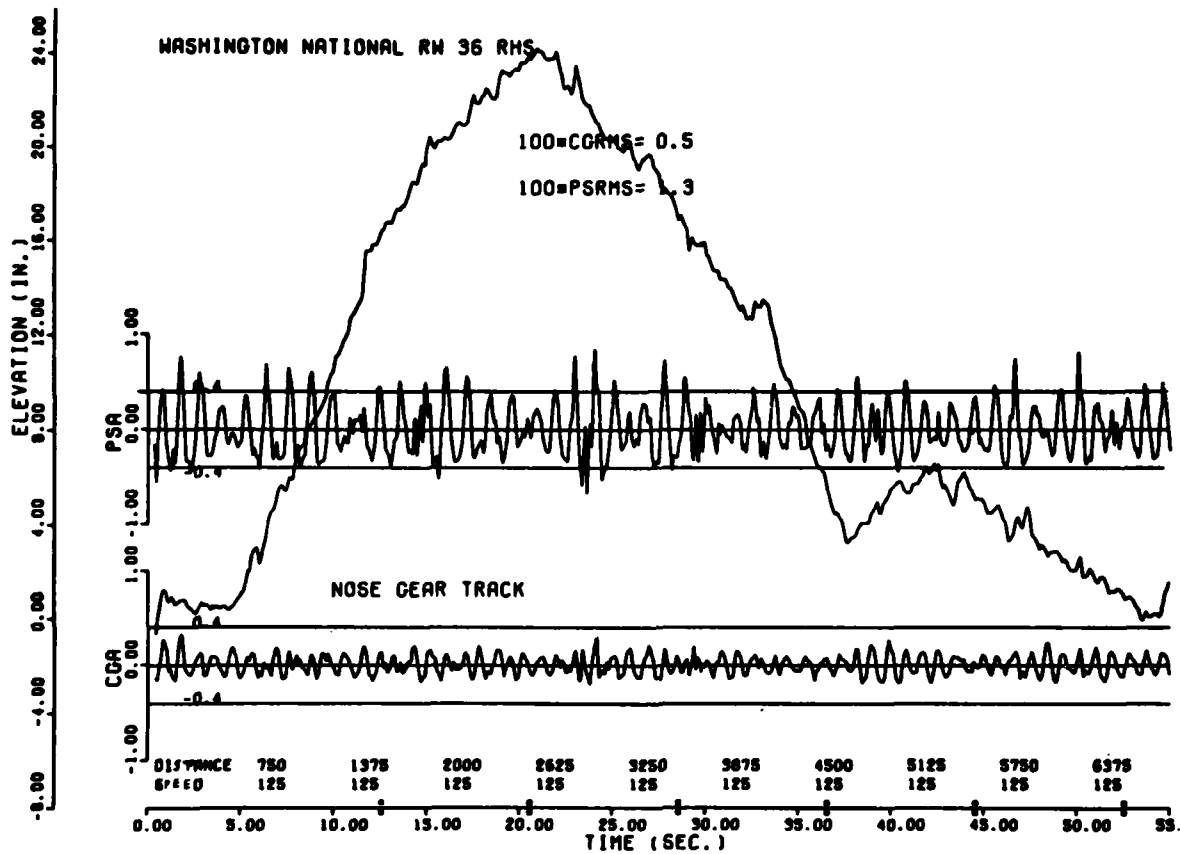


Figure 8. Boeing 727-100 Constant Speed Taxi over the Washington National Profile With a Roll Degree of Freedom

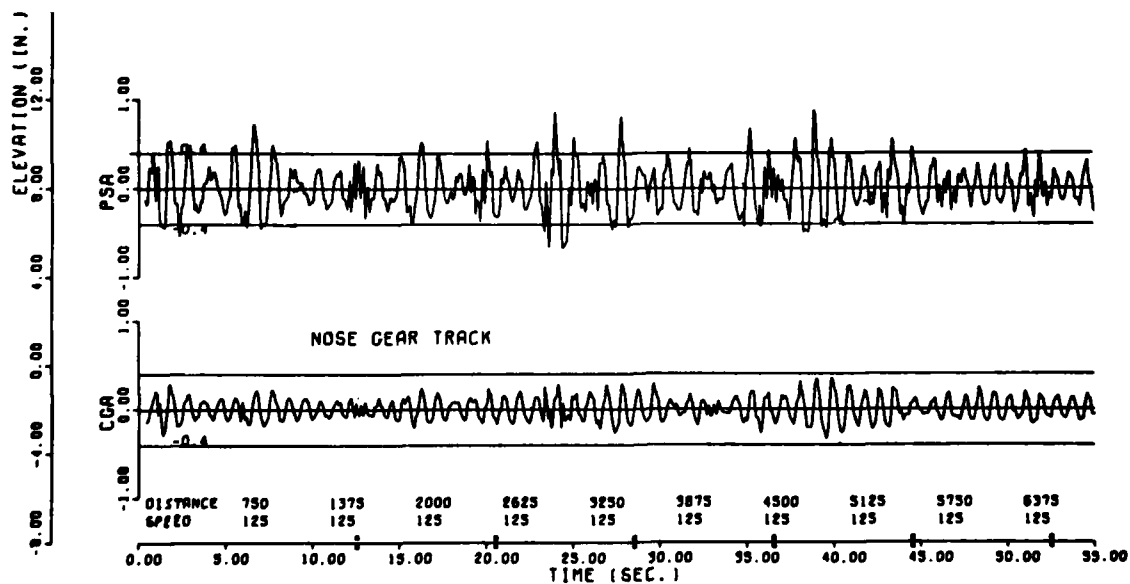


Figure 9. Boeing 727-100 Constant Speed Taxi Simulation over the Washington National Profile Without a Roll Degree of Freedom

bottom of the dip.

Figure 7 shows the plotted results of the same simulation except the approach angle was 45° instead of head-on. The peak pilot's station acceleration occurred at the same point in time but was approximately 10% larger. The peak center-of-gravity acceleration (.6g) was lower, and occurred later than in figure 6. In fact, the c.g. acceleration of figure 7 is in phase with the P.S. acceleration.

It should be pointed out that for the airplane being simulated, the 50 foot per second speed "tuned" the bump wavelength (50 feet) to the aircraft's natural pitching frequency. In figure 7 the effective dip wavelength was 70.7 feet and therefore it was traversed at an "untuned" speed. Running the simulation of figure 7 at the tuned speed of 70 feet per second, the acceleration levels were 1.7g and 1.2g at P.S. and c.g. respectively.

Figures 8 and 9 show the plotted results of the same aircraft traversing a paved but rough runway profile without a roll degree of freedom and with a roll degree of freedom respectively. Both runs were made at the constant speed of 125 feet per second, because this speed produced higher levels of vertical acceleration for this airplane on this particular runway. Comparison of these two figures shows a significant increase in the vertical acceleration at the pilot's station (P.S.) at different locations on the runway. For example, at T=46 seconds, the P.S. acceleration levels more than doubled when 3 lines of profile were used. This is attributed to the fact that the profiles seen by the main landing gear at these runway locations were rougher in the latter case. Figure 10 shows the Power Spectral Density (PSD) levels of each line of survey for the Washington National runway. A PSD is a measure of the relative roughness of a runway versus frequency. It can be seen that the PSD level is significantly different for each line of survey. Differences in elevations of the three profiles account for the change in the aircraft's dynamic response.

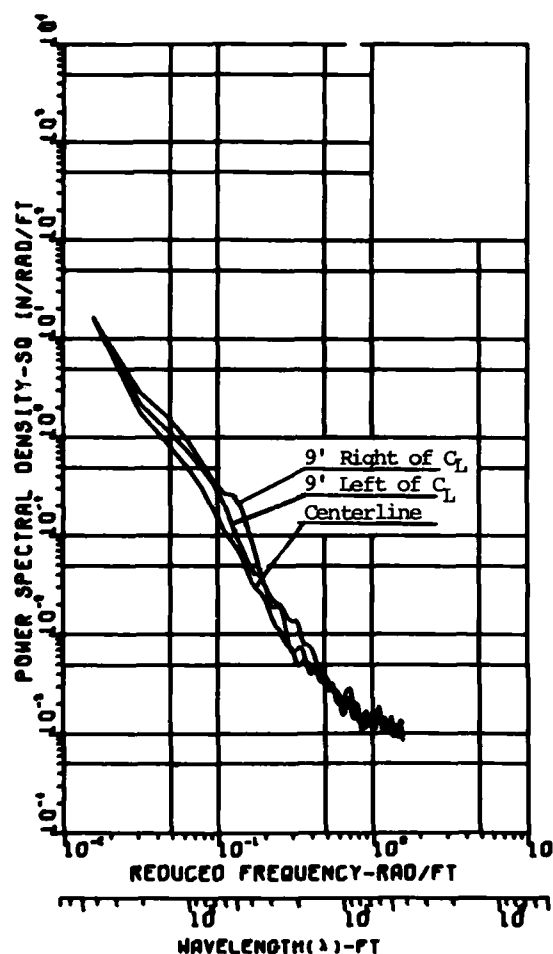


Figure 10. PSD of Washington National Airport Runway 36

TABLE I Comparisons of Simulated and Experimental Data

Experimental Time (sec)	P.S. Vertical Acceleration		C.G. Vertical Acceleration	
	Exp (g's)	Sim. (g's)	Exp (g's)	Sim. (g's)
6.0	.90	.74	.55	.35
14.3	1.30	1.12	.80	.40
20.5		TAKEOFF		

Note: All measurements are peak to peak.

Limited experimental data was available for one aircraft. Figure 11 shows the actual time history plots of vertical acceleration measured during a takeoff of a large commercial jet at 120,000 pounds gross weight from a rough paved runway. Figure 12 shows a simulation of the same aircraft under the same conditions. Some parameters of the test aircraft were unknown, such as exact strut and tire pressures and actual inertias, therefore exact simulation

was not possible. However, Table I shows that comparison of several peak values of vertical accelerations at the P.S. were within 15 percent. The comparisons of C.G. vertical accelerations were not as good. In the simulation the acceleration levels were lower. It appears that main gear strut pressures on the actual airplane were lower than that simulated. This difference would cause the higher response in the plunge mode.

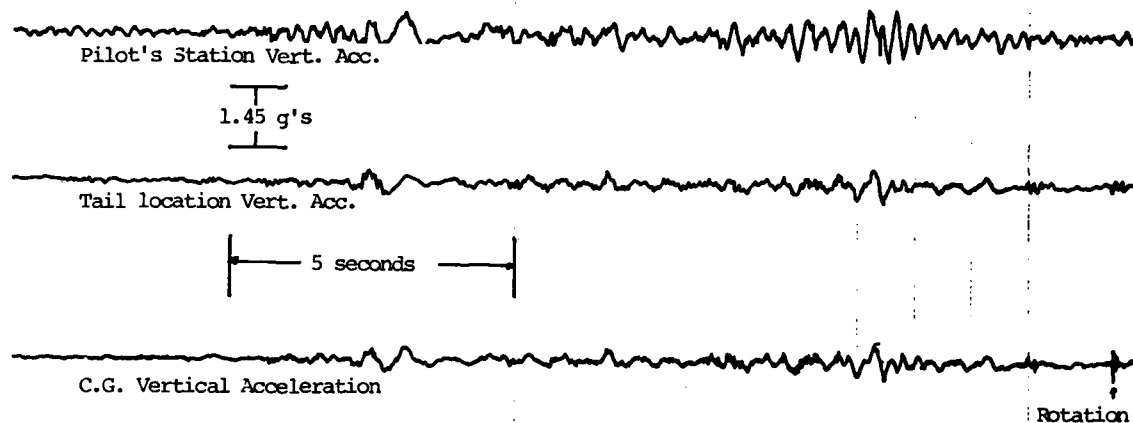


Figure 11. Measured Response of a Boeing 727-100 Takeoff at Washington National Airport Runway 36

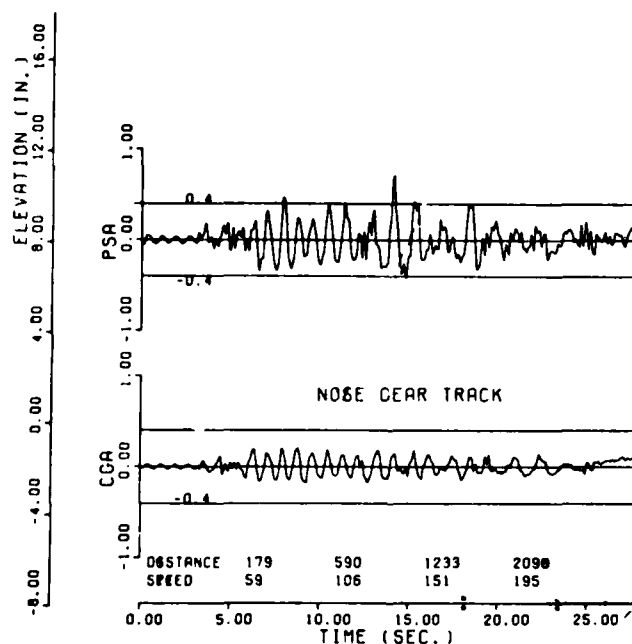


Figure 12. Simulated Response of a Boeing 727-100 Takeoff at Washington National Airport Runway 36

## CONCLUSIONS

In summary, a mathematical model has been formulated and programed for a digital computer and is capable of simulating most flexible aircraft traversing an asymmetric runway profile during constant speed taxi or takeoff. Three different aircraft have been simulated and comparisons have been made with experimental data.

Based on the simulations made, the following conclusions were drawn;

1. The roll degree of freedom can have a significant effect on the pilot's station and center of gravity vertical acceleration levels if the runway profile is asymmetric. The degree of severity of the acceleration is dependent upon the degree of the runway asymmetry.

2. Comparison of the simulated aircraft response with the limited amount of available test data was satisfactory. The roughest parts of the runway were identified and as in the test, pilot station acceleration levels exceeded the  $\pm 4g$  criterion. If exact strut and tire pressures and inertias were known for the test aircraft, the simulated C.G. response would have more closely matched the experimental data.

The simulated takeoff took an additional 5 seconds to reach rotation speed. It is assumed that the actual test aircraft weight was less than 120,000 pounds, because during this test, a series of runs were made with the fuel weight at the beginning of the series being 120,000 pounds. Therefore some of the fuel had been burned off. The fact that the airplane was lighter than that simulated would also contribute to the difference in C.G. response. Also, using a  $15^\circ$  flap setting changed the value of  $C_L$ , which would result in a shorter takeoff distance.

3. This computer program appears to be a very efficient technique for locating the rough areas of an asymmetric runway. Using a CDC 6600 digital computer, a typical commercial jet takeoff simulation with 10 flexible modes and a time interval of .001 seconds required 70 seconds of CPA computer time, which is just 30 seconds over real time.

4. With the addition of the roll degree of freedom, it now becomes possible to expand the computer program to obtain vertical accelerations (and consequently shears and moments) at vital wing stations such as the wing root, and engine and stores pylons. This would be a natural extension of the study.

## REFERENCES

1. Goldman, D.E., and von Gierke, H.E., Effects of Shock and Vibration on Man, Volume III, Chap. 44, Shock and Vibration Handbook (C.M. Harris and C.E. Crede, editors) McGraw Hill Book Co., N.Y. 1961.
2. Gerardi, A.G., Lohwasser, A.K., Computer Program for the Prediction of Aircraft Response to Runway Roughness, AFWL-TR-73-109, Volume I and II, Air Force Weapons Laboratory, Kirtland AFB, New Mexico, September 1973.

CHIANTI - COMPUTER PROGRAMS FOR PARAMETRIC  
VARIATIONS IN DYNAMIC SUBSTRUCTURE ANALYSIS\*

A. Berman and N. Giansante  
Kaman Aerospace Corporation  
Bloomfield, Connecticut

A method and computer program description for parametric variations in dynamic substructure analysis are described. The method models the individual components of a system, forms the appropriate system interface coordinates and calculates the system dynamic response at particular frequencies. Application of the method for prediction of the dynamic response characteristics of a helicopter transmission and a comparison of results with test data is also included.

INTRODUCTION

Substructure methods employing eigen-solutions of the separate components are frequently employed in the dynamic analysis of complex structures. When appropriately applied, they are convenient and economical.

The computer programs described in this paper illustrate an implementation of an alternate technique which, under certain conditions, can result in significant additional savings. The primary limitation on the applicability of this method is that solutions are obtained at individual frequencies of excitation. For problems in which the dynamic response of a linear complex structure and modifications of it are desired at a relatively small number of discrete frequencies, this method has some advantages over the usual modal approaches.

The method which has been implemented in the CHIANTI program has two important features. The first of these relates to the reduction in degrees of freedom. The analysis of each basic component is carried out with as many degrees of freedom as is necessary for a valid analysis. When the resulting analytical model is used, however, the number of degrees of freedom may be drastically reduced and must include only:

- (1) Those which interface other components.
- (2) Those which are to be affected by changes.

- (3) Those at which a force is applied or dynamic response is specifically desired.

This reduction in the number of coordinates is performed only once at each frequency of interest with no loss in the validity of the analytical model, regardless of the extent of this reduction.

The other important feature relates to the ease with which changes may be studied. Structural modifications such as local mass or stiffness changes, the addition of springs or dampers between components, addition of vibration absorbers, changes in boundary conditions may be exactly modeled at virtually no computer cost and without performing a new modal analysis for each change.

The CHIANTI system was developed for use in a study of the noise and vibration of a helicopter gearbox. This application satisfied the limitation that only a small number of forcing frequencies are important. The configuration was naturally quite appropriate to a substructure type analysis. The case and each of the shafts were treated as a substructure which interfaced the other components at the bearings and gear meshes and could be reduced to an analytical model with a small number of coordinates. It was desired to study such effects as bearing stiffness, mass and stiffness changes in the shafts, case vibration absorbers, mounting characteristics. In order to predict radiated noise, the case surface responses were desired, but except for the interface coordinates, virtually all the remaining degrees of freedom could be eliminated. The program system was used quite successfully.

\*This work was performed under Contract No. DAAJ02-74-C-0039 for the U. S. Army Air Mobility Research and Development Laboratory, Eustis Directorate, Fort Eustis, Virginia.

The purpose of this paper is to present the theoretical rationale behind the CHIANTI system and to describe the architecture and operation of the programs.

## THEORETICAL BASIS

A linear structure is often represented in the frequency domain as a finite element model in terms of an impedance matrix. For viscous or "structural" damping the impedance matrix may be alternately represented as:

$$Z = -\omega^2 M + i\omega C + K \quad (1a)$$

or

$$Z = -\omega^2 M + (1 + ig)K \quad (1b)$$

where  $M$ ,  $C$ ,  $K$  are the mass, viscous damping, and stiffness matrices, respectively, and  $\omega$ ,  $i$ ,  $g$  are the frequency of motion,  $\sqrt{-1}$ , and the structural damping coefficient.

The method used here makes no distinction in the way  $Z$  is formed provided that this impedance matrix is an adequate representation of the structure. This will be discussed below. The starting point for the analysis requires a valid impedance matrix for each substructure for each frequency of interest. If the impedance is formulated as in (1a) or (1b) and the degrees of freedom are adequate,  $Z$  at any frequency is easily formed by matrix addition.

From the point of view of the dynamicist, the criteria for a valid impedance matrix is that it correctly predict the motion at the coordinates of interest at each frequency of interest. The relationship between the applied force and the structural response is:

$$Zy = f \quad (2)$$

where  $y$  and  $f$  are vectors representing the displacements (or rotations) and the applied forces (or moments) at the respective coordinates. (In general, all the matrices and vectors are complex.) Except for an undamped system at resonance or for  $\omega = 0$ ,  $Z$  will not be a singular matrix. Thus:

$$y = Z^{-1}f \equiv Yf \quad (3)$$

where  $Y$  is the mobility matrix and is the inverse of the impedance matrix. Note that while  $Z$  may usually be represented as a simple function of  $\omega$ , there is no such simple formulation for the mobility (in terms of the basic  $M$ ,  $C$ ,  $K$  matrices).

The elements of the mobility matrix have individual physical significance. Each element represents the displacement at a point due to a force at some point. The numerical value of

each of these elements is independent of the number and location of the other degrees of freedom. This must be true since this quantity may be directly physically measured on the actual structure. This characteristic is not true of the impedance matrix since the numerical value of the individual elements are specifically dependent on the number and location of all the other degrees of freedom of the analytical model.

Thus, the criteria for a valid impedance matrix is that the elements of its inverse correctly represent the true response characteristics of the structure. This argument leads to a direct method of obtaining a valid reduced impedance matrix, as follows:

- (1) Perform a structural analysis using conventional methods to obtain a valid, full size, impedance matrix at each frequency of interest,  $Z(\omega)$ .
- (2) Invert  $Z$  at each  $\omega$  to obtain valid, full size mobility matrices  $Y(\omega)$ . Alternately, a modal approach or a direct integration technique may be used to obtain  $Y(\omega)$ .
- (3) Select elements from  $Y$  at each  $\omega$  corresponding to the coordinates to be retained. These elements are then formed into a new reduced mobility matrix,  $Y_R(\omega)$ .
- (4) The reduced impedance matrix is then formed by inversion of  $Y_R$ :

$$Z_R(\omega) = Y_R^{-1}(\omega) \quad (4)$$

It is to be noted that  $Z_R$  is valid only at the frequency at which it has been computed. There is no necessary or required interpretation of  $Z_R$  in terms of mass, damping, and stiffness matrices. (This is discussed in some detail in Reference (1)).  $Z_R$  represents a physical system which, at the frequency  $\omega$ , behaves precisely as the system under study.

The reason for specifically obtaining the impedance matrix of the reduced system is that the impedance of a complex structure is obtained by simply adding the impedance matrices of the separate components at coordinates where the deflections are common. If  $Z_a$ ,  $Z_b$ ,  $Z_s$  are partitioned impedance matrices of subsystem  $a$ ,  $b$ , and the complete system, respectively, and  $(\cdot)$  refers to interface coordinates,  $(\wedge)$  refers to noninterface coordinates, and  $(\hat{\cdot})$  refers to coupling between interface and noninterface coordinates then (see Reference (1)):

$$Z_s = \begin{bmatrix} \hat{Z}_a & \hat{Z}_a & 0 \\ \hat{Z}_a^T & Z_a + Z_b & \hat{Z}_b \\ 0 & \hat{Z}_b^T & \hat{Z}_b \end{bmatrix} \quad (5a)$$

$$\text{and } Y_s = Z_s^{-1}. \quad (5b)$$

Note that the substructures must be modeled as if they were unrestrained at the interface coordinates.

There are several considerations involved in applying this technique to practical analyses:

- (1) It is not important how the reduced mobilities are computed as long as they are valid.
- (2) For the method to be practical, the number of reduced coordinates must not be so large that matrix inversions become prohibitive.
- (3) Local impedance changes due to addition of spring-mass systems or boundary condition changes are simply added to the reduced component impedances.
- (4) When adding impedance matrices the corresponding elements must represent deflections in the same direction.
- (5) The impedance elements add when their deflections are equal; thus when components are separated by spring-damper devices, the impedance of this device must be added to one of the substructures prior to synthesis.

The CHIANTI programs automatically and conveniently perform the coordinate reductions, coordinate transformations, addition of impedance changes, impedance matrix addition for a number of subsystems, determination of the mobility of the combined system.

The ability to accommodate structural modifications including local mass or stiffness changes, the addition of springs or dampers between components, addition of vibration absorbers or changes in boundary conditions is a valuable feature of a structural dynamics program. With the impedances of each element at frequencies of interest stored in a data bank, variation in structural parameters of the individual components can be readily made. The CHIANTI computer programs allow implementation of these capabilities without performing new and costly analyses for each change.

## SYSTEM OVERVIEW

The CHIANTI system consists of two major programs called ADDRED and SYNTH which uses a common data base. The ADDRED program is designed to modify the structural characteristics of the basic components stored in the data bank. The SYNTH program synthesizes the impedance and mobility matrices of the complete system.

Figure 1 presents a schematic of the CHIANTI Program System. Impedance matrices for the various components comprising the structure are formed at the frequencies of interest and stored, with appropriate identification, in the common data bank. The ADDRED and SYNTH programs operate on these stored impedance matrices according to the selected options, receive new identifications and are optionally stored in the data bank or used in the current analysis. The original component impedance matrices are retained in the data bank.

### CHIANTI PROGRAM SYSTEM

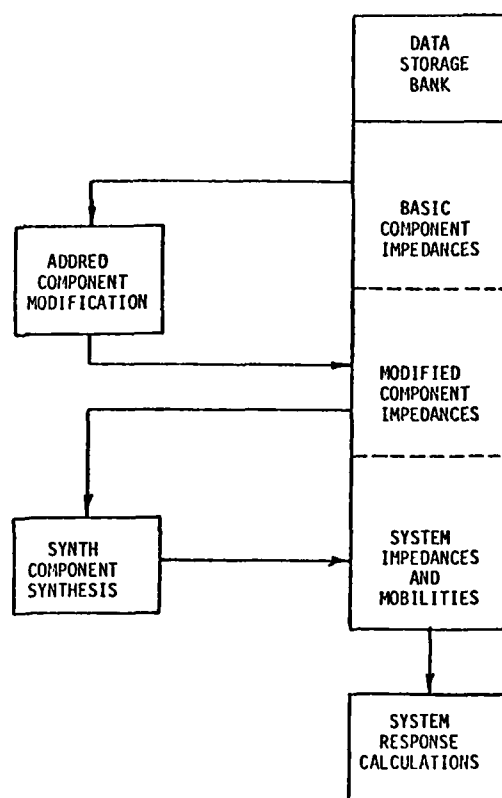


Figure 1. CHIANTI Program Schematic



## ADDRED PROGRAM

The ADDRED program has the capability to modify the characteristics of any dynamic component as follows:

- (1) Add structural damping.
- (2) Add vibration absorbers or concentrated masses at selected coordinates.
- (3) Add spring-damper systems between structural components.
- (4) Add spring-damper systems to ground at selected coordinates.
- (5) Perform coordinate transformations.
- (6) Perform a dynamic coordinate reduction.
- (7) Convert an impedance matrix to a mobility matrix and vice versa.

All of these changes are implemented through a simple set of coded instructions to the computer. Items (5)-(7) are to perform such necessary and convenient operations as converting coordinates from local to global orientation. Additionally, the efficiency of future computations can be increased by retaining only degrees of freedom of interest without loss of accuracy.

### Description of Program Options

The program features listed may be implemented with a minimum of input cards. The first three input cards required for program execution are common to all the options.

#### Card Input

##### Heading Card

- |          |  |
|----------|--|
| Col 1    | Code indicating which modification is to be implemented  |
| Col 2    | Number of items per component  |
| Col 3    | Output print option for original and modified impedance matrices; also data bank storage option for modified matrices  |
| Col 4-10 | Control of particular frequency or range of frequencies at which modification is to be implemented. When a range of frequencies is selected, the modification is performed at each of the frequencies within the range at which a component impedance matrix is stored in the data bank. |

##### Heading Card

Col 21-80 Arbitrary heading

Card 2 Identification of the component which is to be modified. The impedance matrices for the component which have been previously stored in the data bank are retrieved for modification and retained intact in the data bank.

Card 3 Identification of component after modification. The modified impedance matrices with new identification are optionally stored in the data bank.

1. Add Structural Damping - Structural damping may be added in the form  $igK$ , where  $K$  is simply the component impedance matrix at zero frequency which is stored in the data bank. Thus, the component impedance matrix with the addition of structural damping at a particular frequency of interest,  $\omega$ , is:

$$Z_{\text{Mod}}(\omega) = Z_{\text{Orig}}(\omega) + igZ_{\text{Orig}}(\omega=0) \quad (6)$$

where  $g$  is the structural damping coefficient.

This modification is implemented with only the input cards shown below. The program automatically seeks the original impedance matrix and the proper impedance matrix at  $\omega = 0$  and performs the operation of Equation (6). It then returns the new impedance matrix with its new identification to the data bank.

##### Input Card 1

Col 1-10 Structural Damping Coefficient

##### Input Card 2

Col 1-80 Identification of Component Impedance matrix at  $\omega = 0$ ,  $Z(\omega=0) \equiv K$

2. Addition of Vibration Absorber or Lumped Mass - The modification of the component impedance matrix due to vibration absorbers attached at particular coordinates involves a change in both the real and imaginary components of the matrix yielding:

$$\Delta Z = - \frac{[1 - \frac{\omega}{\Omega}]^2 + 4(\frac{\omega}{\Omega})^2 \xi^2}{[1 - (\frac{\omega}{\Omega})^2]^2 + 4\xi^2} \omega^2 m$$

$$+ i \frac{2(\frac{\omega}{\Omega})^3 \xi \omega^2 m}{[1 - (\frac{\omega}{\Omega})^2]^2 + 4\xi^2} \quad (7)$$

where  $\omega$  is the frequency of excitation and  $\Omega$ ,  $m$ , and  $\xi$  are the undamped natural frequencies, the mass and damping ratio of the vibration absorber, respectively. This change is added to the original impedance matrix at the diagonal element corresponding to the attachment point.

The input cards required to accomplish this change are as indicated:

Input Card

- Col 9-10 Local coordinate number of absorber attachments
- Col 11-20 Undamped natural frequency of absorber,  $\Omega$
- Col 21-30 Absorber mass,  $m$
- Col 31-40 Critical damping ratio,  $\xi$

One card is input for each absorber on a particular component. For a torsional absorber the moment of inertia of the absorber in appropriate units replaces the absorber mass.

For the addition of a lumped mass at a local coordinate, the aforementioned cards are applicable; however, the undamped natural frequency and critical damping ratio are omitted yielding a modified impedance matrix of the form:

$$\Delta Z = -\omega^2 m \quad (8)$$

3. Add Spring-Damper in Series - Adding a parallel spring-damper system in series with the structure at a coordinate automatically generates a new coordinate at the free end of the system. Thus, an additional row and column are included in the modified impedance matrix. If  $k$ ,  $c$  are the spring and damping rates, the real and imaginary components of this system are:

$$Z_R = k$$

and

$$Z_I = i\omega c$$

The modified impedance matrix becomes:

$$Z_{Mod} = \begin{bmatrix} \text{Attachment} & \text{Additional} \\ \text{Coordinate} & \text{Column} \\ \cdots (Z_{Orig} + k + i\omega c) \cdots & \begin{bmatrix} 0 \\ \vdots \\ (k + i\omega c) \end{bmatrix} \\ \vdots & \vdots \\ \cdots 0 \cdots (k + i\omega c) \cdots 0 \cdots & \begin{bmatrix} 0 \\ \vdots \\ (k + i\omega c) \end{bmatrix} \end{bmatrix}$$

Additional Row (10)

Input cards necessary to implement this change are:

Input Card

- Col 9-10 Local coordinate number of spring-damper attachment
- Col 11-20 Spring rate
- Col 21-30 Damper rate

One input card is required for each spring-damper system attached to each coordinate. For a torsional spring-damper system appropriate units must be used.

4. Add Spring-Damper to Ground - In this situation, no new coordinate is generated and the modified impedance matrix is simply the original impedance matrix with each diagonal element modified to include any added spring-damper impedance; therefore:

$$Z_{Mod}(i,i) = Z_{Orig}(i,i) + k + i\omega c \quad (11)$$

The input card format is similar to that for a spring-damper system in series.

5. Coordinate Transformation - This option allows for any linear transformation of coordinates on a particular component. This option is used to transform local coordinates into the proper orientation in the global system for component synthesis. In addition, it is often convenient to transform coordinates so they conform to the direction of an applied force such as the line of action of a gear mesh. If the transformation matrix is defined as  $T$ , the impedance matrix for the transformed coordinates becomes:

$$Z_{Mod} = T^{-T} Z_{Orig} T^{-1} \quad (12)$$

where  $y_{New} = T y_{Orig}$ . Rotations, sign changes and combinations of rotation and translation are common applications. Implementation of this transformation is achieved with the following input cards (one card per transformed coordinate,  $T$  is filled with unit diagonal elements for unchanged coordinates):

Input Card 1

- Col 1-10 Number of coordinates to be transformed

Input Card 2

- Col 1-5 Coordinate to be transformed
- 6-10 Number assigned to the transformed coordinate
- 11-17 Coefficient which multiplies a coordinate used in the transformation

#### Input Card 2

Col 18-20 Number of the coordinate which is multiplied by the previous coefficient

21-27 Repeat for each of the original coordinates necessary to the transformation

6. Coordinate Reduction - Coordinate reduction must be performed on the mobility matrix since the elements of this matrix have individual significance, wherein each element represents the response of a point due to a force at the same or any other point. Thus, to accomplish a coordinate reduction the impedance matrix for a component must be retrieved from the data bank and inverted to yield the mobility matrix. The coordinates to be eliminated are removed from the mobility matrix and the resulting matrix inverted to form the desired impedance matrix with reduced coordinates. This can be represented mathematically as:

$$Y_{Orig} = Z_{Orig}^{-1}$$

$$Y_{Mod} = (Y_{Orig})_{Reduced} \quad (13)$$

$$Z_{Reduced} = Y_{Mod}^{-1}$$

The input cards necessary to achieve coordinate transformation are:

#### Input Card

Col 1-2 Number of coordinates to be eliminated

3-5 Coordinate numbers to be eliminated

6-10 Continue with coordinates to be eliminated

11-15

Etc

7. Invert Matrix - This option allows inversion of impedance matrices to yield the mobility matrix and the reverse inversion to yield the impedance matrix. The only cards required for this option are the heading card and identification cards as previously described.

#### SYNTH PROGRAM

The essential features of this program relate to component synthesis. This program synthesizes the system impedance and mobility matrices of the complete system. The complete system is defined by a table of global coordinates and the corresponding local coordinates

of each specified component. Coordinates not listed in the table are automatically eliminated for each component as in ADDRED.

The input cards required for the SYNTH program are:

#### Heading Card

Col 1-2 Number of components in system

3-10 Frequency control (same as described under ADDRED program)

11-20

21-80 Arbitrary heading

#### System Card 1

Col 1-2 Number of global coordinates

Col 3-5 Print controls

#### System Card 2,3

Col 1-80 Identification of Impedance Matrix

Col 1-80 Identification of Mobility Matrix

#### Component Cards

Col 1-16 Identification of First Component

21-36 Identification of Subsequent Components

Etc

as many cards as necessary with maximum of 16 components.

#### Coordinate Table

Col 1-2 Global coordinate number

3-5 Corresponding local coordinate number of first component

6-10 Etc for subsequent components

11-15

#### APPLICATION

The application to the gearbox mentioned in the introduction will be briefly described as an illustration of the capabilities of the system. In addition to the previously described computer programs, programs were necessary to establish the primary data bank. IMODEL, which is also a part of the CHIANTI System was used to generate a model of the transmission case using the method of incomplete models, as described in Reference (2).

Because of the structural and geometric complexity of the case and the need to include gear mesh excitation frequencies extending to 3000 Hz, development of a cost effective and reliable finite element model was considered unlikely. Additionally, an actual transmission case was available for testing, prompting application of the incomplete model method. This method uses measured normal modes, natural frequencies and an intuitively developed approximate mass matrix to yield an analytical model of the structure. The resulting analytical dynamic model of the case correlated with frequency response test data over the range of interest. One further program, RSVP, was used to develop free shaft impedance matrices for coupled bending and torsion modes. The RSVP program considers a lumped mass representation of the shafts with gears attached, generates mobility matrices of the components at frequencies of interest and finally inverts these matrices to yield the component impedance matrices. Special purpose programs to generate impedance matrices may be developed for any application using a standard subroutine to enter these matrices into the data bank.

Figure 2 presents a schematic of the helicopter transmission analyzed. An input spiral bevel gear mesh drives a spur gear set which, in turn, drives a planetary gear system whose output drives the rotor shaft. Sets of roller and ball bearings retain the various shafts to the gearbox case. The ring gear which meshes with the planet gears is also attached to the transmission case.

Table 1 presents a coordinate table of the transmission system including the system coordinates and an identification and coordinate representation of the individual components. As an example of the data shown, the original impedance matrix of the input shaft has been modified to include the addition of springs attached to the input shaft, which are representative of bearings at these locations, at local coordinates 2, 8, 14 and 20. As discussed previously under the description of the program options, number 3, new coordinates are established at the free end of the springs with coordinate numbers 100 plus the old number. Thus, the coordinate which was originally numbered 2 becomes coordinate number 102. Coordinate number 3 on the input shaft had been previously transformed, using the ADDRED program option 5, to the line of action of the spiral bevel gear on the input shaft.

The first column in the table indicates the system or global coordinates and the remaining columns represent the local coordinate numbers associated with the respective component identified by each column heading. Multiple entries in a row headed by a global coordinate indicates an interface between the components at the local coordinates of the respective elements. For example, at system coordinate 1, a connection exists between the input shaft at local coordinate 108 and the transmission case coordinate 24. The SYNTH program eliminates the unwanted coordinates on the individual components yielding a reduced impedance matrix, performs matrix addition for the subsystems and generates the mobility of the combined system. This system mobility when multiplied by the applied force vector yields structural response of the system.

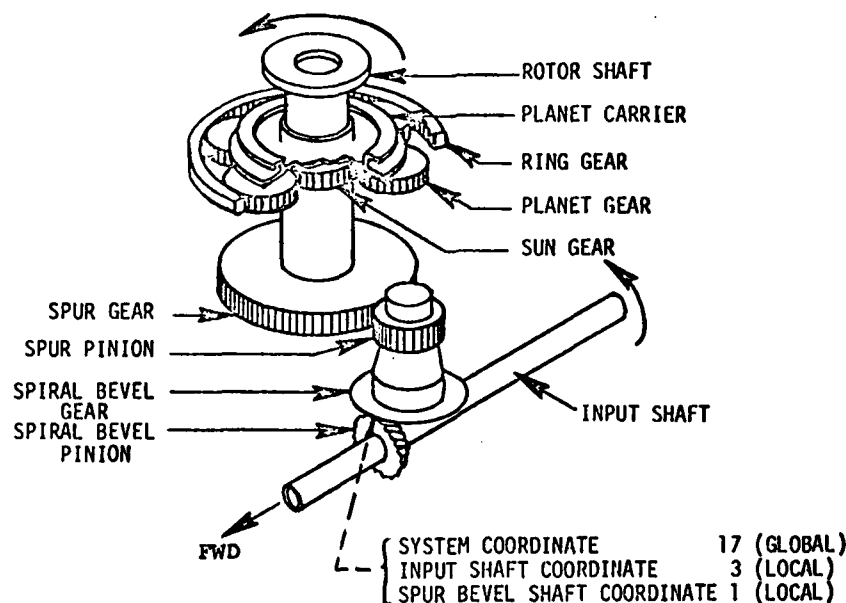


Figure 2. SH2 Main Transmission Schematic

TABLE 1  
Planet System Excitation at 348 Hz, FX

Applicable Frequency Range = 348.0 Hz Only

System Impedance Ident SYS IMP 348 2  
System Mobility Ident SYS MOB 348 2

Coordinate Table

System	IN1 80TS	OUT1 -80S CK3	BVLS PR-8 OTS	SPR- 80TS	CASE GT1
1	108	0	0	0	24
2	120	0	0	0	23
3	102	0	0	0	22
4	114	0	0	0	21
5	0	102	0	0	29
6	0	110	0	0	35
7	0	113	0	0	30
8	0	121	0	0	36
9	0	0	103	0	26
10	0	0	112	0	25
11	0	0	109	0	28
12	0	0	118	0	27
13	0	0	0	101	31
14	0	0	0	107	32
15	0	0	0	104	33
16	0	0	0	110	34
17	3	0	1	0	0
18	0	0	8	2	0
19	0	5	0	0	0
20	0	16	0	0	0
21	0	24	0	0	0
22	0	12	0	0	0
23	0	14	0	0	0
24	0	0	0	0	1
25	0	0	0	0	3
26	0	0	0	0	4
27	0	0	0	0	5
28	0	0	0	0	11
29	0	0	0	0	12
30	0	0	0	0	13
31	0	0	0	0	14
32	0	0	0	0	15
33	0	0	0	0	16
34	0	0	0	0	17
35	0	0	0	0	18
36	0	0	0	0	19
37	0	0	0	0	20
38	0	1	0	0	0
39	0	3	0	0	0
41	0	8	0	0	0
42	0	120	0	11	410
43	0	126	0	14	0
44	0	109	0	0	0
45	0	0	0	5	402

TEST CORRELATION

To validate the dynamic substructure analysis method, analytically derived vibration characteristics were compared to simulated operational test data for a Kaman SH-2D helicopter main transmission. Acceleration response of the transmission case, measured normal to the surface, at fourteen selected points was compared to the respective analytically obtained response. Figure 3 presents a comparison of measured and predicted case surface accelerations in peak g's for excitation applied at the planetary system fundamental frequency of 348 Hz at 80% rotor rpm and a torque loading of 9120 in-lb. The analytically predicted and measured transmission housing accelerations show reasonable agreement promoting confidence in the dynamic substructure analysis method.

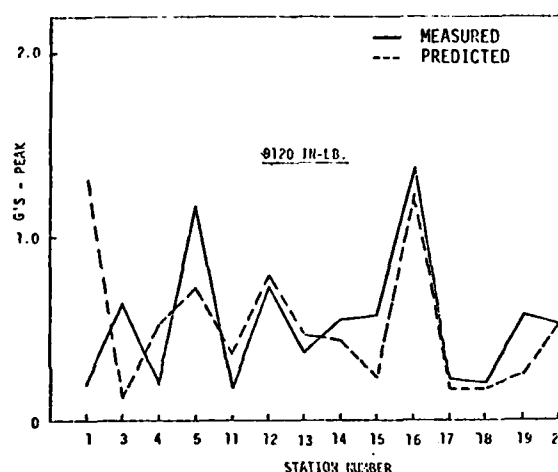


Figure 3. Measured vs Predicted Case Acceleration for 348 Hz Excitation

PARAMETRIC STUDY

The analytical method described in the paper allows rapid and economical evaluation of transmission design changes. Once each basic mechanical component is modeled, modifications can be readily effected without re-evaluation of each element. This technique presents a significant advantage over the usual substructure procedures wherein each component modification requires a new modal analysis. An application study was performed which considered effects of shaft mass and stiffness increases, case mass and stiffness increases, bearing stiffness reduction and bearing relocation. Results of the transmission design changes are presented in Reference (3).

## CONCLUSIONS

1. A computer program has been described which has application in the dynamic analyses of a linear complex structure, including modifications of it at a small number of discrete frequencies.
2. The computer analysis of the linear complex structure can be achieved using a common data bank containing the impedance matrices of the individual components, thereafter a minimum number of input data cards are used in implementation of the program options.
3. The method has been successfully applied in the dynamic analysis of a helicopter main transmission where the components consisted of the gearbox case, the shafts and gears and a planetary system.

## REFERENCES

1. A. Berman, "Vibration Analysis of Structural Systems Using Virtual Substructures", The Shock and Vibration Bulletin 43, NRL, Washington, D. C., June 1973.
2. A. Berman, "System Identification of a Complex Structure", AIAA Paper No. 75-809, AIAA/ASME/SAE 16th Structures, Structural Dynamics, and Materials Conference, Denver, Colorado, May 27-29, 1975.
3. M. A. Bowes, "Development and Evaluation of a Method for Predicting the Vibration and Noise Characteristics of Helicopter Transmissions", AHS Paper No. 77.33-76, American Helicopter Society 33rd Annual National Forum, Washington, D. C., May 1977.

## FREQUENCY RESPONSE ANALYSIS OF COMPLEX STRUCTURES

Hatem R. Radwan and Palanichamy Shunmugavel  
SARGENT & LUNDY  
Chicago, Illinois

This paper discusses the use of the frequency response method based upon the Fourier transform theory for dynamic analysis of complex structural systems. The application of the method to the analysis of a nuclear reactor containment complex subjected to hydrodynamic loads is demonstrated and typical results are presented. The results illustrate the convenience and effectiveness of this method and advantages and limitations of the method as well as other applications are discussed. Several precautions found necessary to obtain sufficiently accurate results are also discussed.

### 1. INTRODUCTION

The analysis of complex structures subjected to arbitrary dynamic loads is, in general, a problem requiring great computational effort. The advent of present day computer capabilities has made possible detailed analysis of many structures that would have been considered prohibitive a decade ago. However, as computer capabilities have grown so have the demands placed on them in terms of capacity and speed due to an increased interest in detailed dynamic as well as static analysis of complex structures.

Structural engineers and stress analysts are continually searching for more efficient and suitable methods to analyze their systems. The response of a structure modeled by finite elements to dynamic loads is usually determined by modal analysis or by direct numerical integration of the governing differential equations. Most commercial general purpose finite element programs available today provide the analyst with the option of using either method. In general, modal analysis is preferred unless too many modes are required to adequately describe the system response to the loading under consideration.

This paper discusses the use of the frequency response method, based upon the Fourier transform theory, for complex structural systems. This

method, used in conjunction with the direct integration approach, is found to be particularly valuable in saving computer time in the analysis of a nuclear reactor containment structure for hydrodynamic loads. In addition, the approach makes possible a considerably enhanced insight into the structural dynamic characteristics, leading to a more satisfactory analysis of the problem. The method is equally applicable to other structural systems and promises to be an additional powerful tool for structural dynamicists.

The introduction of the FFT algorithm [1] in 1965 enables the efficient and rapid numerical calculation of the discrete Fourier transform and inverse Fourier transform for arbitrary functions, which makes the frequency response method a powerful practical tool. It is believed, however, that practical application of this procedure has not been as widespread as it should be for structural analysis. It is recognized, however, that FFT has been used widely and successfully in recent years for analyzing vibration test results, particularly in the aerospace industry. It is hoped that this paper will illustrate the convenience and effectiveness of this method and demonstrate its additional practical value as an analytical capability.

## 2. THE PROBLEM

The problem described here arose during the analysis of a prestressed concrete nuclear reactor containment structure subjected to hydrodynamic loads. The structure is essentially a shell of revolution supported upon a mat foundation, which in turn rests upon a stiff clayey soil with firm rock at a depth of approximately 126 feet. The structural model set up for the analysis is shown in Figure 1. The model includes the soil to bedrock, which is modeled by finite solid elements of revolution, while the structure is modeled by thin shell elements of revolution. The analysis is made using a modified version of the Ghosh and Wilson program [2] developed at the University of California, Berkeley in 1969.

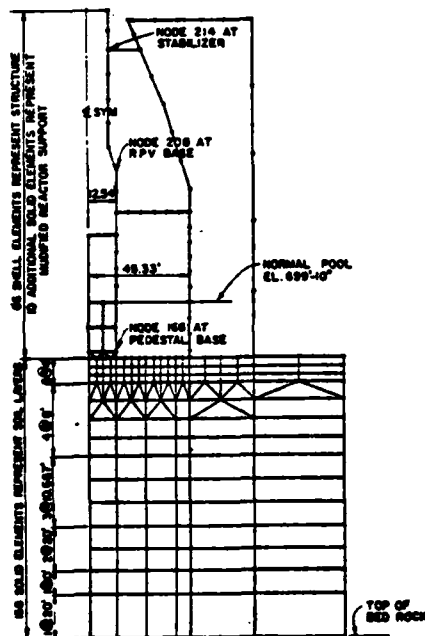


FIGURE 1 - MATHEMATICAL MODEL FOR ANALYSIS OF NUCLEAR CONTAINMENT COMPLEX FOR DYNAMIC SRV DISCHARGE LOADS

The hydrodynamic loads are caused in the suppression pool by a transient discharge phenomenon associated with the operation of safety relief valves. The loads are specified as a decaying oscillatory pressure field of relatively short duration, with upper and lower bounds for the frequency of oscillation. Figures 2 and 3 illustrate typical spatial distribution and time history variation of the load.

The inclusion of the soil in the structural model was deemed necessary for proper evaluation of the structural response in this problem. However, this led to precluding a modal analysis of the system under dynamic loads since too many modes would be required to adequately describe the response of the structure. It was then found necessary to solve the problem by direct integration of the differential equations, a costly process for the complex structural model adopted. Also, since the natural frequencies of the system were not known, it was also necessary to evaluate the response of the system to a large number of excitation frequencies in order to establish the most critical load condition for each component.

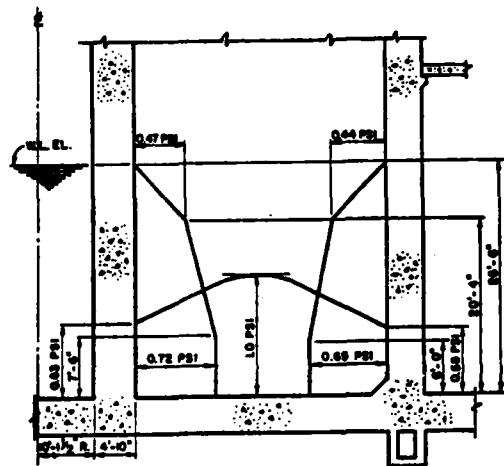


FIGURE 2 - NORMALIZED SPATIAL DISTRIBUTION OF SRV DISCHARGE LOAD

This represented an excessive amount of computational effort and an alternative solution was sought. It was also recognized that even if the natural frequencies of the system were known, the analysis for the load cases with excitation frequency coinciding with each of these natural frequencies would still be an expensive lengthy process. The frequency response method was found to provide a much more satisfactory and efficient solution.



## SRV ANALYSIS

SYMMETRIC 4.0 HZ. 1.0 SEC.

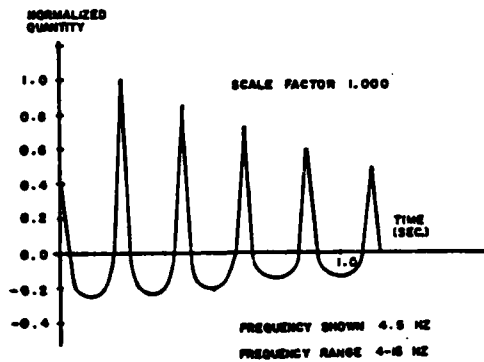


FIGURE 3 - TYPICAL LOAD EXCITATION TIME HISTORY FOR SRV DISCHARGE

### 3. THE FFT ALGORITHM AND ITS USE

The frequency response method of analyzing a linear system is based upon the capability to numerically evaluate the complex Fourier transform and inverse Fourier transforms of arbitrary function. The complex Fourier transform  $F(w)$  of an arbitrary real time function  $f(t)$  is defined by [4]:

$$F(w) = \int_0^T f(t) e^{-iwt} dt \quad (1)$$

Here  $f(t)$  is assumed to be defined over the interval  $0 \leq t \leq T$ ,  $w$  is the frequency in radians/seconds and  $i = \sqrt{-1}$ . The inverse Fourier transform re-creates  $f(t)$  from its transform  $F(w)$ :

$$f(t) = \frac{1}{2\pi} \int_{-\infty}^{\infty} F(w) e^{iwt} dw \quad (2)$$

Equations (1) and (2) represent a Fourier transform pair in continuous form, and allow going back and forth between the time and frequency domains.

If the function  $f(t)$  is defined by a digitized record with  $N$  points at time increments of  $\Delta t$ , the Fourier transform pair can be expressed in discrete form as follows [1]:

$$f(j\Delta t) = \text{Re} \sum_{s=0}^{N/2} F(s\Delta w) e^{is\Delta w j\Delta t} \quad (3)$$

and

$$F(s\Delta w) = \frac{1}{N} \sum_{j=0}^{N-1} f(j\Delta t) e^{-is\Delta w j\Delta t};$$

$$s = 0, N/2 \quad (4a)$$

or

$$F(s\Delta w) = \frac{2}{N} \sum_{j=0}^{N-1} f(j\Delta t) e^{-is\Delta w j\Delta t};$$

$$s = 1, 2, \dots, \left(\frac{N}{2} - 1\right)$$

$$\Delta w = 2\pi / (N\Delta t) \quad (4b)$$

The fast Fourier transform (FFT) is simply an efficient algorithm to calculate the Fourier transform and the inverse Fourier transform in discrete form. In this study a FFT algorithm with radix 2, i.e.  $N$  should be a power of 2, is used. This FFT corresponds to Cooley and Tukey's [1] original algorithm and required  $N/2 \log_2 N$  operations rather than  $N^2$  operations which would be required in the direct method for evaluating a transform. (An operation is a complex multiplication followed by a complex addition). For the value of  $N = 4096$  used in this study, FFT is about 680 times faster than the direct method. It is the computational efficiency of FFT that makes the frequency response method a practical tool in analyzing linear structures. At present, a standard subroutine for the FFT algorithm is available at almost every major computer installation. However, several precautions discussed below should be observed while employing the FFT algorithm.

Equations (3) and (4) are based upon the assumption that the function  $f(t)$  is periodic with period  $T$ . Thus, for analyzing a structure or system subject to a transient excitation of duration  $T_1$ , a quiet period of duration  $(T - T_1)$  should be added at the end of the time history as shown in Figure 4. This quiet period should be long enough to bring the system to rest at the end of  $T$ . The duration of the quiet period should be estimated based upon the structural damping characteristics of the system and the nature of the forcing function.

The constant time interval  $\Delta t$  has to be selected so that the time history of the excitation  $f(t)$  is well defined, and the folding frequency  $(N/2 \Delta w = \pi / \Delta t)$  includes the highest frequency of interest. The total

number of points  $N$  to define the force time history should be chosen so as to be a power of 2, to include an adequate length of quiet period ( $N \Delta t = T$ ) and to have a sufficiently small frequency interval ( $\Delta \omega = 2\pi/N\Delta t$ ) to adequately define the functions in the frequency domain.

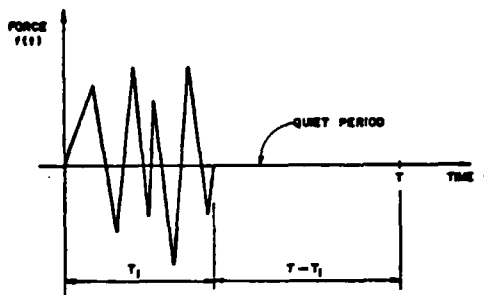


FIGURE 4 - ARBITRARY TRANSIENT FORCING FUNCTION

#### 4. ANALYSIS

The fundamental concept upon which the frequency response method is based, is the complex frequency response function [3], or transfer function  $H(\omega)$ . For a single degree of freedom system, the response  $x(t)$  to an arbitrary excitation  $f(t)$  may be expressed by the convolution integral [3]:

$$x(t) = \int_{-\infty}^t f(\tau) h(t - \tau) d\tau \quad (5)$$

where  $h(t)$  is the impulsive response of the system, i.e. the response of the system with zero initial conditions to a unit impulse  $\delta(t)$  at  $t = 0$ . It follows from equation (5) and the convolution theorem for the Fourier transform theory [4] that

$$X(\omega) = F(\omega) H(\omega) \quad (6)$$

where  $X(\omega)$ ,  $F(\omega)$  and  $H(\omega)$  are the Fourier transforms of  $x(t)$ ,  $f(t)$  and  $h(t)$  respectively.

Under harmonic excitation we have

$$f(t) = \cos \omega_0 t \quad (7)$$

$$F(\omega) = \pi [\delta(\omega - \omega_0) + \delta(\omega + \omega_0)]$$

$$\text{Thus } X(\omega) = \pi H(\omega) [\delta(\omega - \omega_0) + \delta(\omega + \omega_0)]$$

The inverse Fourier transform then gives

$$x(t) = \frac{1}{2} H(\omega_0) e^{i\omega_0 t} + \frac{1}{2} H(-\omega_0) e^{-i\omega_0 t}$$

But  $H(-\omega) = H^*(\omega)$ , so that

$$x(t) = \text{Re } H(\omega_0) e^{i\omega_0 t} \quad (8)$$

which is the steady state response to the harmonic excitation (7). Expression (8) represents the well known relation that  $H(\omega)$  is in fact the complex frequency response for the system.

Equation (8) may also be extended to any linear system such as a complex structure. If the structure is subjected to a loading that has a constant spatial distribution, then the loading time variation is represented by a single function  $f(t)$ . The response of any selected component  $x_i(t)$  may then be expressed by a relation similar to (5)

$$x_i(t) = \int_{-\infty}^t f(\tau) h_i(t - \tau) d\tau$$

where  $h_i(\tau)$  is the corresponding impulsive response. It then follows that

$$X_i(\omega) = F(\omega) H_i(\omega) \quad (9)$$

where  $H_i(\omega)$  is the complex frequency response function, or transfer function, corresponding to the selected response component.

Two points of interest may be realized based upon equation (9):

1. The transfer functions  $H_i(\omega)$  for all response components of interest may be determined if the system response to any one excitation is known.

$$H_i(\omega) = X_i(\omega) / F(\omega) \quad (10)$$

Obviously the transfer functions  $H_i(\omega)$  may also be determined by other means, such as from the significant natural frequencies and mode shapes of the system.

However, the former approach may be more appropriate in cases where a suitable response is already known, or if too many modes are required to adequately represent the system response.

2. Once the transfer functions  $H_i(\omega)$  have been determined, the system response to any other load excitation time history  $g(t)$  may be obtained using equation (9) without having to re-analyze the entire system. Thus, the Fourier transform  $G(\omega)$  of the load is first determined, and the responses  $x_i(t)$  are then determined by utilizing the inverse Fourier transform capability of FFT on  $X_i(\omega)$ . This procedure can be used to great advantage in cases where many different loadings need to be considered, particularly if only a relatively small number of response components are of main interest.

For the problem at hand, as of course in many other problems, determination of the transfer functions provided significant added insight into the dynamic characteristics of the structure. Thus all the significant structural natural frequencies are immediately available from the location of the peaks in the transfer functions, while insignificant natural frequencies are recognized as such. The different frequencies for the different components are also just as easy to establish. Thus the critical frequencies of the loading are relatively easy to establish by comparing the Fourier transform of the loading with the dominant peaks in the transfer functions.

In this manner it was possible to achieve considerable savings in computer time by determining the responses of the various components at their respective critical frequencies without analyzing the entire structure for all frequencies. The other advantages of the flexibility gained by this procedure can also be clearly realized, such as later date assessments or parametric investigations.

For comparison purposes, the time history analysis by direct integration for the problem considered required approximately 40 CPU minutes for each frequency (load case) to be analyzed on the in-house UNIVAC 1106 system. The Fourier transform solution required only 6 CPU minutes for 100 response component calculations per load case after the transfer functions had been determined.

## TRANS FUNS FOR SRV LOADS

WHITE NOISE -0.05 TO 1.45 SEC 30HZ

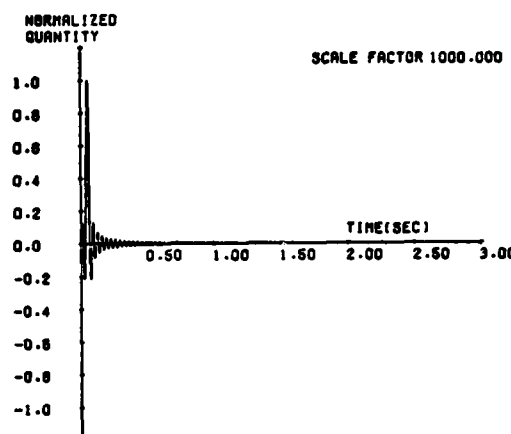


FIGURE 5 - NORMALIZED TRUNCATED BAND - LIMITED WHITE NOISE TIME HISTORY - 30 HZ.

## 5. RESULTS

Typical results obtained using the frequency response method to analyze the nuclear containment complex considered are shown in Figures 5 through 9. While no particular problems were encountered in using the transfer functions to determine the system response, several precautionary measures were found necessary to accurately obtain the transfer functions.

To obtain the transfer functions, the structural response is first determined by a direct integration method for a loading whose time history variation corresponds to a band limited white noise time history, shown in Figure 5. The response of each component of interest is then analyzed separately to determine the corresponding transfer function by equation (10). The Fourier transform of the band limited white noise used is shown in Figure 6, and typical computed transfer functions are shown in Figures 7 and 8. Similar transfer functions are obtained for all significant response components of interest.

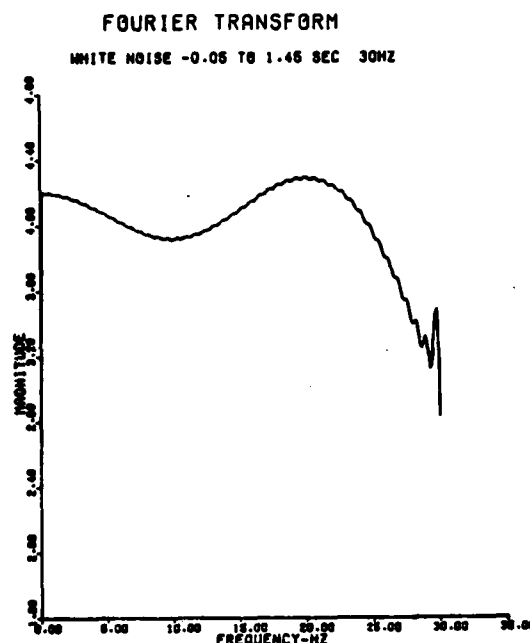


FIGURE 6 - FOURIER TRANSFORM OF BAND LIMITED WHITE NOISE TIME HISTORY

Theoretically, any time history could be used by the above procedure to determine the transfer functions, provided its Fourier transform has a finite magnitude at all values within the frequency range of interest. However, the use of the band limited white noise time history shown in Figure 5 was found to be most appropriate in minimizing numerical problems in using the FFT algorithm to calculate the transfer functions. The use of the white noise time history, described by  $1/w_t \sin w_t$ , also offered the following advantages:

1. The frequency range of interest is easily ensured adequate representation by specifying only one parameter  $w_0$ .
2. The duration of the white noise signal that should be considered in the analysis is relatively small compared to other time histories that would also be suitable for the same frequency range of interest. This meant significant savings in computer time.

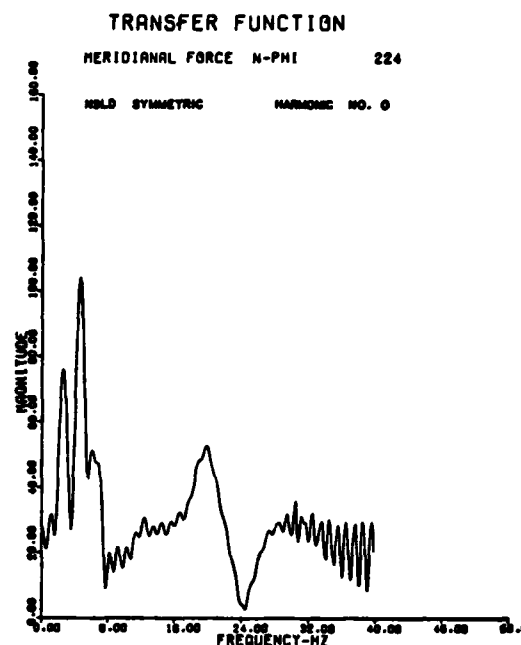


FIGURE 7 - TYPICAL TRANSFER FUNCTION FOR A RESPONSE COMPONENT OF INTEREST

The following precautions were found necessary:

1. The frequency  $w_0$  must clearly be larger than the maximum frequency for which the transfer functions are to be determined.
2. The integration time increment used in determining the response to the white noise signal must be sufficiently small to adequately represent the structural behavior up to the highest frequency desired in the transfer functions.
3. The total time duration for which a numerical solution to the white noise time history should be determined is such as to ensure decay of the response, not just the loading, to sufficiently small magnitudes. Decay to 5% of the peak amplitude was found to be adequate for the containment system investigated.
4. To avoid initial integration error, the peak value of the white noise signal should be shifted a few cycles away from the start of the integration process, as shown in Figure 5, with a small or zero initial function value.

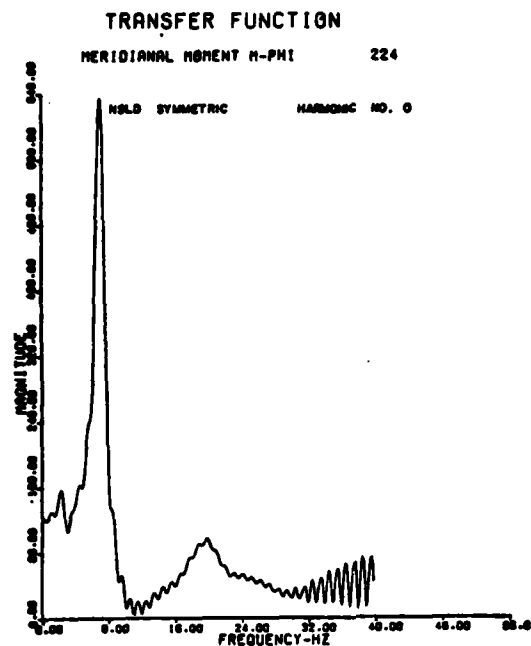


FIGURE 8 - TYPICAL TRANSFER FUNCTION FOR A RESPONSE COMPONENT OF INTEREST

With the above precautionary measures adopted, no problems were encountered in determining consistent and reliable transfer functions such as those shown in Figures 7 and 8. A typical response time history determined using the transfer functions is shown in Figure 9, for the load excitation time history shown in Figure 3. Checks on the responses were made by comparing them to those established by direct numerical integration method for the same load, showing excellent agreement.

#### 6. OTHER APPLICATIONS

The application of the frequency response method as described above is equally applicable to any linear system whose loading time variation is described by a single time history function. The transfer functions provide most convenient response descriptions for steady state loadings such as for loads due to eccentricity in rotating machinery. The transfer functions may of course also be used to determine the responses to arbitrary transient loads, as for the problem described here, as well as to establish critical load frequencies. Another interesting application of this method is the inverse problem of determining the load time history on a structure from measured response time histories.

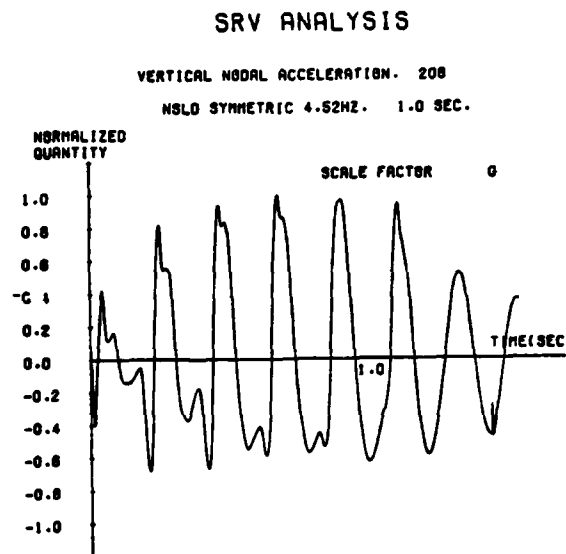


FIGURE 9 - TYPICAL TIME HISTORY OF RESPONSE COMPONENT DETERMINED USING CORRESPONDING TRANSFER FUNCTION

#### REFERENCES

1. Cooley, J. W. and Tukey, J. W., "An Algorithm for the Machine Calculation of Complex Fourier Series", *Mathematics of Computation*, Vol. 19, April, 1965.
2. Ghosh, S. and Wilson E., "Dynamic Stress Analysis of Axisymmetric Structures Under Arbitrary Loading", Report No. EERC 69-10, College of Engineering, University of California, Berkeley, September, 1969.
3. Clough, R. W. and Penzien, J., *Dynamics of Structures*, McGraw-Hill, 1975.
4. Meirovitch, L., *Analytical Methods in Vibrations*, MacMillan, 1967.

# COMPUTER AIDED DERIVATION OF THE GOVERNING DYNAMICAL EQUATIONS FOR A HIGH SPEED GROUND VEHICLE

J. Patten\* and N. Isada  
State University of New York

This paper presents a computer aided methodology for deriving the complete set of nonlinear ordinary differential equations governing the motion of a vehicle. The method, which was successfully employed to generate the governing equations for a five mass 14 degree of freedom system, greatly reduced the effort in deriving equations. The symbolic manipulating language FORMAC was used in conjunction with the IBM 360 computer to formulate and list for inspection the complete set of equations. In addition, the equations were made available to a standard integration technique for solution. Because of the manner in which the vehicle problem was posed, constraint equations did not arise. However, a simple extension of the method is described which will include the case in which geometric and kinematic constraints are present provided they are in the form of equalities.

## Introduction

During the past several years increasing interest has developed in the new forms of ground transportation including tracked vehicles capable of speeds well in excess of 150 mph. Transportation systems with such high speeds will be required to operate, a major portion of the time, on an elevated guideway. Predicting the motion of such systems is a difficult task. Analytical techniques used in the past [1, 2] have relied on simplifying assumptions about the completeness of the vehicle and guideway representation. The majority of the effort to date has concentrated on the two dimensional motions of the vehicle. However, the ride characteristics expected in any high speed vehicle will have to be based on its three dimensional motion. The reasons for this are economical as well as technical. The cost of land for the elevated structures in the congested North-East transportation corridors will not allow the long smooth transitions needed for comfortable high speed travel. The problem of analyzing the interactive suspension capable of producing a comfortable ride is therefore intimately related to developing a system simulation that faithfully predicts the complete vehicle motion.

Predicting the ride characteristics of such a system involves deriving the coupled three dimensional equations for the vehicle and the

structure over which it is traveling. Once these equations are available a thorough parametric analysis of the design can be accomplished using a computer. The system performance can then be evaluated as a prerequisite to developing the specifications for the individual vehicle components.

The analysis presented in this paper is a first attempt to remove simplifying assumptions by developing a methodology for deriving the complete set of second order nonlinear ordinary differential equations that represent the vehicle.

In recent years, the formulation of mathematical models has been facilitated by the use of the digital computer equipped with formula manipulation compilers (FORMAC), and by the development of computer programs designed to perform a variety of non-numerical operations. J. J. Walton [3] has shown how symbolic mathematical computations can be used to obtain the Christoffel symbols of the first and second kind for 12 orthogonal curvilinear coordinate systems. J. C. Howard [4,5] has shown how FORMAC can be used to derive the equations of motion of a particle and the Navier-Stokes equations in any curvilinear coordinates. With these efforts to lead the way, a similar procedure is developed here to derive the governing equations for a vehicle using the formula manipulation capabilities of the computer. Although this task relied on the

\* Present Address: Argonne National Laboratory

FORMAC language more recent work with MACSYMA [6] would also provide a useful language with which to carry out this type of system modeling.

The procedure utilized here assumed that the vehicle can be described by a system of connected rigid bodies. The topology of the system is specified by means of a path matrix describing how the rigid bodies are interconnected. Body-fixed coordinates are chosen for each body and a transformation matrix is defined that allows a vector fixed in the body to be transformed into inertial space. Using this information, an algorithm has been written that develops an expression for the systems kinetic energy. Since the system is considered to be moving in configuration space the coefficients of the quadratic terms in this expression are used as the components of the metric tensor for the space. All the inertial terms in the equations of motion can now be developed, by the algorithm, using tensor methods [7]. Potential functions, for any forces that can be derived from potentials, are differentiated and the resulting forces are included in the equations of motion. Finally, the generalized forces corresponding to all externally applied forces are generated. Generic names are given these forces so that they may be supplied by the solving algorithm at execution. The completed equations are arranged in the form  $[A] \{\ddot{X}\} = [B]$  and supplied to a numerical procedure for solution.

This algorithm has been used successfully in developing the governing equations for a 5 mass, 14 degree of freedom representation of a high speed ground vehicle [8]. However, the algorithm is general and could be used to generate the governing equations for any system of rigid bodies that has a tree-like topology; the limiting factor being the cost of computer time to carry out the computations.

This paper presents a detailed description of the methodology and algorithm that has been developed to generate governing dynamical equations.

#### Preliminary Considerations

As an introduction to configuration space, consider a space of three dimensions in which the position of a point mass,  $P$ , is determined by three coordinates,  $X$ ,  $Y$ , and  $Z$ . To each configuration assumed by this mechanical system there corresponds a point in space. When the mass moves, the coordinates describing its position change, and each set of coordinates represents a distinct point in space and a configuration of the mechanical system. Thus, the whole evolution of the mechanical system is known by calculating the trajectory of the representative point  $P$  in space  $X$ ,  $Y$ ,  $Z$ . This process of reducing a problem in analytical mechanics into one of calculating a trajectory in configuration space

rests mainly upon the concept of the metric tensor and the definition of differentiation in curved space. A brief description of these two concepts follows.

#### The Metric Tensor of a Space

Any point in space can be determined by its coordinates in an orthogonal Cartesian system of axes and we denote such a system by  $(y^1, y^2, y^3)$ . Now consider a functional transformation

$$x^r = x^r(y^1, y^2, y^3) \quad (1)$$

from the Cartesian system and examine what kind of coordinates we obtain. If the Jacobian of the transformation

$$\left| \frac{\partial x^r}{\partial y^s} \right| = \left| \frac{\partial(x^1, x^2, x^3)}{\partial(y^1, y^2, y^3)} \right|$$

is different from zero, then equation (1) can be inverted to give

$$y^r = y^r(x^1, x^2, x^3). \quad (2)$$

Hence, the variables  $x^r$  uniquely determine a point in space and are called the curvilinear coordinates of the point.

Consider  $P$  to be a point  $x^r$  and let  $Q$  be a neighboring point with coordinates  $x^r + dx^r$ . Denote the infinitesimal distance  $PQ$  by  $dS$ , the line-element of length, and express it in terms of differentials  $dx^r$ . Referring to the Cartesian system in which the coordinates of  $P$  are  $y^r$  and those of  $Q$  are  $y^r + dy^r$ , the element of length is

$$dS^2 = (dy^1)^2 + (dy^2)^2 + (dy^3)^2,$$

$$dS^2 = dy^i dy^i \quad \begin{array}{l} \text{Summation} \\ \text{Convention} \end{array} \quad (3)$$

$$= \delta_{ij} dy^i dy^j.$$

But

$$dy^i = \frac{\partial y^i}{\partial x^r} dx^r$$

so that

$$dS^2 = \frac{\partial y^i}{\partial x^m} \frac{\partial y^i}{\partial x^n} dx^m dx^n = g_{mn} dx^m dx^n. \quad (4)$$

The term  $g_{mn}$  is called the metric tensor (7) of the space and it is known to be symmetrical, a fact which will be useful later.

#### The Covariant Derivative

A covariant tensor,  $\bar{a}_{st}$ , by definition has the property that

$$\bar{a}_{st} = \frac{\partial x^n}{\partial \bar{x}^s} \frac{\partial x^p}{\partial \bar{x}^t} a_{np}. \quad (5)$$

In dealing with a generally curved space, a fact should be mentioned about equation (5) which would not arise in the more familiar case of Cartesian tensors. Coefficients  $\partial x^n / \partial \bar{x}^s$  in equation (5) are functions of  $x^r$  and therefore also of  $\bar{x}^s$ . Consequently, if  $a_{np}$  and  $\bar{a}_{st}$  are two sets of quantities satisfying equation (5) for one point in  $x^r$ , the equations will not generally be true at other points. In other words,  $a_{mn}$  is a tensor at point  $x^r$  and is not, in general, a tensor at any other point.

Anticipating the development a little, the problem is to derive an expression for the covariant derivative of a tensor, since this derivative is of fundamental importance in the expression of Newton's Law in curved space.

To define a derivative, the value of a function must be computed at two neighboring points an infinitesimal distance apart. For a curved space, in moving to the neighboring point, not only will the function of interest change its value due to a change in its arguments, i.e.,  $(x^i + x^i dx^i)$ , but it may change due to changes in the coordinate system being used to describe it. For example, consider the known motion in curvilinear space of a point  $x^i(t)$ . This moving point displaces with itself a contravariant vector  $u^i$ . The question, then, is what will be the true variation of the vector as a function of time. The customary way of finding an answer to this problem is to introduce the concept of a parallel vector field. Figure 1 represents the displacement of the vector  $u^i$  parallel to itself, to  $P'$ . At  $P'$  two vectors are now defined, the difference of which is called the absolute differential (or covariant differential). This, then, is a measure of how the vector changes while moving from  $P$  to  $P'$ . Carrying out this procedure leads naturally to the covariant derivative of a vector function. The results are a covariant derivative of a covariant vector.

$$\frac{Du_i}{Dx^k} = \frac{\partial u_i}{\partial x^k} - \Gamma_{ik}^j u_j \quad (6a)$$

and a covariant derivative of the contravariant vector

$$\frac{Du^i}{Dx^k} = \frac{\partial u^i}{\partial x^k} + \Gamma_{jk}^i u^j \quad (6b)$$

The preceding equations tell how to proceed in finding the rate of change of a vector as it moves in a general space. The term  $\Gamma_{jk}^i$  is the Christoffel symbol.

#### Dynamics and the Geometry of Dynamics

Consider a system of  $N$  mass points. These points move in ordinary three-dimensional

Euclidean space. The masses can be subject to external forces and their mutual interaction can obey arbitrary laws. The  $3N$  coordinates of these  $N$  points can form a hyperspace of  $3N$  dimensions which is called configuration space. As long as the different moving points remain free, our space necessarily has the  $3N$  dimensions and remains Euclidean. However, this system may be subject to constraints. Certain points are constrained to move on a given curve or surface. Others must remain a fixed distance from certain moving points.

What is the meaning of a condition of this kind from the geometric point of view? The system of  $N$  real points is represented by a single fictitious point  $P$  with coordinates  $X, Y, Z, \dots, X_n, Y_n, Z_n$  in a space of  $3N$  dimensions. The whole evolution of the system will be known when the trajectory can be calculated for the representative point in its space. The introduction of a holonomic constraint requires the point  $P$  to remain on a certain hypersurface. This point now moves in a reduced space which has only  $3N-1$  dimensions. The reduced space generally loses its Euclidean character and is curved. To study the motion of the representative point  $P$  in this curved space, use must be made of Riemannian Geometry [7].

A fundamental characteristic of a Riemann space is that it possesses a covariant metric tensor of the second order, which is symmetrical. Denoting this tensor by  $g_{rs}$ , the metric form can be written as

$$dS^2 = g_{rs} dx^r dx^s \quad (7)$$

Brillouin [7] has shown that given the expression for the kinetic energy for a system of bodies, the expression can be used to define the metric of the configuration space

$$dS^2 = M_{rs} dq^r dq^s$$

or

$$T = \frac{1}{2} \left( \frac{dS}{dt} \right)^2 = \frac{1}{2} M_{rs} \dot{q}^r \dot{q}^s \quad (8)$$

Thus, once the kinetic energy expression for the system has been developed in the form of equation (8), a metric can be defined for the configuration space. Again, Brillouin has shown that taking equation (8) as the definition of the kinetic energy and applying Lagrange's equations gives

$$\frac{d\dot{q}^i}{dt} - \frac{1}{2} \frac{\partial M_{jh}}{\partial q^i} \dot{q}^j \dot{q}^h + \frac{\partial V}{\partial q^i} + \frac{\partial \mathcal{D}}{\partial \dot{q}^i} = Q_i$$

where the notation  $T = \frac{1}{2} M_{jh} \dot{q}^h \dot{q}^j$  was used for convenience. This result is immediately simplified by using the definition of covariant derivative (equation (6a)). The details can be found in Ref. [7]. Thus,



$$M_{ij} \ddot{q}^j + \left( \frac{\partial M_{ij}}{\partial q^h} - \frac{1}{2} \frac{\partial M_{jh}}{\partial q^i} \right) \dot{q}^i \dot{q}^h + \frac{\partial V}{\partial q^i} + \frac{\partial D}{\partial \dot{q}^i} = Q_i \quad (9)$$

These are the equations of motion for a mechanical system in terms of the generalized coordinates being used to describe it and the elements of the metric tensor for the configuration space in which it moves.

Once the generalized coordinates have been selected and the kinetic energy has been derived in the form of equation (8), the first two terms of equation (9) can be used to derive the "inertial forces." The terms containing,  $V, D$  generate forces derivable from potential expressions and  $Q_i$  is the generalized force generated by all applied external forces.

The most useful feature of equation (9), as opposed to using Lagrange's equations directly, is that differentiation with respect to time has been completed. Differentiation with respect to the generalized coordinates is all that is required and is much simpler to carry out using FORMAC. In addition, the coefficients of the generalized accelerations and velocities appear in an orderly fashion which greatly facilitates the arrangement of the resulting equation in the form  $[A][\ddot{X}] = [B]$  needed by a solving algorithm.

#### The Inertial Terms

The first step in the derivation procedure is to develop the system's kinetic energy in the form of equation (8). Next, any forces which can be derived from a potential are computed. These potential functions are to be supplied by the user as input. Finally, the generalized forces,  $Q_i$ , corresponding to the externally applied forces are derived. The completed equations are then punched out in FORTRAN in the form  $[A][\ddot{X}] = [B]$ .

Consider a mechanical system consisting of  $R$  rigid bodies which are connected in any manner. The only restriction on the system is that topologically it must form a tree (from any body of the system to any other both there is a unique path - a unique system of other bodies). It is evident that the degree of the system depends not only on the number of bodies involved, but also on how the motion of each is restricted physically. Thus, a system of  $R$  rigid bodies with  $p$  equations of constraint have only  $6R-p$  independent degrees of freedom. Assuming that satisfactory generalized coordinates can be determined the transformation equation relating the position coordinates of the  $R$  bodies to their generalized coordinates are:

$$x_i = x_i(q^j). \quad (10)$$

The kinetic energy of any point mass moving in space is then

$$T = \frac{1}{2} m_i |\bar{v}_i|^2 \quad (11)$$

where  $\bar{v}_i$  is the inertial velocity. With the help of equation (10) the position vector to the mass point can be written as:

$$\bar{\rho}_i = \bar{\rho}_i(q^1, \dots, q^n).$$

The velocity becomes:

$$\bar{v}_i = \frac{d\bar{\rho}_i}{dt} = \sum_r \frac{\partial \bar{\rho}_i}{\partial q^r} \dot{q}^r.$$

The velocity squared is:

$$\bar{v}_i \cdot \bar{v}_i = \sum_{r=1}^n \sum_{s=1}^n \frac{\partial \bar{\rho}_i}{\partial q^r} \cdot \frac{\partial \bar{\rho}_i}{\partial q^s} \dot{q}^r \dot{q}^s.$$

The translational kinetic energy of a system of particles is:

$$T = \frac{1}{2} \sum_{i=1}^R m_i \bar{v}_i^2 = \frac{1}{2} \sum_{i=1}^R \sum_{r=1}^n \sum_{s=1}^n m_i \frac{\partial \bar{\rho}_i}{\partial q^r} \cdot \frac{\partial \bar{\rho}_i}{\partial q^s} \dot{q}^r \dot{q}^s$$

If the system happens to include rigid bodies, then the kinetic energy is stored in two modes, rotationally and translationally. The system's kinetic energy would now be expressed as:

$$T = \frac{1}{2} \sum_{i=1}^R \sum_{r=1}^n \sum_{s=1}^n \left[ m_i \frac{\partial \bar{\rho}_i}{\partial q^r} \cdot \frac{\partial \bar{\rho}_i}{\partial q^s} + (\bar{\omega}_q^r)_i \cdot I_i \cdot (\bar{\omega}_q^s)_i \right] \dot{q}^r \dot{q}^s \quad (12)$$

But this is precisely the form of equation (8) with

$$M_{rs} = \sum_{i=1}^R \left( m_i \frac{\partial \bar{\rho}_i}{\partial q^r} \cdot \frac{\partial \bar{\rho}_i}{\partial q^s} + (\bar{\omega}_q^r)_i \cdot I_i \cdot (\bar{\omega}_q^s)_i \right) \quad (13)$$

This, Eq. (13), is an expression for the components of metric tensor for the configuration space in which the mechanical system moves. Again, the  $\bar{\rho}_i$  is the position vector to the  $i^{\text{th}}$  body's center of mass, and  $(\bar{\omega}_q^r)_i$  is a vector component of the  $i^{\text{th}}$  body's angular velocity.

To construct  $\bar{\rho}_i$  for any body, the vector must follow along the tree-like structure from the origin to the body of interest. To accomplish this, an  $n \times m$  path matrix is provided. The  $i^{\text{th}}$  row of this matrix consists of the sequence of body numbers to be followed in constructing the vector to the  $i^{\text{th}}$  body's center of mass. There are as many columns as the maximum number of bodies in any tree.

Consider two adjacent bodies in the system. Figure 2 shows that the vector from the inertial coordinate system to the  $i^{\text{th}}$  body's center of mass has already been formed and the increment which takes us to the  $i+1$  body center of mass (CM) is about to be added. The information

needed to do this is the position of the  $(i + 1)$  CM in the body-fixed coordinates of  $i^{\text{th}}$  body. Thus, the position vector in matrix form is

$$[\rho_{i+1}]_{CM} = [\rho_i]_{CM} + [T]_i [LCG]_{i+1}$$

where  $[T]_i$  is the transformation matrix which transforms the components of the vector given in the  $i^{\text{th}}$  body fixed coordinates into the inertial space. Thus, once the sequence of bodies to be followed is given for a particular body, its position vector can be constructed as: (note the shift in index to account for  $i = 1$ ).

$$[\rho_i] = [LCG]_1 + \sum_{j=2}^{NBD \text{ IN PATH}} [T]_{j-1} [LCG]_j$$

and its partial derivative:

$$\frac{\partial \bar{\rho}_i}{\partial q^\lambda} = \frac{\partial [LCG]_1}{\partial q^\lambda} + \sum_{j=2}^{NBD} \frac{\partial [T]_{j-1}}{\partial q^\lambda} \cdot [LCG]_j + [T]_{j-1} \frac{\partial [LCG]_j}{\partial q^\lambda} \quad (14)$$

It should be restated at this point that the reason for generating the displacement vector is to develop the coefficients of the metric tensor equation (13). These factors are then used in equation (9) to compute the inertial terms in the equations of motion. As the developments of the algorithm progressed, it became convenient to compute not the  $\bar{\rho}_i$ , but rather  $\partial \bar{\rho}_i / \partial q^\lambda$ ,  $\partial^2 \bar{\rho}_i / (\partial q^\lambda)^2$ , since these are the terms required to construct  $M_{rs}$ ,  $\partial M_{rs} / \partial q^\lambda$ . The partial derivatives of the metric tensor are then:

$$\frac{\partial M_{rs}}{\partial q^\lambda} = \sum_{i=1}^{NBD} m_i \left[ \frac{\partial \bar{\rho}_i}{\partial q^r} \cdot \frac{\partial^2 \bar{\rho}_i}{\partial q^s \partial q^\lambda} + \frac{\partial^2 \bar{\rho}_i}{\partial q^r \partial q^\lambda} \cdot \frac{\partial \bar{\rho}_i}{\partial q^s} \right] + \frac{\partial (\bar{\omega}_q)_i}{\partial q^\lambda} \cdot I_i \cdot (\bar{\omega}_q)_i + (\bar{\omega}_q)_i \cdot I_i \cdot \frac{\partial (\bar{\omega}_q)_i}{\partial q^\lambda} \quad (15)$$

The flow diagram, Fig. 3., illustrates the logic for computing the entire set of equations. The logic for the inertial terms is shown in Fig. 4. Prior to the starting point of this diagram, the local position vectors, transformation matrices, and angular velocity vectors have been differentiated with respect to all the generalized coordinates. If a particular derivative evaluates to -1, 0, 1, this value is used directly, otherwise the expression is atomized and the generic name of the derivative is used in the succeeding calculations. This process increases the comprehensiveness of the final equations.

Consider, now, the situation where the inertial terms for the  $q^\lambda$  degree of freedom are being generated. For each body in the system, the previously generated partial derivatives are combined to give the partial derivative of the

position vector (equation (14)). These terms are now combined as prescribed by equation (15) to generate the partial derivatives of the elements of the metric tensor, and these, in turn, are combined according to equation (9) to give the inertial terms.

#### Potential and Generalized Force Computations

The expression, equation (9), has two terms which are the derivatives of potentials  $\bar{V}$  and  $\bar{D}$ . These functions are supplied as input data if any forces can be developed in this manner. Their derivatives are taken with respect to all of the generalized coordinates and are included as terms in the  $[B]$  matrix.

The generalized force  $Q_\lambda$  is calculated from the following formula,

$$\sum_i^{NFOR} \bar{F}_i \cdot \frac{\partial \bar{\rho}_i}{\partial q^\lambda} = Q_\lambda$$

where  $\bar{F}_i$  is an externally applied force which acts on the  $i^{\text{th}}$  body. In this program, these forces are never defined. At execution, a solving algorithm will have to be provided which will generate these forces as a function of the generalized coordinates. The  $\bar{\rho}_i$  is the vector, in inertial space, to the point of application of the force  $\bar{F}_i$ . Finally, the generalized force  $Q_\lambda$  is the sum over all of the external forces of the inner product of the applied force and the partial derivative of this position vector.

As with the kinetic energy expressions, the key computation is the development of the vector from the origin to the point of application of the force. To facilitate this computation, the path matrix is again used which specifies the sequence of bodies between the origin and the position of the force. Using this sequence of body numbers,  $N1, N2, \dots, N_i$ , the program logic could develop the expression:

$$[\rho_i] = [\rho_1] + \sum_{j=2}^{NFOR} [T]_{j-1} \cdot [LCG]_j + [T]_j \cdot [LFOR]_j$$

However, the term which is needed is the partial derivative,  $\partial \bar{\rho}_i / \partial q^\lambda$ , and, as with the inertial terms, it is constructed using the existing partial derivatives. Thus,

$$\frac{\partial \bar{\rho}_i}{\partial q^\lambda} = \frac{\partial [LCG]_1}{\partial q^\lambda} + \sum_{j=2}^{NFOR} \left\{ \frac{\partial [T]_{j-1}}{\partial q^\lambda} \cdot [LCG]_j + [T]_{j-1} \cdot \frac{\partial [LCG]_j}{\partial q^\lambda} + \frac{\partial [T]_j}{\partial q^\lambda} \cdot [LFOR]_j + [T]_j \cdot \frac{\partial [LFOR]_j}{\partial q^\lambda} \right\} \quad (16)$$

Finally, the inner product term is computed for each of the active forces to give  $Q_\lambda$  of equation (9). The flow diagram of the logic used to compute the generalized forces is given in Fig. 5.

#### Specialization of the General System to Represent the TACV

The previous sections discussed the general approach which was followed in generating the governing equations for a system of rigid bodies. To simulate a TACV, a specialized system is assumed consisting of one rigid body, the sprung mass, and four point masses. The FORMAC algorithm, was used to generate the governing equations, and the result is presented in Ref. [8].

Figure 6 is a schematic drawing of the vehicle model illustrating the coordinates. Four coordinate systems are defined in this figure. The inertial coordinate system, XYZ, which is fixed in space, initially  $X'Y'Z'$ , has its origin at the sprung mass C.G. with its axes along the sprung mass principal axes of inertia. The inertial coordinate system is also used as the terrain coordinate system in which terrain elevation and displacement are defined.

The beam coordinate system,  $X_b Y_b Z_b$ , is aligned with the inertial system, but has its origin displaced a distance  $a_2$  in the positive X-direction. The vehicle is assumed, at time zero, to be traveling at constant velocity in the positive X-direction with the front wheels just entering the beam.

Figure 6 also illustrates the generalized coordinates used to describe the vehicle motion.  $X, Y, Z$  are the coordinates of the sprung mass C.G. in the inertial system.  $D_{ij}$  ( $i = 2, 3, 4, 5$ ;  $j = 2, 3$ ) are the displacements of the point masses relative to the sprung mass coordinate system. Their zero position is taken as the point where the secondary suspension produces zero force. In general, the vehicle is composed of five masses (one rigid body, and four point masses) with 14 degrees of freedom. The point masses are capable of moving in the  $y'$ - and  $z'$ -directions (in the sprung mass coordinate system), but not in the  $x'$ -direction. The entire vehicle, however, is capable of three-dimensional motion.

The orientation of the rigid body is described by the three Euler angles,  $\psi$ ,  $\theta$ ,  $\phi$ , (see Fig. 7). Table I gives the definition of these angles. This transformation matrix is used extensively in the derivation for transforming vectors given in the sprung mass coordinate system into vectors in the inertial system. The definitions presented here are consistent with aircraft stability notation, and can be found to Etkin [9].

The interconnection of sprung and unsprung mass is accomplished by means of both linear springs and dampers and non-linear springs and linear dampers. The latter case is presented in Ref. 8. A more complex suspension, suggested by Chiu [10] and others [11], has not been included at this time. Once experimental data for validation are available, a logical extension of the simulation would be to incorporate a more advanced suspension model.

#### The Structure

The generalized forces  $Q_\lambda$  which acts on the vehicle have as components the externally applied forces  $FORX2, \dots$ . These forces are the contact forces acting at the interface between the vehicle and the structure over which it passes. To compute these forces, it is necessary to compute the position in inertial space of each of the contact centers, and, in addition, the dynamic response at this particular point, all at the same time. The vector sum of these two quantities then can be used to compute a first-order approximation to the contact forces. In any case, it is necessary to be able to compute the dynamic response of the elevated structure.

The solution presented in Ref. 8 computes the dynamic response of the beam for an arbitrary distribution of pressure which is moving at constant velocity. It has been specialized for the case of two distinct pressure patches of constant magnitude, separation, and length. This case is representative of the type of loading which a TACV would produce on its guideway. The derivation presented in Ref. 8 follows closely the work of Wilson [12] as presented in the Shock and Vibration Bulletin.

#### Conclusion

An algorithm has been written, using the FORMAC language, to derive the governing equations for a five mass representation of a high speed ground vehicle. This paper presents the mathematical formalisms used to reduce the Lagrangian method to a workable computer program as well as the details of the computational procedure.

One further point should be made regarding the generality of this method. In the vehicle problem discussed in detail here, the generalized coordinates are chosen as the three components of the position vector to the sprung mass C.G. and the corresponding Euler angles. As a result, the sprung mass will have the full complement of six coordinates specifying its position. In addition, all guiding forces acting on the vehicle are considered external forces and therefore are adequately accounted for in the procedure used to generate the generalized forces. Therefore, because of the choice of coordinates and the method used for accounting for the forces acting on the system, constraint

equations do not appear in this problem. However, this situation in general need not be the case. When constraint equations do appear they can be handled using the method of Lagrange multipliers.

Consider the case of a kinematic constraint of the form:

$$\sum a_{lk} dq_k = 0$$

Such a constraint can be accounted for by the inclusion of the term

$$\sum \lambda_l a_{lk}$$

in the [B] matrix and the addition of the differential equations

$$\sum a_{lk} \dot{q}_k = 0$$

to the equations that have already been developed by the FORMAC algorithm. Geometric constraints can also be handled in the same fashion since the equations of the form  $f(q_1 \dots q_n) = 0$  are equivalent to the differential equations

$$\sum \frac{\partial f}{\partial q_k} \dot{q}_k = 0$$

The resulting differential equations as well as the solution procedure used to solve them have been left to the much more detailed analysis of Ref. 8.

#### NOMENCLATURE

X, Y, Z	Inertial coordinate system. Coordinates of the sprung mass C.G. in the inertial frame
X', Y', Z'	Moving coordinate system fixed in the sprung mass. The coordinate axes coincide with the principal axes of the sprung mass so that products of inertia are zero.
$a_i, b_i, c_i$	Coordinates of a point in the sprung mass coordinate system. This point is taken as the spring wheel attachment point when the spring is at its natural length.
$\delta_{i2}, \delta_{i3}$	$i^{th}$ "wheel" deflection coordinate, $\delta_{i2}$ is in the Y' direction, $\delta_{i3}$ is in the Z' direction, relative to the sprung mass coordinate system.
$\bar{\rho}_i$	Displacement vector in the inertial frame of the $i^{th}$ wheel center = $[\rho]_i$ .
$a_{ij}$	Components of the transformation matrix [T].

$\phi, \theta, \psi$	Euler angles which describe the orientation of the sprung mass in inertial space
$I_{x'}, I_{y'}, I_{z'}$	Principal moments of inertia of the sprung mass. Products of inertia are zero since X'-Y'-Z' is a set of principal coordinates.
$M_s$	Mass of the sprung mass.
i	"Wheel" index
$K_{i2}, K_{i3}$	Spring rate: $i^{th}$ "wheel"
$CK_{i2}, CK_{i3}$	Rail-spring rate
$C_{i2}, C_{i3}$	Damping rate: $i^{th}$ "wheel"
i	2-left front      4-right rear 3-right front    5-left rear
$g_{rs}, m_{rs}$	Components of a metric tensor
$q^\lambda$	Generalized coordinate
$m_i$	Mass of body i
$[I]_i$	Inertia matrix of body i
$[T]_i$	Transformation matrix for transforming coordinates in the $i^{th}$ body fixed coordinate system to inertial space
$[LCG]_{i+1}$	Position vector in $i^{th}$ body fixed coordinate system to the center of mass of body (i + 1)
$[LFOR]_i$	Position vector in $i^{th}$ body fixed coordinate system to the point of application of the resultant external force acting on the body i
$Q_\lambda$	Generalized force corresponding to the $\lambda^{th}$ degree of freedom
$[\rho_i]_{CM}$	Position vector, in inertial space, to the center of mass body i (same as $\bar{\rho}_i$ except given in component form)
$[\omega]_i$	Angular velocity of rigid body i, equal to $[(\dot{\phi} - \dot{\psi} \sin \theta), (\dot{\theta} \cos \phi + \dot{\psi} \cos \theta \sin \phi),$ $(\dot{\psi} \cos \theta \cos \phi - \dot{\theta} \sin \phi)]$ expressed as $(\bar{\omega}_g^r)_i \dot{q}^r + (\bar{\omega}_g^s)_i \dot{q}^s + (\bar{\omega}_g^e)_i \dot{q}^e.$

In particular:

$$\bar{\omega}_\theta = \begin{bmatrix} 0 \\ \cos \phi \\ -\sin \phi \end{bmatrix}; \quad \bar{\omega}_\phi = \begin{bmatrix} 1 \\ 0 \\ 0 \end{bmatrix};$$

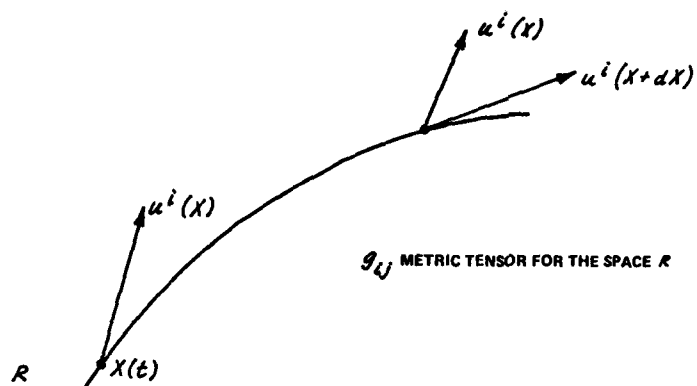
$$\bar{\omega}_\psi = \begin{bmatrix} -\sin \theta \\ \cos \theta \sin \phi \\ \cos \theta \cos \phi \end{bmatrix}$$

See Fig. 9 for coordinate system.

- $\mathbb{T}$  Kinetic energy  
 $\mathbb{V}$  Potential function  
 $\mathbb{D}$  Dissipation function

#### References

1. H. H. Richardson and D. W. Wormley, "Transportation Vehicle/Beam-Elevated Guideway Dynamic Interactions: A State-Of-The-Art Review," ASME Paper No. 74-AUT-P, March 11, 1974.
2. C. C. Smith, A. J. Gilchrist and D. W. Wormley, "Multiple and Continuous Span Elevated Guideway-Vehicle Dynamic Performance," ASME Paper No. 74-WA/AUT-4, February 1974.
3. J. J. Walton, "Tensor Calculations on the Computer," Communications of ACM, Vol. 9, No. 12, 12-66, p. 864.
4. J. C. Howard, "Computer Formulation of the Equations of Motion Using Tensor Notation," Communications of ACM, Vol. 10, No. 9, 9-67, pp. 543-548.
5. J. C. Howard, "An Algorithm for Deriving the Equations of Mathematical Physics by Symbolic Manipulation," Communications of ACM, Vol. 11, No. 12, 12-68, pp. 814-818.
6. J. Moses, "MACSYMA-The Fifth Year," Progress Report, Project MAC Massachusetts Institute of Technology, Cambridge, Mass., 1975.
7. L. Brillouin, Tensors in Mechanics and Elasticity, Academic Press, New York, NY, 1964.
8. J. S. Patten, "A Three-Dimensional Simulation of a High Speed Ground Vehicle Including the Structure Over Which it Travels," Department of Mechanical Engineering, State University of New York at Buffalo, Buffalo, New York, May 1973.
9. B. Etkin, Dynamics of Flight, John Wiley and Sons, Inc., New York, New York, 1957.
10. W. S. Chiu, et al., "Coupled Dynamic Interactions Between High-Speed Ground Transport Vehicles and Discretely Supported Guide-ways," Department of Mechanical Engineering, Massachusetts Institute of Technology, July 1970, Report No. R-76115-1.
11. "The Tracked Air Cushion Research Vehicle (TACRV) System Summary Report," DOT, FRA-RT-72-41, May 1972.
12. J. F. Wilson and S. B. Biggers, "Dynamic Response of Beams to Moving Pressure Loads as Related to Tracked Air Cushion Vehicles," The Shock and Vibration Bulletin, Bulletin 40, Part 4, Dec. 1969, p. 47.



COVARIANT DERIVATIVE OF A CONTRAVARIANT VECTOR

$$\frac{Du^i}{dX^k} = \frac{\partial u^i}{\partial X^k} + \Gamma_{jk}^i u^j$$

$\Gamma_{jk}^i$  CHRISTOFFEL SYMBOL

$$\Gamma_{jk}^i = \frac{1}{2} g^{ir} \left[ \frac{\partial g_{jr}}{\partial X^k} + \frac{\partial g_{kr}}{\partial X^j} - \frac{\partial g_{jk}}{\partial X^r} \right]$$

Figure 1 DERIVATION OF COVARIANT DERIVATIVE

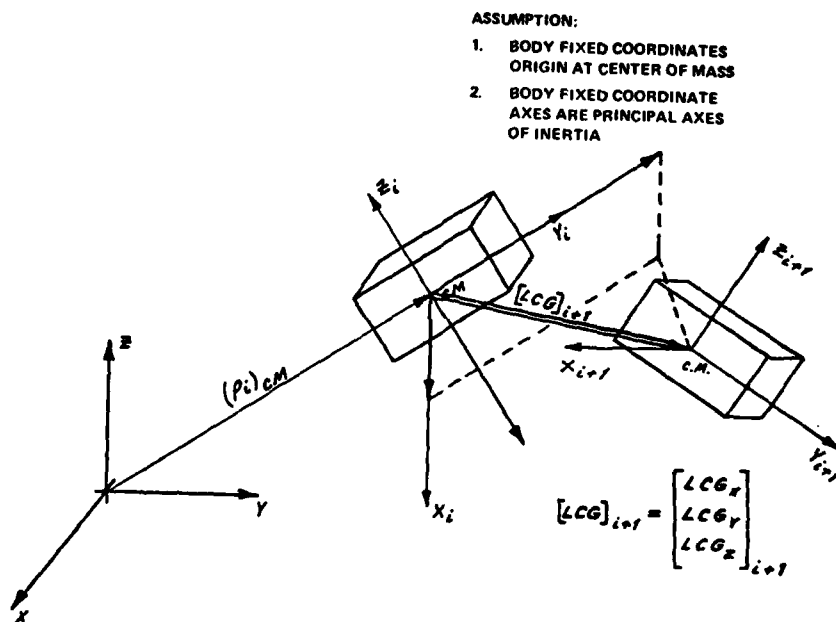


Figure 2 POSITION VECTOR - TWO ADJACENT BODIES

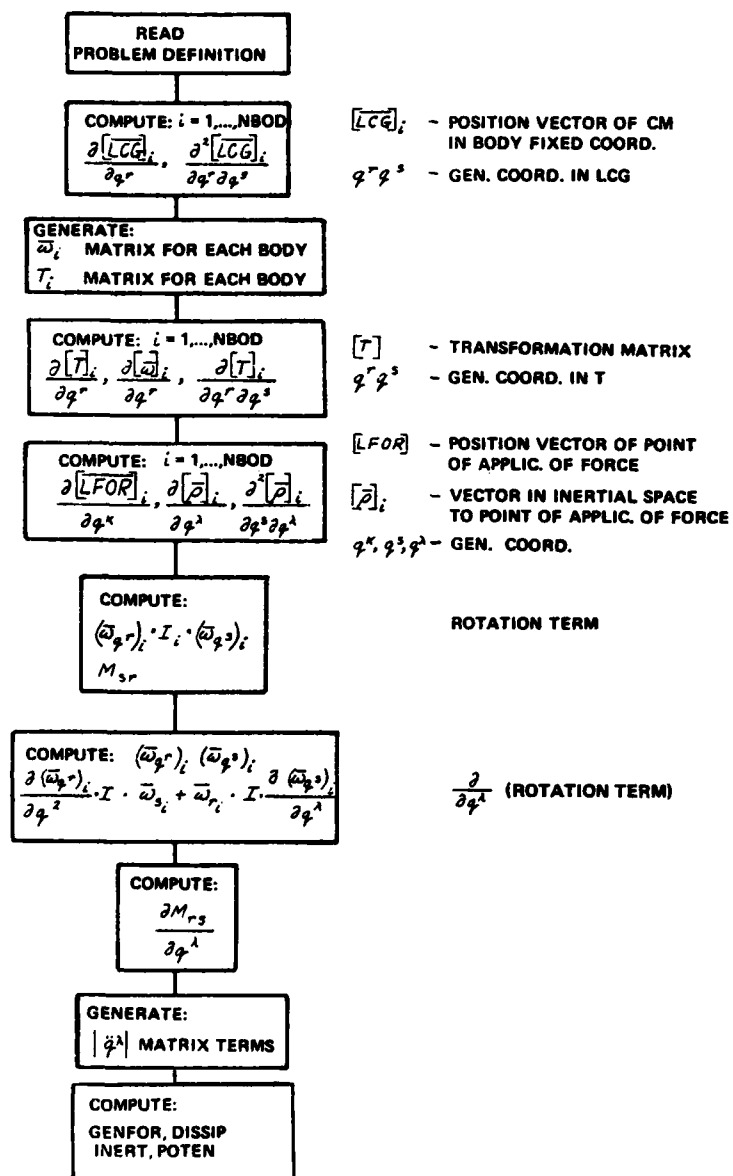


Figure 3 EQUATIONS OF MOTION PROCEDURE

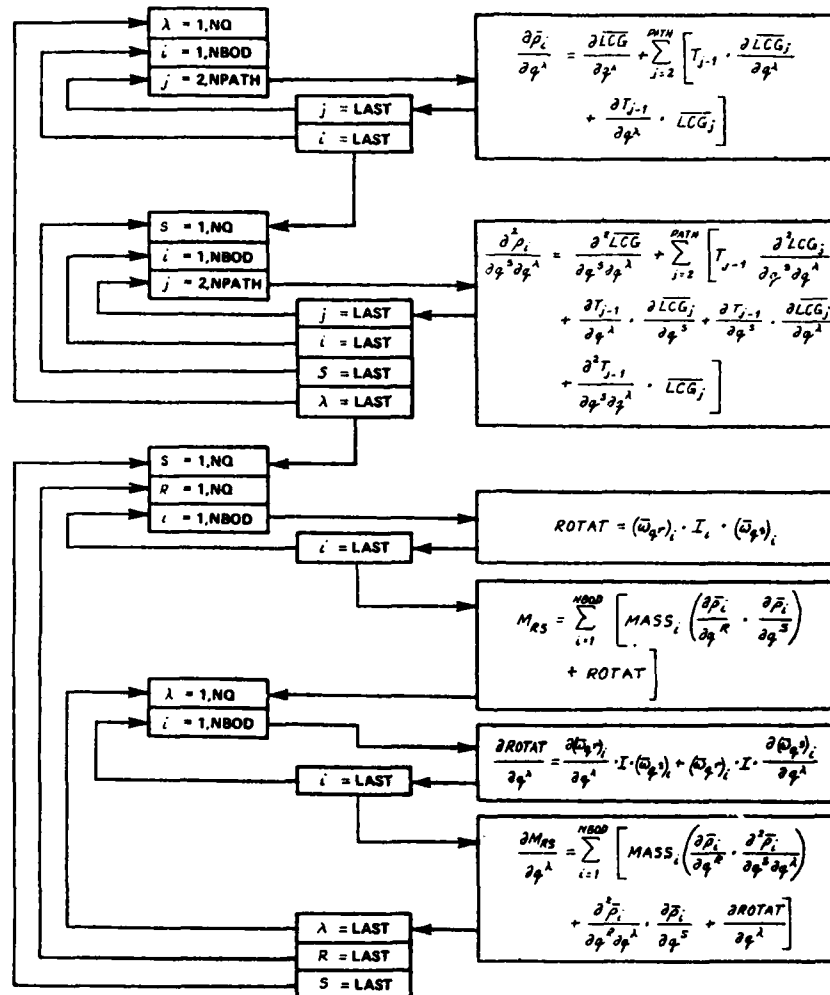


Figure 4 INERTIAL TERM





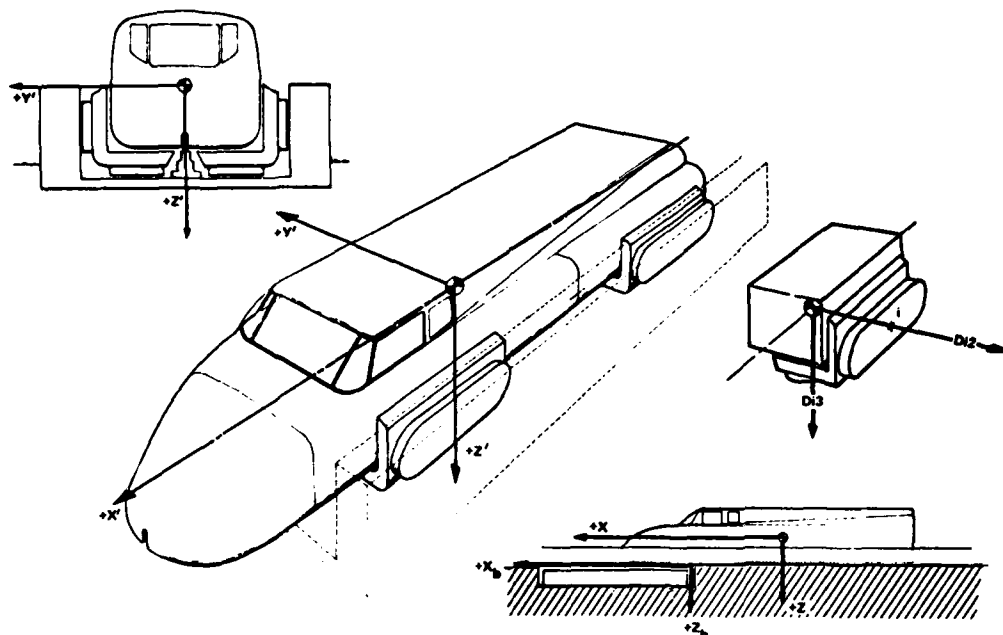


Figure 6 COORDINATES SYSTEMS

NOTE: ROTATIONS BEGIN AROUND  
 $z$ , NOT THE USUAL  $x$ .

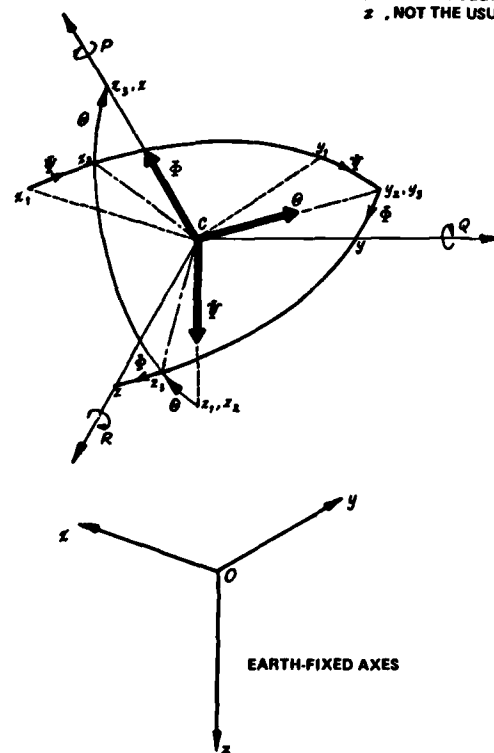


Figure 7 EULER ANGLES VEHICLE SIMULATION

Table I

**TRANSFORMATION MATRIX**  
(Reference 7)

$$T = \begin{bmatrix} \cos \theta \cos \psi & -\cos \phi \sin \psi + \sin \phi \sin \theta \cos \psi & \sin \phi \sin \psi + \cos \phi \sin \theta \cos \psi \\ \cos \theta \sin \psi & \cos \phi \cos \psi + \sin \phi \sin \theta \sin \psi & -\cos \psi \sin \phi + \cos \phi \sin \theta \sin \psi \\ -\sin \theta & \cos \theta \sin \phi & \cos \theta \cos \phi \end{bmatrix}$$

**NOTE:**

THE POSITION OF THE VEHICLE IN THE SPACE COORDINATE SYSTEM IS DEFINED BY THE COORDINATES OF THE SPRUNG MASS C.G. ( $x_{cg}$ ,  $y_{cg}$ ,  $z_{cg}$ ), AND THE ORIENTATION OF THE VEHICLE IN THE SPACE FIXED COORDINATE SYSTEM IS DEFINED BY THE EULER ANGLES ( $\psi$ ,  $\theta$ ,  $\phi$ ) ABOUT THE Z, Y, X AXES OF THE VEHICLE COORDINATE SYSTEM TAKEN IN THE ORDER  $\psi$ ,  $\theta$ ,  $\phi$ .

THE TRANSFORMATION MATRIX FOR TRANSFORMING COORDINATES IN THE VEHICLE COORDINATE SYSTEM INTO COORDINATES IN THE SPACE FIXED COORDINATE SYSTEM IS GIVEN ABOVE.

